FORMULATION DEVELOPMENT, CHARACTERIZATION AND EVALUATION OF ANTI-HIV POTENTIAL OF DENDRIMER-CARBON NANOTUBES CONJUGATES (DENDRITUBES)

Thesis Submitted for the Award of the Degree of

DOCTOR OF PHILOSOPHY

in

Pharmaceutics

By

Neha Srivastava

Registration Number: 41700192

Supervised By

Dr. Vijay Mishra (20352)

Department of Pharmaceutical Sciences (Professor)

Lovely Professional University

LOVELY PROFESSIONAL UNIVERSITY, PUNJAB

2024

DECLARATION

I, hereby declared that the presented work in the thesis entitled "Formulation development, characterization and evaluation of anti-HIV potential of dendrimer-carbon nanotubes conjugates (dendritubes)" in fulfilment of degree of Doctor of Philosophy (Ph. D.) is outcome of research work carried out by me under the supervision Dr. Vijay Mishra, working as Professor, in the School of Pharmaceutical Sciences of Lovely Professional University, Punjab, India. In keeping with general practice of reporting scientific observations, due acknowledgements have been made whenever work described here has been based on findings of other investigator. This work has not been submitted in part or full to any other University or Institute for the award of any degree.

(Signature of Scholar)

Neha Srivastava

41700192

School of Pharmaceutical Sciences

Lovely Professional University,

Jalandhar- Delhi GT road,

Phagwara-144411

Punjab, India

CERTIFICATE

This is to certify that the work reported in the Ph. D. thesis entitled "Formulation development, characterization and evaluation of anti-HIV potential of dendrimer-carbon nanotubes conjugates (dendritubes)" submitted in fulfillment of the requirement for the reward of degree of Doctor of Philosophy (Ph.D.) in the School of Pharmaceutical Sciences, is a research work carried out by Neha Srivastava, 41700192, is bonafide record of his/her original work carried out under my supervision and that no part of thesis has been submitted for any other degree, diploma or equivalent course.

(20352)

(Signature of Supervisor)

Dr.Vijay Mishra

Professor

School of Pharmaceutical Sciences

Lovely Professional University,

Jalandhar- Delhi GT road,

Phagwara-144411

Punjab, India

Abstract

Human immunodeficiency virus (HIV) is responsible for acquired immunodeficiency syndrome (AIDS) is an international concern affecting social and the economic conditions of the affected countries. The disease can be treated with anti-HIV therapy with severe adverse effects with no definite cure. The virus tends to relapse as it accumulates in intracellular cavities. Conventional therapy is incapable of delivering the drugs to the intracellular reservoirs and incapable of managing drug resistance. Hence novel cargo system is required which can bypass the downsides of conventional therapy.

A novel cargo system was designed to deliver the anti-HIV drug Nevirapine (NVP) and Fosamprenavir calcium (FPV) using dendritubes (DT) as a delivery system (NVP-FPV-DT). The drugs were conjugated with covalent bonding on the surface of DT. The designed structure was decorated with mannose for target efficiency (M-NVP-FPV-DT). The developed NVP-FPV-DT and M-NVP-FPV-DT were subjected to different spectroscopic analysis such as "Fourier transform infrared (FTIR)," Raman, "^{1}H Nuclear magnetic resonance (NMR) spectroscopy" and other techniques. The spectroscopic analysis revealed the conjugation of NVP and FPV with DT. Along with drug conjugation, it confirmed the attachment of mannose on the drug-loaded DT. XRD and DSC studies also support the conjugation of drugs NVP and FPV on the surface of DT. Entrapment efficiency of NVP-FPV-DT was found to be 69.65% for NVP and 47.59% for FPV. *In vitro* release studies of NVP-FPV-DT indicated 80.045±1.664% in acetate buffer pH 5 and 73.745±1.524 in PBS pH 7.4 of NVP and 75.787±1.657% in acetate buffer pH 5 and 67.192±1.924% in PBS pH 7.4 of FPV in 96 h. The profile of release of the drug was subjected to various kinetic models and the drug release profile of NVP-FPV-DT was found to follow the Higuchi release pattern.

The cell viability studies indicated that DT shows high cytotoxicity which was found to be reduced with mannosylation. NVP-FPV-DT showed cell viability of 43.1194 ± 2.10% at 100 µg/mL concentration which was later improved upon mannosylation. The cell internalization studies indicated that mannosylation improves and enhances the uptake of the designed delivery system. Biodistribution of prepared formulations showed

that the higher concentration of drug in the liver was due to accumulation, followed by the kidney, spleen, and heart. The hemolysis studies showed that the mannosylation reduces the RBC lysis. No histological evidence was observed with the liver, kidney, heart, and spleen.

The study revealed that a novel cargo system can be designed and developed for efficient delivery of anti-retroviral drugs Nevirapine and Fosamprenavir calcium to the target sites.

ACKNOWLEDGEMENT

Table of Content

List of Tables

List of Figures

Abbreviations

Abbreviations	Full form.
HIV	Human immunodeficiency virus
AIDS	Acquired immunodeficiency virus
SIV	Simian immunodeficiency virus
CD4	Clusters of differentiation
COVID-19	Corona Virus Disease of 2019
HAART	Highly active antiretroviral therapy
ARVs	Anti-retroviral drugs
CNS	Central nervous system
NDDS	Novel drug delivery systems
SNEDDS	Self nano-emulsifying drug delivery system
CNTs	Carbon nanotubes
SWCNT	Single-walled carbon nanotubes
MWCNT	Multi-walled carbon nanotubes
COOH-MWCNT	Carboxylated MWCNT
PPI	Poly(propylene imine)
DT	Dendritubes
CCR5	C-C chemokine receptor type 5
CXCR4	C-X-C motif chemokine receptor 4
RT	Reverse transcriptase
DNA	Deoxyribonucleic acid
RNA	Ribonucleic acid
gp120,41	Envelope glycoprotein120,41
HLA	Human leukocyte antigen
ICAM-1	Intercellular adhesion molecule 1
TAT	Tyrosine Aminotransferase
Rev	Regulator of expression of virion proteins
Vrp	Virus-like replicon particles
Vpu	Viral protein U
Vif	Virion infectivity factor
Nef	Negative regulatory factor
TCR	T-cell receptor
TNF	Tumor necrosis factor
RANTES	Regulated upon activation, normal T cell expressed and secreted
MIP	Macrophage inflammatory protein
GI	Gastrointestinal
ART	Antiretroviral therapy
WHO	World health organization
TDF	Tenofovir disoproxil fumarate
FTC	Emtricitabine
3TC	Lamivudine

EFV	Efavirenz
AZT	Zidovudine
NVP	Nevirapine
d4T	Stavudine
DRV	Darunavir
RAL	Raltegravir
ETV	Etravirine
CAP-EFV-NPs	Cellulose acetate phthalate-efavirenz
NP	Nanoparticles
SLN	Solid lipid nanoparticles
SEDDS	Self-emulsifying drug delivery systems
G	Generation
PAMAM	Poly(amidoamine)
PPI	Poly(propylene imine)
PEI	Polyethylenimine
PPI-HEX-10% PEI	Hexanoate conjugated PPI–PEI
kDa	Kilodalton
CuAAC	Copper-assisted azide-alkyne cycloaddition
TYC	Thiol-yne click reactions
TEC	Thiol-ene click reaction
PAMAMOS	Poly(amidoamine–organosilicon)
OS	Organosilicon
IV	Intravenous
Kyn-13	Kynurenine
SMPPI	Sialic acid-mannosylated PPI
SPPI	Salisylic acid PPI
MPPI	Mannosylated PPI
UV	Ultra-violet
TEM	Transmission electron microscopy
DSC	Differential scanning calorimetry
SEM	Scanning electron microscopy
MS	Mass spectroscopy
PEG	Polyethylene glycol
DAB	Diamino butane
DWCNT	Double-walled carbon nanotubes
TWCNT	Triple-walled carbon nanotubes
PECVD	Plasma-enhanced chemical vapor deposition
IC_{50}	Inhibitory concentration 50
CS	Chitosan
TGA	Thermogravimetric analysis
HNO_3	Nitric acid
H_2SO_4	Sulphuric acid
CNT–COOH	carboxylated carbon nanotubes
AZT	Azidothymidine
FI	Fluorescein isothiocyanate

FA	Folic acid
siRNA	small interfering RNA
XPS	X-ray photoelectron spectroscopy
CuAAC	Copper alkyne-azidecyclo addition
GL	Glycyrrhizin
DOX	Doxorubicin
MTT	3-(4, 5-Dimethylthiazol-2-y1)-2, 5-diphenyl tetrazoliumbromide
CNHs	Carbon nanohorns
MAPK	Mitogen-activated protein kinase
CP	Conducting polymer
FAR	Folic acid receptors
MR	Mannose receptors
CRDs	Carbohydrate recognization domain
MMR	Macrophage mannose receptors
DC	Dendritic cells
APCs	Antigen presenting cells
MHC	Major histocompatibility complex
AmB	Amphotericin B dendrimeric delivery
AFM	Atomic force microscopy
MPPI	Mannose-conjugated 5G PPI
GmcH	Gemcitabine Hydrochloride
AS	Artesunate
SRB	Sulphate Reducing Bacteria (SRB) Test
N-FB	Nuclear factor-B
IR	Infrared
^{1}H	Proton
^{13}C	Carbon
^{15}N	Nitrogen
^{19}F	Florine
^{31}P	Phosphorous
DSC	Differential scanning calorimetry
AUC	Area under curve
BCS	Biopharmaceutical classification
Cmax	Maximum concentration
CYP	Cytochrome P450
HeLa	Henrietta Lacks
XTT	methoxynitrosulfophenyl-tetrazolium carboxanilide
HPCO	High pressure cut out
NVP	Nevirapine
FPV	Fosamprenavir calcium
AVP	Amprenavir
PBS	Phosphate buffer
SS	Stock solution

DMSO	Dimethylsulfoxide
ACN	Acetonitrile
HPLC	High performance liquid chromatography
HQC	Higher quantified concentration
MQC	Medium quantified concentration
LQC	Lower quantified concentration
MWCO	Molecular weight cut off
DMEM medium	Dulbecco's Modified Eagle medium
FICT	Fluorescein isothiocyanate
RH	Relative humidity
NPD	Normal pellet diet
EDTA	Ethylene diamine tetra acetic acid
ICH	International Council for Harmonisation
RSD	Relative standard deviation
SD	Standard deviation
RBC	Red blood cells
WBC	white blood cells
EDTA	Ethylene diamine tetra acetic acid
NMR	Nuclear magnetic resonance
PDI	Polydispersity index
M-DT	Mannosylated Dendritubes
NVP-DEN	Nevirapine loaded dendrimers
NVP-CNT	Nevirapine loaded MWCNT
NVP-DT	Nevirapine loaded DT
FPV-DEN	Fosamprenavir calcium loaded dendrimers
FPV-CNT	Fosamprenavir calcium loaded MWCNT
FPV-DT	Fosamprenavir calcium loaded DT
NVP-FPV-DT	Nevirapine and Fosamprenavir calcium loaded DT
M-NVP-FPV-DT	Mannosylated Nevirapine and Fosamprenavir calcium loaded DT

List of Annexure

Annexure 1: Letter of candidacy

Annexure 2: Approval by Institutional Animal Ethics Committee

Annexure 3: List of publications, patents, presentations and workshops attended

Chapter 1
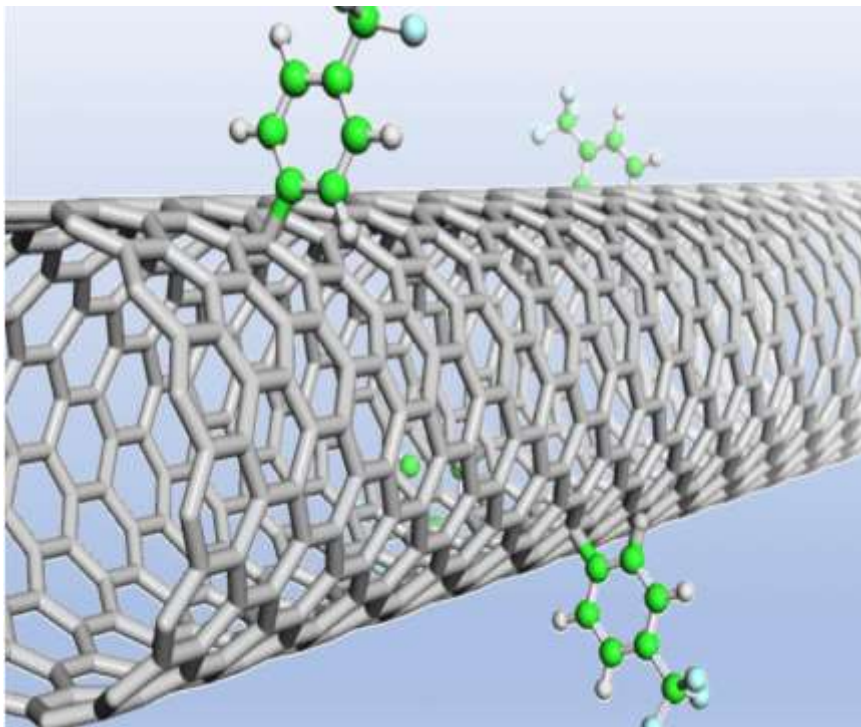
Introduction

The human immunodeficiency virus (HIV) is accountable for the occurrence of acquired immunodeficiency syndrome (AIDS), which is responsible for more than 40.1 million deaths across the world. AIDS is a deadly disease caused by a retrovirus known as HIV. HIV has its impact throughout the world affecting the health system, education system as well as the economic condition of the countries. Presently 38.4 million (33.9 - 43.8 million) people will be suffering from HIV worldwide in 2021. Different health agencies are striving hard for the betterment of HIV patients, which can help them to lead a better life with disease.

1.1 Human Immunodeficiency Virus

HIV leads to the development of the disease AIDS which has catastrophic socioeconomic implications in affected zones of the world. There are approximately 38.4 million HIV infections worldwide (UNAIDS, 2021; WHO, 2021). In 1981, the first case of HIV was found in Los Angeles in healthy gay males, who reported a cluster of Pneumocystis carinii pneumonia. Today we are in the 41st year of HIV with no defined treatment or cure (Becken et al., 2019; Guinto et al., 2021). HIV belongs to the genus lentivirus, of the retrovirus family and orthoretrovirinae subfamily (Eloy et al., 2018). Two types of HIV are identified across the world, i.e. type 1 and type 2. The classification is based on variation in the antigen in the virus as well as on genetic differences. HIV infecting non-human primates also belong to the group lentivirus termed simian immunodeficiency virus (SIV). The study based on phylogenetic analysis revealed that the disease was introduced from 1920 to 1940 in the human population. The disease evolved from the African continent from non-human primate immunodeficiency virus, chimpanzees in Central Africa were the source of HIV-1, whereas sooty mangabeys in West Africa were the first source of HIV-2 (Faria et al., 2014).

HIV-1 has genetic diversity and can be categorized into four different lineages M, N, O, and P. The common lineage of HIV-1 worldwide is M, and N, while O is less common and found in Cameroon only. Group O accounts for one percent of HIV infections and is found to be most prevalent in Gabon and Cameroon in Africa. HIV-1 variant P is the version of the virus that is seen least frequently (Edoul et al., 2020). It is only

responsible for 0.06% of total HIV cases (Bhatti et al., 2016). HIV-2 is dominant in Western Africa in Senegal, Guinea-Bissau with the greatest incidence. There are eight subtypes of HIV-2, each of which is designated as from HIV-A to HIV-H. Group A has been documented in every country in the sub-Saharan area (Exbjornsson et al., 2019). Group B is commonly found on the Ivory Coast (Visseaux et al., 2021). Due to the sporadic nature of the illness group, C-H transmission is known as dead-end transmission since it does not induce future infections (Vallari et al., 2010). Figure 1 shows the types of HIV. HIV has an impact on all the countries of the world. Infection is commonly spread by infected syringes, infected blood transfusion, mother-to-child, and unprotected sex. Once the virus enters the body, it starts multiplying and infecting many healthy immune cells (WHO, 2021).
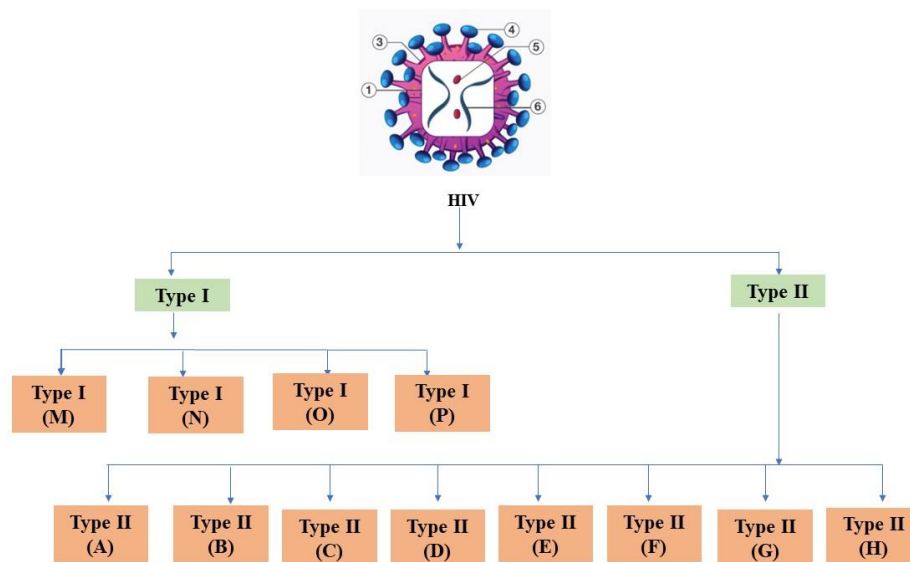
Fig 1: Types of HIV

The immune system consists of $CD4^+$ cells commonly targeted by a virus, which has the effect of lowering the immunity of the infected individual. Even after the virus enters the body, many people are unaware and asymptomatic. Some can develop symptoms such as flu, tiredness, and enlargement of lymph nodes, these symptoms subside within a week and the person remains normal. This phase can last for years, sometimes even for 10 years. After infection, the disease can develop in a few weeks, or it can even take years

depending on individual immunity. HIV affects the immune system primarily on CD4$^+$ cells and leads to chronic medical condition developments such as pulmonary disorders, lung cancers, pulmonary hypertension, asthma, and various others. These co-morbidities develop due to viral load, immune dysfunction, immune activation, or even due to toxicity of anti-HIV drugs (Cribbs et, al. 2020).

1.2 Worldwide statistics

HIV has its impact throughout the world affecting the health system, education system as well as economic condition of the countries. Presently 38.4 million (33.9 - 43.8 million) people will be suffering from HIV worldwide in 2021. Among these, 1.7 million were children of age 0 to 19. From the data, it was revealed that around 850 children were infected with HIV, and around 330 died due to AIDS-associated problems. The deaths were the majority due to scarce accessibility to the treatment, care, or prevention of the disease. Around 15.4 million children had lost their parents because of AIDS (Wang et al., 2020). Worldwide statistics are represented in Figure 2.
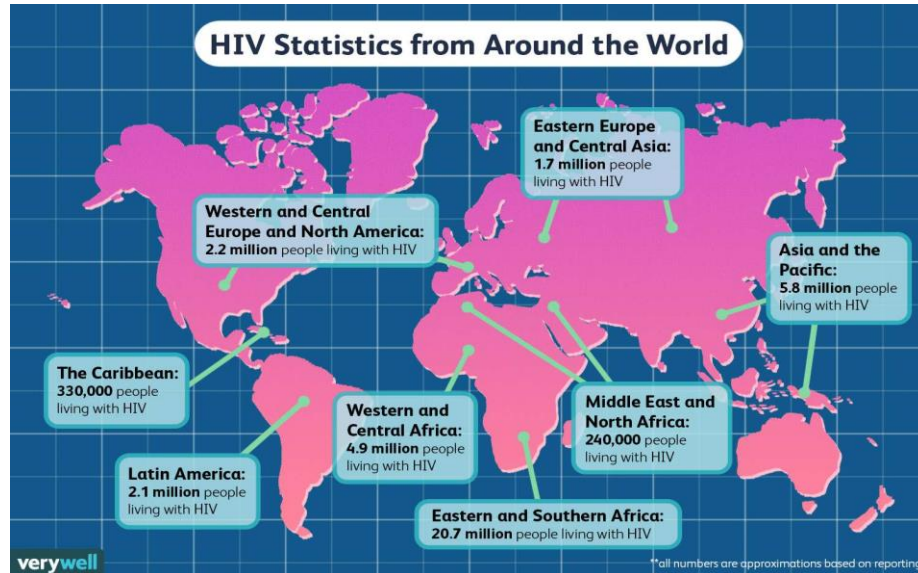
Figure 2: Worldwide statistics of HIV- AIDS (Charles, 2021)

As per the report by HIV.gov, 1.5 million newly infected HIV people were there in 2020. The disease is causing its impact and leading to the death of 650,000 million people by AIDs related illnesses. Most HIV-positive people live in low-income countries. According to the statistics from 2020, 20.6 million were infected in East and South Africa

(representing 55% of the total), 4.7 million people suffered from HIV in West and Central Africa (representing 13% of total), 5.7 million people suffering from HIV in Asia and the Pacific (representing 15% of total), and 2.2 people suffering with HIV in American northern continent and in the central and west part of Europe and (representing 6% of the total). In this group, 27.5 million individuals participated in antiretroviral treatment in the year 2020. The people suffering from HIV had more severe effects and higher co-morbidities from HIV. In mid-2021, very few HIV patients got COVID-19 vaccines. From the studies, it was observed that the risk of death is almost double in HIV-infected individuals as compared to non-infected patients. Almost 67% of HIV patients used to live in the sub-Saharan region but till July 2021 only 3% with a minimum of one dose were vaccinated with the COVID-19 vaccine (WHO, Gov report, 2020).

1.3 Impact of COVID-19

COVID-19 contributed more to HIV problems, increasing the risk of poverty, homelessness, discrimination, as well as school dropout. Most of the children infected with HIV live in the sub-Saharan region. As a result of measures, to control the transmission of infection from mother to offspring, the rate of newly acquired HIV infections in children aged 0 to 9 years old fell by around 52 percent. Lockdowns also had an impact on HIV testing, diagnosis, and referral. Although the scientific understanding of diseases is increasing, efforts are put down by different organizations for the betterment of diseases but still, the prevention, care, and treatment are not accessible to all and there is no ultimate cure for the diseases. Along with the health of an individual at risk, it also greatly impacted household development. and the economic growth of nations (Brown et al., 2021).

1.4 Therapy for HIV-AIDS

Highly active antiretroviral therapy (HAART) is the presently available treatment used to treat HIV and to improve the lifestyle of the patients. HAART therapy includes different anti-retroviral drugs (ARVs) given in combinations that help in the management of disease and increase the life expectancy of the patient. However, the therapy is associated with several limitations. Most of the drugs possess short half-lives and need to be administered frequently, adhesion to a strict regimen reduces patient compliance.

Inappropriate dosing responsible for drug resistance in HIV patients. Another major limitation is the inaccessibility of anti-retroviral drugs (ARVs) to the intracellular locations, as HIV tends to accumulate in the central nervous system (CNS), immune cells, and lymphatic systems. The routine therapy is not efficient in delivering and localizing the drug at intracellular target sites, leading to failure of therapy and also the development of multidrug resistance. Apart from this, anti-HIV drugs showed severe adverse effects at the therapeutics level, due to which the dose of the drugs has to be compromised which contributes to the poor bioavailability of the majority of ARVs (Maitre et al., 2019).

1.5 Strategies for Novel Cargo System

Different strategies were explored for overcoming the limitation of ARVs such as new chemical entity development, altering existing moieties, and modifying the dose and dosage regimen. These approaches did not lay down any promising solution. Novel drug delivery systems (NDDS) are an optimistic approach that can increase the efficacy of the drugs, reduce the potential adverse effects as well, and help to manage drug resistance. The nano delivery system can accommodate the drugs to intracellular locations targeting the intracellular reservoirs. In recent times, NDDS has been explored by different researchers for the delivery of ARVs to overcome different above-mentioned problems (Rizvi et al., 2018). Different novel nanocarriers were explored for the development of anti-HIV drugs such as nanoparticles (Dharshini et al., 2021), liposomes (Okafor et al., 2020), Self-nano-emulsifying drug delivery systems (Reddy et al., 2020), dendrimers (Pagroo et al., 2021), carbon nanotubes (Zuru et al., 2019), and various others.

Dendrimers are hyperbranched structured artificial polymers getting enormous attention for diverse therapeutic agents (Sherje et al. 2018). This nanosized complex molecule was first put forward by Fritz Vogtle in 1978, named cascade molecules. After many years of basic discoveries, Tomalia and co-workers formulated an improved category of cascade molecules, termed dendrimers which is a from the Greek word *dendrons* means branched-like structure (Abbasi et al. 2014). Newkome and co-workers published the development of a similar kind of structure and termed them *arborol* derived from the Latin term arbor (Kaur et al., 2016). Biological applications of dendrimers are due to high water

solubility (Choudhary et al. 2017), polyvalency, biocompatibility, and accurate molecular weight (Santos et al., 2020). Because of these characteristics, it is considered an appropriate cargo for the efficient delivery of drugs and site-specific targeting to the particular sites.

Carbon nanotubes, also known as CNTs, are molecules with a cylindrical shape that are comprised of carbon atoms. Graphene sheets are taken together and rolled down to form a cylinder without any seams making the basic structure of CNTs. The aspect ratio of this cylinder is quite high, with a nano-range diameter, and its length is many micrometers. CNTs have an open end or a capped end. Single-walled carbon nanotubes (SWCNT) are the outcome of CNTs being formed by using one sheet of graphene, whereas multi-walled carbon nanotubes (MWCNT) are the product of numerous graphene sheets being combined. Pristine CNTs are practically insoluble in water. The solubility of the pristine CNTs can be improvised by surface functionalization with an organic group improvises the solubility and opens the doors to the possibility of CNTs being used in bio-applications. They can conjugate with a different medicinal compound because of the vast surface area that they possess. CNTs can have their surfaces engineered, or functionalized, to increase their dispersibility or improve the target efficiency. This allows CNTs to be used to produce a therapeutic effect. The linked medicinal molecule may have an easier time penetrating through the target cell with the assistance of CNTs, which may then be used to cure ailments (Mishra et al., 2020).

MWCNT- Dendrimers conjugates (Dendritubes) are the novel supramolecular delivery system comprised of surface-engineered dendrimers with carbon nanotubes. The structure is fabricated by attaching dendrimers to the outer structure of functionalized carbon nanotubes by covalent linking. As carbon nanotubes have many active peripheral functional groups, dendrimers are attached by an amide linkage to these functional groups.

The failure of HAART therapy is due to the inefficiency of retaining the required amount of drugs at target sites. Dendritubes contain carbon nanotubes that can entrap drugs or bind on their surface and a large number of drug-loaded dendrimers are adjoined on the surface of CNTs. The structure is further treated with mannose which acts as an anchor for the dendritubes. Macrophages have mannose receptors in abundance which will help in

6

targeting the prepared conjugates to the viral reservoirs. This enhances the effectiveness of the drug at the desired location and overcomes the problems of HAART therapy.

For the study two anti-HIV drugs are being selected, the first one is Nevirapine which belongs to non-nucleoside reverse transcriptase inhibitors (NNRTI) and other one is protease inhibitors. Both drugs are selected from different categories so that the action can be exerted at two levels. The two drugs, Nevirapine and Fosamprenavir calcium belong to BCS class II and showed poor bioavailability after oral administration. The two drugs are selected to produce independent action and for better efficacy.

The research work involves the synthesis of the newer drug delivery system by conjugating carboxylic functionalized MWCNT (COOH-MWCNT) with 5G poly(propylene imine) (PPI) dendrimers termed dendritubes (DT). The outer surface engineering of MWCNT with 5G PPI dendrimers increases the surface area which upsurges the drug-loading capacity of the structure. Dendrimers also help to improve the solubility of the MWCNT. Mannosylation of the prepared dendritubes helps them target the macrophages, the target sites for viral reservoirs. The novel system has a much higher drug-loading capacity and improves drug solubility due to its dendritic attachments. The developed dendritubes have a solid intact structure that has better stability compared to other novel delivery systems. The nano delivery system will help in the uptake of the cargo system at the level of the target cells. Anti-HIV drugs, Nevirapine, and Fosamprenavir calcium are the two anti-HIV drugs respectively are selected for loading drugs to DT.

Chapter 2

Literature Review

2.1 Human Immunodeficiency Virus-Acquired Immunodeficiency Syndrome

AIDS leads to a significant weakening of the body's defense system, which results in a dramatic drop in $CD4^+$ T cells. This, in turn, makes patients more susceptible to a variety of opportunistic infections that can be fatal. Once the gp120 which is the exterior glycoprotein of the virus comes in contact with $CD4^+$ T cells, the virus utilizes CXCR4 and CCR5 co-receptors to penetrate the immune cells (Campbell et al., 2018; Mishra et al., 2014). The genetic RNA material and many enzymes, including integrase, protease, ribonuclease, and reverse transcriptase are then discharged inside the cellular structure of the host. According to the findings, the enzyme known as reverse transcriptase is one of the primary targets that researchers are focusing on when developing AIDS medicaments (Javan et al., 2017). Inhibitors of reverse transcriptase have been developed; nevertheless, they have a few drawbacks, such as the development of resistance strains and dose-related toxic effects (Himmel and Arnold., 2020). According to Yetisgin et al.'s research from 2020, nanotechnology makes it possible to distribute drugs for HIV in a regulated and/or targeted way. This results in an increase in drug bioavailability as well as residence duration at target areas, leading to a substantial upliftment in the overall living quality of patients with HIV. Study reveals that nano vehicles can function effectively against viruses and can lead to the annihilation of the virus from intracellular viral deposits such as those observed in the CNS, the cerebrospinal fluid, the lymphatic system, and the macrophages which are inaccessible for current HIV treatment. Nanomedicines will help in achieving the therapeutic concentration at the desired location with higher retention time (Colino et al., 2020; Das et al., 2016). Because resistance was developing to the various categories of anti-HIV drugs, testing for resistance needed to be done to choose a combination of medications that would be more beneficial for individual patients. According to Lu et al. (2018), exceptionally long HAART treatment regimens are associated with low compliance of patients, intolerance to medication, toxicity, and eventual viral recurrence. Patients who were treated with HAART revealed higher incidences of diabetes, heart disease, cancer, liver disease, and accelerated aging; this is a cause for worry because adverse effects produced by the toxicities of the medications are a major problem. (Alvi et

al., 2019). Apart from these, disease management is challenging as the virus tends to reside in intracellular sites that are inaccessible to the traditional delivery system as well as the development of latent cells which are formed by the integration of viral DNA in normal cells which can trigger *in vivo* activation and viral multiplication (Aggarwal et al., 2021).

Considering the toxicity and inaccessibility in the intracellular compartment, it is an urgent necessity to advance a novel delivery system that can target the virus reservoirs and also reduce the toxicity by developing the low dose system. The sustained release system assists in reducing the dose and managing the accurate concentration at the site of action.

2.1.1 Configuration of HIV

HIV is the retrovirus from the lentivirus genus of the retroviridae family broadly classified into two types HIV-1 and HIV-2. Like all retroviruses, HIV consists of two similar sets of RNA molecules with single-stranded structures. The mature virus structure consists of a 100 nm diameter enveloped with an outer membrane rich in lipids. The outer envelope represents 72 knots involving three Env proteins. The envelope of the virus is made of a bilayer of lipids with surface and transmembrane proteins. The trimer of surface protein gp120 is attached to the viral membrane by attaching to transmembrane protein gp41. The attachment of gp120 and gp41 are not covalent which results in the removal of gp120. The envelop proteins cover the outer capsid membrane which consists of matrix proteins. Inside the outer capsid membrane consist of two RNA strands that are identical along with different viral enzymes such as protease, reverse transcriptase, and integrase. The viral structure also constitutes oligopeptides (p55, p160) which are released during the maturation of the virus during proteolytic cleavage. The virus also carries HLA I and II proteins, host membrane proteins, or adhesion proteins such as ICAM-1 which helps in the attachment of the virus with new cells. The genomic structure consists of structure-specific genes (Fanales-Belasio et al., 2010; Cheng et al., 2019).

2.1.2 Genomic structure

Both HIV-1 and HIV-2 consist of similar genomic structures but HIV-1 and HIV-2 can be differentiated by the arrangement of genomes. Apart from these structural genes,

the genome also includes various other regulatory genes. The structural proteins of the capsid shell are coded with gag gene (p24, p7, p6) and matrix protein (p17), the envelop glycoproteins are coded with env gene code for gp120 and gp41 and viral replication enzymes are coded with pol gene responsible for the viral enzyme's integrase, reverse transcriptase and protease. Apart from these, the accessory or regulatory gene is responsible for viral replication. The gene TAT codes for a protein that appears in the initial phase of HIV (Rein et al., 2019).

The Rev gene codes proteins that support the efficient movement of genomic or messenger RNA to the cytoplasm from the nucleus. There are other regulatory proteins whose roles are not clear but play a role in the cell cycle. Vrp protein of HIV-1 is responsible for the interruption of the cell cycle, it also helps in the entry of reverse transcriptase DNA to the nucleus of non-dividing cells. A similar type of function is performed by Vpx in HIV-2. The gene Vpu is responsible for the appropriate virus particle release, and another gene Vif affects the progeny increasing its infectivity. Nef is responsible for different functions facilitating viral budding (Toccafondi et al., 2021)
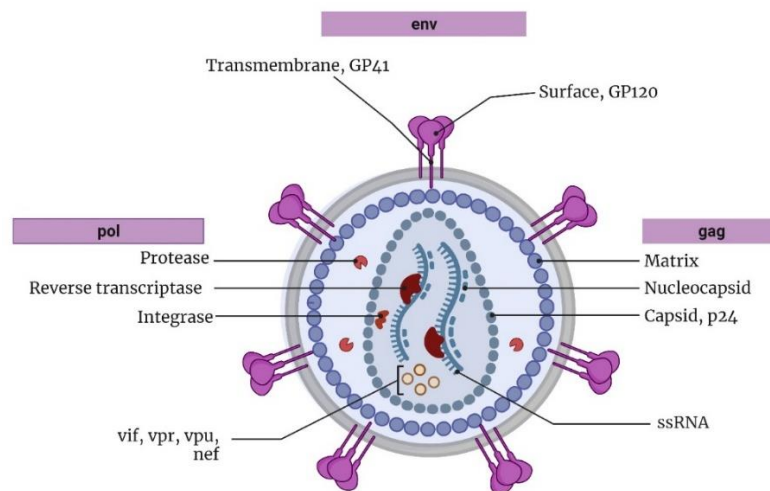
Fig 3: Structure of HIV

2.1.3 Pathogenesis of Acquired Immunodeficiency Syndrome

HIV is communicated from one individual to another by percutaneous inoculation, from mother to infant, and by sexual contact. Among different variants, the CCR5 virus is transmitted by all routes. HIV replicates exponentially and multiples, and alters its genesis, making it difficult to study the molecular structure of the transmitted virus and its identification. Productive clinical infection was observed with sexual transmission from a single virus inefficient in virus transmission. After the transmission of the virus, the host develops a marker for the new infectious agent known as host markers. The virus and host markers can be observed in blood samples (Naif et. al., 2013).

The foremost phase of infection due to HIV is the attachment of a viral structure onto the outer surface of the immune cells. The interaction occurs between gp120 present on the viral surface with host CD4+ along with other receptors specifically found on the T lymphocytes and macrophages, which are primary immune structures. After attachment, the entry is further facilitated with gp 41, a transmembrane protein. Apart from gp 120, chemokines receptors along with other coreceptors provide a parallel pathway for viral entry. HIV binds with different coreceptors present in different cells. The two primary chemokine receptors that are involved in HIV fusion or entrance are CCR5 and CXCR4, respectively (Woodham et al., 2016). Once entered, the cell enzymes are released by the HIV structures including reverse transcriptase and viral integrase. HIV belongs to a retroviral family which carries the RNA as genetic material. Once HIV has been inserted in the cell structure RNA of the virus is converted to viral DNA which can be conveniently introduced into the host DNA. Viral enzymes reverse transcriptase, and integrase plays crucial roles. Reverse transcriptase helps to transcribe single-stranded RNA to DNA (double-stranded structure). This newly formed DNA gets inserted in the genomic structure of the host due to the functioning of the enzyme integrase. Viral DNA gets integrated into host DNA (provirus) is formed by unspliced viral RNA, which is separated from the nucleus through host translation machinery. After the inception of the viral genetic structure, the viral fate is decided whether it will be active or remain latent depends on various cellular mechanisms. The active structure can indulge in transcription and produce

11

new viral structures which can be released by cell lysis or by cellular pores. Viruses can remain latent as proviral structures which can produce new viral structures but are not able to produce viruses as their transcription is blocked. Certain HIV infections are CD4$^+$ independent and occur in astrocytes and renal epithelial cells. The expressed gene is responsible for nephropathy and neurocognitive problems (Freed et al., 2015).
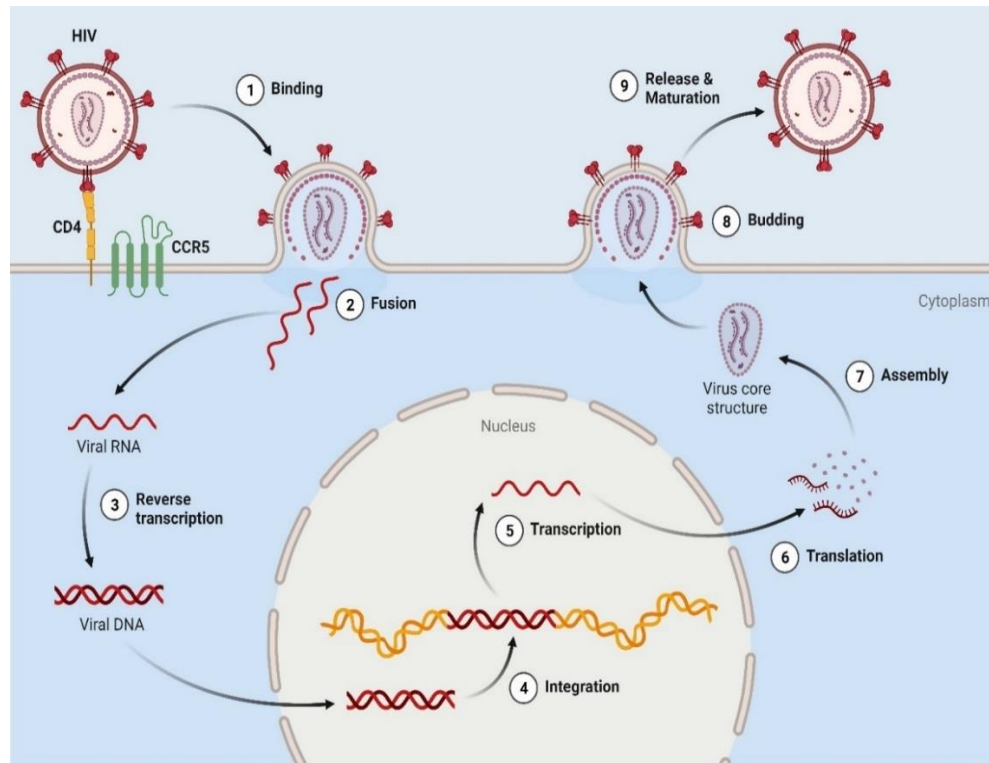
Fig 4: Life cycle of HIV

2.1.4 Host Immune response

The host Immune system starts acting against HIV after the ingress of the virus. T cells are accountable for mediating the death of possibly infected cells via the process of CD8$^+$ killing which is HIV-specific. CD8$^+$ cells which are specific to viruses focus themselves selectively on cells that are infected with viruses. Infected cells present a viral protein that forms a complex with HLA class I molecule, which are identified by virus-specific CD8$^+$ T cells (Perdomo-Celis et al., 2017). Once recognized, it triggers the initiation of events that cause the release of perforin and granzymes which kill the infected cells and inhibit the formation of new virions. Along with this, the activation of T cell

receptors (TCR) results in the development of several cytokines for example tumor necrosis factor (TNF) and interferon as well as chemokines such as RANTES, MIP-1, and MIP, all of which can inhibit viral replication. $CD8^+$ T cells are essential for preventing viral development and replication and are hence very important. Hence, viral load decreases after primary infection. At the onset of infection, $CD4^+$ T cell proliferative property is diminished hence its role in initial control is minor. But as the disease progresses secretes cytokines and interleukins which control viral growth and multiplication (Upadhyay et al., 2018).

In the initial phase of infection, the humoral response is weak and observed in the later stage contributing very little amount of antibodies when the viral load is low. P17 and P24 are the first observed antibodies against structural protein which subsides gradually. Other antibodies are generated later which are specific to proteins that are engaged in the viral entry in the cell. Generated antibodies are specific to $CD4^+$ binding sites, chemokine receptor sites, gp120 variable region, and gp41 transmembrane protein. Neutralizing antibodies are not of much use due to the development of viral escape mutants (Klatt, 2017).

2.1.4.1 Dysfunction of the Immune responses

The response from humoral immunity and cell-mediated immunity against infections are both dependent on $CD4^+$ T cells as a fundamental component. HIV attacks T cells, which causes a drop in the cell count of $CD4^+$ cells, alternating the function of primary immune cells such as macrophages, and dysregulation in the production of cytokines (Peng et al., 2020). Manipulation in immune function upsurges the risk of opportunistic infection and enhances immune activation. In HIV infection, the collapse of the immune system takes place due to different factors such as direct killing by the virus, and immune system activation leads to the progression of HIV (Deeks et al., 2015).

2.1.4.2 Direct killing by HIV infection

The principal target of HIV is CD4$^+$ T cells, which go on depletion with the progression of the disease. The depletion is mainly due to increased reduction and lower production of the CD4$^+$ helper T cells. The virus can remain latent and invisible in CD4$^+$ T cells hence unrecognized by CD8$^+$ T cells (Vijayan et al., 2017). This latent virus becomes active in a later stage and produces new virions causing infections. HIV infection causes the reduction of CD4$^+$ helper T cells, and immunological activation results in the death of infected cells, the creation of syncitia, the proliferation of cells, as well as the aging process. At the initial stages of an infection, the rate of cell death and formation of CD4$^+$ helper T cells is increased, and the body is constantly replacing its supply of T cells. But as the disease progresses the infection spreads in the thymus. As the CD4$^+$ helper T cell gets infected, they are eliminated by the thymus T cell selection system which leads to a reduction in CD4$^+$ helper T cell count. CD4$^+$ cells also undergo direct cytolysis due to infection (Conway et al., 2018).

2.1.4.3 Immune system activation

The advancement of HIV illness is associated with increased immunological activation, which causes increased cell division of T cells, B cells, CD8$^+$ cells, and CD4$^+$ cells. It also increases the cell division of T cells (memory cells), and faster self-renewal results in greater cell count (Hileman and Funderburg., 2017). This activation leads to the depletion of immune cells, as explained by Yates et al., CD4$^+$ helper T cells which are activated are lost rapidly due to apoptosis or by activation inducing death of the cell and possess a short life span. An HIV patient's immune activation indicates immune deficiency and serves as a marker for disease progression (Yates et al., 2007).

It is observed in infection with HIV, the process system remains in the hyperactive state with faster T cell turnover polyclonal activation and proliferation of B cells, and increased release of inflammatory cytokines. Hence HIV is producing its targets by acting on the immune system (Ward et al., 2021). Different viral genes such as Nef, Vpr, Tat, and Vpu participated in the immune system activation (Lusic et al., 2017).

2.1.4.4 Immune activation and Inflammation

Circulating chemokines and cytokines are accompanied by chronic immune activation. Cytokine storms have been observed with sudden and rapid increases in cytokine levels in HIV infection indicating the immune system activation and depletion of T lymphocytes. Regular immune activation inhibits the CD4$^+$ and CD8$^+$ T cells production (Vijayan et al., 2017). The result of an alteration of T cell production and depletion shows an immediate effect on the gastrointestinal tract with a vast depletion of immune cells with minimum recovery. It is observed that the concentration of lipopolysaccharides, a microbial product, increased in the plasma due to higher gastrointestinal (GI) permeability, rapid destruction of lymphoid cells in the GI tract along with apoptosis. With the progression of the disease, different factors are responsible for the destruction of CD-naïve and CD8-I T cells including collage deposition, and the diminution of the cell network of the fibroblastic reticular system (Maartens et al., 2014).

2.1.4.5 Cell death by pyroptosis

According to the findings of investigations, it is now obvious that a T cell that has been infected by HIV kills via the process of apoptosis. However, certain subtypes of T cells are resistant to HIV and can prevent its reproduction. These T cells are called non-permissive (Doitsh et al., 2016). Pyroptosis is the mode of death of the cell that happens in these kinds of cells. Pyroptosis is the programmed cell death in which all the inflammatory cytokines are released by the dying cell. The released cytokines target the other T cells and induce cell death by the pyroptosis process is extremely inflammatory resulting in massive T-cell depletion. It is related to two consecutive events, the first is the depletion of T cells followed by chronic inflammation. Cell death leads to a vicious cycle; the dying cells give out all the inflammatory components that trigger more cells to die. These events further damage the immune system causing chronic inflammation that leads to disease progression (Dotish et al., 2017).

2.1.5 Symptoms of HIV

HIV enters the body and can reside in the human body and resides for many years without symptoms. When the infection starts, in the initial time antibodies are formed against HIV due to seroconversion at detectable concentration. Common symptoms observed after the initial infection are muscle aches, fever, rash, swelling in lymph nodes, and other flu-like symptoms. HIV tends to form reservoirs in the cells and tissue due to the continuous growth of the virus. Cytoplasmic mass is formed with multiple nuclei termed syncytium which causes cell death. HIV is resistant to the immune system or develops the condition when the immune system is hijacked by HIV. Sometimes the virus resides in a latent condition for a long period, the condition arises due to low virulent strain or due to the presence of strong cellular immunity (Schank et al., 2021). As discussed, HIV targets the immune cells and weakens them by infecting $CD4^+$ helper T lymphocytes. In the later stage of disease progression with gradual destruction of $CD4^+$ helper T cells triggers immunodeficiency which further results in AIDS (Aavani et al., 2019). There are severe symptoms in the later phase of HIV. It is believed that the gathering of indications known as the AIDS-related complex serves as a prodrome, which is another word for a precursor to AIDS. Various opportunistic infections such as candidiasis, toxoplasmosis, and Mycobacterium tuberculosis develop in the infected individual. The patient is declared as an AIDS patient when the $CD4^+$ count is depleted to 200 mm^3. The symptoms come gradually and may develop in years or sometimes never develop even in a lifetime. The onset of infection and its progression varies widely from patient to patient (Gupta et al., 2019).

2.1.6 Current therapy

The newer HAART therapy has controlled the advancement of the disease and also reduces the chances of opportunistic infections. ART stands for Antiretroviral therapy includes the administration of drugs in combination, introduced in the 1990s, helping to suppress the viral replications and progression of the disease (Barbier et al., 2020). ART therapy manages HIV from progressive illness to manage chronic disease. Health agencies have approved more than 25 anti-retroviral drugs that can block HIV replication at diverse

levels of the replication cycle of the virus. ART is more effective, less toxic, reduces drug resistance, and reduces pill burden and frequency as compared to previous protease inhibitor therapy. In this treatment, nucleoside reverse transcriptase inhibitors are given along with other types of inhibitors. Several combinations can be explored if intolerance or resistance to nucleoside reverse transcriptase is observed (Altice et al., 2019).

HIV is a host-specific infection having complex pathogenesis and varies from patient to patient. Treatments that are available for HIV infection get complex as the viral structure is non-specific and tends to alter frequently (Moranguinho et al., 2020). The virus tends to develop resistance, so the combination of available drugs was given for the effective management of HIV. This therapy is known as ART an anti-retroviral therapy. Standard ART constitutes at least 3 medicines termed HAART. This therapy helps to reduce the multiplication of viral cells and increases the $CD4^+$ cell count in the blood. It helps to prolong the phase of infection termed the asymptomatic phase, which reduces the course of the infection and further lowers its rate of transmission (Pawar et al., 2019).

The selection of drug and dosage regimen depends on the need of the patient which is based on viral load, virologic efficacy, drug-drug interaction, pill burden, dosing frequency, comorbid condition, potential adverse effects, and cost. Even with the continuous effort of scientists, health workers, and the government, the rate at which new infections are taking place remained comparatively unchanged over the past decade. HAART therapy is found to be inefficient in controlling dementia and HIV-associated neurocognitive disorders (Cihlar et al., 2020).

2.1.7 Limitations of HAART therapy

Antiretroviral drug therapy, which became widely accessible in the middle of the 1990s, has been shown to significantly enhance the quality of life of HIV-infected individuals and lower death rates. Existing HAART therapy, on the other hand, has several drawbacks, such as severe adverse effects, resistance to the drug, higher level of viral mutations, a limited and specific target, lesser bioavailability of some compounds, the development of viral reservoirs, and the fact that the therapy is already in use. Even while the overall viral load could be brought down to imperceptible levels, the replication of the virus will

continue as long as typical highly active anti-retroviral therapy (HAART) medications are unable to enter certain cells. Patients have to follow strict regimens of several medications and dietary restrictions lead to incompliance and withdrawal (UNAIDS., 2023).

HAART has improved the lifestyle and expectancy of HIV-infected patients by reducing the load of the virus but has shown its inability to penetrate cells having viral reservoirs. The virus tends to affect and multiply in the intracellular environment primarily $CD4^+$ T, dendritic, and macrophage cells, even after the systemic viral load is reduced to an unidentifiable level. The virus tends to develop resistance due to continuous mutation and genetic diversity to specific combinations of drugs which fail in failure of the HAART treatment. Apart from strict regimen modern therapy shows severe side effects such as peripheral neuropathy, lipodystrophy, anemia, hepatotoxicity, neutropenia, thrombocytopenia, CNS disturbances like suicidal tendency, anxiety, bone marrow toxicity, and rashes which lead to failure or interruption of the therapy as well as the progression of the diseases. Side effects are precipitated because the drug binds with different receptor sites at the different organs and can be overcome by target-specific delivery of anti-HIV treatments. A new treatment for HIV involves the delivery of anti-HIV medications specifically to the cells that are infected with the virus (Lu et al., 2018).

As time progressed, the efforts of health workers and the governments created awareness of the disease, reduced new infections, and controlled AIDS-related deaths. Different health agencies also work for the proper distribution and availability of the treatment and are also funded to reduce the cost of antiretroviral therapy. Despite all the efforts, some countries still have significantly high HIV cases. This is due to limited testing services, lack of awareness, and unavailability of HIV treatment, COVID-19 worsens the case even more (Bekker et al., 2018).

Literature review*

Table 1: FDA Approved Anti-HIV drug classes

Anti- HIV drug classes-	Definition	Examples	Reference
Reverse Transcriptase	To prevent HIV from replicating itself, reverse transcriptase enzyme inhibitors can attach to enzymes responsible for viral replication and stop it from functioning. Non-nucleoside reverse transcriptase inhibitors (NNRTIs) and nucleoside reverse transcriptase inhibitors (NRTIs and NNRTIs, respectively).	didanosine, abacavir, combivir, tenofovir, zidovudine	(de Béthune, 2010;)
Protease inhibitor	For appropriate assembly and generation of HIV, controlling the protease enzyme is most significant. In	Amprenavir, nelfinavir, Indinavir, lopinavir/ritonavir	(Hughes et al., 2011)

	CD4$^+$ cells that are acutely or chronically infected with HIV, the use of protease inhibitors can limit the working of protease enzymes. When HIV protease enzymes are inhibited, immature virus particles that cannot cause infection are released into the bloodstream.		
Fusion inhibitor	These drugs exhibit action by averting HIV from accessing the CD4$^+$ cells of people already infected with the virus. They prevent the HIV particles from fusing with the CD4$^+$ cells in the body.	Enfuvirtide	(Xiao et al., 2021)

Chemokine receptor	The chemokine receptor 5 (CCR5) antagonist receptors are blocked which is found on CD4$^+$ T cells is the way this class of antiviral agents works to protect against infection. HIV is unable to enter the cell and infect it if the CCR5 receptors on the cell's surface are not occupied.	Maraviroc	(Sojka et al, 2021)
Integrase strand transfer inhibitor	Inhibitors of strand transfer hinder the ingress of the structure of DNA into the genomic structure of the CD4$^+$ cells of the host, which is carried out by an enzyme called integrase. Integrase inhibition is an effective means of	Dolutegravir Elvitegravir Raltegravir	(Tzou et al., 2020)

	preventing HIV replication.		

2.1.8 Latest World Health Organization Recommendations for ART

World Health Organization (WHO) recommended first-line, second-line, and third-line treatment detailed below (World Health Organization, 2015).

2.1.8.1 First-line ART

The first-line antiretroviral therapy (ART) regimen typically consists of single NNRTIs and two NRTIs. For this form of antiretroviral therapy (ART), the combination of emtricitabine (FTC), tenofovir disoproxil fumarate (TDF), and lamivudine (3TC), and efavirenz (EFV) in a fixed dosage for the treatment. The usage of zidovudine (AZT) lamivudine and efavirenz (EFV), zidovudine and 3TC, and Nevirapine (NVP), of TDF plus 3TC (or FTC) plus Nevirapine (NVP) is recommended as alternatives to this medication combination when it is either not safe to use or not accessible (Patrikar et al., 2017).

2.1.8.2 Second-line ART

When an ART therapy of the first line is unsuccessful, an ART treatment of the second line needs to be used. The second-line treatment consists mostly of one protease inhibitor (PI) and two nucleotides reverse transcriptase or non-nucleoside reverse transcriptase inhibitors that have been increased with ritonavir. The combination of AZT and 3TC as the NRTI is the antiretroviral therapy (ART) option that is recommended for second-line treatment. After an initial treatment regimen based on AZT or stavudine (d4T) + 3TC has been tried and shown to be ineffective, the option of using 3TC or FTC along with TDF as the NRTI can be examined. When treatment based on NNRTIs of first-line fails, a combination of two NRTIs and a PI in a boosted dose is indicated (Patrikar et al., 2017).

2.1.8.3 Third-line ART

ART integrase inhibitors and other second-generation protease inhibitors, non-nucleoside reverse transcriptase inhibitors, such as Darunavir (DRV), Raltegravir (RAL), Etravirine (ETV) are some examples of new medications that the WHO recommends if first and second-line antiretroviral therapy (ART) are ineffective (Patrikar et al., 2017).

2.2 Targeted delivery system

As HAART is facing challenges in targeting the drug to the infected cells and the intracellular reservoirs. The targeting of the intracellular reservoir is inefficient leads to the development of resistance and also contributes to various adverse effects. Targeting the drug to the virus-infected cells or reservoirs helps to achieve a higher drug therapeutic index by specifying the pharmacological action by localizing the drug and helps to decrease the drug-associated adverse effects and improve the treatment efficiency. HIV causes infection in the $CD4^+$ T-cells ($CD4^+$), dendritic cells, and macrophages (Nayak et al., 2016). The basic goal of targeting a drug is to enhance the therapeutic action of the drug by carefully localizing the pharmacological action of the drug to the target organ where the action is required. This is accomplished by reducing the amount of systemic distribution of the drug. The targeting helps in a considerable reduction in the toxicity caused due to drug molecules, a reduction in the drug dose, and an increase in the treatment's overall effectiveness. In HIV infection, only macrophages, dendritic cells, and $CD4^+$ T cells are infected by HIV, hence directing anti-HIV medications to these cells increases therapeutic efficacy. Adding the surface markers on targeting macrophages, $CD4^+$ T-cells, dendritic cells, and the central nervous system helps selective drug transfer to HIV-infected tissues and cells. This can also help deliver drugs to the CNS. Targeting these receptors has the potential to have two different outcomes: either (i) more selective absorption of a nanocarrier that is laden with anti-viral drugs, or (ii) protection of the cell in a prophylactic fashion, the occupation of the receptor required for cell-virus contact. In this regard, several compounds with origins in both the virus and the host cell have been characterized in modern times, and the delivery system shows the potential to enable targeted medication administration for HIV infection (Ramana et al., 2014).

Therefore, directing the medicine to particular cells to improve the effectiveness of the treatment can be accomplished by targeting surface indicators that are present on the infected cells. Targeting the drugs helps by blocking the receptor site for the attachment of the viral particles and easy uptake of the drug-loaded nanostructures.

2.2.1 Nanocarriers for HIV treatment

A controlled release delivery system is another approach to improve patient compliance. Controlling the release rate and targeting specific receptors on infected cells not only increases the duration of action, improves patient compliance, and reduces drug-related adverse effects but also controls resistance. To control the adverse effects of the therapy and to enhance the effectiveness of the drugs, different carrier systems have been formulated for example liposomes, nanoemulsions, dendrimers, carbon nanotubes, solid lipid nanoparticles, and polymeric nanoparticles[9]. This delivery system helps to administer the medicaments in a controlled released manner to the target cells controlling the adverse drug effect and enhancing the efficiency of drugs (Chamundeeswari et al., 2019).

Date et al. created a nano delivery system for microbial agents including cellulose acetate phthalate which is an HIV-1 entrance inhibitor and an anti-HIV agent efavirenz for the prevention of HIV. Nanoprecipitation of nanoparticles of efavirenz and cellulose acetate phthalate is examined for zeta potential and size of nanoparticles and efavirenz entrapment efficiency. The thermosensitive nanoparticle-loaded gel was prepared. The nanoparticles, gel, and efavirenz solution were tested on Henrietta Lacks (HeLa) cells for cytotoxicity and HIV-1 prophylaxis in TZM-bl cells derived from HeLa cell lines for 1 and 3 days. Formulated nanoparticles have particle size found to be less than 100 nm, negative surface charge, with 98% efavirenz entrapment effectiveness. The prepared nanoparticles and nanoparticle-loaded gel were less hazardous ($P < 0.01$) to HeLa cells than the plain efavirenz solution (Date et al., 2018).

Godbole et al., developed liposomes of lamivudine using 32 factorial designs by hydration of thin film. The formulated structures were evaluated by the size of the vesicle, % drug entrapment efficiency, and polydispersity index. Rats are used for biodistribution studies and pharmacokinetic studies of the drug lamivudine and lamivudine-loaded liposomes. The results reveal that the optimized liposomes have 276.20 ± 13.36 nm of vesicle size, show $60.20 \pm 2.86\%$ entrapment efficiency, and have 0.291 ± 0.053 polydispersity. It is observed by *in vivo* studies that prepared liposomes are readily

removed from plasma and show 1in the spleen and liver.38 ± 0.52 and 10.97 ± 0.72 times deposition in liver and spleen tissues respectively (Godbole et al., 2020).

Roy et al., utilized the nanodiamond for brain delivery. The nanodiamonds are biocompatible and non-toxic compared to other carbon-based materials, making them an efficient drug carrier. Efavirenz, an anti-HIV drug is loaded in carboxylic and amine surface-modified nanodiamonds and the prepared structure was characterized. It is observed from the studies that surface-modified nanodiamonds have comparatively lower drug loading efficiency than unmodified nanodiamond conjugated drugs with minimum toxicity. Then a new drug formulation was evaluated for drug dissolution profile and therapeutic effects. The prepared formulation of nanodiamonds is studied for biological characterizations such as *in vivo* pharmacodynamics and pharmacokinetics of nanodiamond-based delivery systems (Roy et al., 2018).

2.2.1.1 Polymeric Nanoparticles

Nanoparticles are nanosized constructions in the nano range of 1 to 1000 nm designed to target the drug, gene, and diagnostic materials to the target site. Nanoparticles include nanosphere and nanocapsules both vary in morphological structure. Nanospheres encase the drug in the polymeric matrix throughout the structure, whereas in nanocapsules, the medicament is enclosed inside the core and surrounded by a polymeric matrix on all sides. Both structures are used to deliver the medicine. Polymeric nanoparticles are gaining importance due to their nano size, targeting efficiency, controlled release, keeping the medicament safe in the physiological environment, and increasing bioavailability as well as therapeutic index (Zielińska et al., 2020). Nanoparticles can be functionalized to enhance blood circulation time and target specific cells or tissues using peptides, antibodies, and aptamers as targeting ligands (Prabhu et al., 2015).

2.2.1.2 Solid lipid nanoparticles

Solid lipid nanoparticles (SLN) are a biodegradable system for delivering aqueous soluble drugs. SLNs can incorporate different therapeutic components such as polysaccharides, peptides, drug molecules, DNA/RNA, and antigenic materials. The SLNs are formulated by melting solid lipids, dispersing them in water, and stabilizing them with

emulsifiers through high-pressure homogenization. Depending on the production conditions or the makeup of the product, the drug molecule may be included in the matrix, the shell, or the core. The nanosize of the SLNs offers the benefit of biopharmaceutical trafficking across the biological membrane and assists in managing the release of the medication from the designed delivery system in conjunction with the target specification (Prabhu et al., 2015, Scioli et al., 2020).

2.2.1.3 Nanoemulsion

Nanoemulsions are colloidal systems consisting of two immiscible liquids like water and oil, along with surfactant and co-surfactant. The oil in the water (o/w) system tends to develop interfacial tension which is stabilized with the help of surfactant and co-surfactant. Nanoemulsions are classified as o/w type emulsion, w/o type emulsions, bi-continuous emulsions, and multiple emulsions such as o/w/o or w/o/w. Different surfactants (anionic, cationic, non-ionic) can be used for the formulation of such systems. To hold the oil and water together in the system both hydrophobic and hydrophilic surfactants are used together (Gurpreet et al., 2018). The system is thermodynamically stable and prevents the system from different instabilities such as cracking, creaming, and flocculation due to steric stabilization of sub-micron droplet size (Che Marzuki et al., 2019)

2.2.1.4 Liposomes

Liposomes are lipid bilayers enclosing a hydrophilic core to create a spherical vesicle. This vehicle may be utilized to transport hydrophilic and lipophilic medications to the target region. Liposomes are formed when lipid bilayers are sandwiched around an aqueous core. The bilayer can be classified as either a unilamellar vesicle (consisting of a single bilayer) or a multilamellar vesicle. This vesicle acts as a carrier for biologically active substances to be delivered to the designated location (Wang et al., 2012). However, the half-life time of these compounds in the blood is significantly shorter. PEGylated liposomes, also known as stealth liposomes, can be created by coating liposomes with polymeric molecules such as polyethylene glycol. Because it can avoid removal by the reticuloendothelial system, this stealth liposome has better stability and prolonged circulation time. As a result, it produces a prolonged drug release. The drug molecules that are included in the liposomes

increase the pharmacokinetics as well as the biodistribution of the drug that is incorporated. For example, the drug doxorubicin encased in a stealth liposome has been shown to have a lower distribution of the drug in plasma as well as a lower concentration of the drug in healthy cells. This is in comparison to the drug when it is dissolved in a solution. (Rosenblum et al., 2018)

2.2.1.5 Self-Emulsifying Drug Delivery System

Self-Emulsifying Drug Delivery Systems is the emulsion system that is produced by peristaltic agitation. The system consists of oil, surfactant, drug, cosolvent, or co-surfactant which can produce emulsion using aqueous fluid from the stomach. This system improves absorption by increasing the solubility of the system and remains solubilized during dispersions and digestion. The factors governing the characteristics of SEDDS are the concentration and physiochemical properties of the surfactants and co-surfactants (Maji et al., 2023).

2.2.1.6 Dendrimers

Dendrimers are 3D structures having tree-like branches with a center core with outer branches. It is also called cascade molecules. They have unique properties like monodispersity, spherical and symmetrical shape, and highly branched with a terminal functional group. Dendrimers are available in different generations G1, G2, G3, G4, and G5. It has a surface functional group that serves as a carrier of various agents such as genes, antibodies, siRNA, and targeting agents (Sherje et al., 2018).

2.2.1.7 Carbon nanotubes

Carbon nanotubes are elongated chain-like structures with a repeated pattern of carbon atoms with sp^2 hybridization which is wrapped to form the cylinder structure. The size of the structure is 2.5-100 nm in diameter in range. The tube with end caps is formed by rolling together sheets of carbon, which are then sealed off. Pristine carbon nanotubes are insoluble in water and need to functionalize by different functional groups which improve the water solubility and make it suitable for drug delivery. Different biomolecules, such as DNA, protein, and antibodies, improve the target efficiency. CNTs can penetrate

through cells easily, and improve drug delivery to the nucleus and cytoplasm (Kiran et al., 2020).

2.3 Dendrimers

Dendrimers are hyperbranched supramolecular structures that have a size that is uniform and controlled with the functional groups on the periphery in abundance. They are formed with successive attachment of branching units to a central core. It is feasible to exert specific control over the shape and size of dendrimers, and changed surface functional groups as a result of the methods that are employed to synthesize dendrimers (Palmerston et al., 2017). Therefore, for the dendrimers to selectively engage with the HIV envelope protein as well as receptors on the host cells, they have been engineered with definite functional terminal groups. This is done to inhibit the combination of HIV and the cells of the host, as well as the final phases of HIV replication. In addition to this, dendrimers that include a significant number of terminal groups and inner spaces act as vectors for the drug delivery, genes, and peptides that suppress HIV. Hydrogen bonds, electrostatic interactions, and hydrophobic interactions can bind these materials to dendrimer peripheral groups or cavities. Either way, they are capable of performing both of these functions. Dendrimers would make chemical medications more stable and would enable the absorption of such drugs by cells through the use of functional end groups (Lyu et al., 2019).

2.3.1 Chemistry

Dendrimers are the heavily branched macromolecular structure with an abundance of functional groups present on the external surface along with low molecular volume. The structure of the dendrimer includes three basic parts: core, building block, and terminal functional groups. The core comprises of an atom or set of atoms with a minimum of two identical functional groups called a core.

The structure begins with the core. On this core branches of other atoms grow with the help of a variety of chemical reactions (Saluja et al., 2019). Further different layers can be grown by adding repeating units at the terminal end. On the peripheral end, multiple functional groups are present which help the structure to bind with different moieties

altering the physical and biological properties. The structure of dendrimers is considered to be semi-globular to globular in shape, although it is still not clear that the end groups are fully extended or folded back. Dendrimer chemistry is an attractive and fast-growing area in the world of chemistry (Patel et al., 2020).
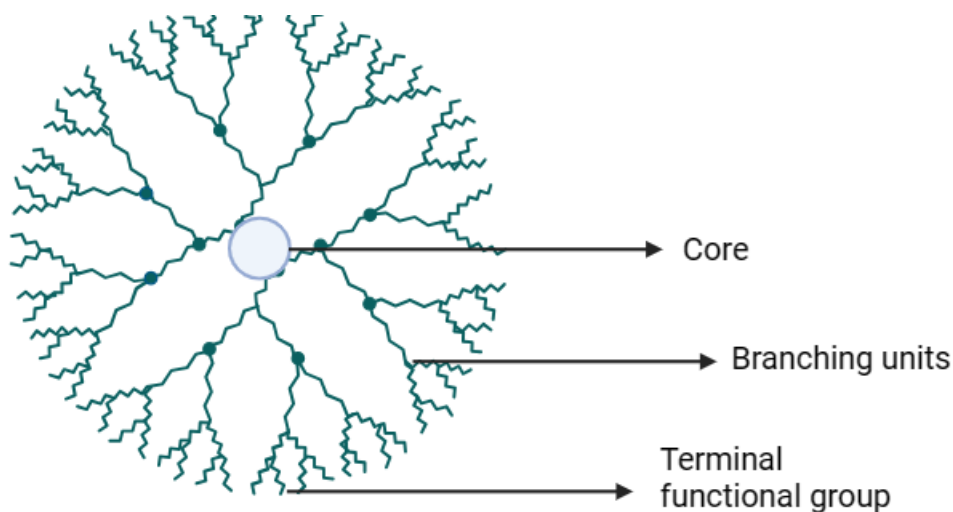
Fig 5: Structure of dendrimers

2.3.2 Synthesis

2.3.2.1 Divergent Synthesis

This type of synthesis starts from the core material and on this core material, the building up of the molecule takes place in a stepwise manner toward the periphery based on two operations. As the steps proceed, branching units get added to the structure resulting in an increase in generation number by one. The reaction begins when monomers are attached, then the monomer surface group is changed or altered, creating a new surface that is reactive and coupling fresh monomers to the structure. In this, the synthesis takes place in an ascending manner. The method is simple and efficient but needs to be very precise as multiple steps take place simultaneously. This method is useful in developing different dendritic structures such as Poly(amidoamine) dendrimers (PAMAM), phosphorous-based dendrimers, poly(propylene imine) (PPI) etc (Chauhan et al., 2018).

The 3rd generation poly(propyleneimine) (G3-PPI) dendrimers were created by Alavi et al., 2017 and were synthesized by employing a divergent growth technique using

1, 4-diaminobutane as a core initiator. The structure of the dendrimer generates toxicity due to the terminal amine group. The structure is conjugated with alkylcarboxylate which boosts the lipophilicity of the dendrimers and lowers the toxicity. Conjugation of the alkylcarboxylate–PPIs to branched polyethylenimine (PEI), which helps to maintain the buffering capacity of the system and enhances transfection, was then performed. It has been shown that the modified PPI can build complexes of 60 nm or less in size, and 20 mV surface charge (Alavi et al., 2017).

2.3.2.2 Convergent synthesis

Convergent synthesis is different from divergent synthesis as it starts from the opposite direction. This synthesis is initiated from the periphery and progresses toward the core. The peripheral branches get attached by the one-to-one coupling of monomers. The core is the last one to get attached to the structure. In this, on the branching unit, two groups get linked with the branching unit. These dendrons are connected to the branching unit so that together they can create dendrons of a higher generation. The continuation of the procedure results in an increment in the structure's size by 1. Adding a core at the very end of the process that involves two or more dendritic structures ultimately results in the synthesis of dendrimers (Prajapati et al., 2020; Mishra et al., 2019).

Haghighi et al., formulated different nanostructures for improving the adsorption of drug 5-Flurouracil using dendrimers of PAMAM G0 generation using Becke, 3-parameter, Lee–Yang–Parr (B3LYP) for surface functionalization. The prepared structure reduces the toxicity of the 5- Fluorouracil drug and the carrier PAMAM G0 acts as a drug release facilitator. The study conducted by atom in molecule shows that pseudo hydrogen and hydrogen bonds are essential in the functionalization of PAMAM G0 and drug. The study concluded that 5-Flurouracil interacts with PAMAM G0 via the carboxyl functional group is the most stable one (Haghighi et al., 2016).

Polyanionic carbosilane dendrimers were synthesized with antiviral drugs in developing innovative microbicides to inhibit the spread of HIV-1 by sexual intercourse (Vacas-Cordoba et al., 2016). The research investigated the process behind the formation of sulfated and naphthylsulphonated functionalized carbosilane dendrimers, specifically

generation 3 sulfated 16 and generation 2 napthylsulfonated 16. They can prevent viral infections at the stage of fusion and the stage of entrance. The study demonstrates that dendrimers have the power to stop HIV from spreading from one cell to another and also stop the formation of difficult infectious synapses (Vacas-Córdoba et al., 2016).

Dendrimers comprising 9 to 18 molecules of tryptophan at the outer surface were successfully synthesized by Rivero-Buceta et al., These chemicals prevent the virus from entering its target cell, which is thought to be the start of the HIV life cycle. According to the findings that have been gathered up to this point, there is a need for just 9 tryptophan residues on the surface of the molecule to achieve effective gp120/gp41 binding and anti-HIV activity (Rivero-Buceta et al., 2015).
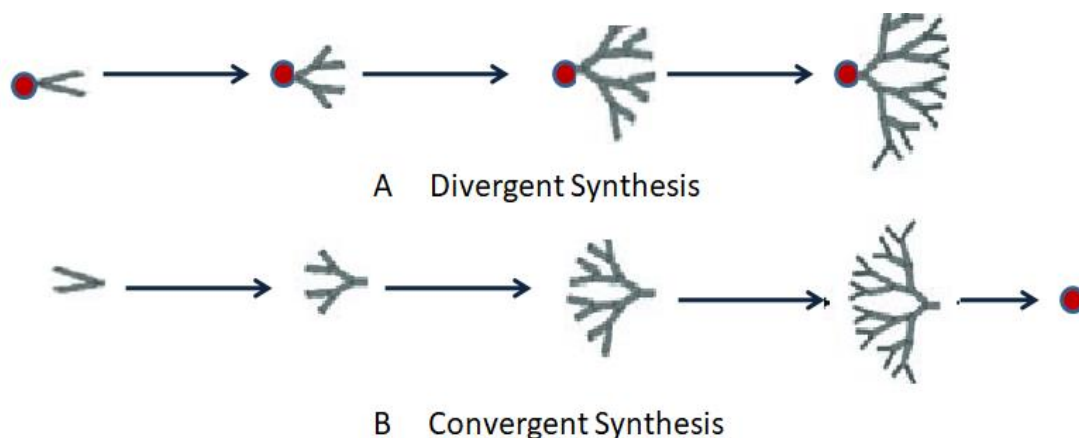
Fig 6: Synthesis of dendrimers a) Divergent method b) Convergent method

2.3.2.3 Lego chemistry

In Lego chemistry, phosphorous dendrimers are made by combining cores with branching monomers that have more functional groups than the cores themselves. This approach increases surface groups from 48 to 250 in one step. (Mishra et al., 2019).

2.3.2.4 Hypercores and branched monomer growth

In this technique, monomers required for the growth in divergent or convergent manner are synthesized from the single starting material. The two products that are created using the procedures described above are then processed together to create the trimer structure. This trimer is utilized in the process of iteratively growing dendrimers (Mishra et al., 2019).

2.3.2.5 Click chemistry

This is a new technique that is involved in the reaction of high yield. As a result, this method has been put to use in the creation of a great deal of brand-new dendrimer molecules. The aim is to develop environment-friendly and carbon-rich dendrimer (Mishra et al., 2019).

2.3.3 Types of Dendrimers

2.3.3.1 PAMAM Dendrimer

PAMAM dendrimers are the commonly used dendrimers. The development of poly amidoamine dendrimers (PAMAM) begins with the utilization of ethylenediamine or ammonia as the center reagent as a core for the initiation of the reaction. This is followed by a repeating series of double Micheal adding method of methyl acrylate to the main amino group, amidation, and amidation of the carbomethoxy intermediate to form 5-generation dendrimers with a mol. weight of 9,30,000 g/mol. The brand name of the PAMAM dendrimers is Starburst. PAMAM dendrimers dissolved in methanol are easily available. The name is assigned because of the star-like assembly of the high-generation dendrimers (Rajora et al., 2021).

2.3.3.2 PPI dendrimers

PPI dendrimers are commonly synthesized by divergent methods with amine-terminated macromolecules. The structure is hyper-branched with different nitrogen atoms one with a primary amine and the other with a tertiary amine. The development of PPI dendrimers involves the recurrent sequencing of double Michael adding method of acetonitrile to primary amine, after that the hydrogenation of the nitrile group was done. With each replication, primary amines get doubled. The core of this PPI dendrimer comprised of 1, 4 diaminobutane which is commonly been used. Apart from these various molecules containing primary and secondary amine can be used as core molecules (Kesharwani et al., 2014).

2.3.3.3 Liquid crystalline dendrimers

These are commonly known as carbosilane dendrimers. These are the liquid crystalline monomers termed mesogenic monomers. In these dendrimers, the end groups

are functionalized with a total of 36 mesogenic units that are joined through a C-5 spacer. This results in the creation of liquid crystalline dendrimers at temperatures ranging from 17 to 300 °C (Higuchi et al., 2020).

2.3.3.4 Chiral dendrimers

Chiral dendrimers have chemically similar branches to the chiral core but are constitutionally different. Non-racemic, chiral dendrimers have specific stereochemistry. It is a fascinating type of dendrimer and has applications in chiral chemistry and asymmetric catalysis (Agrahari et al., 2020).

2.3.3.5 Glycodendrimers

These structures have carbohydrates in the structure of dendrimers termed 'Glycodendrimers'. They are further classified as carbohydrate-centered, carbohydrate-coated, and fully carbohydrate-based. These glycodendrimers have potential bio-applications and commonly participate in protein-carbohydrate interactions. Dendrimers with carbohydrates on the surface are extensively studied for drug targeting to different organs. Sugar can readily get access through different carbohydrate-specific receptors such as mannose receptors, and fucose receptors help to evaluate the carbohydrate-protein interactions. Different fields where glycodendrimers are used such as formulation of gels, delivery systems for drugs and genes, targeting MRI contrast agents, and others (Agahari et al., 2020).

2.3.3.6 Hybrid dendrimers

The name suggests that it is a cross-breed between linear and dendritic polymers, and the end product is either a graft copolymer graft or a hybrid block. The structure binds with many reactive chain ends which are provided surface active agents, adhesives, and compatibilizers (Agahari et al., 2020).

2.3.3.7 PAMAMOS dendrimers

These are poly(amidoamine–organosilicon) (PAMAMOS) dendrimers. These are the micelles whose interiors consist of nucleophilic, hydrophilic poly (amidoamine), while their exteriors are adorned with organosilicon (OS). They are used as precursors for the

making of networks like honey-comb with nanoscopic OS and PAMAM domain (Mishra et al., 2019).

2.3.3.8 Peptide dendrimers

In these dendrimers, peptides are surfaced on the exterior of the structure of the dendrimers. The dendrimers with amino acids as core or branching units are also categorized as peptide dendrimers. Even the incidence of peptide bonds in the structure can also be termed peptide dendrimers. As peptide molecules are relevant for drug delivery and other biological procedures, peptides play diverse roles such as cancer, antimicrobials, CNS, asthma, antiviral, and various others. Peptides are specifically taken up by different cells which are beneficial for drug delivery. Peptide dendrimers are utilized for magnetic resonance angiography, magnetic resonance imaging, serodiagnosis, and fluorogenic imaging (Kesharwani et al., 2014).

2.3.4 Properties of dendrimers

2.3.4.1 Pharmacokinetic property

It is considered to be the most important property that governs drug delivery, imaging, photodynamic therapy, and others. Several modifications can be done on the surface of the dendrimer structure such as peptides, antibodies, and protein molecules that can be attached to the surface. This structure can help to alter the pharmacokinetics of the entrapped drug. Different factors affecting the pharmacokinetics of the dendrimers are anatomical structure and the physiology of the target organ, characteristics of macromolecules, and their interaction with biological molecules at target sites.

Dendrimers are commonly administered by intravenous (IV) route, introducing the system in blood. From blood, the dendrimer is distributed to different organs followed by the elimination of these macromolecules. The uptake of macromolecules is affected by organ blood flow, capillary permeability, and the nature of macromolecules. Dendrimers show potential absorption across different epithelial barriers, intestines, and skin. Dendrimers can be targeted to specific tissues reducing drug toxicity and thus preventing the non-infected healthy cells and improving therapeutic levels. Target specificity can be achieved by surface decoration as well as improved pharmacokinetics profiles. With

amine-terminated 3G and 4G dendrimers, it showed rapid clearance along with a high volume of distribution. Uncharged dendrimers are excreted through urine and feces and it takes 7 days for complete excretion (Yellepeddi et al., 2019).

2.3.4.2 Polyvalency

The structure of dendrimers is polyvalent which makes it versatile for functionalization. This polyvalent nature facilitates multiple interactions with different receptors at target sites.

2.3.4.3 Nanoscale size

A dendrimer is a nano-range structure with many protein properties also termed artificial protein. If dendrimers are developed in a controlled manner, they will closely resemble the structure of enzymes, proteins, and antibodies. Due to its nanostructure, it can penetrate with ease through bio-membranes including the blood-brain barrier, cell membrane, and tumor membrane. The nano-size also reduces the removal through urine. The high permeability and reduced clearance make it suitable for targeting the drug molecules.

2.3.4.4 High solubility potential

Dendrimers are hydrophilic polymers with good water solubility. This property has been investigated to increase the drug solubility. Terminal groups are responsible for the solubilization of the drug which helps to improve the bioavailability and efficacy of different therapeutic and diagnostic agents. The solubility is enhanced by different chemical interactions at the terminal functional group. Apart from a functional group other properties which affect the solubility are core moiety, generation number, and nature of the repetition unit (Tunki et al., 2020, Santos et al., 2020).

2.3.4.5 Self-assembling dendrimers

Self-assembling is the characteristic feature of chemical species due to intermolecular forces which are complementary to each other. Due to the amphiphilic nature, the smaller structure of dendrimers tends to self-assemble and results in the formation of supramolecules by different weak interactions. This newly created structure has a similar drug loading capacity as the conventional one (Lyu et al., 2020).

2.3.4.6 Monodispersibility

A controlled synthesis process and multiple purification steps render the multivalent nature to the dendrimers with a low level of impurities. The monodispersible nature helps to judge the pharmacokinetic nature of the prepared formulation in biological systems (Tunki et al., 2020; Santos et al., 2020).

2.3.4.7 Multivalency

Multivalency also termed polyvalency is the numeral of terminal functional groups that are available on the periphery and can bind with receptors on biological membranes including polymers, proteins, cell structure, and others. It also facilitates surface modification to mimic biological structures such as substrates, co-factors, and inhibitors. The terminal functional group can also form conjugates with a drug or ligands (Santos et al., 2020).

2.3.4.8 High loading capacity

Dendrimers can carry a wide variety of organic and inorganic molecules. It can carry the molecules by; (i) electrostatic interactions, (ii) conjugation of drug to molecules, (iii) encapsulation of drug (iv) by micelle formation. Dendrimer's loading capacity depends on its architectural design and the number of functional groupings on the outer surface. The surface function group goes on increasing with the increase in generations (Santos et al., 2020).

2.3.5 Dendrimers as cargo for anti-HIV drug

Dendrimers can be used for entrapment of the drug by entrapping the drug molecules in void spaces, branching of dendrimers by hydrogen bonding, and on the terminal of dendrimers. Drug molecules interact mostly with the outer surface of the dendrimers. The generation and structural complexity determine whether medicinal compounds can interact or integrate into dendrimers. Modulation of the capacity of drug loading of the dendrimers is carried out by the interaction of the drug with terminal functional moieties. The drug loading is based on the number of generations of dendrimer structure. With the increase of the generation the space for incorporation of the drug also

increases. Hydrophobic, electrostatic, or hydrogen bonding can introduce drugs into the core. (Nikzamir et al., 2021).

Maingi et al., work was based on atomized molecular dynamics stimulators to analyze the pattern of release of the ligands which are entrapped inside the ethylenediamine-cored polyamidoamine dendrimers (PAMAM) by docking method. The four ligands included two water-insoluble drugs viz, phenylbutazone and primidone, and two drugs that are water-soluble namely L-alanine and salicylic acid. The potential of mean force variation was measured using umbrella sampling for the drug and 5G dendrimers complex. The result concluded that the water-soluble drug has a lower energy barrier than water-insoluble drugs. It was also observed that higher pH facilitates the entrapment of the drug in the PAMAM dendrimers. As the drug-loaded dendrimers enter the body at a neutral pH, it limit the drug release in the blood in a controlled fashion (Maingi et al., 2021).

Jain et al., explored two other drugs Famotidine and Indomethacin with 5G ethylene diamine-cored PPI dendrimers with fully atomistic molecular dynamics at varying pH conditions. This study also supported that a higher pH helps to stabilize the drug dendrimer complex as compared to a lower pH tends to destabilize the complex. Calculating the mean force potential using the umbrella sampling technique revealed that there was spontaneous drug release at low pH (Jain et al., 2013).

Fluorescence spectroscopy was employed to understand the interaction between polyamidoamine dendrimers (PAMAM) and lipopeptide antibiotics like daptomycin. A shift in fluorescence took place because of the interaction between daptomycin dendrimers. The fluorescence difference plotted for daptomycin at 460 nm from ordinary kynurenine (Kyn-13) in the absence or presence of dendrimers revealed some interesting results. The ionized Asp-9 residue of the drug daptomycin largely interacts with a positive charge surface amine of PAMAM. (Chanyorachote et al., 2015).

Gajbhiye et al., conjugated sialic acid-mannosylated PPI (SMPPI) dendrimers to target zidovudine, an HIV medication, dually. Fourth-generation PPI dendrimers were developed and evaluated by spectroscopic analysis., size exclusion chromatography, and DSC. The dendrimers were examined and characterized for different evaluation

parameters. ZDV-loaded SMPPI, salicylic acid PPI (SPPI), and mannosylated PPI (MPPI) had decreased hemolytic, cytotoxic, and drug release. SMPPI increased macrophage cell ZDV absorption significantly (P > 0.001) more than dendrimer and plain drugs. Blood and biodistribution studies in albino rats showed the promise of a dual-targeted method targeting carbohydrate receptors and sialoadhesin. SMPPI increased the accumulation of the drug in lymph nodes by 28 times compared to the free drug during the 6th hour. SMPPI, this system may increase biocompatibility and site-specific administration of ZDV, an antiviral medicine. (Gajbhiye, 2013).

Cordoba et al., performed an anti-HIV action of the various combinations of the drug maraviroc with polyanionic carbosilane dendrimers in the HIV-1 strain. The study included the in-vitro cellular model using TZM.bl cells of breast cancer and peripheral blood mononuclear cells. The study revealed the synergistic profile of the drug maraviroc against CCR5 (Cardoba et al., 2013).

Kumar et al., generated and evaluated PEGylated G4 and G5 PAMAM dendrimers for the lamivudine. PAMAM dendrimers were constructed using the core of ethylene diamine and PEGylated to alter the structure. PEGylation of PAMAM dendrimers has been shown to lower the surface toxicity of the dendrimers while simultaneously increasing their capacity for drug loading. In addition, PEGylated PAMAM dendrimers released the medicine over a period that was both regulated and extended (Kumar et al., 2013).

Sepúlveda-Crespo et al., the study examined the synergistic effects of carbosilane dendrimers, with tenofovir, and maraviroc. Triple combinations were tested for cell toxicity, anti-HIV-1 efficacy, irritation at the viginal cavity, and histology. CalcuSyn calculated the median effective concentration and investigated combination effects. The combination medications have broader anti-HIV-1 efficacy than conventional therapy, even in acidic conditions or seminal fluid. Weighted average combination indices from 0.06 to 0.38 indicated considerable synergistic action. Their indices were 0.06–0.38. Female BALB/c mice showed no irritation. Combining these three medicines boosts their antiviral activity and may act as a microbicide. (Sepulveda-Crespo et al., 2015).

Pyreddy et al., reported that innovative PEGylated PAMAM (poly-amidoamine) dendrimers were created to facilitate the administration of the anti-HIV medication efavirenz. It takes around 5.0 g equivalents of ethylene diamine core to create PAMAM dendrimers using the Michael addition divergent technique. Polyethylene glycol 600 acts as the linker during the PEGylation process, which requires epichlorohydrin. Studies on FTIR spectroscopy, DSC analysis, scanning electron microscopy (SEM), drug release, and stability are being conducted on efavirenz (EFV) loaded PEGylated PAMAM dendrimers (5G). The findings demonstrate that this approach requires significantly less time, is more economical, and is easier to replicate. According to the findings of drug-release experiments, PEGylated 5G PAMAM-EFV dendrimers have demonstrated a sustained drug-release characteristic. (Pyreddy et al., 2014)

Pargoo et al., have produced a 2nd generation of a linear globular nano-biopolymer dendrimer. This dendrimer was loaded with the drugs efavirenz and lamivudine of the anti-HIV category. The prepared structure was characterized by several different analytical procedures, including elemental analysis, Zetasizer, FTIR, and liquid chromatography-mass spectroscopy, among others. In addition, a human embryonic kidney cell (HEK293) T cell that had been infected was used to test lamivudine conjugation and loaded efavirenz with PEGylated G2 dendrimer. The results of these tests were analyzed using the methoxynitrosulfophenyl-tetrazolium carboxanilide (XTT) test and the HIV-1 P24 protein load. The findings demonstrated that lamivudine-loaded dendrimers considerably reduced the amount of retroviral activity with minimum or no cell damage. A similar effect was approximately seen by G2 which had been loaded with efavirenz (Pargoo et al., 2021).

2.3.6 Dendrimer as an HIV agent

Garcia-Gallego et al., established a new way for the inhibition of progression of HIV-1 disease. PPI dendrimers with ethylenediamine core were functionalized as sulfonated and carboxylated. This functionalized complex with metal (Cu^{2+}, Ni^{2+}, Co^{2+}, and Zn^{2+}) was found to be an effective antiviral agent. The prepared structure was evaluated for antiviral properties and it was observed that both functionalized dendrimer and metal-conjugated dendrimers showed antiviral activity. VK-2 and HEC-1A are the models for the

epithelial cell line which is the first barrier against HIV and is used to study antiviral activity. The structure showed excellent inhibition of HIV activity and also reduced the virus internalization of virus in the cell. The second barrier was peripheral blood mononuclear cells, the prepared structure showed preventive and therapeutic behavior in PBMC cell lines (Garcia-Gallego et al., 2015).

Maciel et al., developed three generations of anionic dendrimers with terminal groups of sulphonate and carboxylate functional moiety. The dendrimers are initiated from the family of poly(alkylidene amine) with a terminal nitrile group. The terminal functional amino structure facilitates the structure to work against HIV. Characterization of prepared dendrimers was carried out by NMR, mass spectroscopy (MS), FTIR, and zeta potential methods. The stability studies confirm the stability of prepared dendrimers for one and a half years in solid and solution states. The prepared dendrimers were evaluated for anti-HIV activity. The study indicated that the dendrimers were cytocompatible and prepared structures have anti-HIV activity against specific isolates which blocks the viral entry and acts on the viral structure. It also showed inhibitory action at different pH levels against the viral particles. Similarly, a tropical application was explored by carrying out a vaginal irritational assay designed and studied in BALB/c mice to confirm the safety of prepared dendrimers (Maciel et al., 2019).

Perisé-Barrios et al., studied second-generation carbosilane dendrimers for anti-HIV activity. These dendrimers were evaluated on macrophage phenotype and studied for developing an inflammatory response. The nanoconjugates provide an efficient reduction in HIV-1 replication. Prepared dendrimers were safe and effective since they did not increase $CD4^+$ T cell proliferation or macrophage interleukins and tumor necrosis factor release. It reduces phagocytic activity (Perise-Barrios et al., 2014).

2.3.7 Biocompatibility

Dendrimers can be anionic terminated, cationic terminated, or neutral which alters their toxicity as well as biocompatibility. The study showed that amine-terminated dendrimers have more toxicity and hemolysis as compared to anionic and neutral dendrimers. Toxicity is mainly due to the exterior functional structures of the dendrimers

and can be surpassed by altering the cationic groups with the anionic or neutral group. Amino-terminated PAMAM tends to increase the toxicity with an increase in generation while PPI behaves differently. The cell lysis takes place due to the adhesion of the dendrimer with the cell membrane interaction between a positive surface charge of dendrimers and a negative surface charge of the cell membrane. Masking cationic end groups or converting them to anionic or neutral groups leads to the generation of dendrimers with reduced toxicity and even non-toxicity (Santos et al., 2020).

2.3.8 Toxicity of dendrimers

Dendrimer has a free surface amino group which leads to toxicities when administered in the body. This toxicity can be overcome by one of the two approaches. The masking of the surface group can be done either by biocompatible/biodegradable dendrimers such as polyester, polyether-imine, polyether copolyester, citric acid, polyether, peptide or melamine dendrimers or by acetylation or pegylation of the surface functional group. Surface functional groups can be covered with a diverse functional groups such as amino acids, carbohydrates, folic acid, and antibodies which reduce the positive charges that cause toxicity due to the surface amino group. Dendrimers toxicity was tested with different cell lines as it is used as a carrier for various molecules. The toxicity of dendrimers is due to different factors such as the cytotoxicity of dendrimers, number of generations, number of surface functional groups, and its nature. Toxicity tends to increase with progression in generations as surface charges increase. Scientists explored different ways to reduce cytotoxicity by peripheral chemical modifications of dendrimers. Dendrimers fabricated with an acetyl group, carbohydrate, or polyethylene glycol (PEG) show slight or no change in cell viability while other properties are maintained without any effect. (Janaszewska et al., 2019).

The smaller size and surface functional group of dendrimers in the nano-range enable it to penetrate the cell or interact with cell organelles, proteins, and cell membranes. Dendrimers tend to react with the lipid structure of the bilayer membrane structure enhance the cell wall permeability and affect the integrity of the biological membrane. Dendrimers initially engage with cell membranes, which speeds up the leaking of cytosolic proteins

including lactate dehydrogenase and luciferase, which ultimately results in the lysis of the cell. The study revealed and proved that the toxicity is more with anionic dendrimers or cationic dendrimers (Thiagarajan et al., 2013).

Oral acute toxicity tests were performed on PAMAM dendrimers using CD-1 mice, who are capable of mounting an immunological response. The size of dendrimers as well as their charges were taken into consideration during the research. It may be deduced from these findings that cationic dendrimers, in contrast to their anionic counterparts, are more hazardous to human health. Dose-escalation research was carried out to ascertain the highest dosage of dendrimers that was safe for human consumption. It was found that dendrimers are suitable for consumption via the mouth. In low-dose forms, G7-NH2 and G7-OH are the only ones that exhibit evidence of toxicity (Yellepeddi et al., 2019).

The dendrimers having a cationic group on their external surface tend to interact with RBCs which causes hemolysis. Auclair et al, worked on the toxicity of generations of the PAMAM dendrimers with general antibiotic minocycline in treated wastewater when treated with hepatocytes. The results showed that higher generations of dendrimers are more toxic than lower generations. 5G dendrimers possess toxicity at a lower concentration of 7 µg/mL while 2G dendrimers were toxic at higher doses of 20 µg/mL. Antibiotics alone was well tolerated by hepatocytes even at higher doses of 100 µg/mL. But when introduced with 2G dendrimers (20 µg/mL) it causes toxicity at 70 µg/mL. As toxicity tends to increase when introduced with PAMAM dendrimers but the potency of the antibiotic minocycline was also improved when given with 5G dendrimers. 5G dendrimers double the potency of the drug at the conc. of 35 µg/mL (Auclair et al, 2017).

2.3.9 PPI dendrimers

PPI dendrimers are synthetic polymers discovered by Voegtle et al., in 1978. It is a spherical vesicle consisting of primary and tertiary alkyl amine side chains, commercially available in G0 to G5 generations. PPI dendrimer consists of three parts, center core material, interior branching, and surface branching. The core can be ethylene diamine or 1,4 diamino butane, interior branching consists of tertiary tris-propylene amine and surface branching of primary amine. It is also known as DAB dendrimers based on core material

or POPAM dendrimers due to the presence of polypropylene amine. PPI is comparatively more hydrophobic than any other dendrimers which may be due to the extensive branching of PPI dendrimers (Idris et al., 2020).

2.3.9.1 Synthesis of PPI dendrimers

PPI dendrimers can be synthesized by – the convergent method and the divergent method. The divergent synthesis method starts from the center and progresses toward the surface by coupling with branching units while the convergent synthesis method starts from the exterior towards the center core by conjugating with a branching dendritic structure. Parallelly modern techniques such as Lego chemistry, click chemistry, and hyper core monomeric growth methods can be utilized for the synthesis of the dendrimers. The production process starts from central core moiety. Double Michael's addition of acetonitrile with core material initiates the process of synthesis. In half-generation, -CN is the surface group on which catalytic hydrogenation in the presence of Raney nickel and methanol is converted to -NH2 developing full-generation dendrimers (Kesherwani et al., 2018; Kaur et al., 2016). Another method was given by Majoros et al., who utilized a divergent growth process in two steps, The Initial step includes the Micheal addition of amino group to double bonded methyl acrylate, and in the second step progression of chain length takes place by amidation of the methyl ester with ethylene diamine (Majoros et al., 2008; Mishra et al., 2016).

2.3.9.2 Toxicity and biocompatibility

It has also been proven that the amount of toxicity increases proportionately with increments in generations in dendrimers. In his research, Kesharwani and colleagues found that dendrimers of generation 5G were substantially more harmful than dendrimers of generation 4 (Kesherwani et al., 2014). One of the main reasons that is responsible for cytotoxicity is the incidence of a cationic group on the periphery of the substance. The process of acetylation, pegylation, and amination of dendrimers results in an enhancement in the biocompatibility of these dendrimers (Singh et al., 2021).

2.3.9.3 Comparison of PPI and PAMAM

PAMAM is the commonly used dendrimer with tertiary amine as core material with branching of polyamides. PAMAN dendrimers are readily accessible in different generations (G0 to G5) (Tomalia et al., 2012 A, B). These dendrimers are extensive studied by scientists for diagnostics and delivery of bioactives.

- **Structure**: PPI is the polar vesicle as it contains an alkyl chain with primary and tertiary amine functional groups while the PAMAM dendrimers have an enclosed pocket-like structure. PAMAM contains an alkyl amido chain and like PPI dendrimers it also contains primary and tertiary amine functional groups (Shao et al., 2011).

- **Size and length**: The size and length of PPI dendrimers are smaller as compared to PAMAM dendrimers as PPI dendrimers contain 3 bonds while PAMAM contains 7 bonds.

- **Shape**: PPI dendrimers are spherical while PAMAN dendrimers are globular in shape. The globular shape offers a large surface area for the entrapment of biomolecules (Alamry et al., 2015; Mishra et al., 2011).

- **Generations**: PPI is commercially available in G0 to G5 generation while PAMAM is available in G0 to G10. There are 32 amino groups in the third-generation of PPI dendrimers and fourth-generation PAMAM (Shao et al., 2011).

- **Reactivity**: Both PAMAM and PPI dendrimers can undergo condensation of DNA because of the surface positive charge of the dendrimers. DNA Condensation takes place by transfection.

- **Toxicity and biocompatibility**: Dendrimers tend to show toxicity related to surface amino groups. PPI dendrimer toxicity is related to the amount of surface amine functional group, while the PAMAM shows dose-dependent toxicity. PPI structure shows good biocompatibility while PAMAM dendrimers are commonly conjugated with polyethylene glycol for enhancing biocompatibility (Pyreddy et al., 2014; Kaur et al., 2014)

2.4 Carbon nanotubes

Carbon nanotubes, also known as CNTs, are molecules comprised of cylindrical shapes that are comprised of carbon atoms. Graphene sheets are rolled into a cylinder without any seam which makes the basic structure of CNTs. The aspect ratio of this cylinder is quite

high, its diameter is around 1 nanometer, and its length is numerous micrometers. CNTs have an open end or a capped end. SWCNTs are the outcome of CNTs being formed from a single sheet of graphene, whereas MWCNTs are the product of numerous graphene sheets being combined with MWCNTs. Pristine CNTs are insoluble in water. To improve the solubility of pristine CNTs, surface functionalization with an organic group improves solubility and opens the doors to the possibility of CNTs being used in bioapplications. They can adsorb or react with a different pharmacologically active compound due to the vast surface area that they possess. CNTs can be functionalized to enhance their water dispersibility or to render the correct functional groups that can attach to the therapeutic substance or desired tissue to activate a beneficial effect. This allows CNTs to be used to produce a therapeutic effect. The linked medicinal molecule may have an easier time penetrating through the target cell with the assistance of CNTs, which may then be used to cure ailments (Mishra et al., 2020).

2.4.1 Classification of Carbon nanotubes based on the arrangement

2.4.1.1 Single-walled carbon nanotubes

The SWCNT structure consists of hexagonal rings designed up of carbon atoms like a structure of benzene and consists of only one layer of cylindrical graphene. The graphene sheet structure looks like a honeycomb lattice of crystalline graphite. The cylinder is seamless. The diameter of the cylinder varies from 0.4 to 2 nm. The diameter is affected by the temperature of the process during its synthesis, with the increment of temperature the diameter increases. The structure of SWCNT can be helical, arm-chair, chiral, or zig-zag depending on the wrapping of the cylinder. Nanotubes are considered one-dimensional structures that show a much greater length vs diameter ratio (aspect ratio) of around 1000. SWCNT is suitable for drug entrapment and conjugates because of its higher surface area and exhibits high drug loading capacity. SWCNTs show efficient binding with different kinds of proteinaceous structures as binding is important for cell internalization by phagocytosis. As the structure is internalized in the endosomes, it changes to lysosomes and further to phagosomes by phagocytes (Pandey et al., 2016, Srivastava et al., 2023).

2.4.1.2 Multiwalled Carbon nanotubes

Multiwalled Carbon nanotubes are produced by rolling up two or more graphene sheets. The layers in MWCNT are separated on average by approximately 0.34 nm. All the sheets are rolled down together, forming an individual tube that has a larger diameter than others ranging the diameter from 2.5 to 100 nm. MWCNT possesses more structural defects as compared to SWCNT. It is a less stable nanostructure but continued to be used due to its ease of processing by various researchers. Based on their arrangements of graphite layers, MWCNT structures are further classified into two types: one has a graphene sheet rolled up around it like a parchment-like structure and another is where layers of graphene sheets are arranged within a concentric structure termed the Russian doll model (Karimi et al., 2015). Badea et al., 2018 prepared carboxyl functionalized MWCNT loaded with cisplatin. The biological properties of the formulation were studied using mda-mb-231 cells. Different concentrations were applied to the cells for 24 and 48 hrs. Morphological changes were observed at higher concentrations of the drug cisplatin (1.26 and 2.52g/mL) and MWCNT-loaded cisplatin (2-4g/mL). Cellular viability decreases by 40% after 48 hr for 2.52g/mL cisplatin and 4g/mL MWCNT-loaded cisplatin (Badea et al., 2018, Srivastava et al., 2023).

| a | b |
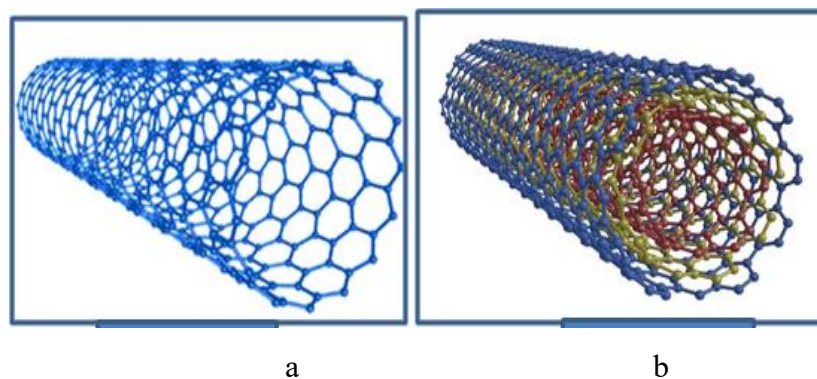
Fig 7: Types of carbon nanotubes (a) SWCNT (b) MWCNT

2.4.1.3 Double-walled Carbon nanotubes

Double-walled carbon nanotubes (DWCNTs) are constructed from two CNTs that are arranged concentrically, so that the outer tube encases the inner tube. The internal and

external diameters of the double-walled carbon nanotubes measure 0.8-1.2 and 1.6-2.0 nm, respectively, as determined by TEM and Raman spectroscopy. The arc-discharge method is used to produce DWCNTs in an environment consisting of a combination of argon and mercury with a volume ratio of one to one and three hundred fifty torrs. The catalyst is made by heating a combination of powders containing Ni, Co, Fe, and S in an environment containing inert gas for one hour at a temperature of 500 degrees Celsius. The majority of the DWCNT bundles have an outside diameter of 1.9-5.0 nm and internal tube diameters that lie between 1.10-4.20 nm utilizing a hydrogen arc discharge method, DWCNTs were produced on a large scale by graphite powder or CNTs as initial material in presence of Fe/Co/S as co-catalyst and growth promoters (Anzar et al., 2020).

2.4.1.4 Triple-walled carbon nanotubes

Triple-walled carbon nanotubes (TWCNTs) stand for 3 graphene sheet layers if they are present (Mehra et al., 2014). TWCNTs have the potential to either be commensurate or incommensurate based on the symmetry and periodicity in the multi-walled tubes. It was previously thought that unequal systems would not provide interactions of IL which can change the electrical and vibrational characteristics of the individual SWCNTs that make up the multi-walled carbon nanotubes. However, recent research has shown that this is not the case (Clancy et al., 2018).

2.4.2 Synthesis of MWCNTs

In the last two decades, many methodologies have been suggested and evolved to meet the growing need for CNTs of consistently excellent quality that can be produced in large quantities. CNTs are synthesized in two ways, as a powder that is substrate-free, and on a substrate. They are arranged in parchment arrangement and arm-chair arrangement.

The first type consists of CNTs that are oriented vertically, which are typically implemented in sensors and other electrical devices. The most prevalent methods for producing nanotubes are known as chemical vapor deposition, arc discharge, and laser ablation. Other techniques are flame synthesis, pyrolysis, electrolysis, ball milling, and high pressure cut out (HPCO) can also be employed for the synthesis. Different techniques used for the commercial production of CNTs are given below.

2.4.2.1 Laser Ablation Method

This method includes the employment of a steady laser of high power to vaporize graphite targets while the targets are contained within a furnace that is heated to 1200 degrees Celsius and pressurized with 500 torrs of argon or helium gas. The CNTs that are synthesized using this process produce roughly 70% and have chirality, high purity, and regulated sizes. Additionally, there are fewer structural flaws in the CNTs. Both SWCNT and MWCNT may be synthesized with the use of this technique. This approach is capable of producing carbon nanotubes that have a high degree of crystallinity. The finished product does, however, contain amorphous carbon as well as catalysts and fullerenes (Kesharwani et al., 2015).

2.4.2.2 Catalytic chemical vapor deposition method

Araga and Sharma employed a process called plasma-enhanced chemical vapor deposition, or PECVD, to generate multi-walled carbon nanotubes at a lower temperature (450 degrees Celsius) straight onto the charcoal of the coconut shell. The minerals act as catalysts in the process of the synthesis of CNTs. Calcium, magnesium, sodium, and potassium act as catalysts that can function at lower temperatures and can bypass the role of iron. X-ray spectroscopy, Raman spectroscopy, SEM, as well as other structural properties, were used to analyze the MWCNTs that were produced. The sizes of the formed CNTs were anywhere between 25 and 30 nm. (Araga and Sharma., 2017).

2.4.2.3 Electrolysis

In this technique, the current was passed through two electrodes by immersing them in molten forms of ionic salts. Lithium chloride heated at 600 ^{0}C, further dissolved in distilled water leads to the extraction of carbon matter. This procedure contributes to the synthesis of 10-15 walled MWCNTs having a diameter ranging from 10-20 nm and a length of >500 nm (Grobert et al., 2007).

2.4.2.4 Pyrolysis

Pyrolysis with the spray pyrolysis method can be used for the synthesis of the MWCNTs. This method contributes to the production of MWCNTs in aligned bundles that have constant diameters throughout. Using ferrocene as a catalyst and ethanol as both a

carbon source and a solvent, at the temperature of 8000 °C. An ultrasonic nebulizer was used to spray the catalyst solution that was dissolved in ethanol into the tubular furnace. Adding feed continuously to the furnace is all that is required to easily scale up the production method (Rao et al., 2004).

2.4.3 Properties of CNT

2.4.3.1 Chirality

A tube-like shape is prepared by rolling the sheet of graphene into a cylindrical structure. The rolled graphite sheet is denoted by the integers n and m, which together are referred to as the chiral vectors. In the honeycomb crystal structure of graphene, the numbers n and m denote the number of unit vectors as well as the two directions. The Zig-zag structure of nanotubes will be represented when m is 0 and appear V-shaped perpendicular to the structure of the axis. If the two integers are equal (m,n), the nanotubes represent the structure of the armchair which has the perpendicular structure of the chair to the axis of the tube. The rest of the vectors are termed chiral when the values lie between m and n. Chirality affects the conductivity of the structure (Wu et al., 2020).

2.4.3.2 CNT dispersion and solubility

Solubility and hydrophilicity are the most important characteristics for any component to be used as pharmaceutical excipients for its biocompatibility and therapeutic delivery. Pristine carbon nanotubes are insoluble, which is the major obstacle in a delivery system. Graphene sidewalls are hydrophobic and assemble as a bundle due to strong p-p interaction between the individual tubes. To utilize the CNT as a delivery system it should possess wettability and alteration of the surface structure to avoid aggregation. Immobilization on CNT sidewalls by covalent binding, transition metal complexes, surface functionalization by chemical modification of sidewall, wet mechano-chemical method, use of surfactants, coating with polymers, biological molecules, binding of pyrroles and pyrenes, and other macrostructures attaching to CNTs are some of the strategies (Naqvi et al., 2020, Srivastava et al., 2024).

2.4.3.3 Physical strength

Carbon nanotubes show a sp2 type of bonding between the carbon atoms which makes them extremely stronger along their axis. This makes carbon nanotubes an extremely strong metal and shows the largest elastic modulus which makes them highly resistant to damage from physical forces. The diameter and chirality of the SWCNT affect elastic modulus while defects in MWCNT affect the elastic characteristics of the CNT. Due to its physical strength and large elastic modulus, it can be bent by pressing on the tip of nanotubes without damaging the tip. The elastic modulus helps to regain its original structure as soon as the force has been removed (Shirasu et al., 2017).

2.4.3.4 Electrical Properties

CNTs behave as metal and exhibit good conducting capacity. The conductive nature depends on the chirality, diameter, and arrangement. Their conductivity is a function of their degree of twist, chirality, and diameter. CNT behaves in a complex manner concerning the electric property. CNT exhibits the properties of metal as well as a semiconductor. Some structures appear to be better than others in conduction. The arm-chair structure shows better conductivity as compared to others. Multiwalled CNT tends to distribute electric current non-uniformly across the cross wall while the SWCNT shows no change in current (Singh et al., 2013).

2.4.4 Toxicity and Biocompatibility of MWCNTs

Different investigations were carried out to study the biocompatibility of carbon material across the cell membrane, osteoblast, neutral cell, fibroblast, immune cells, and various other proteins and ionic systems. CNTs have unique properties, and the electronic properties of CNTs have laid forward the newer way for neural applications.

Carbon nanotubes have enormous potential as a drug delivery vehicle and target delivery system owing to their nano size and size-to-surface ratio, but at the same time nano size and higher surface ratio tend to impart toxicity. Toxicity is due to the smaller size and complete distribution in the biological system. Different physical and dose-related factors affect the toxicity of the CNTs. The concentration of CNTs or the number of CNTs

given to particular organs alters the toxicity of CNTs. Different factors such as the length of CNTs, surface topology, functionalization, and method of manufacturing affect toxicity.

CNT can travel through different biological barriers, enter the blood, transverse through the cell membrane, and can locate intracellularly. CNTs are commonly excreted through the urinary excretion method. They are generally targeted by immune cells and help in the excretion of the CNTs, in case the immune cells fail to identify or eliminate them, they start accumulating in secondary organs. The research suggests that the pristine MWCNT and CNTs which are non-covalently bounded tend to accumulate in organs while the cationic MWCNTs are excreted via urine, this may be due to the solubility of the pristine and non-covalently functionalized CNTs is lesser that cationic functionalized MWCNTs. Dispersibility also contributes to the toxicity of the CNTs, the lesser the dispersibility more the accumulation, which leads to more toxicity. Length of CNT affects the toxicity but during the functionalization process length of CNTs tends to alter which makes it difficult to relate the altered length with toxicity.

Studies revealed that higher concentration SWCNTs are likely to cause toxic effects on neurons and glial cells. CNT tends to agglomerate and due to this it causes reduced cell viability. A study revealed that pristine and functionalized MWCNTs showed a toxic effect on T cells and caused cell death (Prajapati et al., 2022).

Genotoxicity was observed with MWCNTs, primary genotoxicity was due to the direct interaction of CNTs with the cells and secondary genotoxicity takes place by the formation of reactive oxygen species. CNTs also contributed to mutation in animals. The CNTs also contribute to carcinogenicity in animals and humans.

Recent reports suggest the safety and biocompatibility of carbon nanotubes, after IV administration acute toxicity was not observed. CNTs showed long-term accumulation with low toxicity (Francis et al., 2018).

2.4.5 Functionalization for drug delivery

Raw carbon nanotubes have extremely hydrophobic surfaces, which prevents them from being soluble in aqueous solutions. Pure CNTs, on the other hand, are not soluble in any solution at all. Functionalization is one approach that may be taken to solve this issue.

Functionalization of CNTs is a technique of chemical synthesis in which required functional groups may be placed into the surface of CNTs to manufacture functionalized carbon nanotubes (f-CNT). This procedure results in the production of functionalized CNTs. This procedure aims to improve the biocompatibility of the substance within the body, as well as its encapsulation propensity and solubility, multimodal drug delivery, and imaging capabilities, while also imparting particular features that are directly connected to the desired function. Covalently bonded modifications and non-covalently bonded modifications are the two categories that may be used to classify changes made to CNTs (Mallakpour and Soltanian 2016; Mehra et al., 2014).

Iannazzo et al., created a formulation that comprises carboxyl functionalized MWCNT that are loaded with anti-HIV drugs and a hydrophilic functional group. This causes improvement in the hydrophilicity and dispersibility of the structure. The very hydrophilic structure has strong antiviral action; the inhibitory concentration (IC_{50}) values for oxidized MWCNT (ox-MWCNT) were 11.43 lg/mL, and the IC_{50} values for MWCNT-C-CHI360 were 4.56 lg/mL, respectively. According to the findings of the study, integrating carboxylic groups as a functional group makes the structure hydrophilic and demonstrates improved dispersibility, both of which are critical for applications. (Iannazzo et al., 2015).

Pistone et al., studied the antiviral capability of COOH-MWCNTs and their activity as HIV inhibitors *in vitro*. This demonstrated their capacity to react with different enzymes of the virus and suppress HIV *in vitro*. This study used 3TC, a well-known nucleoside antiretroviral medication, and two recently synthesized benzimidazolones, CHI360 and CHI415, which are active NNRTIs. CHI360 and CHI415 treat HIV. This research found that the hydrophilicity and dispersibility of these nanoparticles are the most critical factors affecting antiviral activity. The most successful oxidized samples were hydrophilic and dispersible. with acceptable IC_{50} values (Pistone et al., 2014).

Raw carbon nanotubes are hydrophobic and insoluble in water solutions. Functionalization improves solubility. Functionalized carbon nanotubes (f-CNTs) are produced by chemically introducing functional groups onto CNT walls for diverse uses.

This technique improves biocompatibility, encapsulation, solubility, multimodal drug administration, and imaging with qualities linked to the target purpose. CNT modifications can be covalent or non-covalent (Mallakpour and Soltanian 2016; Mehra et al., 2014).

Afshari et al., synthesized acid and amide functionalized carbon nanotube drug delivery systems which are grafted with chitosan (CS) attached covalently with f-MWCNT and MWCNT bonded with chitosan nanoparticles as a sustained-release system for tenofovir. FTIR, thermogravimetric analysis (TGA), and SEM were used to analyze NPs for drug delivery systems. *In vitro*, MWCNT bonded with chitosan nanoparticles released the most tenofovir (90%) after 120 hours. MWCNT bonded with chitosan nanoparticles had the best cumulative release rate of tenofovir. MWCNT–chitosan is also dispersible and stable in aqueous media, unlike ungrafted CNTs. This confirms MWCNT solubilization and CS grafting. (Afshari et al., 2015).

Zuru et al., acid oxidized CNTs using 3:1 nitric acid (HNO_3) and sulphuric acid (H_2SO_4) to generate carboxylated functionalized carbon nanotubes. Acylation was carried out by thionyl chloride to generate CNT-COCl moieties which are more reactive. Refluxing the acyl chloride with ursonic acid (UA)-pyridine produces the CNT–UA drug matrix. The terpene's C-28 position should covalently connect. The Dakin–The west reaction will exhaust the HIV-gp120 entrance inhibition of CNT-AU in the pyridine. The 4-dimethylaminopyridine catalyst converts the viral glycoprotein into a keto amide. This idea may lead to permanent HIV/AIDS therapy if studied (Zuru et al., 2019).

Hatami et al., suggested that the HIV medication known as azidothymidine (AZT) reacts with both nanotubes and carboxylated nanotubes. The calculations were carried out with the assistance of the hybrid density function of a B3LYP and the basic function 6-31G (d,p) in the solution and gas, polarization of the model for the effects of the solvent, and covalent and non-covalent drug capture on SWCNT. The bond interactions were examined via the amine group, utilizing the anti-HIV drug Azidothymidine (AZT) by Ultrasonic resonance, FTIR spectroscopy, and X-ray diffraction (XRD) methods. This was done to better understand the nature of the bond interactions. CNT groups affect the energy required for non-covalent capture. Interactions between zidovudine and SWCNT that take

place via the amino group generate the most powerful non-covalent complex. Investigations on SWCNT medicine absorption suggest that it is determined by hardness and chemical potential. The FT-IR spectra of the medication including functionalized nanotubes show a peak of acidic functionalized nanotubes that overlaps with the N-H peak of azidothymidine. Because of these conditions, combining medications and interacting with functionalized nanotubes was not possible. Before sonication with carbon nanotubes, the peaks of azidothymidine in the XRD spectrum were quite distinct; however, after interactions with both non-functionalized and functionalized nanotubes, these peaks were less distinct. The non-functionalized form of carbon nanotubes exhibits the least loss in sharpness and differences when compared to pure azidothymidine (Hatami et al., 2019).

Xu et al., investigated EFV delivery through *boron nitride nanotubes* (BNNTs) and CNTs. Dry film thickness was utilized to study EFV's electrical properties and interactions with BNNTs and CNTs. EFV-nanotube intermolecular interactions were studied by analyzing the optimum structure and interaction energy. The findings showed that CNTs may physically absorb EFV while remaining stable. CNTs may deliver EFV. The investigations show that EFV adsorption on nanotubes does not change their electronic properties. The computed interaction energies suggest that CNTs adsorb EFV better than BNNTs because EFV interacts strongly with CNTs. Thus, carbon nanotubes might transfer antiviral drugs intracellularly (Xu et al., 2018).

2.5 Dendrimer–Carbon nanotubes conjugate

To increase drug loading and target to the desired cellular level different approaches have been designed. Supramolecular complexes or conjugates can be prepared in the aspect of increasing the intracellular drug concentration. Dendrimers-carbon nanotube conjugates provide supramolecular chemistry with a high potential for drug loading. The complex is further tagged to designate the target site of action.

To target cancer cells and photograph them, Shi et al., presented an advanced approach for the modification of CNTs using multifunctional PAMAM dendrimers. Within the framework of this methodology, 5G PAMAM dendrimers were conjugated on acid-treated MWCNT. MWCNT was surface architecture with dendrimers with amine terminals. The

conjugated structure was further decorated with fluorescein isothiocyanate and folic acid, followed by acylation of the free amine group on the terminal. This conjugated structure is stable, biocompatible, and dispersible in water. The generated MWCNT/G5NHAcFI-FA conjugate can target desired cancer cells that overexpress folic acid receptors with high affinity, as shown by the findings of *in vitro* flow cytometry and confocal microscopy (Shi et al., 2009).

Herrero et al., created several MWCNT derivatives functionalized with dendrons. These derivatives are distinguished from one another due to a distinguishable large number of tetraalkyl ammonium salts which are positively in charge around the perimeter of the synthesized dendron. Due to positive charges on the surface of MWNTs and the exceptional capacity of CNTs to pass through membranes of cells, the newly developed derivatives serve as excellent vectors for the delivery of siRNA. Using a sequence of noncoding siRNA that has been fluorescently labeled. Herrero et al., were able to show that there is a significant increase in the amount of nucleic acid that is delivered into the cytoplasm of dendrons as they go through successive generations (Herrero et al., 2009).

Garcia et al., created both SWCNTs and MWCNTs, with the SWCNTs yielding 238 mol and the latter 511 mol of pyrrolidine groups per gram, respectively. Both the Kaiser test and thermogravimetric studies were used to determine the total amino groups that were incorporated into the system. Carbodiimide chemistry was utilized in the subsequent stage of the process, which was the inclusion of dendrimers. Thermogravimetric Analysis, Raman Spectroscopy, and Atomic Force Microscopy have been used to characterize the final CNT–dendrimer conjugate (Garcia et al., 2008).

Desmecht et al., established non-covalent contacts among the 2 different components, showing the excellence of grafting procedures, such as click chemistry and xanthene procedure. Desmecht covalently immobilized PAMAM dendrimers on MWCNTs by using two different 'grafting to' strategies. Before reacting with PAMAM or azido-PAMAM dendrimers, MWCNT exteriors were reacted with active ester and propargylic moieties. They examined PAMAM generations, 0 to 3 grafting using XPS, TGA, and TEM. Post-functionalization sequences employing copper alkyne-azidecyclo

addition (CuAAC) provided evidence of the adaptability of our hybrids (Desmecht et al., 2018).

Chopdey et al., demonstrated the cargo system of glycyrrhizin (GL) conjugated dendrimers (GL-PPI) and MWCNTs (GL-MWCNTs) in the direction of liver targeting of doxorubicin (DOX), which is a model anti-cancer agent. FTIR, 1H-NMR, and morphological analyses all came back positive in confirming the synthesis. In the case of DOX-loaded GL-PPI and DOX-loaded GL-MWCNT, a higher DOX loading was detected (43.020.64% and 87.260.57%, respectively), in comparison to the loading seen in the parent nanocarriers. hepatoblastoma cell line (HepG2) cells were used for cytotoxicity experiments using MTT as well as flow cytometry and assessments of cell shape. The IC_{50} value of DOX was decreased from 4.190.05 M to 2.00.01 and 2.70.03 M, respectively, when it was treated with either GL-PPI-DOX or GL-MWCNT-DOX (Chopdey et al., 2015). Phase-contrast microscopy and flow cytometry indicated that GL-conjugated formulations were considerably targeting more cancer cells observed in the initial stage of apoptosis.

To minimize cytotoxicity and improve cellular absorption of the nanoparticles, Pan et al., treated the surfaces of SWCNTs with PAMAM dendrimer. They used MTT and TEM to evaluate the results of cellular absorption of un-coated and dendrimer-coated SWCNT on a human cancer cell line called MCF-7 cells. According to the results of the MTT test, SWCNTs were hazardous to MCF-7 cells; on the other hand, dendrimer-coated SWCNTs were largely non-toxic. Analysis using transmission electron microscopy revealed that dendrimer-coated SWCNTs penetrated the cytoplasm, but uncoated SWCNTs were rejected; this suggested that the SWCNTs-based material's behavior during endocytosis was reliant on surface features (Pan et al., 2006).

Guerra et al. synthesized and analyzed new hybrid materials using carbon nanohorns (CNHs) as a base and various PAMAM dendrimers as a carrier for siRNA. CNHs become more soluble and physiologically favorable once PAMAM dendrimers with different amino groups are added. When PAMAM dendrimers are added, generate a uniform positive charge, improving bio-compatibility. t Au nanoparticles of 1–2 nm

determined PAMAM dendrimers CNH surface localization. The hybrid of newly synthesized compounds' transfection efficiency is displayed. 4th generation PAMAM dendrimers and CNHs link siRNA without cytotoxicity at 25 µg/mL. Unmodified PAMAM dendrimers were hazardous at identical levels in propidium iodide experiments. These non-viral vectors have promising biological data, especially since f-CNH3 and siRNA complex can decrease house-keeping glyceraldehyde 3-phosphate dehydrogenase (GAPDH), messenger RNA, and the protein p42 (Guerra et al., 2012).

Buber et al., (2018) studied the amperometric ability of biosensors of conducting polymer (CP), MWCNTs, and (PAMAM) dendrimer. Graphite electrode was improved by using poly[9,9-di-(2-ethylhexyl)-fluorenyl-2,7-diyl] end-capped with N,N-bis(4-methylphenyl)-4-aniline, MWCNTs, and PAMAM. Glutaraldehyde was used to crosslink Glucose oxidase (Gox) to the modified surface. Then, an examination of biosensors was performed based on kinetics and analytical properties. The result revealed that a linear response was observed. Finally, the constructed biosensor detected glucose in drinks (Buber et al., 2017).

Wen et al., 2013 developed dendrimer-conjugated MWCNTs to target and pH-responsively deliver doxorubicin to cancer cells. This study covalently linked 5G PAMAM dendrimers with amine terminal to acid-treated MWCNTs. The surface potential which was due to remaining dendrimer terminal amines was acetylated. Fluorescein isothiocynates and folic acid-modified acylated PAMAM 5G dendrimers. MWCNT and fluorescein isothiocynates and folic acid-modified acylated PAMAM were characterized using many approaches. The MWCNT and modified dendrimers were loaded with doxorubicin for pH-sensitive delivery to cancer cells that overexpress folic acid receptors. The entrapment efficiency was found to be 97.8%. pH governs the drug release from the designed structure. They also targeted high-affinity cancer cells and suppressed their growth. The dendrimer-modified MWCNTs can be employed for a pH-responsive delivery strategy for many cancer cell types (Wen et al., 2013).

2.6 Mannose as targeting agents

2.6.1 Mannose receptors

Mannose receptors (MR) are the receptors of the C-type lecithin family which consist of glycoproteins. There are four types of receptors of the C-type lecithin family such as gp200-MR6, M-type *phospholipase* A2 *receptor*, DEC-205, and mannose receptors. Mannose receptors are categorized as type-1 transmembrane receptors which have a large extracellular domain consisting of carbohydrate recognization domain (CRDs; 8-10 in numbers), fibronectin type 2 domain, N-terminal cysteine-rich domain and small cytoplasmic chain (Dalle Vedove et al., 2018).
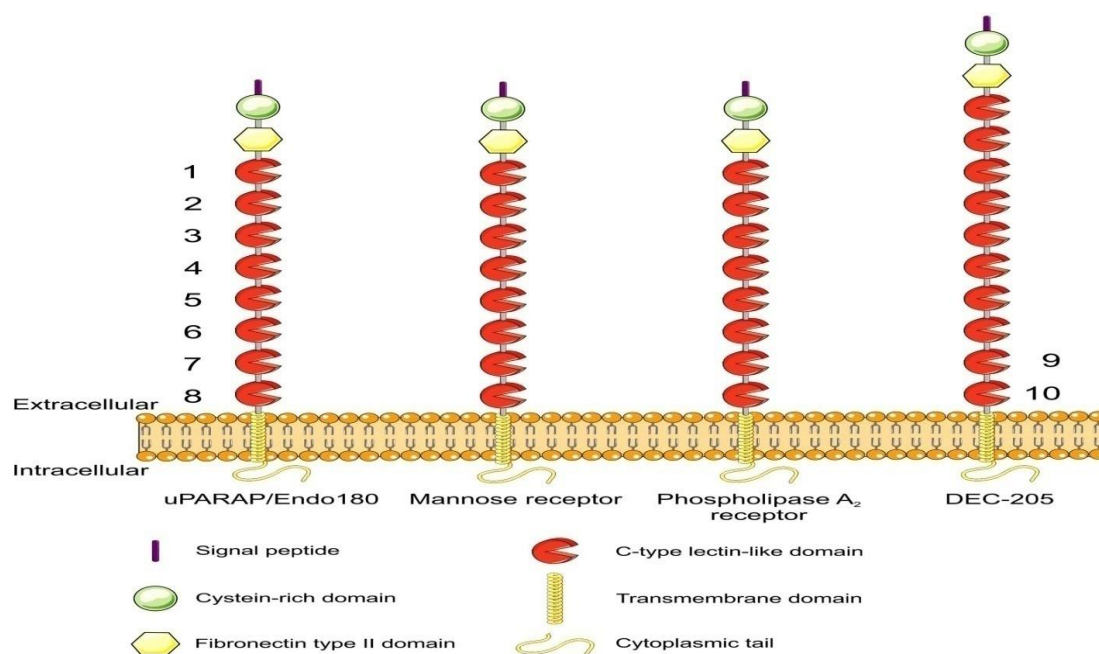
Fig 8: Structure of mannose receptor family (Taylor et al., 2005)

Among all the domains, the CRDs domain can react and bind with fucose, N acetyl glucosamine, and mannose while sulfated sugar binds with the N-terminal domain. There are eight CRDs, among them, CRDs 4 and 5 tend to bind with multivalent glycoconjugates. The CRD protein binds and facilitates the movement of the ligands inside the cells as the protein can shift between the endosomal apparatus and plasma membrane (Dalle Vedove et al., 2018).

MR has also been termed macrophage mannose receptors (MMR) as it was first observed in macrophages, which are expressed in large amounts by immune cells including endothelial cells, macrophages, and dendritic cells. MR is involved in the endocytosis and phagocytosis of the microorganism. It is important in primary defense from external microorganisms as well as a secondary defense mechanism by reserving the antigen and presenting it when required. Immediate immunity in the initial hour of infection was achieved by macrophages and leucocytes. These cells engulf the microorganism and degrade them in lysosomes/phagolysosomes. MR plays another role in adaptive immunity which is commonly found on dendritic cells that engulf the antigen and transfer them to the major histocompatibility complex compartment (Jahagirdar et al., 2019).
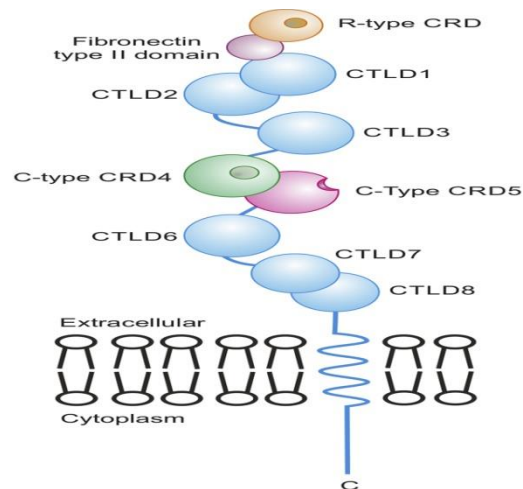
Fig 9: Organization of domains of mannose receptors (Feinberg et al., 2021)

Microphage belongs to the mononuclear phagocyte series, formed by circulating monocytes. These cells are formed by differentiating from monocytes circulating in the blood. Monocytes leave the blood vessels and travel to nearby tissue and turn into macrophages. They govern primary and secondary immunity and function effectively in other pathogenic circumstances. It has an abundance of MR receptors that can bind with glycoconjugates (Ceciliani et al., 2021).

Along with macrophages, MR is present in other immune cells such as Dendritic cells (DC). DC are the immune cells that belong to the leukocyte family and excel in starting and processing innate and secondary immunity. DC internalizes the bacterial or

viral particles and presents antigenic peptides to T and B lymphocytes. DCs are the effective antigen-presenting cells (APCs) with MR for producing immune responses (Dalle Vedove et al., 2018).

2.6.2 Functioning of MR receptors

The receptors facilitate the phagocytosis and endocytosis of the mannose-containing components. This uptake by MR receptors is dependent on their pattern and expression in different cell structures. It also helps in the phagocytosis of a microorganism containing carbohydrates including parasites, gram-positive and negative bacteria, yeast, and similar microbes. In the process of endocytosis, coated pits present in the cytoplasmic region of MRs deal through motifs that recognize and bind with carbohydrate-containing antigens. After the attachment of the antigen to the coated pit, the antigen is internalized and converted into a coated vesicle which further opens and results in the formation of early endosomes. Early endosomes send MR receptors back toward the surface of the cell or the late endosomes. In phagocytosis, antigen binds at the cell surface by their specific structure. The antigen is taken up by actin-dependent movement by membrane forms phagosomes. The phagosome undergoes continuous fusion which generates mature phagolysosomes which are degradative (Filatova et al., 2018).

Mannose receptors are commonly found in macrophages of the liver Kupffer cells, in the alveolar region of lungs, connective tissues such as histiocytes, and the red pulp of the brain cells, spleen, bone marrow, and lymph nodes. It is also observed in dendritic cells, a subset of endothelial cells. It engulfs the antigen and presents it to the Major histocompatibility complex called MHC class I and MHC class II. Many endocytosed compounds undergo dissociation and present it to MHC class I which activates the CD8$^+$ T cells in its early stage. MR receptors also facilitate the soluble antigen fragment to late endosomes and lysosomes where proteolytic degradation takes place. This antigen protein fragment is further taken up and presented in MHC class II molecules which activate CD4$^+$ cells. MRs also help in the release of different cytokines, different enzymes, and the alteration of different surface receptors (Patil et al., 2020).

2.6.3 Mannosylation of the delivery system

Mannose receptors can bind with glycosylated structures and can internalize them. This concept helps in targeting the delivery vehicles to the immune system where MRs are found in abundance. HIV resides in the immune cells making the MR cells the most promising target for anti-HIV drugs. The delivery system is conjugated with mannose, a natural ligand for MRs. The observations suggested that if an antigen is uptaken by Mannose receptors leads to many times a better presentation of antigen to T cells. Mannose binds by non-covalent conjugation or by covalent linkage with the carrier backbone of the delivery system. In the case of covalent linkage, the ligand remains permanently attached to the structure and does not show premature detachment. The non-covalent linkage is formed by excessive non-specific weak bonding between the carrier surface and mannose. As the weak forces are involved which leads to premature detachment of ligands before reaching the target site. Sometimes ligands get detached near the target leading to the binding sites saturation and limiting the uptake of the delivery system (Nahar et al., 2022).

2.6.4 The fate of mannosylated structures

The mannosylated structure expresses a good immune response at the MR of different APCs. After administration, it identifies the APCs (antigen-presenting cells) which are responsible for recognition. Mannosylated structures are rapidly cleared by MMR of liver cells and macrophages in red pulp along with DCs. Targeting the structure of the immune cells requires ligand specificity or specific MMR constructs. When the specific ligand interacts with the mannose receptors, it has its unique pathway of antigen processing and signaling. Mannose on the nanostructure can bind with different receptors on different antigen-presenting cells. Once internalized its fate depends on endosomal enzymes which break down the structure and make the drugs available from the nanostructures (Torrelles et al., 2010).

Jain et al., conducted a study to enhance amphotericin B dendrimeric delivery (AmB). After being synthesized, linked with mannose, and characterized with FTIR, 1H-NMR, and atomic force microscopy (AFM), fifth-generation PPI dendrimers (5G) were shown to be effective. Mannose-conjugated 5G PPI (MPPI) dendrimers were conjugated

with AmB and characterized for different evaluation parameters along with different *ex-vivo* and *in-vivo*. MPPI dendrimers were nanometric and almost spherical, according to AFM. The conjugate entrapped AmB and released drugs pH-sensitively. Without affecting AmB's antiparasitic effectiveness, human erythrocyte, and macrophage toxicity decreased significantly. The formulation selectively uptakes macrophages *in vitro*. Pharmacokinetic and organ distribution studies clarified the formulation's regulated administration. The drug localization index increased considerably in macrophage-rich tissues. MPPI was biocompatible and antileishmanial *in vivo*. According to findings, surface-engineered dendrimers have the potential to be the most effective AmB delivery carrier owing to their high activity and lower toxicity. (Jain et al., 2015).

4G MPPI dendrimers delivered bioactive Gemcitabine Hydrochloride (GmcH) to lung tumor cells by Soni et al. In sodium acetate buffer of pH 4.0, ethylenediamine-cored 4G PPI dendrimers were linked with mannose by Schiff's reaction. IR, NMR, and SEM characterized PPI and mannose-conjugated dendrimers. Equilibrium dialysis into PPI and MPPI dendrimers produced GmcH-PPI and GmcH-MPPI. Drug loading, release kinetics, stability, hemolytic toxicity, cytotoxicity, pharmacokinetics, and biodistribution were assessed. pH-sensitive GmcH dendrimeric formulation showed faster release at pH 4.0 than at pH 7.4. MPPI conjugate decreased human erythrocyte hemolysis compared to 4G PPI dendrimers. GmcH-MPPI demonstrated the lowest A-549 lung cancer cell line cytotoxicity IC$_{50}$. Free drug, PPI-loaded drug, and mannosylated PPI-loaded drug in albino Sprague–Dawley rats were subjected to biodistribution and kinetic studies indicated that the conjugate had a much longer mean residence time of nearly 24 h than the other two. Plain drugs and PPI-loaded drugs demonstrated lower lung drug deposition than GmcH-M-PPI (Soni et al., 2015).

Pruthi et al., explored polysaccharide (mannose) coupled engineered MWCNTs with amphotericin B for targeted macrophage delivery. Dialysis diffusion loaded mannosylated treated CNTs with AmB. Mannosylated MWCNTs were described using SEM, FTIR, TEM, drug entrapment, drug release and kinetics, MTT assay, and *in vivo* studies. 500-nm, tubular amphotericin B-loaded mannosylated MWCNTs showed 75.46 ±

1.40% entrapment efficiency. At pH 4, 7.4, and 10, amphotericin B-loaded mannosylated MWCNTs produced controlled AmB, boosting cell uptake and disposal in macrophage-rich areas and delivering drugs site-specifically (Pruthi et al., 2012).

Gulbake et al., produced artesunate-loaded mannose-linked multi-walled carbon nanotubes for brain-targeted cerebral malaria therapy. Selective oxidation purifies MWCNTs, which were subsequently chemically functionalized by acylation, carboxylation, D-mannose conjugations, and by modification of amine. Equilibrium dialysis loaded artesunate (AS) in a molar ratio of 1:3 of different functionalized sonicated MWCNTs. FTIR, TEM, elemental analysis, and drug entrapment were performed on functionalized MWCNTs. The *in vitro* drug release investigation used AS-M-MWCNTs. An albino rat bio-distribution research quantified AS in organs and blood. M-MWCNTs were open tubular in TEM images, whereas AS-MWCNTs showed AS entrapment. AS-M-MWCNT had 80.29±3.4% drug entrapment. AS-M-MWCNTs released AS *in vitro* at pH 7.4. Bio-distribution experiments show that AS-M-MWCNTs increase brain AS accumulation better than conventional therapy (Gulbake et al., 2019).

Gupta et al., construct sulfasalazine (SSZ)-loaded fucosylated MWCNT for liver kupffer cell targeting to treat cytokine-induced liver injury. After dialysis membrane functionalization (carboxylation, acylation, amidation), sulfasalazine was added to fucosylated MWCNTs. *In vitro* and *in vivo* research on macrophages J 774 targeting Kupffer cells. Sulfasalazine-loaded fucosylated MWCNTs showed 87.7 ± 0.11% of drug loading. Sulfasalazine-loaded fucosylated MWCNTs released 89.12 ± 0.71% of SSZ at 48 hr. Sulfasalazine-loaded fucosylated MWCNTs decreased hemolysis from 21.62 ± 0.24% to 9.01 ± 0.23%. Sulfasalazine-loaded fucosylated MWCNTs were more cytotoxic than raw and SSZ-MWCNTs in the SRB test. Sulfasalazine-loaded fucosylated MWCNTs inhibited interleukin-12 p40 secretion better in the cytokine test. Sulfasalazine-loaded fucosylated MWCNTs decrease nuclear factor-B activation in Western blot (Gupta et al., 2014).

2.7 Characterization

2.7.1 Fourier transform Infrared Spectroscopy

Fourier transforms infrared Spectroscopy is a useful tool for understanding different functional groups in the chemical structure. It is also used to study biological specimens. The technique is simple, efficient, and reproducible. It doesn't require any additional reagent and is non-destructive. The sample size required for sample preparation is very low, ranging from nanograms to micrograms (Su et al., 2020). IR range used for the spectral analysis is 400-4000 cm-^{1}. This region supports the conversion of transitional energy to vibrational energy for the majority of the function group. Based on the position of IR bands, wave numbers can be co-related with different chemical components (Mohamed et al., 2017).

2.7.2 Nuclear Magnetic Resonance Spectroscopy

Nuclear magnetic resonance spectroscopy is a promising method for understanding the structures of chemical molecules. The first technique of NMR is proton NMR reported in 1963. There are different types of NMR such as Proton (^{1}H), Carbon (^{13}C), Nitrogen (^{15}N), Florine (^{19}F), Phosphorous (^{31}P), and ^{1}H have frequently been used method due to higher sensitivity and short relaxation time. ^{19}F and ^{31}P are used for higher specificity of the molecular structure. NMR spectroscopy has a quantitative nature to the signal, which can be directly related to the number of nuclei. This technique can be for small as well as for macromolecules and gives accurate results for single as well as multi-component complex mixtures (Bharti et al., 2012).

2.7.3 Raman Spectroscopy

Raman spectral method of analysis is the specialized method for determining the shift in frequency of light scattered from the sample when the applied light hits the molecule and produces the scattering. When the scattering light of a lower frequency comes out from the sample than the incident light it is termed stroke Raman scattering and when a higher frequency is observed termed anti-stroke Raman scattering. A higher frequency can be observed when the proton takes up energy from bonds that are already in an excited state of vibration. The energies are either gained or lost based on the energy level of the

molecule. The spectra plotted correspond to the wave number of the incident light. Raman shift is the difference between incident and Raman scattered light which is specific for a particular molecule and is detected by the detector (Movasaghi et al., 2007; Rostron et al., 2016).

2.7.4 Differential scanning calorimetry

Differential scanning calorimetry (DSC) is the thermal method of analyzing the uptake of heat energy by the sample in increasing and decreasing temperature in a controlled manner. A calorimeter is the device used to study the phase transition. It helps study the single molecular transition of molecules from one phase to another. DSC helps to determine the glass transition temperature, melting point, related enthalpy, entropic changes, and other changes related to latent heat or heat changes. An equal amount of heat is applied to the sample cell as well reference cell. The difference in the amount of energy taken up by the sample cell concerning the reference cell as compared to input energy governs whether heat is released or absorbed. If heat is released during the process, it is termed an endothermic process and if heat is evolved during the process, the process is exothermic (Gill et al., 2010).

2.7.5 X-ray diffraction

X-ray diffraction is the technique that helps to investigate the crystal lattice and the physio-chemical properties of the powdered material. The crystal structure shows the periodic arrangement of the atoms which tends to diffract light at a particular angle. The principle of powder XRD relates to the X-ray scattering that produces the pattern to elucidate the arrangement of atoms in the crystalline structure. For diffraction patterns, the particles should be in a periodic array like in crystal structures. Amorphous material does not have long-range periodic order; hence no diffraction peak pattern is observed.

In X-ray diffraction, X-rays are produced and targeted on the crystal structure leading to diffraction of the incident radiations which is processed and displayed by the diffraction pattern. The intensity of light is plotted against the angle of the detector, 2θ (Raja et al., 2022). Bragg's law defines the relationship between the angle of incident of an X-ray and the d-spacing between the atoms of the crystals. The technique is simple,

reliable, non-destructive, and highly sensitive and can be used to analyze crystalline to amorphous materials (Chouhan et al., 2014; Khan et al., 2020).

2.7.6 Field emission scanning electron microscopy

Field emission scanning electron microscopy (FE-SEM) is the microscopic technique used for the analysis of the surface morphology and chemical characteristics of micro/nanostructures. FE-SEM is used to magnify the image by 3,00,000x to 10,00,000 based on models. The system consists of a sample holder with a pressure system. The emitted signals from the samples are collected by detectors. The instrument consists of a source to produce electrons of high energy with the help of an electron gun. Long column for electron traveling across many electromagnetic lenses and scan coils for deflection. Two types of electron detectors are available for the detection of images (backscattered and secondary electron detectors). The system includes a sample chamber and computer system for displaying the scanned image (Mohammed et al., 2018; Inkson et al., 2016).

2.7.7 High-resolution transmission electron microscope

Transmission electron microscopy is an effective method of determining the dimensions of 100nm or less. It is an effective tool for studying the morphology of nanosized structures, film composite, and reverse osmosis membranes. The instrument includes an electron gun generating electron beam, metal aperture, and electromagnetic lens. The electrons are deflated by magnetic and electric fields due to the negatively charged particles. A specific electron beam is subjected to the surface of the specimen placed on a metal frame and carbon-based film. Different factors such as composition or thickness affect the TEM electron (Inkson et al., 2016).

2.8 Drug profile

2.8.1 Nevirapine

Description: Nevirapine is a white to off-white powder. It is crystalline.

Molecular structure:
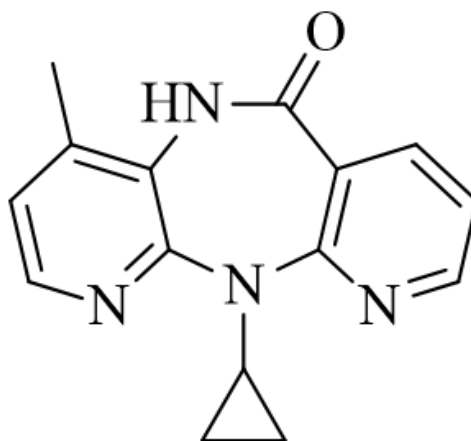
IUPAC name: 2-cyclopropyl-7-methyl-2,4,9,15-tetrazatricyclopentadeca-1(11),3,5,7,12,14-hexane-10-one

Molecular formula: $C_{15}H_{14}N_4O$

Molecular weight: 266.30

Melting point: 247-249 °C

Solubility: 0.7046 mg/L in water

Log p: 2.5

Pka: 2.8

Category: Non-nucleoside reverse transcriptase inhibitor (NNRTI) (PubChem)

Pharmacodynamics

Nevirapine is an effective drug for the treatment of HIV-1 type while found ineffective against HIV-2 and human DNA polymerase. It is non-nucleoside reverse transcriptase (NNRTI). The drug tends to develop resistance if taken alone hence always taken with other drugs. The drug is usually prescribed after the decline of the immune system (Usach et al., 2013).

Mechanism of action

Nevirapine attaches with reverse transcriptase and inhibits the DNA polymerase effect by interrupting the catalytic site of enzymes.

Pharmacokinetics

Absorption and Bioavailability

After a 200 mg single dose, the peak plasma concentration reached 2 ± 0.4 µg/mL. The peak plasma concentration gradually increases with multiple dosing regimens. Nevirapine absorption is not affected by food and therefore can be administered before or after a meal. Nevirapine shows 90% absorption in healthy individuals and HIV-infected persons. The bioavailability of immediate-release tablets and suspensions is almost similar and comparable and can be interchanged at the dose of 200 mg.

Distribution

Nevirapine showed 60% plasma proteins binding in plasma. The concentration of the drug in cerebrospinal fluid was found to be 45% contributing to the non-bounded fraction of the drug. The drug remains almost non-ionized in physiological pH due to its lipophilic nature. The apparent volume of distribution was found to be 1.21 L/kg indicating the thorough distribution of the drug in the body fluids.

Metabolism and elimination

The drugs are metabolized extensively in the liver by cytochrome p450 metabolism to hydroxylate metabolites. The drug undergoes metabolism by cytochrome P450 enzymes, conjugating with glucuronides and eliminated through urine. Only 3% of the non-metabolized drug is excreted through urine thus it shows that the drug is transformed by the liver. The half-life also tends to decrease with multiple injections due to the alteration of hepatic activity (RxList virumine).

Adverse effect

Patients who were given Nevirapine have been reported to experience severe, and even fatal hepatic toxicity. This includes cholestatic hepatitis, fulminant hepatitis, necrosis of hepatic cells, and hepatic failure. Over many days, the manifestations proceeded to liver failure with elevated transaminases, with or without hyperbilirubinemia, extended partial

thromboplastin time, and/or eosinophilia, and many others. If Nevirapine treatment is stopped due to hepatitis, it should be stopped for good, and starting back up again should not be considered an option (RxList virumin; Pawar et al., 2015).

Interactions

When Nevirapine is given in conjunction with a protease inhibitor, extreme caution is essential since the level in the blood of the protease inhibitors may drop to levels below those considered therapeutic as a result of the accelerated hepatic metabolism caused by Nevirapine.

Cimetidine and Nevirapine used together can cause an increase in the steady-state concentration of Nevirapine at its lowest point, therefore adjusting the dose might be required.

Nevirapine lowers the AUC values of oral contraceptives containing estrogen; hence, oral contraceptives are not supposed to be used if Nevirapine is recommended to women of reproductive age. Nevirapine lowers the AUC values of oral contraceptives containing estrogen. When ketoconazole and Nevirapine are taken at the same time, there is a considerable decrease in the level of the blood ketoconazole with little increase in the concentrations of Nevirapine. Taking these two drugs at the same time is not advised (PubChem virumine)

Marketed formulation: There marketed formulations are available as immediate-release tablets, sustained-release tablets, and oral suspensions.

2.8.2 Fosamprenavir calcium

Description: White to off-white powder, a prodrug of amprenavir

Molecular structure:
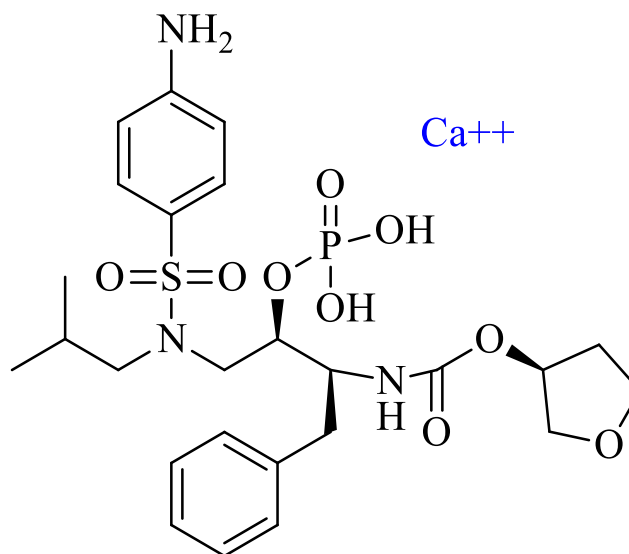
IUPAC name: [(3*S*)-oxolan-3-yl] *N*-[(2*S*,3*R*)-4-[(4-aminophenyl)sulfonyl-(2-methylpropyl)amino]-1-phenyl-3-phosphonooxybutan-2-yl]carbamate

Molecular formula: $C_{25}H_{36}N_3O_9PS$

Molecular weight: 585.6

Melting point: 315-318 °C

Solubility: 0.31 mg/mL in water

Log P: 2.2

Pka: 1.7

Category: Protease inhibitor (PubChem Fosamprenavir compound)

2.8.3 Amprenavir

Description: It is a white crystalline powder.

Molecular structure
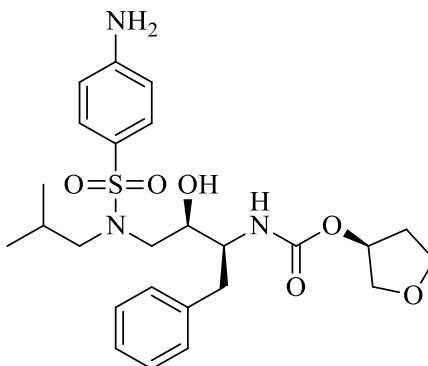
IUPAC name: [(3*S*)-oxolan-3-yl] *N*-[(2*S*,3*R*)-4-[(4-aminophenyl)sulfonyl-(2-methylpropyl)amino]-3-hydroxy-1-phenylbutan-2-yl]carbamate

Molecular formula: $C_{25}H_{35}N_3O_6S$

Molecular weight: 505.628 g/mol

Melting point: 72-74 °C

Solubility: 0.0491 mg/mL in water

Log P: 2.2

Pka: 2.39

BCS class: BCS class II

Pharmacodynamics

To produce the antiretroviral protease inhibitor amprenavir, Fosamprenavir must first be digested by cellular phosphatases. This hydrolysis enables a delayed release of amprenavir, which in turn decreases the total number of tablets that a patient needs to consume.

Mechanism of action

Fosamprenavir is a prodrug that, once it is taken into the body, is quickly converted to amprenavir by cellular phosphatases in the epithelium lining the stomach. (Crowe et al., 2017; Rxlist Agenerase).

Pharmacokinetics

Absorption and Bioavailability

It has not been determined whether or not acyclovir increases the absolute bioavailability of amprenavir in people when taken by mouth following the administration of amprenavir. Both acyclovir oral suspension and acyclovir tablets provided similar amprenavir exposures (AUC) following administration of a 1,400 mg dose in the fasted state.

Distribution

Extremely high (about 90%), with the majority of it being attached to alpha 1-acid glycoprotein. When there is a higher quantity of amprenavir in the serum, there is also a greater amount of free amprenavir.

Metabolism and elimination

In the epithelium of the stomach, during the process of absorption, Fosamprenavir calcium is digested almost entirely into amprenavir and inorganic phosphate. This happens before Fosamprenavir enters the systemic circulation. The cytochrome P450 3A4 (CYP3A4) enzyme system is responsible for the metabolic breakdown of amprenavir in the liver. The amount of unmodified amprenavir that is eliminated in feces and urine is quite low. Because the renal elimination of unaltered amprenavir accounts for only about one percent of the total dosage, renal impairment is not anticipated to have a substantial influence on the elimination of amprenavir. The metabolite amprenavir has an elimination half-life in plasma of approximately 7.7 hours (RxList Agenerase).

Adverse effect

There have been reports of skin responses that are either extremely severe or potentially fatal. Diarrhea, rash, nausea, vomiting, and headache were the most prevalent adverse effects that ranged from mild to severe in severity throughout clinical studies of Lexiva.

Interactions

Amprenavir, the active metabolite of Fosamprenavir, inhibits CYP3A4 metabolism and should not be given with narrow-therapeutic-window CYP3A4 substrates. Amprenavir seems to stimulate CYP3A4.

CYP3A4 metabolises amprenavir. Lexiva and CYP3A4 inducers like rifampin may diminish amprenavir concentrations and efficacy. Lexiva with CYP3A4 inhibitors may raise amprenavir levels and have undesirable consequences.

Ritonavir, a powerful CYP3A4 inhibitor, reduces Lexivab 's medication interaction risk. Lexiva with ritonavir may influence the amount of CYP3A4-mediated medication interactions (impact on amprenavir or co-administered medicine). Lexiva with ritonavir may interact with CYP2D6-metabolized medications due to ritonavir's inhibition. Other drugs can cause life-threatening interactions (Drug bank Amprenavir).

Marketed formulation

Fosamprenavir calcium is available in film-coated tablets, capsules, and oral suspension.

Chapter 3

Rational of the study

3.1 Hypothesis

Acquired immunodeficiency syndrome (AIDS) is a life-threatening disease caused by a human immunodeficiency virus (HIV) belonging to the Reoviridae family. This disease has marked its global presence with approximately 38.4 million people suffering from the disease, concentrated in sub-Saharan Africa. The disease progresses gradually and may take 10 years to develop the disease. The virus preliminary targets T-lymphocytes destroying the host immune system and making individuals vulnerable to various preliminary infections, autoimmune diseases, and malignancies (Merino et al., 2017). The virus tends to form preliminary reservoirs in different target organs which are inaccessible to regular anti-retroviral therapy (ART) (Chun et al., 2015).

This disease lacks effective treatment for its complete cure but continuous treatment with ART improves the quality of life and extends the normal life span of an infected person. Treatment focuses on increasing the $CD4^+$ cell count, decreasing the HIV reservoirs, and controlling opportunistic infections. A combination of drugs is given to the patients termed highly active antiretroviral therapy (HAART) to control resistance developed by viruses. HAART has improved the life expectancy of patients. In 2021, 75% of infected people accessing the HAART, showed viral suppression. But HAART has many limitations such as adherence to the strict regimen, drug resistance, adverse effects of the drugs, and cost of the drug. Viral reservoirs are the intracellular reservoirs of HIV that are inaccessible to traditional HAART. As the drug itself cannot be targeted to the intracellular locations, a nanosized delivery system can be designed to carry the drugs to the desired site in an intracellular location and reduce the viral load (Maitre et al., 2015).

Dendrimers are highly branched structures developed in a step-wise pattern starting from the central core towards the periphery. The structure of dendrimers comprises a central core, with layers of repeating units, followed by terminal functional groups. The terminal functional groups control the pharmacokinetic properties of the structure. Dendrimers can alter the pharmacokinetics of the attached drug molecules by conjugating them with peptides, proteins, and specific antibodies (Yellepeddiet al., 2019). Dendrimers are polyvalent and possess high solubility potential, which improves the solubility of

hydrophobic drugs. It also possesses the self-assembling property due to intermolecular forces which balance the individual forces. Due to the self-assembling supramolecular structure is generated, which possesses high drug-loading capacity. PPI dendrimers are polar vesicles with spherical shapes (Murugan et al., 2013). PPI dendrimer consists of three parts, center core material, interior branching, and surface branching. PPI is comparatively more hydrophobic than any other dendrimers which may be due to the presence of extensive branching of PPI dendrimers (Idris et al., 2020). PPI dendrimers have good biocompatibility as compared to PAMAM dendrimers and hence selected for further studies.

Carbon nanotubes are cylindrical nanostructured carriers made by rolling graphene sheets. In the year 1991, a Japanese scientist by the name of Sumio Iijima published the first report on them. Single-walled carbon nanotubes (SWCNTs) are CNTs made from a single graphene sheet, whereas multi-walled carbon nanotubes (MWCNTs) are made by rolling up many graphene sheets. SWCNTs and MWCNTs both have diameters in the nm range, but their lengths may reach several mm (Mishra et al., 2018). The unique structural, mechanical, electrical, and thermal characteristics of the CNTs are thought to make them suitable candidates for therapeutics and diagnostics. The vast surface area of CNTs makes it possible to adsorb or link substantial concentrations of the drug onto them. Controlled drug administration may also be accomplished by modifying CNTs with stimuli-responsive materials (Mishra et al., 2022). Carboxylated MWCNT are selected for further studies.

The proposed research work worked on designing of novel conjugate structure using 5g PPI dendrimers and COOH-MWCNT (Dendritubes) for effective and targeted treatment of HIV. Dendritubes are designed using COOH functionalized carbon nanotube which is surface decorated with 5G PPI dendrimers. Dendrimers have good drug-loading capacity but contribute to potential toxicity due to terminal amine groups. COOH-MWCNT also has good loading capacity but with compromised water solubility. The surface engineering of MWCNT with 5G PPI dendrimers magnified the surface area many times as dendrimers attached to the externals of COOH-MWCNT, which enhances the drug loading capacity of the dendritube structure. Dendrimers also help to improve the solubility

of the MWCNT as dendrimers are highly hydrophilic. The conjugation took place between the amine group of 5G PPI dendrimers and COOH of MWCNT, reducing the surface amine groups of dendrimers, which reduces the toxicity of dendrimers. Thus, the novel structure, dendritubes have high drug loading capacity with lesser toxicity and better water solubility.

Anti-HIV drugs of two different categories such as Nevirapine belonging to the NNRTI class and Fosamprenavir calcium belonging to the protease inhibitor category were selected to be loaded on dendritubes. The drugs used for HIV treatment have severe side effects due to which the dose of the drug needs to be compromised. Dendritubes enabled higher loading of the drugs due to higher loading capacity.

HIV tends to accumulate in the intracellular spaces making ART inefficient. The target specificity is achieved by tagging the dendritubes with mannose. The primary sites of HIV localization are the immune cells, including monocytes, and macrophages. These cells are primarily found in the blood, liver, spleen, and lungs. Immune cells especially the macrophages have abundant mannose receptors (MR) that can bind with glycoconjugates and internalize them. Thus, tagging the delivery system with mannose will help to target the dendritubes to the macrophages. Mannose will assist in conjugating dendritubes with MR of macrophages followed by internalization of drug-loaded dendritubes in the intracellular vicinity. Hence the structure gets direct access to viral reservoirs and can deliver the drug in the required quantity at target sites.

Thus, the present work is focused on developing a delivery system with COOH-MWCNT and 5G PPI dendrimers termed dendritubes for the treatment of HIV. Anti-HIV drugs Nevirapine and Fosamprenavir calcium are loaded individually on dendrimers, COOH-MWCNT, and dendritubes (DT). Finally, both drugs are loaded on DT. The drug-loaded dendritubes are further mannosylated to enhance the target efficiency. The formulated drug-loaded formulations are evaluated by different characterization techniques. The novel delivery system dendritubes enhances the drug loading capacity, reduces toxicity, and improves dose efficiency, and target specificity. The system can efficiently and specifically be targeted to viral reservoirs.

3.2 Aim

Formulation Development, Characterization and Evaluation of Anti-HIV Potential of Dendrimer-Carbon Nanotubes Conjugates (Dendritubes)

3.3 Objective

❖ To develop and characterize dendrimer-carbon nanotube conjugates (dendritubes).

❖ To develop and characterize drug-loaded mannosylated dendrimer-carbon nanotube conjugates (dendritubes).

❖ To perform *in vitro* cytotoxicity and cell internalization studies.

❖ To perform *in vivo* biodistribution studies of developed formulations.

Chapter 4

Experimental work

The list of materials used throughout the study was listed in Table 2 along with the respectivesource.

Table 2. Various materials used in the research work

Material	Source
Acetic acid	S.D Fine Chemicals, India
Acetone	Loba Chemie Private Limited, India
Acetonitrile (HPLC grade)	Rankem, India Limited., India
Amprenavir	S and G lab supplies, Chandigarh, India
Buffer capsules pH 7.0 ± 0.05	Qualigens Fine Chemicals, India
Chloroform	Loba Chemie Private Limited, India
COOH-MWCNTs	Adnano Technologies Pvt Ltd, India
PPI Dendrimers	Gift sample from Prof. N.K. Jain, H. S. Gour Central University, Sagar, India
Dialysis membrane-110 (LA395)	Himedia Lab Private Limited, India
FITC dye	Sigma Aldrich, USA
Formaldehyde	Loba Chemie Private Limited, India
Formic acid	Loba Chemie Private Limited, India
Fosamprenavir calcium	Gift sample from Lupin Laboratories, Pune, India
Hydrochloric acid	Loba Chemie Private Limited, India
Mannose	Sigma Aldrich, USA
Methanol AR grade	S.D Fine Chemicals, India
Methanol HPLC grade	Rankem, Avantor Performance Materials India Ltd., India
Millipore water	Bio-Age Equipment Ltd., India
Nevirapine	Gift sample from Emcure Pharmaceuticals, Pune India
n-octanol	Loba Chemie Private Limited, India

Potassium dihydrogen orthophosphate anhydrous purified	Central Drug House Pvt. Ltd., India
Sodium chloride 99.5% extra pure	Loba Chemie Private Limited, India
Sodium hydroxide	Loba Chemie Private Limited, India
Sodium acetate	S.D Fine Chemicals, India
Sodium phosphate dibasic anhydrous 98% Purified	Loba Chemie Private Limited, India

Instruments and equipment

Instruments and equipment used in various stages of research work were enlisted in Table 3 along with its model/manufacturer details.

Table 3. List of instruments and equipment used in various stages of work

Instruments/equipment	Model/Manufacturer details
Analytical balance	AX200 Shimadzu Analytical Pvt. Ltd., India
Atomic force microscopy	Veeco (XE100), Plainview, New York, United States
Differential scanning calorimetry	Perkin Elmer, Waltham, Massachusetts, United States
Digital ultrasonic cleaner	LMUC-4 Labman Scientific Instruments Serial No: L10321, India
Diode array detector	SPD-M20A Shimadzu, Japan
FTIR spectroscopy	Perkin Elmer, Waltham, Massachusetts, United States
Hot air oven	Q-5247, Navyug, India
Nylon membrane filter (0.45 µm)	Millipore, Germany
Nanoparticle size analyzer	Malvern Zetasizer, Nano ZS90, Malvern Panalytical Ltd., UK
NMR spectroscopy	Avance NEO 500mhz, FT-NMR spectrophotometer, Bruker, Switzerland
Optical microscope	KYOWA, Getner Instruments Pvt. Ltd., Japan
pH meter	Phan, Lab India, India
Raman spectroscopy	Bruker RFS 27 MultiRAM FT Raman Spectrophotometer, Switzerland
Field emission Scanning electron microscopy	Jeol, Akishima, Tokyo, Japan

Transmission electron microscopy	JEM-2100 plus Electron microscope, Jeol Ltd., Japan
Tissue homogenizer	REMI RQ-1, India
Ultracentrifuge	REMI, RM-12C, REMI Elektrotechnik Ltd., India
High-performance liquid chromatography (HPLC) equipped with a degasser unit and pump system	DGU-20 A5 prominence degasser with LC-20AD/T prominence Liquid Chromatograph Shimadzu, Japan
UV Spectrophotometer	UV-1800, Shimadzu Co.Ltd., Kyoto, Japan
Stability chamber	REMI-WSC 100, India
X-Ray Diffraction	Bruker, Switzerland

4.1 Preformulation studies

Preformulation studies extensively cover different physiochemical properties, analytical, pharmaceuticals, and biological characteristics of the newly developed drug molecules. Preformulation studies for dosage form development should include characterization and physiochemical studies of the excipients. These studies give an insight into the development of the dosage form. The pre-formulation studies are important and provide a smooth runway for the formulation of safe, effective, stable, cost-effective, and stable products. Different pre-formulation studies were done for the drug Nevirapine (NVP), Fosamprenavir calcium (FPV), and Amprenavir (AVP). Similarly, the preformulation studies were carried out for dendrimers and COOH-MWCNT (Chaurasia et al., 2016).

4.1.1 Physical properties

The physical appearance of FPV and NVP was noted visually. The following common physical properties were noted:

❖　　Colour

❖　　Odor

❖　　Appearance

4.1.2 Melting point detection of the drug

Estimation of melting point is the foremost technique for representing the purity of the sample. The temperature at which the solid co-exists with liquid in equilibrium under external pressure is termed the melting point. The presence of impurity was indicated by lowering or broadening the melting point range.

The sample of NVP and FPV was subjected to melting point determination by the capillary tube method. The drug was packed in the glass capillary tube by sealing at one end and fitted in a melting point determination apparatus. The sample was observed continuously until it was completely melted. The melting range (from the onset of melting till completely melted) reading was noted thrice (Jobli et al., 2019).

4.1.3 Solubility studies

Solubility of both the drugs, FPV and NVP was determined in methanol, water, and phosphate buffer saline (PBS) of pH 7.4 and acetate buffer pH 5.0. The drug was added in a surplus to each solvent separately. The systems were shaken for a certain period. Small increments in the amount of drug were done in each solution separately until a saturated solution was formed. Saturation was confirmed by the presence of undissolved material in the solution. Then all the solutions were kept on a rotary shaker for 24 h at ambient temperature. After 24 h, the solutions were filtered, and the filtrate was diluted and spectrophotometrically analyzed at 265 nm for FPV and 283 nm for NVP in a UV-Visible spectrophotometer (UV-1800 series Shimadzu). The experiment was performed three times, and the average was noted (Bhandaru et al., 2015).

4.1.4 Partition Co-efficient Studies

The partition coefficient is an important measurement in the process of preformulation. It gives a clear idea about the diffusion of the drug by passive mode. The Hansch method helps to estimate the partition coefficient of drugs using water and *n*-octanol. The drug NVP and FPV were added to the n-octanol: water system separately and kept aside for 24 h. The solvent from both layers was collected and a UV spectrophotometer was used to analyze at 283 nm for NVP and 265 nm for FPV (Chimiel et al., 2019).

4.1.5 Determination of ultraviolet absorbance maxima (λmax)

For determining the absorbance maxima (λmax), scanning was carried out in methanol. With the appropriate dilution of the standard stock solution with respective solvents, (UV-1800, Shimadzu) against a blank solution. FPV and NVP solutions (10 μg/mL) were used to record the spectrum. From the spectra obtained, the absorbance maxima (λ_{max}) were determined for both NVP and FPV (Bhavyasri et al., 2019; Cyganowski et al., 2022).

4.1.6 Preparation of standard calibration curves (pH 5 and pH 7.4)

The standard calibration curves of NVP and FPV were prepared in methanol: phosphate buffer (40:60) in the range of 5.0-27.5 μg/mL concentration at 265 nm and NVP were prepared in methanol: phosphate buffer (40:60) and methanol: acetate buffer pH 5.0 (40:60) in the concentration range of 5.0-25.0 μg/mL at 283 nm. For the standard

calibration curve of FPV and NVP, 10 mg of each FPV and NVP were weighed and placed in a separate volumetric flask. To this sufficient quantity of methanol: phosphate buffer pH 7.4 and methanol: acetate buffer pH 5 (40:60) in a volumetric flask of 10 mL. The desired volume was maintained with methanol: PBS pH 7.4 and methanol: acetate buffer pH 5.0 (40:60) which gives 1000 µg/mL standard stock solution-I (S-I). 1mL was withdrawn from the stock solution-I (SS-I), shifted into another volumetric flask of 100 mL, and the volume was maintained with methanol: phosphate buffer pH 7.4 and acetate buffer pH 5.0 (40:60) to get a second stock solution-II (SS-II), having a concentration of 100 µg/mL. From the second stock solution (SS-II) various concentrations were prepared respectively. The absorbance of final solutions was measured at 265 nm for FPV and 283 nm for NVP in a UV-visible spectrophotometer (UV-1800 series Shimadzu). The calibration curve was plotted using the Microsoft Excel program and statical parameters were applied and determined (Bhavyasri et al., 2019; Cyganowski et al., 2022).

4.2 Characterization of drug NVP, FPV, dendrimers, and carbon nanotubes

4.2.1 UV spectrophotometer

For determining the absorbance maxima (λmax), scanning was carried out in methanol. With the appropriate dilution of the standard stock solution with respective solvents, the solutions were scanned between 200-400 nm with a UV-visible spectrophotometer (UV-1800, series Shimadzu) against a blank solution. Dendrimers and carbon nanotube solutions (10 µg/mL) were used to record the spectrum. From the spectra obtained the absorbance maxima (λ_{max}) of the drug was determined.

4.2.2 FTIR spectrophotometer

The spectra of FTIR of 5G PPI dendrimers and COOH-MWCNTs were taken separately to study the structural characteristics. KBr pellets were prepared with the samples of MWCNT and dendrimers by triturating KBr pellets uniformly. The pellets were exposed to the IR beam and the spectrum was determined between 4000-400 cm^{-1}. The instrument used was FTIR spectrophotometer (Perkin Elmer 100 Series, USA). The spectra of the drugs, dendrimers, and MWCNT were studied (Mirali et al., 2021).

4.2.3 Differential Scanning Calorimetry

Differential Scanning Calorimetry studies are the thermal studies that help to study the thermal properties such as melting point, exothermic onset temperature, reaction order, activation energy, and extent of reactions. The drugs FPV and NVP were subjected to thermal analysis to confirm the melting point and to study the purity of the drug. The sample was placed on the aluminum pan and packed properly. The heating rate was set from 2 °C/min using DSC (Perkin Elmer, Massachusetts, United States), (Hsieh et al., 2010; Chountoulesi et al., 2019).

4.2.4 X-Ray Diffraction

X-ray diffraction is the nondestructive method to study the crystallinity of the samples. The crystal nature of the drug can be studied with a high-intensity X-ray beam exposed to the samples and a diffractogram was studied. The degree of crystallinity depends on the width of the peaks of the diffractogram. The XRD pattern of the drugs was studied using XRD diffractogram (Bruker, Massachusetts, United States). The monochromatic Kα1 radiation with Johansson monochromators for Cu at the wavelength of 1.5406 A°, with an electric potential difference of 40 kV and current of 30 mA. The silicon substrate was used to cast the samples and then exposed to X-rays. The X-ray diffractogram was developed in the range of 0-80θ between 2θ angle (Hamedi and Koosha, 2020).

4.2.5 Nuclear Magnetic Resonance Spectroscopy

Nuclear magnetic resonance spectroscopy is the confirmatory and most desirable analytical method to evaluate the chemical structure of raw materials. FPV and NVP were subjected to NMR spectroscopy for structural confirmation. The drugs were subjected to proton NMR (Bruker Advance II) at an operational frequency of 400 MHz in Dimethylsulfoxide (DMSO). The drug samples were dissolved in DMSO (Zhang et al., 2014).

4.2.6 Field emission scanning electron microscopy

FE-SEM helps to examine the outer surface characteristics such as porosity, cracks, and defects in the dendrimer structures. It also provides structural confirmation of the samples. Surface morphology studies were carried out using FE-SEM (Jeol, USA, Inc)

having 1.0 nm (15kV) resolution. The detector used was secondary. The sample was prepared by coating with a thin layer of gold using a JFC ion sputter coater. The scanning was carried out at an accelerated voltage of 15 kV (Shi et al., 2022).

4.2.7 High-resolution transmission electron microscopy

HR-TEM helps to study the morphology and structure of DT and drug-loaded DT. For morphological studies, the samples were kept on copper grids which are coated with holey carbon support film. For in situ heating, was carried out on silicon nitride support film of thickness 50 mm. For the TEM study, a JEOL 2010 instrument operating at 120 kV and fitted with a Gatan heating stage, an Oxford Instruments INCA EDS system, and a Gatan SC1000 ORIUS CCD camera were used. To guarantee that the samples remained stable at each temperature, the rate of heating was around 10 °C/min, and the dwell duration was less than five min or even longer (Benjamin, 2008).

4.3 HPLC Method Development and Validation

4.3.1 Spectral Analysis

10 µg/mL solution of drugs FPV and NVP was prepared separately using methanol. The samples were scanned against methanol as blank using a UV spectrophotometer 1800 (Shimadzu, Japan) in the range of 200-400 nm. The physical mixture of 10 µg/mL of both drugs was prepared. The prepared solution was scanned using a UV spectrometer.

4.3.2 Method Development by HPLC

A simultaneous method was developed for drug NVP and FPV using the HPLC method (Shimadzu LC-20AD Prominence, Japan) using a Nucleodur C18 column with dimensions 250 mm x 4.6 mm and bead diameter of 5µm, with a photodiode array detector (SPD-M20A; Shimadzu, Japan) and a Rheodyne injector (7725i). The pump used was the LC20AD pump. LabSolution version 5.82 was used for chromatographic integration, recording, and statistical evaluation. The rate of flow was adjusted to 1 mL/min. The mode was isocratic. The volume of sample injection was set at 20 µL for the sample injection.

The mobile phase used for isocratic elution was Methanol: Water in the ratio of 80:20. Different solvent systems were used for the elution of the two drugs FPV and NVP in the same chromatogram. The composition of the mobile phase was selected based on

chromatographic peak parameters such as peak purity, sharpness, resolution, and tailing factors of the peaks. The solvent system should support the complete resolution of two peaks. Different trials were carried out to better elution of the two drugs. Solvent mixtures used for method development are Buffer: Methanol, Buffer: Acetonitrile (ACN), Formic acid: ACN, Formic acid: Methanol, and Methanol: Water.

4.3.3 Preparation of the stock solution for FPV and NVP

10 mg of FPV and NVP were weighed accurately and shifted to a volumetric flask of 10 mL. To the flask, a small quantity of methanol was added and mixed properly to solubilize the drugs NVP and FPV. Finally, the volume was adjusted to 10 mL with methanol.

4.3.4 Preparation of the working solution

1 mL of liquid sample was taken from the stock preparation and shifted to a volumetric flask of 10 mL and methanol was used to adjust the volume up to 10 mL which gives the concentration of 100 µg/mL. For the working solution from the above solution of 100 µg/mL, 1 mL was withdrawn and shifted to a volumetric flask of 10 mL, and methanol was used to adjust the volume up to 10 mL. The concentration of the working solution was 10 µg/mL each for FPV and NVP.

4.3.5 Method Validation

Validation of the optimization of a simultaneous estimate of FPV, APV, and NVP has been performed in accordance with the requirements provided by the *International Council for Harmonisation* (ICH, 2023) 45 Q2 (R1). The assessing system, appropriateness, LOD and LOQ, accuracy, range, specificity, linearity, robustness, and precision are all aspects that are covered by the rules [ICH, 2023].

4.3.5.1 System suitability

The validation of the optimization of the simultaneous estimation of FPV and NVP has been accomplished in compliance with the requirements that have been established by ICH 45 Q2 (R1). The guidelines address a variety of parameters, including system assessment, appropriateness, LOQ and LOD, range, linearity, accuracy, specificity, robustness, and precision (ICH, 2023).

4.3.5.2 Preparation of calibration curve

The calibration curve was plotted using the standard working solution. From the 10 µg/mL working solution, further dilution was made of concentrations 2.0, 4.0, 6.0, 8.0, and 10.0 µg/mL. The dilution was made by withdrawing 2.0, 4.0, 6.0, 8.0, and 10.0 mL of working stock solution in the five different volumetric flasks, and methanol was used to make up the volume up to 10 mL. The sample was analyzed using HPLC, and the curve used for calibration was displayed with a peak area on the y-axis and the concentration was plotted on the x-axis. To calculate the mean peak area, each injection was performed six times. Using the analytical technique, we were able to determine the calibration curve's slope, intercept, and coefficient of correlation.

4.3.5.3 Linearity and Range

Plotting the concentration against the mean area of peaks of each concentration allowed for the development of the calibration curve. Using the analytical technique, we were able to determine the coefficient of correlation, intercept, and calibration curve's slope (Kumar et al., 2020).

4.3.5.4 Accuracy study

The accuracy was calculated by recovery calculations (absolute) of the two drugs from the prepared samples. The study was performed at three levels, qualified as 80, 100, and 120% of the middle concentration of the calibration curve. For FPV, the mid concentration was 7.18 µg/mL and for NVP mid concentration was 7.74 µg/mL. The three levels of quantification were classified as higher quantified concentration, medium quantified concentration, and lower quantified concentration abbreviated as HQC, MQC, and LQC respectively. In the case of FPV, the LQC was 5.98 µg/mL, MQC 7.18 µg/mL, and HQC was 8.38 µg/mL and for NVP the LQC was 6.54 µg/mL, MQC was 7.74 µg/mL and HQC was 8.94 µg/mL.

4.3.5.5 Precision studies

The examination of the accuracy of the developed method was divided into two parts: the first portion focused on the repeatability of the method, while the second part investigated its intermediate precision. To investigate repeatability, the samples were injected six times at LQC, MQC, and HQC, maintaining similar chromatographic conditions on the same day. The intermediate precision was achieved by injecting six times as many LQC, MQC, and HQC samples at the same chromatographic settings but on separate days (interday). Additionally, each sample was analyzed by a different analyst. The data were summarized by noting the mean, and the % relative standard deviation (RSD) was computed.

Formula

$$Absolute\ recovery = Actual\ concentration\ recovered/$$
$$Theoretical\ concentration\ X\ 100$$

4.3.5.6 Determination of LOD and LOQ

The LOD and LOQ calculations of FPV and NVP and metabolite APV were carried out with the use of an equation for linear regression that depends on the standard deviation (SD) of the slope and intercept. The formula for determining LOD and LOQ is given below:

Formula:

$$\text{LOD} = 3.3\frac{Q}{S} \qquad \text{LOQ} = 10(\text{SD/S})$$

4.3.5.7 Robustness

There have been several planned and subtle adjustments made to the chromatographic settings, particularly the rate of flow and wavelength. These adjustments have been made in an array of different methods. These adjustments were also assessed for their effects on the separation of FPV, and NVP (Gupta et al., 2020).

4.4 Formulation development

4.4.1 Synthesis and characterization of DT (Conjugation of carboxylated MWCNT and dendrimers)

Accurately weighed 200 mg of 5G PPI dendrimers and 1000 mg of COOH-MWCNT were taken in the round bottom flask. 10 mL of water and methanol was added in a 2:1 ratio. The prepared mixture was sonicated on a bath sonicator for 60 min. The sonicated preparation was rotated using a magnetic stirrer (Remi) for 24 h at 50 $^{\circ}$C. After 24 h collect the sample and wash the mixture properly with water. The resultant product was dried in a hot air oven at 50 $^{\circ}$C till it was completely dried. The dried product was collected and stored in an air-tight container for further characterization (Pan et al. 2006).

4.4.2 Mannosylation of DT

Accurately weighed 500 mg of the D-mannose was taken in a round bottom flask. To this round bottom flask, 10 mL of acetate buffer (pH 4.0) was added. Then 100 mg DT was added. The flask was heated for 2 h at 60 $^{\circ}$C. The solution was further stirred for 72 h to complete the reaction using a magnetic stirrer. Following a period of 72 h, the solutions were dialyzed in a cellulose dialysis membrane bag (Molecular weight cut off (MWCO) 7000 Da, Himedia, India) against water and methanol in a ratio of 2:1 while the sink

condition was maintained. This process lasted for 15 min. This process helps to remove unconjugated mannose. The resultant product was collected and dried at 50 °C till it was completely dried. The dried product was collected and stored in an air-tight container for further characterization (Pruthi 2012; Mirali 2021).

4.4.3 Formulations loaded with NVP

4.4.3.1 Formulation development and characterization of NVP-loaded dendrimers

100 mg of drug NVP was weighed accurately and taken in a 10 mL volumetric flask. 20 mL methanol was added upto the mark and mixed. The drug methanol solution was sonicated for 10 min to solubilize the drug completely. The above solution was transferred to a round bottom flask and into this accurately weighed 50 mg of dendrimers was added. The preparation was stirred using a magnetic stirrer for 48 h. Following a period of 48 h, the solutions were dialyzed in a cellulose dialysis membrane bag (MWCO 7000 Da, Himedia, India) against a water and methanol at a ratio of 2:1 while the sink condition was maintained. This process lasted for 15 min. The resultant product was collected and dried at 50±1 °C till it was completely dried. The dried product was collected and stored in an air-tight container for further characterization (Kaur et al. 2017).

4.4.3.2 Formulation development and characterization of NVP-loaded carbon nanotubes

Accurately weighed 200 mg of drug NVP was taken. 20 mL of methanol was mixed with the drug NVP. The drug methanol solution was sonicated for 10 min to solubilize the drug completely. The above solution was transferred to a round bottom flask and then 10 mL water was added and to this accurately weighed 200 mg of carbon nanotubes was mixed. The preparation was stirred using a magnetic stirrer for 48 h. Following a period of 48 h, the solutions were dialyzed in a cellulose dialysis membrane bag (MWCO 7000 Da, Himedia, India) against water and methanol at a ratio of 2:1 while the sink condition was maintained. This process lasted for 15 min. The resultant product was collected and dried at 50±1 °C till it was completely dried. The dried product was collected and stored in an air-tight container for further characterization (Zhu et al., 2019).

4.4.3.3 Formulation development and characterization of NVP-loaded DT

Accurately weighed 200 mg of drug NVP was taken. 20 mL of methanol was mixed with the drug. The drug methanol solution was sonicated for 10 min to solubilize the drug completely. The above solution was transferred to a round bottom flask and then 10 mL water was added and to this accurately 200 mg of DT was added. The preparation was stirred using a magnetic stirrer for 48 h. Following a period of 48 h, the solutions were dialyzed in a cellulose dialysis membrane bag (MWCO 7000 Da, Himedia, India) against water and methanol at a ratio of 2:1 while the sink condition was maintained. This process lasted for 15 min. The resultant product was collected and dried at 50 ± 1 $^{\circ}$C till it was completely dried. The dried product was collected and stored in an air-tight container for further characterization (Singh et al., 2021; Zhu et al., 2019).

4.4.4 Formulations loaded with FPV

4.4.4.1 Formulation development of FPV-loaded dendrimers

100 mg of drug FPV was weighed accurately. 20 mL of methanol was added to the drug and mixed well. The drug methanol solution was sonicated for 10 min to solubilize the drug completely. The above solution was transferred to a round bottom flask and then 10 mL water was added and to this accurately weighed 200 mg of carbon nanotubes was added. The preparation was stirred for 48 h using a magnetic stirrer. Following a period of 48 h, the solutions were dialyzed in a cellulose dialysis membrane bag (MWCO 7000 Da, Himedia, India) against water and methanol at a ratio of 2:1 while the sink condition was maintained. This process lasted for 15 min. The resultant product was collected and dried at 50 $\pm$ 1^{0}C till it was completely dried. The dried product was collected and stored in an air-tight container for further characterization (Singh et al., 2021).

4.4.4.2 Formulation development and characterization of FPV-loaded carbon nanotubes

Accurately weighed 200 mg of drug FPV was taken. 20 mL of methanol was added to the drug and mixed. The drug methanol solution was sonicated for 10 min to solubilize the drug completely. The above solution was transferred to a round bottom flask and then 10 mL water was added and to this accurately weighed 200 mg of carbon nanotubes was

added. The preparation was stirred using a magnetic stirrer for 48 h. Following a period of 48 h, the solutions were dialyzed in a cellulose dialysis membrane bag (MWCO 7000 Da, Himedia, India) against water and methanol at a ratio of 2:1 while the sink condition was maintained. This process lasted for 15 min. The resultant product was collected and dried at 50±1 °C till it was completely dried. The dried product was collected and stored in an air-tight container for further characterization (Zhu et al., 2019).

4.4.4.3 Formulation development and characterization of FPV-loaded DT

Accurately weighed 200 mg of drug FPV was taken. 20 mL of methanol was added and mixed well. The drug methanol solution was sonicated for 10 min to solubilize the drug completely. The above solution was transferred to a round bottom flask and then 10 mL water was added and to this accurately weighed 200 mg of DT was added. The preparation was stirred using a magnetic stirrer for 48 h. Following a period of 48 h, the solutions were dialyzed in a cellulose dialysis membrane bag (MWCO 7000 Da, Himedia, India) against water and methanol at a ratio of 2:1 while the sink condition was maintained. This process lasted for 15 min. The resultant product was collected and dried at 50±1 °C till it was completely dried. The dried product was collected and stored in an air-tight container for further characterization (Singh et al., 2021; Zhu et al., 2019).

4.4.5 FPV and NVP loaded DT

4.4.5.1 Formulation development and characterization of NVP and FPV-loaded DT

200 mg of drug NVP was accurately weighed was placed in a round bottom flask. To this methanol, 20 mL was added and mixed well. The drug methanol solution was sonicated for 10 min to solubilize the drug completely. 200 mg of FPV was added and sonicated for 2 min to solubilize the drug. The above solution was transferred to a round bottom flask and into this accurately weighed 400 mg of DT was mixed. The preparation was stirred using a magnetic stirrer for 48 h. Following a period of 48 h, the solutions were dialyzed in a cellulose dialysis membrane bag (MWCO 7000 Da, Himedia, India) against a mixture of water and methanol at a ratio of 2:1 while the sink condition was maintained. This process lasted for 15 min. The resultant product was collected and dried at 50±1 °C

till it was completely dried. The dried product was collected and stored in an air-tight container for further characterization (Kaur et al. 2017).

4.4.5.2 Mannosylation of NVP and FPV-loaded DT

Accurately weighed 500 mg of the D-mannose was taken in a round bottom flask. To this round bottom flask, 10 mL of acetate buffer (pH 4.0) was added. Then 100 mg NVP and FPV-loaded DT were incorporated into the flask. The flask was heated for 2 h at 60 ^{0}C. The solution was further stirred for 72 h to complete the reaction using a magnetic stirrer. Following a period of 72 h, the solutions were dialyzed in a cellulose dialysis membrane bag (MWCO 7000 Da, Himedia, India) with water as the receptor medium while the sink condition was maintained. This process lasted for 15 min. The process helps to remove unconjugated mannose. The resultant product was collected and dried at 50±1 $^\circ$C till it was completely dried. The dried product was collected and stored in an air-tight container for further characterization (Gulbake et al., 2019; Rathod et al., 2019).

4.5 Characterization of DT and developed formulations

4.5.1 Physiochemical properties

The physicochemical properties were studied such as colour, odour, and texture.

4.5.2 Spectrophotometric analysis

4.5.2.1 UV spectroscopy

The absorption spectra of the different formulations were determined using a UV spectrophotometer (Shimadzu). The sample was studied with a 10-mm quartz cell. The UV–visible spectra of different formulations were studied in the range of 190–420 nm (Noordadi et al. 2018).

4.5.2.2 FITR Spectroscopy

FTIR spectroscopy analysis helps to detect the structure of DT and drug loading in DT, dendrimers, and MWCNT using the PerkinElmer Spectrum IR Version 10.6.1. The absorbance spectrum was obtained using KBr pellets. A beam of light was utilized at different frequency levels and absorption was noted. Different functional groups present in the sample correspond to specific wave numbers. This is an important technique for identifying and confirming the specific functional group in a particular sample (Samsodien

et al., 2017). The samples of dendrimers, COOH-MWCNT, and dendritubes, different formulations were subjected to FTIR spectroscopy for the confirmation of the functional groups (Razzazan et al. 2016).

4.5.2.3 Raman Spectroscopy

The spectra provide details about the diameter of the carbon structure, the presence of any interactions as well as defects in the carbon structures. It also gives a clear indication of the sp^2 hybridized structure. The prepared conjugate, DT, and drug-loaded formulations were subjected to Raman spectroscopy (Bruker) equipped with three wavelengths. Raman spectroscopy measurements were carried out on powdered samples with a **BRUKER RFS 27 MultiRAM FT Raman Spectrometer** instrument at an excitation wavelength of 785 nm. The source used was Nd-YAG laser (1064 nm) in addition there was a white light source. The spectral range applied was 50-4000 cm^{-1} (Piao et al., 2021).

4.5.2.4 Nuclear Magnetic Resonance Spectroscopy

Nuclear magnetic resonance spectroscopy is the confirmatory and most desirable analytical method to evaluate the chemical structure of DT and developed formulations. Different formulations containing NVP and FPV were subjected to NMR spectroscopy for structural confirmation. The drugs were subjected to proton NMR (Bruker Advance II) at an operational frequency of 400 MHz in Dimethylsulfoxide (DMSO). The drug samples were dissolved in DMSO (Zhang et al., 2014).

4.5.3 X-ray diffraction

X-ray diffraction is the nondestructive method to study the crystallinity of the samples. To study the crystal nature of the novel conjugate system DT and drug loaded formulations, a high-intensity X-ray beam was exposed to the samples, and a diffractogram was studied. The degree of crystallinity depends on the width of the peaks of the diffractogram. The XRD pattern of the DT and different formulations was studied using an XRD diffractogram (Bruker, Massachusetts, United States). The monochromatic Kα1 radiation with Johansson monochromators for Cu at the wavelength of 1.5406 A°. The silicon substrate was used to cast the samples and then exposed to X-rays. The X-ray diffractogram was developed in the range of 0-80θ between 2θ angle (Hamedi 2020).

4.5.4 Differential scanning calorimeter

Differential Scanning Calorimetry studies are the thermal studies that help to study the thermal properties such as exothermic onset temperature, melting point, reaction order, activation energy, and extent of reactions. DT and the FPV and NVP loaded formulations were subjected to thermal analysis to confirm the melting point and to study the possible interaction during conjugations. The sample was placed on the aluminum pan and packed properly. The heating rate was set from 2 °C/min using DSC (Perkin Elmer, Massachusetts, United States) (Heise 2010; Chountoules et al 2019).

4.5.5 Morphological analysis

4.5.5.1 Field emission scanning electron microscopy

FE-SEM helps to study the outer surface characteristics such as porosity, cracks, and defects in the DT and the drug-loaded structures. It also provides structural confirmation of the DT and the different formulations. Surface morphology studies were carried out using FE-SEM (Jeol, USA, Inc) having 1.0 nm (15kV) resolution. The detector used was secondary. The sample was prepared by coating with a thin layer of gold using a JFC ion sputter coater. The scanning was carried out at an accelerated voltage of 15 kV (Shi et al., 2022).

4.5.5.2 Transmission electron microscopy

Transmission electron microscopy helps to study the morphology and structure of DT and drug-loaded formulations. For morphological studies, the samples were kept on copper grids which are coated with holey carbon support film. For in situ heating, was carried out on silicon nitride support film of thickness 50 mm. For the HR-TEM study, a JEOL 2010 instrument operating at 120 kV and fitted with a Gatan heating stage, an Oxford Instruments INCA EDS system, and a Gatan SC1000 ORIUS CCD camera were used. To guarantee that the samples remained stable at each temperature, the rate of heating was around 10 °C/min, and the dwell duration was less than five min or even longer (Benjamin 2008).

4.5.5.3 Atomic force microscopy

Atomic force microscopic studies were studies to confirm the spherical structure of the dendrimers. AFM images precisely provide the 3D structure of the sample. The method is efficient and accurate and can be carried out with a small amount of samples. The sample was prepared with mica deposition by cooling it at 120 ºC for 3-4 min. For the analysis single beam cantilever was used in tapping mode. The scanning range used was 5-10 nm and the scanning rate was 0.5 Hz. The frequency of resonance was 300 kHz. The scanner used was a 7 µm scanner. The sample solution was dropped on the surface of the mica film. The images were captured using a Veeco Digital Instruments Multimode Nanoscope (Model: XE100) (Sharma et al., 2018).

4.5.6 Particle size and zeta potential

The particle size and zeta potential of the prepared DT and drug-loaded formulations were estimated by measuring the dispersion by Zetasizer Ver. 7.13, Malvern, using the light scattering method (Youssry et al. 2020). Zeta potential affects the different aspects of the CNTs such as electroosmosis, flocculation, and stability.

4.5.7 Dispersibility test

The dispersibility test was ~~carried out~~done to study the ~~rate~~ stability of dispersion with respect to time. 5 mg of MWCNT, DT, and the different formulations were weighed and dispersed using deionized water (5 mL), and the dispersion was sonicated ~~(Brand)~~using a bath sonicator for 5 min. The dispersions were observed manually for 24 h (Pruthi et al., 2012).

4.5.8 Drug entrapment

Entrapment efficiency helps to estimate the amount of drug enclosed inside the prepared conjugates. It is an indirect method, that determines the drug content in the solvent system, and the difference between the loaded drug initially and the amount in solvent gives the amount of drug entrapped. After drug loading the prepared dispersion was shifted into a dialysis bag (MWCO 7000 Da, Himedia, India). The bag was shifted to the solution of methanol: water (40:60) and kept for stirring for 15 min. After 15 min the solvent was withdrawn and the drug content was analyzed using a UV spectrophotometer (Shimadzu

UV/Vis, Japan) at 265 nm for FPV and 283 nm for NVP (Parashar et al., 2018). % entrapment efficiency was determined using the formula given below:

% Entrapment Efficiency = $\dfrac{\text{Total weight - Weight of unloaded drug X 100}}{\text{Total weight}}$

4.5.9 *In vitro* drug release

In vitro release study was performed by equilibrium dialysis tube diffusion technique. 5 mL of individual drug-loaded dendrimers/MWCNT/DT solution in methanol (10 mg/5 mL) was taken in a dialysis bag (MWCO 7000 Da, Himedia, India) and tied in hermetical fashion. The prepared tube was dialyzed using methanol: buffer (PBS pH 7.4 and acetate buffer pH 5) under sink conditions. 1 mL of the liquid sample was withdrawn at hourly intervals till 8 h, then at 24, 30, 48, 72, and 96 h. Fresh solvent (1 mL) was added back to maintain the sink condition. The withdrawn sample was diluted with a suitable solvent system and analyzed using a UV spectrophotometer (Shimadzu UV/vis, Japan) at 265 nm for FPV and 283 nm for NVP (Tan et al., 2014). The formulation containing dual drugs in DT and mannosylated dual drug-loaded DT samples were analyzed by HPLC (Shimadzu, Japan) (Ramanunny et al., 2021).

4.5.10 Release kinetic

The drug release data were subjected to different mathematical models such   as first order, zero order, Hixon-Crowell, Korsmeyer-Peppas model, and Higuchi models. The R^2 value was estimated to judge the best model fitting to the release profile. The first-order release indicates that the reaction rate is related to the amount of drug. The zero-order indicates constant drug release from the conjugates. Higuchi's model illustrates the release of both hydrophilic and sparingly soluble drugs by dissolution or by diffusion. Korsmeyer-Peppas model helps to co-relate the diffusion of the drug through the polymeric matrix. The n value (release exponent) can be co-related with release mechanisms. The diffusion pattern can be studied with the help of the n value. If the value of n is less than 0.5 suggests diffusion by fickian mode and a value more than 0.5 to 1.0 indicates non-fickian diffusion.

Hixon-Crowell model indicates that the release of the drug was related to alteration in the total area or diameter of the particles of the drug (Lee et al., 2015; Chudoba et al., 2021) The equation of different models is as follows:

a) Zero order model: $M_t = kt + M_0$

b) First order kinetics: $M_t = M_0^{ekt}$

c) Higuchi Model: $M_t/M_\infty = kt^{1/2}$

d) Korsmeyer-Peppas Model: $M_t/M_\infty = kt^n$

M_t stands for the amount of released drug from the conjugated system at time t, and M_0 is the total amount of the drug in the conjugated system. M_t/M_∞ is the fraction of released drug, n is the diffusion exponent and k is the rate constant.

4.6 Stability studies

Stability studies help to govern the shelf life of the formulated products. It is the time in which the product retains its chemical, physical, and pharmacokinetic properties and characteristics throughout the life of the pharmaceuticals. ICH guideline of stability testing of new drug substances and products Q1A(R2) was followed for the stability studies of the prepared formulations. The prepared formulations of NVP-DT, FPV-DT, and NVP-FPV-DT were subjected to stability studies to evaluate the stability of the product for 3 months. The prepared NVP-DT, FPV-DT, and NVP-FPV-DT were dispersed in PBS pH 7.4 (5 mL) kept at 4±2 °C, at room temperature (25±2 °C) and accelerated temperature (40±2 °C) for six weeks and studied at the interval of 1 week. The prepared formulations of NVP-DT, FPV-DT, and NVP-FPV-DT were evaluated for colour change, texture, consistency, turbidity, precipitation, and leakage of a drug. A drug leakage test was performed using a dialysis bag (MWCO 7000 Da, Himedia, India), 1 mL of the aliquot was placed and the dialysis bag was sealed from both ends. The dialysis bag was kept in PBS pH 7.4 and methanol in the ratio of 60:40. The sample was analyzed after 1h and the leaked amount of drug was evaluated using a UV-spectrophotometer at 283 nm for NVP and 265 nm for FPV. The same procedure was repeated weekly for 6 weeks (Jose et al., 2016; Singh et al., 2016).

4.7 *In vitro* cell line studies

4.7.1 Cytotoxicity studies

The cytotoxicity of DT, mannosylated DT, drug NVP, and FPV, both drug-loaded DT and mannosylated both drug loaded DT was examined in Raw 264.7 (Monocyte Macrophage) cells using the MTT assay. In a 96-well plate, cells were grown at a density of 2 x 10^4 cells per well in Dulbecco's Modified Eagle (DMEM) medium that was augmented with 10% FBS, 1% penicillin, and 1% streptomycin. The incubator was maintained at 37 °C with a 5% CO_2 atmosphere. After the incubation of 24 h, varying concentrations (5-100 dispersed in media) of DT, mannosylated DT, drug NVP, and FPV, both drugs-loaded DT and mannosylated drug-loaded DT were added in the wells in a triplicate manner. After an incubation period of twenty-four hours, the wells were cleaned with PBS, and then 200 µL of MTT (0.5 mg/mL) was added. Crystals of formazan that had been growing for 4 h were dissolved in 200 µL of isopropanol. With the use of a microplate reader, the optical absorbance was measured to be 570. (Epoch2, BoiTek) (Varshosaz et al., 2018). The results were stated as the percentage of cell survival and calculated using the following formula:

$$\% \text{ Cell survival} = \left(\frac{\text{A570 nm of treated cell}}{\text{A570 nm of untreated control cells}} \right) \text{x } 100$$

4.7.2 Cell internalization studies

On coverslips, raw 264.7 cells, also known as monocyte-macrophage cells, were placed at a density of 2 x 10^5 cells per well. The uptake efficiency of prepared formulations was evaluated by treating cells with Fluorescein isothiocyanate (FICT; Green Chanel) tagged drug-loaded DT, and mannosylated drug-loaded DT. These treatments were carried out to examine the efficacy of the prepared structure. After a total of 4 h, the conjugates-containing medium was discarded, and the cells were fixed with 4% paraformaldehyde for twenty min. After mounting the coverslips on slides, uptake was seen with a confocal microscope equipped with a Leica sp5 system (Biagiotti et al, 2018).

4.8 *In vivo* studies

4.8.1 Animals

81 female Wister rats were procured from the Center of Animal House, Panjab University, Chandigarh, India for the bioanalytical methods development. The rats were

kept at room temperature (25 ± 2 °C) and relative humidity (RH) of 55 ± 10%. In the animal house light-dark cycle of 12:12 was followed. Cages for rats were made up of polypropylene layered with husk. The rat was selected from the age group of 10-12 weeks and the weight range was 250-350 g. The feeding routine includes the standard

pellet diet and water. The protocol was approved by The Institutional Animal Ethical Committee of the School of Pharmaceutical Sciences, Lovely Professional University (Protocol no: LPU/IAEC/2022/03) (Khursheed et al., 2022).

The details of the different animal groups required are given below:

Table 4: Animal grouping representing diet, dose, route of administration, and number of animals in each group

Group No.	Sample code	Diet, dose, and route of drug treatment	No of animals
Group 1	Vehicle Control	NPD, Normal saline (Vehicle), IV route	9
Group 2	DT	NPD, 10 mg/kg (DT plain), single dose, IV route	9
Group 3	Mannosylated DT	NPD, 10 mg/kg (DT plain), single dose, IV route	9
Group 4	Drug –NVP	NPD, 10 mg/kg (NVP), single dose IV route	9
Group 5	Drug – FPV	NPD, 70 mg/kg (FPV), single dose IV route	9
Group 6	NVP loaded DT	NPD, equivalent to 10 mg/kg (NVP), single dose, IV route	9
Group 7	FPV loaded DT	NPD, equivalent to 70 mg/kg (FPV), single dose IV route	9
Group 8	NVP and FPV loaded DT	NPD, 70 mg/kg, single dose IV route	9
Group 9	Mannosylated NVP and FPV DT	NPD, 70 mg/kg, single dose IV route	9

* NPD: Normal pellet diet, IV: Intravenous route

4.8.2 Bioanalytical Method Development

4.8.2.1 Spectral Analysis

The solution of drugs FPV, APV, and NVP was prepared separately using methanol as a solvent. 10 µg/mL solution was prepared for each drug. Methanol was used as a blank solution for the analysis using a UV-Vis spectrometer (UV-1800, Shimadzu, Japan). The scanning was carried out in the range of 400-200 nm (Goku et al., 2020; Shokouhi et al., 2020).

4.8.2.2 Method development

A simultaneous bioanalytical method was developed using High-performance liquid chromatography (HPLC) (Waters, Model no: 515 se: J07515777a, India) using ODS C-18 column (Serial no: 015231308138) with dimensions 250 mm x 4.6 mm and 5μm bead size, with photodiode array detector (2998; Waters, Milford, MA) and the instrument is equipped with an autosampler (717). The pump used was the Water's 515 pump. Empower 2.0 software was used for chromatographic integration, recording, and statistical evaluation. The mode was isocratic and the volume of injection was set to 20 μg/mL for the sample injection with a flow rate of 0.5 mL/min. The mobile system used for isocratic elution was Methanol: Water: ACN (800 mL: 200 mL: 50 mL). Different solvent system was used for the elution of the three drugs FPV, APV, and NVP in similar chromatographic conditions. The composition of the mobile phase was selected based on chromatographic peak parameters such as peak purity, sharpness, resolution, and tailing factors of the peaks. The solvent system should support the complete resolution of two peaks. Different trials were carried out to better elution of the two drugs. Solvent mixtures used for method development are Water: Methanol, and Water: ACN in different ratios.

4.8.2.3 Extraction of plasma

In rats, the sample of blood was taken from the retro-orbital cavity by puncturing with a capillary tube. The blood sample was collected in ethylene diamine tetra acetic acid (EDTA) crystals containing radioimmune assay vials. The rat was anesthetized before the blood collection. The neck of the rat was held tightly making the eyes bulge. The fine capillary tube was inserted into the eye's medial canthus, the blood started coming out through the capillary tube. The blood was collected in EDTA-containing vials to prevent blood coagulation. The blood-containing tube was centrifuged at 5213 g for 15 min. After centrifugation, the above liquid was collected with the help of a micropipette and stored at -20 °C in a deep freezer (Gadag et al., 2022; Duse et al.,2021).

4.8.2.4 Preparation of blank solution of plasma

To precipitate the proteins of plasma, 1 mL of extracted plasma was obtained, and then 2 mL of acetone and acetic acid in combination with a volume-to-volume ratio of 1:1

was added. The prepared was then vortexed for five min. After collecting the supernatant, it was centrifuged at a speed of 5213 g for fifteen min. After collecting the supernatant in a volumetric flask of 100 mL and final volume was made up to 100 mL (Mohan et al., 2021).

4.8.2.5 Preparation of the stock solution for FPV, APV, and NVP

Plasma was dissolved in ACN to create the standard stock solution, which included a combination of FPV, APV, and NVP at a concentration of 10 μg/mL each. To prepare the stock solution with plasma, two mL of plasma were obtained and 10 mg of FPV, APV, and NVP were added to it respectively. After agitating the mixture for ten min with a vortex, two mL of an acetone and acetic acid mixture with a volume-to-volume ratio of one to one was added to the matrix that had been spiked, and the combination was then centrifuged once more to separate different proteins in plasma proteins. The whole contents were subjected to a 15-minute centrifuge at a speed of 5213 g. After collecting the supernatant in a volumetric flask, the volume was brought up to 100 mL to prepare a stock solution of 1000 mg/mL (stock solution A) (Mohan et al., 2021).

4.8.2.6 Preparation of the working solution

After taking an aliquot (1 mL) from the stock solution and transferring it to a volumetric flask with a capacity of 10 mL, the volume was brought up to 10 mL with ACN, which resulted in a concentration of 100 μg/mL. From the solution described above (100 μg/mL), 1 mL was removed, and placed in a volumetric flask of 10 mL, and the volume was brought up to 10 mL with ACN. The FPV, APV, and NVP working solutions all had a concentration of 10 μg/mL when they were added to the working solution (Mohan et al., 2021).

4.8.2.7 Method Validation

Validation of the optimization of a simultaneous estimate of FPV, APV, and NVP has been performed in accordance with the requirements provided by the *International Council for Harmonisation* (ICH) 45 Q2 (R1). The assessing system, appropriateness, LOD and LOQ, accuracy, range, specificity, linearity, robustness, and precision are all aspects that are covered by the rules [ICH].

4.8.2.7.1 System suitability

The validation of the optimization of the simultaneous estimation of FPV, APV, and NVP has been accomplished in compliance with the requirements that have been established by ICH 45 Q2 (R1). The guidelines address a variety of parameters, including system assessment, appropriateness, LOQ and LOD, range, linearity, accuracy, specificity, robustness, and precision (ICH, 2023).

4.8.2.7.2 Preparation of calibration curve

Different concentration for calibration curves was prepared using the working solutions (10 µg/mL). From the 10 µg/mL solution, further dilutions were made ranging from 0.2, 0.8, 1.6, 2.4, and 3.2 µg/mL by withdrawing 0.2, 0.8, 1.6, 2.4, and 3.2 µg/mL from working solution (10 µg/mL) and diluting up to 10 mL. The working stock solution was withdrawn in increments of 0.2, 0.8, 1.6, 2.4, and 3.2 mL in each of the five volumetric flasks, and the volume was brought up to 100 mL with ACN. The sample was analyzed using HPLC, and the curve used for calibration was displayed with a peak area on the y-axis and the concentration was plotted on the x-axis. To calculate the mean peak area, each injection was performed six times. Using the analytical technique, we were able to determine the calibration curve's slope, intercept, and coefficient of correlation (Mangla et al., 2020).

4.8.2.7.3 Linearity and Range

Plotting the concentration against the mean area of peaks of each concentration allowed for the development of the calibration curve. Using the analytical technique, we were able to determine the coefficient of correlation, intercept, and calibration curve's slope (Mangla et al., 2020).

4.8.2.7.4 Accuracy study

The absolute recovery of the two drugs and their metabolite from the samples that were prepared allowed for the determination of how accurate the approach was. The research was carried out at three different intensities: 80%, 100%, and 120% of the concentration that was found in the middle of the curve used for calibration. The median value of the FPV and APV concentrations was 1.6 µg/mL, while the median value of the

NVP concentration was 1.6 µg/mL. HQC, MQC, and LQC make up the three levels of quantification. In the case of FPV and NVP, the LOQ was 1.066 µg/mL, the MQC was 1.6 µg/mL, and the HQC was 1.92 µg/mL (Eswarudu et al., 2019).

4.8.2.7.5 Precision studies

The examination of the accuracy of the developed method was divided into two parts: the first portion focused on the repeatability of the method, while the second part investigated its intermediate precision. To investigate repeatability, the samples were injected six times at LQC, MQC, and HQC, maintaining similar chromatographic conditions on the same day. The intermediate precision was achieved by injecting six times as many LQC, MQC, and HQC samples at the same chromatographic settings but on separate days (interday). Additionally, each sample was analyzed by a different analyst. The data were summarized by noting the mean, and the % relative standard deviation (RSD) was computed (Gupta et al, 2020).

Formula

$$\text{Absolute recovery} = \frac{\text{Actual concentration recovered}}{\text{Theoretical concentration}} \times 100$$

4.8.2.7.6 LOD and LOQ

The LOD and LOQ calculations of FPV and NVP and metabolite APV were carried out with the use of an equation for linear regression that depends on the standard deviation (SD) of the slope and intercept. The formula for determining LOD and LOQ is given below:

Formula

$$\text{LOD} = \frac{3.3\,Q}{S}$$

$$\text{LOQ} = \frac{10\,Q}{S}$$

4.8.2.7.7 Robustness.

There have been several planned and subtle adjustments made to the chromatographic settings, particularly the rate of flow and wavelength. These adjustments have been made in an array of different methods. These adjustments were also assessed for their effects on the separation of FPV, APV, and NVP (Gupta et al., 2020).

4.8.2.7.8 Stability study

FPV, APV, and NVP spiked plasma samples were frozen-thawed in triplicate for three hours at room temperature and three weeks at -20 °C for stability testing. One Ria vial included 3 mL plasma for freeze-thaw stability. This vial was vortexed for 5.0 min with 1 mg of FPV, APV, and NVP for 1000 mg/mL concentration. -20 °C frozen sample. Normal temperature thawed the tube. The first cycle utilized 1 mL of thawed plasma, whereas the second used 2 mL. Centrifuged 1 mL drug-containing plasma. The centrifuged clear supernatant was diluted to 100 mL with ACN to attain 100 mg/mL. Diluted to 1.066 µg/mL (LQC), 1.6 (MQC), and 1.92 (HQC). For the second cycle, 1 mL of the sample of frozen plasma (2 mL) was thawed at room temperature. The rest was frozen. Thawing the third sample. Cycles 2 and 3 followed Cycle 1 for LQC, MQC, and HQC samples. HPLC analyzed triplicate dilutions at 258 nm. Each concentration had a mean, SD, and % RSD (Gupta et al., 2022).

FPV, APV, and NVP-spiked plasma samples were examined for short-term stability at room temperature. Short-term stability was tested before extraction. 3 mL plasma was added to the Ria vial with 3 mg of FPV, APV, and NVP for 1000 µg/ml. Vortexed for 5 min. Ria vial. To create LQC, MQC, and HQC samples, pharmaceuticals were extracted from plasma from 1, 2, and 3 mL samples. HPLC analyzed triplicate dilutions at 258 nm. Each concentration had a mean, standard deviation, and % RSD (Harish et al., 2022)

In three Ria vials, 1 mL plasma was added to 1 mg of FPV, APV, and NVP to attain 1000 µg /mL for long-term stability. Vortexing for 5 min froze all 3 vials at -20 °C. The vials were thawed after 1, 2, and 3 weeks. Plasma medicines were processed for LQC, MQC, and HQC samples at each interval. HPLC analyzed triplicate dilutions at 258 nm. Each concentration has a mean, SD, and RSD (Reddy et al., 2019).

4.8.3 Biodistribution studies

The Wister rats of either sex were selected for the biodistribution studies. The rats were equally divided into nine groups. Each group contains three rats (n=3). The drugs, DT (DT), and formulations were dispersed in normal saline (0.9% w/v) and were administrated by the intravenous route via a jugular vein (equivalent dose of NVP 10 mg/kg

and FPV 70 mg/Kg body weight) into animals. The animals (n=3 at each time point) after injection were sacrificed at time intervals of 1,8, and 24 h. These time points were decided based on t1/2 of drugs. After sacrificing, different organs such as the spleen, liver, kidney, and heart. were separated, cleaned, weighed, and stored at freezing temperature till further use. The organ was taken and placed in the required quantity of ACN and homogenized well-using tissue homogenizer and then centrifuged at 3000 rpm for 10 min. The supernatant was decanted, collected, and assayed by the HPLC method (Shegokar et al., 2011). The procedure is shown in Figure 10.

Fig 10: Schematic representation of biodistribution study

4.8.4 Haemolysis studies

Blood was obtained from Wister rats, placed in anti-clot vials, and then centrifuged at 3000 rpm for 15 min using a centrifuge (Remi, India). To obtain the suspension, the red blood corpuscles (RBCs) will first be sorted out, washed, and then resuspended in a saline solution that has a weight-to-volume ratio of 0.9%. After mixing 1 mL of prepared suspension with 4.5 mL of normal saline containing 0.9% water by volume and 0.5 mL of each sample, the mixture was allowed to react while being incubated for 60 min. Absorbance readings were obtained at 540 nm (Shimadzu 1601, Kyoto, Japan) using a 0.9

% w/v NaCl solution and deionized water to simulate 0% and 100% hemolysis, respectively. The proper dilutions were produced first, and then the readings were taken. The following equation was used to calculate the proportion of hemolysis in the sample (Mehra and Jain, 2013; Mishra et al., 2010).

$$\text{Hemolysis (\%)} = \frac{Ab_s - Ab_{S0}}{Abs_{100} - Ab_{S0}}$$

4.8.5 Haematological studies

Analyses of hematological parameters, including hemoglobin, red blood cells (RBCs), and white blood cells (WBCs), are going to be performed on rats of either sex that are healthy Wister strains and have the same weight and size. Up to twenty-four h will pass during which every animal will continue to consume the same diet that they are accustomed to. After 24 h had passed, samples of blood were taken using the retro-orbital plexus procedure, and these samples were tested at the local pathology laboratory to determine various hematological parameters (Jain et al., 2015).

Fig 11: Steps of Hemolysis studies and hematological studies

The list of materials used throughout the study was listed in Table 2 along with the respectivesource.

Table 2. Various materials used in the research work

Material	Source
Acetic acid	S.D Fine Chemicals, India
Acetone	Loba Chemie Private Limited, India
Acetonitrile (HPLC grade)	Rankem, India Limited., India
Amprenavir	S and G lab supplies, Chandigarh, India
Buffer capsules pH 7.0 ± 0.05	Qualigens Fine Chemicals, India
Chloroform	Loba Chemie Private Limited, India

COOH-MWCNTs	Adnano Technologies Pvt Ltd, India
PPI Dendrimers	Gift sample from Prof. N.K. Jain, H. S. Gour Central University, Sagar, India
Dialysis membrane-110 (LA395)	Himedia Lab Private Limited, India
FITC dye	Sigma Aldrich, USA
Formaldehyde	Loba Chemie Private Limited, India
Formic acid	Loba Chemie Private Limited, India
Fosamprenavir calcium	Gift sample from Lupin Laboratories, Pune, India
Hydrochloric acid	Loba Chemie Private Limited, India
Mannose	Sigma Aldrich, USA
Methanol AR grade	S.D Fine Chemicals, India
Methanol HPLC grade	Rankem, Avantor Performance Materials India Ltd., India
Millipore water	Bio-Age Equipment Ltd., India
Nevirapine	Gift sample from Emcure Pharmaceuticals, Pune India
n-octanol	Loba Chemie Private Limited, India
Potassium dihydrogen orthophosphate anhydrous purified	Central Drug House Pvt. Ltd., India
Sodium chloride 99.5% extra pure	Loba Chemie Private Limited, India
Sodium hydroxide	Loba Chemie Private Limited, India
Sodium acetate	S.D Fine Chemicals, India
Sodium phosphate dibasic anhydrous 98% Purified	Loba Chemie Private Limited, India

Instruments and equipment

Instruments and equipment used in various stages of research work were enlisted in Table 3 along with its model/manufacturer details.

Table 3. List of instruments and equipment used in various stages of work

Instruments/equipment	Model/Manufacturer details
Analytical balance	AX200 Shimadzu Analytical Pvt. Ltd., India
Atomic force microscopy	Veeco (XE100), Plainview, New York, United States
Differential scanning calorimetry	Perkin Elmer, Waltham, Massachusetts, United States
Digital ultrasonic cleaner	LMUC-4 Labman Scientific Instruments Serial No: L10321, India
Diode array detector	SPD-M20A Shimadzu, Japan
FTIR spectroscopy	Perkin Elmer, Waltham, Massachusetts, United States
Hot air oven	Q-5247, Navyug, India
Nylon membrane filter (0.45 μm)	Millipore, Germany
Nanoparticle size analyzer	Malvern Zetasizer, Nano ZS90, Malvern Panalytical Ltd., UK
NMR spectroscopy	Avance NEO 500mhz, FT-NMR spectrophotometer, Bruker, Switzerland
Optical microscope	KYOWA, Getner Instruments Pvt. Ltd., Japan
pH meter	Phan, Lab India, India
Raman spectroscopy	Bruker RFS 27 MultiRAM FT Raman Spectrophotometer, Switzerland
Field emission Scanning electron microscopy	Jeol, Akishima, Tokyo, Japan
Transmission electron microscopy	JEM-2100 plus Electron microscope, Jeol Ltd., Japan
Tissue homogenizer	REMI RQ-1, India

Ultracentrifuge	REMI, RM-12C, REMI Elektrotechnik Ltd., India
High-performance liquid chromatography (HPLC) equipped with a degasser unit and pump system	DGU-20 A5 prominence degasser with LC-20AD/T prominence Liquid Chromatograph Shimadzu, Japan
UV Spectrophotometer	UV-1800, Shimadzu Co.Ltd., Kyoto, Japan
Stability chamber	REMI-WSC 100, India
X-Ray Diffraction	Bruker, Switzerland

4.1 Preformulation studies

Preformulation studies extensively cover different physiochemical properties, analytical, pharmaceuticals, and biological characteristics of the newly developed drug molecules. Preformulation studies for dosage form development should include characterization and physiochemical studies of the excipients. These studies give an insight into the development of the dosage form. The pre-formulation studies are important and provide a smooth runway for the formulation of safe, effective, stable, cost-effective, and stable products. Different pre-formulation studies were done for the drug Nevirapine (NVP), Fosamprenavir calcium (FPV), and Amprenavir (AVP). Similarly, the preformulation studies were carried out for dendrimers and COOH-MWCNT (Chaurasia et al., 2016).

4.1.1 Physical properties

The physical appearance of FPV and NVP was noted visually. The following common physical properties were noted:

❖ Colour

❖ Odor

❖ Appearance

4.1.2 Melting point detection of the drug

Estimation of melting point is the foremost technique for representing the purity of the sample. The temperature at which the solid co-exists with liquid in equilibrium under external pressure is termed the melting point. The presence of impurity was indicated by lowering or broadening the melting point range.

The sample of NVP and FPV was subjected to melting point determination by the capillary tube method. The drug was packed in the glass capillary tube by sealing at one end and fitted in a melting point determination apparatus. The sample was observed continuously until it was completely melted. The melting range (from the onset of melting till completely melted) reading was noted thrice (Jobli et al., 2019).

4.1.3 Solubility studies

Solubility of both the drugs, FPV and NVP was determined in methanol, water, and phosphate buffer saline (PBS) of pH 7.4 and acetate buffer pH 5.0. The drug was added in a surplus to each solvent separately. The systems were shaken for a certain period. Small increments in the amount of drug were done in each solution separately until a saturated solution was formed. Saturation was confirmed by the presence of undissolved material in the solution. Then all the solutions were kept on a rotary shaker for 24 h at ambient temperature. After 24 h, the solutions were filtered, and the filtrate was diluted and spectrophotometrically

analyzed at 265 nm for FPV and 283 nm for NVP in a UV-Visible spectrophotometer (UV-1800 series Shimadzu). The experiment was performed three times, and the average was noted (Bhandaru et al., 2015).

4.1.4 Partition Co-efficient Studies

The partition coefficient is an important measurement in the process of preformulation. It gives a clear idea about the diffusion of the drug by passive mode. The Hansch method helps to estimate the partition coefficient of drugs using water and *n*-octanol. The drug NVP and FPV were added to the n-octanol: water system separately and kept aside for 24 h. The solvent from both layers was collected and a UV spectrophotometer was used to analyze at 283 nm for NVP and 265 nm for FPV (Chimiel et al., 2019).

4.1.5 Determination of ultraviolet absorbance maxima (λmax)

For determining the absorbance maxima (λmax), scanning was carried out in methanol. With the appropriate dilution of the standard stock solution with respective solvents, (UV-1800, Shimadzu) against a blank solution. FPV and NVP solutions (10 µg/mL) were used to record the spectrum. From the spectra obtained, the absorbance maxima (λ_{max}) were determined for both NVP and FPV (Bhavyasri et al., 2019; Cyganowski et al., 2022).

4.1.6 Preparation of standard calibration curves (pH 5 and pH 7.4)

The standard calibration curves of NVP and FPV were prepared in methanol: phosphate buffer (40:60) in the range of 5.0-27.5 µg/mL concentration at 265 nm and NVP were prepared in methanol: phosphate buffer (40:60) and methanol: acetate buffer pH 5.0 (40:60) in the concentration range of 5.0-25.0 µg/mL at 283 nm. For the standard calibration curve of FPV and NVP, 10 mg of each FPV and NVP were weighed and placed in a separate volumetric flask. To this sufficient quantity of methanol: phosphate buffer pH 7.4 and methanol: acetate buffer pH 5 (40:60) in a volumetric flask of 10 mL. The desired volume was maintained with methanol: PBS pH 7.4 and methanol: acetate buffer pH 5.0 (40:60) which gives 1000 µg/mL standard stock solution-I (S-I). 1mL was withdrawn from the stock solution-I (SS-I), shifted into another volumetric flask of 100 mL, and the volume was maintained with methanol: phosphate buffer pH 7.4 and acetate buffer pH 5.0 (40:60) to get a second stock solution-II (SS-II), having a concentration of 100 µg/mL. From the second stock solution (SS-II) various concentrations were prepared respectively. The absorbance of final solutions was measured at 265 nm for FPV and 283 nm for NVP in a UV-visible spectrophotometer (UV-1800 series Shimadzu). The calibration curve was plotted using the Microsoft Excel program and statical parameters were applied and determined (Bhavyasri et al., 2019; Cyganowski et al., 2022).

4.2 Characterization of drug NVP, FPV, dendrimers, and carbon nanotubes

4.2.1 UV spectrophotometer

For determining the absorbance maxima (λmax), scanning was carried out in methanol. With the appropriate dilution of the standard stock solution with respective solvents, the solutions were scanned between 200-400 nm with a UV-visible spectrophotometer (UV-1800, series Shimadzu) against a blank solution. Dendrimers and carbon nanotube solutions (10 µg/mL) were used to record the spectrum. From the spectra obtained the absorbance maxima (λ_{max}) of the drug was determined.

4.2.2 FTIR spectrophotometer

The spectra of FTIR of 5G PPI dendrimers and COOH-MWCNTs were taken separately to study the structural characteristics. KBr pellets were prepared with the samples of MWCNT and dendrimers by triturating KBr pellets uniformly. The pellets were exposed to the IR beam and the spectrum was determined between 4000-400 cm^{-1}. The instrument used was FTIR spectrophotometer (Perkin Elmer 100 Series, USA). The spectra of the drugs, dendrimers, and MWCNT were studied (Mirali et al., 2021).

4.2.3 Differential Scanning Calorimetry

Differential Scanning Calorimetry studies are the thermal studies that help to study the thermal properties such as melting point, exothermic onset temperature, reaction order, activation energy, and extent of reactions. The drugs FPV and NVP were subjected to thermal analysis to confirm the melting point and to study the purity of the drug. The sample was placed on the aluminum pan and packed properly. The heating rate was set from 2 °C/min using DSC (Perkin Elmer, Massachusetts, United States), (Hsieh et al., 2010; Chountoulesi et al., 2019).

4.2.4 X-Ray Diffraction

X-ray diffraction is the nondestructive method to study the crystallinity of the samples. The crystal nature of the drug can be studied with a high-intensity X-ray beam exposed to the samples and a diffractogram was studied. The degree of crystallinity depends on the width of the peaks of the diffractogram. The XRD pattern of the drugs was studied using XRD diffractogram (Bruker, Massachusetts, United States). The monochromatic Kα1 radiation with Johansson monochromators for Cu at the wavelength of 1.5406 A°, with an electric potential difference of 40 kV and current of 30 mA. The silicon substrate was used to cast the samples and then exposed to X-rays. The X-ray diffractogram was developed in the range of 0-80θ between 2θ angle (Hamedi and Koosha, 2020).

4.2.5 Nuclear Magnetic Resonance Spectroscopy

Nuclear magnetic resonance spectroscopy is the confirmatory and most desirable analytical method to evaluate the chemical structure of raw materials. FPV and NVP were subjected to NMR spectroscopy for structural confirmation. The drugs were subjected to proton NMR (Bruker Advance II) at an operational frequency of 400 MHz in Dimethylsulfoxide (DMSO). The drug samples were dissolved in DMSO (Zhang et al., 2014).

4.2.6 Field emission scanning electron microscopy

FE-SEM helps to examine the outer surface characteristics such as porosity, cracks, and defects in the dendrimer structures. It also provides structural confirmation of the samples. Surface morphology studies were carried out using FE-SEM (Jeol, USA, Inc) having 1.0 nm (15kV) resolution. The detector used was secondary. The sample was prepared by coating with a thin layer of gold using a JFC ion sputter coater. The scanning was carried out at an accelerated voltage of 15 kV (Shi et al., 2022).

4.2.7 High-resolution transmission electron microscopy

HR-TEM helps to study the morphology and structure of DT and drug-loaded DT. For morphological studies, the samples were kept on copper grids which are coated with holey carbon support film. For in situ heating, was carried out on silicon nitride support film of thickness 50 mm. For the TEM study, a JEOL 2010 instrument operating at 120 kV and fitted with a Gatan heating stage, an Oxford Instruments INCA EDS system, and a Gatan SC1000 ORIUS CCD camera were used. To guarantee that the samples remained stable at each temperature, the rate of heating was around 10 °C/min, and the dwell duration was less than five min or even longer (Benjamin, 2008).

4.3 HPLC Method Development and Validation

4.3.1 Spectral Analysis

10 µg/mL solution of drugs FPV and NVP was prepared separately using methanol. The samples were scanned against methanol as blank using a UV spectrophotometer 1800 (Shimadzu, Japan) in the range of 200-400 nm. The physical mixture of 10 µg/mL of both drugs was prepared. The prepared solution was scanned using a UV spectrometer.

4.3.2 Method Development by HPLC

A simultaneous method was developed for drug NVP and FPV using the HPLC method (Shimadzu LC-20AD Prominence, Japan) using a Nucleodur C18 column with dimensions 250 mm x 4.6 mm and bead diameter of 5µm, with a photodiode array detector (SPD-M20A; Shimadzu, Japan) and a Rheodyne injector (7725i). The pump used was the LC20AD pump. LabSolution version 5.82 was used for chromatographic integration, recording, and statistical

evaluation. The rate of flow was adjusted to 1 mL/min. The mode was isocratic. The volume of sample injection was set at 20 µL for the sample injection.

The mobile phase used for isocratic elution was Methanol: Water in the ratio of 80:20. Different solvent systems were used for the elution of the two drugs FPV and NVP in the same chromatogram. The composition of the mobile phase was selected based on chromatographic peak parameters such as peak purity, sharpness, resolution, and tailing factors of the peaks. The solvent system should support the complete resolution of two peaks. Different trials were carried out to better elution of the two drugs. Solvent mixtures used for method development are Buffer: Methanol, Buffer: Acetonitrile (ACN), Formic acid: ACN, Formic acid: Methanol, and Methanol: Water.

4.3.3 Preparation of the stock solution for FPV and NVP

10 mg of FPV and NVP were weighed accurately and shifted to a volumetric flask of 10 mL. To the flask, a small quantity of methanol was added and mixed properly to solubilize the drugs NVP and FPV. Finally, the volume was adjusted to 10 mL with methanol.

4.3.4 Preparation of the working solution

1 mL of liquid sample was taken from the stock preparation and shifted to a volumetric flask of 10 mL and methanol was used to adjust the volume up to 10 mL which gives the concentration of 100 µg/mL. For the working solution from the above solution of 100 µg/mL, 1 mL was withdrawn and shifted to a volumetric flask of 10 mL, and methanol was used to adjust the volume up to 10 mL. The concentration of the working solution was 10 µg/mL each for FPV and NVP.

4.3.5 Method Validation

Validation of the optimization of a simultaneous estimate of FPV, APV, and NVP has been performed in accordance with the requirements provided by the *International Council for Harmonisation* (ICH, 2023) 45 Q2 (R1). The assessing system, appropriateness, LOD and LOQ, accuracy, range, specificity, linearity, robustness, and precision are all aspects that are covered by the rules [ICH, 2023].

4.3.5.1 System suitability

The validation of the optimization of the simultaneous estimation of FPV and NVP has been accomplished in compliance with the requirements that have been established by ICH 45 Q2 (R1). The guidelines address a variety of parameters, including system assessment, appropriateness, LOQ and LOD, range, linearity, accuracy, specificity, robustness, and precision (ICH, 2023).

4.3.5.2 Preparation of calibration curve

The calibration curve was plotted using the standard working solution. From the 10 µg/mL working solution, further dilution was made of concentrations 2.0, 4.0, 6.0, 8.0, and 10.0 µg/mL. The dilution was made by withdrawing 2.0, 4.0, 6.0, 8.0, and 10.0 mL of working stock solution in the five different volumetric flasks, and methanol was used to make up the volume up to 10 mL. The sample was analyzed using HPLC, and the curve used for calibration was displayed with a peak area on the y-axis and the concentration was plotted on the x-axis. To calculate the mean peak area, each injection was performed six times. Using the analytical technique, we were able to determine the calibration curve's slope, intercept, and coefficient of correlation.

4.3.5.3 Linearity and Range

Plotting the concentration against the mean area of peaks of each concentration allowed for the development of the calibration curve. Using the analytical technique, we were able to determine the coefficient of correlation, intercept, and calibration curve's slope (Kumar et al., 2020).

4.3.5.4 Accuracy study

      The accuracy was calculated by recovery calculations (absolute) of the two drugs from the prepared samples. The study was performed at three levels, qualified as 80, 100, and 120% of the middle concentration of the calibration curve. For FPV, the mid concentration was 7.18 µg/mL and for NVP mid concentration was 7.74 µg/mL. The three levels of quantification were classified as higher quantified concentration, medium quantified concentration, and lower quantified concentration abbreviated as HQC, MQC, and LQC respectively. In the case of FPV, the LQC was 5.98 µg/mL, MQC 7.18 µg/mL, and HQC was 8.38 µg/mL and for NVP the LQC was 6.54 µg/mL, MQC was 7.74 µg/mL and HQC was 8.94 µg/mL.

4.3.5.5 Precision studies

The examination of the accuracy of the developed method was divided into two parts: the first portion focused on the repeatability of the method, while the second part investigated its intermediate precision. To investigate repeatability, the samples were injected six times at LQC, MQC, and HQC, maintaining similar chromatographic conditions on the same day. The intermediate precision was achieved by injecting six times as many LQC, MQC, and HQC samples at the same chromatographic settings but on separate days (interday). Additionally, each sample was analyzed by a different analyst. The data were summarized by noting the mean, and the % relative standard deviation (RSD) was computed.

Formula

$$Absolute\ recovery = Actual\ concentration\ recovered/$$
$$Theoretical\ concentration\ X\ 100$$

4.3.5.6 Determination of LOD and LOQ

The LOD and LOQ calculations of FPV and NVP and metabolite APV were carried out with the use of an equation for linear regression that depends on the standard deviation (SD) of the slope and intercept. The formula for determining LOD and LOQ is given below:

Formula:

$$\text{LOD} = 3.3\frac{Q}{S} \qquad \text{LOQ} = 10(\text{SD}/\text{S})$$

4.3.5.7 Robustness

There have been several planned and subtle adjustments made to the chromatographic settings, particularly the rate of flow and wavelength. These adjustments have been made in an array of different methods. These adjustments were also assessed for their effects on the separation of FPV, and NVP (Gupta et al., 2020).

4.4 Formulation development

4.4.1 Synthesis and characterization of DT (Conjugation of carboxylated MWCNT and dendrimers)

Accurately weighed 200 mg of 5G PPI dendrimers and 1000 mg of COOH-MWCNT were taken in the round bottom flask. 10 mL of water and methanol was added in a 2:1 ratio. The prepared mixture was sonicated on a bath sonicator for 60 min. The sonicated preparation was rotated using a magnetic stirrer (Remi) for 24 h at 50 ˚C. After 24 h collect the sample and wash the mixture properly with water. The resultant product was dried in a hot air oven at 50 ˚C till it was completely dried. The dried product was collected and stored in an air-tight container for further characterization (Pan et al. 2006).

4.4.2 Mannosylation of DT

Accurately weighed 500 mg of the D-mannose was taken in a round bottom flask. To this round bottom flask, 10 mL of acetate buffer (pH 4.0) was added. Then 100 mg DT was added. The flask was heated for 2 h at 60 ˚C. The solution was further stirred for 72 h to complete the reaction using a magnetic stirrer. Following a period of 72 h, the solutions were dialyzed in a cellulose dialysis membrane bag (Molecular weight cut off (MWCO) 7000 Da, Himedia, India) against water and methanol in a ratio of 2:1 while the sink condition was maintained. This process lasted for 15 min. This process helps to remove unconjugated mannose. The resultant product was collected and dried at 50 ˚C till it was completely dried. The dried product was collected and stored in an air-tight container for further characterization (Pruthi 2012; Mirali 2021).

4.4.3 Formulations loaded with NVP

4.4.3.1 Formulation development and characterization of NVP-loaded dendrimers

100 mg of drug NVP was weighed accurately and taken in a 10 mL volumetric flask. 20 mL methanol was added upto the mark and mixed. The drug methanol solution was sonicated for 10 min to solubilize the drug completely. The above solution was transferred to a round bottom flask and into this accurately weighed 50 mg of dendrimers was added. The preparation was stirred using a magnetic stirrer for 48 h. Following a period of 48 h, the solutions were dialyzed in a cellulose dialysis membrane bag (MWCO 7000 Da, Himedia, India) against a water and methanol at a ratio of 2:1 while the sink condition was maintained. This process lasted for 15 min. The resultant product was collected and dried at 50±1 $^{\circ}$C till it was completely dried. The dried product was collected and stored in an air-tight container for further characterization (Kaur et al. 2017).

4.4.3.2 Formulation development and characterization of NVP-loaded carbon nanotubes

Accurately weighed 200 mg of drug NVP was taken. 20 mL of methanol was mixed with the drug NVP. The drug methanol solution was sonicated for 10 min to solubilize the drug completely. The above solution was transferred to a round bottom flask and then 10 mL water was added and to this accurately weighed 200 mg of carbon nanotubes was mixed. The preparation was stirred using a magnetic stirrer for 48 h. Following a period of 48 h, the solutions were dialyzed in a cellulose dialysis membrane bag (MWCO 7000 Da, Himedia, India) against water and methanol at a ratio of 2:1 while the sink condition was maintained. This process lasted for 15 min. The resultant product was collected and dried at 50±1 $^{\circ}$C till it was completely dried. The dried product was collected and stored in an air-tight container for further characterization (Zhu et al., 2019).

4.4.3.3 Formulation development and characterization of NVP-loaded DT

Accurately weighed 200 mg of drug NVP was taken. 20 mL of methanol was mixed with the drug. The drug methanol solution was sonicated for 10 min to solubilize the drug completely. The above solution was transferred to a round bottom flask and then 10 mL water was added and to this accurately 200 mg of DT was added. The preparation was stirred using a magnetic stirrer for 48 h. Following a period of 48 h, the solutions were dialyzed in a cellulose dialysis membrane bag (MWCO 7000 Da, Himedia, India) against water and methanol at a ratio of 2:1 while the sink condition was maintained. This process lasted for 15 min. The resultant product was collected and dried at 50 ±1 $^{\circ}$C till it was completely dried. The dried product was collected and stored in an air-tight container for further characterization (Singh et al., 2021; Zhu et al., 2019).

4.4.4 Formulations loaded with FPV

4.4.4.1 Formulation development of FPV-loaded dendrimers

100 mg of drug FPV was weighed accurately. 20 mL of methanol was added to the drug and mixed well. The drug methanol solution was sonicated for 10 min to solubilize the drug completely. The above solution was transferred to a round bottom flask and then 10 mL water was added and to this accurately weighed 200 mg of carbon nanotubes was added. The preparation was stirred for 48 h using a magnetic stirrer. Following a period of 48 h, the solutions were dialyzed in a cellulose dialysis membrane bag (MWCO 7000 Da, Himedia, India) against water and methanol at a ratio of 2:1 while the sink condition was maintained. This process lasted for 15 min. The resultant product was collected and dried at 50 ± 1^{0}C till it was completely dried. The dried product was collected and stored in an air-tight container for further characterization (Singh et al., 2021).

4.4.4.2 Formulation development and characterization of FPV-loaded carbon nanotubes

Accurately weighed 200 mg of drug FPV was taken. 20 mL of methanol was added to the drug and mixed. The drug methanol solution was sonicated for 10 min to solubilize the drug completely. The above solution was transferred to a round bottom flask and then 10 mL water was added and to this accurately weighed 200 mg of carbon nanotubes was added. The preparation was stirred using a magnetic stirrer for 48 h. Following a period of 48 h, the solutions were dialyzed in a cellulose dialysis membrane bag (MWCO 7000 Da, Himedia, India) against water and methanol at a ratio of 2:1 while the sink condition was maintained. This process lasted for 15 min. The resultant product was collected and dried at 50±1 $^{\circ}$C till it

was completely dried. The dried product was collected and stored in an air-tight container for further characterization (Zhu et al., 2019).

4.4.4.3 Formulation development and characterization of FPV-loaded DT

Accurately weighed 200 mg of drug FPV was taken. 20 mL of methanol was added and mixed well. The drug methanol solution was sonicated for 10 min to solubilize the drug completely. The above solution was transferred to a round bottom flask and then 10 mL water was added and to this accurately weighed 200 mg of DT was added. The preparation was stirred using a magnetic stirrer for 48 h. Following a period of 48 h, the solutions were dialyzed in a cellulose dialysis membrane bag (MWCO 7000 Da, Himedia, India) against water and methanol at a ratio of 2:1 while the sink condition was maintained. This process lasted for 15 min. The resultant product was collected and dried at 50 ± 1 $^{\circ}$C till it was completely dried. The dried product was collected and stored in an air-tight container for further characterization (Singh et al., 2021; Zhu et al., 2019).

4.4.5 FPV and NVP loaded DT

4.4.5.1 Formulation development and characterization of NVP and FPV-loaded DT

200 mg of drug NVP was accurately weighed was placed in a round bottom flask. To this methanol, 20 mL was added and mixed well. The drug methanol solution was sonicated for 10 min to solubilize the drug completely. 200 mg of FPV was added and sonicated for 2 min to solubilize the drug. The above solution was transferred to a round bottom flask and into this accurately weighed 400 mg of DT was mixed. The preparation was stirred using a magnetic stirrer for 48 h. Following a period of 48 h, the solutions were dialyzed in a cellulose dialysis membrane bag (MWCO 7000 Da, Himedia, India) against a mixture of water and methanol at a ratio of 2:1 while the sink condition was maintained. This process lasted for 15 min. The resultant product was collected and dried at 50 ± 1 $^{\circ}$C till it was completely dried. The dried product was collected and stored in an air-tight container for further characterization (Kaur et al. 2017).

4.4.5.2 Mannosylation of NVP and FPV-loaded DT

Accurately weighed 500 mg of the D-mannose was taken in a round bottom flask. To this round bottom flask, 10 mL of acetate buffer (pH 4.0) was added. Then 100 mg NVP and FPV-loaded DT were incorporated into the flask. The flask was heated for 2 h at 60 ^{0}C. The solution was further stirred for 72 h to complete the reaction using a magnetic stirrer. Following a period of 72 h, the solutions were dialyzed in a cellulose dialysis membrane bag (MWCO 7000 Da, Himedia, India) with water as the receptor medium while the sink condition was

maintained. This process lasted for 15 min. The process helps to remove unconjugated mannose. The resultant product was collected and dried at 50±1 °C till it was completely dried. The dried product was collected and stored in an air-tight container for further characterization (Gulbake et al., 2019; Rathod et al., 2019).

4.5 Characterization of DT and developed formulations

4.5.1 Physiochemical properties

The physicochemical properties were studied such as colour, odour, and texture.

4.5.2 Spectrophotometric analysis

4.5.2.1 UV spectroscopy

The absorption spectra of the different formulations were determined using a UV spectrophotometer (Shimadzu). The sample was studied with a 10-mm quartz cell. The UV–visible spectra of different formulations were studied in the range of 190–420 nm (Noordadi et al. 2018).

4.5.2.2 FITR Spectroscopy

FTIR spectroscopy analysis helps to detect the structure of DT and drug loading in DT, dendrimers, and MWCNT using the PerkinElmer Spectrum IR Version 10.6.1. The absorbance spectrum was obtained using KBr pellets. A beam of light was utilized at different frequency levels and absorption was noted. Different functional groups present in the sample correspond to specific wave numbers. This is an important technique for identifying and confirming the specific functional group in a particular sample (Samsodien et al., 2017). The samples of dendrimers, COOH-MWCNT, and dendritubes, different formulations were subjected to FTIR spectroscopy for the confirmation of the functional groups (Razzazan et al. 2016).

4.5.2.3 Raman Spectroscopy

The spectra provide details about the diameter of the carbon structure, the presence of any interactions as well as defects in the carbon structures. It also gives a clear indication of the sp^2 hybridized structure. The prepared conjugate, DT, and drug-loaded formulations were subjected to Raman spectroscopy (Bruker) equipped with three wavelengths. Raman spectroscopy measurements were carried out on powdered samples with a **BRUKER RFS 27 MultiRAM FT Raman Spectrometer** instrument at an excitation wavelength of 785 nm. The source used was Nd-YAG laser (1064 nm) in addition there was a white light source. The spectral range applied was 50-4000 cm^{-1} (Piao et al., 2021).

4.5.2.4 Nuclear Magnetic Resonance Spectroscopy

Nuclear magnetic resonance spectroscopy is the confirmatory and most desirable analytical method to evaluate the chemical structure of DT and developed formulations.

Different formulations containing NVP and FPV were subjected to NMR spectroscopy for structural confirmation. The drugs were subjected to proton NMR (Bruker Advance II) at an operational frequency of 400 MHz in Dimethylsulfoxide (DMSO). The drug samples were dissolved in DMSO (Zhang et al., 2014).

4.5.3 X-ray diffraction

X-ray diffraction is the nondestructive method to study the crystallinity of the samples. To study the crystal nature of the novel conjugate system DT and drug loaded formulations, a high-intensity X-ray beam was exposed to the samples, and a diffractogram was studied. The degree of crystallinity depends on the width of the peaks of the diffractogram. The XRD pattern of the DT and different formulations was studied using an XRD diffractogram (Bruker, Massachusetts, United States). The monochromatic Kα1 radiation with Johansson monochromators for Cu at the wavelength of 1.5406 A°. The silicon substrate was used to cast the samples and then exposed to X-rays. The X-ray diffractogram was developed in the range of 0-80θ between 2θ angle (Hamedi 2020).

4.5.4 Differential scanning calorimeter

Differential Scanning Calorimetry studies are the thermal studies that help to study the thermal properties such as exothermic onset temperature, melting point, reaction order, activation energy, and extent of reactions. DT and the FPV and NVP loaded formulations were subjected to thermal analysis to confirm the melting point and to study the possible interaction during conjugations. The sample was placed on the aluminum pan and packed properly. The heating rate was set from 2 °C/min using DSC (Perkin Elmer, Massachusetts, United States) (Heise 2010; Chountoules et al 2019).

4.5.5 Morphological analysis

4.5.5.1 Field emission scanning electron microscopy

FE-SEM helps to study the outer surface characteristics such as porosity, cracks, and defects in the DT and the drug-loaded structures. It also provides structural confirmation of the DT and the different formulations. Surface morphology studies were carried out using FE-SEM (Jeol, USA, Inc) having 1.0 nm (15kV) resolution. The detector used was secondary. The sample was prepared by coating with a thin layer of gold using a JFC ion sputter coater. The scanning was carried out at an accelerated voltage of 15 kV (Shi et al., 2022).

4.5.5.2 Transmission electron microscopy

Transmission electron microscopy helps to study the morphology and structure of DT and drug-loaded formulations. For morphological studies, the samples were kept on copper grids which are coated with holey carbon support film. For in situ heating, was carried out on silicon nitride support film of thickness 50 mm. For the HR-TEM study, a JEOL 2010 instrument operating at 120 kV and fitted with a Gatan heating stage, an Oxford Instruments INCA EDS system, and a Gatan SC1000 ORIUS CCD camera were used. To guarantee that the samples remained stable at each temperature, the rate of heating was around 10 °C/min, and the dwell duration was less than five min or even longer (Benjamin 2008).

4.5.5.3 Atomic force microscopy

Atomic force microscopic studies were studies to confirm the spherical structure of the dendrimers. AFM images precisely provide the 3D structure of the sample. The method is efficient and accurate and can be carried out with a small amount of samples. The sample was prepared with mica deposition by cooling it at 120 ºC for 3-4 min. For the analysis single beam cantilever was used in tapping mode. The scanning range used was 5-10 nm and the scanning rate was 0.5 Hz. The frequency of resonance was 300 kHz. The scanner used was a 7 µm scanner. The sample solution was dropped on the surface of the mica film. The images were

captured using a Veeco Digital Instruments Multimode Nanoscope (Model: XE100) (Sharma et al., 2018).

4.5.6 Particle size and zeta potential

The particle size and zeta potential of the prepared DT and drug-loaded formulations were estimated by measuring the dispersion by Zetasizer Ver. 7.13, Malvern, using the light scattering method (Youssry et al. 2020). Zeta potential affects the different aspects of the CNTs such as electroosmosis, flocculation, and stability.

4.5.7 Dispersibility test

The dispersibility test was ~~carried out~~done to study the ~~rate~~ stability of dispersion with respect to time. 5 mg of MWCNT, DT, and the different formulations were weighed and dispersed using deionized water (5 mL), and the dispersion was sonicated ~~(Brand)~~using a bath sonicator for 5 min. The dispersions were observed manually for 24 h (Pruthi et al., 2012).

4.5.8 Drug entrapment

Entrapment efficiency helps to estimate the amount of drug enclosed inside the prepared conjugates. It is an indirect method, that determines the drug content in the solvent system, and the difference between the loaded drug initially and the amount in solvent gives the amount of drug entrapped. After drug loading the prepared dispersion was shifted into a dialysis bag (MWCO 7000 Da, Himedia, India). The bag was shifted to the solution of methanol: water (40:60) and kept for stirring for 15 min. After 15 min the solvent was withdrawn and the drug content was analyzed using a UV spectrophotometer (Shimadzu UV/Vis, Japan) at 265 nm for FPV and 283 nm for NVP (Parashar et al., 2018). % entrapment efficiency was determined using the formula given below:

$$\% \text{ Entrapment Efficiency} = \frac{\text{Total weight - Weight of unloaded drug}}{\text{Total weight}} \times 100$$

4.5.9 *In vitro* drug release

In vitro release study was performed by equilibrium dialysis tube diffusion technique. 5 mL of individual drug-loaded dendrimers/MWCNT/DT solution in methanol (10 mg/5 mL) was taken in a dialysis bag (MWCO 7000 Da, Himedia, India) and tied in hermetical fashion. The prepared tube was dialyzed using methanol: buffer (PBS pH 7.4 and acetate buffer pH 5) under sink conditions. 1 mL of the liquid sample was withdrawn at hourly intervals till 8 h, then at 24, 30, 48, 72, and 96 h. Fresh solvent (1 mL) was added back to maintain the sink condition. The withdrawn sample was diluted with a suitable solvent system and analyzed

using a UV spectrophotometer (Shimadzu UV/vis, Japan) at 265 nm for FPV and 283 nm for NVP (Tan et al., 2014). The formulation containing dual drugs in DT and mannosylated dual drug-loaded DT samples were analyzed by HPLC (Shimadzu, Japan) (Ramanunny et al., 2021).

4.5.10 Release kinetic

The drug release data were subjected to different mathematical models such as first order, zero order, Hixon-Crowell, Korsmeyer-Peppas model, and Higuchi models. The R^2 value was estimated to judge the best model fitting to the release profile. The first-order release indicates that the reaction rate is related to the amount of drug. The zero-order indicates constant drug release from the conjugates. Higuchi's model illustrates the release of both hydrophilic and sparingly soluble drugs by dissolution or by diffusion. Korsmeyer-Peppas model helps to co-relate the diffusion of the drug through the polymeric matrix. The n value (release exponent) can be co-related with release mechanisms. The diffusion pattern can be studied with the help of the n value. If the value of n is less than 0.5 suggests diffusion by fickian mode and a value more than 0.5 to 1.0 indicates non-fickian diffusion. Hixon-Crowell model indicates that the release of the drug was related to alteration in the total area or diameter of the particles of the drug (Lee et al., 2015; Chudoba et al., 2021)

The equation of different models is as follows:

a) Zero order model: $M_t = kt + M_0$

b) First order kinetics: $M_t = M_0{}^{ekt}$

c) Higuchi Model: $M_t/M_\infty = kt^{1/2}$

d) Korsmeyer-Peppas Model: $M_t/M_\infty = kt^n$

M_t stands for the amount of released drug from the conjugated system at time t, and M_0 is the total amount of the drug in the conjugated system. M_t/M_∞ is the fraction of released drug, n is the diffusion exponent and k is the rate constant.

4.6 Stability studies

Stability studies help to govern the shelf life of the formulated products. It is the time in which the product retains its chemical, physical, and pharmacokinetic properties and characteristics throughout the life of the pharmaceuticals. ICH guideline of stability testing of new drug substances and products Q1A(R2) was followed for the stability studies of the prepared formulations. The prepared formulations of NVP-DT, FPV-DT, and NVP-FPV-DT were subjected to stability studies to evaluate the stability of the product for 3 months. The prepared NVP-DT, FPV-DT, and NVP-FPV-DT were dispersed in PBS pH 7.4 (5 mL) kept at 4±2 °C, at room temperature (25±2 °C) and accelerated temperature (40±2 °C) for six weeks

and studied at the interval of 1 week. The prepared formulations of NVP-DT, FPV-DT, and NVP-FPV-DT were evaluated for colour change, texture, consistency, turbidity, precipitation, and leakage of a drug. A drug leakage test was performed using a dialysis bag (MWCO 7000 Da, Himedia, India), 1 mL of the aliquot was placed and the dialysis bag was sealed from both ends. The dialysis bag was kept in PBS pH 7.4 and methanol in the ratio of 60:40. The sample was analyzed after 1h and the leaked amount of drug was evaluated using a UV-spectrophotometer at 283 nm for NVP and 265 nm for FPV. The same procedure was repeated weekly for 6 weeks (Jose et al., 2016; Singh et al., 2016).

4.7 *In vitro* cell line studies

4.7.1 Cytotoxicity studies

The cytotoxicity of DT, mannosylated DT, drug NVP, and FPV, both drug-loaded DT and mannosylated both drug loaded DT was examined in Raw 264.7 (Monocyte Macrophage) cells using the MTT assay. In a 96-well plate, cells were grown at a density of 2×10^4 cells per well in Dulbecco's Modified Eagle (DMEM) medium that was augmented with 10% FBS, 1% penicillin, and 1% streptomycin. The incubator was maintained at 37 °C with a 5% CO_2 atmosphere. After the incubation of 24 h, varying concentrations (5-100 dispersed in media) of DT, mannosylated DT, drug NVP, and FPV, both drugs-loaded DT and mannosylated drug-loaded DT were added in the wells in a triplicate manner. After an incubation period of twenty-four hours, the wells were cleaned with PBS, and then 200 µL of MTT (0.5 mg/mL) was added. Crystals of formazan that had been growing for 4 h were dissolved in 200 µL of isopropanol. With the use of a microplate reader, the optical absorbance was measured to be 570. (Epoch2, BoiTek) (Varshosaz et al., 2018). The results were stated as the percentage of cell survival and calculated using the following formula:

$$\% \text{ Cell survival} = \left(\frac{\text{A570 nm of treated cell}}{\text{A570 nm of untreated control cells}} \right) \times 100$$

4.7.2 Cell internalization studies

On coverslips, raw 264.7 cells, also known as monocyte-macrophage cells, were placed at a density of 2×10^5 cells per well. The uptake efficiency of prepared formulations was evaluated by treating cells with Fluorescein isothiocyanate (FICT; Green Chanel) tagged drug-loaded DT, and mannosylated drug-loaded DT. These treatments were carried out to examine the efficacy of the prepared structure. After a total of 4 h, the conjugates-containing medium was discarded, and the cells were fixed with 4% paraformaldehyde for twenty min. After mounting the coverslips on slides, uptake was seen with a confocal microscope equipped with a Leica sp5 system (Biagiotti et al, 2018).

4.8 *In vivo* studies

4.8.1 Animals

81 female Wister rats were procured from the Center of Animal House, Panjab University, Chandigarh, India for the bioanalytical methods development. The rats were kept at room temperature (25 ± 2 °C) and relative humidity (RH) of $55 \pm 10\%$. In the animal house light-dark cycle of 12:12 was followed. Cages for rats were made up of polypropylene layered with husk. The rat was selected from the age group of 10-12 weeks and the weight range was 250-350 g. The feeding routine includes the standard

pellet diet and water. The protocol was approved by The Institutional Animal Ethical Committee of the School of Pharmaceutical Sciences, Lovely Professional University (Protocol no: LPU/IAEC/2022/03) (Khursheed et al., 2022).

The details of the different animal groups required are given below:

Table 4: Animal grouping representing diet, dose, route of administration, and number of animals in each group

Group No.	Sample code	Diet, dose, and route of drug treatment	No of animals
Group 1	Vehicle Control	NPD, Normal saline (Vehicle), IV route	9
Group 2	DT	NPD, 10 mg/kg (DT plain), single dose, IV route	9
Group 3	Mannosylated DT	NPD, 10 mg/kg (DT plain), single dose, IV route	9
Group 4	Drug –NVP	NPD, 10 mg/kg (NVP), single dose IV route	9
Group 5	Drug – FPV	NPD, 70 mg/kg (FPV), single dose IV route	9
Group 6	NVP loaded DT	NPD, equivalent to 10 mg/kg (NVP), single dose, IV route	9
Group 7	FPV loaded DT	NPD, equivalent to 70 mg/kg (FPV), single dose IV route	9
Group 8	NVP and FPV loaded DT	NPD, 70 mg/kg, single dose IV route	9
Group 9	Mannosylated NVP and FPV DT	NPD, 70 mg/kg, single dose IV route	9

* NPD: Normal pellet diet, IV: Intravenous route

4.8.2 Bioanalytical Method Development

4.8.2.1 Spectral Analysis

The solution of drugs FPV, APV, and NVP was prepared separately using methanol as a solvent. 10 µg/mL solution was prepared for each drug. Methanol was used as a blank solution for the analysis using a UV-Vis spectrometer (UV-1800, Shimadzu, Japan). The scanning was carried out in the range of 400-200 nm (Goku et al., 2020; Shokouhi et al., 2020).

4.8.2.2 Method development

A simultaneous bioanalytical method was developed using High-performance liquid chromatography (HPLC) (Waters, Model no: 515 se: J07515777a, India) using ODS C-18 column (Serial no: 015231308138) with dimensions 250 mm x 4.6 mm and 5μm bead size, with photodiode array detector (2998; Waters, Milford, MA) and the instrument is equipped with an autosampler (717). The pump used was the Water's 515 pump. Empower 2.0 software was used for chromatographic integration, recording, and statistical evaluation. The mode was isocratic and the volume of injection was set to 20 μg/mL for the sample injection with a flow rate of 0.5 mL/min. The mobile system used for isocratic elution was Methanol: Water: ACN (800 mL: 200 mL: 50 mL). Different solvent system was used for the elution of the three drugs FPV, APV, and NVP in similar chromatographic conditions. The composition of the mobile phase was selected based on chromatographic peak parameters such as peak purity, sharpness, resolution, and tailing factors of the peaks. The solvent system should support the complete resolution of two peaks. Different trials were carried out to better elution of the two drugs. Solvent mixtures used for method development are Water: Methanol, and Water: ACN in different ratios.

4.8.2.3 Extraction of plasma

In rats, the sample of blood was taken from the retro-orbital cavity by puncturing with a capillary tube. The blood sample was collected in ethylene diamine tetra acetic acid (EDTA) crystals containing radioimmune assay vials. The rat was anesthetized before the blood collection. The neck of the rat was held tightly making the eyes bulge. The fine capillary tube was inserted into the eye's medial canthus, the blood started coming out through the capillary tube. The blood was collected in EDTA-containing vials to prevent blood coagulation. The blood-containing tube was centrifuged at 5213 g for 15 min. After centrifugation, the above liquid was collected with the help of a micropipette and stored at -20 °C in a deep freezer (Gadag et al., 2022; Duse et al.,2021).

4.8.2.4 Preparation of blank solution of plasma

To precipitate the proteins of plasma, 1 mL of extracted plasma was obtained, and then 2 mL of acetone and acetic acid in combination with a volume-to-volume ratio of 1:1 was added. The prepared was then vortexed for five min. After collecting the supernatant, it was centrifuged at a speed of 5213 g for fifteen min. After collecting the supernatant in a volumetric flask of 100 mL and final volume was made up to 100 mL (Mohan et al., 2021).

4.8.2.5 Preparation of the stock solution for FPV, APV, and NVP

Plasma was dissolved in ACN to create the standard stock solution, which included a combination of FPV, APV, and NVP at a concentration of 10 µg/mL each. To prepare the stock solution with plasma, two mL of plasma were obtained and 10 mg of FPV, APV, and NVP were added to it respectively. After agitating the mixture for ten min with a vortex, two mL of an acetone and acetic acid mixture with a volume-to-volume ratio of one to one was added to the matrix that had been spiked, and the combination was then centrifuged once more to separate different proteins in plasma proteins. The whole contents were subjected to a 15-minute centrifuge at a speed of 5213 g. After collecting the supernatant in a volumetric flask, the volume was brought up to 100 mL to prepare a stock solution of 1000 mg/mL (stock solution A) (Mohan et al., 2021).

4.8.2.6 Preparation of the working solution

After taking an aliquot (1 mL) from the stock solution and transferring it to a volumetric flask with a capacity of 10 mL, the volume was brought up to 10 mL with ACN, which resulted in a concentration of 100 µg/mL. From the solution described above (100 µg/mL), 1 mL was removed, and placed in a volumetric flask of 10 mL, and the volume was brought up to 10 mL with ACN. The FPV, APV, and NVP working solutions all had a concentration of 10 µg/mL when they were added to the working solution (Mohan et al., 2021).

4.8.2.7 Method Validation

Validation of the optimization of a simultaneous estimate of FPV, APV, and NVP has been performed in accordance with the requirements provided by the *International Council for Harmonisation* (ICH) 45 Q2 (R1). The assessing system, appropriateness, LOD and LOQ, accuracy, range, specificity, linearity, robustness, and precision are all aspects that are covered by the rules [ICH].

4.8.2.7.1 System suitability

The validation of the optimization of the simultaneous estimation of FPV, APV, and NVP has been accomplished in compliance with the requirements that have been established by ICH 45 Q2 (R1). The guidelines address a variety of parameters, including system assessment, appropriateness, LOQ and LOD, range, linearity, accuracy, specificity, robustness, and precision (ICH, 2023).

4.8.2.7.2 Preparation of calibration curve

Different concentration for calibration curves was prepared using the working solutions (10 µg/mL). From the 10 µg/mL solution, further dilutions were made ranging from 0.2, 0.8, 1.6, 2.4, and 3.2 µg/mL by withdrawing 0.2, 0.8, 1.6, 2.4, and 3.2 µg/mL from working solution (10 µg/mL) and diluting up to 10 mL. The working stock solution was withdrawn in increments

of 0.2, 0.8, 1.6, 2.4, and 3.2 mL in each of the five volumetric flasks, and the volume was brought up to 100 mL with ACN. The sample was analyzed using HPLC, and the curve used for calibration was displayed with a peak area on the y-axis and the concentration was plotted on the x-axis. To calculate the mean peak area, each injection was performed six times. Using the analytical technique, we were able to determine the calibration curve's slope, intercept, and coefficient of correlation (Mangla et al., 2020).

4.8.2.7.3 Linearity and Range

Plotting the concentration against the mean area of peaks of each concentration allowed for the development of the calibration curve. Using the analytical technique, we were able to determine the coefficient of correlation, intercept, and calibration curve's slope (Mangla et al., 2020).

4.8.2.7.4 Accuracy study

The absolute recovery of the two drugs and their metabolite from the samples that were prepared allowed for the determination of how accurate the approach was. The research was carried out at three different intensities: 80%, 100%, and 120% of the concentration that was found in the middle of the curve used for calibration. The median value of the FPV and APV concentrations was 1.6 µg/mL, while the median value of the NVP concentration was 1.6 µg/mL. HQC, MQC, and LQC make up the three levels of quantification. In the case of FPV and NVP, the LOQ was 1.066 µg/mL, the MQC was 1.6 µg/mL, and the HQC was 1.92 µg/mL (Eswarudu et al., 2019).

4.8.2.7.5 Precision studies

The examination of the accuracy of the developed method was divided into two parts: the first portion focused on the repeatability of the method, while the second part investigated its intermediate precision. To investigate repeatability, the samples were injected six times at LQC, MQC, and HQC, maintaining similar chromatographic conditions on the same day. The intermediate precision was achieved by injecting six times as many LQC, MQC, and HQC samples at the same chromatographic settings but on separate days (interday). Additionally, each sample was analyzed by a different analyst. The data were summarized by noting the mean, and the % relative standard deviation (RSD) was computed (Gupta et al, 2020).

Formula

$$\text{Absolute recovery} = \frac{\text{Actual concentration recovered}}{\text{Theoretical concentration}} \times 100$$

4.8.2.7.6 LOD and LOQ

The LOD and LOQ calculations of FPV and NVP and metabolite APV were carried out with the use of an equation for linear regression that depends on the standard deviation (SD) of the slope and intercept. The formula for determining LOD and LOQ is given below:

Formula

$$\text{LOD} = \frac{3.3\ Q}{S}$$

$$\text{LOQ} = \frac{10\ Q}{S}$$

4.8.2.7.7 Robustness.

There have been several planned and subtle adjustments made to the chromatographic settings, particularly the rate of flow and wavelength. These adjustments have been made in an array of different methods. These adjustments were also assessed for their effects on the separation of FPV, APV, and NVP (Gupta et al., 2020).

4.8.2.7.8 Stability study

FPV, APV, and NVP spiked plasma samples were frozen-thawed in triplicate for three hours at room temperature and three weeks at -20 °C for stability testing. One Ria vial included 3 mL plasma for freeze-thaw stability. This vial was vortexed for 5.0 min with 1 mg of FPV, APV, and NVP for 1000 mg/mL concentration. -20 °C frozen sample. Normal temperature thawed the tube. The first cycle utilized 1 mL of thawed plasma, whereas the second used 2 mL. Centrifuged 1 mL drug-containing plasma. The centrifuged clear supernatant was diluted to 100 mL with ACN to attain 100 mg/mL. Diluted to 1.066 µg/mL (LQC), 1.6 (MQC), and

1.92 (HQC). For the second cycle, 1 mL of the sample of frozen plasma (2 mL) was thawed at room temperature. The rest was frozen. Thawing the third sample. Cycles 2 and 3 followed Cycle 1 for LQC, MQC, and HQC samples. HPLC analyzed triplicate dilutions at 258 nm. Each concentration had a mean, SD, and % RSD (Gupta et al., 2022).

FPV, APV, and NVP-spiked plasma samples were examined for short-term stability at room temperature. Short-term stability was tested before extraction. 3 mL plasma was added to the Ria vial with 3 mg of FPV, APV, and NVP for 1000 µg/ml. Vortexed for 5 min. Ria vial. To create LQC, MQC, and HQC samples, pharmaceuticals were extracted from plasma from 1, 2, and 3 mL samples. HPLC analyzed triplicate dilutions at 258 nm. Each concentration had a mean, standard deviation, and % RSD (Harish et al., 2022)

In three Ria vials, 1 mL plasma was added to 1 mg of FPV, APV, and NVP to attain 1000 µg /mL for long-term stability. Vortexing for 5 min froze all 3 vials at -20 °C. The vials were thawed after 1, 2, and 3 weeks. Plasma medicines were processed for LQC, MQC, and HQC samples at each interval. HPLC analyzed triplicate dilutions at 258 nm. Each concentration has a mean, SD, and RSD (Reddy et al., 2019).

4.8.3 Biodistribution studies

The Wister rats of either sex were selected for the biodistribution studies. The rats were equally divided into nine groups. Each group contains three rats (n=3). The drugs, DT (DT), and formulations were dispersed in normal saline (0.9% w/v) and were administrated by the intravenous route via a jugular vein (equivalent dose of NVP 10 mg/kg and FPV 70 mg/Kg body weight) into animals. The animals (n=3 at each time point) after injection were sacrificed at time intervals of 1,8, and 24 h. These time points were decided based on t1/2 of drugs. After sacrificing, different organs such as the spleen, liver, kidney, and heart. were separated, cleaned, weighed, and stored at freezing temperature till further use. The organ was taken and placed in the required quantity of ACN and homogenized well-using tissue homogenizer and then centrifuged at 3000 rpm for 10 min. The supernatant was decanted, collected, and assayed by the HPLC method (Shegokar et al., 2011). The procedure is shown in Figure 10.

Fig 10: Schematic representation of biodistribution study

4.8.4 Haemolysis studies

Blood was obtained from Wister rats, placed in anti-clot vials, and then centrifuged at 3000 rpm for 15 min using a centrifuge (Remi, India). To obtain the suspension, the red blood corpuscles (RBCs) will first be sorted out, washed, and then resuspended in a saline solution that has a weight-to-volume ratio of 0.9%. After mixing 1 mL of prepared suspension with 4.5 mL of normal saline containing 0.9% water by volume and 0.5 mL of each sample, the mixture was allowed to react while being incubated for 60 min. Absorbance readings were obtained at 540 nm (Shimadzu 1601, Kyoto, Japan) using a 0.9 % w/v NaCl solution and deionized water to simulate 0% and 100% hemolysis, respectively. The proper dilutions were produced first, and then the readings were taken. The following equation was used to calculate the proportion of hemolysis in the sample (Mehra and Jain, 2013; Mishra et al., 2010).

$$\text{Hemolysis (\%)} = \frac{Ab_s - Ab_{S0}}{Abs_{100} - Ab_{S0}}$$

4.8.5 Haematological studies

Analyses of hematological parameters, including hemoglobin, red blood cells (RBCs), and white blood cells (WBCs), are going to be performed on rats of either sex that are healthy Wister strains and have the same weight and size. Up to twenty-four h will pass during which every animal will continue to consume the same diet that they are accustomed to. After 24 h had passed, samples of blood were taken using the retro-orbital plexus procedure, and these samples were tested at the local pathology laboratory to determine various hematological parameters (Jain et al., 2015).

Fig 11: Steps of Hemolysis studies and hematological studies

Chapter 5

Result and Discussion

5.1 Characterization of drugs

5.1.1 Physical properties

The drugs were studied through visual examination. Various organoleptic properties of NVP and FPV were observed which are described below in Table 5.

Table 5: Physical parameters of drugs, NVP and FPV

Physical parameters	NVP	FPV
Colour	White	White
Odour	Odourless	Odourless
Physical observation	Micronized powder	Micronized powder

5.1.2 Melting point

The melting point of drugs was measured to confirm their purity and the values are listed in Table 6. The melting point of NVP was in the range 247-250 °C and FPV was in the range 313-316 °C which was within the reported range. The sample results coincide with the results of the standard confirming the purity of the drug.

Table 6: Melting point of drugs, FPV and NVP

Drug	Melting point	Reported melting point	References
NVP	247-250 $^\circ$C	246-249 °C	Sarkar et al., 2008
FPV	313-316 $^\circ$C	318-321 °C	Leksic E et al., 2011

5.1.3 Solubility studies

The solubility study of NVP and FPV was studied in different solvents and tabulated in Table 7. The results of the solubility study of the two drugs NVP and FPV indicated that both the drugs were insoluble in water whereas freely soluble in methanol and slightly soluble in phosphate buffer pH 7 and acetate buffer pH 5.

Table 7: Solubility studies of drugs, NVP and FPV

S.No	Drug	Solvents	Solubility (mg/mL)
1.	NVP	Distilled water	0.058 ± 0.02
		Sodium Acetate buffer (pH 5)	0.133 ± 0.06
		PBS (pH 7.4)	0.098 ± 0.04
2.	FPV	Distilled water	0.025 ± 0.04
		Sodium Acetate buffer (pH 5)	0.042 ± 0.03
		PBS (pH 7.4)	0.026 ± 0.03

5.1.4 Partition Coefficient

The partition coefficient is the ratio of the drug distributed in a unionized form in the water phase and organic phase. It is indicated as Log P, which helps to study the drug partitioning in an organic phase and water phase which can be correlated with the ability of the drug to cross the lipophilic membrane. The partition coefficient was an effective parameter for the absorption of the drug (Amwzqueta et al., 2020). The partition coefficient is calculated as

Log P = C_{oil} / C_{water}

The value can be correlated to the lipophilicity and hydrophilicity of the drug. If the value of Log P is zero, this indicates that there is no difference in the distribution of the medication between water and the partition solvent. A value of Log P that is larger than 1 indicates that the substance has a higher solubility in lipids, whereas a value of Log P that is less than 1 indicates that the substance has a higher solubility in water (Turchi et al., 2019).

Table 8: Log P value of the drug

S.No	Drug	Log P value	Reported Log P	Reference
1.	NVP	2.48	2.5	Pubchem
2.	FPV	2.68	2.69	Drug bank

The results of the partition coefficient of both drugs are tabulated in Table 8. The value of Log P was found to be 2.48 for drug NVP and 2.69 for drug FPV. Both drugs have a log P value greater than 1 which showed that both the drugs are lipophilic. The drug FPV was found to be more hydrophobic as compared to NVP.

5.1.5 Ultra violet Maxima (λ_{max})

The Ultraviolet absorbance maxima were determined spectrophotometrically and it was found to be 282.5 nm for NVP (Bhavyasri et al., 2019) and 265 nm for FPV (Pekamwar et al., 2015). Figure 12 and 13 shows absorbance maxima obtained in PBS: Methanol (60:40).
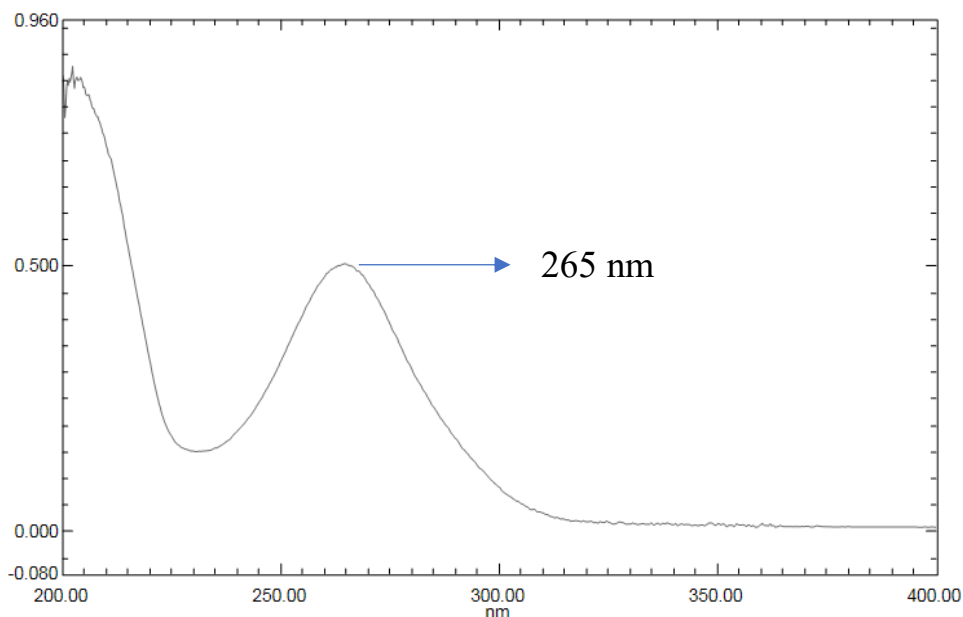
Figure 12: Absorbance maxima of FPV in PBS pH 7.4: Methanol (60:40)
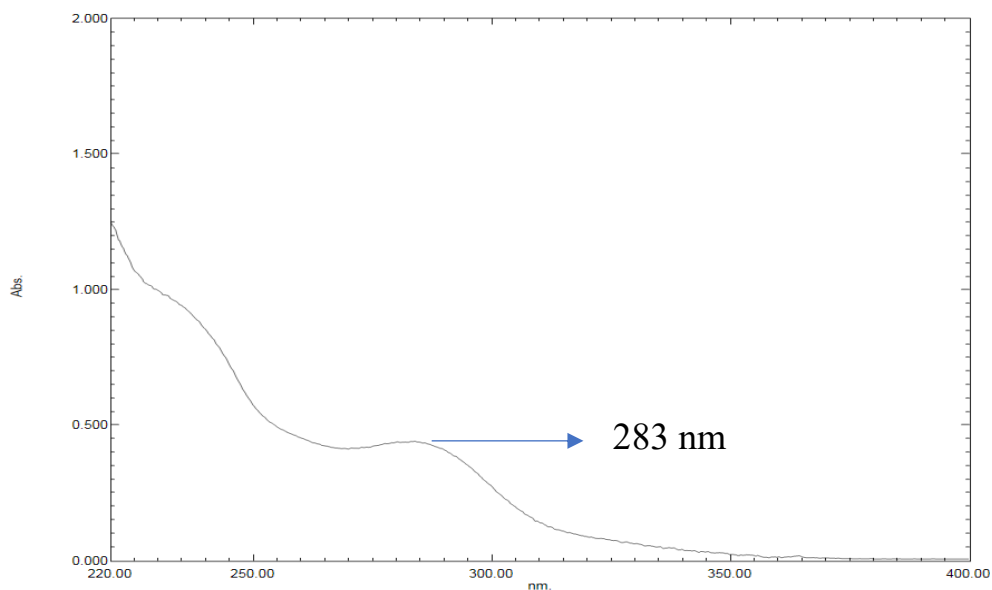
Figure 13: Absorbance maxima of NVP in PBS pH 7.4: Methanol (60:40)

5.1.6 Standard calibration curves of drugs in different solvents

5.1.6.1 Calibration curve in PBS pH 7.4: Methanol (60:40)

To estimate NVP and FPV in experimental protocols, standard calibration curves were prepared in PBS pH 7.4 Methanol (60:40). The various statistical values are recorded in Table 9 and Table 10. Linear standard curves of NVP and FPV are shown in Figure 14 and Figure 15. The procedure showed linearity, reproductivity, and

110

sensitivity in the range of 5.0 - 27.5 µg/mL at λ_{max} 283 nm for NVP and 5.0 – 25.0 µg/mL at λ_{max} 265 nm for FPV. This indicates that both the drug follows Beer's–Lambert law in the concentration ranging 5.0 - 27.5 µg/mL for NVP and 5.0 – 25.0 µg/mL for FPV (Bavyasri et al., 2019; Pekamwar et al., 2015).

Table 9: Standard curve of NVP in PBS pH 7.4: Methanol (60:40)

Sr. No	Concentration (µg/mL)	Absorbance
1	5.0	0.15 ± 0.04
2	7.5	0.27 ± 0.05
3	10.0	0.35 ± 0.03
4	12.5	0.44 ± 0.06
5	15.0	0.48 ± 0.04
6	17.5	0.56 ± 0.05
7	20.0	0.60 ± 0.06
8	22.5	0.70 ± 0.04
9	25.0	0.74 ± 0.07
10	27.5	0.83 ± 0.08

*Absorbance represented as Mean value ± SD (n=3)
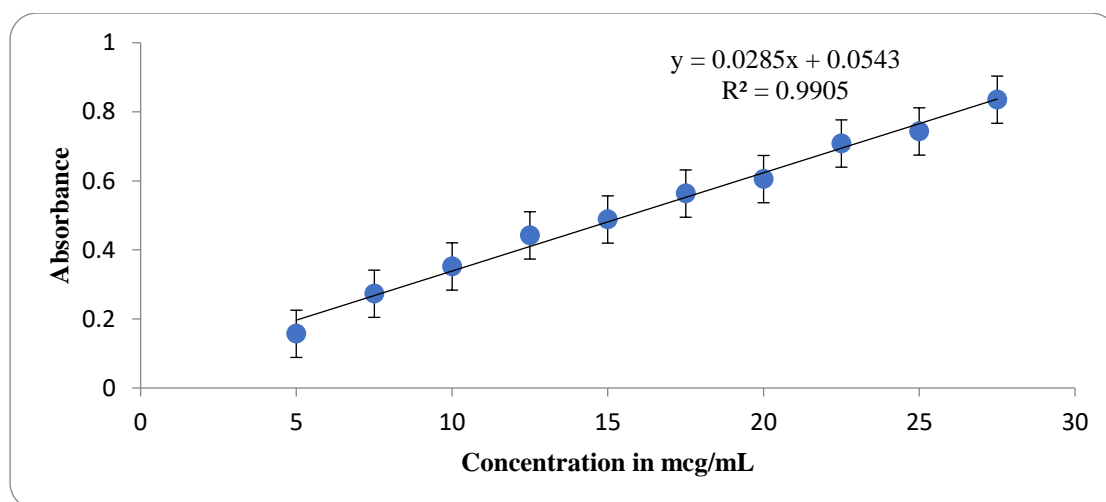
Figure 14: Standard curve of NVP in PBS pH 7.4: Methanol (60:40) (n=3)

Table 10: Standard curve of FPV in PBS pH 7.4: Methanol (60:40)

Sr. No	Concentration (µg/mL)	Absorbance
1	5.0	0.16 ± 0.12
2	7.5	0.21 ± 0.17
3	10.0	0.35 ± 0.20
4	12.5	0.40 ± 0.32
5	15.0	0.50 ± 0.12
6	17.5	0.53 ± 0.40
7	20.0	0.68 ± 0.62
8	22.5	0.78 ± 0.28
9	25.0	0.87 ± 0.67

*Absorbance represented as Mean value±S.D. (n=3)
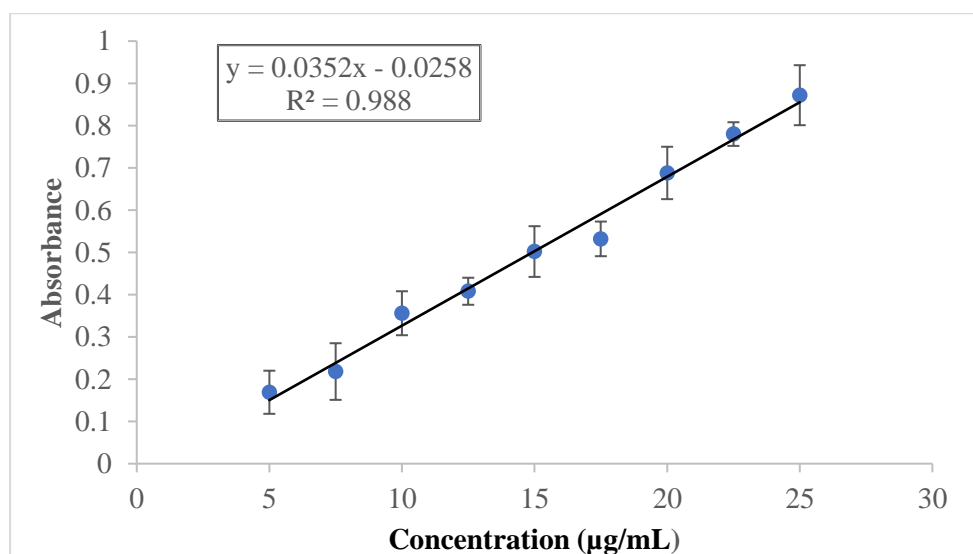
Figure 15: Standard calibration curve of FPV in PBS pH 7.4: Methanol (60:40) (n=3)

5.1.6.2 Calibration curve in acetate buffer pH 5: Methanol (60:40)

To estimate NVP and FPV in experimental protocols, standard calibration curves were prepared in acetate buffer pH 5: Methanol (60:40). The various absorbance data are recorded in Table 11 and Table 12. Standard calibration curves of NVP and FPV are shown in Figure 16 and Figure 17. The procedure showed linearity, reproductivity, and sensitivity in the range of 5.0 - 22.5 µg/mL at λ_{max} 283 nm for NVP and 5.0 – 25.0 µg/mL at λ_{max} 265 nm for FPV. This indicates that the drug follows

Beer's–Lambert law in the concentration range of 5.0 - 27.5 µg/mL for NVP and 5.0 – 25.0 µg/mL for FPV (Bavyasri et al., 2019; Pekamwar et al., 2015).

Table 11: Standard curve of NVP in acetate buffer pH 5: Methanol (60:40)

Sr. No	Concentration (µg/mL)	Absorbance
1	5.0	0.18 ± 0.05
2	7.5	0.23 ± 0.06
3	10.0	0.38 ± 0.02
4	12.5	0.44 ± 0.04
5	15.0	0.56 ± 0.06
6	17.5	0.61 ± 0.02
7	20.0	0.69 ± 0.05
8	22.5	0.73 ± 0.02
9	25.0	0.86 ± 0.03

*Absorbance represented as Mean value±S.D. (n=3)
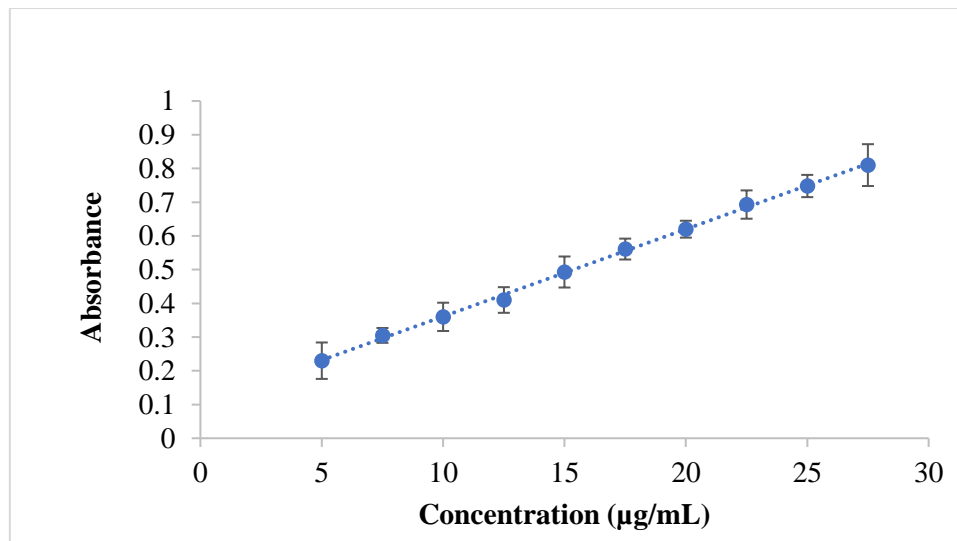
Figure 16: Standard calibration curve of NVP in acetate buffer pH 5: Methanol (60:40) (n=3)

Table 12: Standard curve of FPV in acetate buffer pH 5: Methanol (60:40)

Sr. No	Concentration (µg/mL)	Absorbance
1	5.0	0.23 ± 0.05
2	7.5	0.30 ± 0.02
3	10.0	0.36 ± 0.04
4	12.5	0.41 ± 0.03
5	15.0	0.49 ± 0.04
6	17.5	0.56 ± 0.03
7	20.0	0.62 ± 0.02
8	22.5	0.69 ± 0.04
9	25.0	0.74 ± 0.03
10	27.5	0.81 ± 0.06

*Absorbance represented as Mean value±S.D. (n=3)

$y = 0.0334x + 0.0217$
$R^2 = 0.9866$
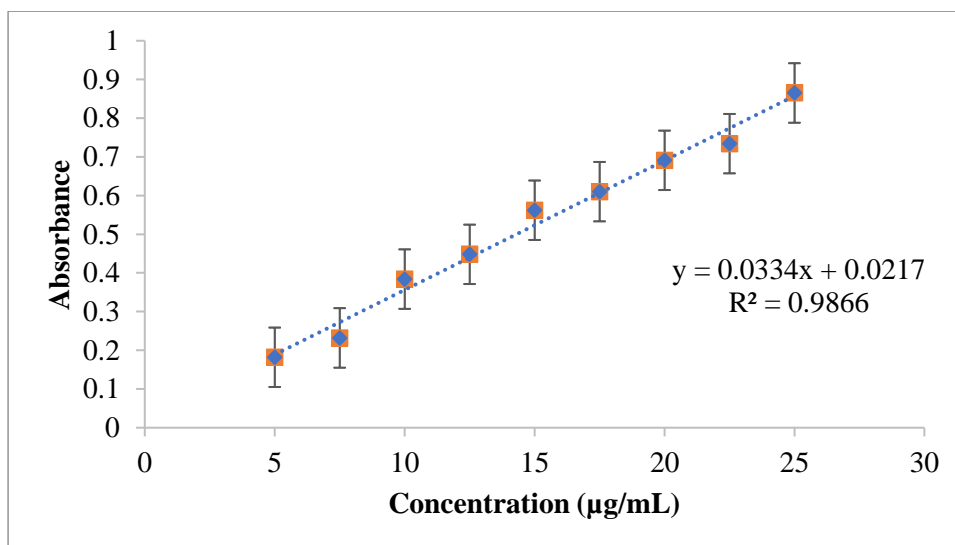
Figure 17: Standard calibration curve of FPV in acetate buffer pH 5: Methanol (60:40) (n=3)

5.1.7 FTIR Spectrum of drugs
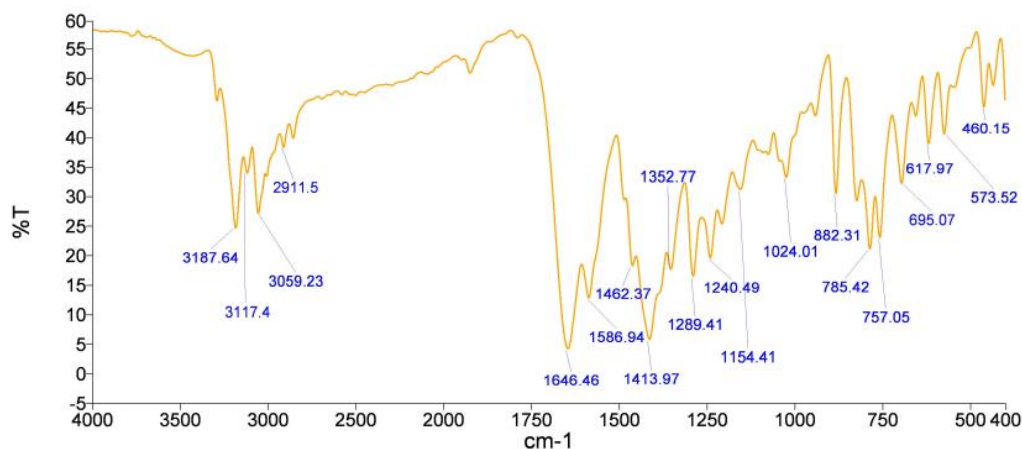
Figure 18. FTIR spectrum of plain drug NVP

Table 13: FTIR spectrum of plain drug NVP

Observed peaks frequency (cm^{-1})	Standard FTIR range (cm^{-1})	Corresponding functional Group
3187.64	3500-3100	Peak of N-H stretching
3059.23	3150-3050	C-H aromatic stretching
1646.46	1760-1630	C=O stretch
1586.94	1475-1600	Cyclopropyl C=C
1289.41	1350-1000	C-N stretching
1240.49	1350-1000	C-N stretching
882.31	900-690	C-H bending (out of plane)

FTIR spectrum of NVP was determined and represented in Figure 18. The FTIR spectrum of NVP revealed the presence of the characteristic peak of the drug. The major peaks are observed at 3187.64 cm^{-1}, a broad peak corresponds to stretching of N-H, the peak at 3059.23 cm^{-1} indicates stretching of C-H, 1646.46 cm^{-1} indicates the carboxyl stretch, the peak at 1413.97 cm^{-1}, 1586.94 cm^{-1} corresponds to the aromatic carbons (C=C), the peak at 1289.41 represents stretching of C-N and the peak at 882.31 cm^{-1} and 757.05 cm^{-1} indicates C-H bending (Varshosaz et al., 2018). Figure 18 represents the spectrum of plain drug NVP and Table 13 summarizes different peaks and their corresponding functional groups in FTIR spectra of NVP.
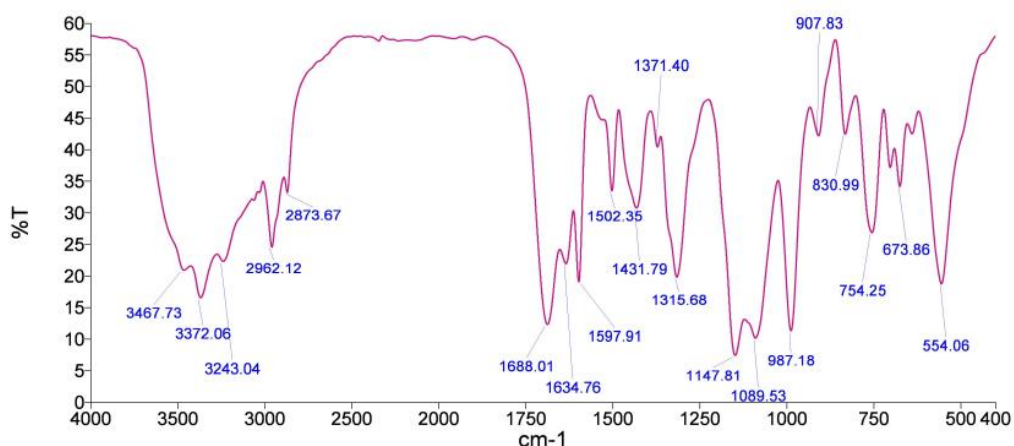
Figure 19. FTIR spectrum of FPV

Table 14: FTIR spectrum of plain drug FPV

Observed peaks frequency (cm^{-1})	Standard FTIR range (cm^{-1})	Corresponding functional group
3243.04	3500-3100	-NH stretching
1688.01	1690-1630	-C=O Carbonyl group
1597.91	1640-1550	-C=C aromatic carbon
1502.35	1600-1475	-C=C aromatic carbon
1431.79	1375-1450	-C-H isopropyl stretch
1315.68	1300-1000	-C-N stretch
1089.53 and 1147.81	1050-1375	-S=O
987.18	900-690	-C-H aromatic (out of plane)

The FTIR spectrum of FPV shows that stretches of O-H are present in an intense peak at 3372.08 cm^{-1}, whereas stretches of an amino group (N-H), which corresponds to amide and amine functional groups, are detected in a medium-intensity peak at 3243.04 cm^{-1}. The asymmetrical stretch of S=O is represented by peaks 1089.53 and 1147.81 cm^{-1}, while medium-intensity stretching of C=H of the aliphatic isopropyl chain is observed at 1431.79 cm^{-1} and 1315.68 cm^{-1}. The peak at 1688.01 cm-1 was the peak of stretched aliphatic C=O, and the peaks of higher intensity were observed at 1597.91 cm^{-1} and 1502.3 cm^{-1}, confirming the stretches of C=C; a region with high intensity, at 987.18 cm^{-1} the peak of high intensity due to stretching of C-O of ether and phosphate esters (Cordeiro et al. 2020; Pavia et al., 1962, Srivastava et al., 2023). Figure 19 represents the spectrum of plain drug NVP and Table 14 summarizes different peaks and their corresponding functional groups in FTIR spectra of NVP.

116

5.1.8 NMR spectroscopy
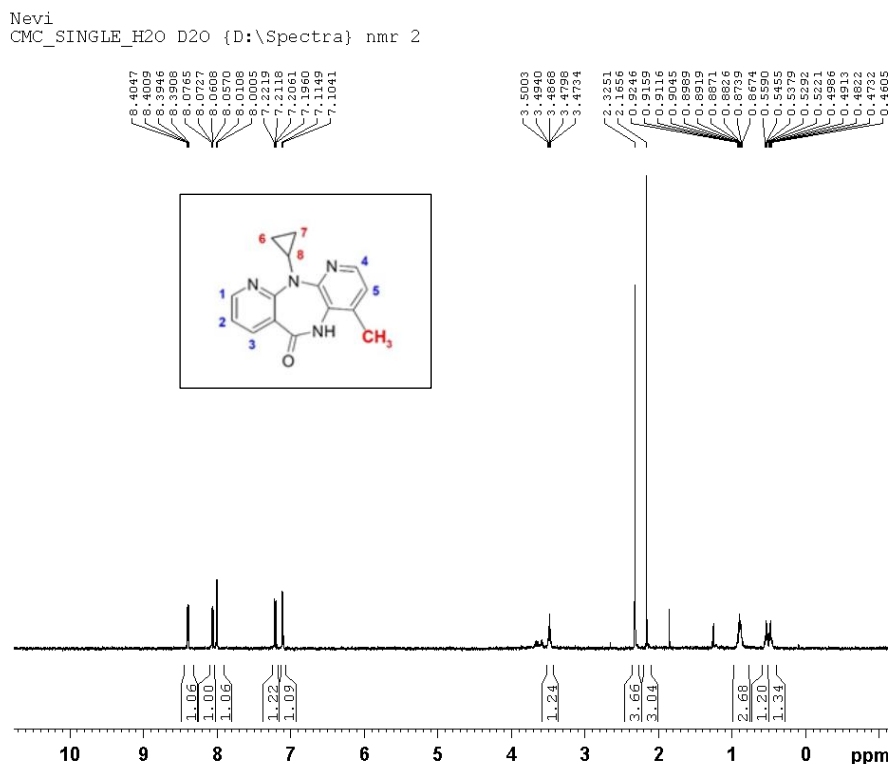
Figure 20. NMR spectrum of Plain drug NVP

The drug NVP was subjected to ^{1}H NMR spectroscopy and studied for the presence of different peaks of different protons in the NVP structure confirming the purity of the drug shown in Figure 20. Multiplets were observed between δ 0.50 and 1.30 ppm corresponding to -CH_2 of methylene groups of cyclopropane (H5, H6), the chemical shifts between δ 3.79 ppm correspond to the protons of cyclopropane (H8), the peak at δ 2.325 ppm corresponds to CH_3, peaks between δ 7.10-8.40 ppm corresponds to the protons associated with aromatic ring (H1, H2, H3, H4, H5). The single peak at δ 8.407 ppm corresponds to NH (da Silva et al., 2021; Silverstein et al., 1962).

117
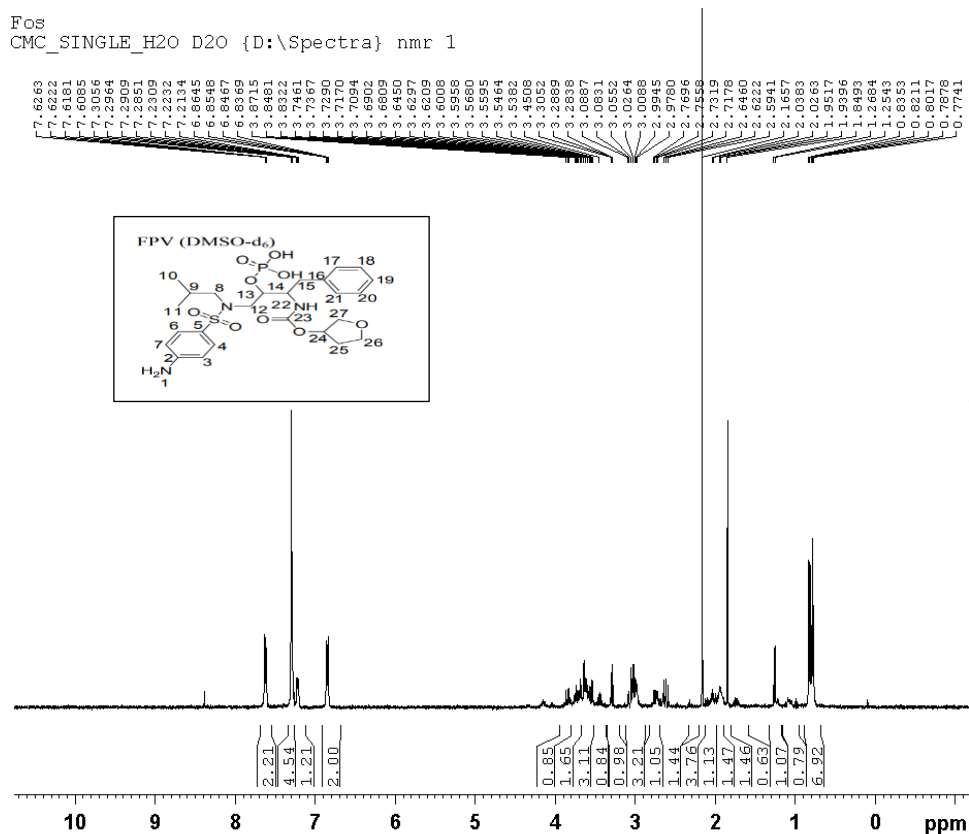
Figure 21. NMR spectrum of Plain drug FPV

The drug was subjected to ^{1}H NMR spectroscopy and studied for the presence of different peaks corresponding to different protons in the FPV structure confirming the purity of the drug shown in Figure 21. H3 and H7 aromatic protons show their presence at H3 and H7 at δ 6.83 ppm, and other aromatic protons H4 and H6 show their doublet at δ 7.62 ppm. The H18, H19, and H20 show resonance at δ 7.21 to δ 7.23 ppm, a pair of doublets corresponding aromatic methine proton at H17 and H21 found at δ 7.30 ppm. Doublets observed at δ 0.77 and 0.78 ppm correspond to H10 and H11 of methyl proton. Five pairs of multiplets for methyl protons containing non-equivalent protons at δ 2.59-2.64 ppm, δ 2.97-2.99 ppm responded to H8 a,b, δ 2.71- 2.76 ppm, δ 3.53-3.54 ppm responded to H-12a,b, δ 2.55-2.59 ppm, δ 3.00-3.03 ppm responded to H-15a,b, δ 1.8 ppm, δ 1.93-1.95 ppm corresponded to H-25a,b, δ 3.2838-3.2889 ppm, δ 3.53-3.54 ppm corresponding to H-26a,b. Multiplets at δ 1.93 ppm, δ 3.7.3-8 ppm correspond to methine proton H9, H-13, H-14, and H-24. The H 27 a,b corresponds to δ 3.59-3.68 ppm, and doublets at δ 6.86 ppm corresponds to the carbamate group (Singh et al., 2019).

5.1.9 X-ray diffraction studies

(a)

(b)
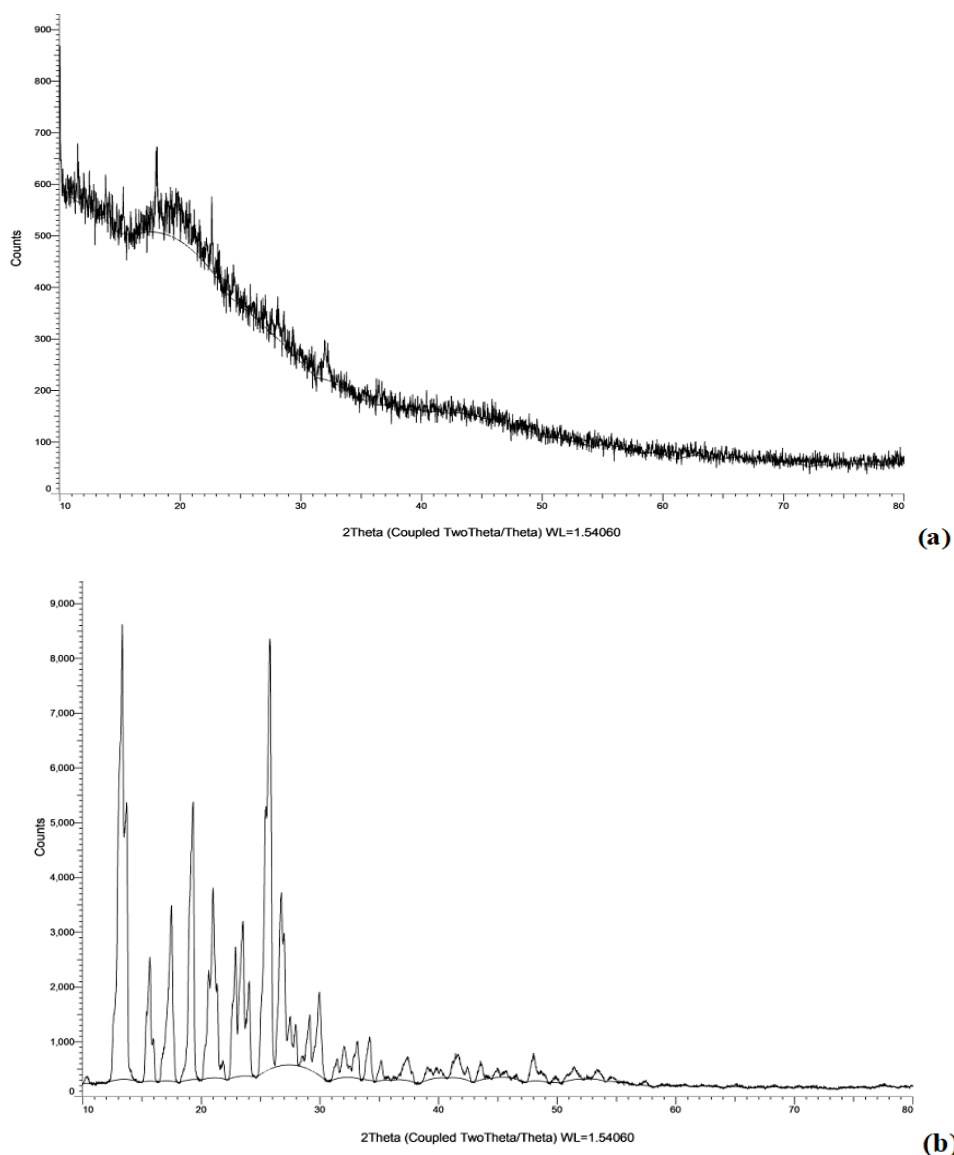
Figure 22. XRD pattern of (a) plain drug FPV (b) plain drug NVP

XRD pattern of NVP confirms the three-dimensional crystalline nature of the drug. The powder sample gives sharp peaks in the diffraction pattern and the scattering angle was observed at 13.915˚ and 25.455˚ (Monteiro et al., 2013). The XRD pattern of FPV does not reflect any prominent peak which indicates that the drug was amorphous (Corderio et al., 2013). Figure 22 represents the XRD pattern of plain drug FPV and plain drug NVP.

5.1.10 Differential Scanning Calorimetry of Drugs
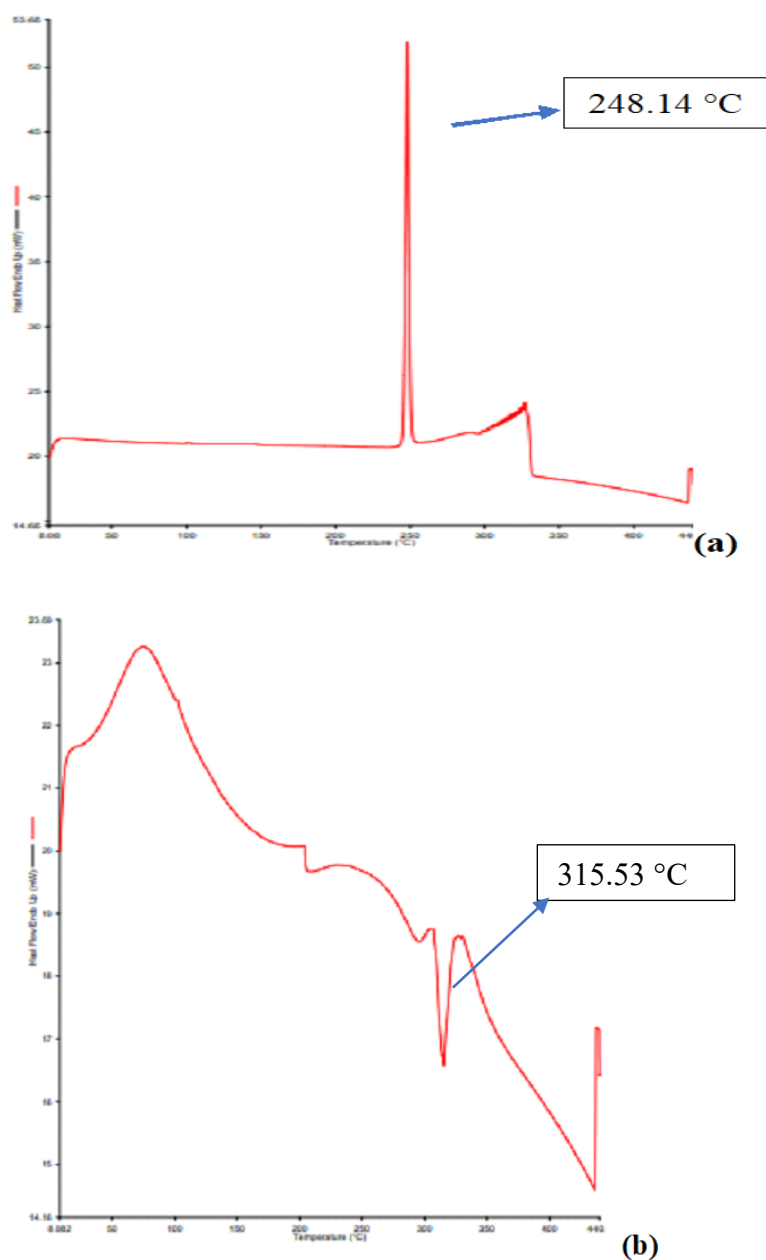
Figure 23. DSC thermogram of (a) Plain drug NVP (b) Plain drug FPV

The DSC image of the drug NVP and FPV is shown in Figure 23. The DSC image of NVP shows the sharp endothermic peak at 248 ºC. The reported DSC peak observed at 245 ºC confirms the purity of the drug NVP (Ramana et al., 2010). The melting point of the drug was represented by a sharp endothermic peak. The DSC image of FPV shows the sharp endothermic peak at 315.53 ºC. The reported DSC peak was observed at 319 ºC confirming the purity of the drug FPV (Leksic et al., 2011).

5.2 Characterization of Dendrimers

5.2.1 UV spectroscopy

The absorbance maxima were determined spectrophotometrically and it was found to be 263 nm for dendrimers shown in Figure 24.
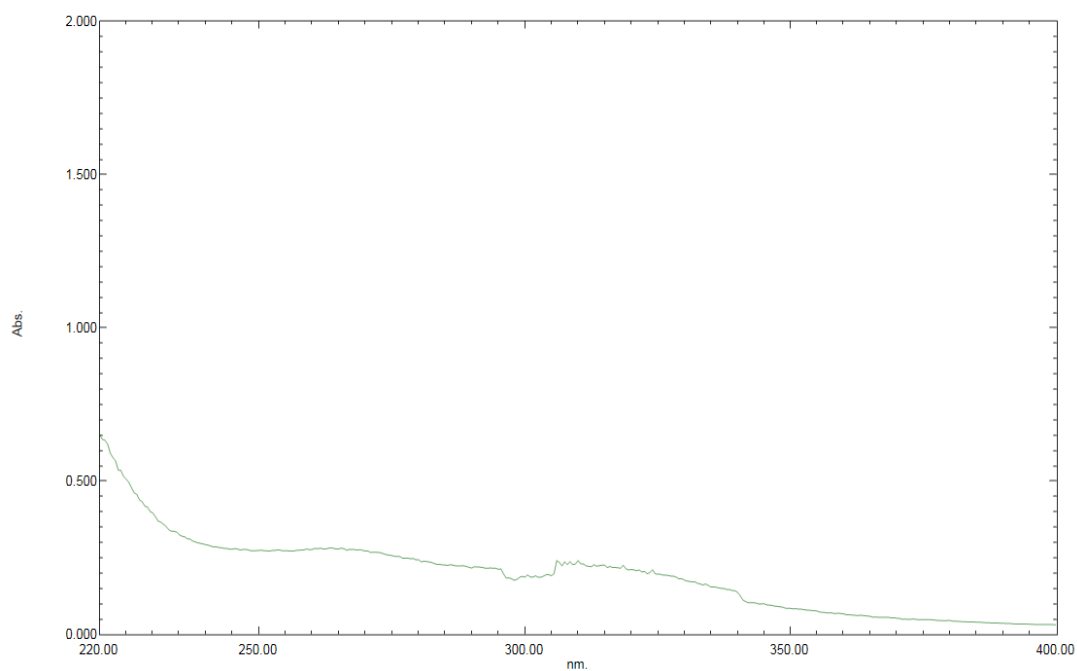
Figure 24. UV spectrum of dendrimers

5.2.2 FT-IR spectroscopy
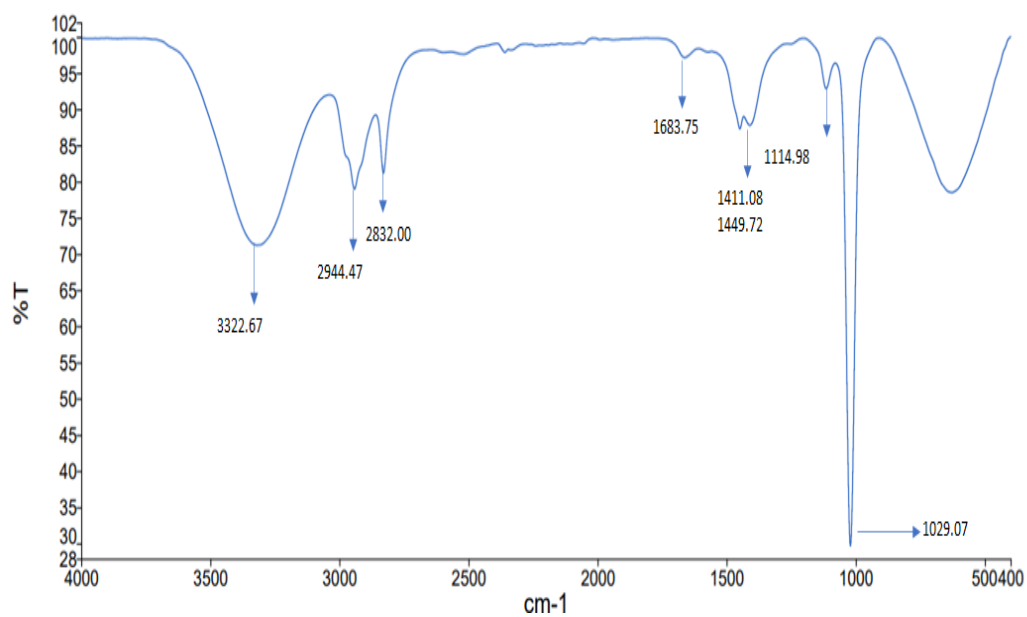
Figure 25. FTIR spectrum of 5G PPI dendrimers

Table 15: FTIR spectrum of 5G PPI dendrimers

Observed peaks frequency (cm^{-1})	Standard FTIR range (cm^{-1})	Corresponding functional group
3322.67	3500-3100	Primary amine
2944.47	3150-3000	-C-H stretching
2832.0	3150-3000	-C-H stretching
1683.75	1640-1550	N-H deflection of amine
1447.72	1450-1365	twin peak corresponding
1411.08		to the CH bend
1114.98	1300-1000	C-N stretching
1029.07	1000-650	-C-H bend

FTIR spectra of 5G dendrimers are represented in Figure 25. The spectrum of dendrimers showed peaks such as a peak at 3322.67 cm^{-1} was the peak for primary amine confirms amine present on the surface of dendrimers, peak at 2832.0 cm^{-1} and peak at 2944.47 cm^{-1} was due to stretching of -C-H of alkene, peak at 1683.75 cm^{-1} indicated N-H deflection of amine, a peak at 1411.08 cm^{-1} and 1449.72 cm^{-1} are the twin peak of -CH band, a peak at 1114.98 cm^{-1} due to –C-N stretching, 1029.07 cm^{-1} which corresponds to bending of C-H bending. All the peaks correspond to the peaks of dendrimers as per literature and tabulated in Table 15 (Kaur et al., 2017).

5.2.3 NMR Spectroscopy

The NMR spectrum of the 5G PPI dendrimer is shown in Figure 26. The NMR spectra of dendrimers confirm the presence of protons as per the literature. Multiplets were observed between δ 0.9 ppm corresponding to -CH$_2$ of methylene groups of EDA. The chemical shifts between δ 1.74 ppm corresponding to -CH2-CH2-, the peak at δ 2.34-2.36 ppm corresponds to -NH2, multiple peaks at δ 2.40–2.69 ppm due to N[C]C and multiplets between δ 2.71–2.79 ppm corresponds to -CH2-NH2 (Kumar et al., 2006; Gajbhiye et al., 2013).
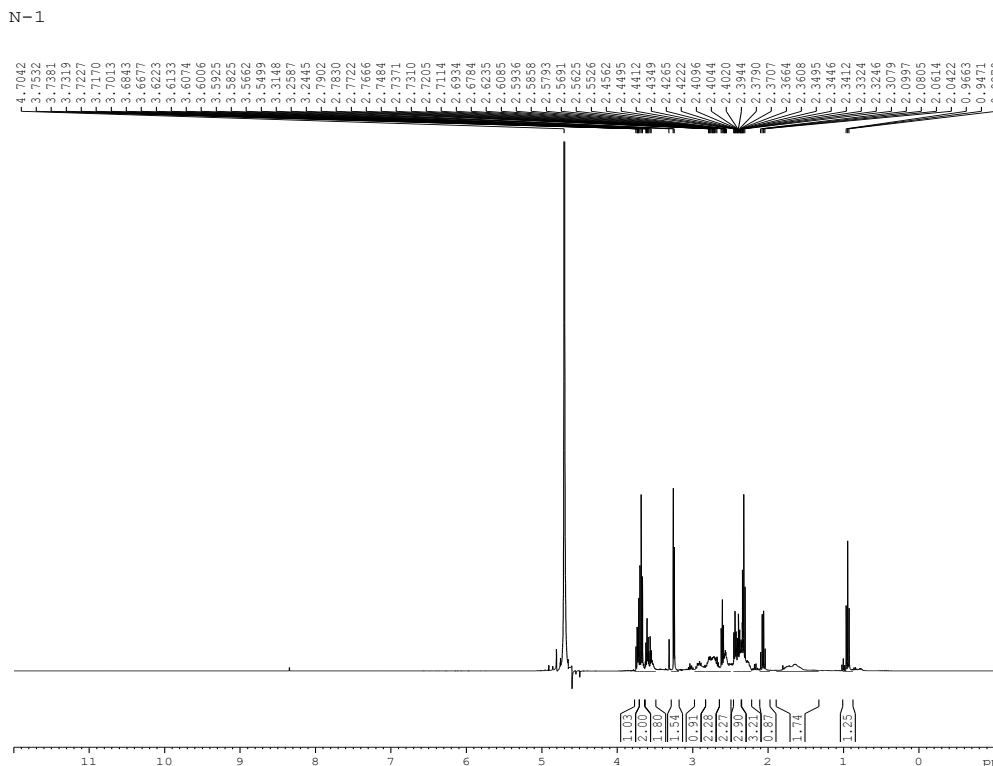
Figure 26. NMR spectrum of 5G PPI dendrimers

5.2.4 Differential scanning calorimetry
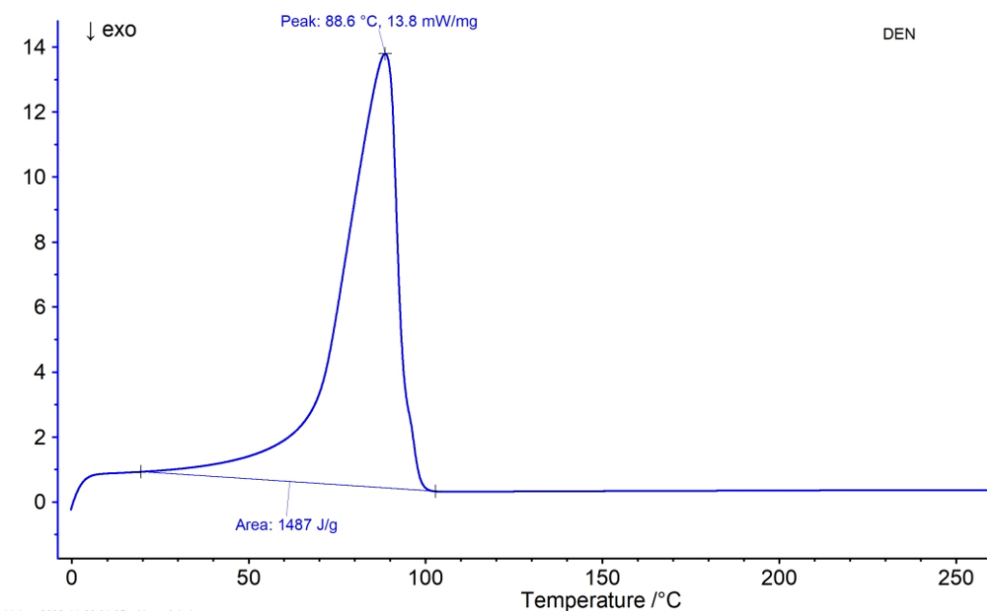
Figure 27. DSC thermogram of 5G PPI dendrimers

The DSC is the thermal analysis that was done to study the crystallinity, melting point, and heat stability of the components at different ranges of temperatures. Dendrimers were subjected to varying temperatures using DSC. The DSC of

dendrimers displayed a peak at 88.6 ℃, this co-related to a sharp melting point of dendrimers. Figure 27 represents the DSC thermogram of 5G PPI dendrimers.

5.2.5 Field emission scanning electron microscopy

The morphology of the surface of dendrimers is shown in Figure 28. FE-SEM of dendrimers clearly showed that the structure was in the nanoscale range and distinct. The image indicates the spherical branching arrangement of the dendrimers originating from the center core (Kaur et al., 2017).
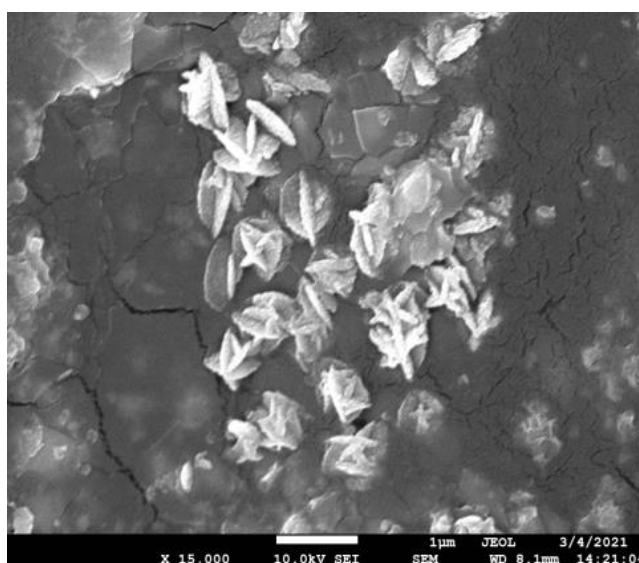
Figure 28. FE-SEM image of 5G PPI dendrimers

5.2.6 High-resolution transmission electron microscopy
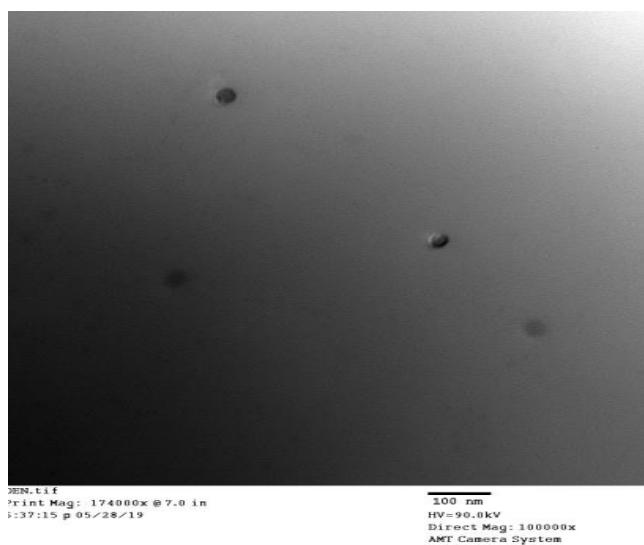
Figure 29. TEM image of 5G PPI dendrimers

Figure 29 shows the HR-TEM image of 5G PPI dendrimers. The image reflects the spherical structure of the dendrimers. The size of a particle of dendrimers was found to be less than 100 nm. This spherical structure of the polymer supports the non-polar interior structure with a polar surface structure (Ordonez et al., 2022).

5.2.7 Particle size and zeta potential

The particle size of the dendrimer was found to be 41.9 nm and PDI was found to be 0.379. The size of the particle was determined by the Delsa nanoparticle size counter. The PDI was found to be slightly higher because of cluster formation due to the self-aggregation of dendrimers. Figure 30 shows the particle size distribution of 5G PPI dendrimers (Ordoñez et al., 2022).

The zeta potential of 5G PPI dendrimer was found to be +24.64 mV. The positive zeta potential was due to the amine group (NH_2) present on the periphery of dendrimers.
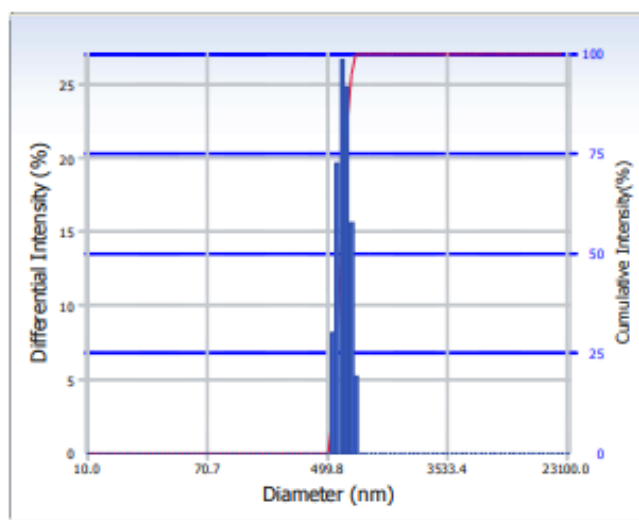
Figure 30. Particle size of 5G PPI dendrimers

5.3 Characterization of carbon nanotubes

5.3.1 UV spectroscopy
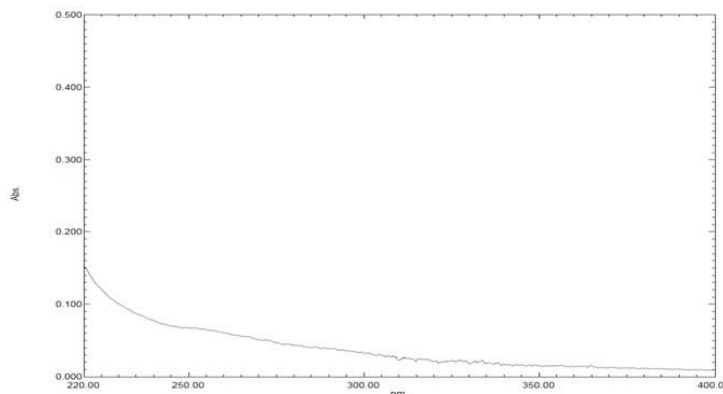
Figure 31. UV spectrum of COOH-MWCNT

The Ultraviolet absorbance maxima were determined spectrophotometrically and no prominent peak was observed in the UV spectrum as shown in Figure 31 (Kaynak et al., 2018).

5.3.2 FT-IR spectroscopy
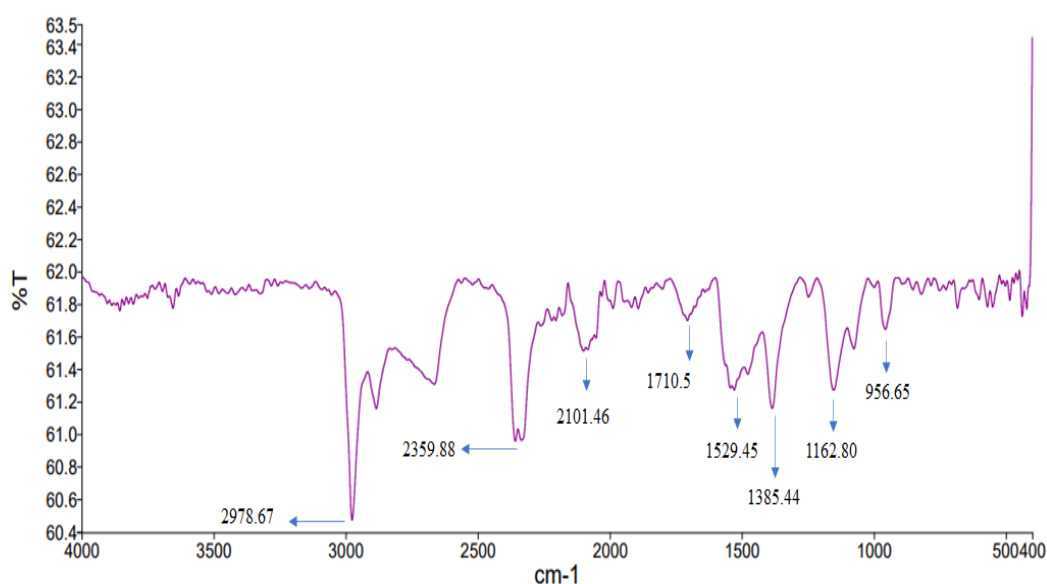
Figure 32. FTIR spectrum of COOH-MWCNT

Figure 32 indicates FTIR peaks for MWCNT-COOH. MWCNT-COOH spectrum indicated an intense peak at 2978.67 cm^{-1} due to the stretching of hydroxyl bond (OH) and a peak at 1710.50 cm^{-1} peak corresponds to the carbonyl group confirming the presence of carboxylic acids at the exterior of MWCNT. The peak observed at 1385.44 cm^{-1} corresponds to the hydroxyl (O–H) bond in the carboxylic

group. The peak at 956.65 corresponds to the out-of-plane bending of aromatic C-H. The existence of the peaks attested to the presence of a significant functional group on COOH-MWCNT. tabulated in Table 16. (Zhang et al., 2018).

Table 16: FTIR spectrum of COOH-MWCNT

Observed peaks frequency (cm^{-1})	Standard FTIR range (cm^{-1})	Corresponding functional group
2978.67	3400-2400	-OH group of COOH
1710.50	1725-1700	-C=O group
1385.44	1390-1440	-OH group of COOH
956.65	900-690	Aromatic C-H (out of plane bend)

5.3.3 Raman Spectroscopy

Raman spectrum of COOH-MWCNT is represented in Figure 33. Raman spectroscopy is a useful technology to study structural characterization. It is also a reliable tool that can help to confirm the conjugation of dendrimers on the periphery of MWCNTs. Raman spectra of COOH-MWCNT.
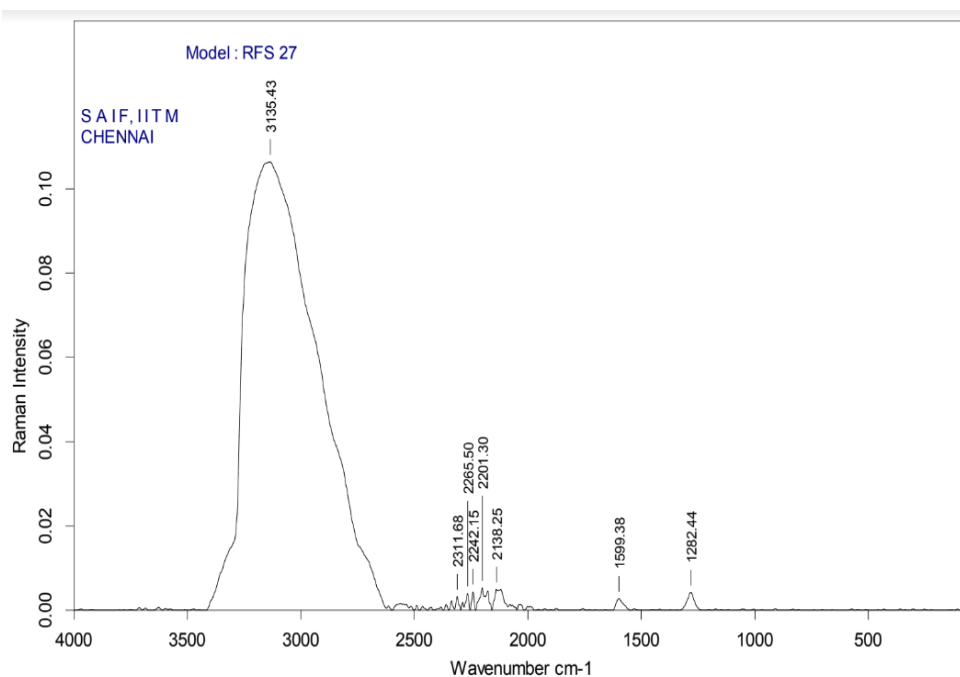
Figure 33. Raman Spectrum of COOH-MWCNT

Both spectra display two bands. The D band for COOH-MWCNT was observed at 1282.44 cm^{-1}. This band was due to a defect or disorder in the COOH-MWCNT structure. The G band was observed at 1599.38 cm^{-1} for COOH-MWCNT. This band relates to the crystalline structure of graphite. Further, the ratio of two bands helps to

analyze the addition of functional groups on the COOH-MWCNT structure. The ratio of ID/IG value acts as an indicator of alteration of electronic structure. The D and G band intensity ratio (ID/IG) of COOH-MWCNT was calculated to be 1.538 (Sedaghat et al., 2014; Muda et al., 2017).

5.3.4 NMR Spectroscopy

^{1}H NMR studies were performed to determine the proton of carboxylic acid made on the surface of COOH-MWCNT. ^{1}H NMR analysis of COOH-MWCNT showed the presence of protons in δ 1.16 to1.23 ppm corresponds to the C-H in the COOH-MWCNT. In the COOH-MWCNT the singlet peak between δ 2.0 to 2.2 ppm indicated the presence of –CH$_2$COOH. The peak at δ 3.0-3.2 ppm was the characteristic peak that indicates the presence of proton of –CH$_2$OH (Singhai et al., 2020). Figure 34 represents the NMR spectra of COOH-MWCNT.
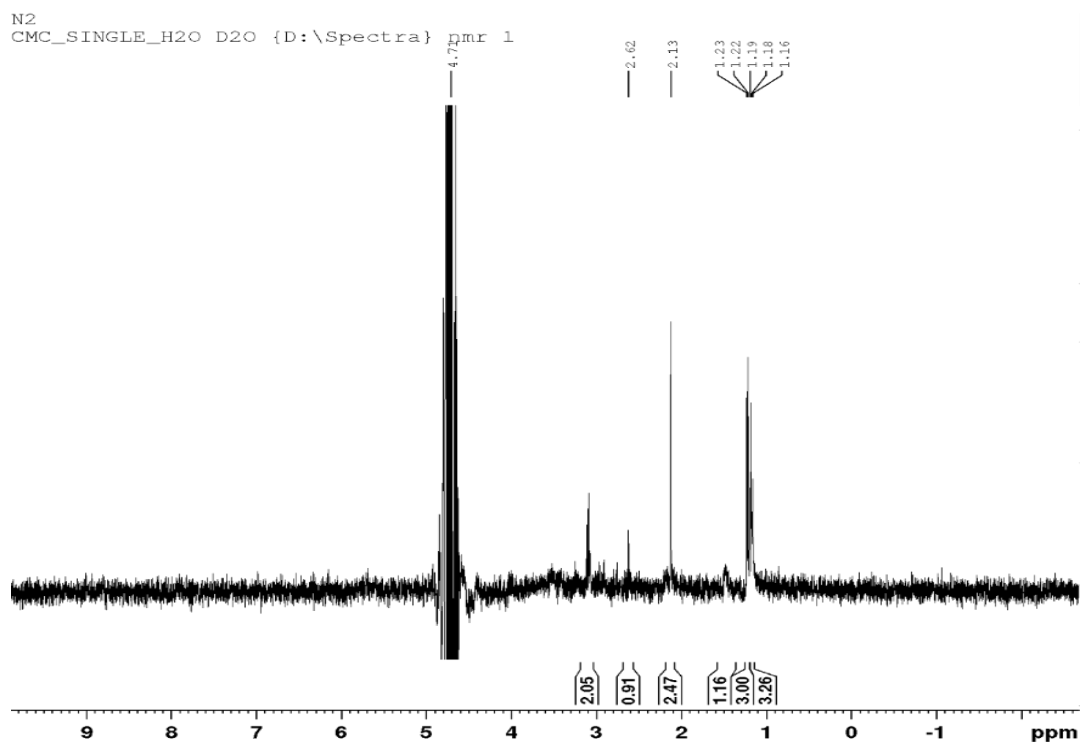
Figure 34. NMR spectrum of COOH-MWCNT

5.3.5 XRD pattern
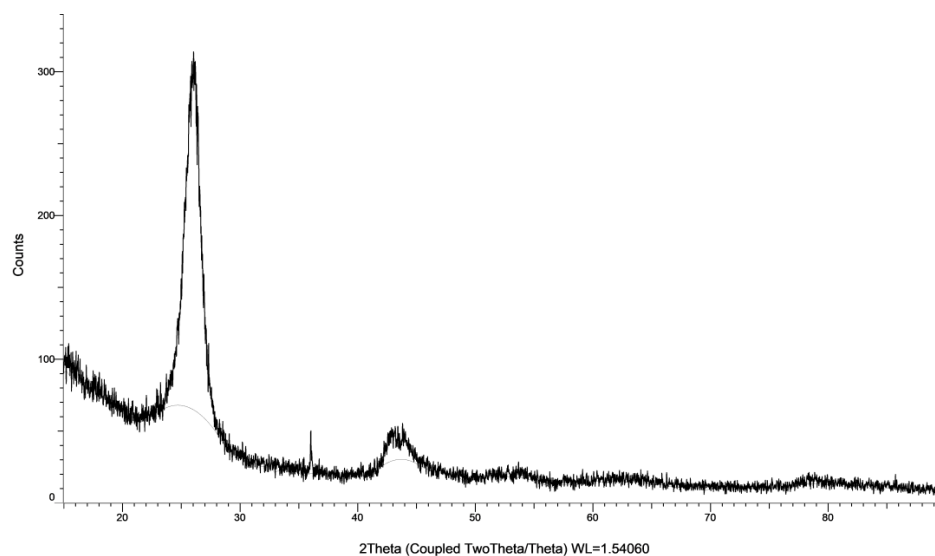
Figure 35. XRD of COOH-MWCNT-COOH

The XRD studies indicated the semi-crystallinity of the MWCNTs structure. Figure 35 indicates the XRD diffraction pattern of COOH-MWCNT. The pattern of COOH-MWCNT had a characteristic peak at 25.959º and another small peak at 42.252 ° (Zhou et al., 2022).

5.3.6 Differential Scanning Calorimetry

The DSC was carried to evaluate the crystallinity, melting point, and thermal stability of the components at different ranges of temperature. COOH-MWCNT was subjected to varying temperatures using differential scanning calorimetry. COOH-MWCNT does not show any enthalpic event till 400 °C (Massourni et al., 2015). The DSC thermogram of COOH-MWCNT is shown in Figure 36.
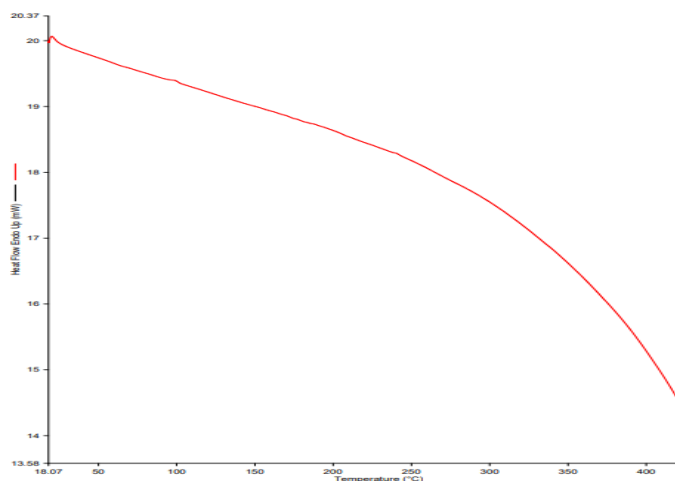
Figure 36: DSC thermogram of COOH-MWCNT

129

5.3.7 Field emission scanning electron microscopy
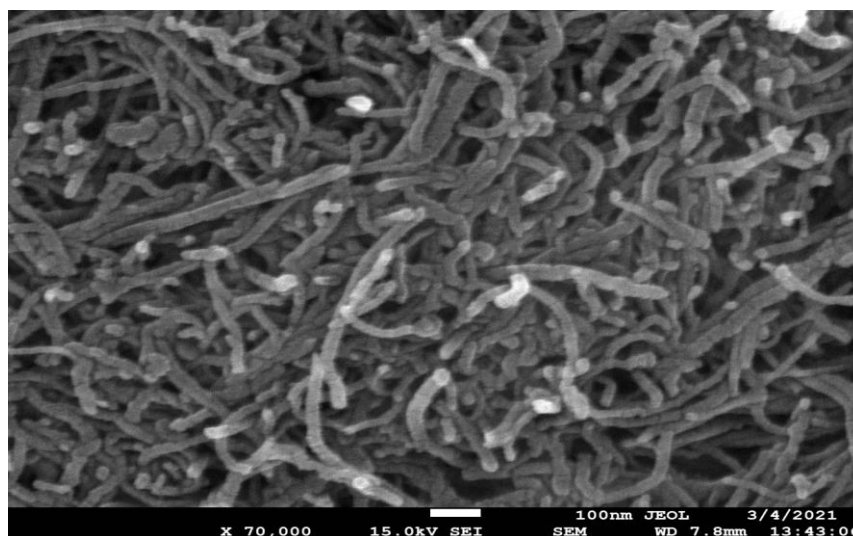
Figure 37: FE-SEM image of MWCNT-COOH

The FE-SEM images of carboxylic functionalized COOH-MWCNT at 70,000 magnifications as shown in Figure 37 revealed the microscopic image of functionalized MWCNT. The image indicated the nanosized long thread-like structure of COOH-MWCNT. FE-SEM images help to examine the surface of the structure and enable the observation of fracture surfaces (Takashi et al., 2016).

5.3.8 High-resolution transmission electron microscopy
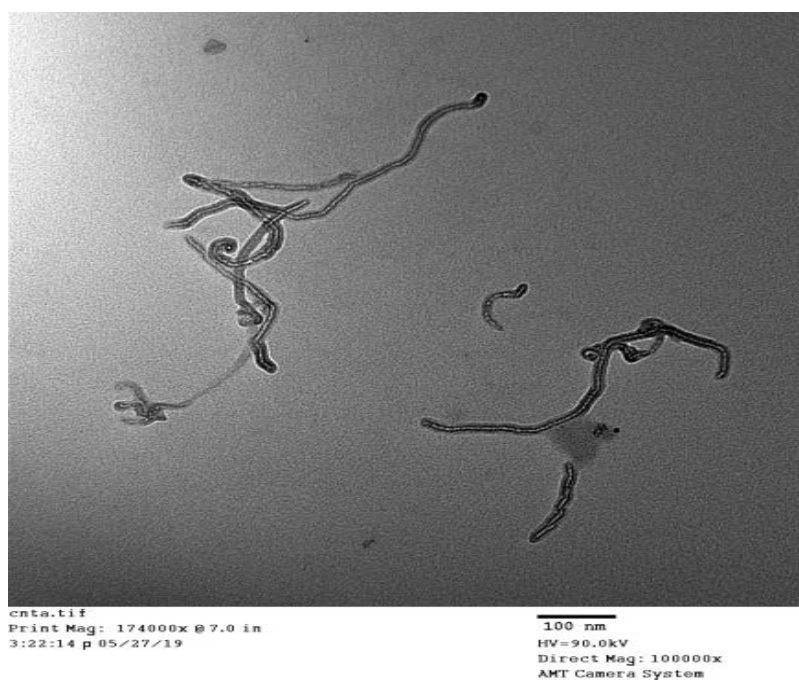
Figure 38. HR-TEM image of COOH-MWCNT

Figure 38 indicates the TEM images of COOH-MWCNT. The image indicates the presence of a hollow tube-like structure of multi-walled walled nanotubes. Thickness around the wall indicated the presence of a multiwall across the carbon tube. The length of carboxylated MWCNTs was investigated by TEM. TEM images revealed the size of COOH-MWCNT was around 100 nm which confirms the nano size of the delivery system (Hassani et al., 2022).

5.3.9 Particle size

Particle size determination helps to determine the size of the nanostructure formed. The particle size was found to be 262.5 nm confirming that the new nanostructure was in the nanosize range. The polydispersity index was found to be 0.590. The PDI indicates that the particle size was narrow and indicates that there was no such aggregation in the size of the particles (Thakur et al., 2022). Particle size distribution is shown in Figure 39.
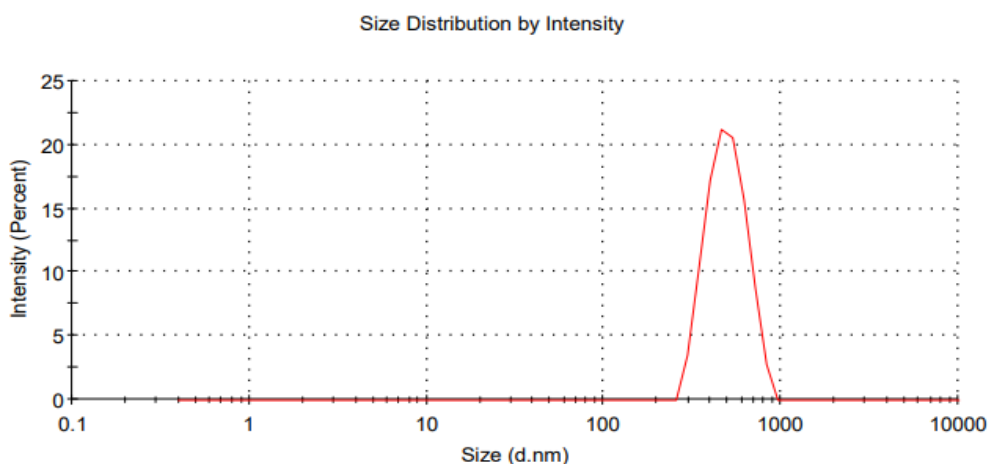
Figure 39. Particle size distribution of COOH-MWCNT

The Zeta potential was found to be -12.5 mV. The negative charge may be contributed by the ionized carboxylic group on the surface (Thakur et al., 2022).

5.4 HPLC Analytical Method Development

5.4.1 Spectral analysis

10 μg/mL solution was prepared and scanned at 400 to 200 nm using a UV spectrophotometer. The absorption maxima were found to be 265 nm for FPV and 283 nm for NVP. The isosbestic point of two drugs in the mixture of the drugs was found to be 258 nm. The UV scan results are shown in Figure 40. Method development and validation were carried out at 258 nm.
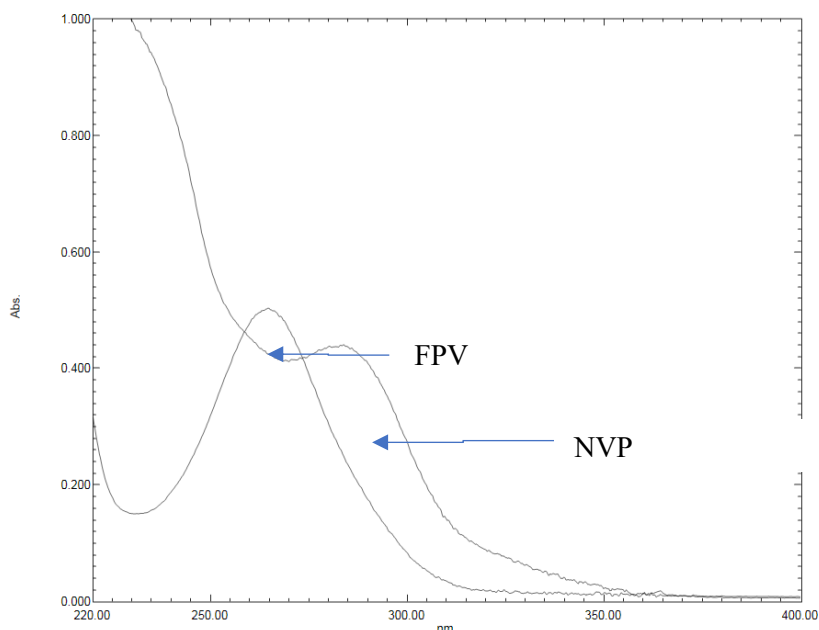
Figure 40. UV spectra of FPV and NVP showing isosbestic point

5.4.2 Method Development and Optimization

Different trials were carried out using different solvent systems in varying ratios for the isolation of two drugs and the results were analyzed. The retention time of drugs tends to change with changes in mobile phage. Trial 1, Acetonitrile (ACN): Formic acid (FA 0.1%) in the different ratios was carried out, and the resultant peaks were broad. In trial 2, ACN: Buffer pH 5 and 2 were used, at 90:10 and 60:40 no peak was observed, with a 40:60 peak with a broad tail observed. Trial 3, ACN: water (40:60) peak was observed but tends to retain the drug. In trial 4, Methanol buffer at varying ratios was used sharp peak was observed but with tails. Trail 5, Methanol: Formic acid 0.1%, peaks were observed but have a broad tail. Trial 6, Methanol: Water (70:30) peaks were resolved properly at retention time 3.352 and 7.042 for FPV and NVP respectively. When Methanol: Water (80:20) was used good peaks were observed at 3.385 and 6.509. The peak was sharper than the peak observed at Methanol: Water 70:30 for the drug NVP at a rate of flow of 1mL/min. Thus, the solvent system Methanol: Water (80:20) was considered for the further development of the calibration curve and validation. Figure 41-48 shows the HPLC chromatogram in different solvents. Figure 49 shows the chromatogram of the blank solution.
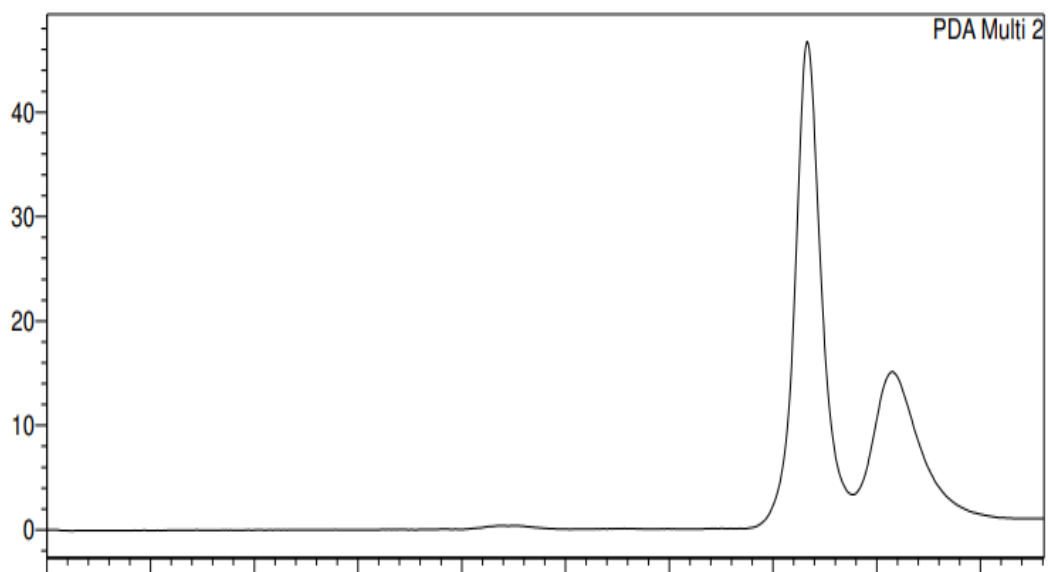
Figure 41. HPLC chromatogram using Acetonitrile (ACN): Buffer pH 5
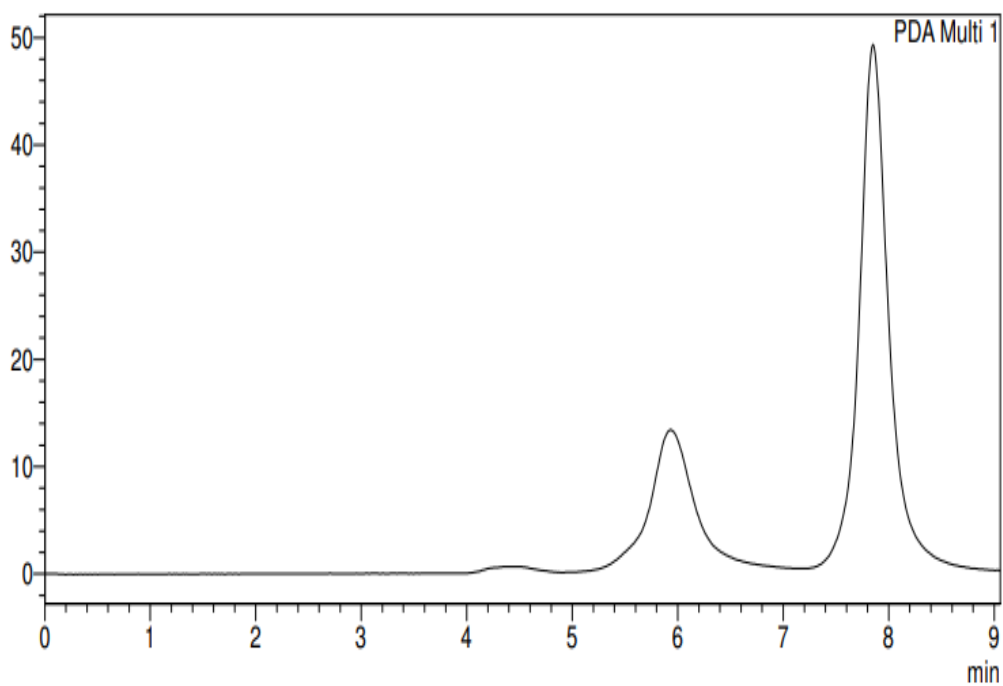
Figure 42. HPLC chromatogram using Acetonitrile (ACN): Buffer pH 2
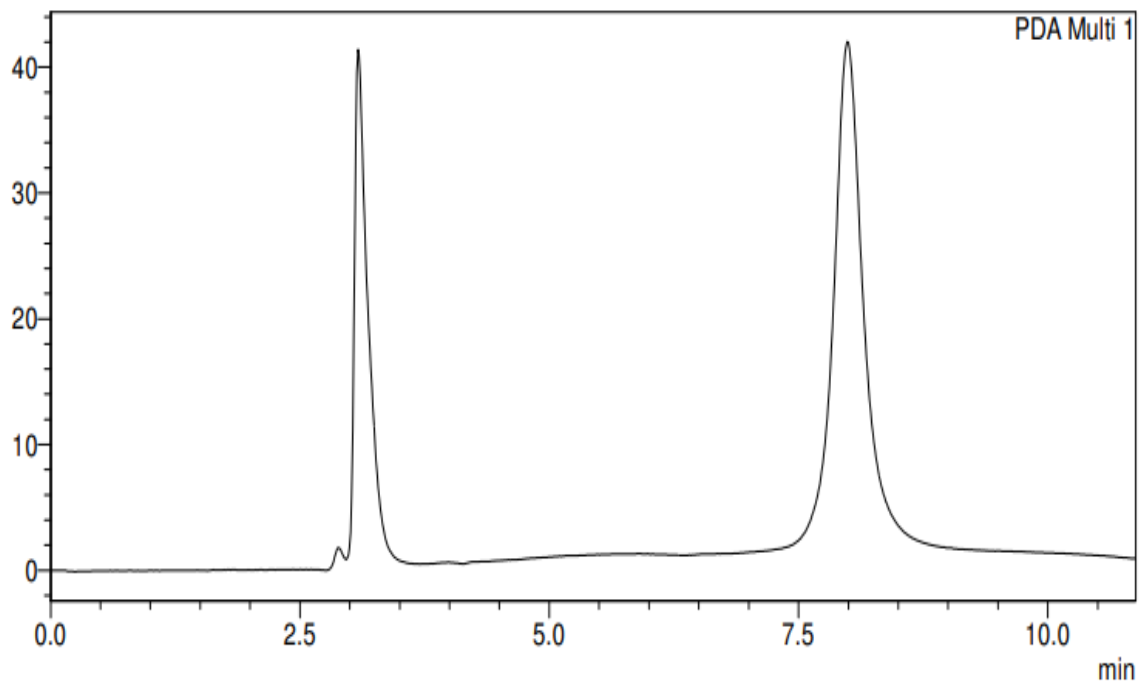
Figure 43. HPLC chromatogram using Acetonitrile (ACN): Water
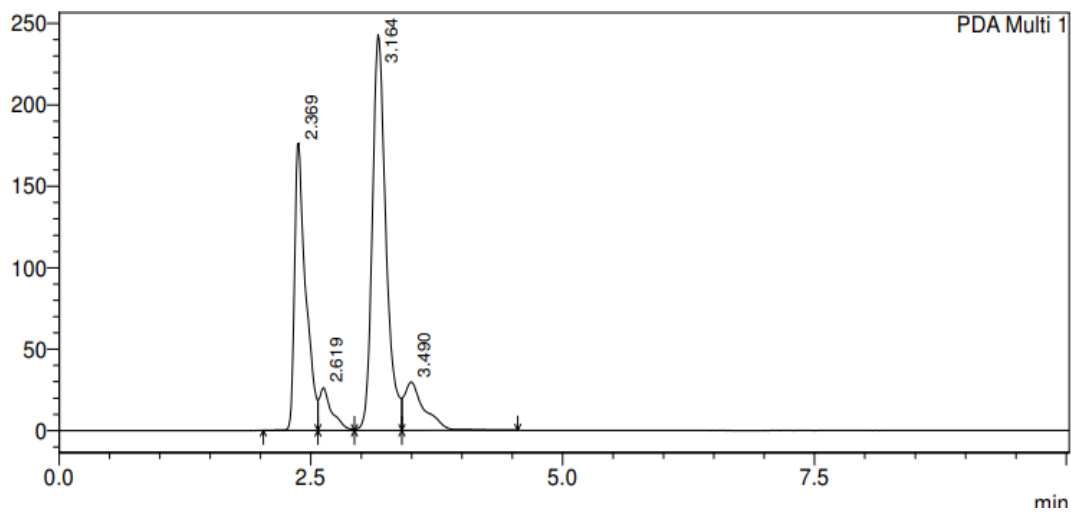
Figure 44. HPLC chromatogram using Methanol: Buffer pH 5
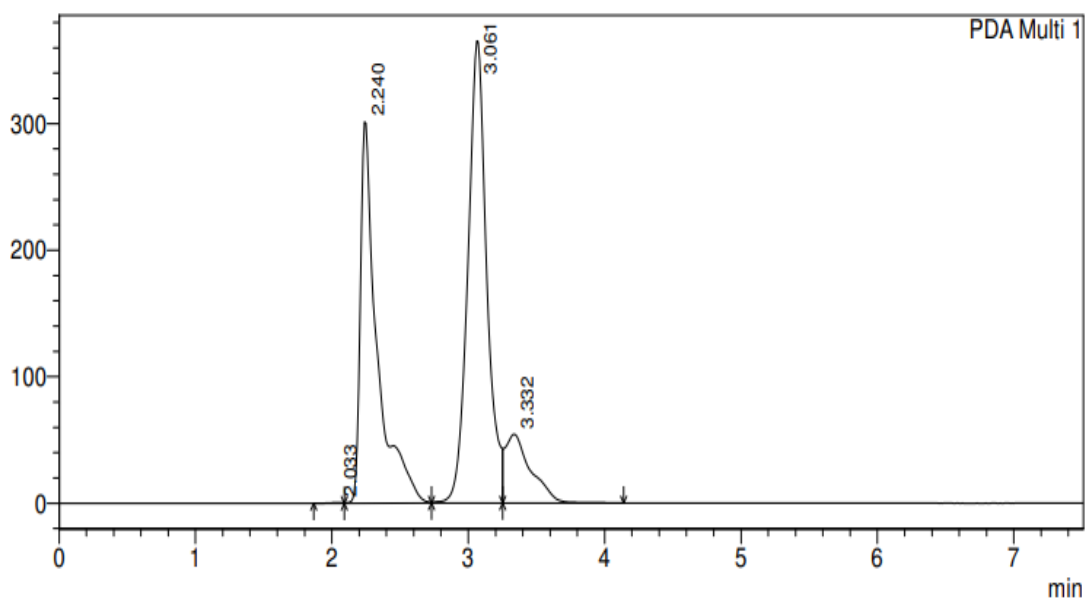
Figure 45. HPLC chromatogram using Methanol: Formic acid (1%)
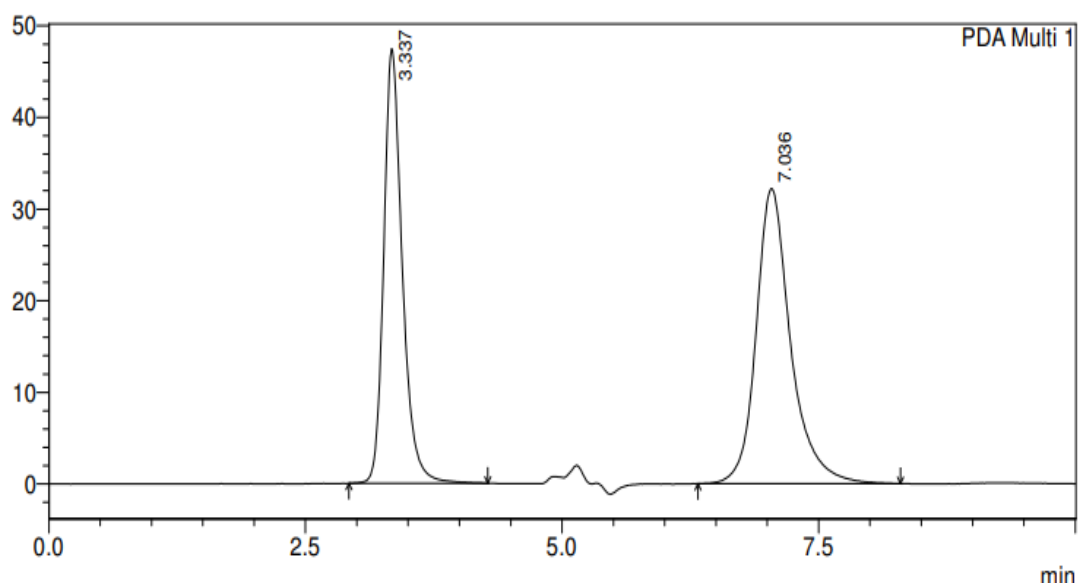
Figure 46. HPLC chromatogram using Methanol: Water (70:30)
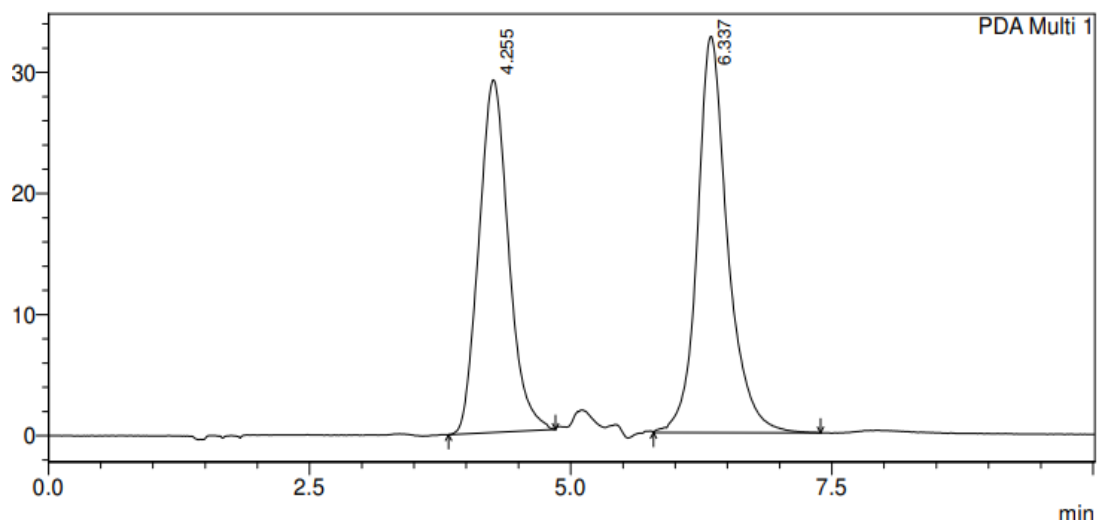
Figure 47. HPLC chromatogram using Methanol: Water (80:20)
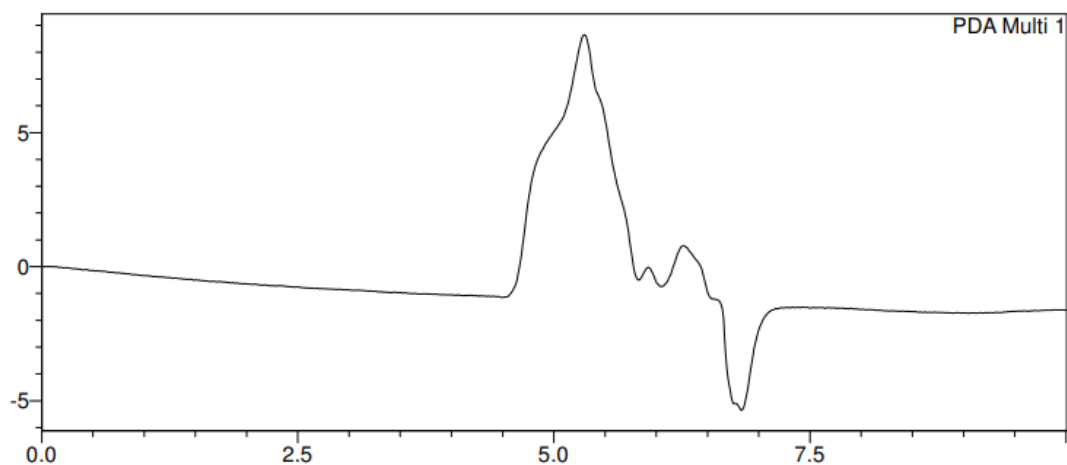
Figure 48. Blank peak

5.4.3 Method validation

5.4.3.1 System suitability

Table 17 shows the parameters describing the system's suitability parameters. Before a chromatographic system is put to use, it must first pass a test called the system suitability test, which evaluates the system to see whether it will perform as expected or not. When used consistently, the efficacy of any chromatographic system has the potential to undergo ongoing shifts, which can have an impact on the validity of the analytical findings. Better column efficiency is indicated when the value of the theoretical plate is greater than 2,000, the value of HETP is lower, and the tailing factor is less than 2%. The findings that we received from this research suggested that the

136

approach that was created has very excellent system adaptability (Ramadan et al., 2020).

Table 17: System suitability parameters for FPV and NVP

Sr.no	Parameters	Values		Limits
		FPV	NVP	
1	Theoretical plates	1034.26	2606.77	Depends on theoretical plates
2	Theoretical plates/meter	6895.102	17819.581	> 20,000
3	HETP	145.030	57.542	>2000
4	Tailing factor	1.182	1.195	> 2

5.4.3.2 Linearity and Range

The calibration curve for FPV and NVP were plotted. The calibration curves were linear in a specified range of 2-10 µg/mL. The coefficient of correlation (R^2) was found to be 0.9905 for FPV and 0.9896 for NVP. The calibration curves are shown in Figures 49 and 50.

$$y = 60574x - 368.98$$
$$R^2 = 0.9905$$
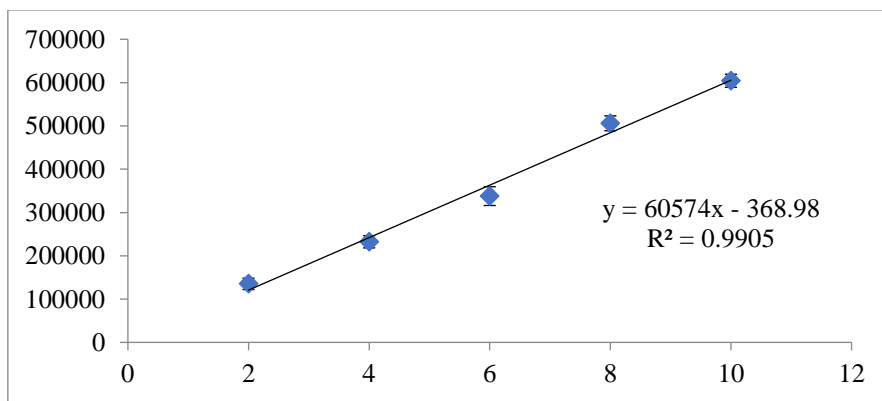
Figure 49. Calibration curve of FPV (n=3)

$$y = 60250x + 53161$$
$$R^2 = 0.9896$$
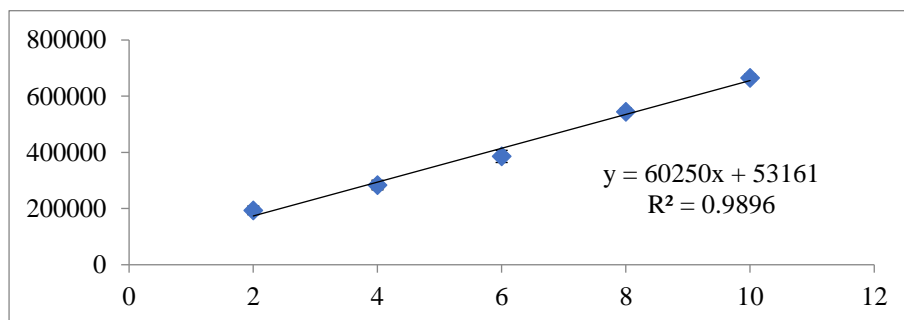
Figure 50. Calibration curve of NVP (n=3)

5.4.3.4 Accuracy

According to the findings, the median recovery percentage was within the allotted range, which was from 95% to 105% (Table 18). This was the case for all three levels. This demonstrates that the technique that was devised is reliable.

Table 18: Accuracy study results for FPV and NVP

Drugs	Levels	Theoretical concentration of the standard solution (µg/mL)	Actual concentration recovered from mobile phase (µg /mL) (mean±SD) (n = 6)	RSD (%)	Recovery (%)	Mean recovery
FPV	LQC	5.98	5.9189 ± 0.1014	1.5414	98.9799	99.7657
	MQC	7.18	7.1122 ± 0.1167	1.5590	99.0565	
	HQC	8.94	8.4856 ± 0.1180	2.1453	101.2609	
NVP	LQC	6.54	6.5281 ±0.0984	1.5073	99.8190	99.6630
	MQC	7.74	7.7650 ±0.0742	0.9567	100.3235	
	HQC	8.94	8.8368 ± 0.1333	1.5107	98.8466	

5.4.3.5 Precision

To determine the precision of the method by measuring % RSD of LQC, MQC, and HQC six times each in interday, interanalyst, and intraday under similar conditions for experimentation. Injecting LQC, MQC, and HQC allowed for the completion of both interday and intraday trials with successful results. Over three consecutive days, the peak locations that were independently discovered for FPV, and NVP were repeatable and exact. The findings for both intraday and interday provide evidence that the devised approach has a high level of repeatability and accuracy. In this method, all the data were expressed in % RSD, and they were consistently below the acceptable limit of % RSD <2 (Binge et al., 2014). Table 19 presents the findings of the intraday and interday accuracy of FPV, and NVP measurements (Kumar R et al., 2020).

Table 19: Precision study results for FPV and NVP

Parameters	Levels	A 1	A2	A3	A4	A5	A6	Mean Area (cm^2)	SD	%RSD
FPV										
Repeatability (Intraday)	LQC	345809	366106	357355	359659	354633	355676	356539.67	6075.062	1.703895
	MQC	430543	430215	428138	435698	429876	432143	431102.17	2366.239	0.548881
	HQC	507627	508765	512345	501987	508734	518767	509704.17	5079.394	0.996538
Intermediate Precision										
Interday 1	LQC	353978	349001	366008	366757	363166	356795	359284.17	6534.736	1.818821
	MQC	430310	427788	437078	421263	421036	417148	425770.50	6703.45	1.574428
	HQC	506153	509164	502204	507535	491052	491529	501272.83	7366.32	1.469523
Interday 2	LQC	373880	364291	360541	358830	371134	360807	364913.83	5663.793	1.552091
	MQC	447474	443668	440573	457260	463460	440552	448831.17	8663.045	1.930134
	HQC	507037	508305	500416	509182	500416	509182	505756.33	3843.707	0.759992
Interday 3	LQC	365489	368436	346319	357522	356746	359771	359047.17	7068.699	1.968738
	MQC	434975	437046	425668	422957	426785	439137	431094.67	6183.284	1.434322
	HQC	510562	508823	503073	508447	504744	508945	507432.33	2622.893	0.516895
Interanalyst	LQC	360757	360758	354587	352819	363568	354856	357890.83	3968.938	1.10898
	MQC	425623	430123	439271	419470	428345	421956	427464.67	6388.571	1.494526
	HQC	504563	502341	510984	520341	515290	500043	508927.00	7261.127	1.426752

NVP										
Repeatability (Intraday)	LQC	453421	447560	440658	460130	446681	445676	449021.00	6211.666	1.38338
	MQC	514356	523987	529876	513056	523045	505674	518332.33	8075.942	1.558063
	HQC	595007	581505	591092	587609	593247	591265	589954.17	4402.178	0.74619
Intermediate Precision										
Interday 1	LQC	444895	454543	457048	449892	432988	442737	447017.17	8012.089	1.792345
	MQC	513483	520731	518472	519580	518341	505792	516066.50	5120.251	0.992169
	HQC	585427	591786	595444	585790	591756	597778	591330.17	4553.902	0.770112
Interday 2	LQC	447474	443668	440573	457260	463460	440552	448831.17	8663.045	1.930134
	MQC	530918	536035	523677	524860	520616	528156	527377.00	5063.643	0.960156
	HQC	589133	585992	586540	597999	590729	597828	591370.17	4887.335	0.826443
Interday 3	LQC	436756	444161	450908	440916	430478	440872	440681.83	6275.62	1.424071
	MQC	521692	532543	507066	522430	531910	526978	523769.83	8550.377	1.632468
	HQC	593265	589678	587730	587646	581314	597616	589541.50	5060.416	0.858365
Interanalyst	LQC	457809	454937	444512	446349	435689	445896	447532.00	7233.07	1.616213
	MQC	512384	521839	514829	519834	512834	521294	517169.00	3938.925	0.761632
	HQC	596294	589362	590017	596723	582396	571238	587671.67	8779.969	1.494026

*A represents Area

5.4.6 LOD and LOQ

The LOD was 0.277 and 0.290 µg/mL for FPV and NVP, respectively, whereas, the LOQ was 0.839 and 0.879 µg/mL for FPV and NVP, respectively.

5.4.7 Robustness

The fact that changing a few chromatographic conditions did not result in any noticeable shifts in the results indicated that the approach was resistant to the introduction of even a relatively large amount of arbitrary variation in the wavelength or flow rate. In every instance, the FPV, and NVP peaks were symmetric (tailing factor less than 2) and were distinguishable (resolution more than 2). According to Awasthi et al., the fact that the % RSD of FPV, APV, and NVP retention periods were less than 1% implies that the established approach was reliable (Awasthi et al, 2022).

Table 20: Robustness study results for FPV and NVP

Variables	Value	Conc. (µg/mL)	Avg. Area (cm²)	Std. Dev.	% RSD	% Recover
FPV						
Flow rate	0.8	10	603462	1417.7491	0.2349	99.6848
	1	10	581272	2010.3046	0.3458	96.0215
	1.2	10	551290	2948.6353	0.5349	91.0719
Wavelength	256	10	528365	688.0149	0.1302	87.2873
	258	10	571295	2582.3540	0.4520	94.3745
	260	10	629845	1483.5100	0.2355	104.0403
NVP						
Flow rate	0.8	10	643947	9122.3846	1.4166	9.7601
	1	10	679384	1174.5044	0.1729	10.0246
	1.2	10	667406	678.1154	0.1016	10.1947
Wavelength	256	10	669920	3545.4334	0.5292	10.3786
	258	10	656295	2588.7179	0.3944	9.9371
	260	10	635757	2513.7646	0.3954	9.6853

5.5 Characterization of Dendritubes

5.5.1 Physiochemical properties

The sample obtained was black in colour and odourless. The obtained material was free-flowing granular material.

5.5.2 UV spectroscopy
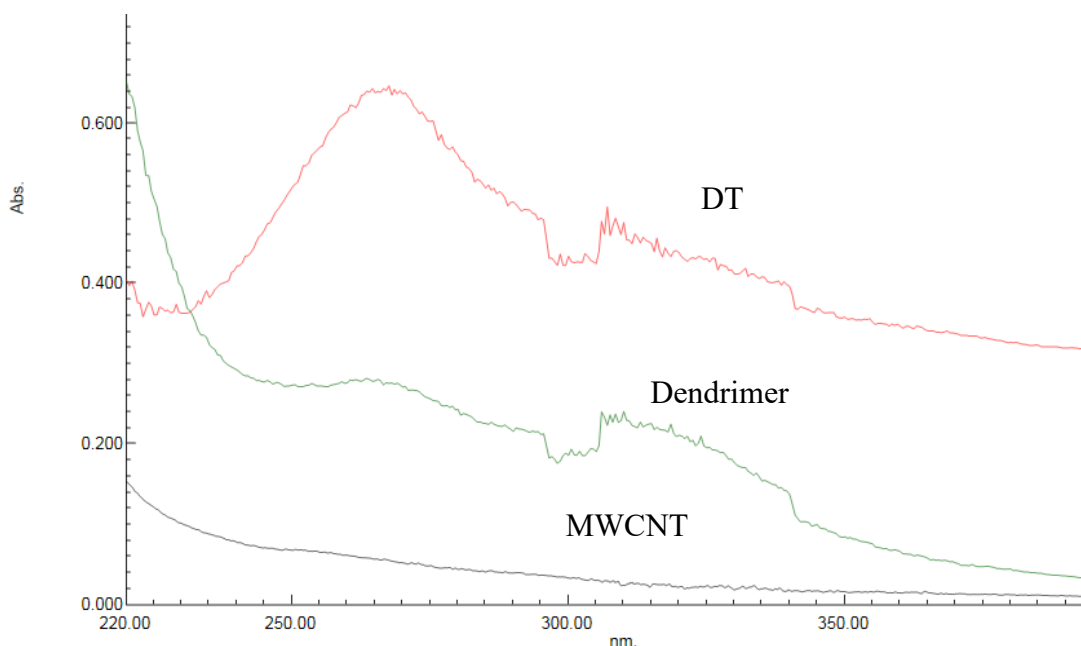
Figure 51: UV spectrum overlay spectra of dendrimers, MWCNT, and DT

The dendrimers, MWCNT, and DT (10 µg/mL) solution were scanned using a UV-Vis spectrophotometer (UV-1800, Shimadzu Co. Ltd). The UV maxima for DT were observed at 269 nm as shown in Figure 51.

5.5.3 FT-IR spectroscopy
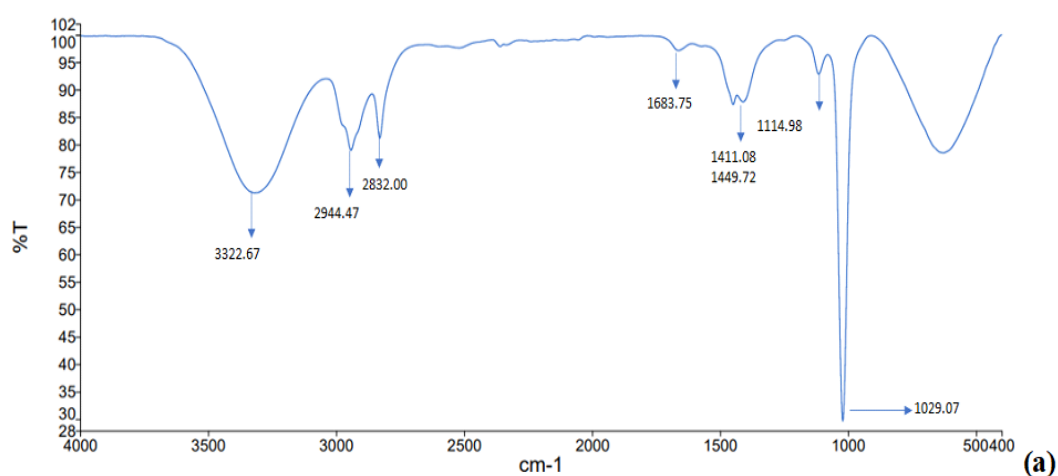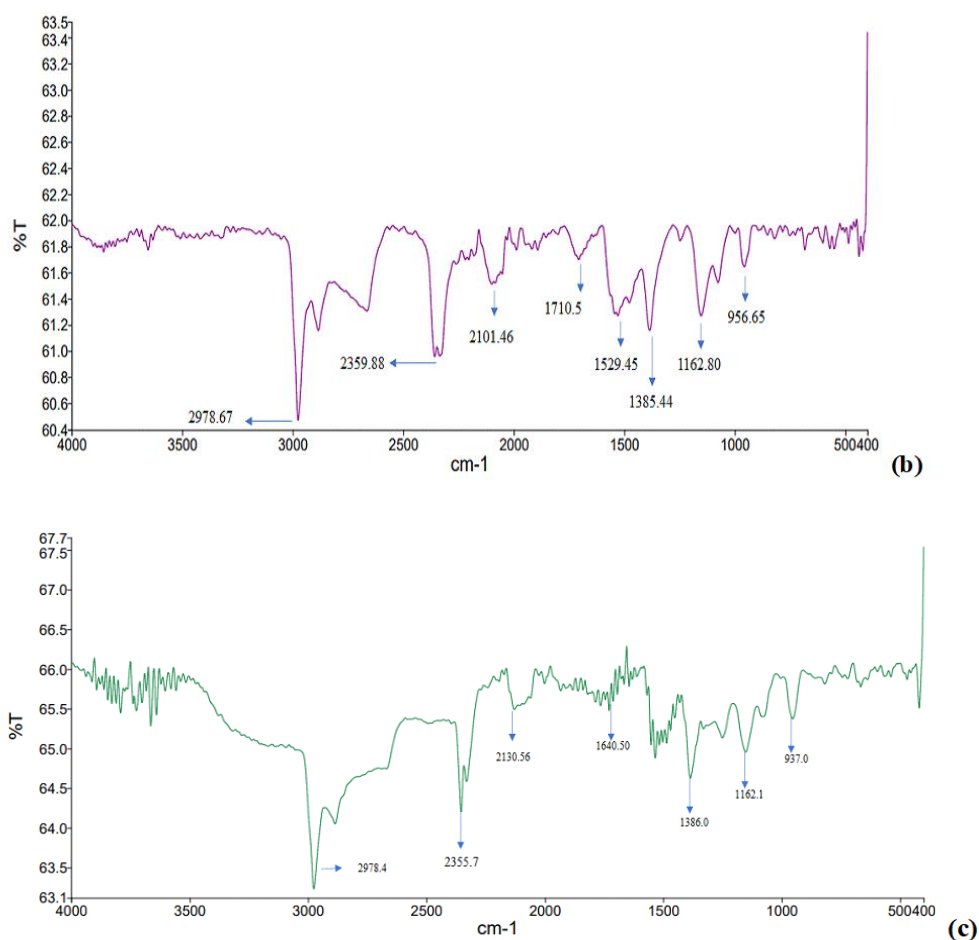
Figure 52. FTIR spectra of (a) MWCNT, (b) Dendrimers, (c) DT

Table 21: FTIR spectrum of DT

Observed peaks frequency (cm^{-1})	Standard FTIR range (cm^{-1})	Corresponding functional group
3643.53	3500-3300	Primary amine
2978.40	3400-2400	-OH group of COOH
1640.50	1680-1630	-CO-NH (amide peak)
1386.00	1390-1440	-OH group of COOH
1162.10	1300-1000	-C-O stretch
937.00	900-690	Aromatic C-H out of plane bend

The conjugates were evaluated with FTIR spectroscopy (Perkin Elmer) using KBr pellets and spectra are shown in Figure 52 and observed frequency is tabulated in Table 21. FTIR spectrum of COOH-MWCNT, dendrimers, and dendrimers MWCNTs conjugate was determined and studied. FTIR of MWCNT showed characteristic peaks such as 2978.67 cm^{-1} peak corresponding to alkene, a broad peak at 1710.05 cm^{-1} was the characteristic peak for carboxylic acid, 1529.45 cm^{-1} was the peak for carboxylate

144

ion stretching, 1385.44 cm^{-1} peak due to OH bending, 1152.80 cm^{-1} peak of C-O stretching and 956.65 cm^{-1} being the peak for out-of-plane bend of alkene.

The spectrum of dendrimers showed peaks such as a peak at 3322.67 cm^{-1} was the peak for primary amine confirming the amine present on the exterior of dendrimers, a peak at 2944.47 cm^{-1} and a peak at 2832.0 cm^{-1} was due to stretching of -C-H of alkene, peak at 1683.75 cm^{-1} due to N-H deflection of amine, a peak at 1411.08 cm^{-1} and 1449.72 cm^{-1} are the twin peak conforming to CH band, a peak at 1114.98 cm^{-1} due to stretching of –C-N, and 1029.07 cm^{-1} which corresponds to bending of C-H bending. All the peaks of MWCNTs and dendrimers indicate all the major functional groups and confirm the presence of the structure.

The spectrum of MWCNT, dendrimers, and DT is represented in Figure 52. The spectrum of DT revealed characteristics peaks of at 2978.4 cm^{-1} primary alkene, 1640.50 cm^{-1} small peak amide, 1386.0 cm^{-1} OH bending, 1162.1 cm^{-1} corresponding to stretching of C-O, and 937.00 cm^{-1} aromatic C-H out of plane bending. The bulge in the region of 3000-3500 cm^{-1} was due to the conjugation of the primary amine of dendrimer with the MWCNT structure. The absence of a stretching peak at 1710.50 cm^{-1} indicates that the COOH group was altered by covalently binding with amine present on the surface of dendrimers.

5.5.4 Raman Spectroscopy

Raman spectroscopy is a useful technology to study structural characterization. It is also a reliable tool that can help to approve the conjugation of dendrimers on the periphery of MWCNTs. Raman spectra of COOH-MWCNT and dendrimers conjugated MWCNTs were recorded to evaluate the attachment of PPI dendrimers on the surface of MWCNT as represented in Figure 53. Both spectra display two bands. The D band for MWCNT was observed at 1282.44 cm^{-1} and for DT was observed at 1286.29 cm^{-1}. This band was due to a defect or disorder in the MWCNT structure. The G band was observed at 1599.38 cm^{-1} for MWCNT and 1601.16 cm^{-1} for dendrimers conjugated MWCNT. This band relates to the crystalline structure of graphite. Further, the ratio of two bands helps to analyze the addition of functional groups on the MWCNT structure. Figure 53 represents the Raman spectra of MWCNT and DT. The ratio of ID/IG value acts as an indicator of alteration of electronic structure. The D and G band intensity ratio (ID/IG) of MWCNT was found to be 1.538 and the ratio of

dendrimers conjugated MWCNTs was found to be 1.460. The change in the value was due to the addition of a newer structure on the surface of MWCNTs which alters the sp2 bonding structure of MWCNTs and leads to the breaking of π bonds holding the hexagonal carbon structure (Muda et al., 2017; Sedaghat et al., 2014).
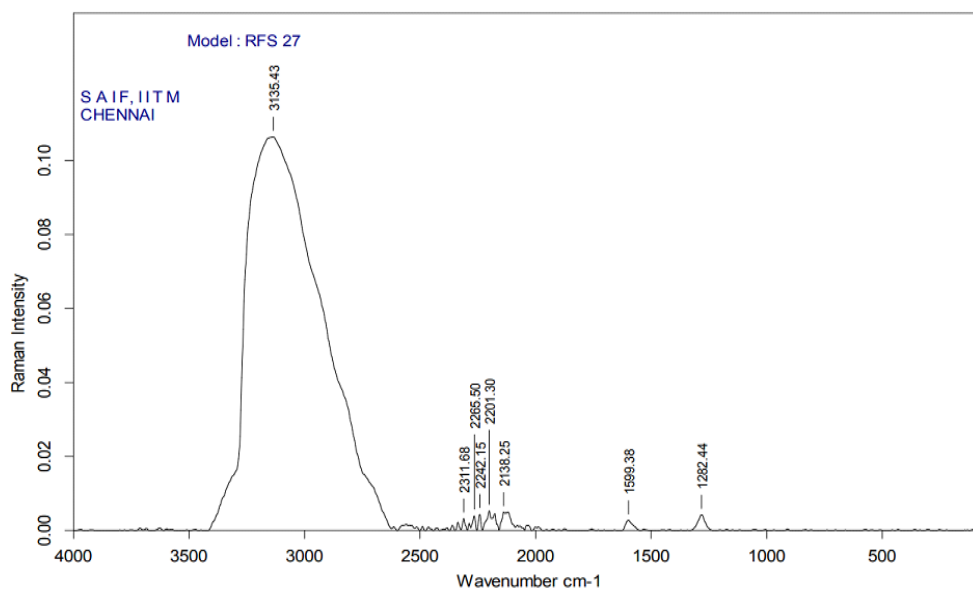
(a)
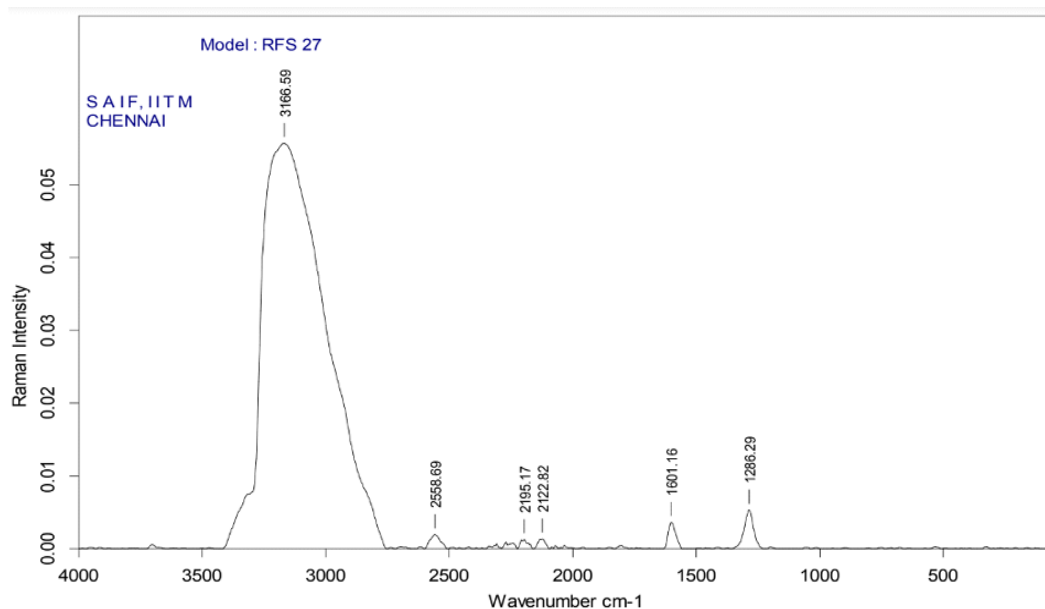
(b)

Figure 53. RAMAN spectra of (a) MWCNT and (b) DT

146

5.5.5 NMR Spectroscopy

N-1

(a)

N2
CMC_SINGLE_H2O D2O {D:\Spectra} nmr 1

(b)
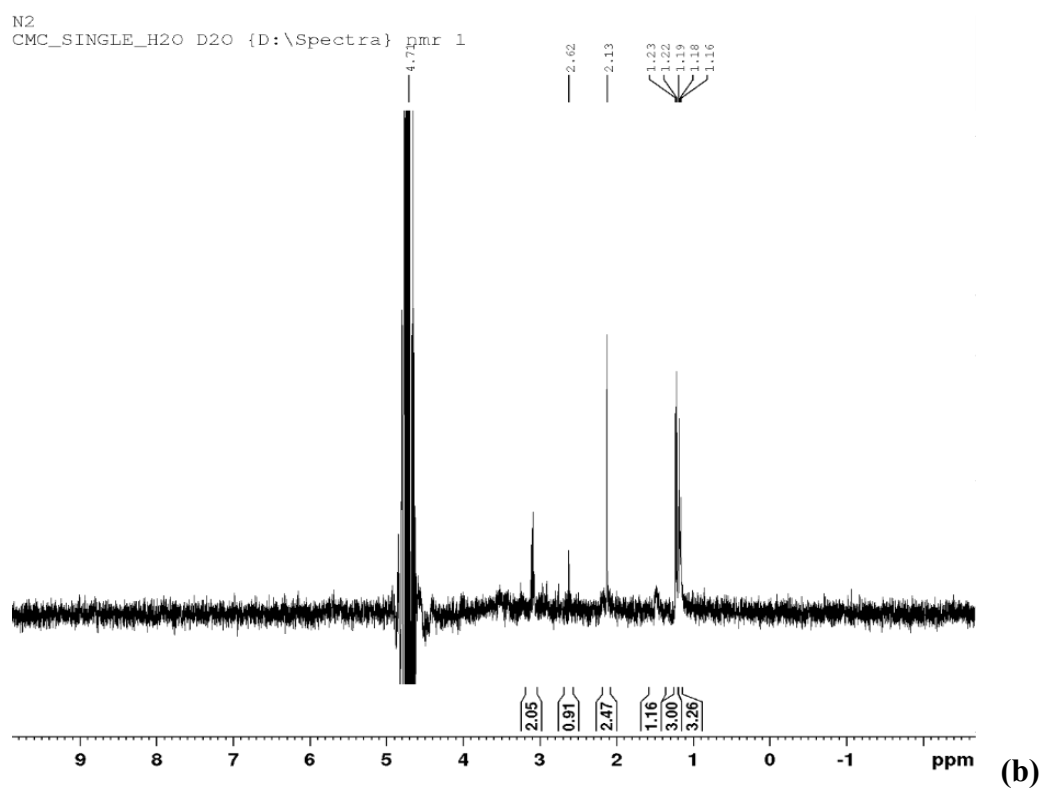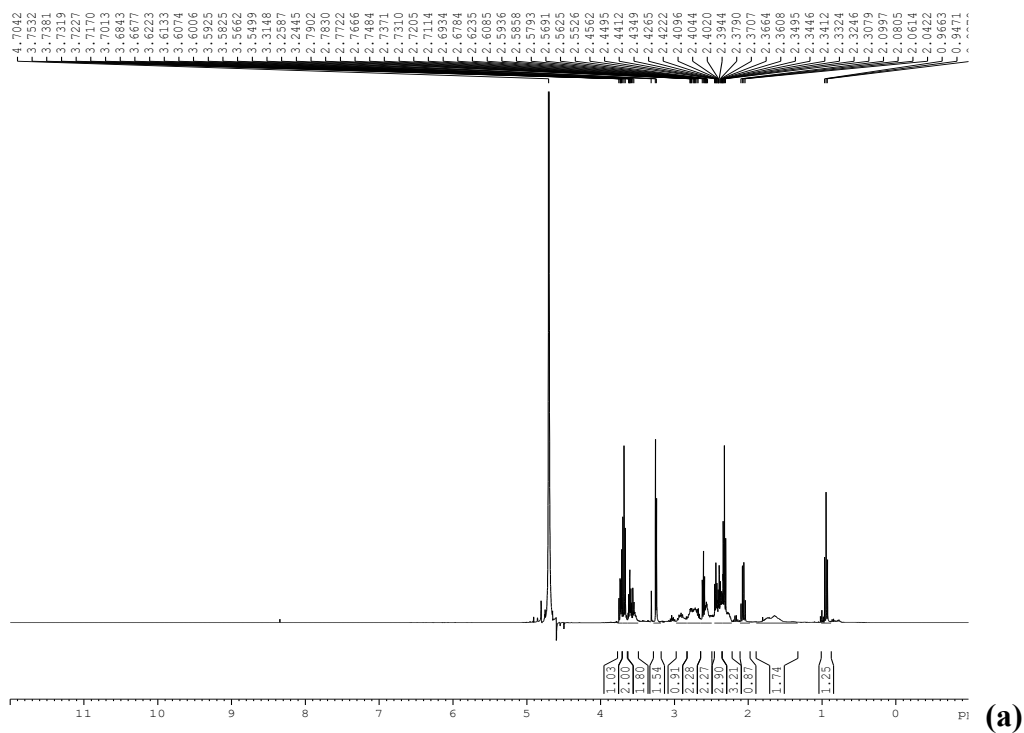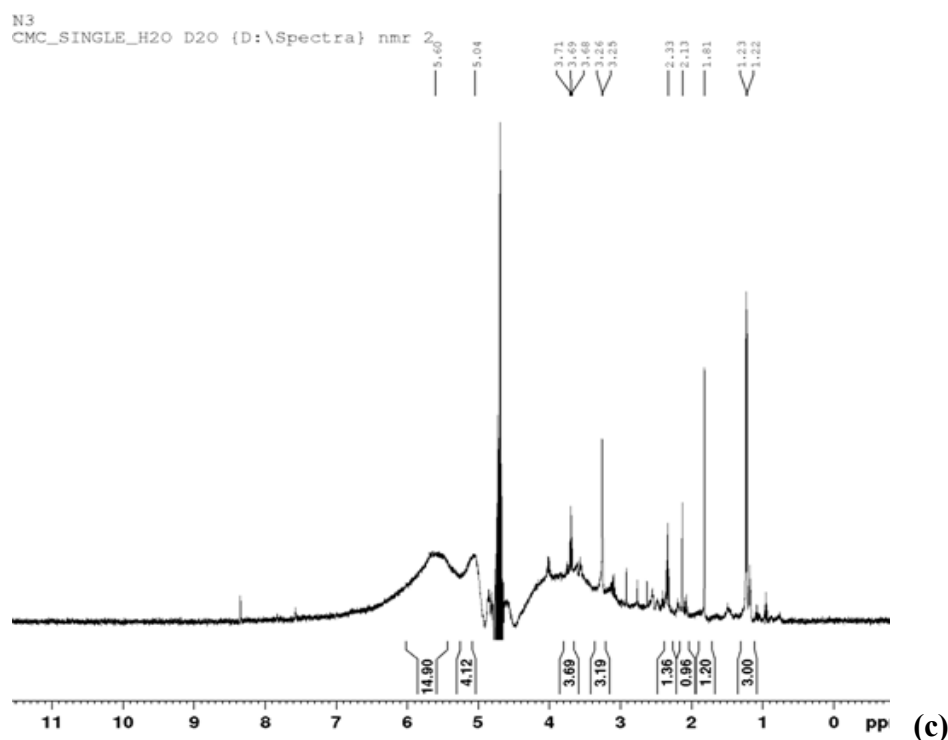
Figure 54. NMR spectra of (a) 5G PPI dendrimers, (b) MWCNT, (c) DT

The NMR spectra of dendrimers confirm the presence of protons as per the literature and represented in Figure 54. Multiplets were observed between δ 0.9 ppm corresponding to $-CH_2$ of methylene groups of EDA, the chemical shifts between δ 1.74 ppm corresponding to $-CH_2-CH_2-$, the peak at δ 2.34-2.36 ppm corresponds to $-NH_2$, multiple peaks at δ 2.40–2.69 ppm due to N[C]C and multiplets between δ 2.71–2.79 ppm corresponds to $-CH_2-NH_2$ (Kumar et al., 2006; Gajbhiye et al., 2013).

^{1}H NMR study of MWCNT showed the presence of protons in δ 1.16 to 1.23 ppm which confirms the presence of the C-H in the MWCNT. In the MWCNT the singlet peak in between δ 2.0 to 2.2 ppm indicated the presence of $-CH_2COOH$. A peak at δ 3.0-3.2 ppm was the characteristic peak that indicates the presence of a proton of $-CH_2OH$.

The NMR spectroscopy results confirmed the attachment of MWCNT with dendrimers. Multiplex between δ 3.2-3.7 ppm corresponds to the -OH protons of MWCNT. Peak at δ 1.01 ppm corresponds to C-H protons, and multiplets at δ 0.8-1.2 ppm correspond to the CH_2 of dendrimer structure. The conjugation took place between the NH_2 of dendrimer and COOH of MWCNT. The peaks of NH_2 and the peak of COOH were observed at δ 2.3 ppm and in between δ 2.13 ppm were found to be altered

148

which confirms the formation of conjugates. The 5G dendrimer's structure has an abundance of protons in its surroundings due to a heavily conjugated and complex structure that corresponds to various peaks and splitting patterns. Thus, from the NMR spectra, the conjugation of MWCNT and dendrimers was confirmed.

5.5.6 X-ray Diffraction
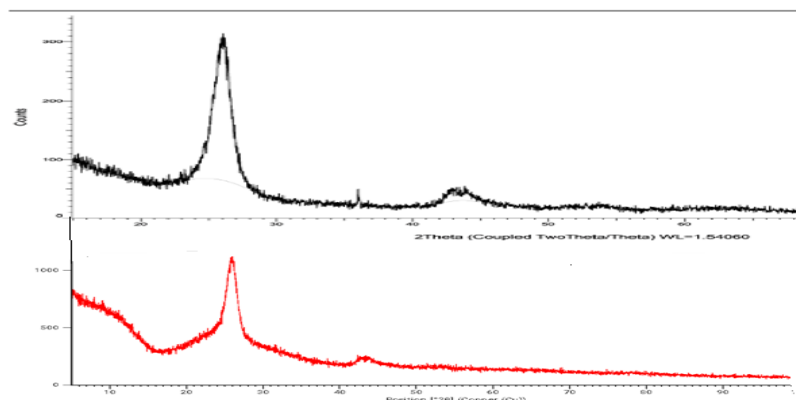
Figure 55: XRD of MWCNTs and DT

XRD is used to study the powder characteristics of a given sample. The XRD pattern indicated the crystallinity of the prepared DT. Figure 55 indicates the XRD diffraction pattern of MWCNT and DT. The pattern of MWCNT had a characteristic peak at 25.959º and another small peak at 42.252º. The conjugate of dendrimers and MWCNT (DT) also exhibits peaks at the same region as MWCNT at 25.907º and 42.562º. XRD pattern indicated that conjugation of the dendrimers with MWCNT did not affect the structural characteristics of MWCNT and crystallinity was similar to MWCNT (Neelgund et al., 2012)

5.5.7   Differential Scanning Calorimetry

| (a) | (b) | (c) |
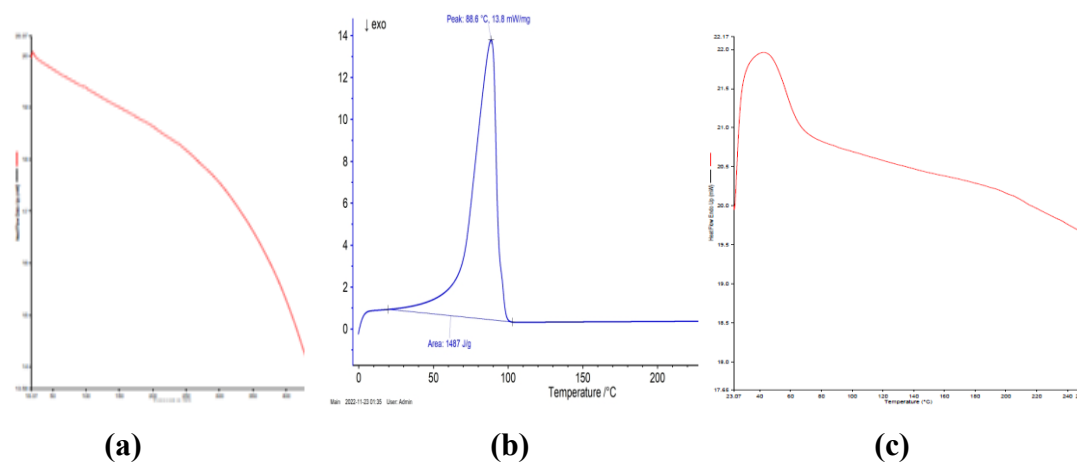
Figure 56: DSC of (a) MWCNT, (b) Dendrimers and (c) DT

149

The DSC was done to study the crystallinity, melting point, and thermal stability of the components at different ranges of temperatures. MWCNT, dendrimers, and DT were subjected to varying temperatures using Differential scanning calorimetry. MWCNT does not show any change in heat event till 400 ˚C. The DSC of dendrimers displayed an intense peak at 88.6 ˚C, this represents a sharp melting point of dendrimers. In the DSC thermogram of DT broad peak was observed at 40 ˚C. The broad peak and the absence of a sharp peak indicate that the dendrimer MWCNT complex had been formed (Barbosa et al., 2014; Garbhiye et al., 2013). DSC of MWCNT, dendrimers, and DT is shown in Figure 56.

5.5.7 Field emission scanning electron microscopy

The FE-SEM of dendrimers clearly shows that the structure was in the nanoscale range and distinct. The image indicated the spherical branching arrangement of the dendrimers originating from the center core. FE-SEM of COOH-MWCNTs indicated an elongated and thread-like structure. The structure did not show any kind of facture on the surface. FE-SEM of dendrimers conjugated MWCNTs indicates the conjugation of dendrimers on the surface of MWCNT. As it was a surface conjugation it was better observed by the study of surface morphology. Figure 57 indicates the SEM images of MWCNT, dendrimers, and DT. The image shows the presence of a tube-like structure of carbon nanotubes with the spherical structure - dendrimer present on the surface of the MWCNT. The image indicates that the supramolecule structure was formed by conjugation of MWCNT and dendrimers, which was further confirmed with TEM images.

(a)   (b)
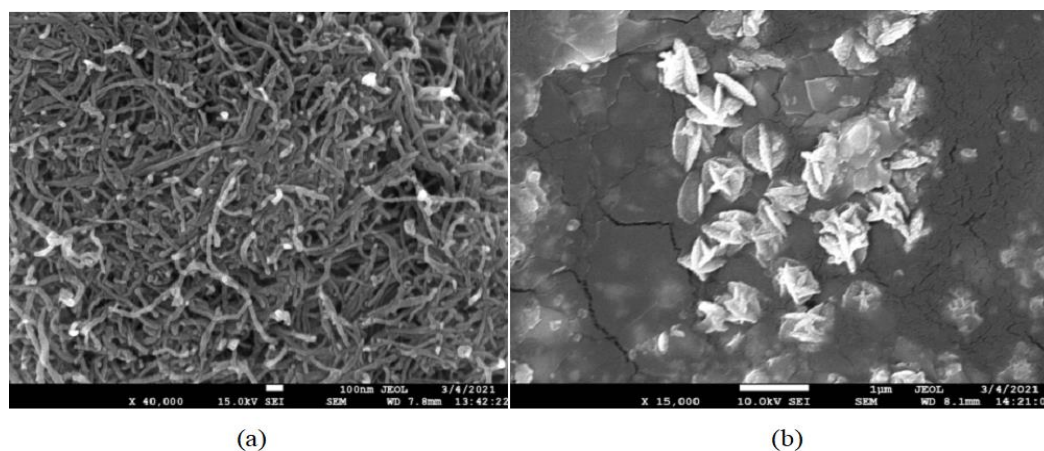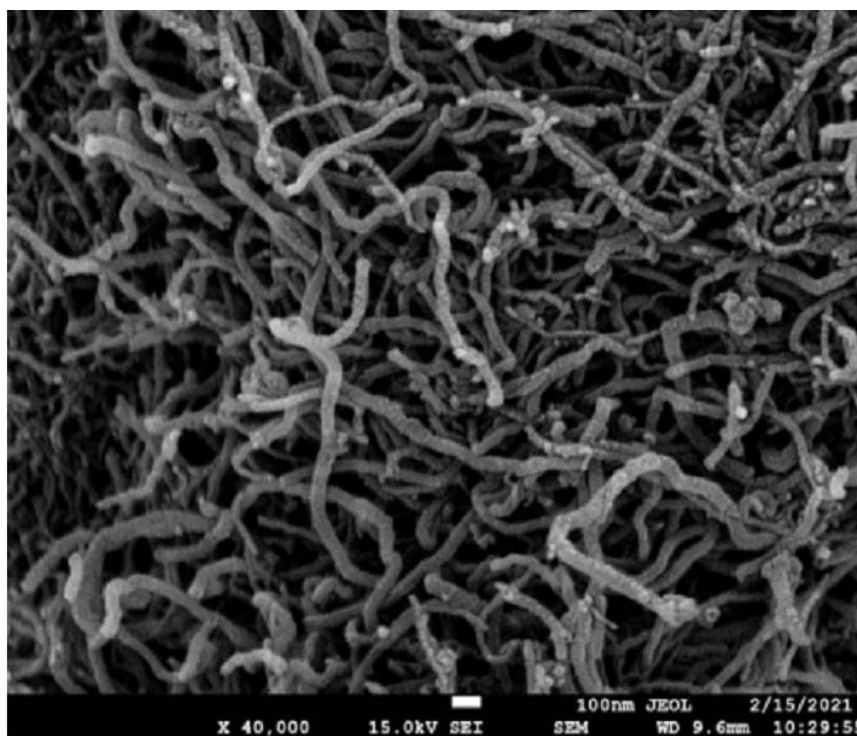
(c)

Figure 57: FE-SEM images of (a) COOH-MWCNTs, (b) Dendrimers

(c) DT

5.5.7.1 High-resolution transmission electron microscopy

Figure 58 indicates the HR-TEM images of DT. The image indicates the presence of a hollow tube-like structure of single-walled nanotubes with the presence spherical structure - dendrimer on the surface of the COOH-MWCNT. The image confirms that the supramolecule structure was formed by the conjugation of COOH-MWCNT and dendrimers. The lengths of carboxylated MWCNTs, dendrimers, and DT were investigated by HR-TEM. HR-TEM images showed that the size of dendrimers and COOH-MWCNT were around 100 nm, while the DT image showed a size around 500 nm which may be due to the addition of dendrimers structure on the outer surface of the COOH-MWCNTs. Comparing the structure of COOH-MWCNT and dendrimer-conjugated COOH-MWCNT, no significant change was observed on the surface of COOH-MWCNTs.
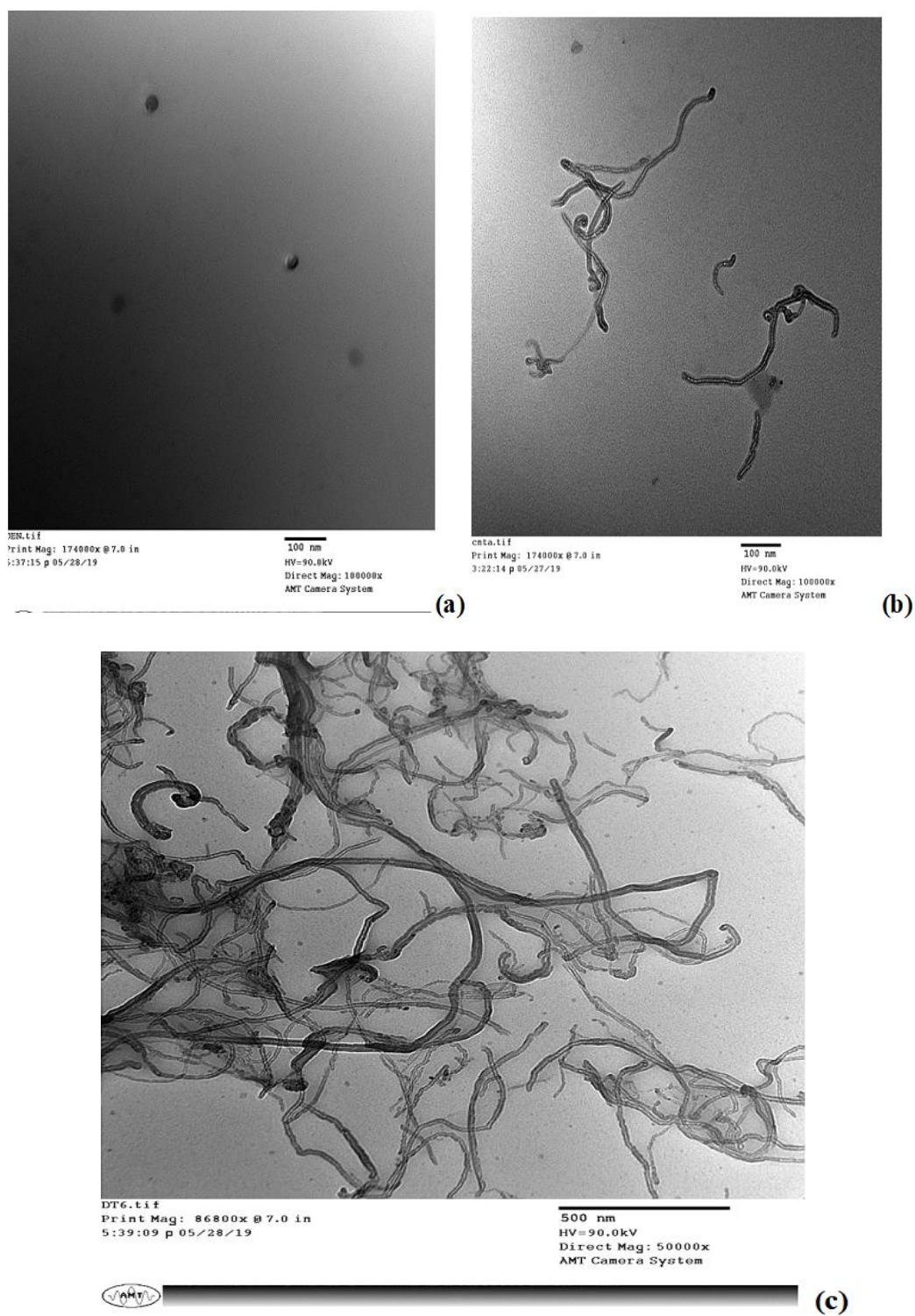
Figure 58: HR-TEM images of (a) Dendrimers (b) COOH-MWCNT (c) DT

5.5.10 Atomic force spectroscopy

| (a) | (b) |
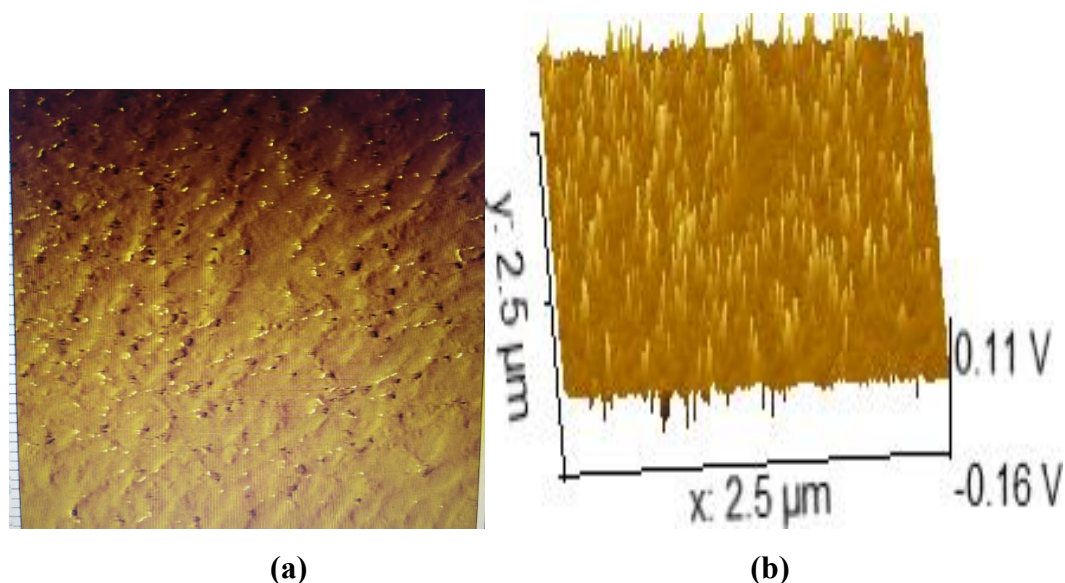
Figure 59: (a) 2D AFM images of DT (a) 3D AFM images of DT

AFM is non-atomic resolution equipment that helps to resolve larger structures like MWCNTs and dendrimers. The image shown in Figures 59 and 60 confirms the tube-like structure below the film surface. This image confirms the structure of MWCNT present in the polymer matrix. The image reflects a rod-like structure present below the matrix indicating the presence of MWCNT structure. The white spots correspond to the free ends of carbon nanotubes protruding out of the matrix. The length of the nanotube was found to be between 2 to 6 μm while diameters were estimated in the XY-plane in the range from 200 to 400 nm. The closed and circular structure near the tube-like structure indicates the presence of the dendrimers, which confirms that dendrimers are associated with MWCNTs (Singh et al., 2016; Mohammed et al., 2017).

5.3.11 Particle Size

Particle size determination helps to determine the size of the nanostructure formed. The average particle size was found to be 288.4 nm confirming that the new nanostructure was in the nano size range. The polydispersity index (PDI) was found to be 0.385. The PDI indicates that the particle size was narrow and indicates that aggregation was not prominent for DT particles. Figure 60 represents the particle size distribution of DT.

153
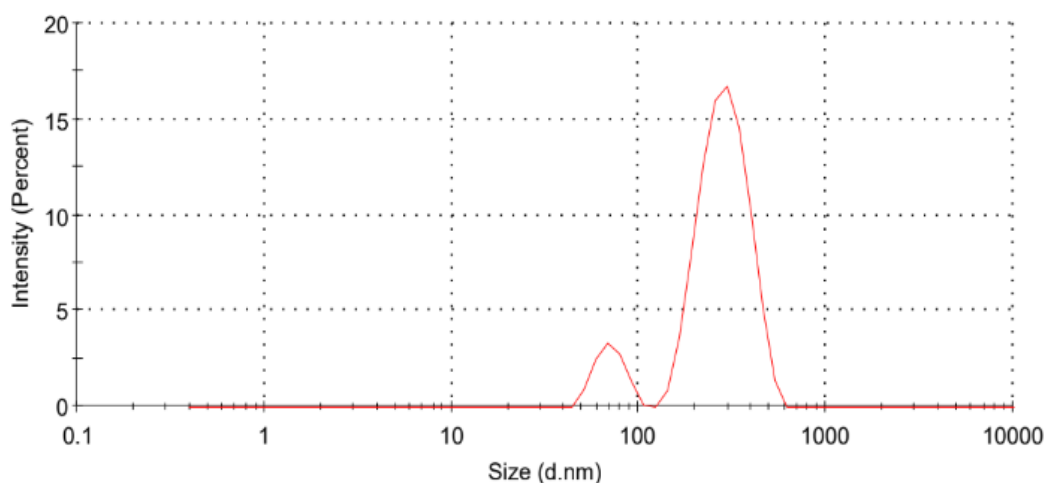
Figure 60: Particle size distribution of DT

5.5.12 Zeta potential

The value of Zeta potential was found to be -2.48. The negative charge may be contributed by the ionized carboxylic group on the surface. The zeta potential was found to be reduced as compared to COOH functionalized CNT and Dendrimers. This indicates that the free surface functional group was reduced in the new structure. Figure 61 represents the zeta potential of DT.
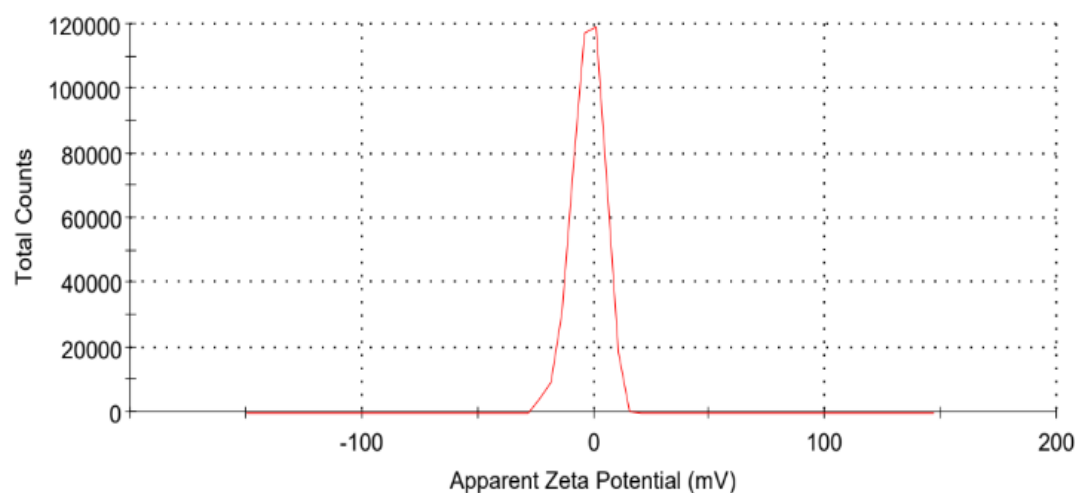
Figure 61: Zeta Potential of DT

Table 22 represents the comparative data of particle size, PDI, and zeta potential MWCNT, dendrimers, and DT. The particle size of DT was found to be greater than MWCNT and dendrimers due to the conjugation of dendrimers and MWCNT. The PDI of DT was found to be improved than MWCNT as conjugation with dendrimer increases the static charges which reduces the entanglement of the MWCNTs. The zeta

potential of MWCNT was -12.5 while dendrimers have positive zeta potential, hence upon conjugation the zeta potentail of DT drastically shifted to the positive side. The data of particle size and zeta potential supports the conjugation of MWCNT and dendrimers in DT.

Table 22: Particle size distribution, PDI and zeta potential of MWCNT, dendrimers, and DT

	Z-average (nm)	PDI	Zeta potential (mV)
MWCNTs	262.5	0.590	-12.5
Dendrimers	41.9	0.379	+24.64
DT	288.4	0.530	-2.48

5.6 Characterization of Mannosylated Dendritues

5.6.1 FTIR spectroscopy
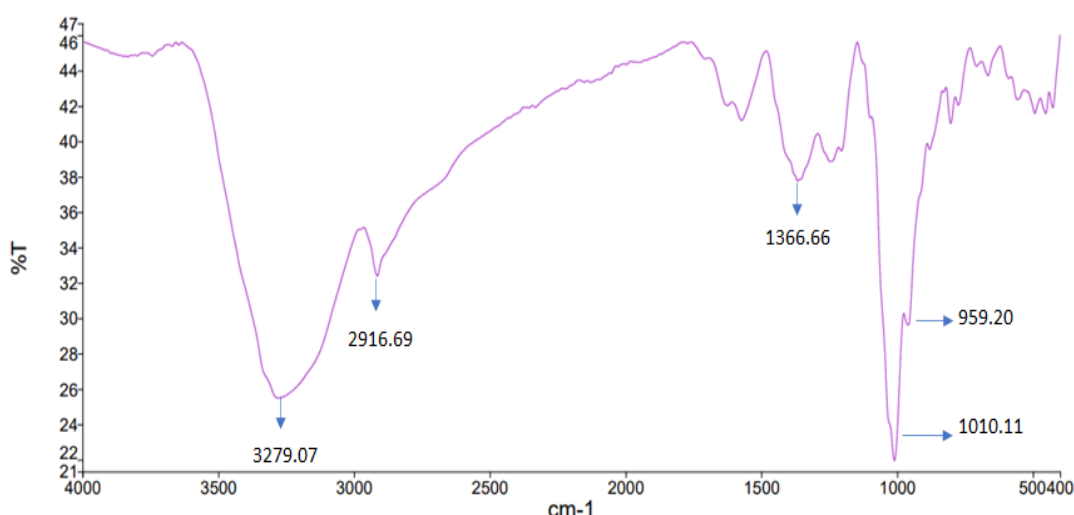
Figure 62: FTIR spectrum of mannosylated DT

FTIR peaks of mannosylated drug-loaded DT were compared and evaluated for different functional groups present. The main peaks are due to stretching of C-N at 1018.92 cm^{-1}; N-H deformation of primary amine at 1410 cm^{-1}; N-H deflection of amine (1639 cm^{-1}); broad peak at 3183 cm^{-1} due to OH group. The peak at broad peak 3183.99 cm^{-1} and C-N deformation at 1410 cm^{-1} confirmed the formation of Schiff base and amines due to the conjugation of mannose and terminal amine group of dendrimers. Figure 62 represents the FTIR spectrum of mannosylated DT.

155
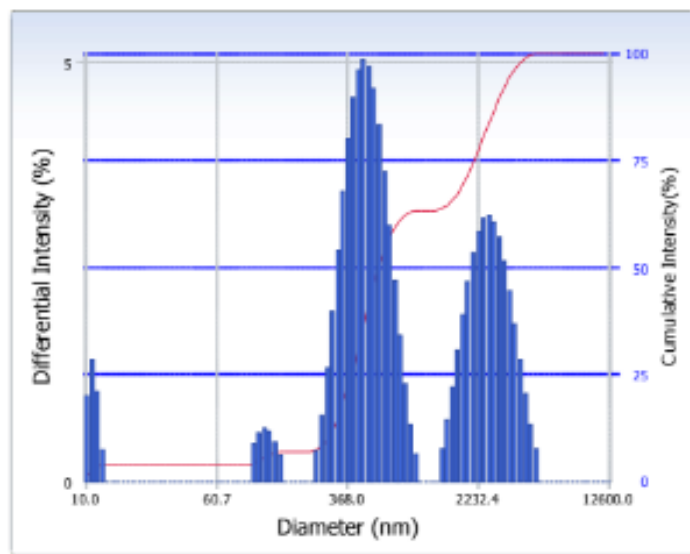
5.6.2 Particle size

Figure 63: Particle size distribution of DT-M

The average particle size was estimated to be 682.5 nm confirming that the new nanostructure was in the nanosize range. The polydispersity index was found to be 0.325. The PDI indicates that the particle size was narrow and that there was no such aggregation in the size of particles as shown in Figure 63.

5.7 Formulation and Characterization

5.7.1 Formulation development and characterization of Nevirapine-loaded dendrimers

5.7.1.1 Formulation development of Nevirapine-loaded dendrimers

The drug NVP was loaded on the 5G PPI dendrimers (NVP-DEN) with constant stirring for 48 h using a magnetic stirrer. The drug binds with the surface amine group of the dendrimers by covalent linkage and by trapping in the dendritic structure. The structure was characterized using different characterization techniques such as spectroscopic analysis, morphological studies, and *in-vitro* drug release studies.

5. 7.1.2 Characterization of NVP-DEN

5. 7.1.2.1 FTIR spectroscopy
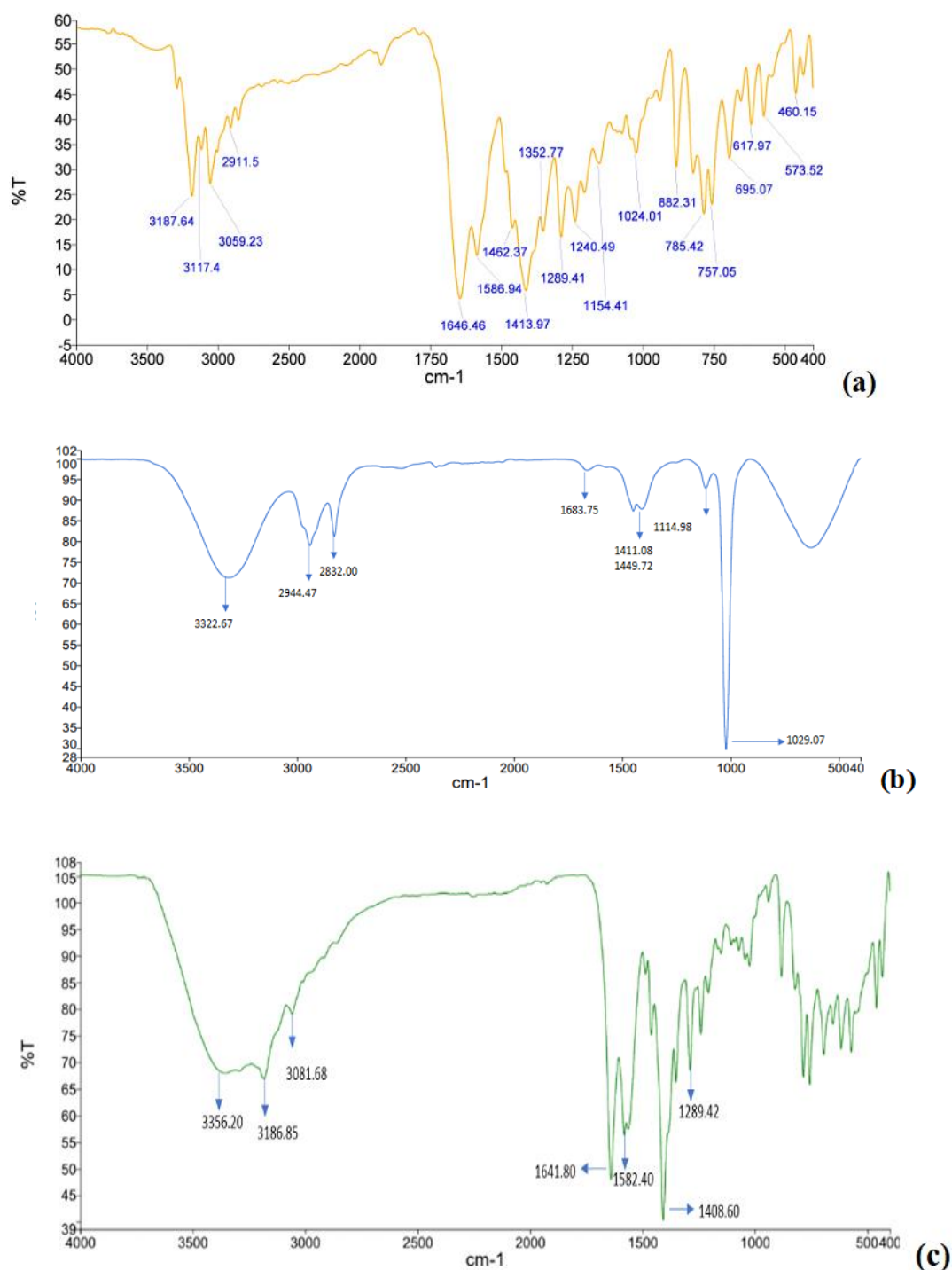
Figure 64: FTIR Spectra (a) Plain drug NVP (b) Dendrimers (c) NVP-DEN

The FTIR spectra of NVP, dendrimers, and NVP-DEN are represented in Figure 64. The FTIR spectrum of NVP revealed the presence of all the characteristic peaks of

157

the drug. The major peaks are observed at 3187.64 cm^{-1}, a broad peak corresponds to stretching N-H, the peak at 3059.23 cm^{-1} indicates stretching C-H at 1646.46 cm^{-1} indicates the C=O stretch, the peak at 1413.97 cm^{-1}, 1586.94 cm^{-1} corresponds to the aromatic carbons (C=C), the peak at 1289.41 cm^{-1} represents C-N stretching and the peak at 882.31 cm^{-1} and 757.05 cm^{-1} indicates C-H bending (Varshosaz et al., 2018).

The spectrum of dendrimers showed peaks such as a peak at 1021.07 cm^{-1} corresponds to stretching of C-N, a peak at 1114.98 cm^{-1} due to –C=C- bond, a peak at 1400.08 cm^{-1} and 1449.72 cm^{-1} are the twin peak corresponding to CH band, peak at 1663.75 cm^{-1} indicates deflection of N-H, peak at 2823.0 cm^{-1} corresponds to NH stretching, peak at 2944.47 cm^{-1} was due to an alkene, and at 3322.0 cm^{-1} was the peak for primary amine confirms the presence of amine present on the periphery of dendrimers.

In the FTIR spectrum of NVP-DEN, the peak of a primary amine present in the dendrimer was found to be altered with NVP-DEN. The peaks of NVP were observed with NVP-DEN at 3186.85 cm^{-1} corresponding to N-H, 3081.68 cm^{-1} peak corresponding to C-H, the peak at 1641.80 cm^{-1} was the peak of -C=O- (amide). Alteration confirms the conjugation of NVP with 5G PPI dendrimers. The other peaks such as peaks at 1408.69 cm^{-1}, 1582.40 cm^{-1} a peak of C=C, peak at 1289.42 cm^{-1} (-C-N) of NVP were also observed in the spectrum of NVP-DEN (Samsodien et al., 2017).

Table 23: FTIR spectrum of NVP-DEN

Observed peaks frequency (cm^{-1})	Standard FTIR range (cm^{-1})	Corresponding functional group
3186.85	3500-3100	A broad band of N-H stretching
3061.68	3150-3050	C-H aromatic stretching
1641.80	1630-1680	C=O (amide) group
1582.40	1475-1600	Cyclopropyl C=C
1408.69	1350-1000	Cyclopropyl C=C
1289.42	1350-1000	C-N stretching

5.7.1.2.2 NMR Spectroscopy

Nevi
CMC_SINGLE_H2O D2O {D:\Spectra} nmr 2

(a)

N-1

(b)

Nevi Den
CMC_SINGLE_H2O D2O {D:\Spectra} nmr 30
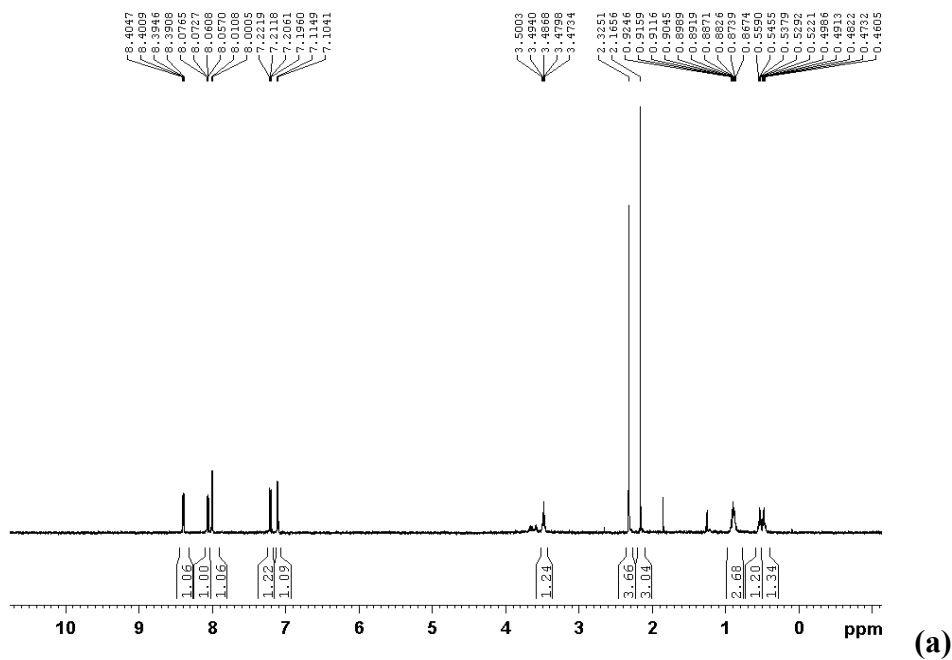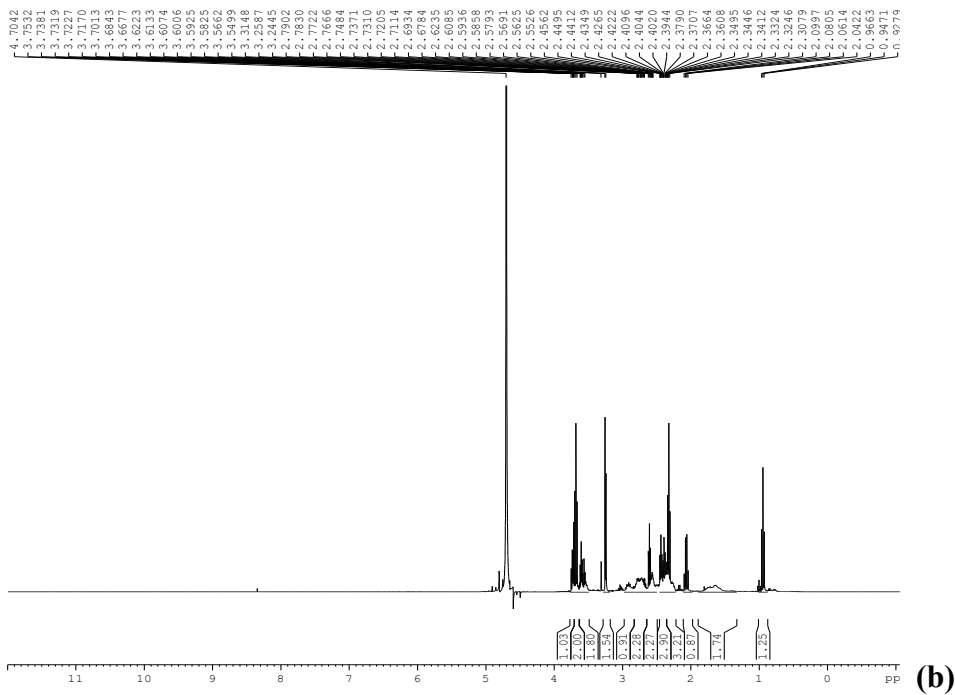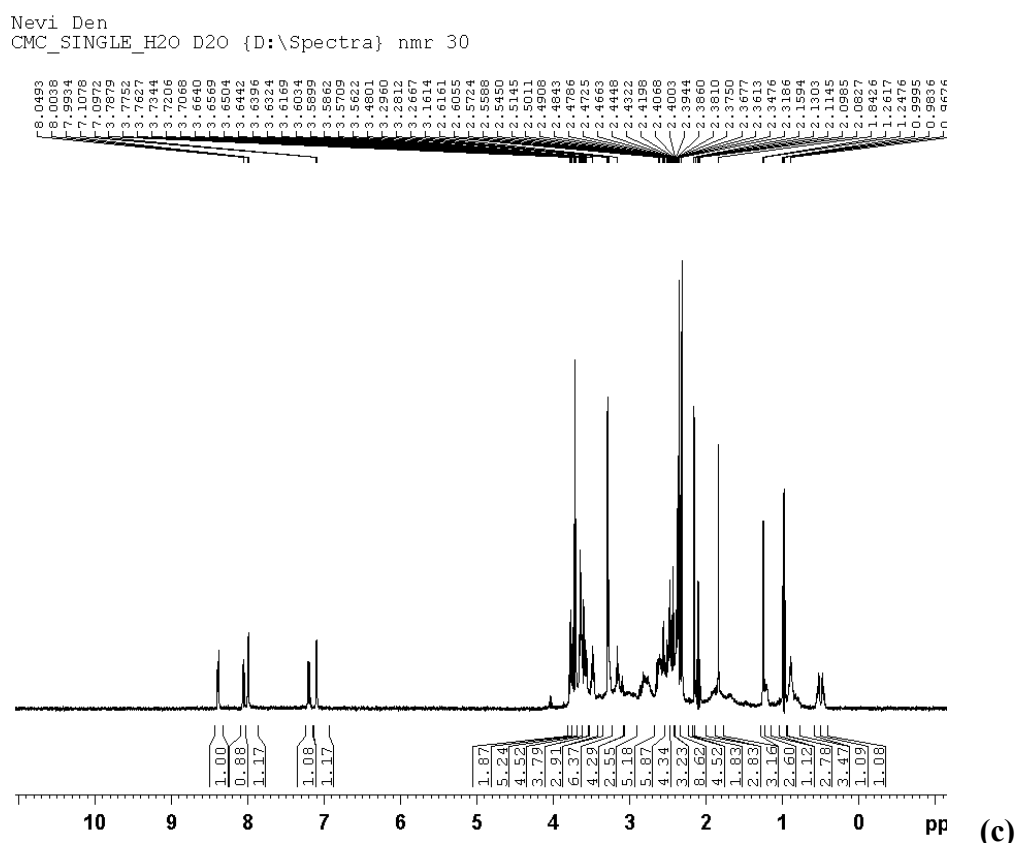
Figure 65: NMR Spcetra (a) Plain drug NVP (b) 5G PPI Dendrimers (c) NVP-DEN

The NMR spectra of NVP, dendrimers, and NVP-DEN are shown in Figure 65. Multiplets were observed between δ 0.50 and 1.30 ppm corresponding to -CH$_2$ of methylene groups of cyclopropane (H5, H6), the chemical shifts between δ 3.79 ppm correspond to the protons of cyclopropane (H8), the peak at δ 2.325 ppm corresponds to CH$_3$, peaks between δ 7.10-8.40 ppm corresponds to the protons associated with aromatic ring (H1, H2, H3, H4, H5). The single peak at δ 8.407 ppm corresponds to NH (da Silva et al., 2021; Silverstein et al., 1962).

The NMR spectrum of dendrimers confirms the presence of protons as per the literature. Multiplets were observed between δ 0.9 ppm corresponding to -CH$_2$ of methylene groups of EDA, the chemical shifts between δ 1.74 ppm corresponding to -CH2-CH2-, the peak at δ 2.34-2.36 ppm corresponds to -NH2, multiple peaks at δ 2.40–2.69 ppm due to N[C]C and multiplets between δ 2.71–2.79 ppm corresponds to -CH2-NH2 (Kumar et al., 2006; Gajbhiye et al., 2013).

160

The NMR spectrum of NVP-DEN revealed the presence of proton peaks between δ 7.09-8.04 ppm corresponding to the protons associated with the aromatic ring. The single peak at δ 8.049 ppm corresponds to NH, and the peaks between δ 0.0-1.0 ppm correspond to the proton of cyclopropane. The incorporation of many multiplets between δ 2.0-3.0 ppm indicated that interaction took place between the amino group (δ 2.7-2.9 ppm) present on the outer periphery of dendrimers and the methyl group (δ 2.39 ppm) of NVP. The 5G dendrimer's structure has an abundance of protons in its surroundings due to a heavily conjugated and complex structure that corresponds to various peaks and splitting patterns. Thus, the NMR spectrum confirms the interaction of the drug NVP with dendrimers (Srivastava et al., 2023).

5.7.1.2.3 Field emission scanning electron microscopy
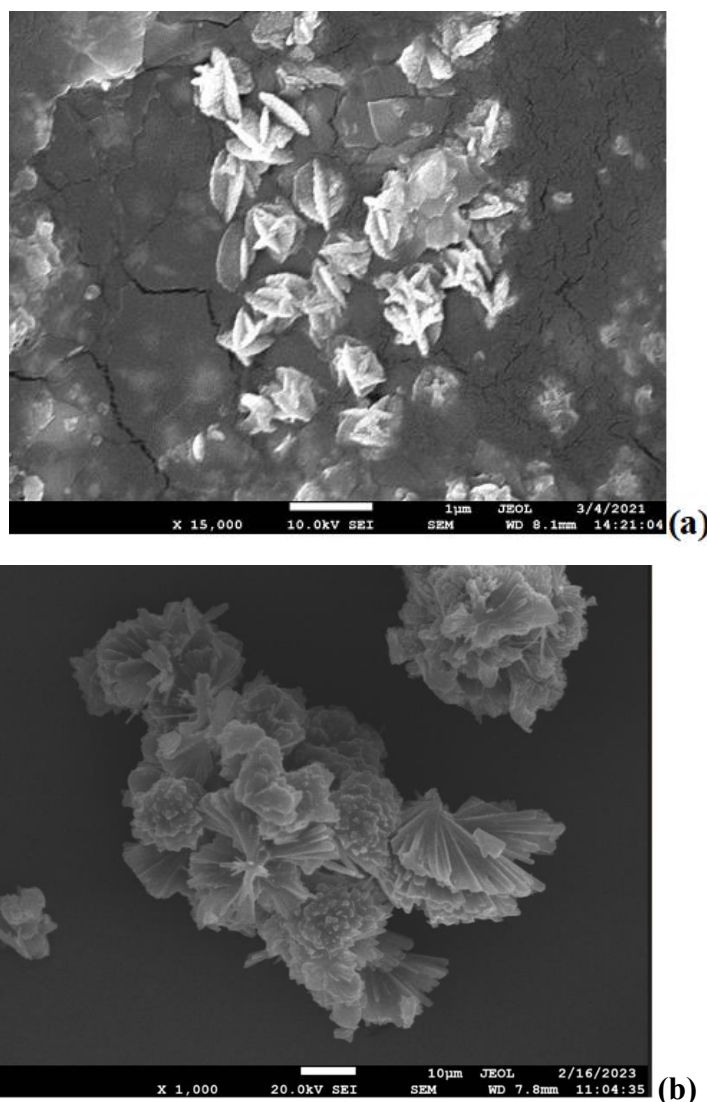
Figure 66: FE-SEM images of (a) Dendrimers (b) NVP-DEN

The NVP-DEN were subjected to morphological studies such as SEM to understand the external morphology and shape of the prepared conjugated structure. Figure 66 represents the FE-SEM image of dendrimers and NVP-DEN. The structure showed a smooth and nearly spherical shaped structure. The structure was further evaluated with atomic force microscopy for better imaging of the drug-loaded dendrimers.

5.7.1.2.4 Atomic force microscopy

AFM is a unique method of studying topographic images of high resolutions in the nanoscale range. Figure 67 represents the 2D and 3D AFM images of NVP-DEN. All the images were carried out using tapping mode. The samples are deposited on the mica surface in monolayer formation at a lower concentration. The spherical structure was observed on the mica surface. The images show individual particles and a few clusters were also observed. The carrier has a relatively rough surface due to the reaction of the drug NVP to the outer surface of the dendrimers (Jain et al., 2015; Haji et al., 2019).
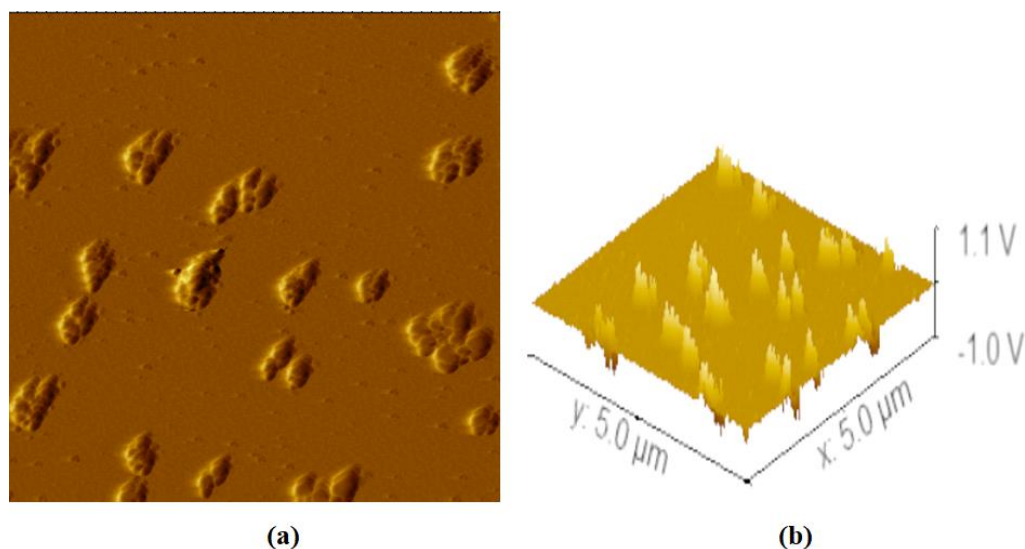
Figure 67: AFM images (a) 2D image of NVP-DEN (b) 3D image of NVP-DEN

5.7.1.2.5 Particle size distribution and zeta potential

The particle size of dendrimers and NVP-DEN were determined using Delsa nano (Beckman counter) and shown in Figure 68. The size of the particle of the dendrimers was found to be 41.9 nm and PDI was found to be 0.379. The size of the particle of drug-loaded dendrimers was found to be 281.5 nm and PDI was found to be 0.17. The result indicated that the prepared drug-loaded dendrimers were found to be

in the nano range and PDI revealed that the structure was distributed uniformly without aggregations.
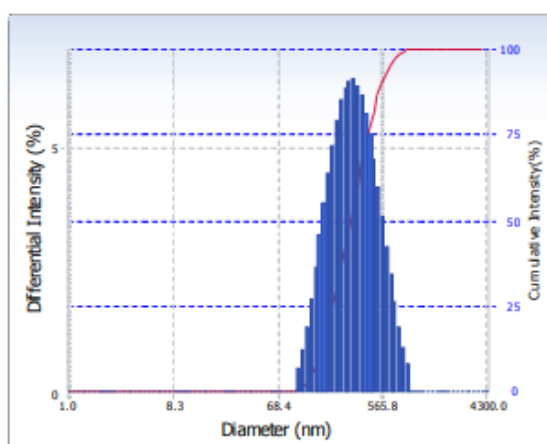
Figure 68: Particle size distribution of NVP-DEN

Table 24. Particle size, PDI and zeta potential of dendrimers and NVP-DEN

Formulations	Particle size (nm)	PDI	Zeta potential (mV)
5G PPI Dendrimer	41.9	0.379	+24.64
NVP-DEN	281.5	0.17	-7.13

The zeta potential of 5G PPI dendrimer was found to be +24.64 due presence of 5G PPI dendrimers. The zeta potential of NVP-DEN was found to be -7.13, the negative shift in zeta potential was due to the conjugation of NVP on the surface amino group reducing free amino groups.

5.7.1.2.6 Drug entrapment

The drug entrapment efficiency was studied by an indirect method using a dialysis membrane (MWCO 7000 Da, Himedia, India). % drug entrapment was found to be $72.05 \pm 0.53\%$. The drug loading was based on a number of surface amino groups. The drug loading was found to be less may be due to steric hindrances due to the 5G structure of the dendrimers. As the generation increases in dendrimers complexity of the structure also increases. Along with covalent bonding other physical interactions such as hydrophobic interaction and hydrogen bonding also govern in drug entrapment (Singh et al., 2021).

5.7.1.2.7 *In vitro* **drug release**

     In vitro release studies of NVP-DEN were determined in PBS media pH 7.4 and acetate buffer media pH 5. Figure 69 represents the *in vitro* release studies of NEV-DEN in acetate buffer pH 5 and PBS pH 7.4. The drug release was found to be 77.89 ± 2.11% in PBS pH 7.4 and the release was found to be 84.12 ± 1.63 % in acetate buffer pH 5. The higher drug release was observed in pH 5 owing to the high solubility of NVP at low pH. The drug tends to be released in a sustained manner because entrapment takes place in hydrophobic cavities of dendrimers. Also, the 5G structure of dendrimers tends to possess steric hindrance, owing to the surface conjugation of primary amines (Patel et al., 2016). At lower pH, due to the surface amine group, the structure of dendrimers also develops a positive charge. NVP also tends to develop a positive charge which develops electrostatic repulsive force, which also promotes the drug release from dendrimer structures (Garkal et al., 2022). The microenvironment in the macrophages has pH 5, thus the higher dissolution favors that the drug gets better dissolved in macrophages.

Table 25: Drug release Profile of NVP from NVP-DEN

Time (h)	% Cumulative drug release	
	Acetate buffer pH 5	**PBS pH 7.4**
0	0±0	0±0
1	3.65±0.07	5.16±2.76
2	16.68±3.32	16.17±2.29
3	32.27±2.272	27.33±3.77
4	37.13±1.85	36.12±0.79
5	42.86±2.07	39.77±1.30
6	45.48±0.90	43.73±1.22
7	51.70±2.19	47.57±2.27
8	55.10±2.93	50.33±2.61
24	73.11±2.14	67.56±1.64
30	74.78±2.49	69.54±1.59
48	77.88±2.86	74.88±2.33
72	79.84±2.60	76.88±2.25
96	84.12±1.63	77.89±2.11

*The data was represented as Mean±SD (n=3)
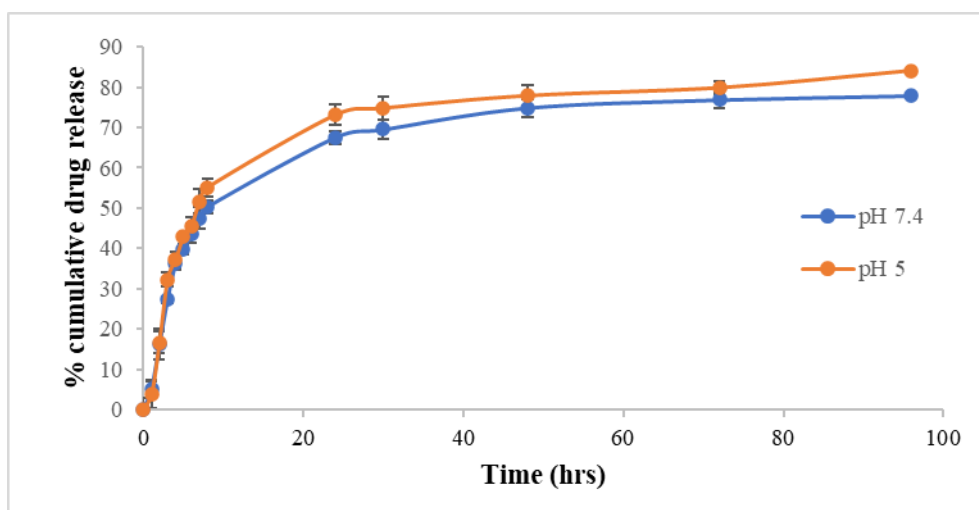
Figure 69: Drug release profile of NVP-DEN for 96 h (n=3)
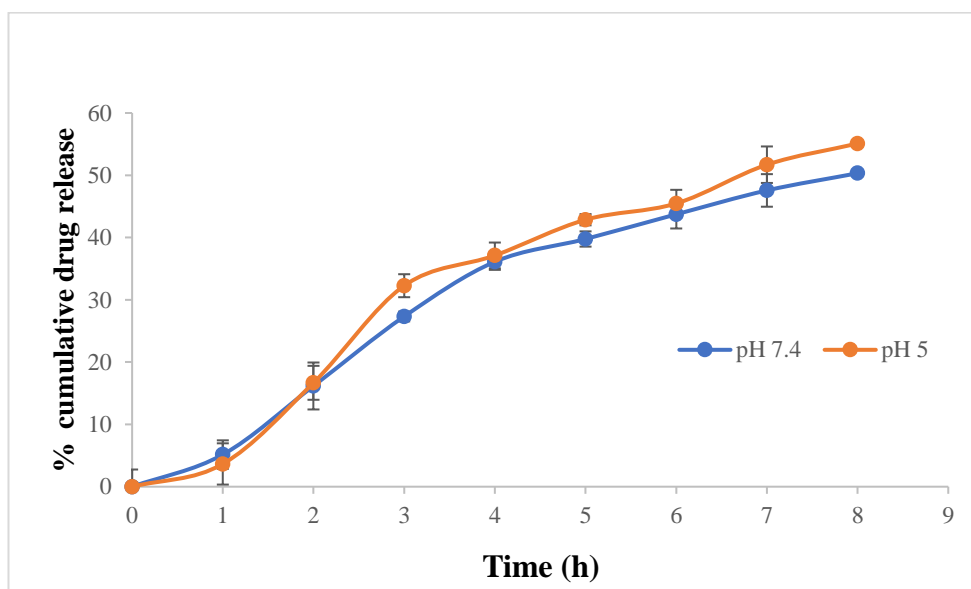
Figure 70: Drug release profile of NVP-DEN for 8 h (n=3)

5.6.1.2.8 Drug release kinetics

Table 26: Drug release kinetics of NVP from NVP-DEN representing regression coefficient and n value

Sr. No.	Release	pH 5		pH 7.4	
		R^2	n	R^2	n
1	First-order.	0.7904	-	0.8076	-
2	Zero-order	0.5856		0.5911	
3	Korsmeyer-Peppas	0.6363	0.6873	0.6398	0.6555
4	Higuchi	0.9103		0.9187	
5	Hixon	0.7374		0.7627	

Various release kinetic models were used for the drug release profile such as the Hixon Crowell model, the Korsmeyer-Peppas model, the Higuchi model, and first, and zero-order release kinetics. The profiles of release patterns at pH 5 and pH 7.4 were subjected to the release kinetics model. Among the different models, the best-suited model was the Higuchi model. The most fitted model was selected based on the R^2 value, the R^2 for release profile pH 5 was found to be 0.9103 and for pH 7.4 was found to be 0.9187. The Higuchi model helps to understand the drug release from an insoluble matrix, wherein the factors affecting the release of drug from dendrimers were owing to the higher solubility of NVP in the release medium. The pattern of release showed a faster release in the initial time point followed by a decrease in release with time. In this system concentration of the drug was much higher than it releases and acts as a driving force. As time proceeds concentration gradient changes reducing the diffusion subsequently reducing the drug release (Golshan et al., 2017).

The n component from the Korysmeyer-Peppas equation helps to study the release of drug mechanism from the drug carrier system. Fickian diffusion was expected to occur if the value of n was less than 0.5; a non-Fickian mechanism was used if the value was between 0.5 and 1. A super case II model is present if n > 1 and if n is 1, in this case, the release occurs by swelling and diffusion and falls under non-fickian diffusion (Case II). For pH 5, the value of exponential n was determined to be 0.6873, and for pH 7.4, 0.6555. The value indicates that the non-fickian diffusion model governed the release. (Hooshyar et al., 2019).

The drug release was subjected to other release models, lowest R^2 value was found to be for the first order. The value for the first order was found to be 0.7904 for pH 5 and 0.8076 for pH 7.4, a lower value of R^2 makes it unsuitable. The zero-order model was not fitting as the correlation coefficient value was 0.5856 for pH 5 and 0.5911 for pH 7.4. The Korsmeyer-Peppas model also showed a lesser R^2 value of around 0.6363 for pH 5 and 0.6398 for pH 7.4. The Hixon-Crowell model was also found unsuitable as the value of R^2 was found to be 0.7374 for pH 5 and 0.7627 for pH 7.4.

Thus, the most fitted model was the Higuchi model for the release mechanism.
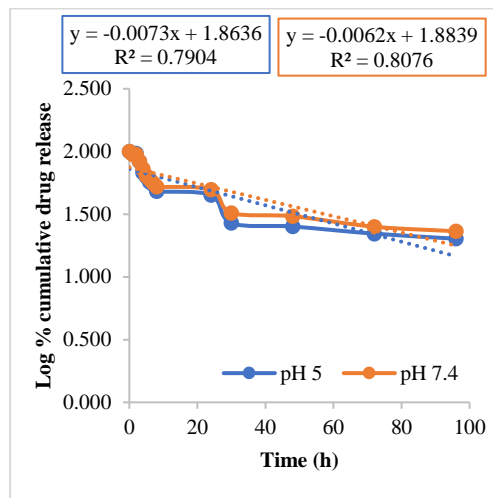
(a) First order release kinetics
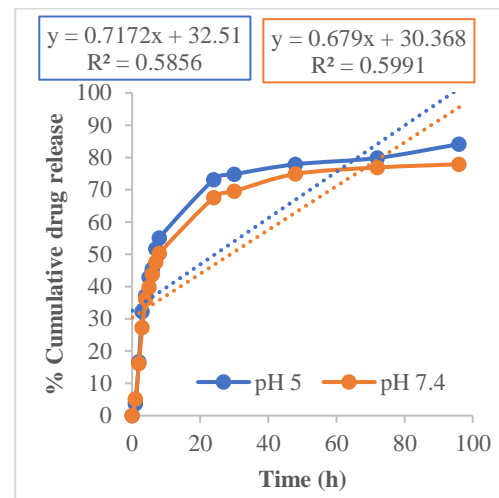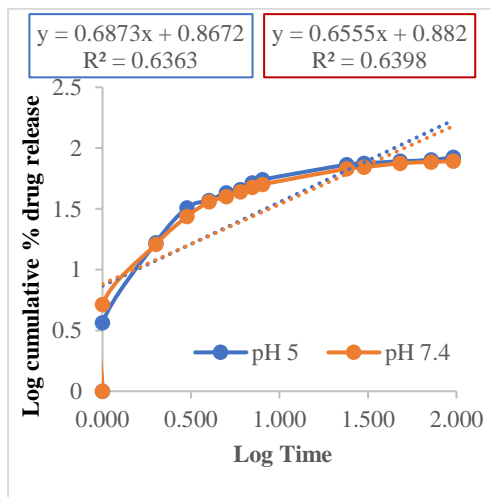
(b) Zero order release kinetics

(c) Korsmeyer Peppas release kinetics
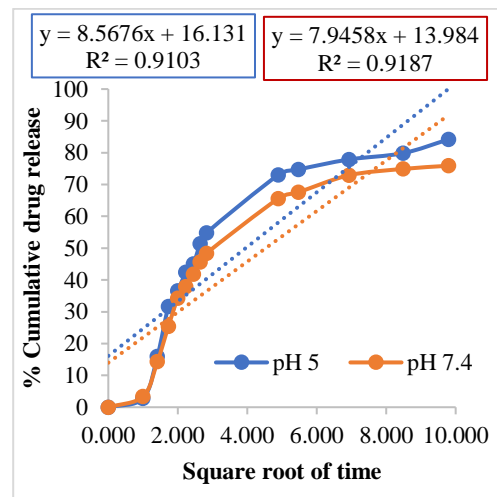
(d) Higuchi release kinetics
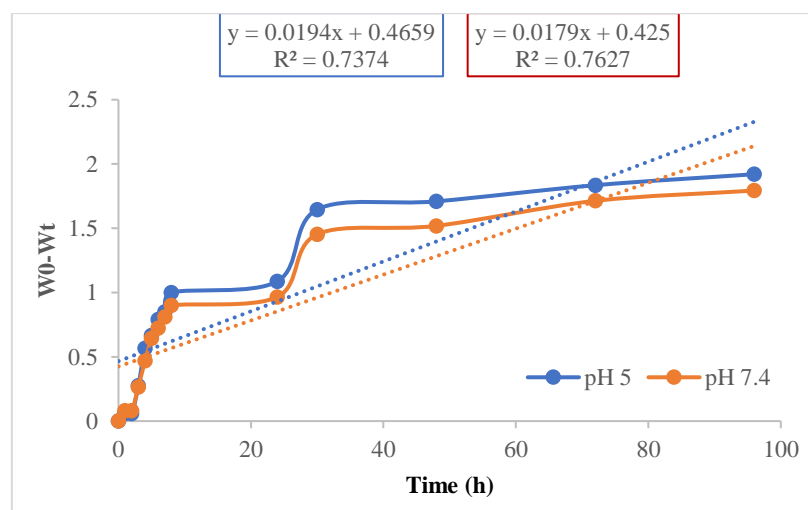
(e) Hixon-Crowell release kinetics

Figure 71. Kinetics of drug release of NVP-DEN at pH 5 and pH 7.4

5.7.2 Formulation development and characterization of Nevirapine-loaded COOH-MWCNT

5.7.2.1 Formulation development of Nevirapine-loaded COOH-MWCNT

The drug NVP was loaded on the COOH-MWCNT (NVP-CNT) with constant stirring for 48 h using a magnetic stirrer. The drug binds with the surface COOH group of the MWCNT by covalent linkage and by π- π stacking on the surface of COOH-MWCNT. The structure was characterized using different characterization techniques such as spectroscopic analysis, morphological studies, and *in-vitro* drug release studies.

5.7.2.2 Characterization of NVP-CNT

5.7.2.2.1 FTIR Spectroscopy

(a)

(b)
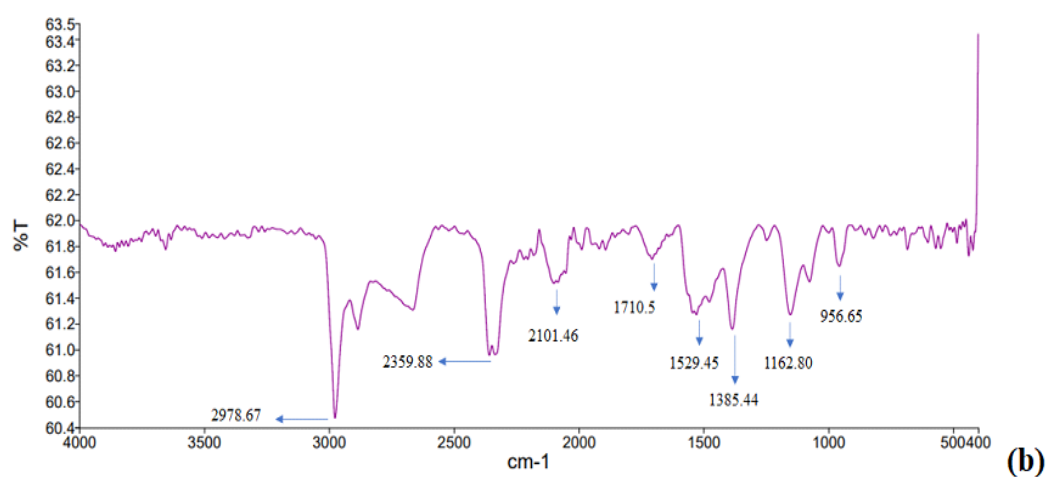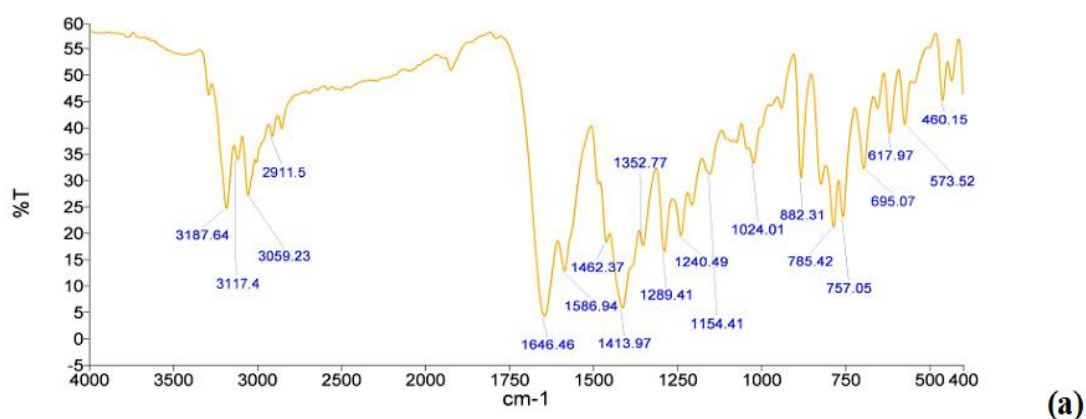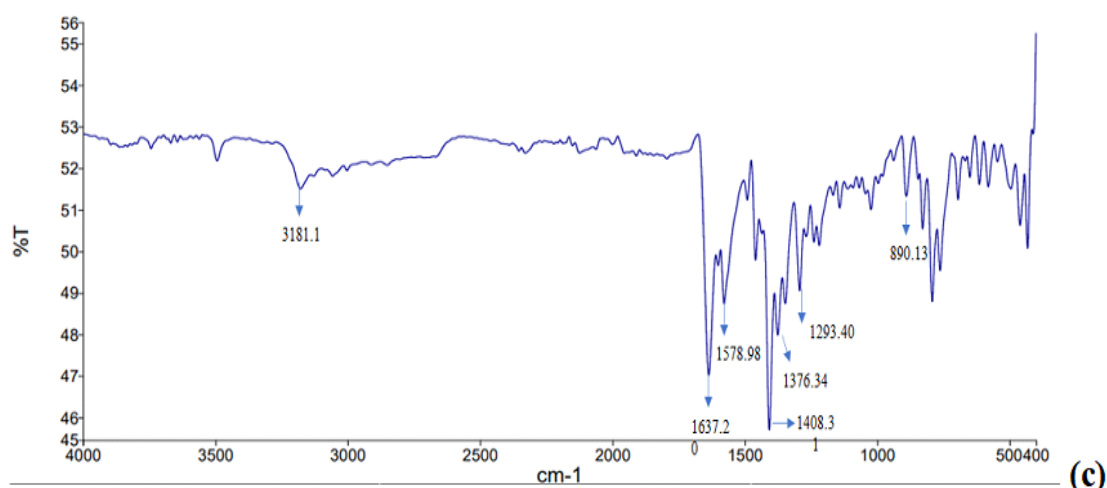
Figure 72: FTIR spectra of (a) Plain drug NVP (b) COOH- MWCNT (c) NVP-CNT

The FTIR spectra of drugs NVP, COOH-MWCNT, and NVP-CNT were determined and shown in Figure 72. The FTIR spectrum of NVP revealed the presence of all the characteristic peaks of the drug. The major peaks are observed at 3187.64 cm^{-1}, a broad peak corresponds to stretching of N-H, the peak at 3059.23 cm^{-1} indicates stretching of C-H, at 1646.46 cm^{-1} indicates the -C=O stretch, the peak at 1413.97 cm^{-1}, 1586.94 cm^{-1} corresponds to the aromatic carbons (C=C), the peak at 1289.41 cm^{-1} represents C-N stretching and a peak at 882 cm^{-1} and 757 cm^{-1} indicates C-H bending (Varshosaz et al., 2018).

FTIR of COOH-MWCNT showed peaks at 1710.5 cm^{-1} which is the peak of carboxylic acid of COOH-MWCNT; other peaks present at 1152.80 cm^{-1} and 1385.44 cm^{-1} are the peaks of C-O stretching and OH bending. The peaks at 956.65 cm^{-1} and 2978.67 cm^{-1} indicate the carbon structure of alkenes (Zhang et al., 2018).

FTIR peaks of NVP-CNT confirm the incorporation of the drug NVP in COOH-MWCNT. The results were correlated with the IR spectra of COOH-MWCNT and NVP. IR peaks show all the prominent peaks of NVP. The peak at 3181.10 cm^{-1} corresponds to the stretching of NH of NVP. The characteristic peak of NVP, -C=C- of cyclic alkene was observed at 1637.20 cm^{-1}, N-H deflection of amine at 1578.98 cm^{-1}, -OH bend at 1408.31 cm^{-1}, C-H bend at 1376.34 cm^{-1}, 1293.40 cm^{-1} relates to the C-N stretching, C-C bend of aromatic alkene corresponds to 890.13 cm^{-1}. The binding of NVP with COOH-MWCNT takes place by forming a covalent bond between the CH$_3$

of NVP and the surface COOH of COOH-MWCNT. The bonding was further confirmed with the disappearance of the peak of CH_3 at 3059.23 cm^{-1} and the carboxylic peak of MWCNT at 1710.5 cm^{-1} in the FTIR of NVP-CNT. This confirms the attachment of the surface COOH group with NVP. All peaks of NVP, COOH-MWCNT, and NVP-CNT are tabulated in Table 27. (Samsodien et al., 2017; Varshosaz et al., 2018; Nalte et al., 2015).

Table 27: FTIR spectrum of NVP-CNT

Observed peaks frequency (cm^{-1})	Standard FTIR range (cm^{-1})	Corresponding functional group
3181.1	3500-3100	Peak of N-H stretching
1637.2	1630-1680	C=O carbonyl stretching
1578.98	1475-1600	Cyclopropyl C=C
1376.34	1365-1390	C-H bending
1293.40	1350-1000	C-N stretching
890.13	900-690	-C-H bend of aromatic alkene

5.7.2.2.2 Raman Spectroscopy

(a)

170

Model : RFS 27

S A I F, I I T M
CHENNAI

(b)
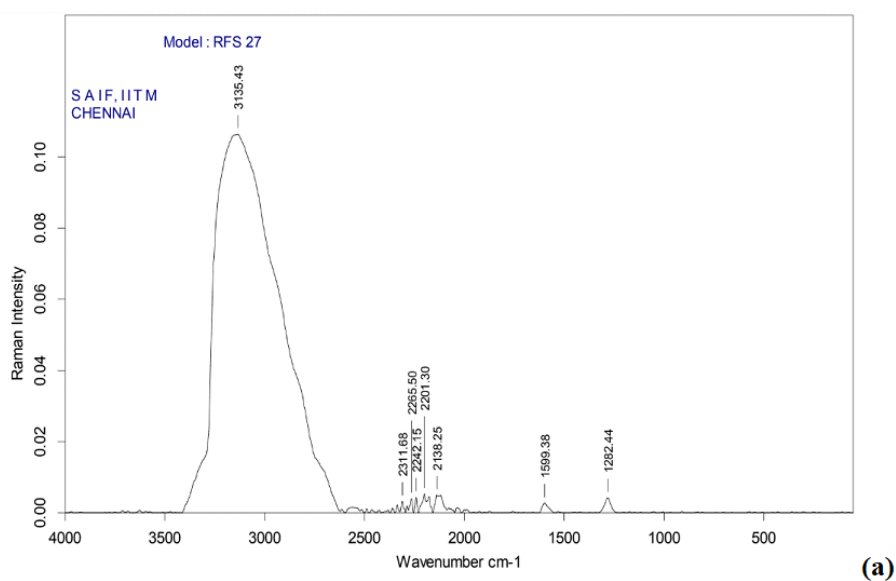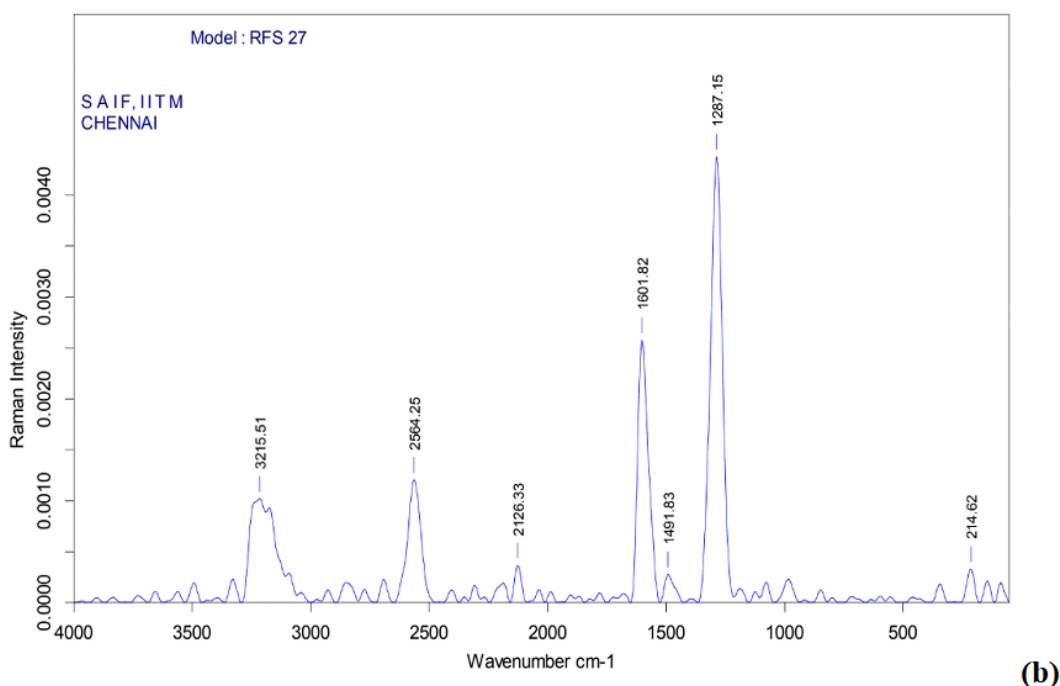
Figure 73: Raman spectra of (a) MWCNT-COOH (b) NVP-CNT

Raman Spectroscopy helps to identify the allotropic form of different carbons and helps to study their defects. Raman spectroscopy works in the range of 0-4000 cm^{-1} for NVP, COOH-MWCNT, and NVP-CNT formulation and the spectra are shown in Figure 73. Raman spectra of COOH-MWCNT show characteristics peak at 1282.44 cm^{-1} (D band peak) and 1599.38 cm^{-1} (G band peak). G band peak is associated with the vibration of the sp2 carbon atom in the 2-dimensional structure of carbon nanotubes. The D bands are related to the defects of sp2-bonded carbon atoms. When MWCNT is functionalized or loaded with a drug the surface defects of the MWCNT tend to increase which will increase the value of the D band. In COOH-MWCNT loaded NVP spectrum. The value of the D bands slightly increases to 1287.15 cm^{-1} and the value of the G band was found at 1601.59 cm^{-1}. The alteration of a peak at 3215.51 cm^{-1} indicates the incorporation of NVP in the COOH-MWCNT structure (Sathisran et al., 2021; Piao et al., 2021).

The I_D/I_G ratio of MWCNT was found to be 1.538 and the I_D/I_G ratio of NVP-CNT was found to be 1.793. The increment in I_D/I_G ratio of NVP-CNT indicated that the conjugation of NVP took place on the CNT surface which alters the sp^2 bonding structure of MWCNTs and leads to the breaking of π bonds holding the hexagonal carbon structure.

171

5.7.2.2.3 Nuclear Magnetic Resonance

Nevi
CMC_SINGLE_H2O D2O {D:\Spectra} nmr 2

(a)

N2
CMC_SINGLE_H2O D2O {D:\Spectra} nmr 1

(b)

(c)
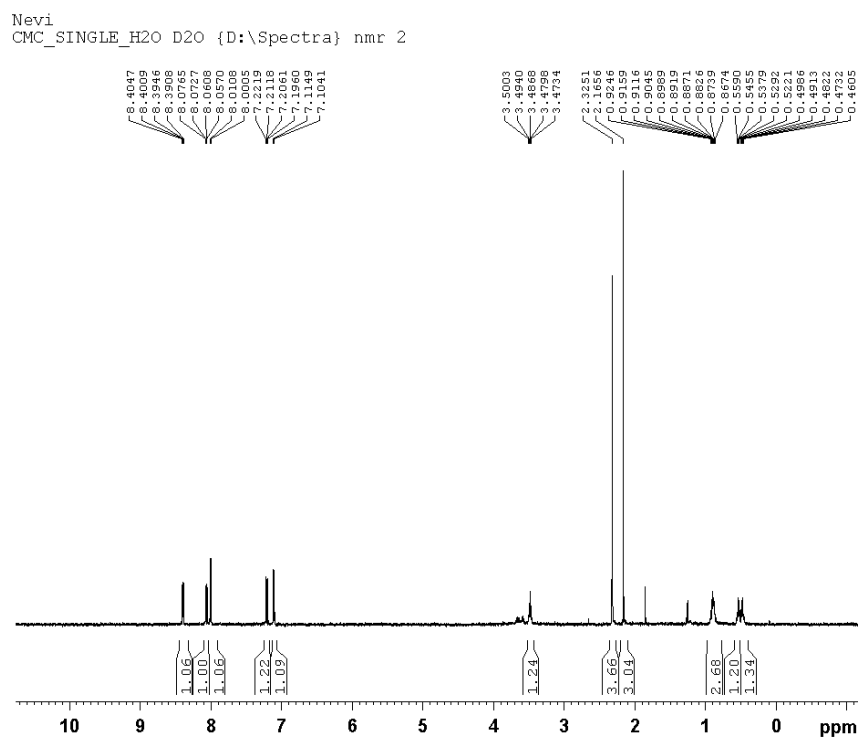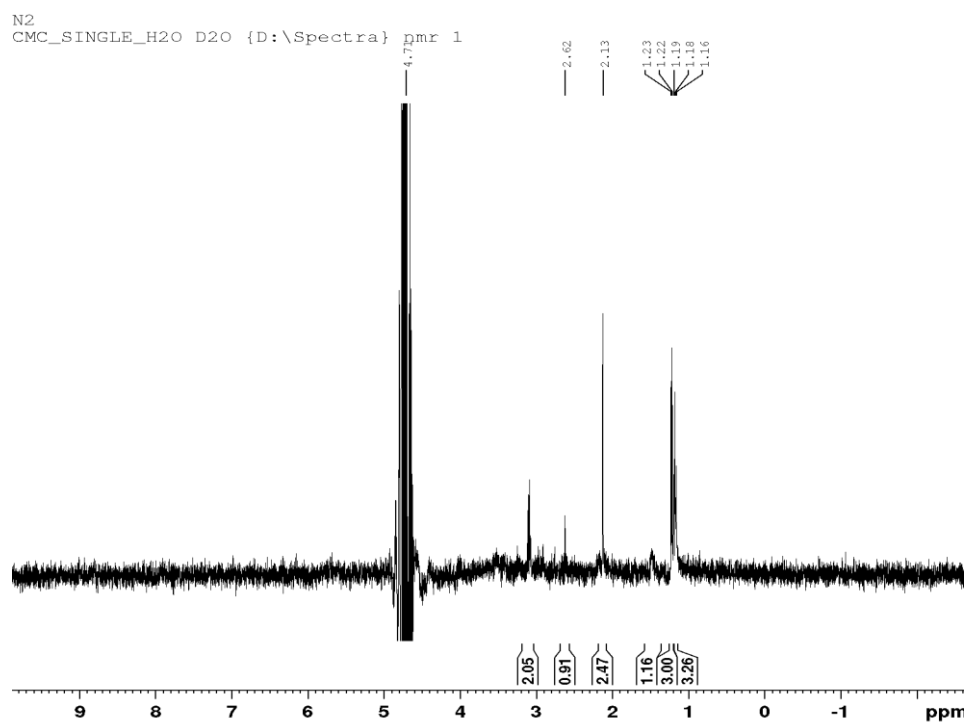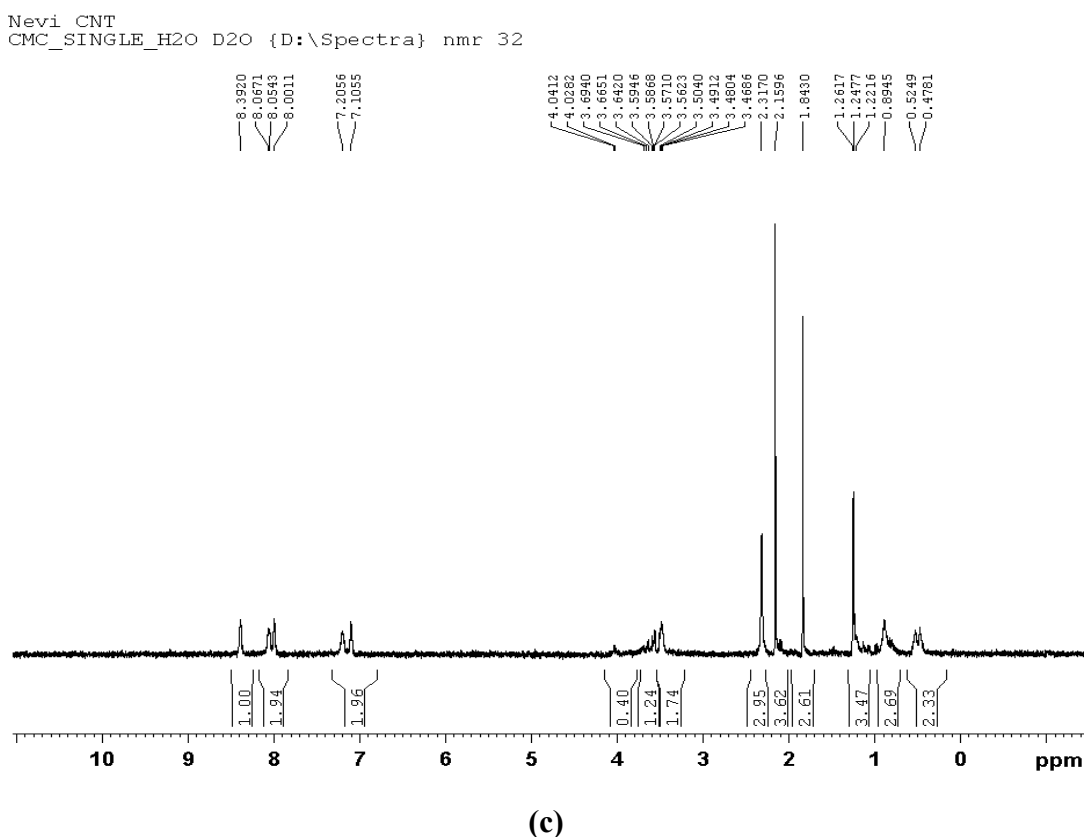
Figure 74: NMR spectra of (a) Plain drug NVP (b) COOH-MWCNT

(c) NVP-CNT

The NMR spectra of NVP, COOH-MWCNT, and NVP-CNT are shown in Figure 74. The NMR of NVP revealed that the multiplets were observed between δ 0.5 and 1.3 ppm corresponding to methylene groups -CH_2 of cyclopropane (H5, H6), the chemical shifts between δ 3.79 ppm correspond to the protons of cyclopropane (H8), the peak at δ 2.325 ppm corresponds to CH_3, peaks between δ 7.10-8.40 ppm corresponds to the protons associated with aromatic ring (H1, H2, H3, H4, H5). The single peak at δ 8.407 ppm corresponds to NH (da Silva et al., 2021; Silverstein et al., 1962).

^{1}H NMR studies were performed to determine the proton of carboxylic acid made on the surface of MWCNT. ^{1}H NMR analysis of MWCNT showed the presence of protons in δ 1.16 to1.23 ppm which was related to the C-H in the MWCNT. In the spectra of MWCNT, the singlet peak between δ 2.0 to 2.2 ppm indicated the presence of –CH_2COOH. The peak at δ 3.0-3.2 ppm was the characteristic peak that indicates the presence of a proton of –CH_2OH (Singhai et al., 2020).

173

The NMR spectroscopy results confirmed the attachment of the drug NVP with COOH-MWCNT. The chemical shift from δ 7.105-8.471 ppm corresponds to the aromatic proton (H1-H5) of the drug NVP. The singlet peak at δ 8.3920 ppm corresponds to the NH proton, and the multiplex between δ 3.0-4.0 ppm corresponds to the -COO-CH- linking of NVP and COOH-MWCNT, similar peaks were absent in NMR spectra of MWCNT. The peak at δ 2.3251 ppm corresponds to CH_3 in NVP having higher intensity as compared to the δ 2.3170 ppm peak of NVP-CNT. The peak δ 1.2 ppm corresponds to the alkyl group of MWCNT and δ 2.13 ppm corresponds to the R-OH group. These peaks are present in the NMR chemical shift (Mallakpour et al., 2017; Singh et al., 2016).

5.7.2.2.4 X-Ray Diffraction

X-ray diffraction was used to study to evaluate the crystallinity of the drug after its incorporation into the COOH-MWCNT. The XRD studies were performed for the drug NVP and drug-loaded COOH-MWCNT, as shown in Figure 75. XRD of COOH-MWCNT revealed a sharp peak at $25.917^{°}$ and a small broader peak between $40\text{-}60^{°}$. This indicates the semi-crystalline structure of COOH-MWCNT. XRD spectrum of NVP-CNT has many peaks as compared to pure COOH-MWCNT. This approves the attachment of NVP on the outer surface of the COOH-MWCNT. Analyzing the data of NVP indicates the sharp peaks between 10-23° indicated that the NVP did not alter its crystalline nature after incorporation in MWCNT. The powder sample gives sharp peaks in the diffraction pattern and the scattering angle was observed at 13.915° and 25.455°. Thus, from the XRD of drug-loaded CNT, it can be confirmed that the drug NVP has been inserted into the structure of MWCNT (Monteiro et al., 2016).
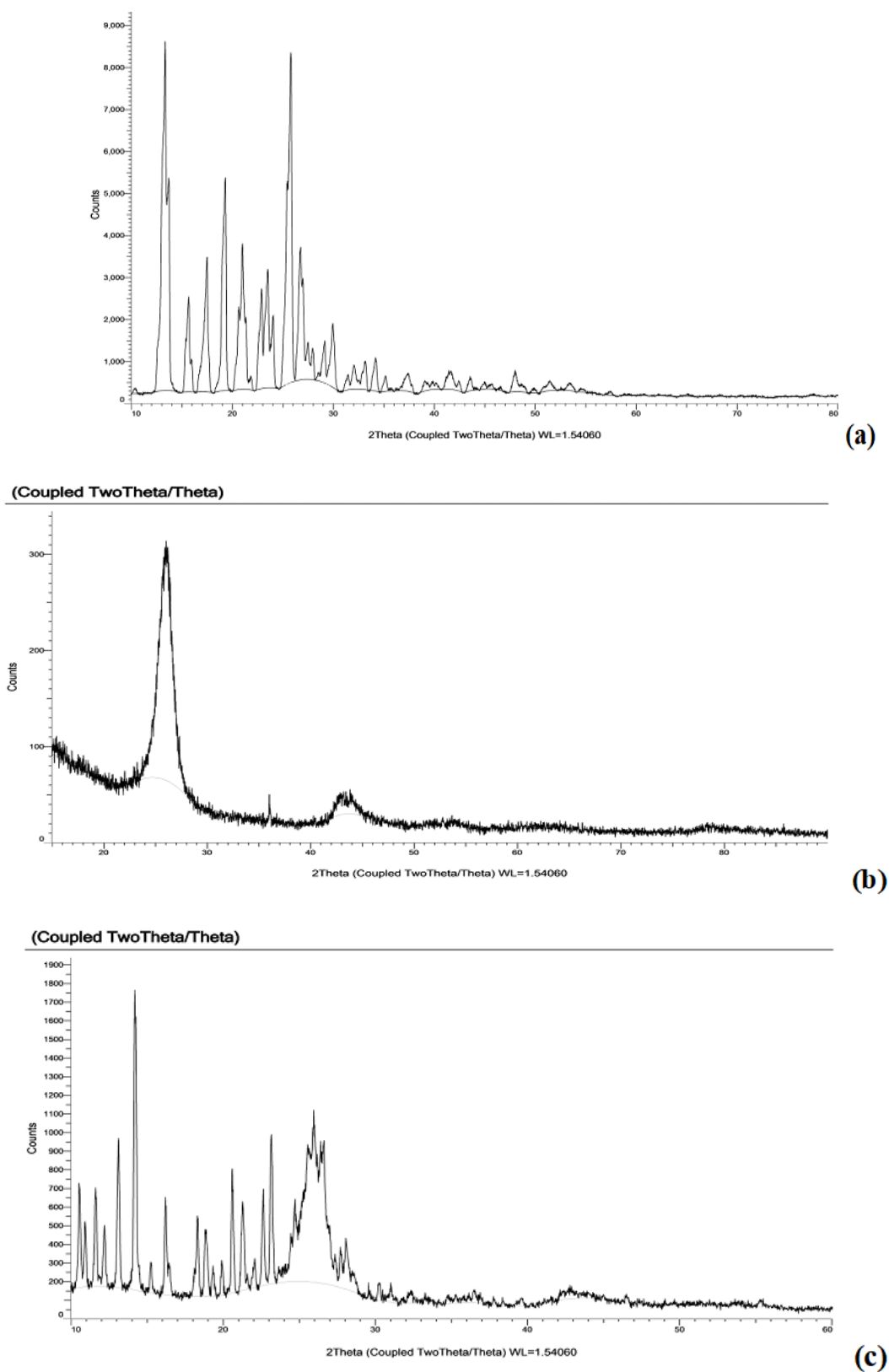
Figure 75: XRD of (a)NVP (b) MWCNT-COOH (c) NVP-CNT

5.7.2.2.5 Differential Scanning calorimetry

| (a) | (b) | (c) |
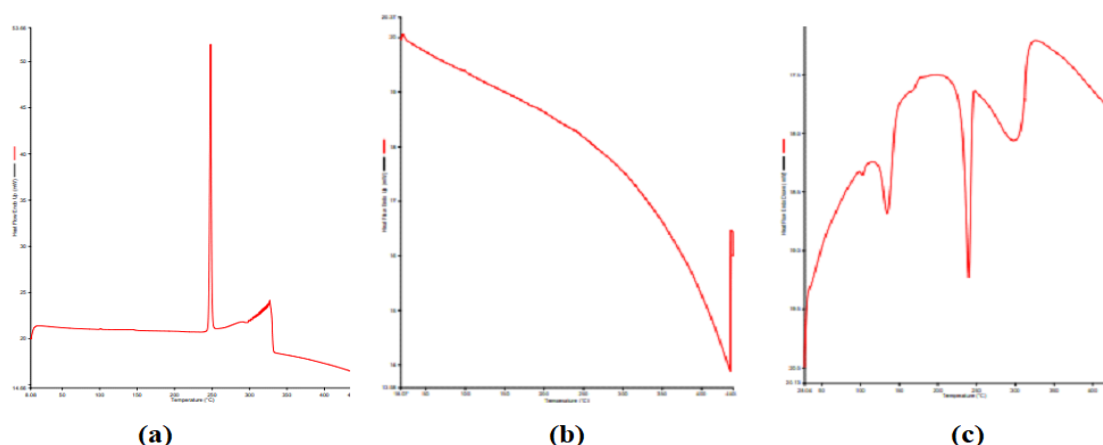
Figure 76: DSC thermogram of (a) Plain drug NVP (b) MWCNT-COOH (c) NVP-CNT

The DSC thermograms of NVP, COOH-MWCNT, and NVP-CNT are represented in Figure 76. Differential scanning calorimetry indicated the presence of sharp melting peaks at 248 ºC which confirms the purity of the drug. The literature revealed the sharp endothermic peak representative of the melting point of the drug NVP at 247 ºC. The DSC of NVP-CNT was performed to evaluate the thermal conduct of the drug after conjugation. The sharp endothermic peak was observed at 239 ºC indicating the conjugation between the drug and MWCNT which leads to the sifting of the peak from 248 ºC to 239 ºC. (Neto et al., 2021; Guo et al., 2018).

5.7.2.2.6 Field emission scanning electron microscopy

The FE-SEM image indicates surface topography did not change when the drug was loaded in the MWCNT structure. The FE-SEM images of MWCNTs revealed the open tube-like nature of MWCNT and there was no observed breakage in the structure of CNT in the plain COOH-MWCNT and NVP-CNT (Zhu et al., 2019). Figure 77 represents the FE-SEM images of COOH-MWCNT and NVP-CNT. The image indicated that no structural changes or defects were observed in the structure of COOH-MWCNT on the attachment of NVP on the surface of COOH-MWCNT.
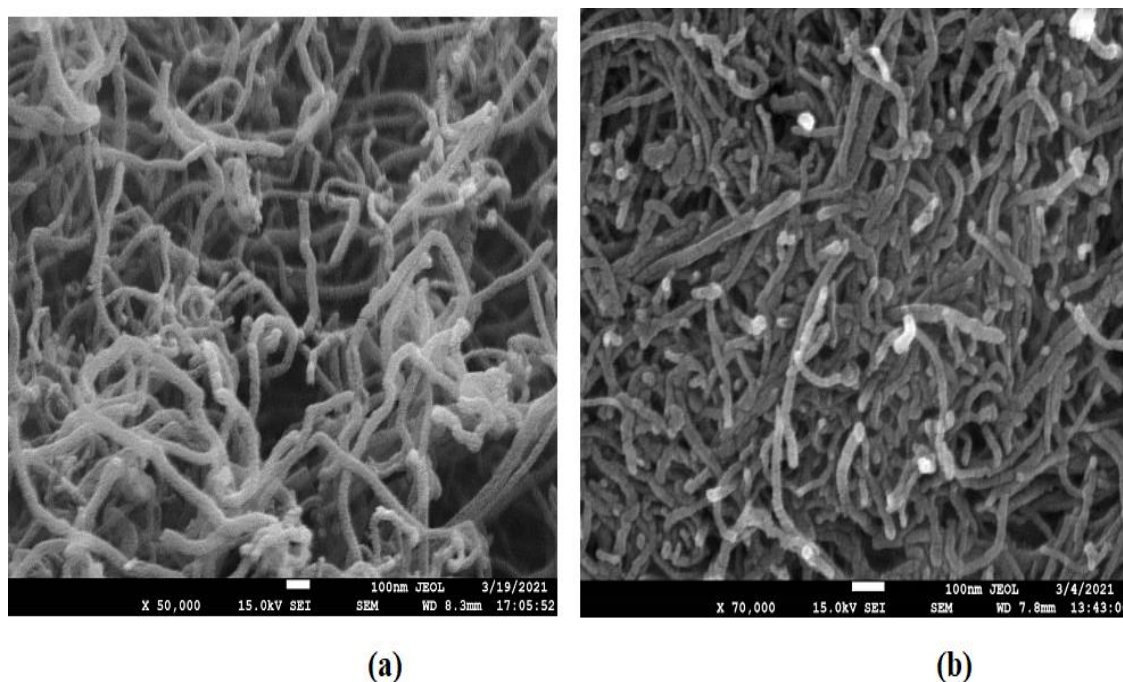
Figure 77: FE-SEM images of (a) MWCNT-COOH (b) NVP-CNT

5.7.2.2.7 Particle size and zeta potential

The particle size and zeta potential of MWCNT-COOH and NVP-CNT were performed with a Delsa nanoparticle sizer. The particle size, polydispersity index, and zeta potential are tabulated in Table 28 and the particle size distribution of NVP-CNT is shown in Figure 78.
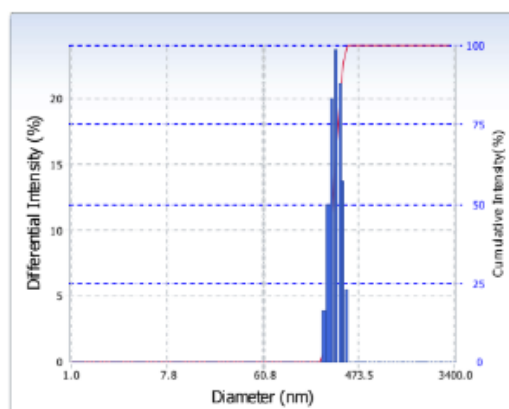
Fig 78: Particle size analysis of NVP-CNT

The particle size of MWCNT was found to be 166.9 nm which on conjugation increases to 247.2 nm. The PDI was found to be 0.566 which reduces to 0.102 indicating that the MWCNT shows a higher aggregation of the nanostructure may be due to entanglement which reduces due to conjugation with the drug. The zeta potential was

177

found to be -10.0 mV which reduces to -7.64 mV. This may be due to the conjugation of NVP with MWCNT-COOH, reducing the surface COOH group (Modi et al., 2011; Dong et al., 2017).

Table 28: Particle size and zeta potential of MWCNT-COOH and NVP-CNT

Formulation	Particle size (nm)	PDI	Zeta potential (mV)
MWCNT-COOH	166.9	0.566	-10.0
NVP-CNT	247.2	0.102	-7.64

5.7.2.2.8 Dispersibility Test

10 mg of COOH-MWCNT and NVP-CNT were dispersed in 5 mL of distilled water. The system was sonicated for 5 mins. Upon sonication, the system was kept aside for observation for 24 hours. Both COOH-MWCNT and NVP-CNT tend to form stable dispersion in deionized water (Zawani et al., 2016). The dispersibility images of COOH-MWCNT and NVP-CNT are shown in Figure 79.
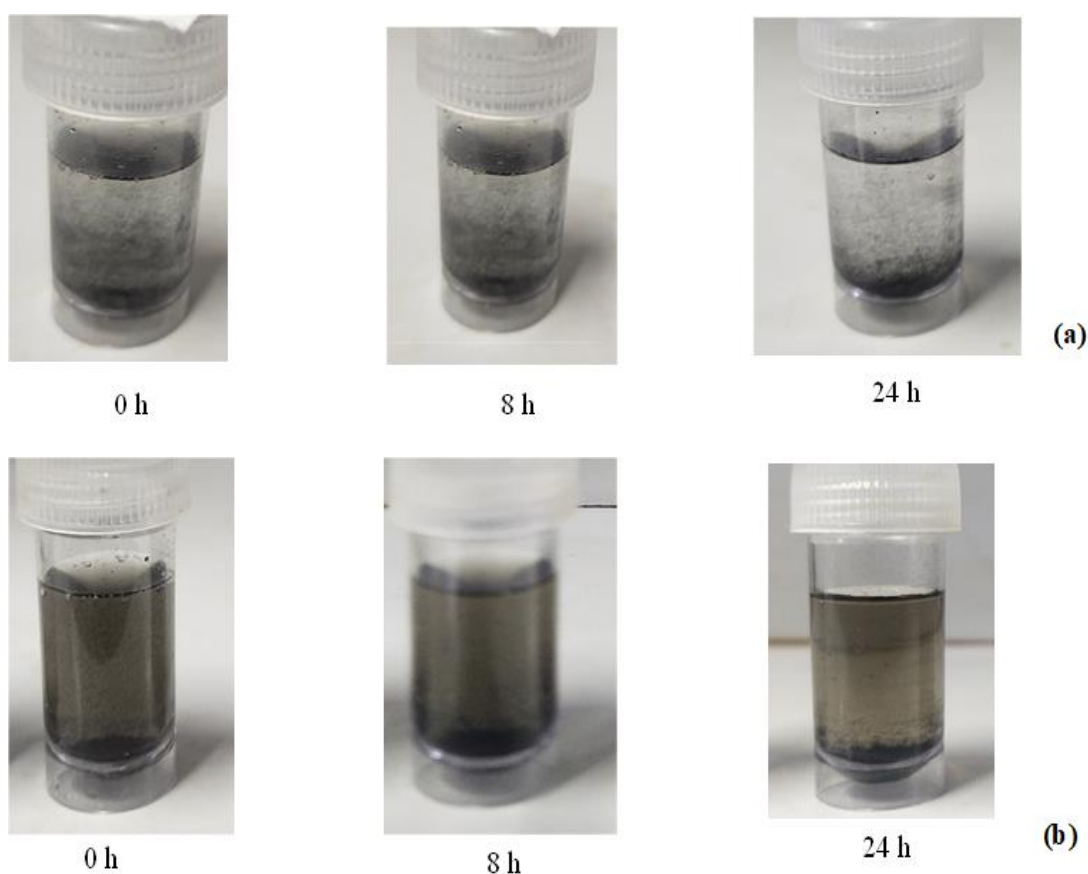
Figure 79: Dispersibility test (a) MWCNT-COOH (b) NVP-CNT at 0 h, 8 h, and 24 h

5.7.2.2.9 Drug entrapment

The drug NVP was entrapped inside the COOH-MWCNT by an indirect method using a dialysis membrane (MWCO, 7000 Da, Himedia, India). The procedure estimated the quantity of unentrapped drug and from that, the quantity of the entrapped drug was calculated. The entrapment efficiency of COOH-MWCNT was found to be $87.98 \pm 0.93\%$. The entrapment was affected by bundling or aggregation of MWCNT. The higher loading of the drug was due to the surface conjugation of 5G PPI dendrimers on COOH-MWCNT. The drug binds to the side wall of MWCNT by π-π stacking and electrostatic interactions (Tripathi et al., 2020).

5.7.2.2.10 *In vitro* drug release

NVP-CNT was subjected to release studies at two different pH, at acetate buffer pH 5 corresponds to the internal structure of macrophages, and PBS pH 7.4 corresponds to the pH of the blood. The release study was performed using 100 mL of dissolution media at 37 ºC for 96 h. The medium consists of 40% of methanol and 60% of the respective buffer. The NVP-CNT showed $91.99 \pm 2.083\%$ release of drug at pH 5 and $86.98 \pm 0.87\%$ of drug release at pH 7.4 at the end of 96 h. The data on the release of the drug is tabulated in Table 29 and shown graphically in Figure 80 for 96 h and 81 for 8 h. The release took place in a sustained manner for 96 h. The release of the drug was higher at acetate buffer pH 5 when compared to PBS pH 7.4. This may be due to the weekly basic nature of the drug NVP which ionizes readily at lower pH and leads to the destruction of π-π interaction resulting in disruption of the carrier system. Due to the disruption of the carrier system repulsion forces increase between the delivery system and the drug, releasing the drug in the release system (Huang et al., 2011). The lower pH leads to the formation of free H+ from the medium which can positively compete with H bond-forming groups. This causes the weakening of the drug-carrier interaction which results in increased drug release of the drug from the delivery system (Manyarara et al., 2018). The formulation can easily disrupt its structures and release drug NVP at a lower pH. The internal pH of macrophages is pH 5, hence maximum drug release can take place at the site of action.

Table 29: Drug release Profile of NVP from NVP-CNT

Time	% Cumulative drug release	
	Acetate buffer pH 5	**PBS pH 7.4**
0	0	0
1	9.98±2.73	1.23±0.42
2	23.49±0.63	2.79±0.85
3	23.75±1.86	4.20±0.36
4	26.61±0.68	6.40±6.19
5	29.26±0.30	15.32±3.30
6	30.63±0.48	19.94±4.99
7	34.03±0.23	24.88±2.69
8	36.26±0.62	34.34±2.29
24	54.98±2.12	46.97±2.99
30	65.22±2.86	53.64±2.60
48	70.24±2.50	69.14±1.02
72	78.54±0.54	77.82±2.39
96	91.99±2.08	86.98±0.87

*The data was represented as Mean±SD (n=3)
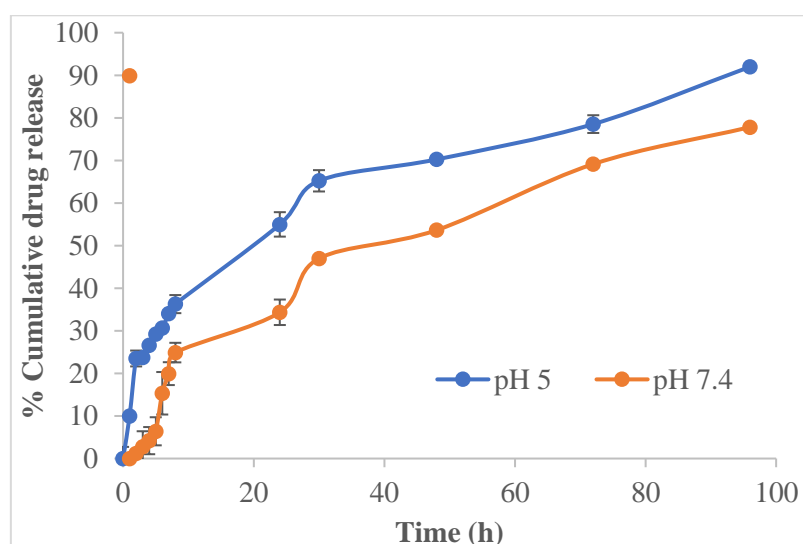
Figure 80: Drug release profile of NVP-CNT for 96 h (n=3)

180
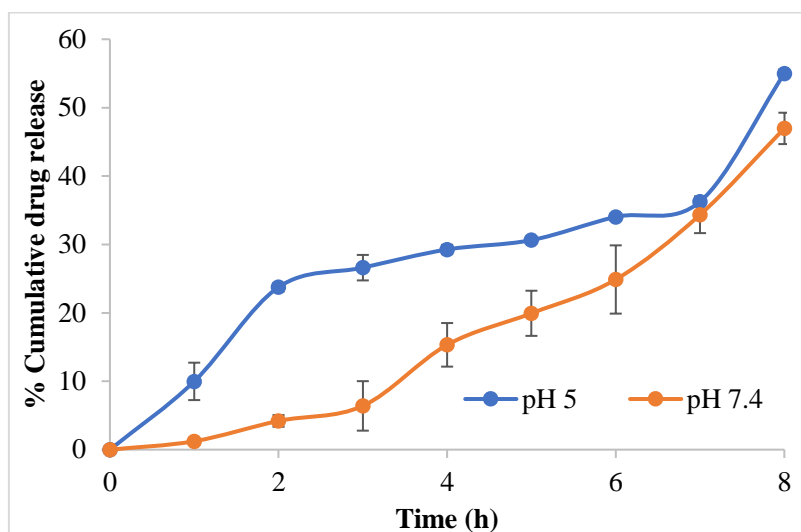
Figure 81: Drug release profile of NVP-CNT for 8 h (n=3)

5.7.2.2.11 Drug release kinetics

Table 30: Drug release kinetics of NVP from NVP-CNT representing R^2 value and n

S.No	Release	pH 5		pH 7.4	
		R^2	n	R^2	n
1	First-order	0.9445	-	0.9807	-
2	Zero-order	0.8522		0.8919	
3	Korsmeyer-Peppas	0.7748	0.8841	0.8905	1.0165
4	Higuchi	0.9701		0.9667	
5	Hixon	0.913		0.9683	

The release data of NVP-CNT were subjected to kinetics models to study the release mechanism. The different kinetics equations are the Higuchi equation which co-relates % cumulative drug release with the square root of time, first order equation relates the log cumulative drug remaining with log time and depends on initial concentration, zero order equation relates cumulative % drug release with time and is independent of initial concentration, Korsmeyer-Peppas equation correlate log cumulative drug released with log time, Hixon-Crowell equations relates a group of particles area to the cube root of its volume. From the data of different equations regression constant and release constant were determined and the regression value helped to determine the most fitted model (Dlamini et al., 2019).

The NVP-CNT was studied for drug release kinetics at different pH and tabulated in Table 30. At pH 5 and pH 7.4. The best-suited model for both the release profile was the Higuchi model as the R^2 value for the data of the release profile at pH 5 was found to be 0.9701 and the R^2 value of release data at pH 7.4 was found to be 0.9667 followed by Hixon Crowell equation where the R^2 was found to be 0.931 for pH 5 and 0.9668 for pH 7.4. The Higuchi model helps to understand the NVP release from an insoluble matrix. The release pattern showed a faster initial release followed by a decrease in release with time. In this system concentration of the drug is much higher than it releases and acts as a driving force. As time proceeds concentration gradient changes reducing the diffusion and subsequently reducing the drug release (Haroun et al., 2018).

Another model that follows the Higuchi model of drug releases is the Hixon Crowell model and first-order model. The release pattern followed the Hixon-Crowell rule indicating that the diameter and surface area are changing concerning time. Diameter and surface area tend to change with the detachment of the drug as time progresses.

The n component from the Korysmeyer-Peppas equation is used to understand the release pattern of the drug NVP from the delivery system. For pH 5, the value of exponential n was determined to be 0.8841, and for pH 7.4, it was 1.016. The value suggests that the non-fickian diffusion model governed the release.

The drug release was subjected to other release models, lowest R^2 value was found to be for the first order. The value for the first order was found to be 0.9445 for pH 5 and 0.9807 for pH 7.4, a lower value of R^2 makes it unsuitable (Albayati et al., 2019). The zero-order model was not fitting due to the low value of the correlation coefficient. It was 0.8522 for pH 5 and 0.8919 for pH 7.4. The Korsmeyer-Peppas model also showed a lesser R^2 value of around 0.7748 for pH 5 and 0.8905 for pH 7.4. Thus, the best-suited model was the Higuchi model followed by the Hixon Crowell release mechanism. Figure 82. Drug release kinetics of NVP-CNT at pH 5 and pH 7.4 in First order release kinetics, Zero order release kinetics, Korsmeyer Peppas release kinetics, Higuchi release kinetics, Hixon-Crowell release kinetics.

(a) **First order release kinetics**

(b) **Zero order release kinetics**

(c) **Korsmeyer Peppas release kinetics**

(d) **Higuchi release model**

(e) **Hixon-Crowell release kinetics**
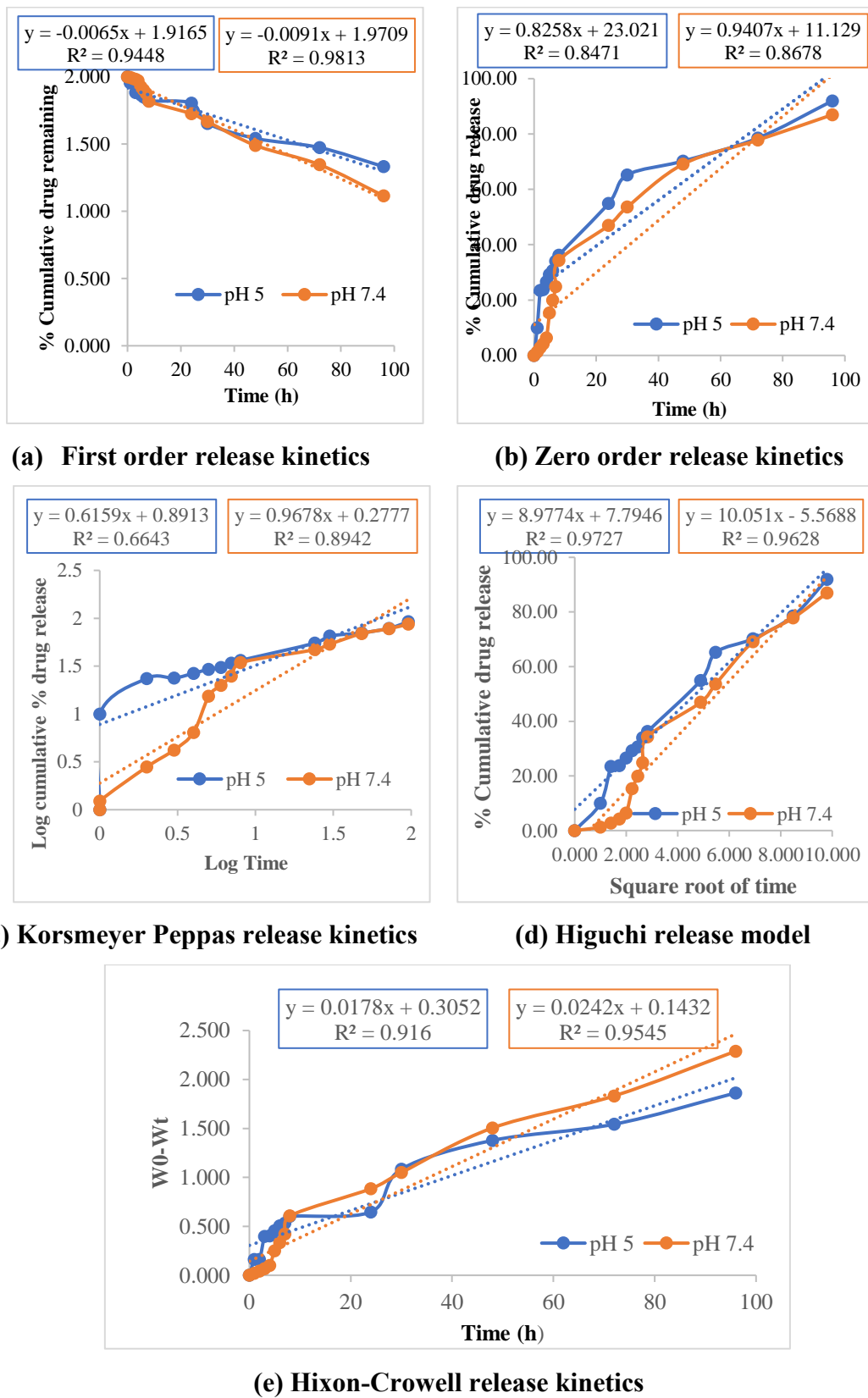
Figure 82. Drug release kinetics of NVP-CNT at acetate buffer pH 5 and PBS pH 7.4

5.7.3 Formulation development and characterization of Nevirapine-loaded dendritubes

5.7.3.1 Formulation development of Nevirapine-loaded dendritubes

The drug NVP was loaded on the DT (NVP-DT) with constant stirring for 48 h using a magnetic stirrer. The drug binds with the surface amine group of the DT by covalent linkage with dendrimers and can be entrapped within the dendrimer structure as well as form π-π stacking. The structure was characterized using different characterization techniques such as spectroscopic analysis, morphological studies, and cytotoxicity studies.

5.7.3.2 Characterization of Nevirapine-loaded dendritubes

5.7.3.2.1 FTIR Spectroscopy

(a)

(b)
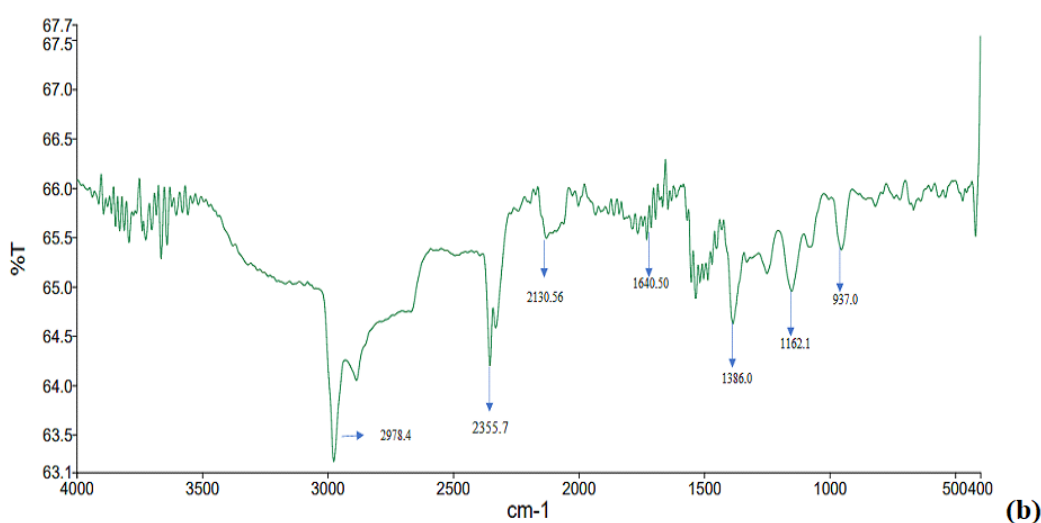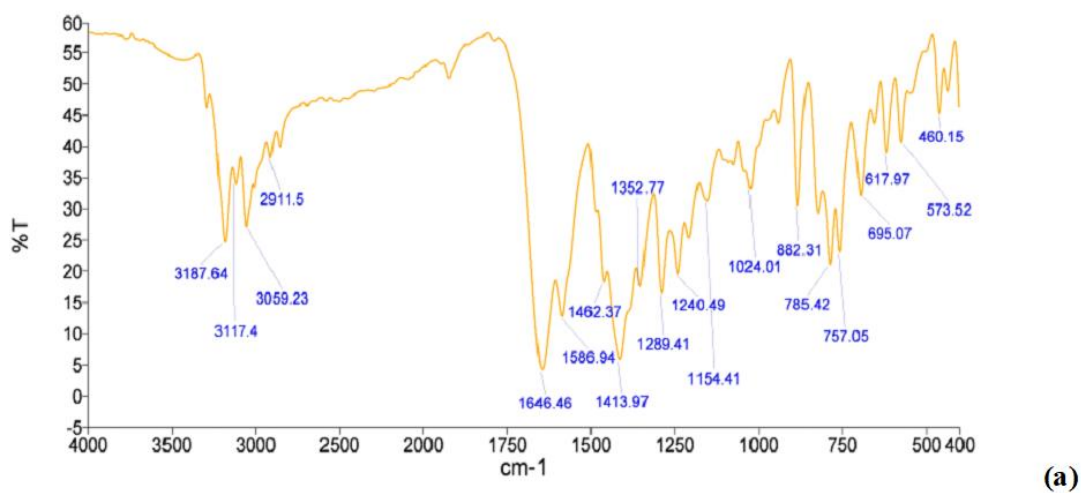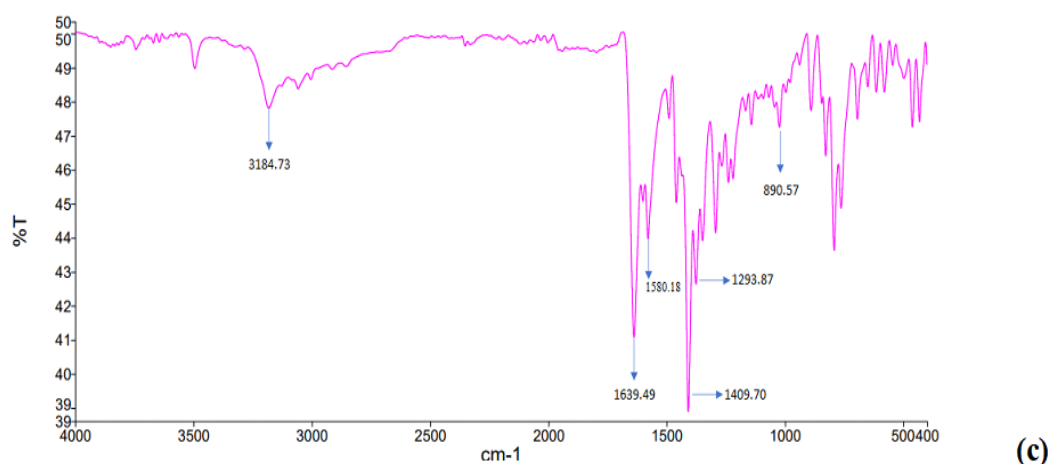
Figure 83: FTIR spectra of (a) NVP (b) DT (c) NVP-DT

The FTIR spectra of plain drug NVP, DT, and NVP-DT were determined and shown in Figure 83. The FTIR spectrum of NVP revealed the presence of all the characteristic peaks of the drug. The major peaks are observed at 3187.64 cm^{-1}, a broad peak corresponds to stretching of N-H, the peak at 3059.23 cm^{-1} indicates stretching of C-H, at 1646.46 cm^{-1} indicates the -C=O stretch, a peak at 1586.94 cm^{-1}, and 1413.97 cm^{-1} corresponds to the aromatic carbons (C=C), the peak at 1289.41 cm^{-1} represents C-N stretching and the peak at 882 cm^{-1} and 757 cm^{-1} indicates C-H bending (Varshosaz et al., 2018).

The spectrum of DT showed characteristics at 3643.53 cm^{-1} corresponds to the NH peak. A peak at 2978.4 cm^{-1} primary alkene 1535.5 cm^{-1}, primary amine, peaks of at 1386.0 cm^{-1} OH bending, 1162.1 cm^{-1} C-O stretching, a peak at 937 cm^{-1} aromatic C-H out of plane bending. The absence of a stretching peak at 1710.05 cm^{-1} indicates that the COOH group was altered by covalently binding with amine present on the surface of dendrimers.

The similar characteristics bands observed with NVP-DT showed similar peaks at nearly the same locations. The binding of NVP with DT takes place by covalent linking between the CH$_3$ of NVP and the surface NH$_2$ of DT. The hypothesis was supported by FTIR. The peak of the -C-H group present at 3059.23 cm^{-1} in NVP spectra disappeared in NVP-DT and the peak of primary amine diminished in NVP-DT. This confirms the interaction of NVP with a surface amino group of DT. All the other major peaks were observed at the same location as that of the drug NVP such as 3184.73 cm^{-1} is N-H stretch, 1639.49 cm^{-1} indicated the presence of C=O stretch, 1580.18 cm^{-1} and

185

1409.70 cm⁻¹ corresponds to the C=C, 1293.88 cm⁻¹ corresponds with C-N stretching. The peak at 890.57 cm⁻¹ corresponds to the aromatic carbon out-of-plane bending (Samsodien et al., 2017; Varshosaz et al., 2018; Nalte et al., 2015). Table 31 represents the FTIR spectrum of NVP-DT.

Table 31: FTIR spectrum of NVP-DT

Observed peaks frequency (cm⁻¹)	Standard FTIR range (cm⁻¹)	Corresponding functional group
3184.73	3500-3100	Peak of N-H stretching
1639.49	1630-1680	C=O carbonyl stretching
1580.18	1475-1600	Cyclopropyl C=C
1409.70	1475-1600	Cyclopropyl C=C
1293.40	1350-1000	C-N stretching
890.57	900-690	-C-H bend of aromatic alkene

5.7.3.2.2 Raman Spectroscopy

The DT and NVP-DT were subjected to Raman spectroscopy to study the vibrational behavior of the prepared conjugates in the range of 0 to 4000 cm⁻¹. Figure 84 represents the Raman spectra of NVP and NVP-DT. The D band for MWCNT was observed at 1282.44 cm⁻¹ and for DT was observed at 1286.29 cm⁻¹. This band was due to a defect or disorder in the MWCNT structure. The G band was observed at 1599.38 cm⁻¹ for MWCNT and 1601.16 cm⁻¹ for dendrimers conjugated MWCNT. This band relates to the crystalline structure of graphite (Muda et al., 2017; Sedaghat et al., 2014).

(a)

186
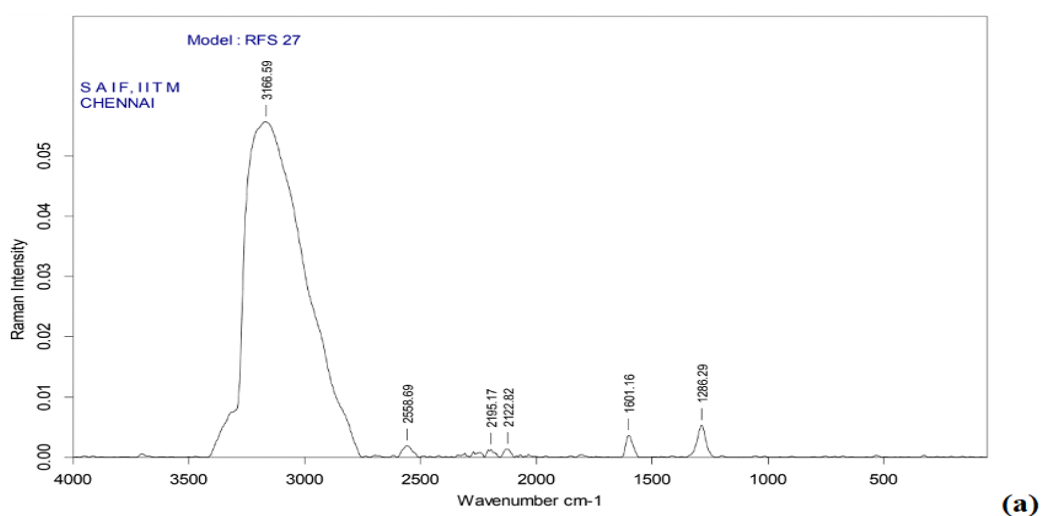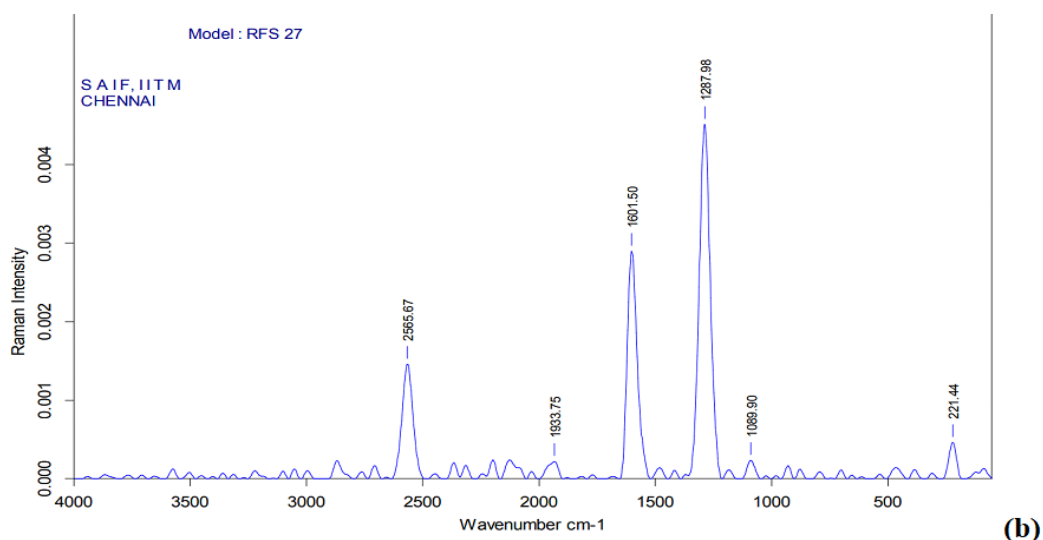
Figure 84: Raman spectra of (a) NVP (b) NVP-DT

The three low-energy energy corresponds to the methyl group. In the spectra of drug-loaded DT, the peaks near the range of 3000 cm^{-1} diminish, indicating the drug attachment on the surface of the DT. The disappearance of the peak supports the hypothesis that the attachment took place in the 4- 4-methyl group (Sathisran et al., 2021).

The I_D/I_G ratio of DT was found to be 1.460 and the ratio of I_D/I_G of NVP-CNT was found to be 1.550. The increment in the I_D/I_G ratio of NVP-DT indicated that the conjugation of NVP took place on the DT surface which alters the sp^2 bonding structure of MWCNTs and leads to the breaking of π bonds holding the hexagonal carbon structure (Muda et al., 2017; Sedaghat et al., 2014).

5.7.3.2.3 NMR Spectroscopy

The NMR spectrum of plain drug NVP, DT, and NVP-DT is shown in Figure 85. The NMR of NVP revealed that the multiplets were observed between δ 0.5 and 1.3 ppm corresponding to -CH$_2$ of methylene groups of cyclopropane (H5, H6), the chemical shifts between δ 3.79 ppm correspond to the protons of cyclopropane (H8), the peak at δ 2.325 ppm corresponds to CH$_3$, peaks between δ 7.10-8.40 ppm corresponds to the protons associated with aromatic ring (H1, H2, H3, H4, H5). The single peak at δ 8.407 ppm corresponds to NH (da Silva et al., 2021; Silverstein et al., 1962).

Nevi
CMC_SINGLE_H2O D2O {D:\Spectra} nmr 2

(a)

N3
CMC_SINGLE_H2O D2O {D:\Spectra} nmr 2

(b)

188

Nevi DT
CMC_SINGLE_H2O D2O {D:\Spectra} nmr 31
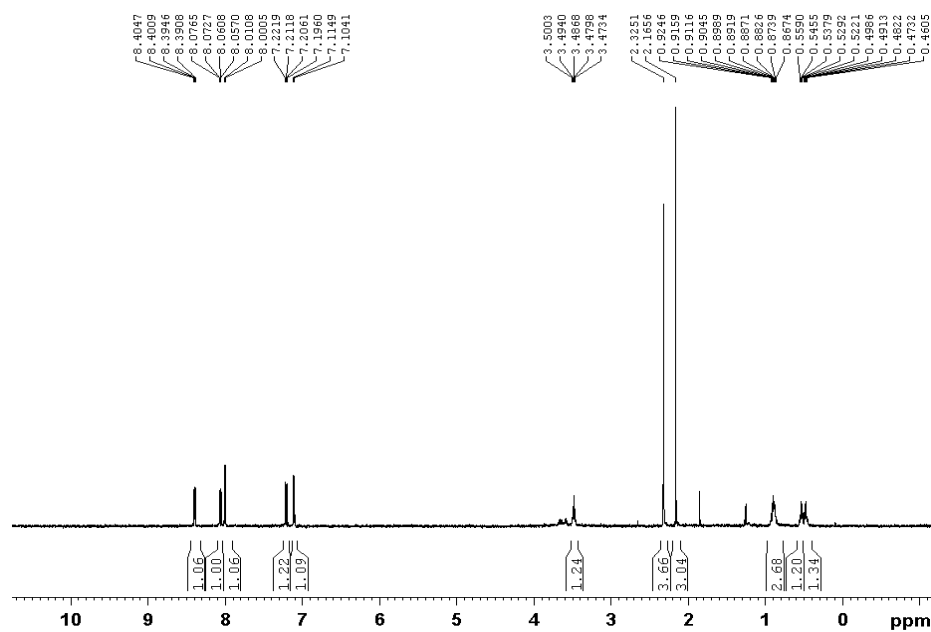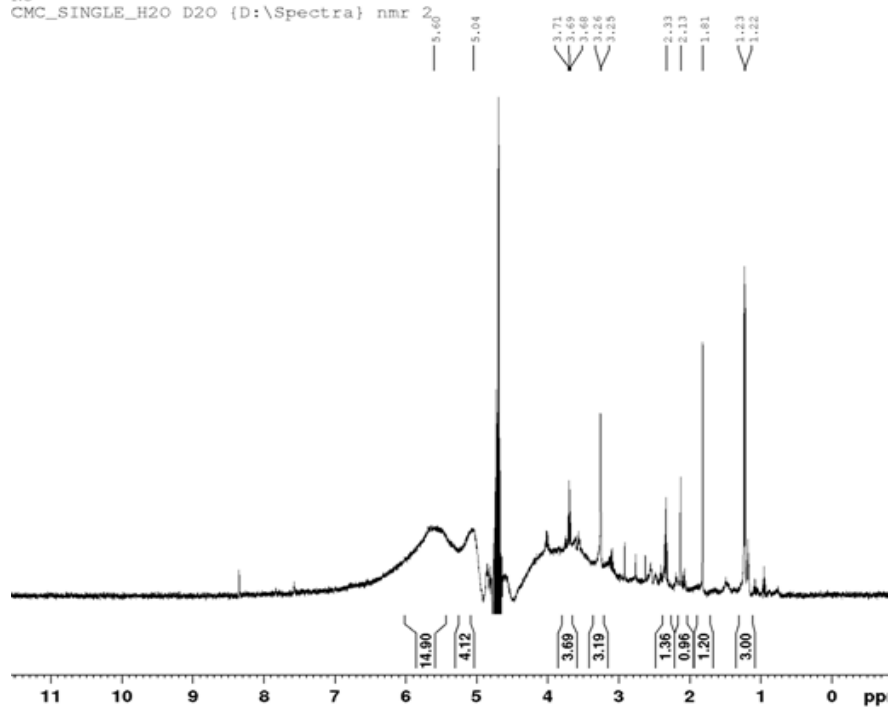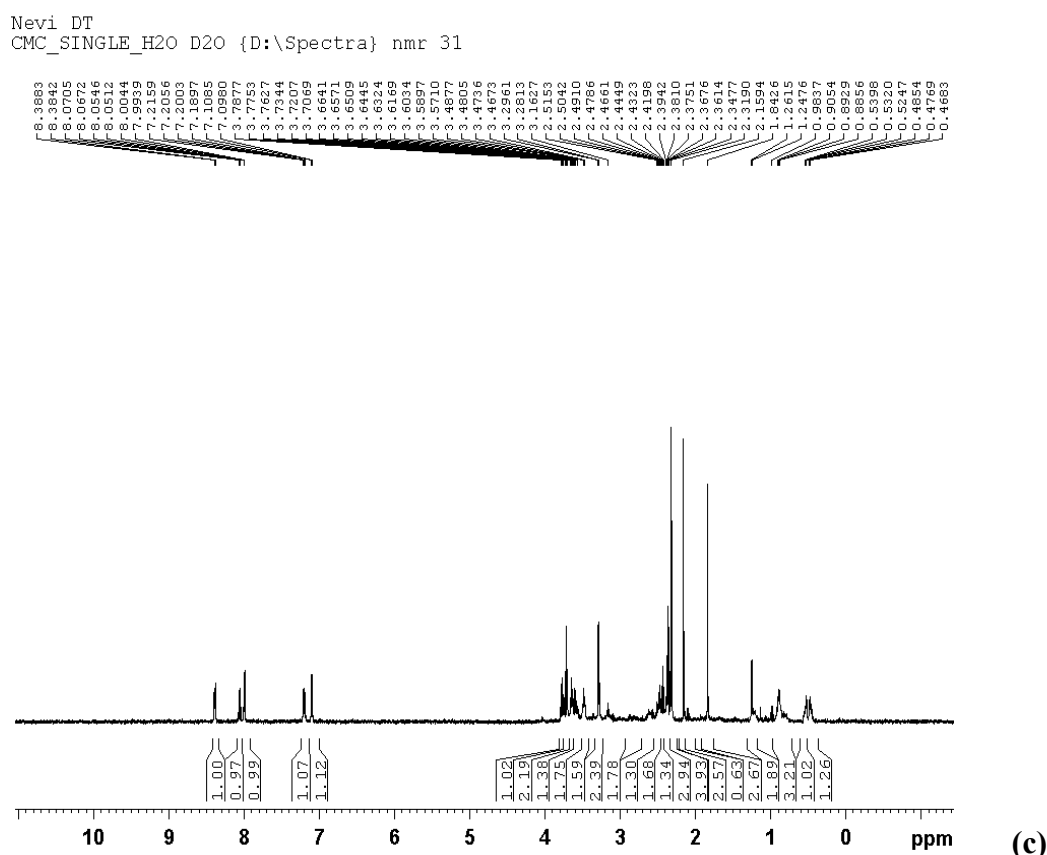
Figure 85: NMR spectra of (a) NVP (b) DT (C) NVP-DT

Multiplex between 3.2-3.7 corresponds to the -OH protons of MWCNT. Peak at 1.01 corresponds to C-H protons, and multiplets at 0.8-1.2 correspond to the CH_2 of the dendrimer structure.

The NMR spectrum of NVP-DT indicates many protons due to the incorporation of the drug NVP in the DT. Alteration in a chemical shift at δ 2.3251 ppm indicated the attachment of the methyl group of drugs with a surface amino group of DT. The peaks at δ 8.3883 ppm indicate the H of NH_2 in the structure. The peaks at δ 3.79 ppm, δ 1.01 ppm, and δ 0.53 ppm correspond to the H of the cyclopropyl group. The H of the aromatic ring was observed between δ 8.51 ppm and δ 6.90 ppm. The dendritube structure has an abundance of protons in its surroundings due to a heavily conjugated and complex structure that corresponds to various peaks and splitting patterns (Monteiro et al., 2016).

189

5.7.3.2.4 X-Ray diffraction

(a)

(b)

(c)
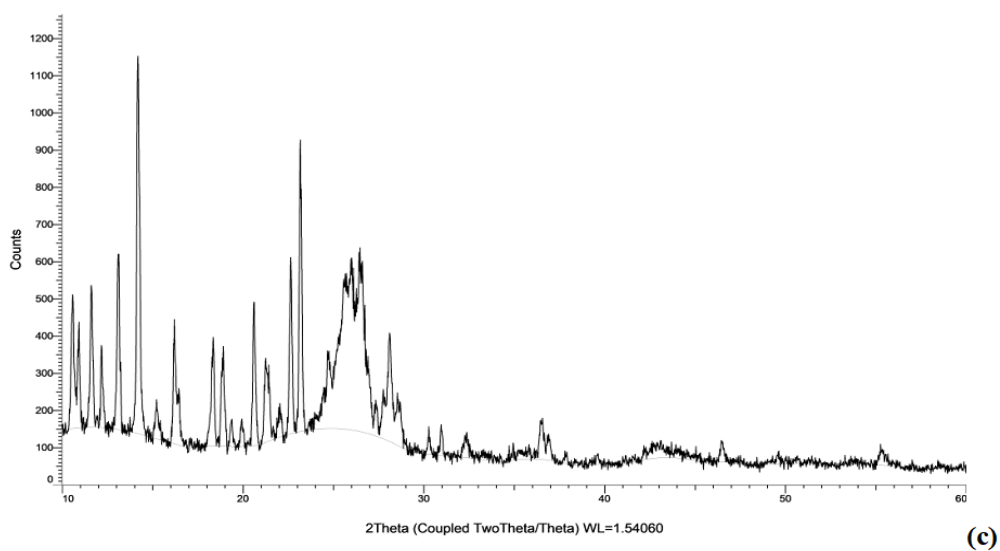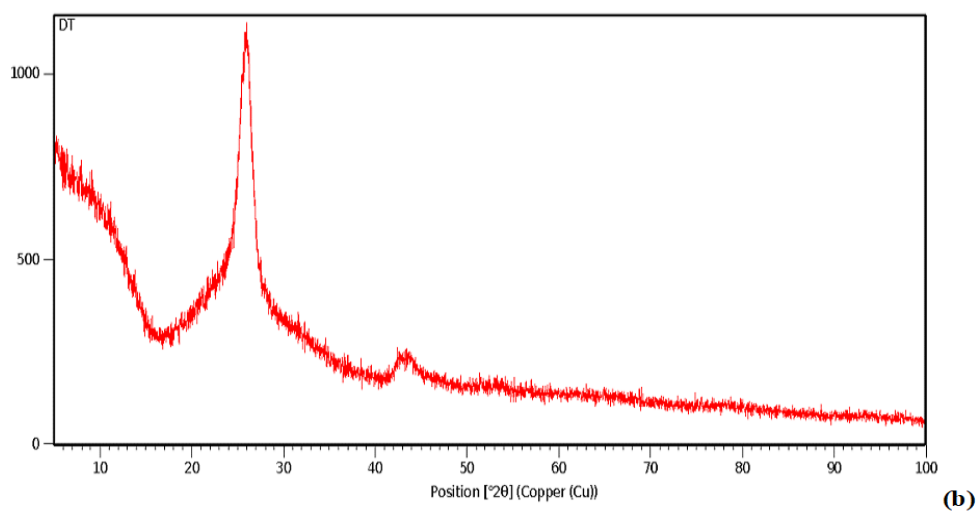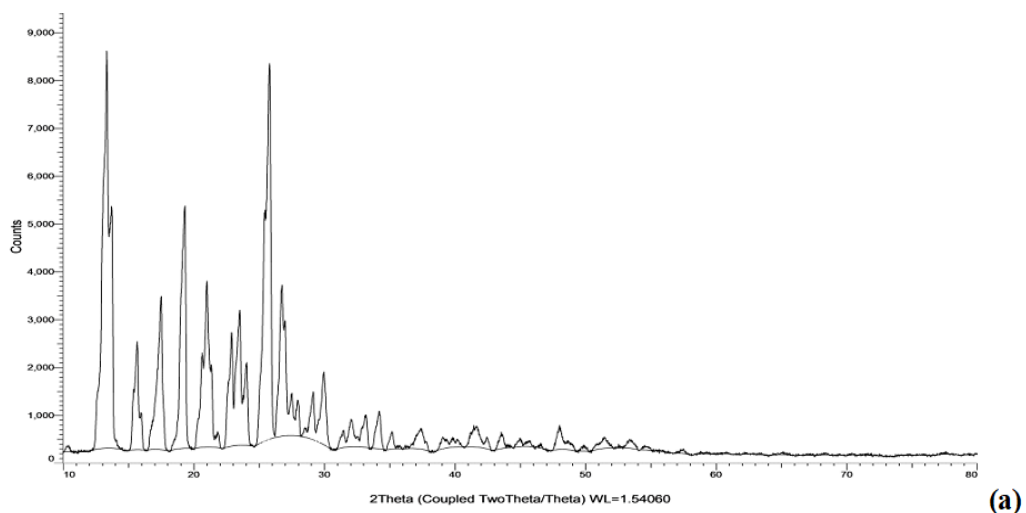
Figure 86: X-ray diffractogram of (a) NVP (b) DT (c) NVP-DT

190

The XRD method was performed to study the crystal structure of the drug after its incorporation in the DT. The XRD of drugs NVP, DT, and NVP-DT was studied and shown in Figure 86. The sharp and intense peaks observed between 2θ = 10 to 23° indicate the crystalline structures of NVP, which further confirms the incorporation of NVP in DT. The peak of NVP was shifted to 14.194° and 26.0° had been shifted in NVP-DT from 13.915° and 25.455° drug NVP. The presence of prominent peaks revealed that the crystalline nature of the drug NVP was not much affected by the conjugation (Monteiro et al., 2016).

5.7.3.2.5 Differential Scanning Calorimetry

(a)   (b)   (c)
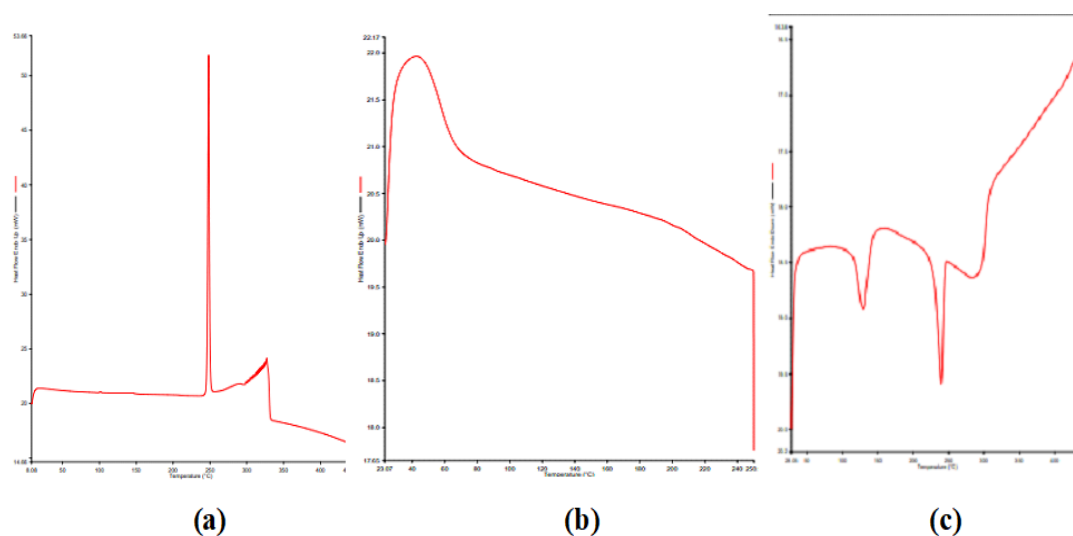
Figure 87: DSC thermogram of (a) NVP (b) DT (c) NVP-DT

The conjugation of NVP with DT was also confirmed by DSC studies and given in Figure 87. The peak was observed at 249.0 for NVP and 239.52 for the drug-loaded DT. It was observed that the transition temperature showed a negative shift confirming the strong interactions between DT and NVP (Ramana et al, 2010). The transition of the peak indicates that the endothermic capability was altered which confirmed that the drug was conjugated with DT (Yang et al., 2022).

5.7.3.2.6 Field emission scanning electron microscopy

Figure 88 represents the FE-SEM image of DT and NVP-DT. FE-SEM images showed the tubular structure of DT with lesser aggregation which was due to surface modification of the MWCNT structure with dendrimers. The drug-loaded structures do not show any kind of breakage or damage or alteration in the long chain structure of CNTs and attachment of dendrimers on the surface (Mallakpour et al., 2018).
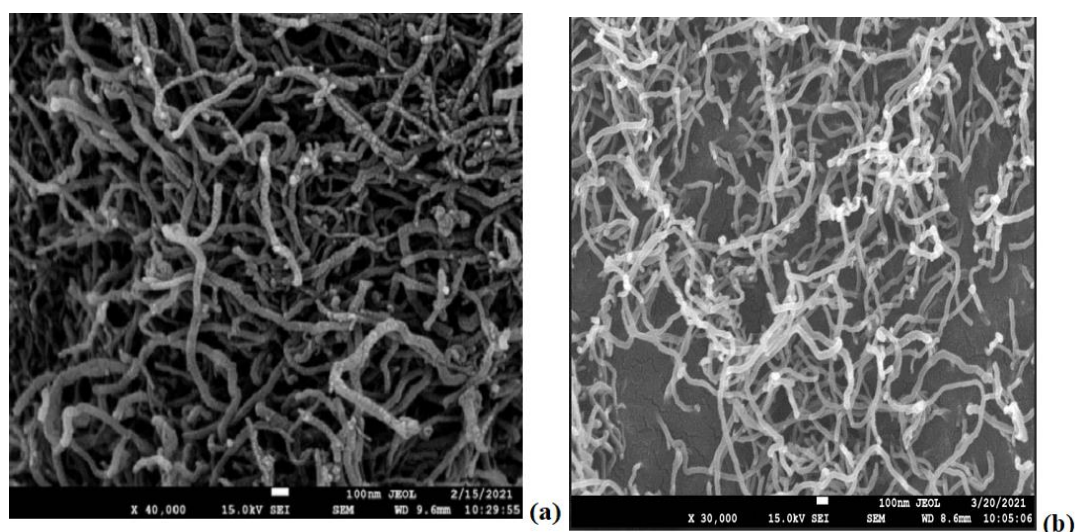
Figure 88: FE-SEM image of (a) DT (b) NVP-DT

5.7.3.2.7 Particle size and zeta potential

The particle size and zeta potential of DT and NVP-DT were evaluated using a Delsa nanoparticle counter. The particle size, polydispersity index, and zeta potential are tabulated in Table 32 and the particle size distribution of NVP-DT is represented in Figure 89. The particle size of DT was found to be 288.4 nm which on conjugation with the drug increases to 481.5 nm. The PDI was found to be 0.385 which reduces to 0.173 indicating that the DT shows a higher aggregation of the nanostructure may be due to entanglement which reduces drastically due to conjugation with the drug. The zeta potential was found to be -2.48 mV for DT which reduces to -8.86 mV. This may be due to the conjugation of NVP with DT, reducing the surface NH_2 group (Modi et al., 2011; Dong et al., 2017).

Table 32: Particle size, PDI and zeta potential of DT and NVP-DT

Formulation	Particle size (nm)	PDI	Zeta potential (mV)
DT	288.4	0.385	-2.48
NVP-DT	481.4	0.173	-8.86
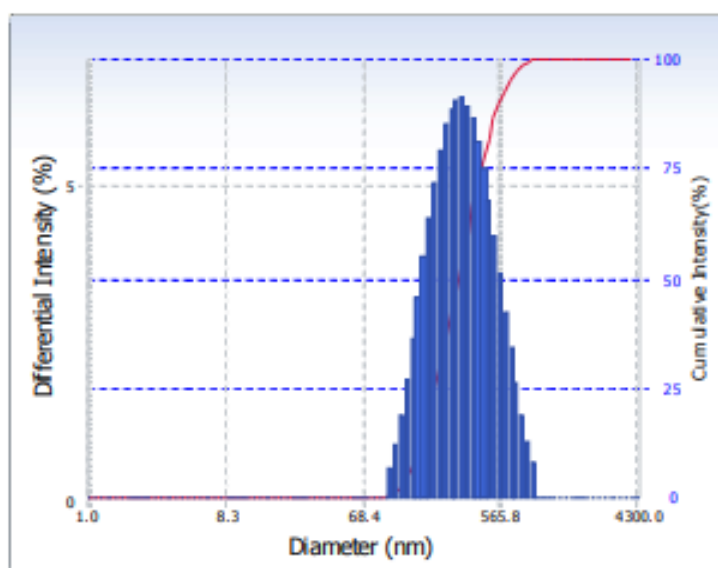
Figure 89: Particle size analysis of NVP-DT

5.7.3.2.8 Dispersibility Test

Dispersion studies were performed to study the dispersion stability of the prepared NVP-DT in deionized water as represented in Figure 90. The dispersibility studies were observed for 24 h without disturbing the sample container. The observation of this study suggests that the NVP-DT remains dispersed for 24 h without settling.

0 h   8 h   24 h
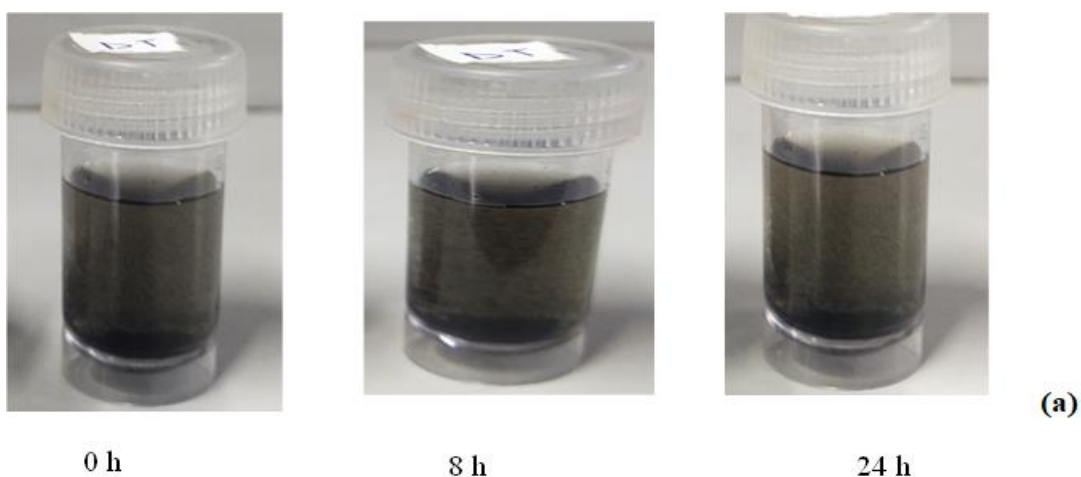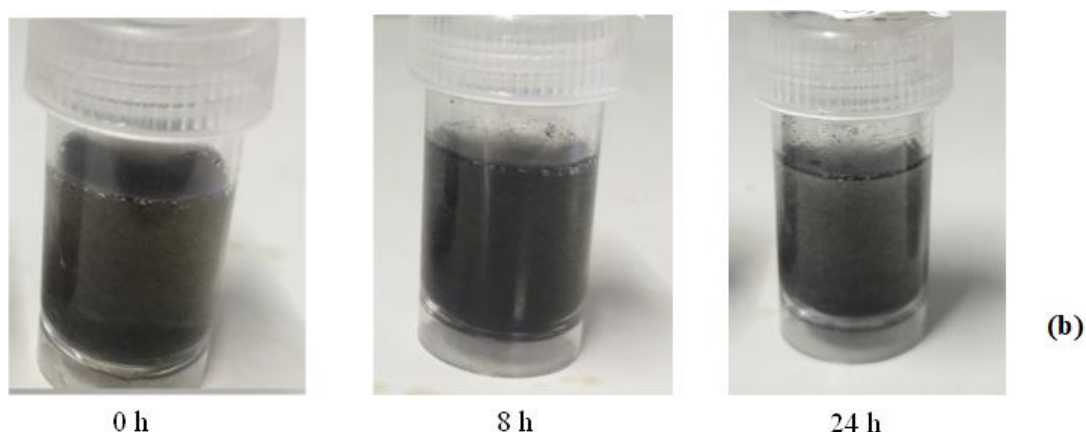
Figure 90: Dispersibility studies of (a) DT (b) NVP-DT

5.7.3.2.9 Drug entrapment

Entrapment efficiency was carried out by dialysis membrane technique using by indirect method (MWCO, 7000 Da, Himedia, India). Singhai et al, reported the method in which the amount of unentrapped drug was calculated and from this amount of entrapped drug was calculated. The entrapment efficiency of DT was found to be 96.57±1.57%. The higher loading of the drug was due to the surface conjugation of 5G PPI dendrimers on COOH-MWCNT. The terminal functional group increases the sites of interaction of drugs by covalent linking and also binds non-covalently by hydrogen bonding or hydrophobic interactions as the drug was also hydrophobic. The drug can also entrap and form bonds inside the dendritic structure. The drug also binds to the side wall of MWCNT by π-π stacking. As with the new conjugate system, multiple binding sites were available which resulted in higher drug loading (Tripathi et al., 2020).

5.7.3.2.10 *In vitro* drug release

The release study was performed to determine the release pattern of the drug NVP from the NVP-DT. The drug release of NVP-DT was determined in acetate buffer pH 5 and PBS pH 7.4 at 37°C was carried out for 96 h. Table 33 represents the drug release profile of NVP-DT in acetate buffer pH 5 and PBS pH 7.4. The formulation, NVP-DT showed drug release of 81.63 ± 2.80 % in acetate buffer pH 5 and 73.31 ± 2.80 % in PBS pH 7.4 at 96 h. The graph indicates that the release takes place in a sustained release manner. The drug NVP is weekly basic which ionizes and leads to the destruction of π-π interaction resulting in disruption of the carrier system. Due to the

disruption of the carrier system repulsion forces increase between the NVP and the delivery system, releasing the drug in the release system (Panzade et al., 2019). Thus, the formulation can effectively release the drug by disruption of the carrier system and the microenvironment of macrophages has pH 5, the drug has better solubility at pH 5, thus ensuring the better release of the drug at the target site.

Table 33: Drug release Profile of NVP from NVP-DT

Time (h)	% Cumulative drug release	
	Acetate buffer pH 5	**PBS pH 7.4**
0	0±0	0±0
1	15.24±1.88	8.32±0.95
2	20.19±1.92	10.29±0.98
3	23.56±1.77	15.24±1.86
4	28.16±2.23	28.93±1.50
5	38.70±0.88	33.47±3.89
6	45.08±3.82	39.05±0.96
7	48.65±2.63	43.32±2.18
8	50.13±1.59	48.08±2.14
24	63.64±2.82	54.62±1.79
30	72.70±3.27	64.65±1.09
48	75.37±2.44	68.78±3.79
72	78.63±3.58	71.65±2.02
96	81.63±2.44	73.31±2.80

*The data was represented as Mean±SD (n=3)
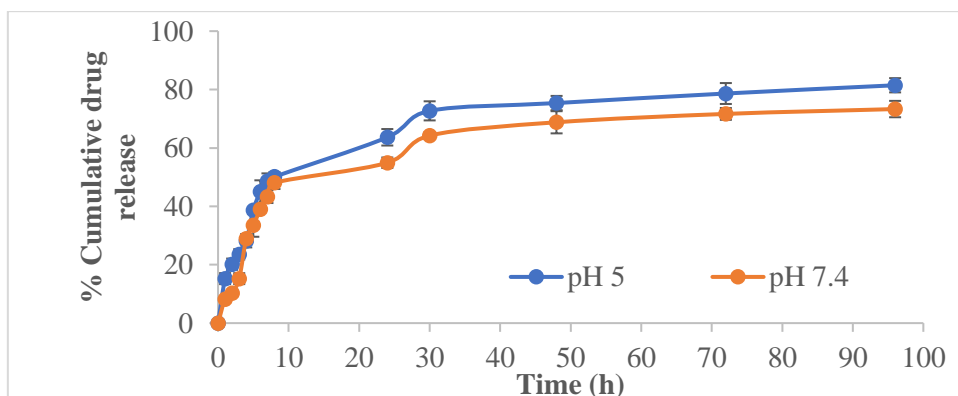
Figure 91: *In vitro* drug release of NVP-DT for 96 h

195
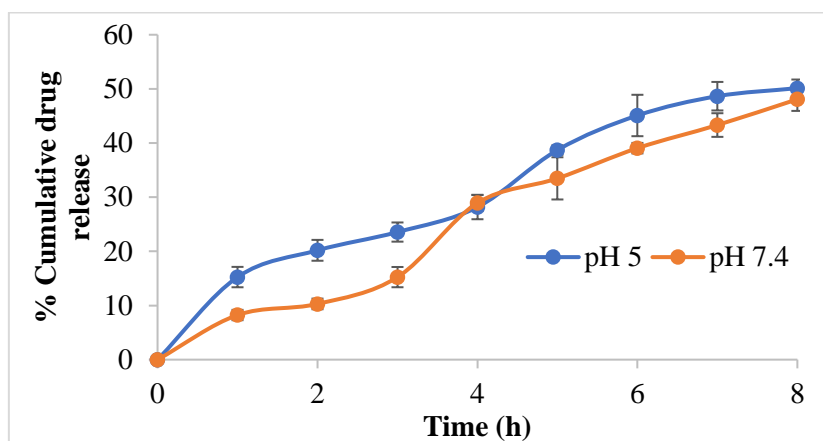
Figure 92: *In vitro* **drug release of NVP-DT for 8 h**

5.7.3.2.11 Drug Release Kinetics

Release kinetic study and the drug release mechanism are studied using different kinetic models such as first order, zero order, Korsmeyer-Peppas equation, Higuchi equation, and Hixon-Crowell equations. The drug release data was subjected to different mathematical models to determine the most fitted model for the drug release was determined based on the regression constant and release constant (Dlamini et al., 2019). Table 34 represents the R^2 values of different kinetic models and Figure 93 represents the different kinetic models studied for the drug release profile of NVP-.

Table 34: Drug release kinetics of NVP from NVP-DT representing R^2 value and n

S.No	Release	pH 5		pH 7.4	
		R^2	n	R^2	n
1	First-order	0.8775		0.8537	
2	Zero-order	0.683		0.6588	
3	Korsmeyer-Peppas	0.6988	0.6926	0.7246	0.6837
4	Higuchi	0.9022		0.9059	
5	Hixon Crowell	0.8332		0.8227	

The most fitted model for the release data of the NVP-DT was the Higuchi model. The exponent of release is indicative of the drug transport mechanism through the polymer. The R^2 value was found to be 0.9022 for pH 5 and 0.9059 for pH 7.4 and the value for exponential n was found to be 0.6926 for pH 5 and 0.6837 for pH 7.4. The value suggests that the non-fickian diffusion model governs the release. The Higuchi model helps to understand the release of drugs from an insoluble matrix. The release pattern showed an initial fast release followed by a decrease in release with time. In this

system concentration of the drug was much higher than it releases and acts as a driving force. As time proceeds concentration gradient changes reducing the diffusion and subsequently reducing the drug release (Haroun et al., 2018).

The drug release was subjected to other release models, lowest R^2 value was found to be for first-order release. The value for the first order was found to be 0.8775 for pH 5 and 0.8537 for pH 7.4, hence found to be unsuitable. The zero-order model was also not fitting due to the low value of the correlation coefficient. It was 0.683 for pH 5 and 0.6588 for pH 7.4. The Korsmeyer-Peppas model also showed a lesser R^2 value of around 0.6988 for pH 5 and 0.7246 for pH 7.4. Hixon- Crowell model also has a correlation coefficient value of less than 9, which made it less appropriate for the drug release model.

NVP- DT follows the Higuchi pattern release pattern showing fickian diffusion.
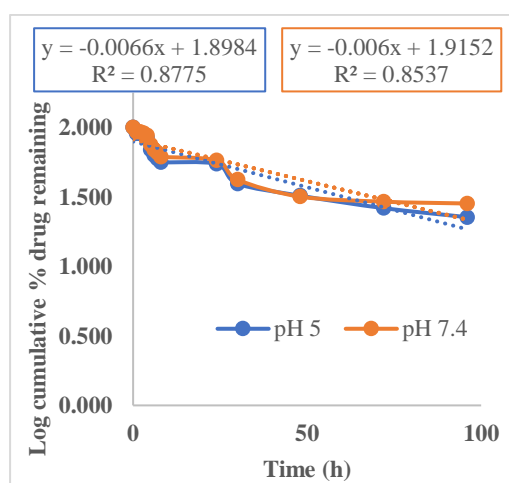
(a) First order release kinetics
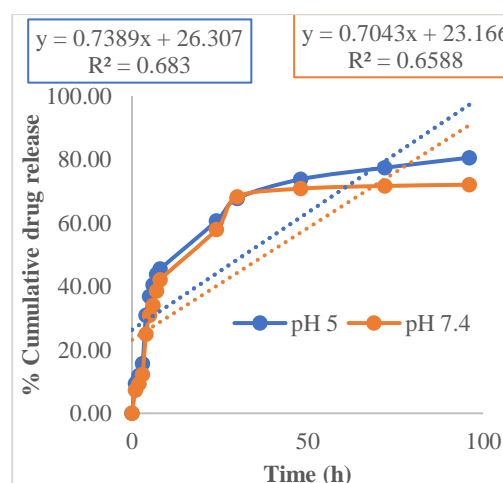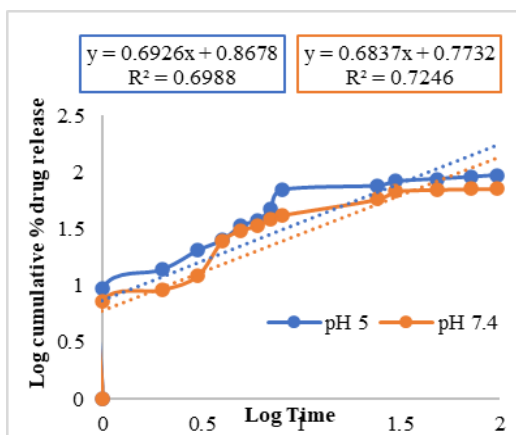
(b) Zero order release kinetics

(c) Korsmeyer Peppas release kinetics

(d) Higuchi release kinetics

197
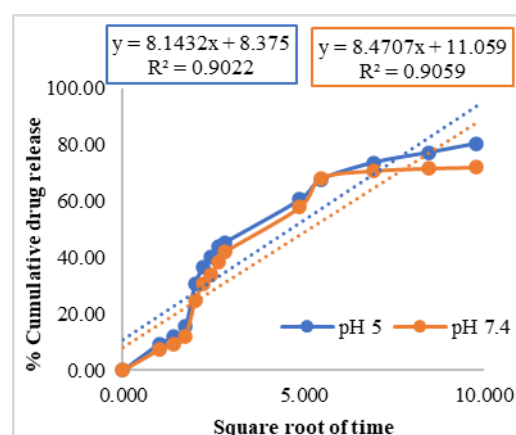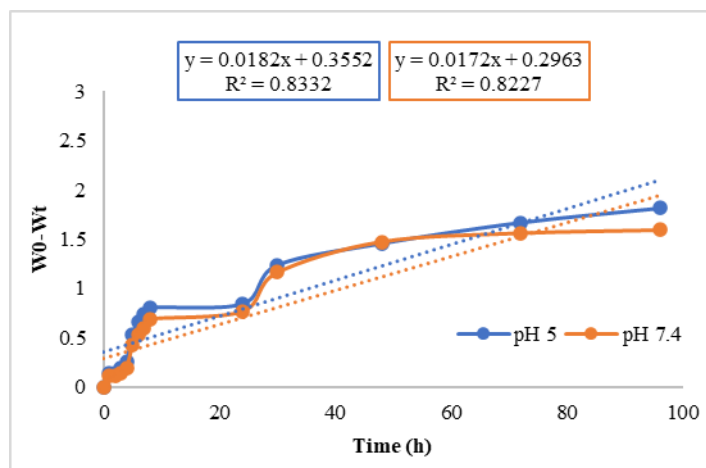
(e) Hixon-Crowell release kinetics

Figure 93. Drug release kinetics of NVP-DT

5.7.4 Formulation loaded with Fosamprenavir calcium

5.7.4.1 Formulation development of Fosamprenavir calcium-loaded dendrimers

Fosamprenavir calcium-loaded dendrimers (FPV-DEN) drug FPV was loaded on the 5G PPI dendrimers with constant stirring for 48 h using a magnetic stirrer. The drug binds with the surface amine group of the dendrimers by covalent linkage and is also trapped in the dendrimer structure. The structure was characterized using different characterization techniques such as spectroscopic analysis, morphological studies, and cytotoxicity studies.

5.7.4.2 Characterization of FPV-DEN

5.7.4.2.1 FTIR Spectroscopy
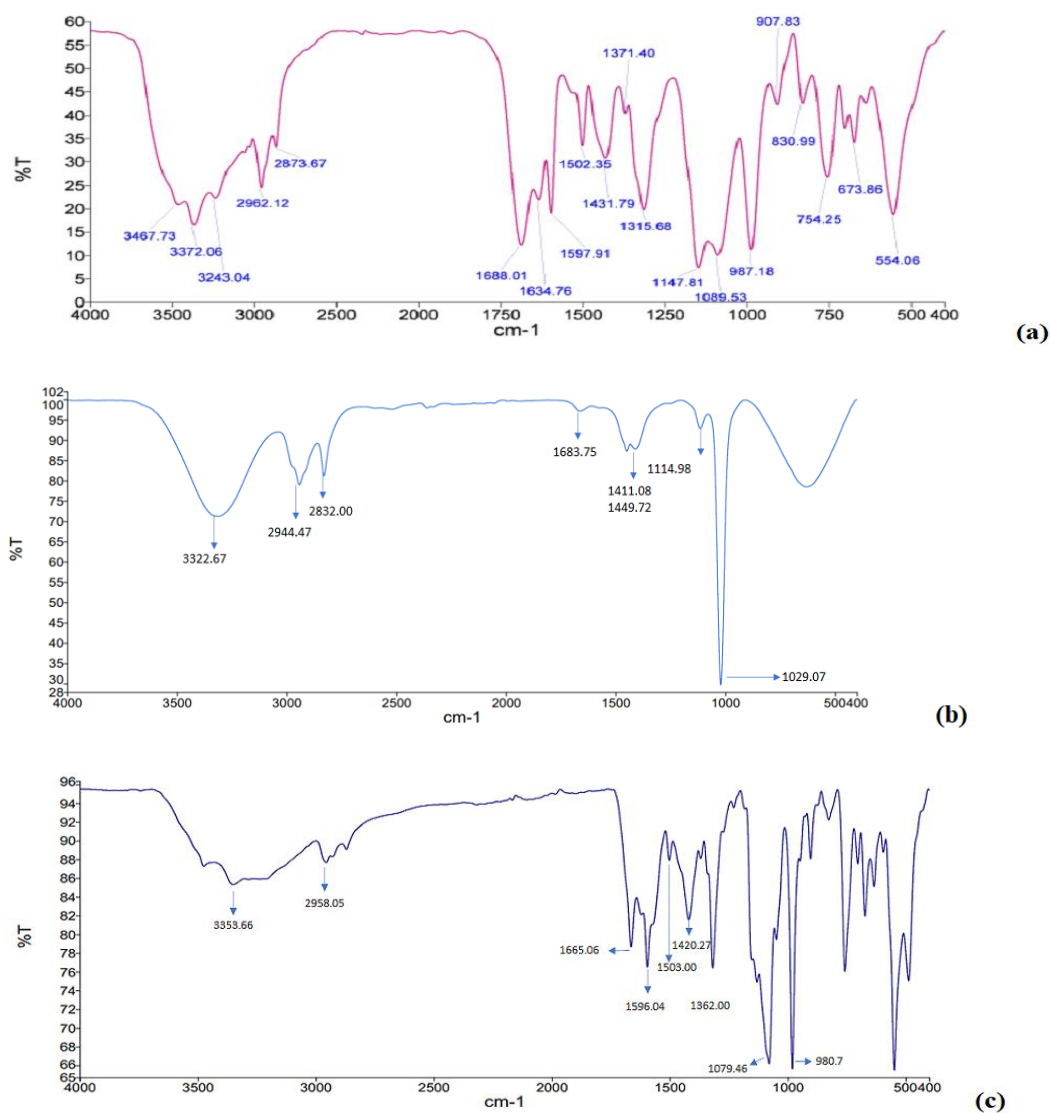
Figure 94: FTIR spectra of (a) FPV (b) Dendrimers (c) FPV-DEN

199

Figure 94 shows the FTIR spectra of FPV, dendrimers, and FPV-DEN. The FTIR spectrum of FPV shows that stretches of O-H are present in an intense peak at 3372.08 cm-1, whereas stretches of an amino group (N-H), which corresponds to amide and amine functional groups, are detected in a medium-intensity peak at 3243.04 cm-1. The asymmetrical stretch of S=O is represented by peaks 1089.53 and 1147.81 cm-1, while medium-intensity stretching of C=H of the aliphatic isopropyl chain is observed at 1431.79 cm-1 and 1315.68 cm-1. The peak at 1688.01 cm-1 was the peak of stretched aliphatic C=O, and the peaks of higher intensity were observed at 1597.91 cm-1 and 1502.3 cm-1, confirming the stretches of C=C; a region with high intensity, at 987.18 cm^{-1} the peak of high intensity due to C-O stretching of ether and phosphate esters (Cordeiro et al. 2020; Pavia et al., 1962; Tan et al. 2014).

The spectrum of dendrimers showed peaks such as a peak at 3322.67 cm^{-1} was the peak for primary amine confirming the presence of amine on the periphery of dendrimers, a peak at 2832.0 cm$^{-1,}$ and a peak at 2944.47 cm^{-1} was due to -C-H stretching of alkene, peak at 1683.75 cm^{-1} indicates N-H deflection of amine, a peak at 1411.08 cm^{-1} and 1449.72 cm^{-1} are the twin peak corresponds to CH band, a peak at 1114.98 cm^{-1} due to stretching of –C-N, and 1029.07 cm^{-1} which corresponds to bending C-H.

The drug conjugation took place between the methyl group of the isopropyl chain of drug FPV and the surface amino group of dendrimers. The spectrum of FPV-DEN showed a characteristic peak at 3353.66 cm^{-1} which corresponds to the broad peak of NH. The peak was found to be altered due to the incorporation of the drug in the dendrimer structure. The peak at 2958.05 cm^{-1} corresponds to the stretching of C-H, and the peak at 1655.06 cm^{-1} corresponds to the carbonyl group (amide) of the drug FPV. The peak at 1596.04 cm^{-1} and 1503.00 cm^{-1} corresponds to C=C of the aromatic structure of drug FPV. The peak of the C-H group of the isopropyl group of FPV was shifted to at 1420.27 cm^{-1} and the peak shape was also altered indicating that the drug structure had been altered due to conjugation of FPV with dendrimers. The C-N peak was observed at 1362.00 cm^{-1} and the characteristics peak of S=O was observed at 1079.46 cm^{-1} confirming the presence of dendrimers. This confirms that the drug FPV was loaded on the surface of dendrimers (Cordeiro et al., 2020). Table 35 represents the FTIR spectrum of NVP-DEN.

Table 35: FTIR spectrum of FPV-DEN

Observed peaks frequency (cm^{-1})	Standard FTIR range (cm^{-1})	Corresponding functional group
3353.66	3500-3100	Broad altered band of N-H stretching
2958.05	3150-3050	C-H stretching
1655.06	1630-1680	C=O (amide) group
1596.04	1475-1600	C=C aromatic carbon
1503.00	1350-1000	C=C aromatic carbon
1420.27	1375-1450	C-H isopropyl stretch
1362.00	1300-1000	-C-N stretch
1079.46	1050-1375	-S=O
980.7	900-690	-C-H aromatic (out of plane)

5.7.4.2.2 NMR spectroscopy

(a)

N-1

(b)

Fos-Den
1H_8scan DMSO {D:\Spectra} nmr 29

u

(c)
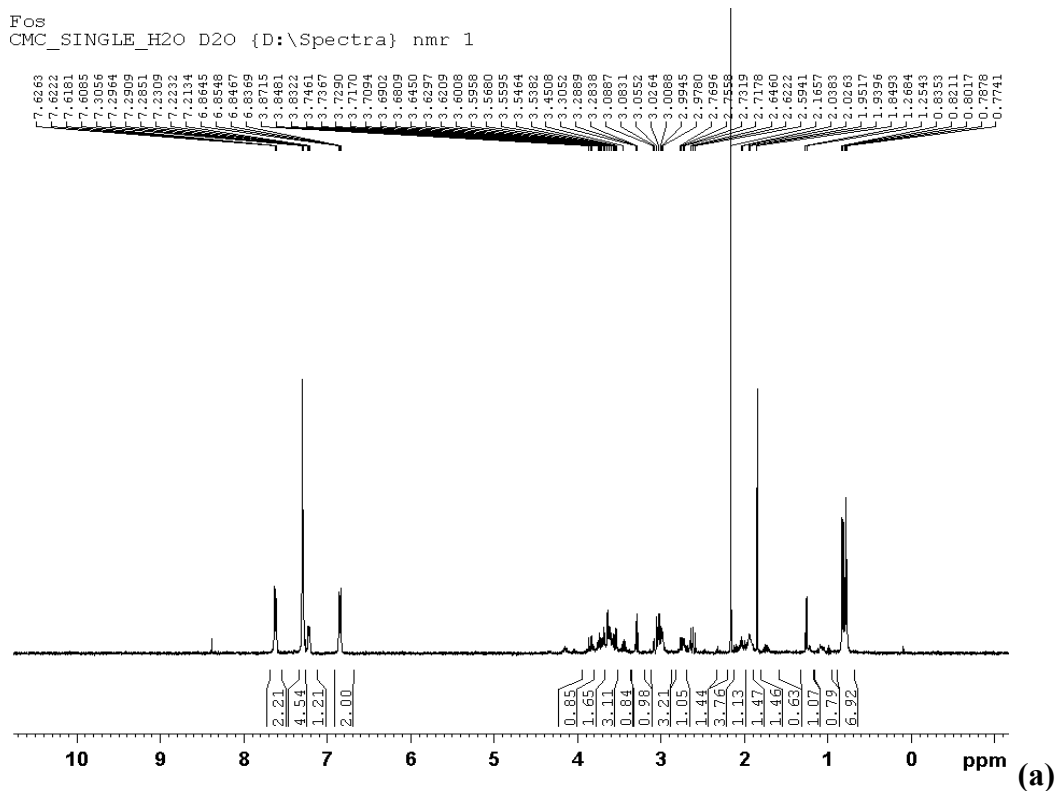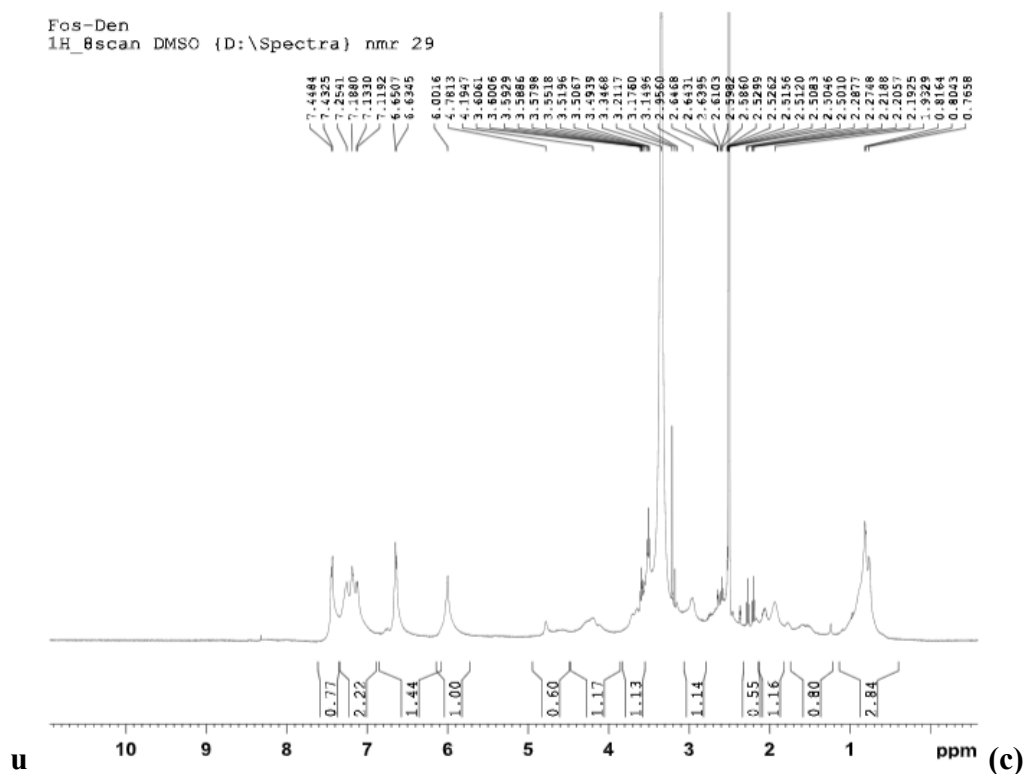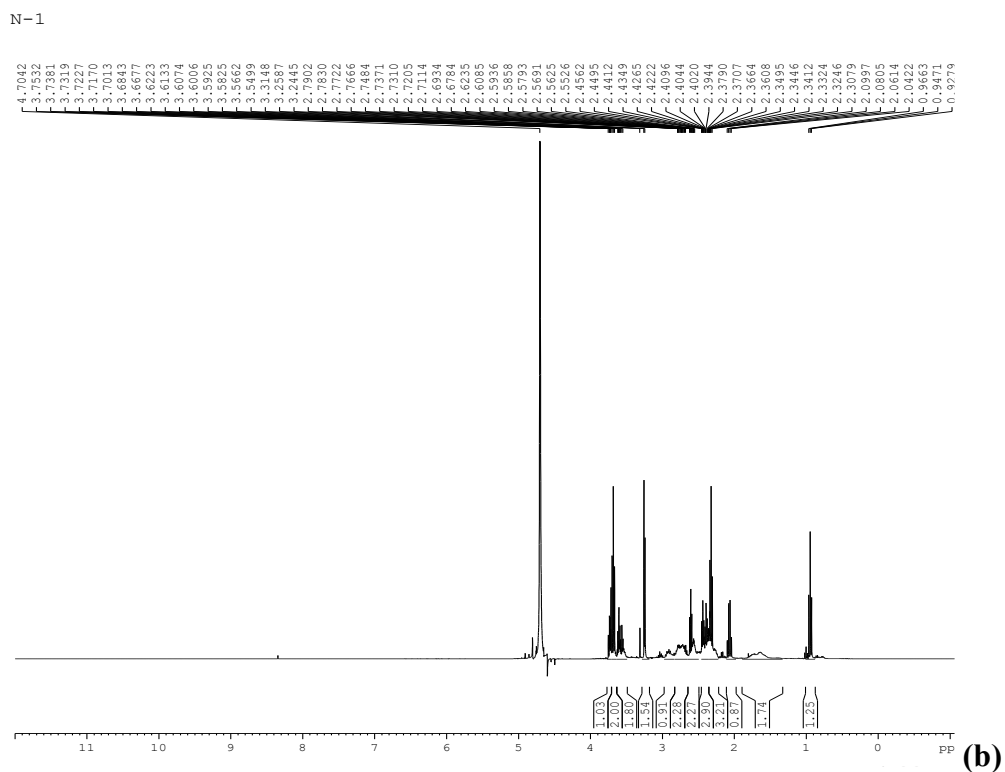
Figure 95: NMR spectra of (a) FPV (b) Dendrimers (c) FPV-DEN

The NMR spectra of plain drug FPV, dendrimers, and FPV-DEN are shown in Figure 95. The drug was subjected to ^{1}H NMR spectroscopy and studied for the presence of different peaks corresponding to different protons in the FPV structure confirming the purity of the drug. H3 and H7 aromatic protons show their presence at H3 and H7 at δ 6.83 ppm, and other aromatic protons H4 and H6 show their doublet at δ 7.62 ppm. The H18, H19, and H20 show resonance at δ 7.21 to δ 7.23 ppm, a pair of doublets corresponding aromatic methine proton at H17 and H21 found at δ 7.30 ppm. Doublets observed at δ 0.77 and 0.78 ppm correspond to H10 and H11 of methyl proton. Five pairs of multiplets for methyl protons containing non-equivalent protons at δ 2.59-2.64 ppm, δ 2.97-2.99 ppm responded to H8 a,b, δ 2.71- 2.76 ppm, δ 3.53-3.54 ppm responded to H-12a,b, δ 2.55-2.59 ppm, δ 3.00-3.03 ppm responded to H-15a,b, δ 1.8 ppm, δ 1.93-1.95 ppm corresponded to H-25a,b, δ 3.2838-3.2889 ppm, δ 3.53-3.54 ppm corresponding to H-26a,b. Multiplets at δ 1.93 ppm, δ 3.7.3-8 ppm correspond to methine proton H9, H-13, H-14, and H-24. The H 27 a,b corresponds to δ 3.59-3.68 ppm, and doublets at δ 6.86 ppm correspond to the carbamate group (Singh et al., 2019).

The NMR spectrum of the 5G PPI dendrimer is shown in Figure 26. The NMR spectra of dendrimers confirm the presence of protons as per the literature. Multiplets were observed between δ 0.9 ppm corresponding to -CH$_2$ of methylene groups of EDA. the chemical shifts between δ 1.74 ppm corresponding to -CH2-CH2-, the peak at δ 2.34-2.36 ppm corresponds to -NH2, multiple peaks at δ 2.40–2.69 ppm due to N[C]C and multiplets between δ 2.71–2.79 ppm corresponds to -CH2-NH2 (Kumar et al., 2006; Gajbhiye et al., 2013).

The NMR spectra of FPV-DEN indicate many protons due to the incorporation of the drug FPV in the dendrimers which were not present in the NMR spectra of dendrimers. Alteration in a chemical shift at δ 2.33 ppm indicated the attachment of the methyl group of the drug with a surface amino group of dendrimers. The multiplets at δ 0.7-0.8 ppm correspond to isopropyl methyl proton altered indicating the attachment of the methyl group of the drug and terminal amine group of dendrimers. Aromatic protons are visible above δ 7.00 ppm, and chemical shift at δ 6.85 ppm corresponds to carbamate proton. The dendrimer structure has an abundance of protons in its surroundings due to a heavily conjugated and complex structure that

corresponds to various peaks and splitting patterns (Monteiro et al., 2016, Srivastava et al., 2023).

5.7.4.2.3 Differential scanning calorimetry

The conjugation of FPV-DEN was also confirmed by DSC studies and given in Figure 96. DSC studies of dendrimer indicated that sharp peak at 88.6 °C. The peak was observed at 315.53 °C for FPV and 104.3 °C for the drug-loaded dendrimers. It was observed that the transition temperature showed a negative shift confirming the strong interactions between dendrimers and FPV (Ramana et al, 2010). The transition of the peak indicated that the endothermic capability was altered which confirmed that the drug was conjugated with dendrimers (Yang et al., 2022).

(a)   (b)   (c)
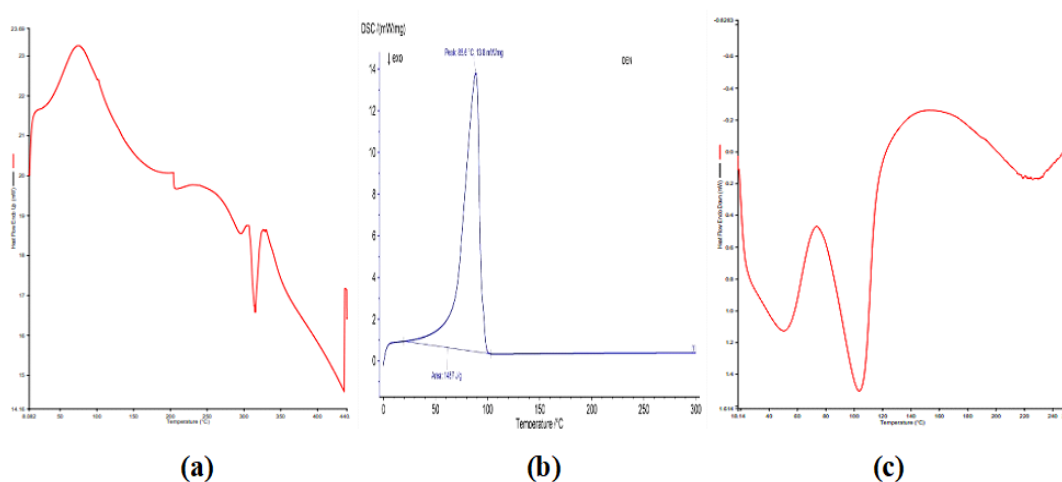
Figure 96: DSC images of (a) FPV (b) Dendrimers (c) FPV-DEN

5.7.4.2.4 Field emission scanning electron microscopy

(a)   (b)
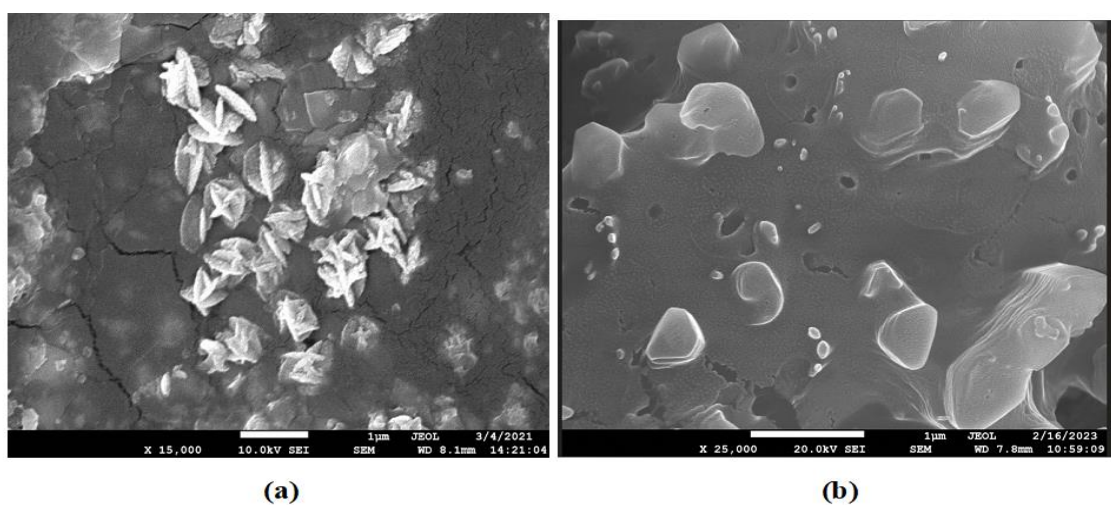
Figure 97: FE-SEM images of (a) Dendrimer (b) FPV-DEN

Figure 97 represents the image of dendrimers and FPV-DEN. The FE-SEM image indicated that the surface topography did not change when the FPV was loaded in the dendrimer structure. The image indicated that the structure of dendrimers in drug-loaded dendrimers remained unchanged as compared to plain dendrimers. Spherical structure dendrimers were observed in the microscopic image indicating that the process of drug loading did not alter the surface topography of the dendrimer. The structural characteristics did not alter the conjugation of the drug.

5.7.4.2.5 Particle size distribution
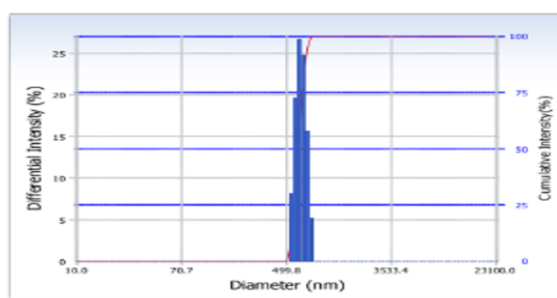
Figure 98: Particle size distribution of FPV-DEN

The size of dendrimers and FPV-DEN were determined using Delsa nano (Beckman counter). Figure 98 shows the particle size distribution of FPV-DEN. The size of a particle of the dendrimers was found to be 41.9 nm and PDI was found to be 0.379. The size of particle of drug-loaded dendrimers was found to be 172.6 nm and PDI was found to be 0.379. The result indicated that the prepared drug-loaded dendrimer was found to be in the nano-range and PDI indicated that the structure is uniformly distributed. Table 36 represents the particle size and PDI of dendrimers and FPV-DEN.

Table 36: Particle size and zeta potential of dendrimers and FPV-DEN

	Particle size (nm)	PDI
5G PPI Dendrimer	41.9	0.379
FPV-DEN	172.6	0.379

5.7.4.2.6 Entrapment efficiency

The drug entrapment efficiency FPV-DEN was determined using an indirect method using a dialysis membrane (MWCO 7000 Da, Himedia, India). The entrapment efficiency was found to be 69.83±0.31%. The terminal functional group increases the sites of interaction of drugs by covalent linking and also binds non-covalently by

hydrogen bonding or hydrophobic interactions as the drug was also hydrophobic. The drug can also entrap and form bonds inside the dendritic structure (Tripathi et al., 2020).

5.7.4.2.7 *In vitro* **drug release**

The drug release studies of FPV-DEN were performed in two different pH mediums, at PBS pH 7.4 which corresponds to systemic pH, and at acetate buffer pH 5 which corresponds to the internal environment of the macrophages. The dialysis membrane method used for the release study revealed initial fast release followed by sustained release in both the release medium. The drug FPV was reported to have higher solubility at lower pH (pH 3.3) which reduces with increases in pH (Ford et al., 2005). The release study revealed the higher drug release at lower pH 5 (80.18±0.64) as compared to pH 7.4 (68.08±1.78). Table 37 includes the drug release profile of FPV from FPV-DT in acetate buffer pH 5 and PBS pH 7.4 for 96 h. Figure 99 and 100 showed the drug release Profile of FPV from FPV-DT in acetate buffer pH 5 and PBS pH 7.4 for 96 h and 8 h. The drug release profile suggests the better release of the drug at lower pH and the macrophage has an acidic environment inside the cell, thus the drug will be better released in the internal environment of the cells.

Table 37: Drug release profile of FPV from FPV-DEN

Time	% Cumulative drug release	
	Acetate buffer pH 5	**PBS pH 7.4**
0	0±0	0±0
1	5.98±3.53	7.56±1.56
2	15.01±3.71	14.61±4.55
3	18.98±2.50	21.66±2.35
4	25.79±0.13	24.63±1.71
5	28.85±1.33	28.13±1.07
6	39.16±0.77	32.69±1.66
7	46.17±0.57	36.27±2.53
8	51.10±0.64	40.35±2.71
24	60.03±2.01	47.82±2.02
30	65.59±2.04	53.27±1.69
48	68.52±1.82	60.90±1.28
72	77.22±1.73	64.39±1.70
96	80.18±0.64	68.08±1.78

*The data was represented as Mean±SD (n=3)
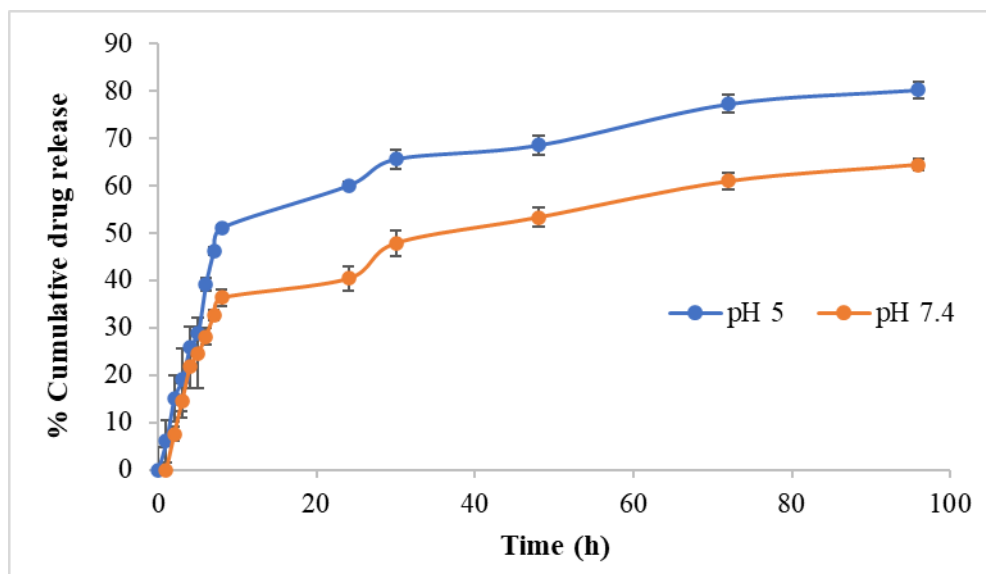
Figure 99: Drug release profile of FPV-DEN for 96 h (n=3)
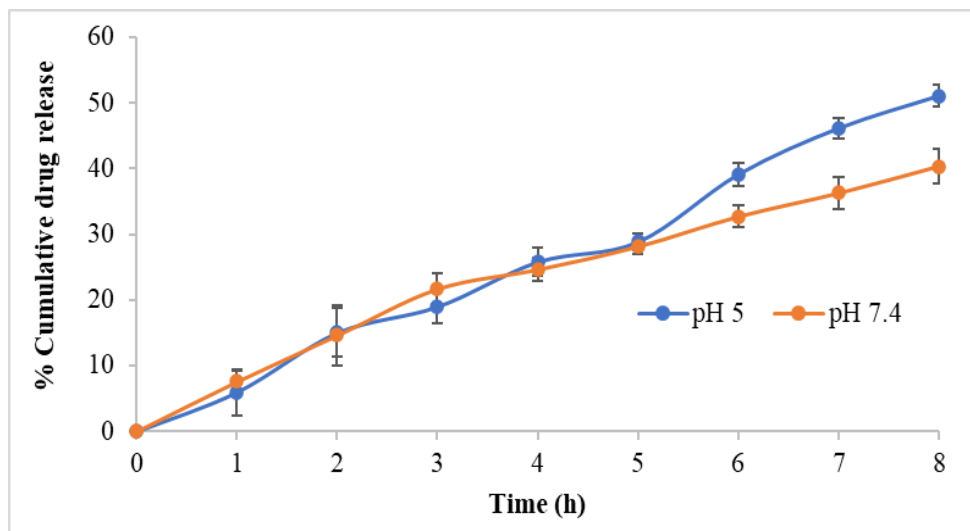
Figure 100: Drug release profile of FPV-DEN for 8 h (n=3)

5.7.4.2.8 Drug release kinetics

Table 38: Drug release kinetics of FPV from FPV-DEN showing R^2 value and n

S.No	Release	pH 5		pH 7.4	
		R^2	n	R^2	n
1	First-order	0.8500		0.8404	
2	Zero-order	0.6800		0.7160	
3	Korsmeyer-Peppas	0.7235	0.6667	0.6816	0.5974
4	Higuchi	0.9052		0.909	
5	Hixon	0.7961		0.8015	

Different mathematical models are used to correlate the release pattern zero and first order, Higuchi model, Korsmeyer-Peppas model, and Hixon-Crowell model. The results were tabulated in Table 38. The most-fitted model was based on the value of regression, the higher the value better the model fitted.

Both the release profile was subjected to the release kinetics model and the R^2 value was calculated. From the kinetics model, it was concluded that the most-fitted model was found to be the Higuchi model with the highest R^2 value of 0.9052 for pH 5 and 0.909 for pH 7.4. The release exponent indicated the drug transport mechanism through the polymer. The Higuchi model helps to understand the drug release from an insoluble matrix. The release pattern showed an initial fast release followed by a decrease in release with time. In this system concentration of the drug is much higher than it releases and acts as a driving force. As time proceeds concentration gradient changes reducing the diffusion and subsequently reducing the drug release (Haroun et al., 2018). For pH 5, the n value was determined to be 0.6667, and for pH 7.4, it was 0.5974. The value suggests that the fickian diffusion model governed the release.

The drug release was subjected to other release models, lowest R^2 value was found to be for the first order. The value for the first order was found to be 0.85 for pH 5 and 0.8404 for pH 7.4, a lower value of R^2 makes it unsuitable. The zero-order model was also unsuitable as the value of the correlation coefficient was 0.68 for pH 5 and 0.716 for pH 7.4. The Higuchi model also showed a lesser R^2 value of around 0.7235 for pH 5 and 0.6816 for pH 7.4. The Hixon Crowell model was also found unsuitable as the value of R^2 was found to be 0.7961 for pH 5 and 0.8015 for pH 7.4
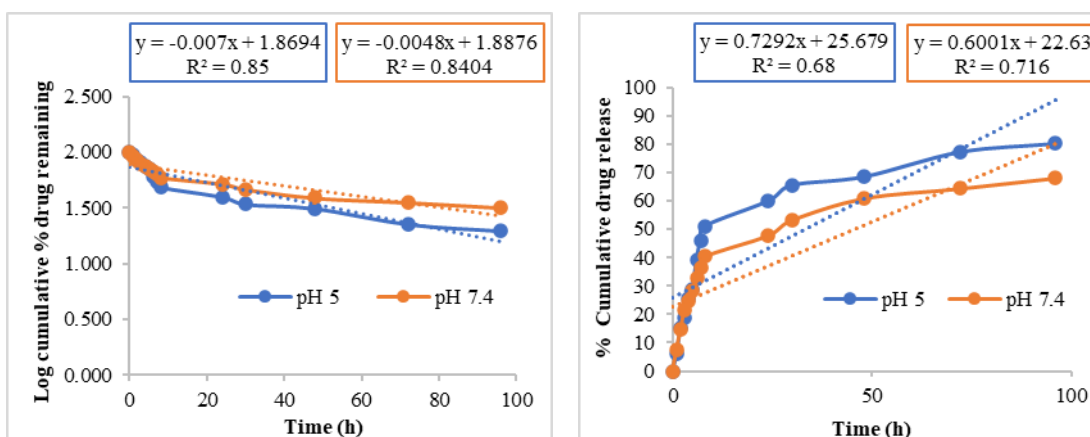
(a) First order release kinetics   (b) Zero order release kinetics
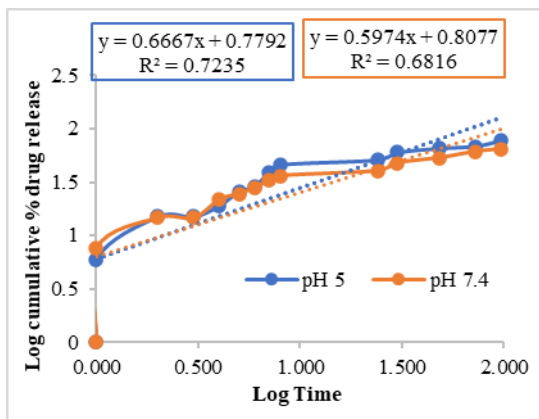
(c)Korsmeyer Peppas release kinetics
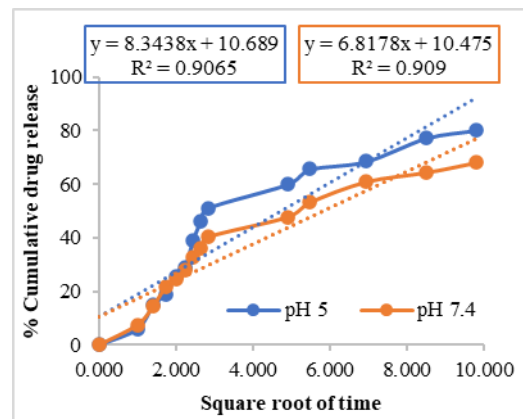
(d) Higuchi release kinetics
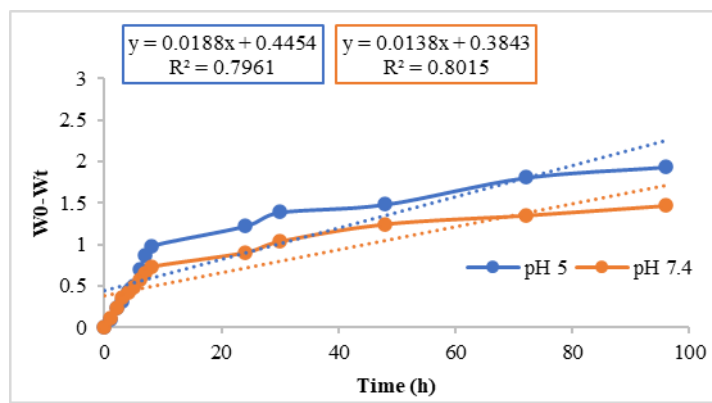
(e) Hixon-Crowell release kinetics

Figure 101. Drug release kinetics of FPV-DEN

5.7.5 Formulation development and characterization of Fosamprenavir calcium-loaded COOH-MWCNT

5.7.5.1 Formulation development of Fosamprenavir calcium-loaded MWCNT

In Fosamprenavir calcium-loaded COOH-MWCNT (FPV-CNT), drug FPV was loaded on the COOH-MWCNT with constant stirring for 48 h using a magnetic stirrer. The drug binds with the surface COOH of the MWCNT by covalent linkage and is also arranged by π- π stacking. The structure was characterized using different characterization techniques such as spectroscopic analysis, morphological studies, and cytotoxicity studies.

5.7.5.2 Characterization of FPV-CNT

5.7.5.2.1 FTIR Spectroscopy
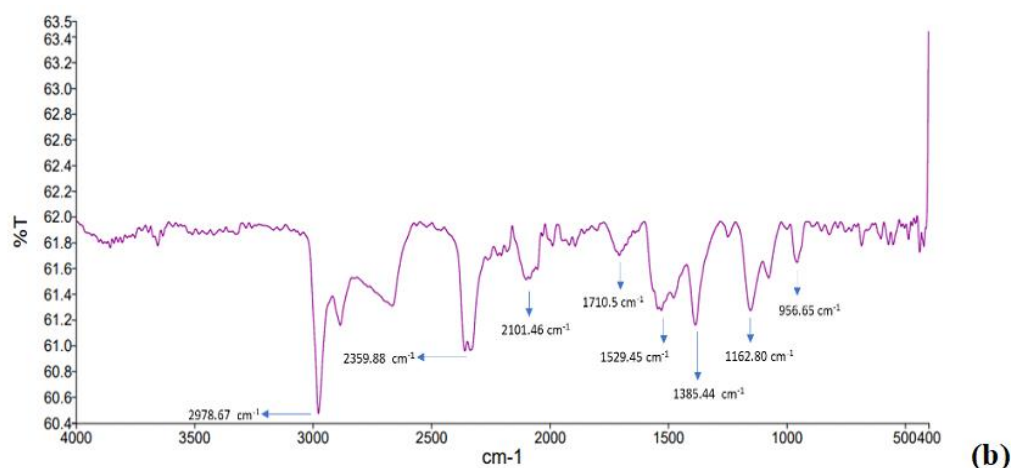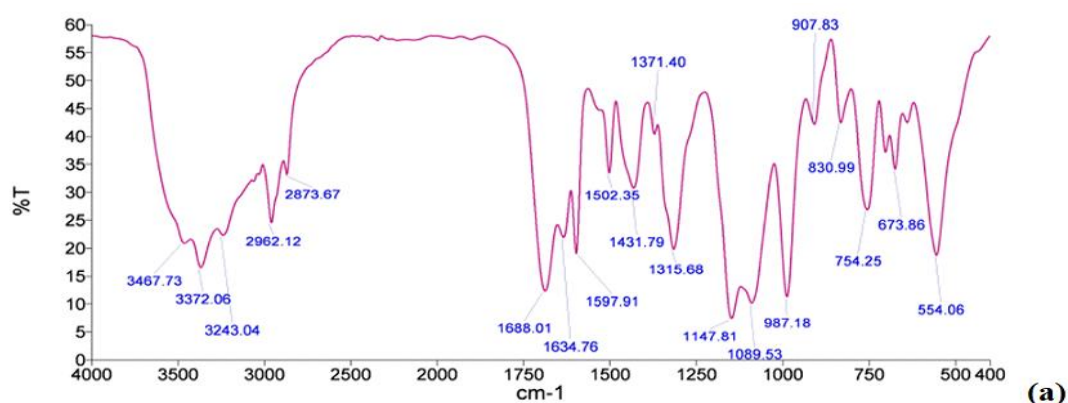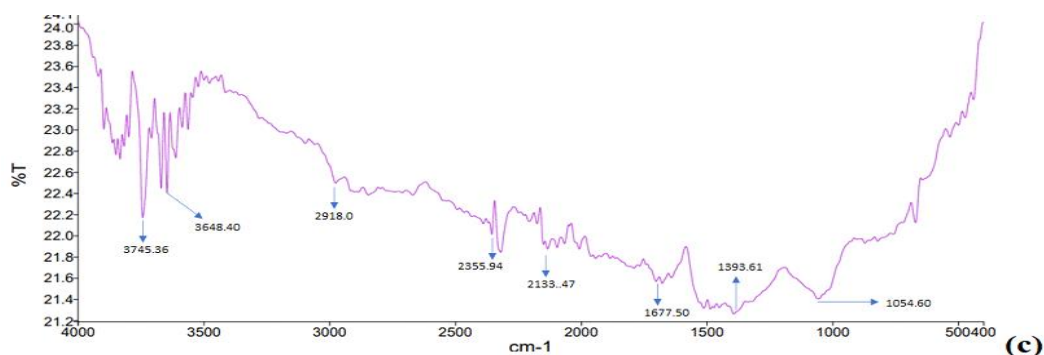
Figure 102: FTIR spectra of (a) FPV (b) COOH-MWCNT (c) FPV-CNT

Figure 102 showed FTIR peaks for FPV, COOH-MWCNT, and FPV-CNT. FTIR spectrum of FPV indicates a sharp peak at 3372.0 cm^{-1} reflecting the presence of stretching of O-H; the medium intensity peak found at 3243.04 cm^{-1} are the stretches of an amino group (N-H) corresponding to amide and amine functional group. The peak at 1688.01 cm^{-1} was the peak of stretched of C=O, the peak of higher intensity was observed at 1597.91 cm^{-1} and 1502.3 cm^{-1} confirms the stretches of C=C; medium intensity C=H stretches of the aliphatic isopropyl chain observed at 1431.79 cm^{-1}, 1315.68 cm^{-1} corresponds to stretching of C-N of the amine group, the peak shows high to medium intensity, 1089.53 cm^{-1} and 1147.81 cm^{-1} peaks correspond to an asymmetrical stretch of S=O; a region with high intensity, at 987.18 cm^{-1} the peak of high intensity due to stretching of C-O of ether and phosphate esters (Cordeiro et al., 2020).

The vibrational stretching of the OH group is represented by a prominent peak at 2978.67 cm^{-1} in the FTIR spectrum of MWCNT-COOH, while the carbonyl group's distinctive peak was found at 1710.50 cm^{-1}. In addition, the peak of OH of COOH is correlated with a peak at 1385.44 cm^{-1}. The aromatic C-H is bent out-of-plane, as indicated by the peak at 956.65 cm^{-1}. The significant functional group on MWCNT was validated by the occurrence of peaks. The presence of MWCNT is confirmed by the presence of all the major peaks (Zhang et al., 2018).

The presence of the NH group is confirmed by FPV-CNTs FTIR spectrum, which also revealed an asymmetric methyl stretching peak at 2918.0 cm^{-1} and peaks at 3648.0 and 3745.0 cm^{-1}. the C-H aliphatic stretching peak at 1677.50 cm^{-1}. The isopropyl group, 1054.60 cm-1 high-intensity asymmetrical stretch S=O, which was the

distinctive peak of FPV, correlates to the medium intensity peak at 1396.61 cm-1. Table 39 shows the FPV-CNT's FTIR spectrum. (Tanet al., 2014; Singh et al., 2016).

Table 39: FTIR spectrum of plain drug FPV-CNT

Observed peaks frequency (cm^{-1})	Standard FTIR range (cm^{-1})	Corresponding functional group
3648.0 and 3745.0	3500-3100	Broad altered band of N-H stretching
2918.0	3150-3050	C-H stretching
1683.90	1630-1680	C=O (amide) group
1396.51	1375-1450	C-H isopropyl stretch
1054.60	1050-1375	-S=O

5.7.5.2.2 Raman Spectroscopy
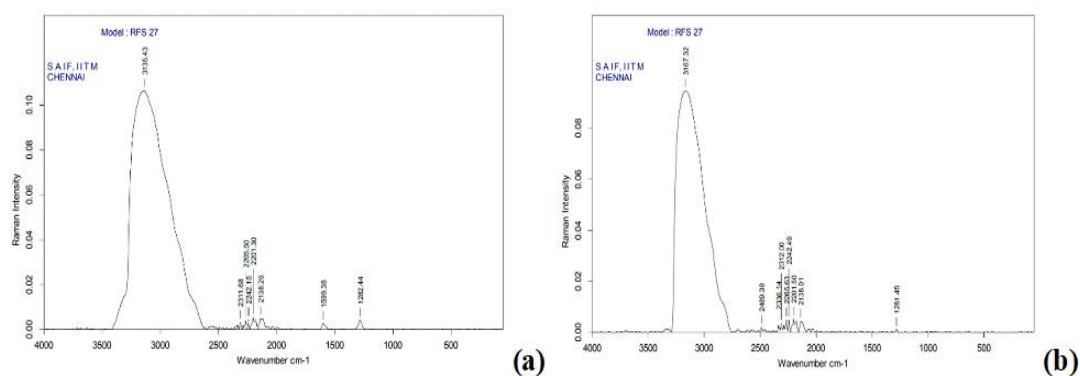
Figure 103: Raman Spectra of (a) COOH-MWCNT (b) FPV-CNT

A potent method frequently used to assess the structural quality of functionalized CNTs is Raman spectroscopy. Figure 103 represents the Raman spectroscopy of COOH-MWCNT and FPV-CNT. There were two distinct peaks visible, one of which was assumed to be the G band, which was produced by the tangential vibrations of the carbon atoms and was placed at 1580 cm^{-1}. Due to the significant imperfections or abnormalities in carbon nanostructures, a second one, measuring approximately 1282.44 cm^{-1}, was dubbed the D band. In contrast to the COOH-MWCNTs, the Raman spectra of the FPV-CNT did not exhibit a discernible G-band, and the D-band peak intensity was significantly weaker and somewhat skewed towards a lower frequency. This indicates that the unique absorption peaks were significantly reduced during the conjugation process, indicating that the interactions between COOH-MWCNTs and drugs are potent enough to alter the nanotubes' structural makeup (Wang et al., 2020, Srivastava et al., 2024).

5.7.5.2.3 XDR spectrum
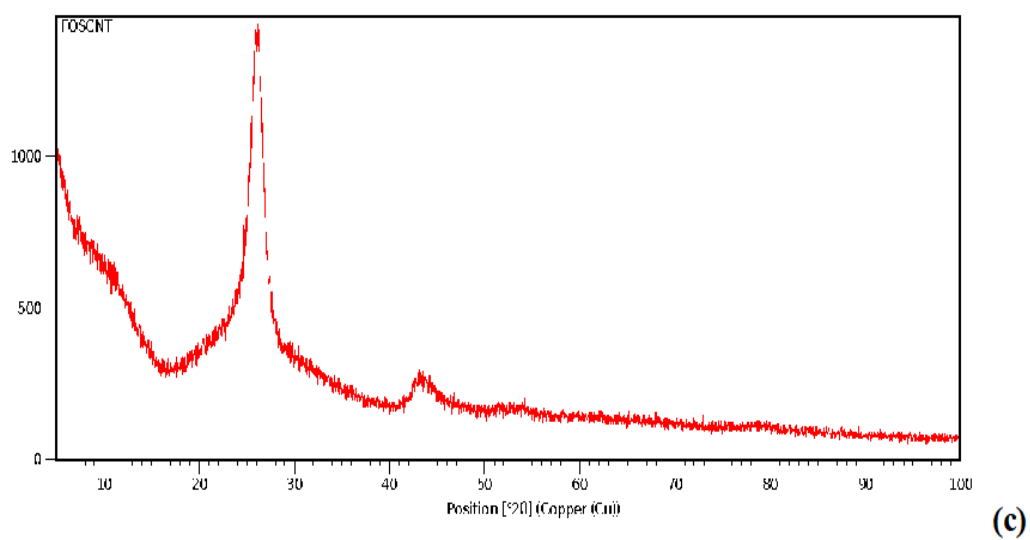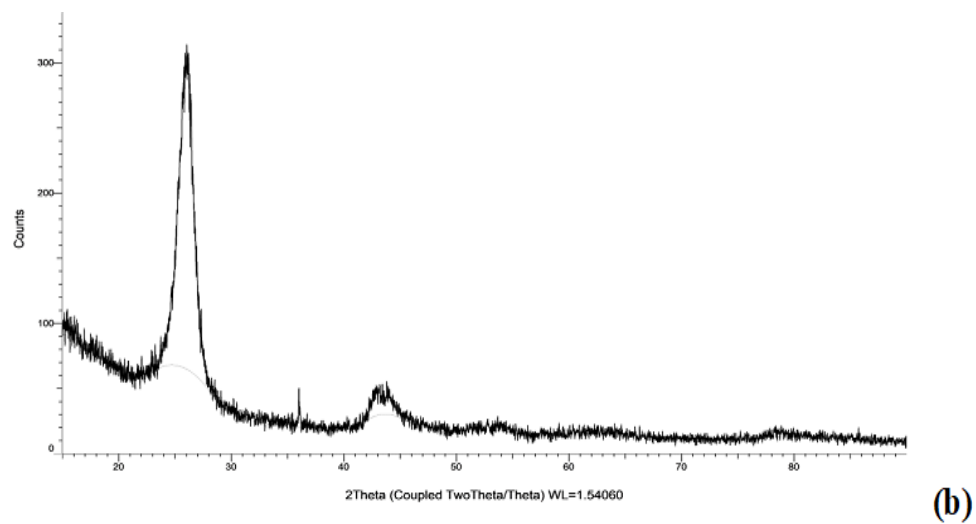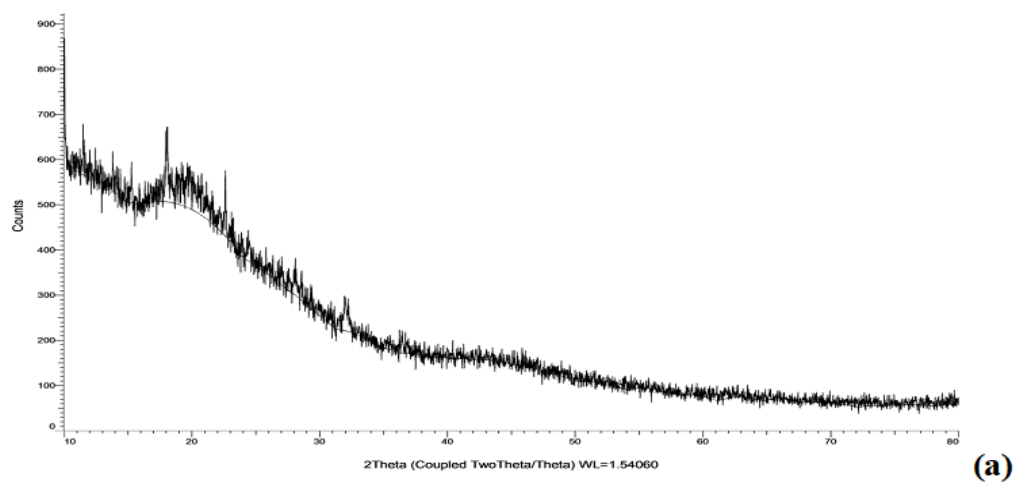
Figure 104: XRD of (a) FPV (b) COOH-MWCNT (c) FPV-CNT

Figure 104 shows the pattern of XRD of plain drug FPV, COOH-MWCNT, and FPV-CNT. Sharp peaks were not observed in the XRD diffraction pattern of plain FPV in the diffractogram, which suggests that the plain drug was in an amorphous form. One broader peak was observed near $20^{°}$ in the diffractogram of MWCNT, which was present in the FPV-CNT diffraction pattern, indicating the loading of FPV in COOH-MWCNTs in molecular form. Observing the diffraction pattern of COOH-MWCNT and FPV-CNT, no new peaks were observed and the pattern remains the same. The unchanged pattern of FPV-CNT reflects that the crystallinity of carbon nanotubes was not affected due to the loading of the drug. Parallel XRD patterns were also obtained by Zheng et al., 2010 and Kayat et al, 2016 on the biomaterial-loaded nanotubes (Zheng et. al., 2010; Kayat et al, 2016).

5.7.5.2.4 Scanning electron microscopy
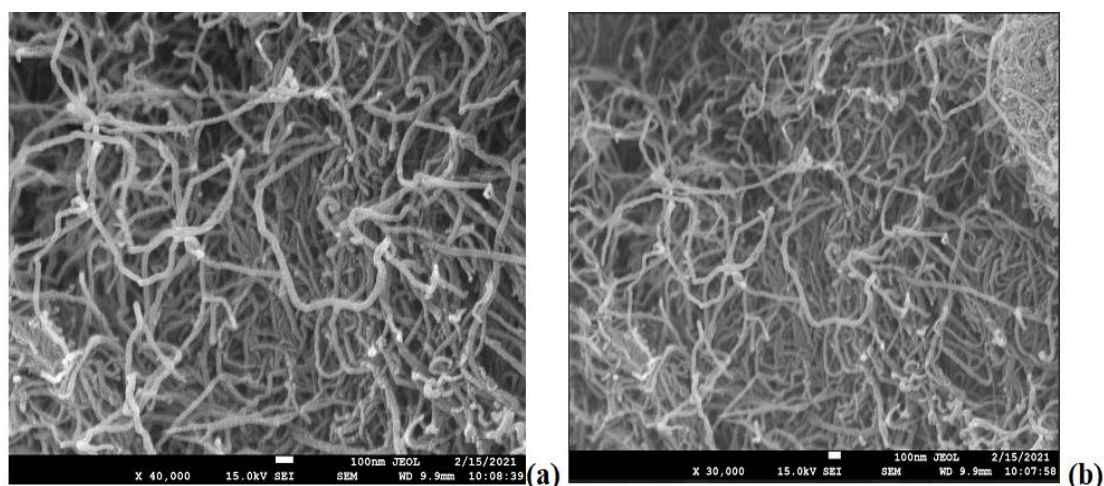
Figure 105: FE-SEM image of (a) COOH-MWCNT (b) FPV-CNT

The SEM images at higher magnifications shown in Figure 105 revealed the microscopic image of functionalized MWCNT and FPV-CNT. The image clearly indicated the nanosized long thread-like structure of COOH-MWCNT. FE-SEM images help to examine the surface of the structure and enable the observation of fracture surfaces. The FPV-CNT structure did not indicate any fracture or breakage on its surface. The size of the FPV-CNT was found to be irregular because of the random attachment of the drug molecules on the surface of the nanotube network (Zhu et al., 2019; Qi et al., 2016).

5.7.5.2.5 Atomic force microscopy

(a)   (b)
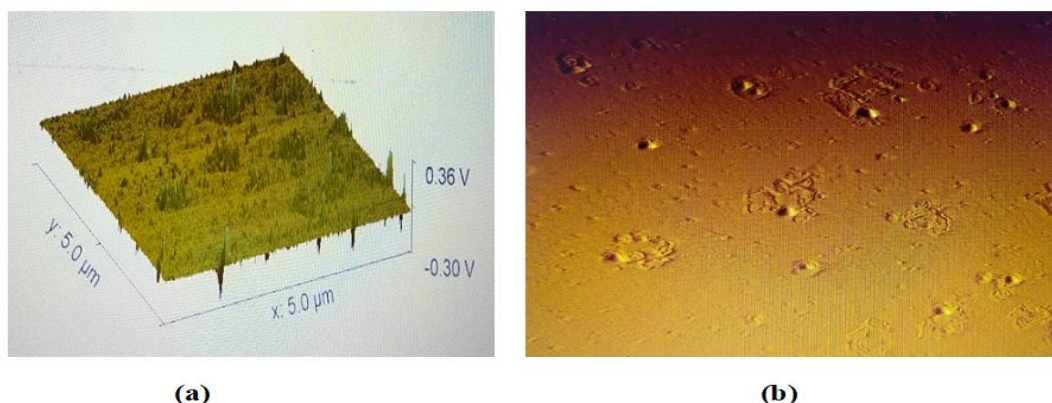
Figure 106: AFM image of FPV-CNT (a) 3D image of FPV-CNT (b) 2D image of FPV-CNT

AFM pictures aid in describing the drug-loaded nanotubes' morphology. The AFM picture, 3D image, and 2D image of FPV-CNT are shown in Figure 106. The picture clearly showed the existence of tube-like morphology all around the picture. At 5 nm, the width and height were recorded. (Singh et al., 2016).

5.7.5.2.6 Particle size distribution and zeta potential
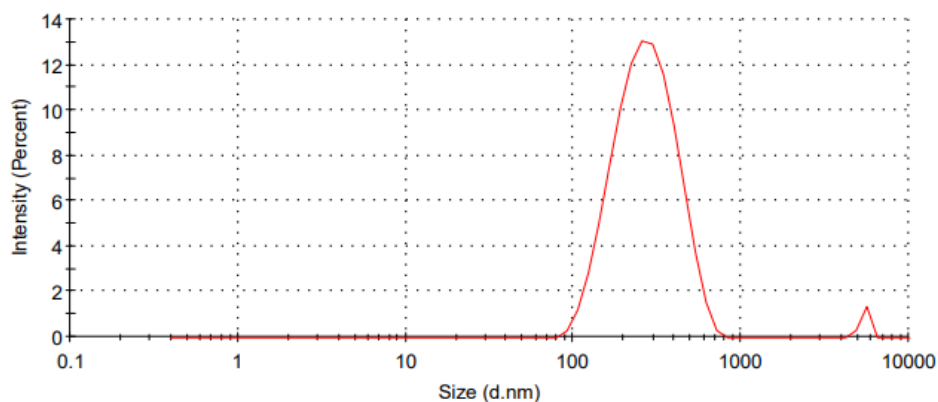
Figure 107: Particle size analysis of FPV-CNT

The principle of the Malvern zeta sizer is based on dynamic light scattering which helps to determine the hydrodynamic diameter of the MWCNT structure which is relatable to the diameter of the particle and the zeta potential of the material. The polydispersity index (PDI) and Z- average diameter were determined using a Malvern metasizer which can be related to the diameter of the prepared nanostructure and its zeta potential. Figure 107 represents the particle size distribution of FPV-CNT. The Z average diameter for COOH-MWCNT was found to be 262.5 d nm with PDI 0.590.

Higher PDI was found for COOH-MWCNT as MWCNT tends to form aggregates of various sizes. The Zeta potential was found to be - 8.01 mV and conductivity was found to be 0.446 mS.cm^{-1}. The MWCNTs possess a negative charge on their surface due to the availability of few free carboxylic groups and the zeta potential of magnitude 8 implies that the MWCNTs are slightly agglomerated (Prajapati et al., 2019, Komane et al., 2018). The Z average diameter was found to be 290.1 and PDI was found to be 0.390. The zeta potential value was found to be 0.230 mV. Zeta potential tends to shift from a negative scale to positive 0.230 which may be due to the cationic group due to the presence of calcium and amino group in FPV which led to the positive zeta potential of FPV-CNTs (Dong et al., 2017). The value still indicates that the structure was aggregated. Change in zeta potential confirms the conjugation of FPV with CNT (Lodhi et al., 2013). Table 40 represents the size distribution, PDI, and zeta potential of FPV-CNT.

Table 40: Size Distribution, PDI and Zeta Potential

Formulations	Particle size (nm)	PDI	Zeta potential (mV)
COOH-MWCNT	262.5	0.590	-12.5
FPV-CNT	290.1	0.390	0.230

5.7.5.2.7 Entrapment efficiency

The drug entrapment efficiency of FPV-CNT was 79.57 ± 0.4 %. As the drug has an aromatic structure helps to bond strongly with the sidewall and ends of the carbon nanotube structure by hydrophobic interaction along with stacking (Sharma et al., 2016).

5.7.5.2.8 *In Vitro* **Drug Release**

Table 41: Drug release Profile of FPV from FPV-CNT

Time (min)	% Cumulative drug release	
	Acetate Buffer pH 5	**PBS pH 7.4**
0	0±0	0±0
0.5	1.59±2.003	5.60±3.093
1	9.39±3.12	7.25±3.161
1.5	13.93±2.01	9.19±1.82
2	20.45±1.66	16.30±3.40
3	25.32±2.25	18.53±3.37
4	33.95±3.93	19.61±4.17
5	37.69±3.99	25.21±3.66
6	47.28±1.03	34.91±2.62
7	55.96±2.24	37.56±1.57
8	67.47±2.00	44.39±2.73
24	83.42±3.36	70.10±4.85
30	87.76±3.02	76.99±1.97
48	89.26±2.34	79.342±2.71
72	91.50±3.22	84.32±3.72
96	94.53±2.88	91.43±2.85

*The data was represented as Mean±SD (n=3)
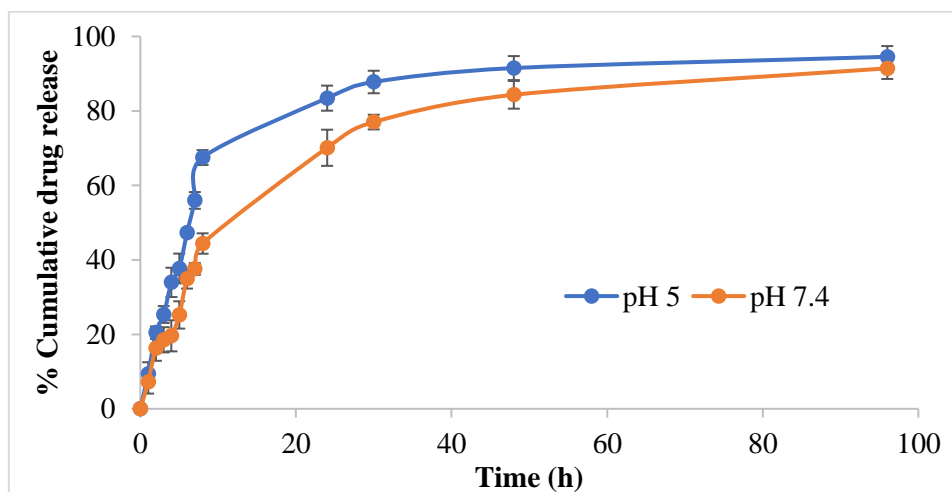
Figure 108: *In vitro* **drug release of FPV-CNT for 96 h (n=3)**
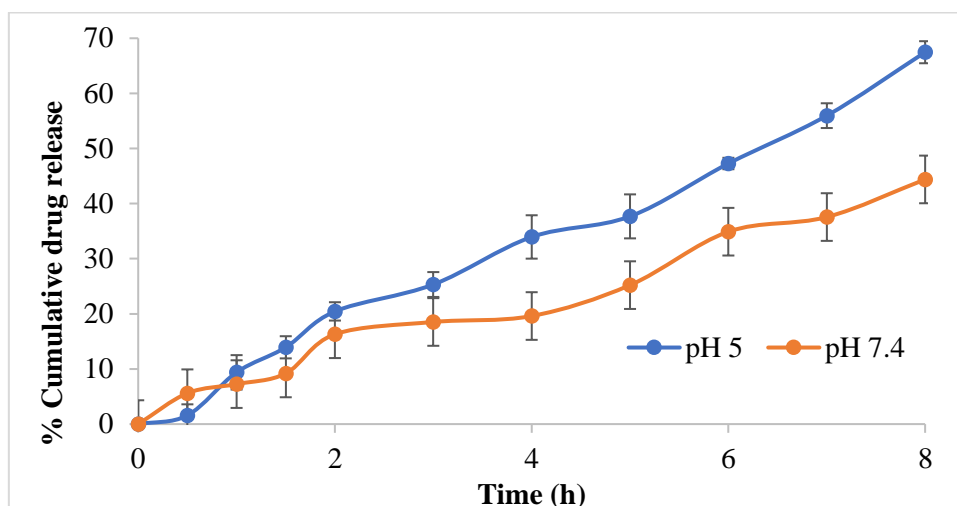
Figure 109: *In vitro* **drug release of FPV-CNT for 8 h (n=3)**

It is important to perform the release behavior and pattern of the delivery system. A sustained release system helps to reduce drug-related toxicity and improves the systemic concentration and bioavailability of the drug. Different factors such as pH, surface properties, carrier characteristics, and particle size affect the release mechanism of the drugs from the delivery system (Milosavljevic et al., 2017). Figures 108 and 109 indicate the *in vitro* releases of the drug from FPV-CNTs for 96 h and 8 h. The system shows initial fast release followed by slow drug release indicating a biphasic release pattern. An *in-vitro* releases study was carried out in acetate buffer pH 5 and PBS pH 7.4 and the release pattern was observed for 96 h. It showed that the prepared FPV-CNT has a sustained release pattern. The cumulative release was found to be 94.53 ± 2.88 % in acetate buffer pH 5 and 91.43 ± 2.58 % in 96 h. The higher release was observed with MWCNT due to carboxylated MWCNT which was hydrophilic and tends to make hydrogen bonds with water molecules. It helps to drag and bind with water and helps to bring water near drug molecules which helps to improve the dissolution rate. The drug molecules that are surface adsorbed but not bound to MWCNTs were responsible for the first release, which was succeeded by the drug that was attached to the MWCNTs' surface and released gradually. (Vatanpour et al., 2017).

5.7.5.2.9 Drug release kinetics

The mechanism and release kinetics of FPV-CNT were determined, and release data was subjected to different kinetics equations. such as the zero-order model, first-order model, Hixson-Crowell model, Higuchi model, Korsmeyer-Peppas model. For

the various models, the regression coefficient and release constant for FPV-CNT were examined. Comprehending the drug release mechanism and its kinetics from the MWCNT delivery device is crucial. (Dlamini et al., 2019). Table 42 represents the drug release kinetics showing R^2 value and n.

Table 42: Drug release kinetics showing FPV from FPV-CNT showing R^2 value and n

S.No	Release	pH 5		pH 7.4	
		R^2	n	R^2	n
1	First-order	0.9276	-	0.9301	-
2	Zero-order	0.6520		0.8300	
3	Korsmeyer-Peppas	0.6988	0.6926	0.7958	0.7222
4	Higuchi	0.9408		0.9558	
5	Hixon	0.9091		0.934	

Various models, including Hixon Crowell, Higuchi distribution model, First order dynamics, zero-order dynamics, and Korsmeyer & Peppas (K–P) equation, were applied to data gathered from the drug release investigation (Nivethaa et al., 2016). The model with the greater value was chosen as the best-fitted model for that release profile, taking into account the degree of coefficient correlation. The zero-order pattern of release for the FPV-CNT release showed the lowest R^2 value. The zero-order dynamics model's correlation coefficient, which stands at 0.711, indicates that it is not appropriate for the FPV-CNT release data. Since the correlation coefficient was 0.755, Korsmeyer-Peppas' model was likewise inappropriate. Additionally, the Hixon Crowell model is less suitable for the drug release model with a correlation coefficient value of less than 9. With a correlation coefficient value of 0.9408 for pH 5 and 0.9558 for pH 7.4, the Higuchi distribution model was found to fit the data from the various kinetic models the best. First-order kinetics came in second with values of 0.9276 and 0.9301 for pH 5 and pH 7.4, respectively. Because the discrepancy between the observed curve and the release profile was the smallest, the Higuchi distribution model outperforms the First-order dynamics model.

Although the release of FPV-CNTs does not conform well to the K-P model, it provides insight into the process of drug release via diffusion exponent n. The paragraph aids in figuring out how the medication is released from the delivery device.

For pH 5 and pH 7.4, the values of n for FPV-CNT release were determined to be 0.6926 and 0.7222, respectively. The value suggests that a non-fickian diffusion model regulated the release. As a result, the Higuchi model and the first-order dynamics model best explained the in vitro drug release of the FPV-CNT formulation, since these graphs demonstrated maximal linearity. (Ghoshal et al., 2014; Hosseini et al., 2016). Figure 110 represents the drug release kinetics of FPV-CNT at pH 5 and pH 7.4
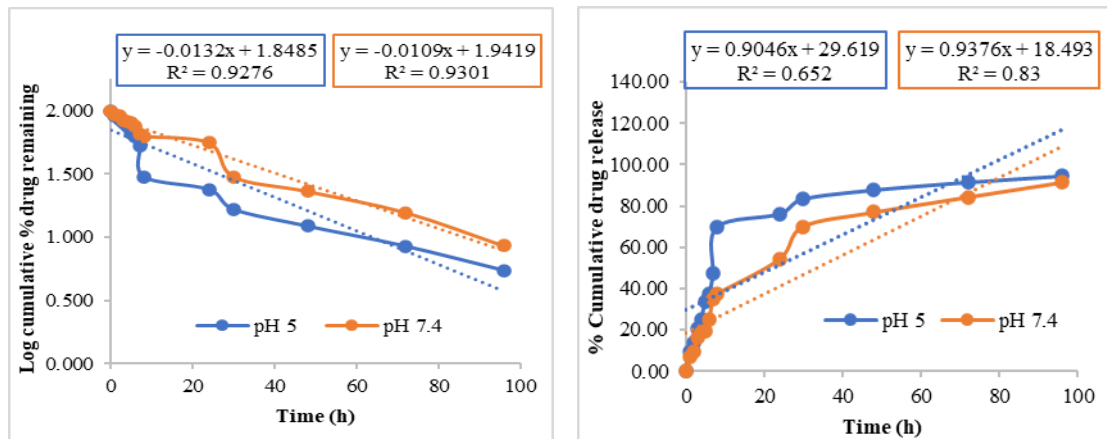
(a) First order release kinetics
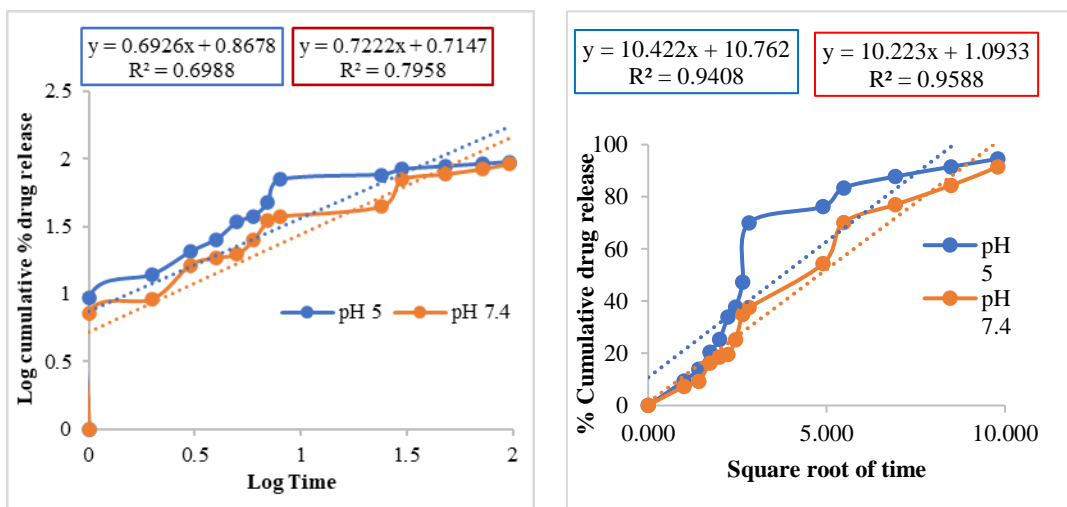
(b) Zero order release kinetics

(c) Korsmeyer-Peppas release kinetics

(d) Higuchi release kinetics
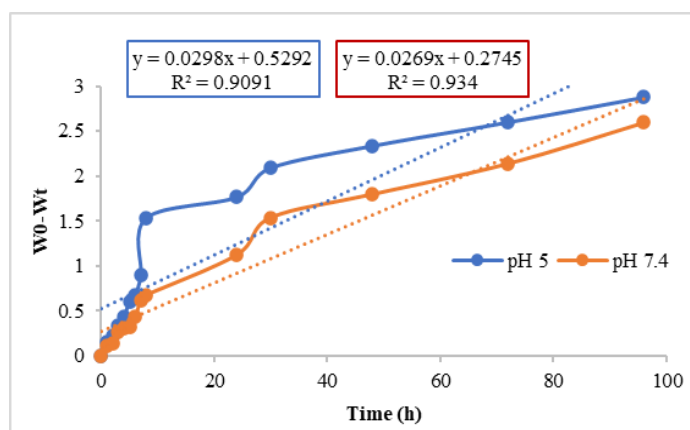
(e) Hixon-Crowell release kinetics

Figure 110. Drug release kinetics of FPV-CNT

5.7.6 Formulation development and characterization of Fosamprenavir calcium-loaded dendritubes

5.7.6.1 Formulation development of Fosamprenavir calcium-loaded DT

In Fosamprenavir calcium-loaded DT (FPV-DT), drug FPV was loaded on the DT with constant stirring for 48 h using a magnetic stirrer. The drug binds with the surface amine group of the dendrimers attached to DT by covalent linkage and by entrapping in dendrimer structure and by π-π stacking. The structure was characterized using different characterization techniques such as spectroscopic analysis, morphological studies, and cytotoxicity studies.

5.7.6.2 Characterization of FPV-DT

5.7.6.2.1 FTIR spectroscopy
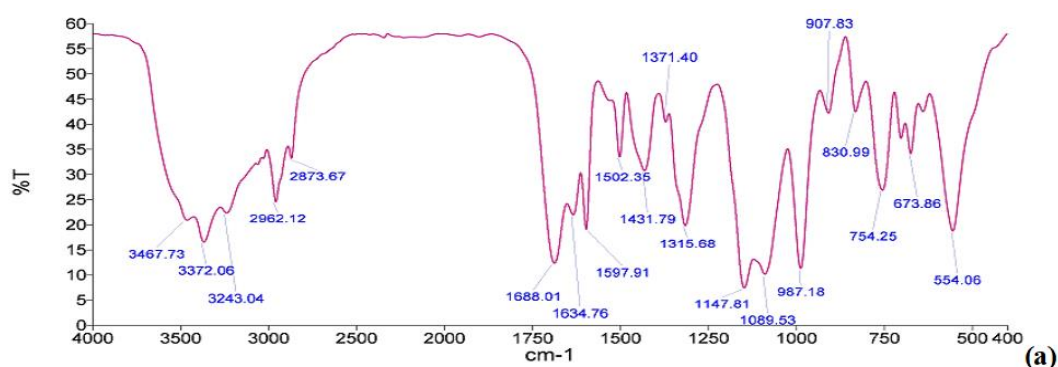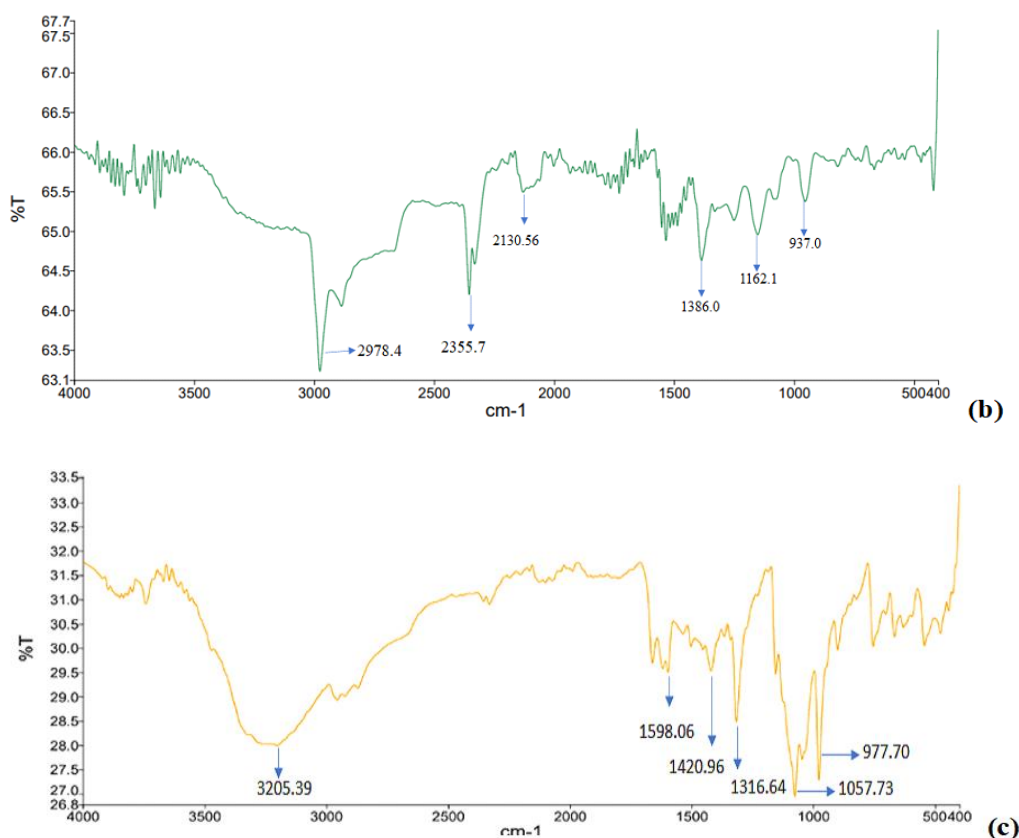
Figure 111: FTIR Spectra (a) Plain drug FPV (b) DT (c) FPV-DT

Figure 111 represents the FTIR spectra of plain drug FPV, DT, and FPV-DT. FTIR spectrum of FPV indicates a sharp peak at 3372 cm^{-1} reflecting the presence of O-H stretches; the medium intensity peak found at 3243.0 cm^{-1} are the stretches of an amino group (N-H) corresponding to amide and amine functional groups. The peak at 1688.01 cm^{-1} was the peak of stretched of aliphatic C-H, the peak of higher intensity was observed at 1597.9 and 1502.3 cm-1 confirms the stretches of C=O correspond to the carbonyl group; C=C stretches of the aromatic ring at 1431.7 cm^{-1}, 1315.1 cm^{-1} corresponds to stretching of C-N of the amine group, the peak shows high to medium intensity, 1089.53 cm^{-1} and 1147.81 cm^{-1} peaks correspond to an asymmetrical stretch of S=O; a region with high intensity, at 984 cm^{-1} the peak of high intensity due to stretching of C-O of ether and phosphate esters (Tan et al. 2014).

The spectrum of DT revealed peaks of 2978.4 cm^{-1} of primary alkene, 1535.5 cm^{-1}, 1640.50 cm^{-1} small peak of amide, 1386.0 cm^{-1} OH bending, 1162.1 cm^{-1} C-O stretching, and 937.00 cm^{-1} aromatic C-H out of plane bending. The bulge in the region of 3000-3500 cm^{-1} was due to the conjugation of the primary amine of a dendrimer with

222

the MWCNT structure. The absence of a stretching peak at 1710.50 cm^{-1} indicates that the COOH group was altered by covalently binding with amine present on the surface of dendrimers.

The spectrum of FPV-DT indicated characteristic peaks at 977.70 cm^{-1} corresponding to C-O Phosphate ether, 1316.64 cm^{-1} corresponding to the sulphonate group of FPV, the peak at 1598.07 cm^{-1} corresponding to the C-C and 1420.96 cm^{-1} corresponds to isopropyl stretch. FPV has a terminal isopropyl group which tends to bind with the primary amine of the DT. The interaction was supported by the FTIR spectrum, the peak primary amine of DT in the range of 3000-3500 cm^{-1} was altered in the spectrum of FPV-DT. Similarly, the peak of the isopropyl group of FPV was also reduced in FPV-DT. This confirms that the drug FPV was loaded on the surface of DT. The covalent bonding was not prominently observed in the spectrum, this may be due to higher π- π stacking in CNT structure as well as due to entrapment of drug in dendrimer molecules (Cordeiro et al., 2020). FTIR spectrum of FPV-DT is tabulated in Table 43.

Table 43: FTIR spectrum of FPV-DT

Observed peaks frequency (cm^{-1})	Standard FTIR range (cm^{-1})	Corresponding functional group
3000-3500	3500-3100	Broad altered band of N-H stretching
1598.07	1475-1600	C=C aromatic carbon
1420.96	1375-1450	C-H isopropyl stretch
1316.64	1300-1000	-C-N stretch
1075.77	1050-1375	-S=O
977.7	900-690	-C-H aromatic (out of plane)

5.6.6.2.2 Raman Spectroscopy

Figure 112 represents the Raman spectra of DT and FPV-DT. The two major bands of DT were observed in the FPV-DT Raman spectra. The G band was observed at 1286.29 cm^{-1} for DT and 1286.67 cm^{-1} for FPV-DT. The D band was observed at 1601.16 cm^{-1} for DT and 1600.11 cm^{-1} for FPV-DT. The G band relates to the crystallinity of the drug and the D band is co-related to the defects of the DT structure. The intensity of the D band and G band of the conjugate of FPV-DT shifted to a very low frequency compared to the D band and G band of DT. This indicated that the conjugation took place between DT and FPV-DT confirming the conjugation.

The I_D/I_G ratio of DT was found to be 1.460 and the I_D/I_G ratio of FPV-DT was found to be 1.904. The increment in the I_D/I_G ratio of FPV-DT indicated that the conjugation of FPV took place on the DT surface which alters the sp2 bonding structure of MWCNTs and leads to the breaking of π bonds holding the hexagonal carbon structure (Muda et al., 2017; Sedaghat et al., 2014).
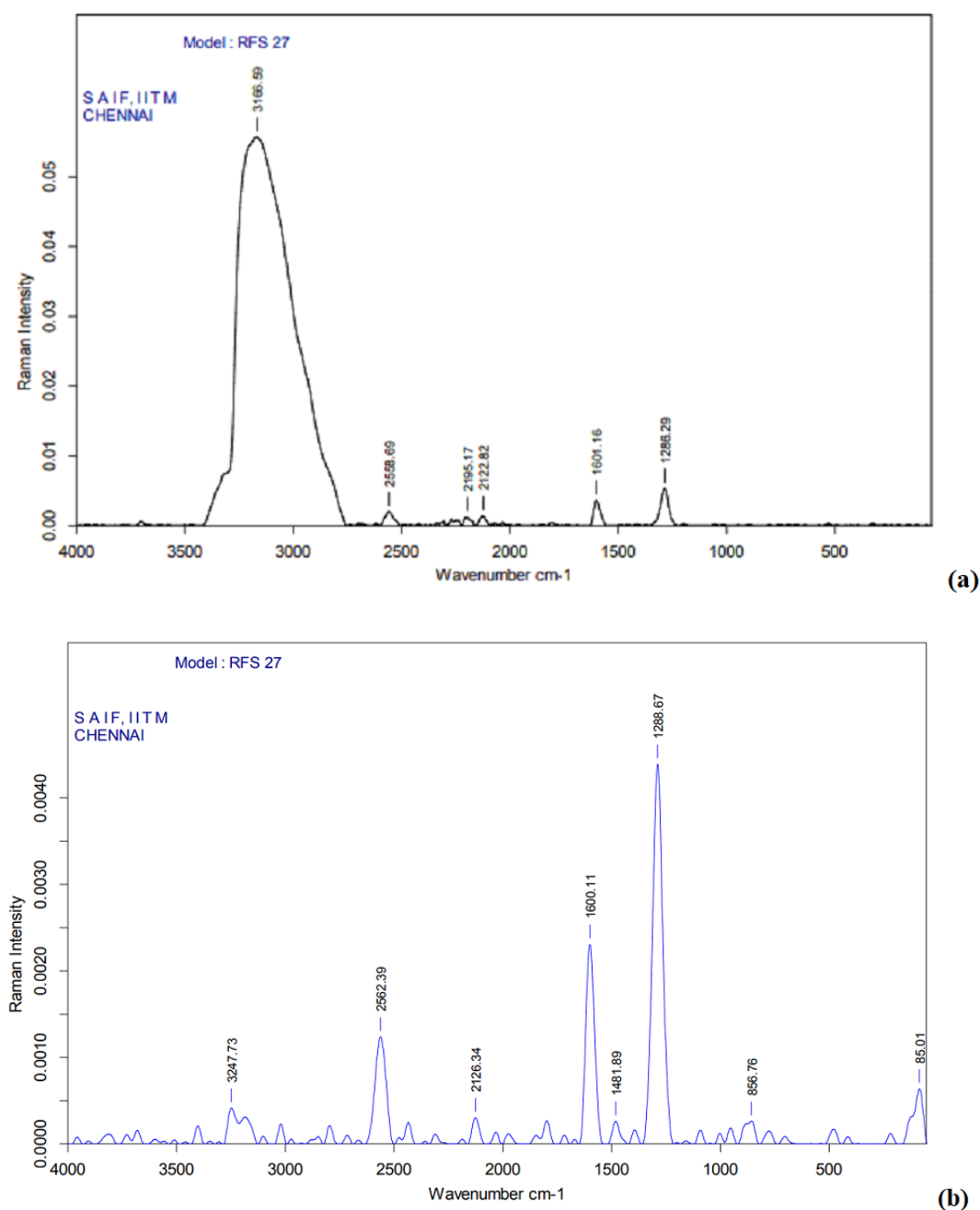
Figure 112: Raman spectra of (a) DT (b) FPV-DT

224

5.7.6.2.3 NMR spectroscopy

(a)

(b)

FosDt
CMC_SINGLE_H2O D2O {D:\Spectra} nmr 29
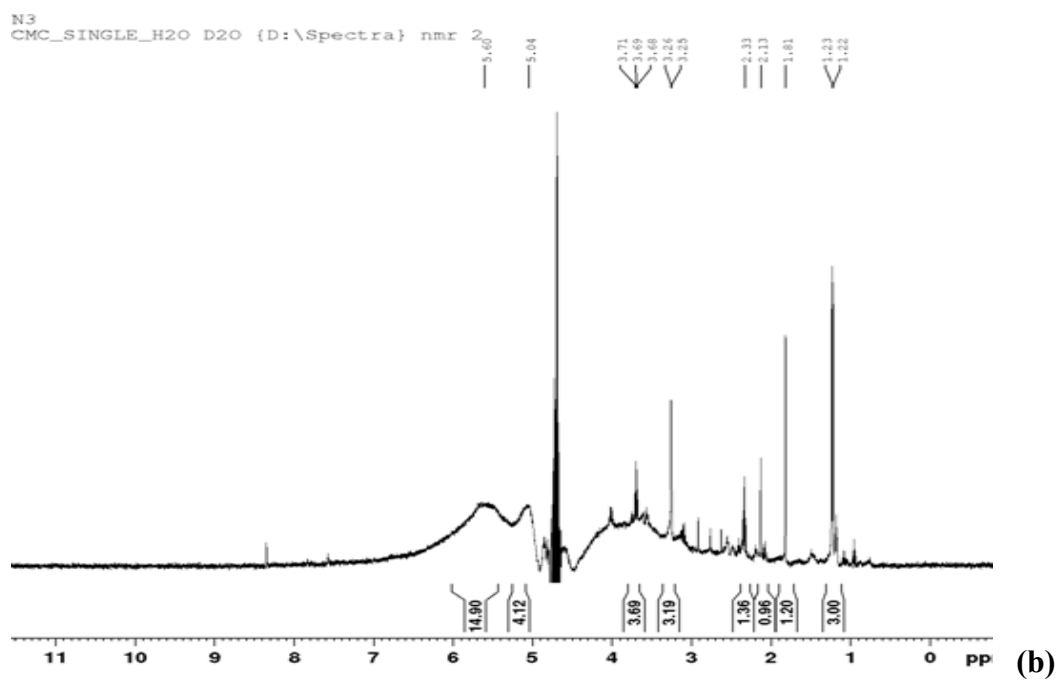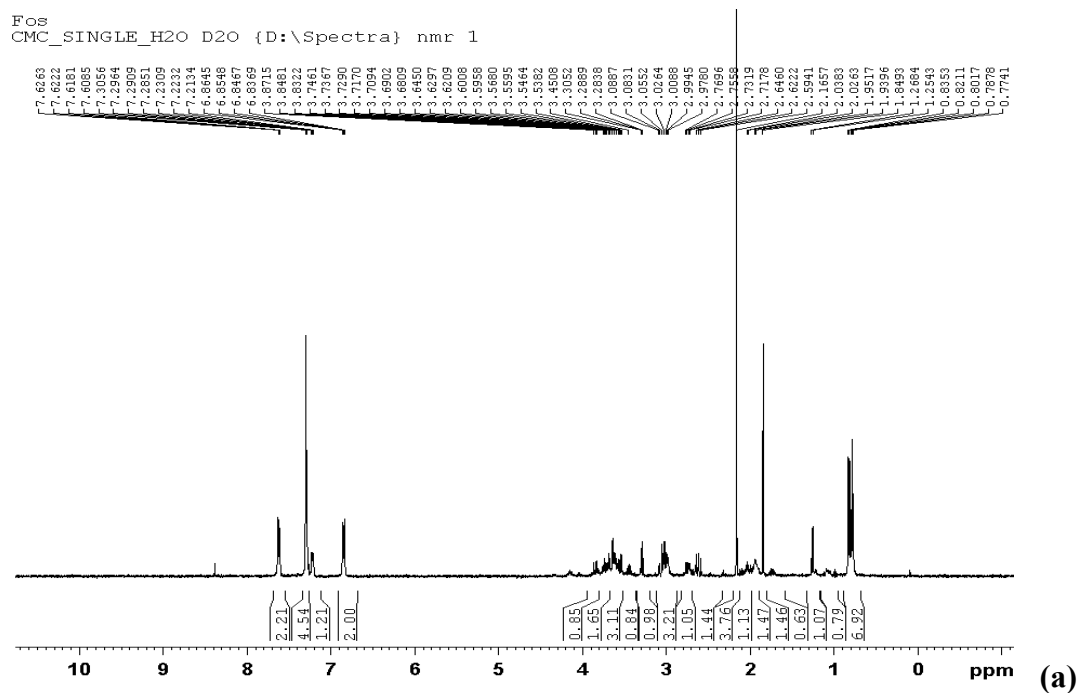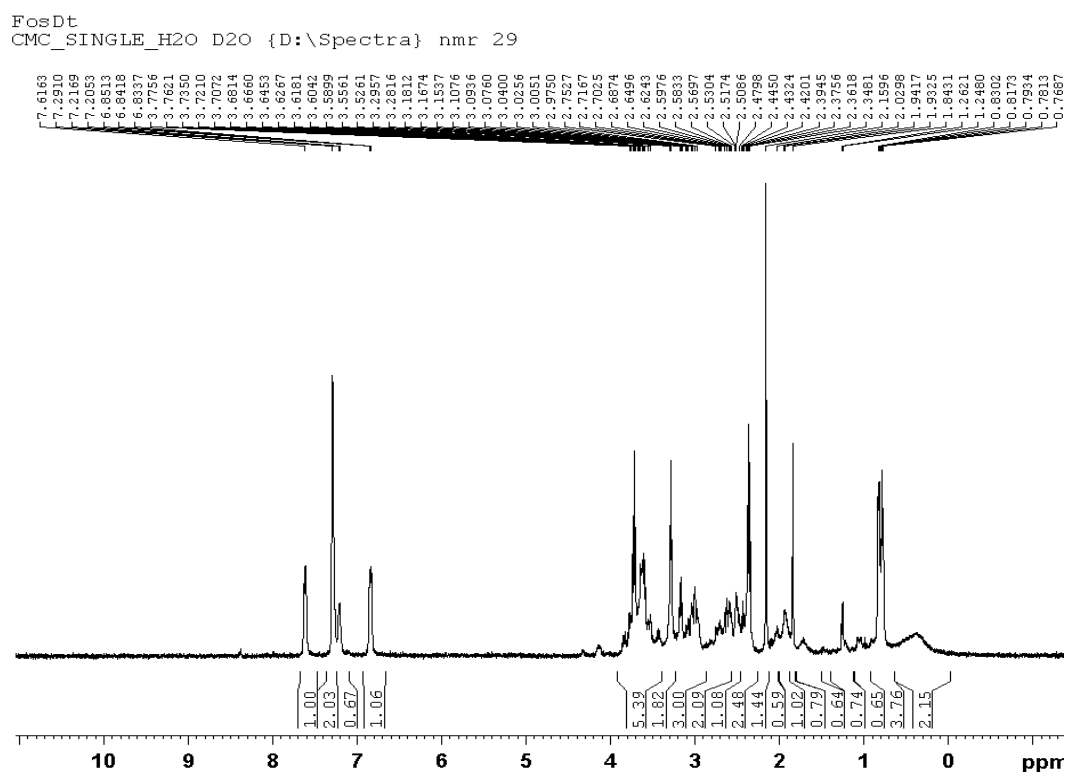
(c)

Figure 113: NMR Spectra (a) Plain drug FPV (b) DT (c) FPV-DT

The NMR spectra of plain drug FPV, DT, and FPV-DT are shown in Figure 113. NMR of FPV showed H3 and H7 aromatic protons show their presence at H3 and H7 at δ 6.83 ppm, and other aromatic protons H4 and H6 show their doublet at δ 7.62 ppm. The H18, H19, and H20 show resonance at δ 7.21 to δ 7.23 ppm, a pair of doublets corresponding aromatic methine proton at H17 and H21 found at δ 7.30 ppm. Doublets observed at δ 0.77 and 0.78 ppm correspond to H10 and H11 of methyl proton. Five pairs of multiplets for methyl protons containing non-equivalent protons at δ 2.59-2.64 ppm, δ 2.97-2.99 ppm responded to H8 a,b, δ 2.71- 2.76 ppm, δ 3.53-3.54 ppm responded to H-12a,b, δ 2.55-2.59 ppm, δ 3.00-3.03 ppm responded to H-15a,b, δ 1.8 ppm, δ 1.93-1.95 ppm corresponded to H-25a,b, δ 3.2838-3.2889 ppm, δ 3.53-3.54 ppm corresponding to H-26a,b. Multiplets at δ 1.93 ppm, δ 3.7.3-8 ppm correspond to methine proton H9, H-13, H-14, and H-24. The H 27 a,b corresponds to δ 3.59-3.68 ppm, and doublets at δ 6.86 ppm correspond to the carbamate group (Singh et al., 2019).

NMR of dendritubes indicated multiplex between δ 3.2-3.7 ppm corresponds to the -OH protons of MWCNT. A peak at 1.01 corresponds to C-H protons, and multiplets at δ 0.8-1.2 ppm correspond to the CH_2 of the dendrimer structure.

226

The NMR spectra of FPV-DT indicate many protons due to the incorporation of the drug FPV in the DT. Alteration in a chemical shift at δ 2.33 ppm indicates the attachment of the methyl group of the drug with a surface amino group of DT. The multiplets at δ 0.7-0.8 ppm correspond to methyl proton altered indicating the attachment of the methyl group of the drug and terminal amine group of dendrimers of DT. Aromatic protons are visible above δ 7.00 ppm, and chemical shift at δ 6.85 ppm corresponds to carbamate proton. The dendritubes structure has an abundance of protons in its surroundings due to a heavily conjugated and complex structure that corresponds to various peaks and splitting patterns (Monteiro et al., 2016).

5.7.6.2.4 X-ray Diffraction

(a)

(b)
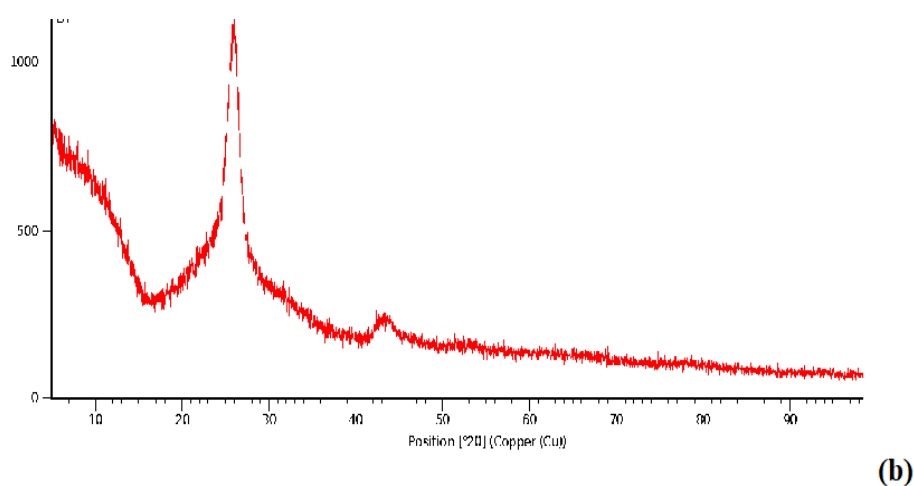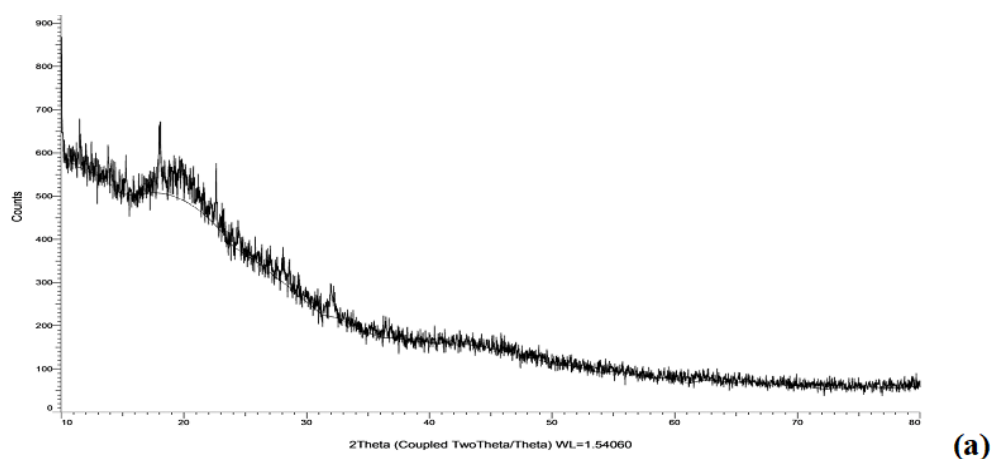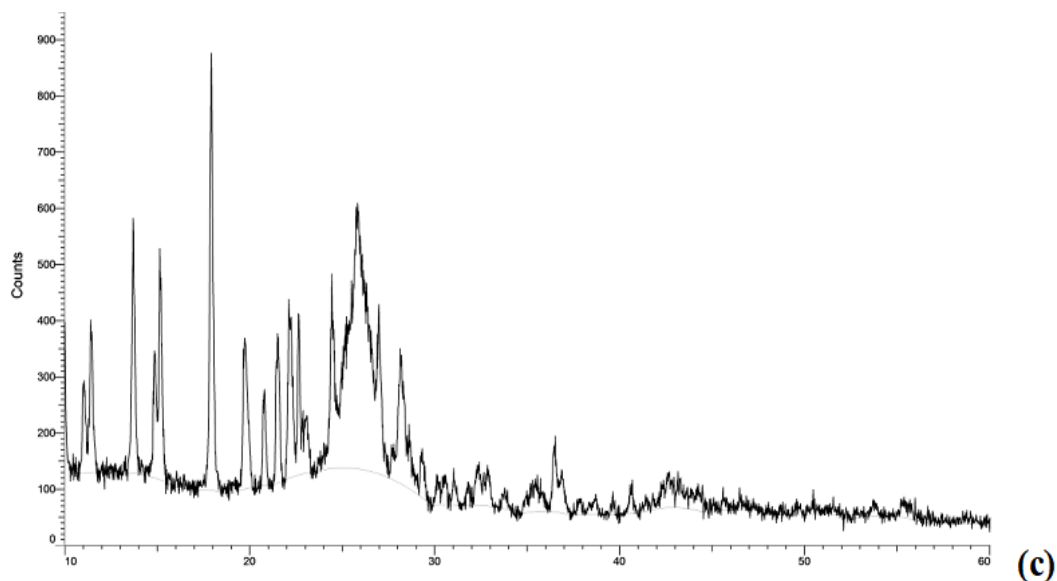
Figure 114: XRD spectra of (a) FPV (b) DT (c) FPV-DT

The XRD studies were performed for the drugs FPV and FPV-DT and are represented in Figure 114. XRD of DT revealed a sharp peak at 25.917° and a small broad peak between $40\text{-}50^{\circ}$. This indicates the semi-crystalline structure of DT. XRD spectrum of FPV-DT has many peaks as compared to pure DT. This confirms the attachment of FPV on the surface of the DT. This also indicates that the drug converted to a crystalline nature due to the attachment of the drug with surface dendrimers. Thus, from the XRD of drug-loaded FPV, it was concluded that the drug FPV has been incorporated into the structure of DT (Monteiro et al., 2016).

5.7.6.2.5 Differential scanning calorimetry
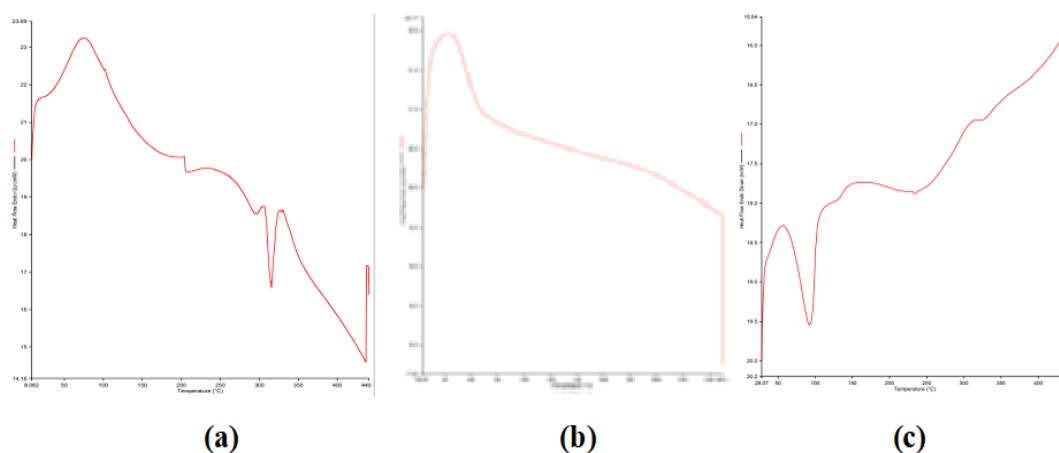
Figure 115: DSC thermogram of (a) Plain drug FPV (b) DT (c) FPV-DT

The conjugation of FPV-DT was also confirmed by DSC studies and given in Figure 115. DSC studies of DT indicated the broad peak at 40 °C. The peak was observed at 315.53 °C for FPV and 92.1 °C for the drug-loaded DT. It was observed that the transition temperature showed a negative shift confirming the strong interactions between dendrimers and FPV (Ramana et al, 2010). The transition of the peak indicates that the endothermic capability was altered which confirmed that the drug was conjugated with dendrimers (Yang et al., 2022).

5.7.6.2.6 Field emission scanning electron microscopy

The surface morphology was studied with FE-SEM for DT and FPV-DT as shown in Figure 116. The FE-SEM image indicating surface topography did not change when the drug was loaded in the DT. The image indicated that the structure of DT in drug-loaded DT remained unchanged as compared to plain DT. Spherical structure dendrimers were observed on the surface of the DT indicating that the process of drug loading did not alter the surface topography of the DT. The image of FPV-DT indicated their open tubular nature with spherical dendrimers and there was no observed breakage in the structure of DT in the plain DT and FPV-DT.

(a)   (b)
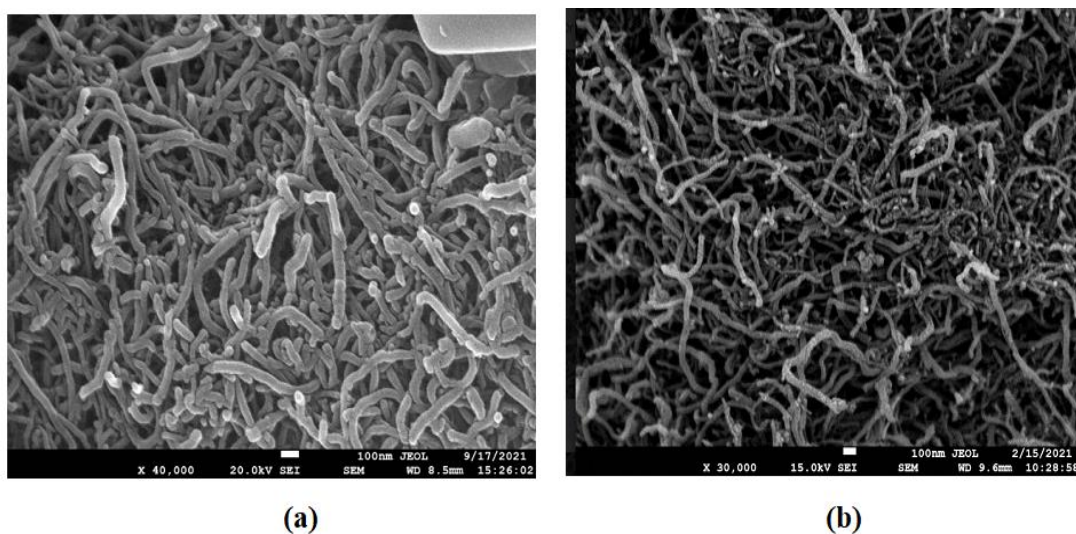
Figure 116: FE-SEM images of (a) MWCNT-COOH (b) FPV-DT

5.7.6.2.7 Particle size distribution and zeta potential
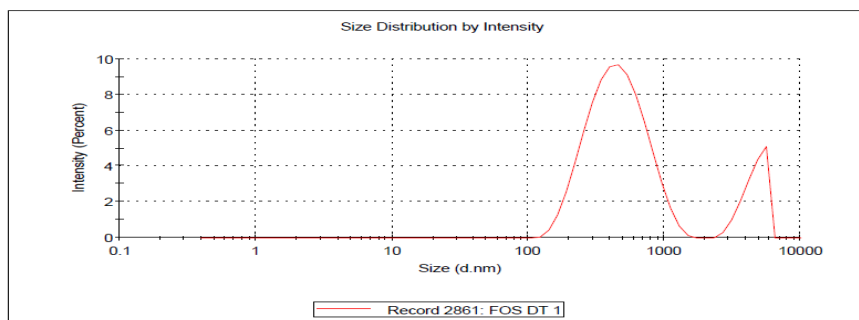
Figure 117: Particle size analysis of FPV-DT

The particle size and zeta potential of DT and FPV-DT were studied with a Delsa nano zeta sizer. The particle size, polydispersity index, and zeta potential are tabulated in Table 44 and the particle size distribution of FPV-DT is shown in Figure 117. The size of a particle of DT was found to be 288.4 nm which on conjugation with the drug increases to 518.9 nm. The PDI was found to be 0.385 which reduces to 0.435 indicating that the FPV-DT shows a higher aggregation of the nanostructure. The zeta potential was found to be -2.48 mV for DT which reduces to -27.0 mV. This may be due to the conjugation of FPV with DT, reducing the surface NH_2 group (Modi et al., 2011; Dong et al., 2017).

Table 44: Particle size and zeta potential of DT and FPV-DT

Formulation	Particle size (nm)	PDI	Zeta potential (mV)
DT	288.4	0.385	-2.48
FPV-DT	518.9	0.435	-27.0

5.7.6.2.8 Dispersibility

The DT and FPV-DT were subjected to the dispersibility test to study the rate of dispersion of the prepared dispersions. The dispersion of DT and FPV-DT was prepared by dispersing 10 mg of the sample in 5 mL distilled water. The system was sonicated for 5 min on the bath sonicator. After sonicating, the samples were kept for 24 h without disturbing the system. The dispersed system was observed at 0 h, 8 h, and 24 h. The system was found to be stable and did not settle down in deionized water. Dispersibility test of DT and FPV-DT at 0 h, 8 h, and 24 h in Figure 118.

0 h
8 h
24 h
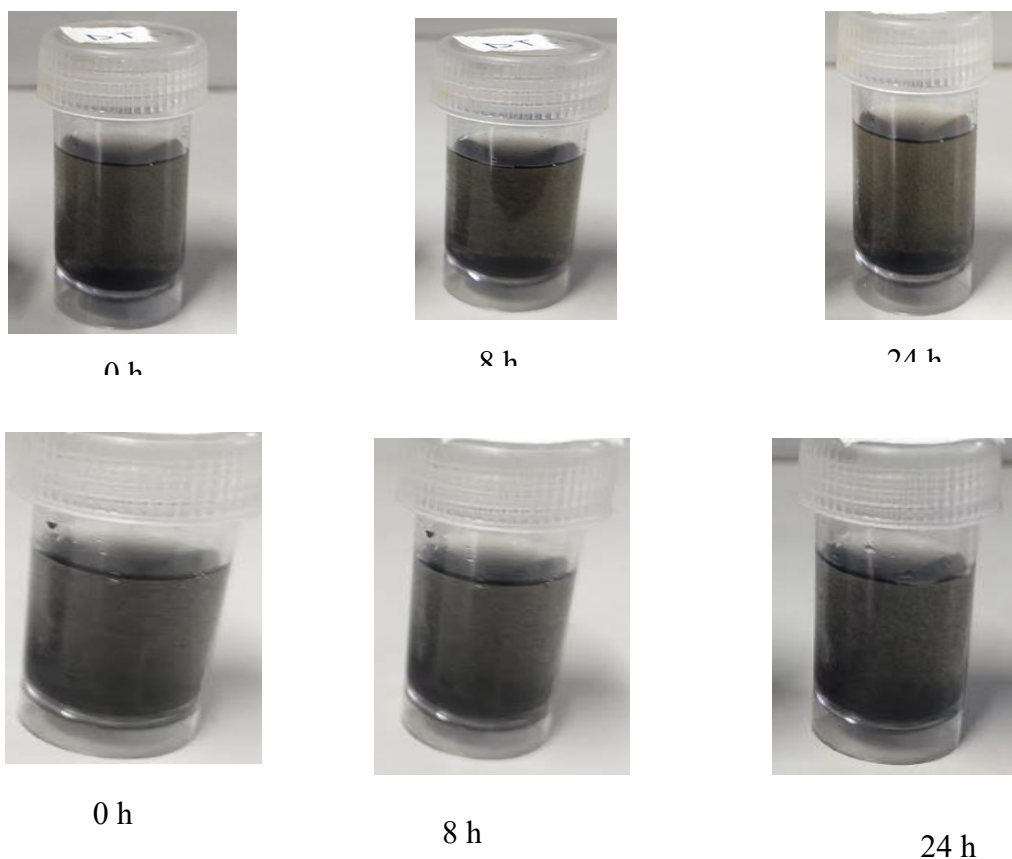
Figure 118: Dispersibility test (a) DT (b) FPV-DT at 0 h, 8 h, and 24 h

5.7.6.2.9 Entrapment efficiency

Entrapment efficiency was performed using a dialysis membrane to determine the amount of drug entrapped in the carrier system. The drug entrapment efficiency FPV-DT was found to be 83.73 ± 0.42% determined using an indirect method using a dialysis membrane (MWCO 7000 Da, Himedia, India). The entrapment was found to be higher due to the conjugate structure of MWCNT and dendrimers. The structure provides higher loading spaces as multiple dendrimers are attached on the surface of the MWCNT increasing the loading spaces of the drug. The terminal functional group increases the sites of interaction of drugs by covalent linking and also binds non-covalently by hydrogen bonding or hydrophobic interactions as the drug was also hydrophobic in nature. The drug can also entrap and form bonds inside the dendritic structure. The drug also binds to the side wall of MWCNT by π-π stacking. As with the new conjugate system, multiple binding sites were available which resulted in higher drug loading (Tripathi et al., 2020).

5.7.6.2.10 *In vitro* drug release

The drug release studies were performed in two different pH mediums, at pH 7.4 which corresponds to systemic pH, and at pH 5 which corresponds to the internal environment of the macrophages. The study involves 50 mL of release medium kept on continuous stirring. The dialysis membrane method used for the release study indicated faster release at initial time points followed by sustained release in both the release medium. The drug FPV was reported to have higher solubility at lower pH (pH 3.3) which reduces with increases in pH (Ford et al., 2005). The release study revealed the higher drug release at lower pH 5 (88.79 ± 1.10) as compared to pH 7.4 (78.59± 2.42). Table 45 represents the drug release profile of FPV from FPV-DT in acetate buffer pH 5 and PBS pH 7.4. Figures 119 and 120 represent the drug release Profile of FPV from FPV-DT in acetate buffer pH 5 and PBS pH 7.4 for 96 h and 8 h.

Table 45: Drug release Profile of FPV from FPV-DT

Time	% Cumulative drug release	
	Acetate buffer pH 5	**PBS pH 7.4**
0	0±0	0±0
1	14.31±3.28	12.22±2.46
2	24.99±2.56	16.91±1.90
3	27.00±2.23	21.09±2.61
4	33.43±2.41	32.66±2.42
5	37.65±1.14	42.60±2.00
6	49.69±3.14	44.76±2.66
7	55.11±2.31	46.07±1.86
8	57.37±2.54	48.34±1.41
24	62.48±2.19	57.56±2.12
30	64.20±3.31	59.89±3.28
48	72.76±3.56	65.29±2.86
72	78.84±3.89	73.97±3.94
96	88.79±1.10	78.59±2.42

*The data was represented as Mean±SD (n=3)
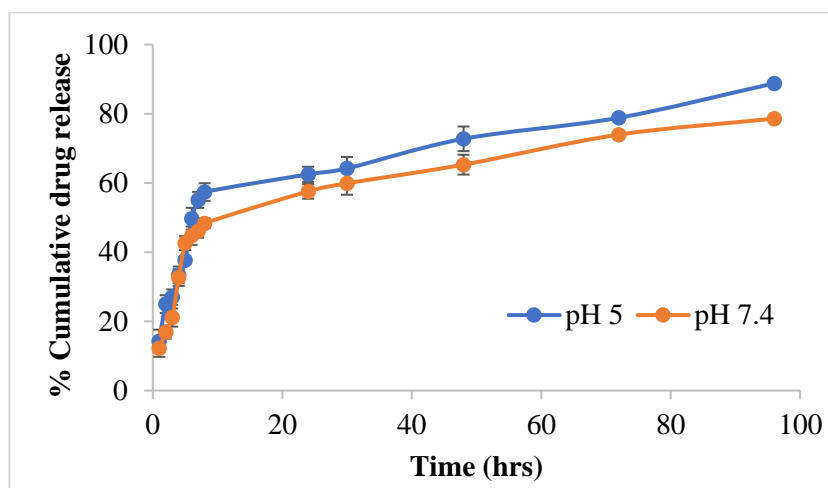
Figure 119: Drug release profile of FPV-DT for 96 h (n=3)
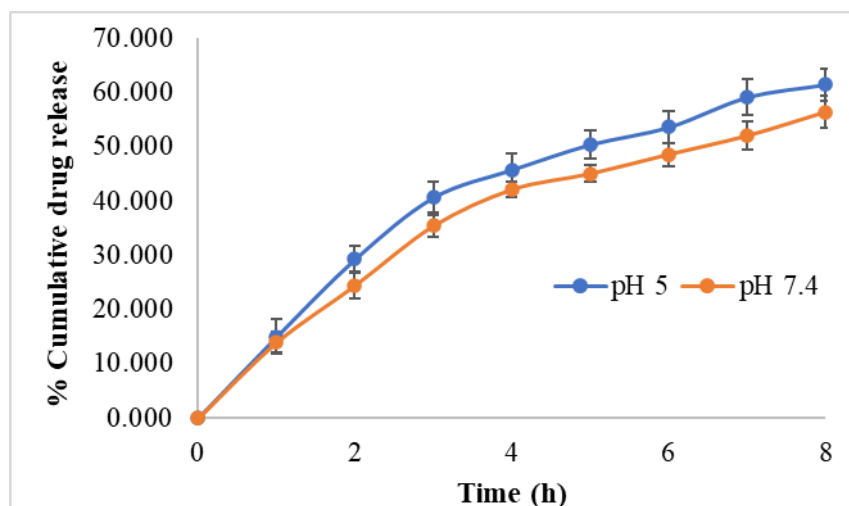
Figure 120: Drug release profile of FPV-DT up to 8 h (n=3)

5.7.6.2.11 Drug Release Kinetics

Table 46: Drug release kinetics of FPV from FPV-DT showing R^2 value and n

S. No	Release	pH 5		pH 7.4	
		R^2	n	R^2	n
1	First-order	0.821	-	0.8101	-
2	Zero-order	0.6641		0.6566	
3	Korsmeyer-Peppas	0.5553	0.5656	0.5891	0.579
4	Higuchi	0.945		0.913	
5	Hixon	0.7668		0.7617	

The release data were subjected to different release kinetics models. The release model defines the release mechanism of the drug release from the delivery system.

233

Different mathematical models are used to correlate the release pattern zero and first order, Higuchi model, Korsmeyer-Peppas model, and Hixon-Crowell model. The results were tabulated in Table 46. The best-suited model was based on the value of regression, the higher the value better the model fitted.

Both the release profile was subjected to the release kinetics model and the R^2 value was calculated. From the kinetics model, it was concluded that the best-fitted model was found to be the Higuchi model with the highest R^2 value of 0.945 for pH 5 and 0.913 for pH 7.4. For pH 5, the n value was determined to be 0.5656, and for pH 7.4, it was 0.579. The value suggests that the fickian diffusion model governed the release.

The drug release was subjected to other release models, lowest R^2 value was found to be for the first order. The value for the first order was found to be 0.821 for pH 5 and 0.8101 for pH 7.4, a lower value of R^2 makes it unsuitable. The zero-order model was not fitted due to the low value of the correlation coefficient was 0.6641 for pH 5 and 0.6566 for pH 7.4. The Korsmeyer Peppas model also showed a lesser R^2 value of around 0.5553 for pH 5 and 0.5891 for pH 7.4. The model of Hixon Crowell was also found unsuitable as the value of R^2 was found to be 0.7668 for pH 5 and 0.7617 for pH 7.4 making them unsuitable. The best-fitted model was the Higuchi model. Figure 121 represents the drug release kinetics of FPV-DT at pH 5 and pH 7.4 such as First order release kinetics, Zero order release kinetics, Korsmeyer Peppas release kinetics, Higuchi release kinetics, and Hixon-Crowell release kinetics.
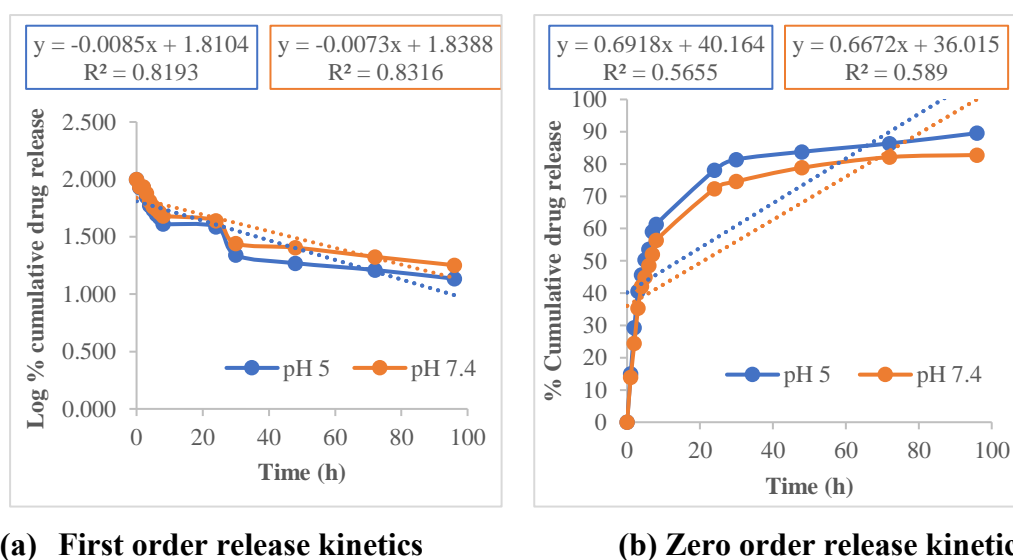
(a) First order release kinetics   **(b) Zero order release kinetics**
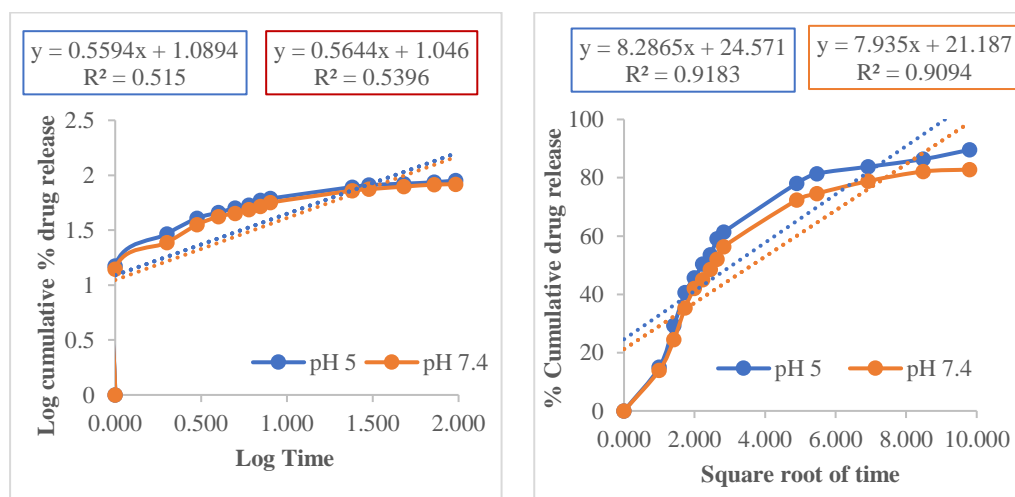
(c) **Korsmeyer-Peppas release kinetics**

(d) **Higuchi release kinetics**
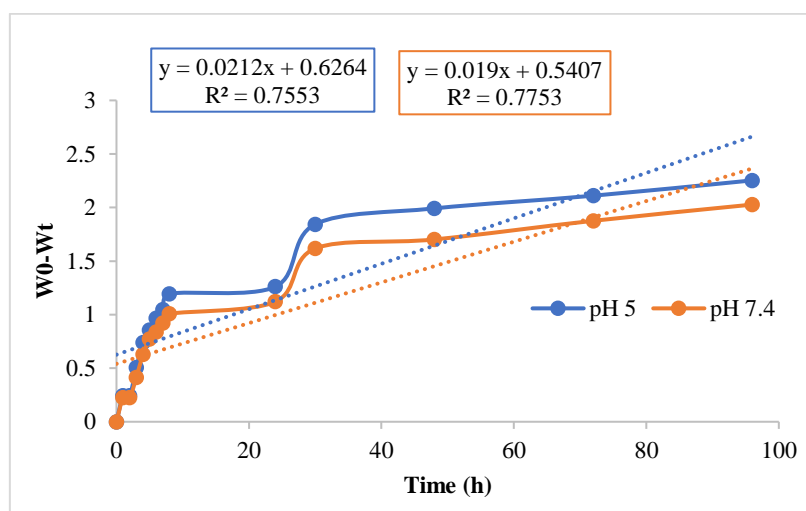
(e) **Hixon-Crowell release kinetics**

Figure 121: Drug release kinetics of FPV-DT

5.7.7 Nevirapine and Fosamprenavir calcium-loaded dendritubes

5.7.7.1 Formulation development of Nevirapine and Fosamprenavir calcium-loaded dendritubes

The drug NVP and FPV were loaded on the DT (NVP-FPV-DT) with constant stirring for 48 h using a magnetic stirrer. The drug binds with the surface amine group of the dendrimers by covalent linkage and by trapping in the dendrimer structures. The structure was characterized using different characterization techniques such as spectroscopic analysis, morphological studies, and *in-vitro* drug release studies.

5.7.7.2 Formulation development of mannosylated Nevirapine and Fosamprenavir calcium-loaded dendritubes

The formulated NVP-FPV-DT was conjugated with D-mannose using acetate buffer (pH 4.0). The flask was heated for 2 h at 60 °C. The solution was further stirred for 72 h to complete the reaction using a magnetic stirrer. The mannose attached with surface NH$_2$ of DT by Schiff base formation reaction. The structure was characterized using different characterization techniques such as spectroscopic analysis, morphological studies, and *in-vitro* drug release studies.   **5.7.7.3 Characterization of NVP-FPV-DT**

5.7.7.3.1 FTIR spectroscopy

5.7.7.3.1.1 FTIR spectroscopy of NVP-FPV-DT
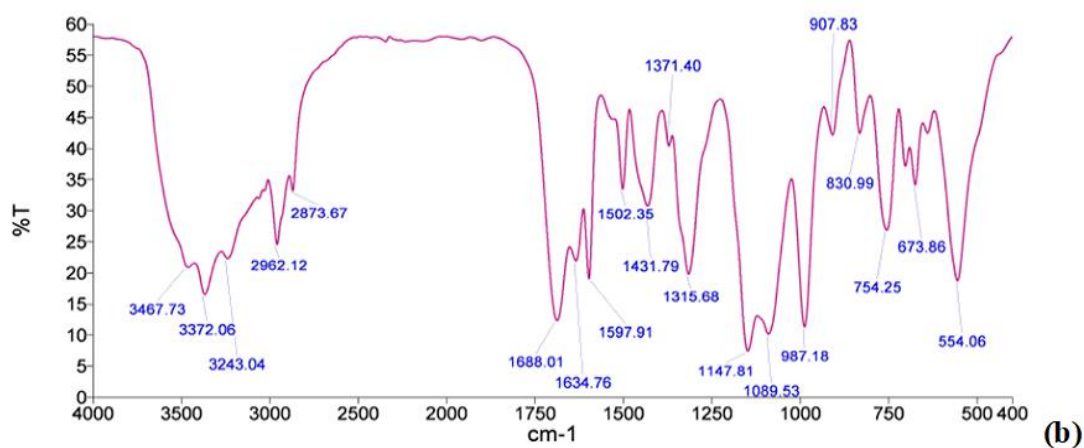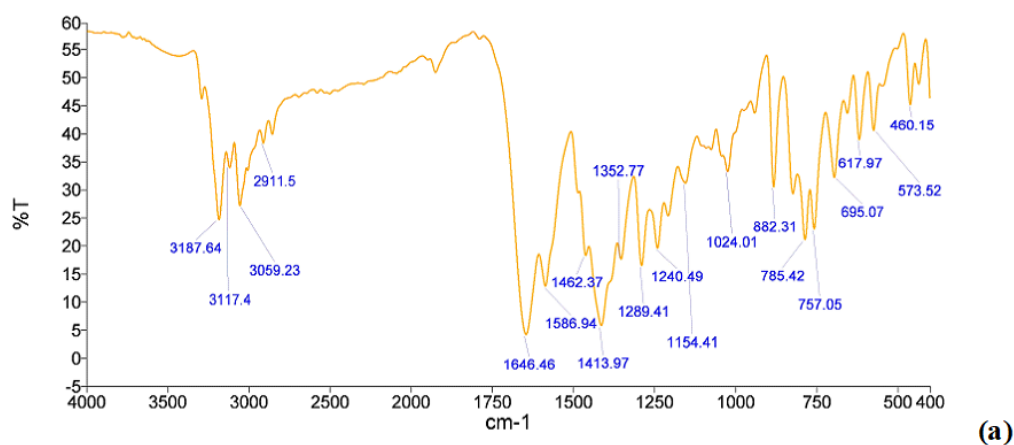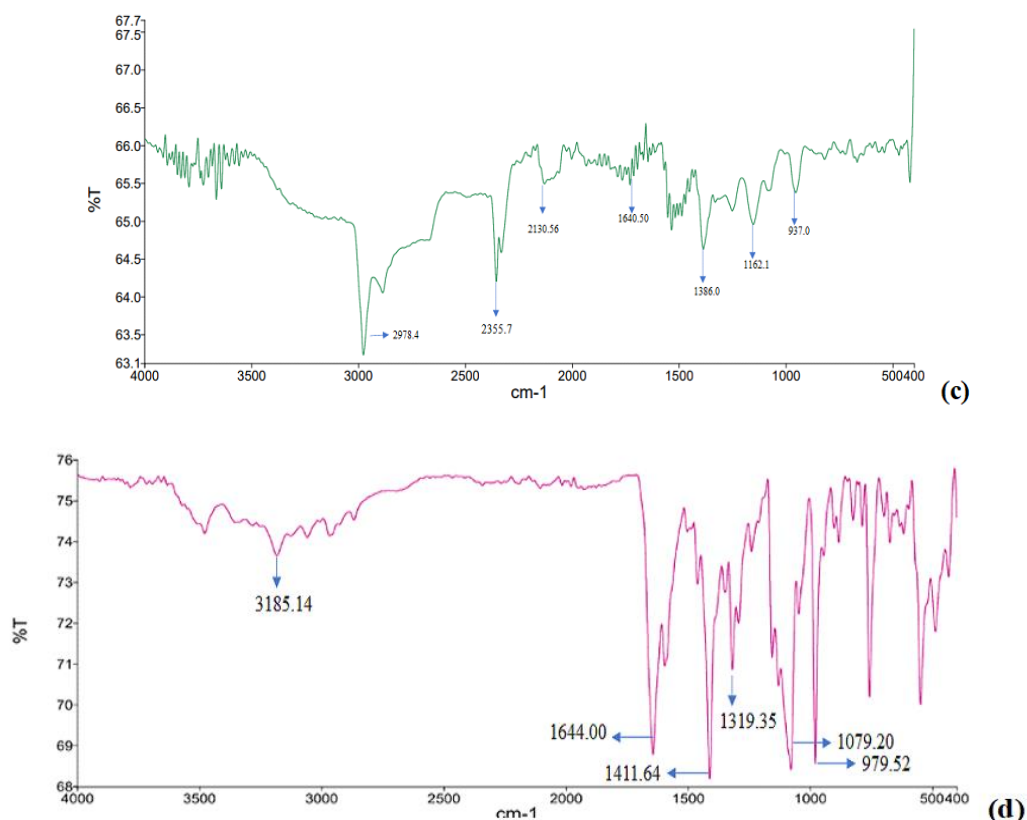
Figure 122: FTIR spectra of a) NVP b) FPV c) DT d) NVP-FPV-DT

The FTIR spectrum of NVP revealed the presence of all the characteristics peak of the drug. The major peaks are observed at 3187.64 cm^{-1} corresponding to the a broad peak of stretching of N-H, the peak at 3059.23 cm^{-1} indicated stretching of C-H, at 1646.46 cm^{-1} indicates the C=O stretching, the peak at 1413.97 cm^{-1}, 1586.94 cm^{-1} corresponds to the aromatic carbons (C=C), the peak at 1289.41 cm^{-1} represents C-N stretching and the peak at 882 cm^{-1} and 757 cm^{-1} indicates C-H bending (Varshosaz et al., 2018).

FTIR spectrum of FPV indicates a sharp peak at 3372 cm^{-1} reflecting the presence of O-H stretches; the medium intensity peak found at 3243.0 cm^{-1} are the stretches of an amino group (N-H) corresponds to amide and amine functional group. The peak at 1688.01 cm^{-1} was the peak of stretched of aliphatic C-H, the peak of higher intensity was observed at 1597.9 cm^{-1} and 1502.3 cm^{-1} confirms the stretches of C=O correspond to the carbonyl group; medium intensity C=C stretches of the aromatic ring; 1431.7 cm^{-1}, 1315.1 cm^{-1} corresponds to stretching of C-N of the amine group, the peak show high to medium intensity, 1089.53 cm^{-1} and 1147.81 cm^{-1} peaks correspond to an

237

asymmetrical stretch of S=O; a region with high intensity, at 984 cm^{-1} the peak of high intensity due to stretching of C-O of ether and phosphate esters (Tan et al. 2014).

The spectrum of DT indicated characteristics peaks of at 2978.4 cm^{-1} primary alkene, 1535.5 cm^{-1}, 1640.50 cm^{-1} small peak amide, 1386.0 cm^{-1} OH bending, 1162.1 cm^{-1} C-O stretching, and 937.00 cm^{-1} aromatic C-H out of plane bending. The bulge in the region of 3000-3500 cm^{-1} was due to the conjugation of the primary amine of a dendrimer with the MWCNT structure.

The results of NVP-FPV-DT are shown in Figure 122 and matched with the spectra of DT and drug NVP and FPV. As per the hypothesis, both drugs are supposed to bind with the primary amine group present on the surface of DT. The methyl group of NVP and isopropyl group of FPV tends to bind with the surface amine group of DT. This was supported by the disappearance of the terminal amine peak of DT at 2978.4 cm^{-1} in the spectrum. Similarly, the peak of the methyl group of NVP at 3059 cm^{-1} and isopropyl peak of FPV was absent confirming the conjugation of the drug with DT. The major peaks were observed at 3185 cm^{-1} corresponds to the N-H bond, peak at 1644.00 cm^{-1} corresponds to stretching of amide, peak at 1411 cm^{-1} corresponding to cyclopropyl C=C, peak at 1319.35 cm^{-1} corresponds to stretching of C-N, 1079 cm^{-1} corresponding to stretching of -S=O, peat at 979.52 cm^{-1} corresponds to bending of -C-H of aromatic alkene were observed at defined wavelength confirm the loading of the drug on DT. Table 47 represented FTIR spectrum of NVP-FPV-DT.

Table 47: FTIR spectrum of NVP-FPV-DT

Observed peaks frequency (cm^{-1})	Standard FTIR range (cm^{-1})	Corresponding functional group
3185.14	3500-3100	Peak of N-H stretching
1644.00	1630-1680	C=O carbonyl stretching
1411.84	1475-1600	Cyclopropyl C=C
1319.35	1350-1000	C-N stretching
1079.20	1050-1375	S=O stretching
979.52	900-690	-C-H bend of aromatic alkene

5.7.7.3.1.2 FTIR of M-NVP-FPV-DT

FTIR peaks of M-NVP-FPV-DT were compared and evaluated for different functional groups present. Figure 123 represented the FTIR spectra of M-NVP-FPV-DT. The main peaks are of C-N stretching at 1018.92 cm^{-1}; N-H deformation of primary amine at 1410 cm^{-1}; deflection of N-H of amine at 1639 cm^{-1}; broad peak at 3183 cm^{-1} due to OH group. The broad peak at 3183.99 cm^{-1} and C-N deformation at 1410 cm^{-1} confirmed the formation of Schiff base and amines due to conjugation of mannose and terminal amine group of dendrimers (Vieira et al., 2016).
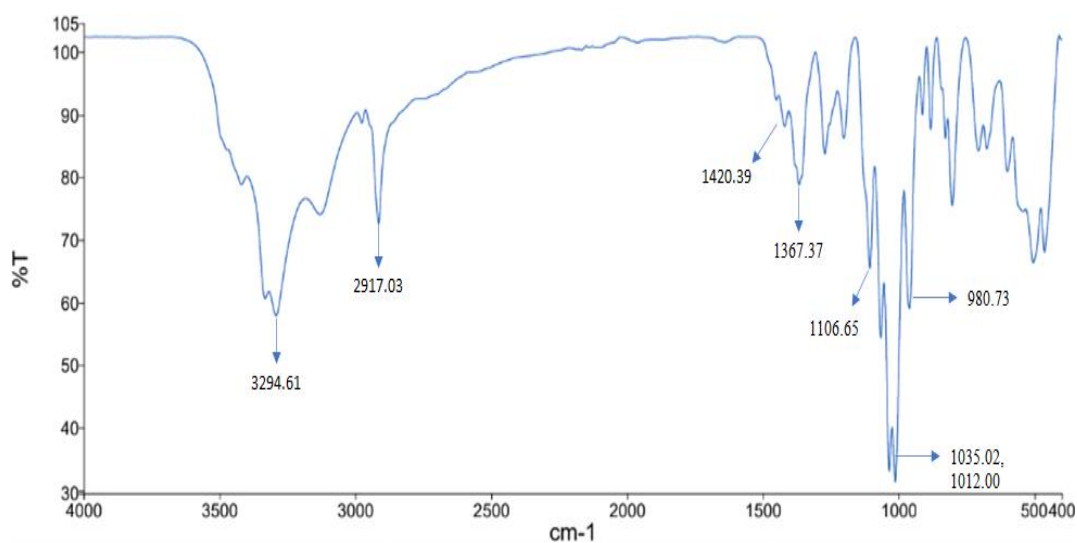
Figure 123: FTIR spectra of M-NVP-FPV-DT

Table 48: FTIR spectrum of M-NVP-FPV-DT

Observed peaks frequency (cm^{-1})	Standard FTIR range (cm^{-1})	Corresponding functional group
3294.61	3500-3100	Peak of N-H stretching
2917.03	3150-3050	C-H aromatic stretching
1420.39	1475-1600	Cyclopropyl C=C
1367.37	1350-1000	C-N stretching
1035.02, 1012.00	1050-1375	S=O stretching
980.73	900-690	-C-H bend of aromatic alkene

5.7.7.3.2 Raman Spectroscopy

Raman spectroscopy was performed in the range of 0-4000 cm^{-1} for DT, NVP-FPV-DT, and M-NVP-FPV-DT, as shown in Figure 124. The D band for DT was observed at 1286.29 cm^{-1}. This band was due to a defect or disorder in the MWCNT

structure. The G band observed at 1601.16 cm^{-1} for DT corresponding to the crystalline structure of DT. The D band for NVP-FPV-DT was observed at 1285.40 cm^{-1}. The G band was observed at 1600.10 cm^{-1} for NVP-FPV-DT. A broad peak was observed near 3166.59 cm^{-1} in DT and at 3224.21 cm^{-1} in NVP-FPV-DT due to the crowding of the N-H group.

(b)

(a)

240
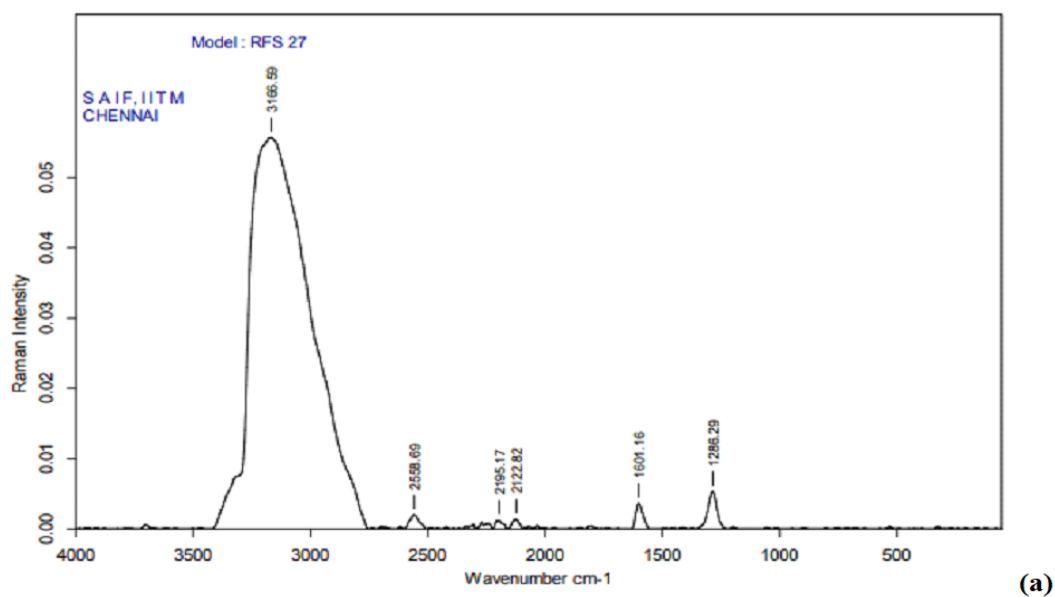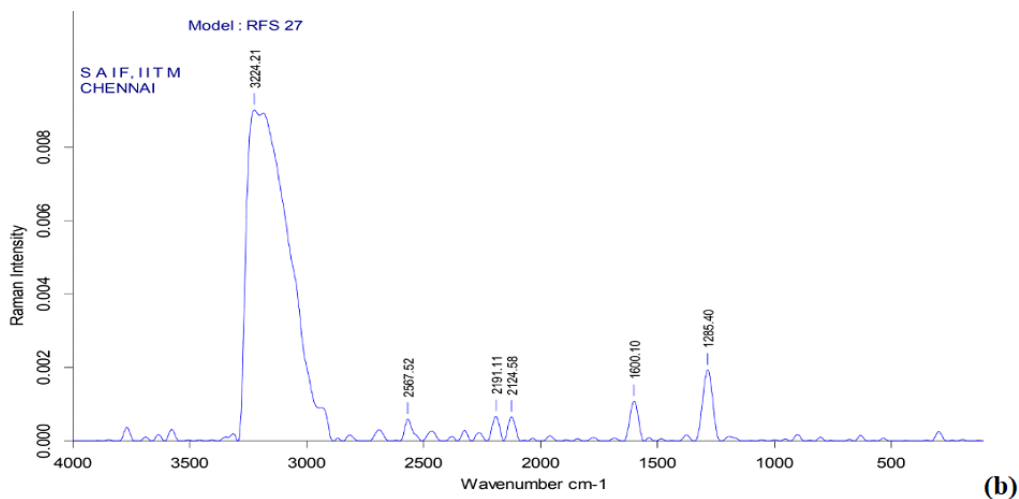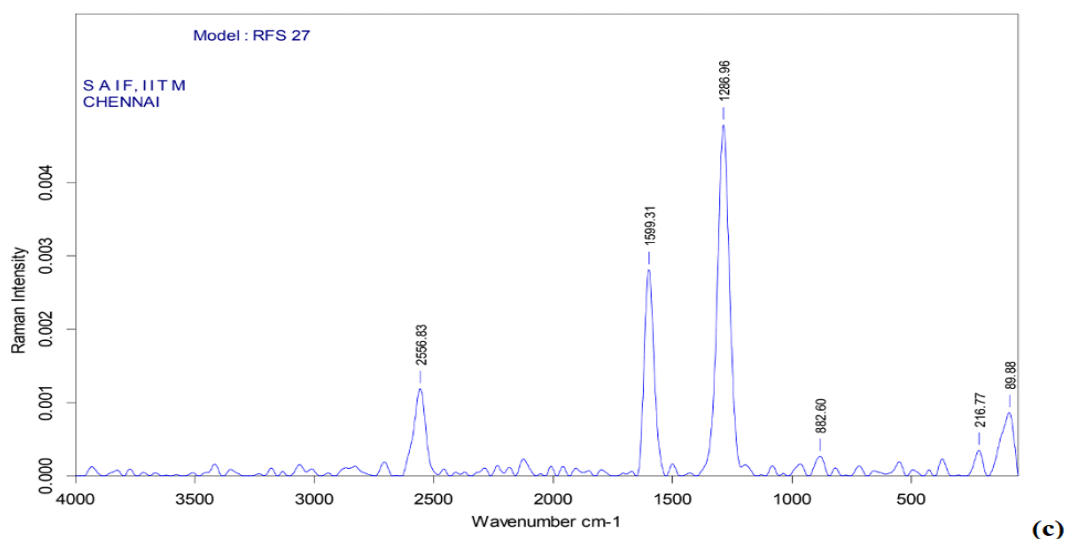
Figure 124: Raman spectra of (a) DT (b) NVP-FPV-DT (c) M-NVP-FPV-DT

Raman spectroscopy was performed in the range of 0-4000 cm^{-1} for M-NVP-FPV-DT. The D band for M-NVP-FPV-DT was detected at 1286.96 cm^{-1}. The G band was detected at 1599.31 cm^{-1} for M-NVP-FPV-DT. A broad peak was detected at 3224.21 cm^{-1} in NVP-FPV-DT due to crowding of the N-H group which was not observed with M-NVP-FPV-DT which confirms the attachment of the mannose with surface amine of DT (Adar et al., 2016).

The I$_D$/I$_G$ ratio of DT was found to be 1.460 and the I$_D$/I$_G$ ratio of NVP-FPV-DT was found to be 1.787. The increment in I$_D$/I$_G$ ratio of NVP-FPV-DT indicated that the conjugation of NVP and FPV took place on the DT surface which alters the sp2 bonding structure of MWCNTs and leads to the breaking of π bonds holding the hexagonal carbon structure.

The I$_D$/I$_G$ ratio of M-NVP-FPV-DT was found to be 2.069. The increment in I$_D$/I$_G$ ratio of M-NVP-FPV-DT indicated that the conjugation of mannose took place on the surface of drug conjugated DT (Muda et al., 2017; Sedaghat et al., 2014).

5.7.7.3.3 NMR spectroscopy

Nevi
CMC_SINGLE_H2O D2O {D:\Spectra} nmr 2

(a)

Fos
CMC_SINGLE_H2O D2O {D:\Spectra} nmr 1

(b)

(c)

(d)
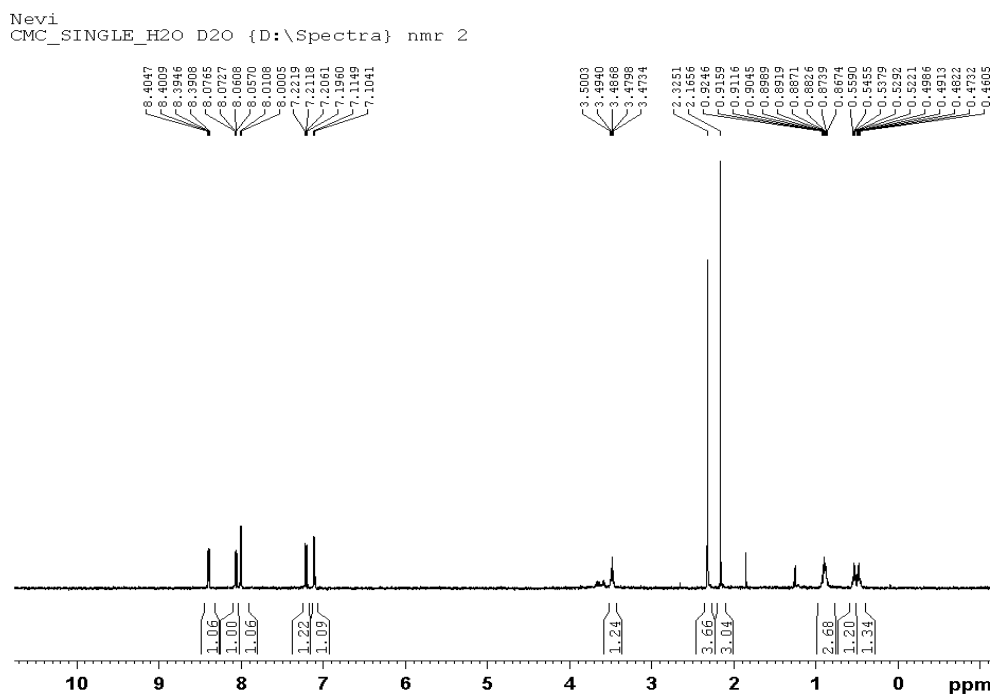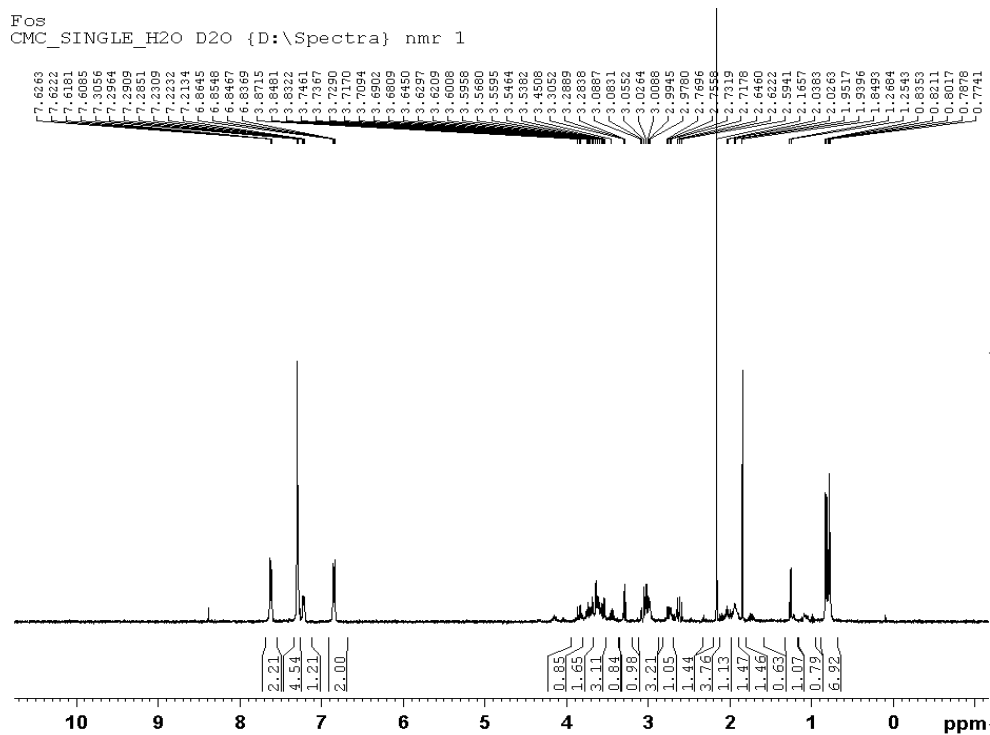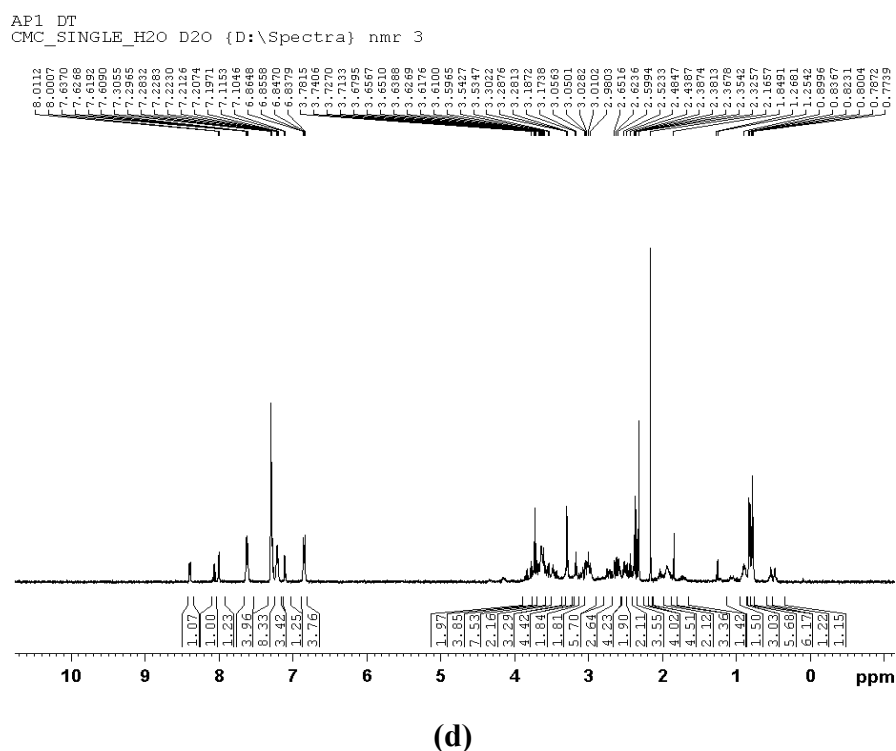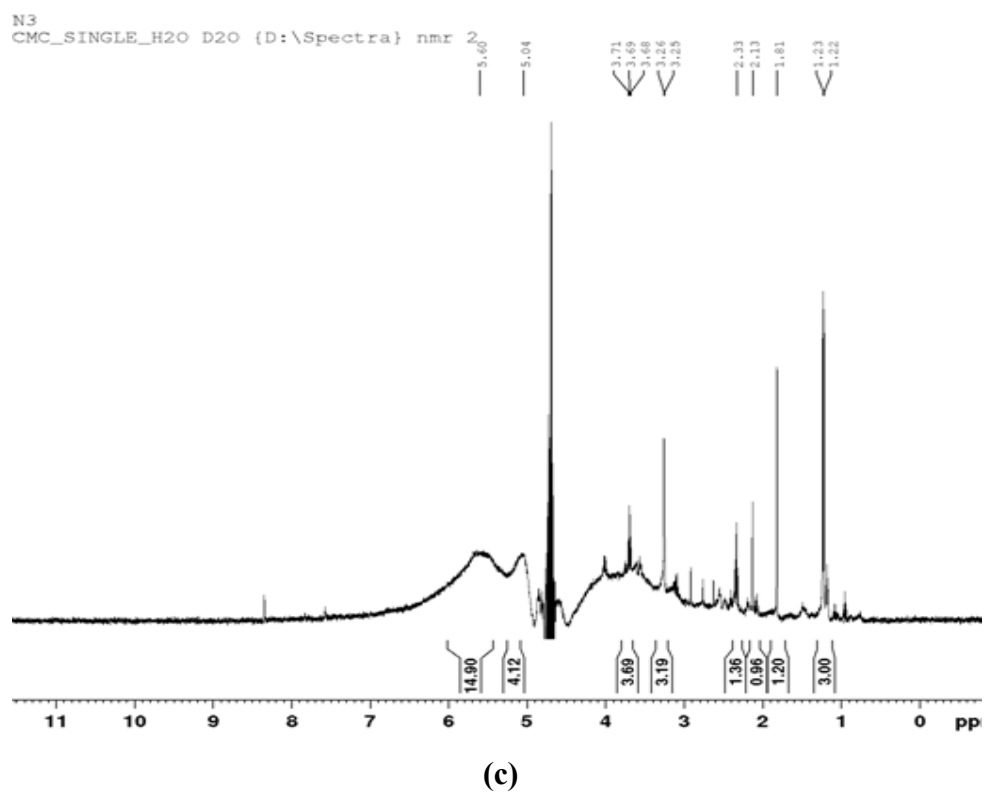
Figure 125: NMR Spectra of (a) NVP (b) FPV (c) DT (d) NVP-FPV-DT

Figure 125 represents the NMR Spectra of NVP, FPV, DT, and NVP-FPV-DT. Multiplets were observed between δ 0.50 and 1.30 ppm corresponding to -CH$_2$ of methylene groups of cyclopropane (H5, H6), the chemical shifts between δ 3.79 ppm

243

correspond to the protons of cyclopropane (H8), the peak at δ 2.325 ppm corresponds to CH₃, peaks between δ 7.10-8.40 ppm corresponds to the protons associated with aromatic ring (H1, H2, H3, H4, H5). The single peak at 8.407 ppm corresponds to NH (da Silva et al., 2021; Silverstein et al., 1962).

H3 and H7 aromatic protons show their presence at H3 and H7 at δ 6.83 ppm, and other aromatic protons H4 and H6 show their doublet at δ 7.62 ppm. The H18, H19, and H20 show resonance at δ 7.21 to δ 7.23 ppm, a pair of doublets corresponding aromatic methine proton at H17 and H21 found at δ 7.30 ppm. Doublets observed at δ 0.77 and 0.78 ppm correspond to H10 and H11 of methyl proton. Five pairs of multiplets for methyl protons containing non-equivalent protons at δ 2.59-2.64 ppm, δ 2.97-2.99 ppm responded to H8 a,b, δ 2.71- 2.76 ppm, δ 3.53-3.54 ppm responded to H-12a,b, δ 2.55-2.59 ppm, δ 3.00-3.03 ppm responded to H-15a,b, δ 1.8 ppm, δ 1.93-1.95 ppm corresponded to H-25a,b, δ 3.2838-3.2889 ppm, δ 3.53-3.54 ppm corresponding to H-26a,b. Multiplets at δ 1.93 ppm, δ 3.7.3-8 ppm correspond to methine proton H9, H-13, H-14, and H-24. The H 27 a,b corresponds to δ 3.59-3.68 ppm, and doublets at δ 6.86 ppm correspond to the carbamate group (Singh et al., 2019).

Multiplex between δ 3.2-3.7 ppm corresponds to the -OH protons of MWCNT. A peak at δ 1.01 ppm corresponds to C-H protons, and multiplets at δ 0.8-1.2 ppm corresponds to the CH₂ of the dendrimer structure. The peak of NH₂ and a peak of COOH was observed at δ 2.3 ppm and in between δ 2.13 ppm were found to be altered which confirms the formation of conjugates. The 5G dendrimer's structure has an abundance of protons in its surroundings due to a heavily conjugated and complex structure that corresponds to various peaks and splitting patterns.

¹H NMR spectrum has confirmed the conjugation of drugs NVP and FPV with the denritubes. Chemical shift at δ 0.773 and 0.7873 ppm are responsible for methyl proton in FPV, shift near δ 0.5 ppm corresponds with a proton of cyclopentane of NVP, shift at δ 2.39 ppm responds to CH₃ group of NVP, peak at δ 3.6 ppm corresponds to C-N proton, δ 6.846 ppm corresponds to aromatic carbon proton near CH₃, peak at δ 7.111 to 7.201 ppm corresponds to aromatic carbon. Similarly, the peak at δ 6.8 ppm corresponds to the amine carbamate structure of Fosamprenavir and quadruplet peaks near δ 1.95 ppm correspond to methane proton. Shift near δ 7.0 ppm corresponds to

aromatic carbons. Thus, from the chemical shift, it can be concluded that both drugs have been incorporated into the structure.
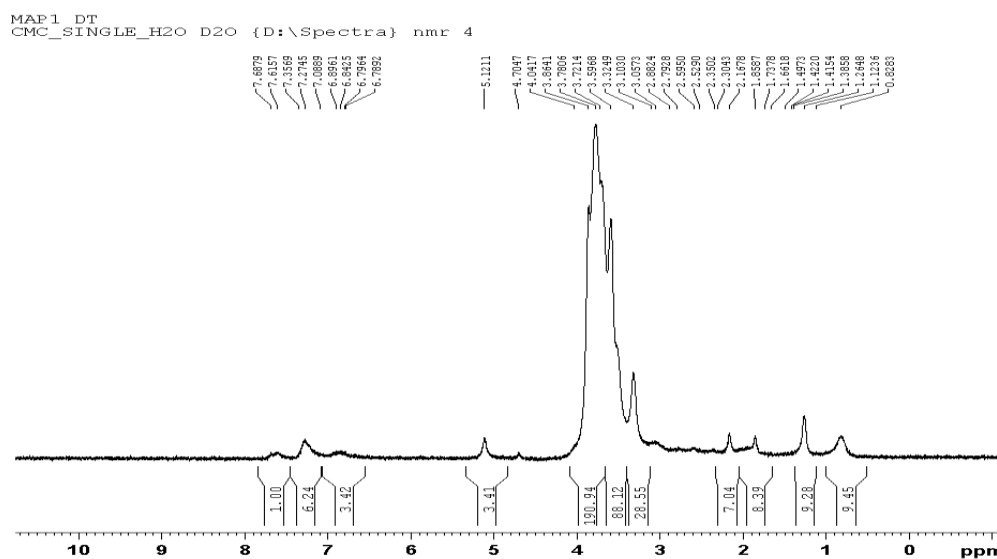
Figure 126: NMR Spectra of M-NVP-FPV-DT

The presence of multiplets at δ 5.121 ppm peak corresponds to the imine of mannose and some other amines developed during the interactions. A broad multiplets at δ 3.057-3.864 ppm responsible for multiple OH groups of mannose. Further, the shift at δ 7.274 ppm confirmed the presence of secondary amide (–NH–) in the drug-conjugated system. From the data, it can be concluded that mannose had been incorporated into the structure. Figure 126 shows the NMR Spectra of M-NVP-FPV-DT.

5.7.7.3.4 X-ray diffraction

(a)

(b)

(c)

(d)
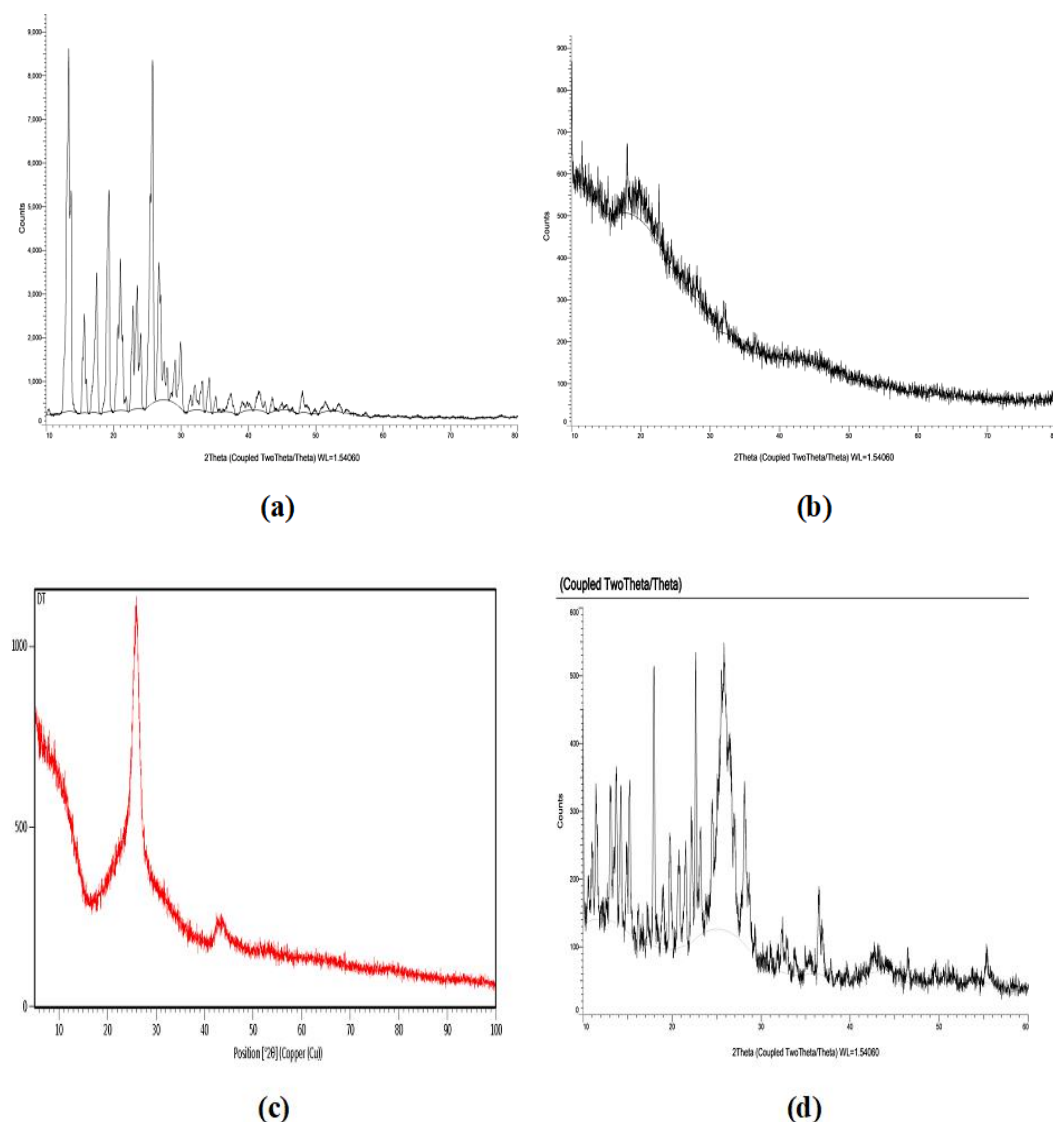
Figure 127: XRD of (a) plain drug NVP (b) plain drug FPV (c) DT

(d) NVP-FPV-DT

Figure 127 represents the XRD pattern of plain drug NVP, plain drug FPV, DT, and NVP-FPV-DT. XRD studies help to determine the crystal nature of the powdered drug samples. XRD pattern of NVP confirms the three-dimensional crystalline nature of the drug. The powder sample gives sharp peaks in the diffraction pattern and the scattering angle was observed at 13.915° and 25.455° (Monteiro et al., 2013). The XRD pattern of FPV does not show any prominent peak which indicated that the drug was amorphous (Corderio et al., 2013). Figure 22 represents the XRD

pattern of plain drug FPV and plain drug NVP. The DT also exhibits peaks at the same region as MWCNT at 25.907º and 42.562º. The XRD pattern of the NVP-FPV-DT showed a different peak as compared to DT which indicated that the crystalline drugs have been incorporated into the structure of DT. Different peaks were observed at 13.130º, 17.956º, and 22.665º were the peaks that were shifted from 13.915º and 25.455º peaks of NVP indicated the conjugation of drugs and delivery system. The broad peak at 25.00º corresponds to the peak of DT. Thus, from the XRD pattern it was observed that both NVP, and FPV had been incorporated in the structure.

5.7.7.3.5 Differential Scanning Calorimetry

(a)　　　　　　　　　　　　　　　(b)

(c)　　　　　　　　　　　　　　　(d)
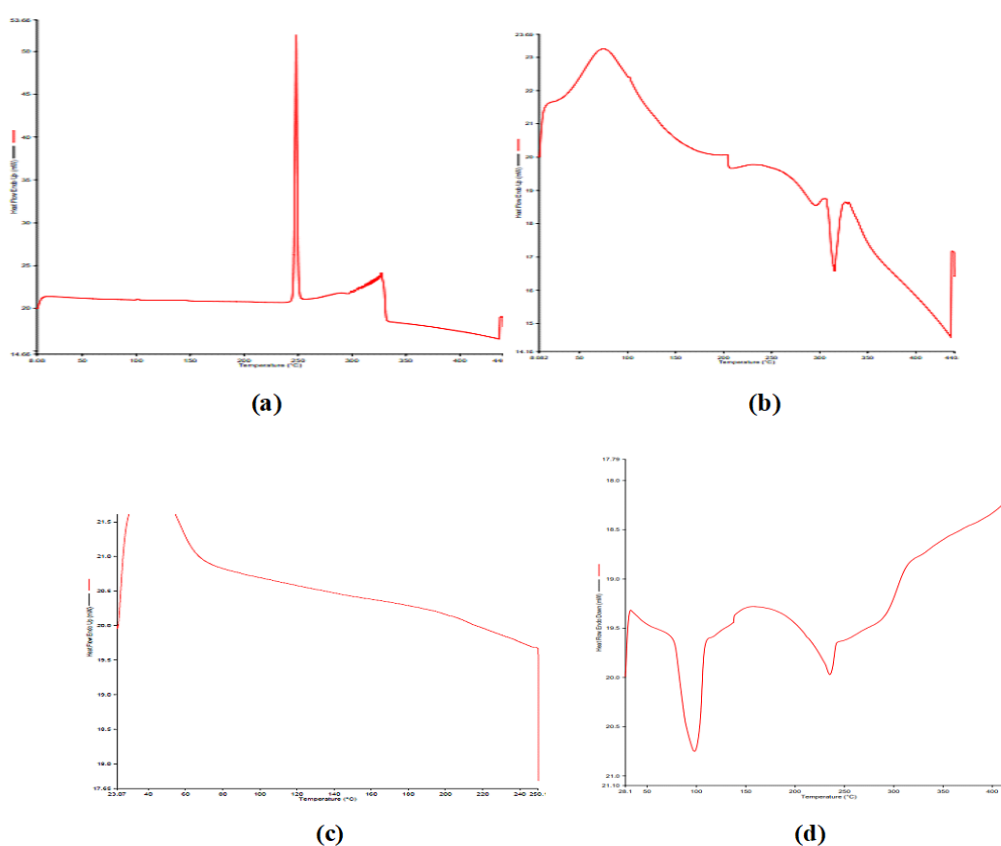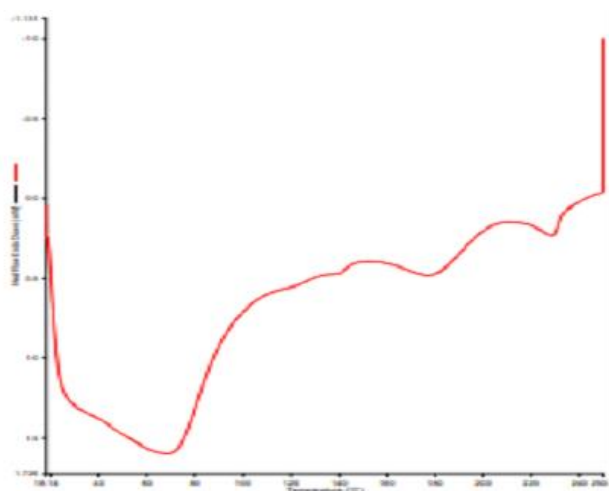
(e)

Figure 128: DSC thermogram of (a) Plain drug NVP (b) Plain drug FPV (c) DT (d) NVP-FPV-DT (e) M-NVP-FPV-DT

The DSC thermogram of the drug NVP and FPV was shown in Figure 128. The DSC image of NVP shows the sharp endothermic peak at 248 ºC. The reported DSC peak observed at 245 ºC confirms the purity of the drug NVP (Ramana et al., 2010). The DSC image of FPV shows the sharp endothermic peak at 315.53 ºC. The reported DSC peak was observed at 319 ºC confirming the purity of the drug FPV (Leksic et al., 2011). In the DSC thermogram of DT broad peak was observed at 40 ºC.

NVP-FPV-DT showed a peak at 235.08 ºC and another peak at 98.22 ºC. It was observed that the transition temperature showed a negative shift confirming the strong interactions between DT and drug NVP and FPV (Ramana et al, 2010). The transition of the peak indicated that the endothermic capability was altered which confirmed that the drug was conjugated with dendrimers (Yang et al., 2022). M-NVP-FPV-DT showed a broad peak at 64.26 ºC, this may be due to the conjugation of mannose which causes distortion or alteration in the basic structure of the delivery system (Vieira et al., 2016).

5.7.3.6 Field emission scanning electron microscopy

Figure 129 indicates the FE-SEM images of DT, NVP-FPV-DT, and M- NVP-FPV-DT. The image shows the presence of a tube-like structure of carbon nanotubes with the spherical structure -dendrimer present on the surface of the MWCNT. The image indicates that the supramolecule structure was formed by the conjugation of

MWCNT and dendrimers, which was also confirmed with TEM images. The image of NVP-FPV-DT and M-NVP-FPV-DT as shown in Figure 129 indicates that the structure remains intact with drug loading and no structural defects were observed on drug loading.

(a)

(b)

(c)
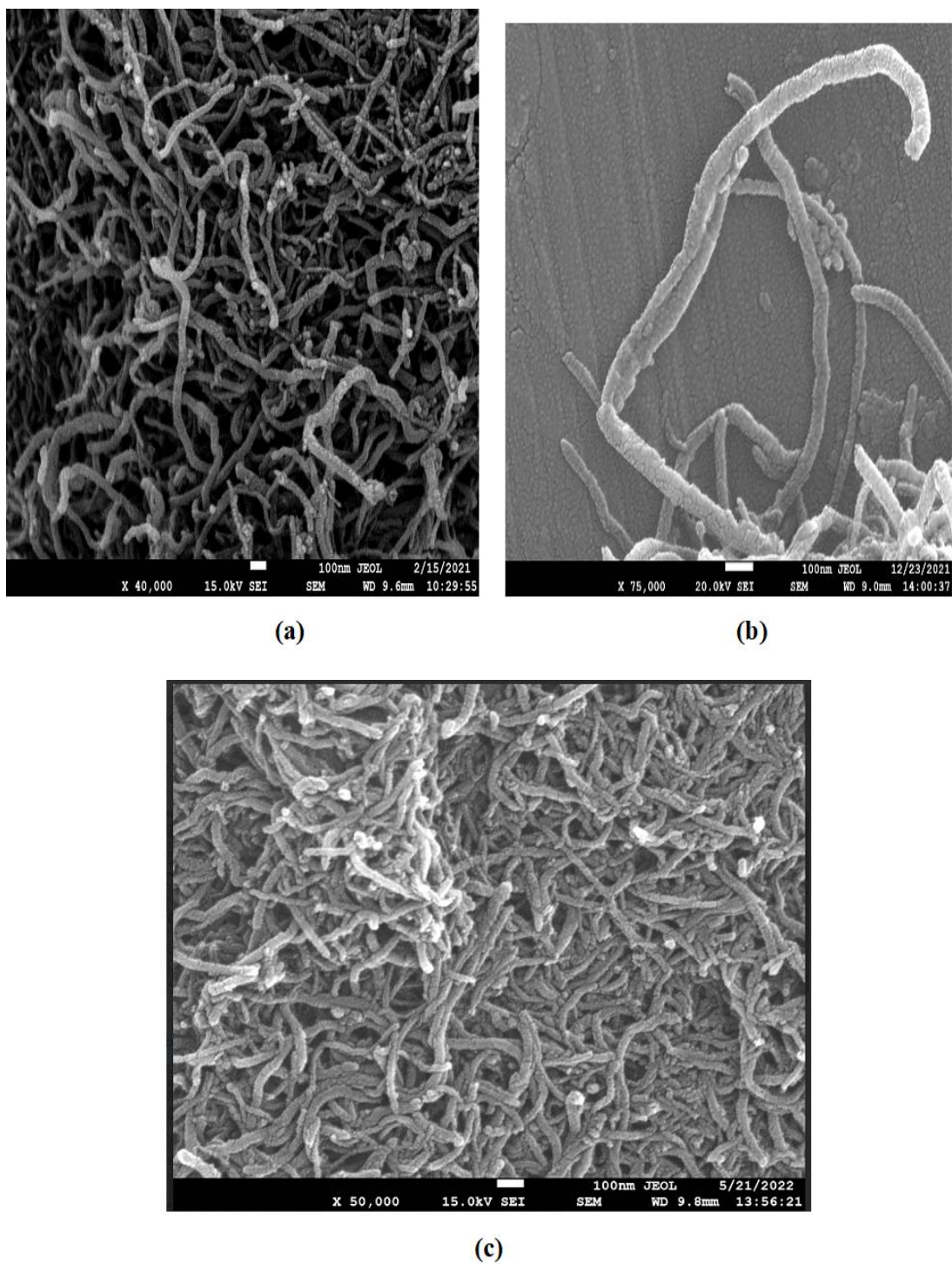
Figure 129: FE-SEM images of Dendritubes, NVP-FPV-DT, M- NVP-FPV-DT

249

5.7.7.3.7 High-resolution transmission electron microscopy
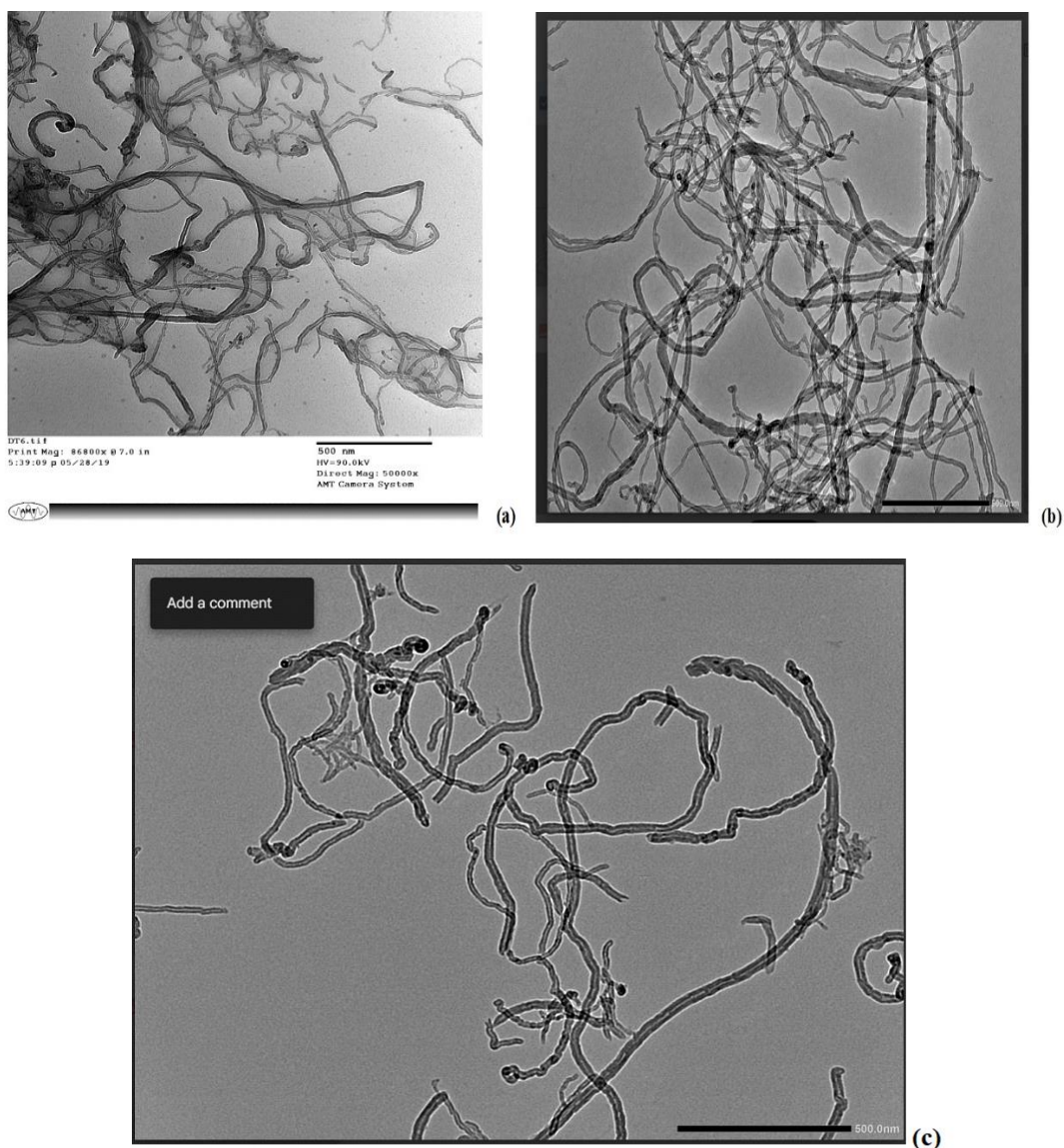
Figure 130: HR-TEM images of DT, NVP-FPV-DT, M- NVP-FPV-DT

Figure 130 indicates the HR-TEM images of DT, NVP-FPV-DT, and M-NVP-FPV-DT. The image shows the presence of a tube-like structure of carbon nanotubes with the spherical structure-dendrimer present on the surface of the MWCNT. The image of NVP-FPV-DT and M-NVP-FPV-DT as shown in Figure 130 indicates that the structure remains intact with drug loading and no structural defects were observed on drug loading.

5.7.7.3.8 Particle Size

(a)

(b)

(c)
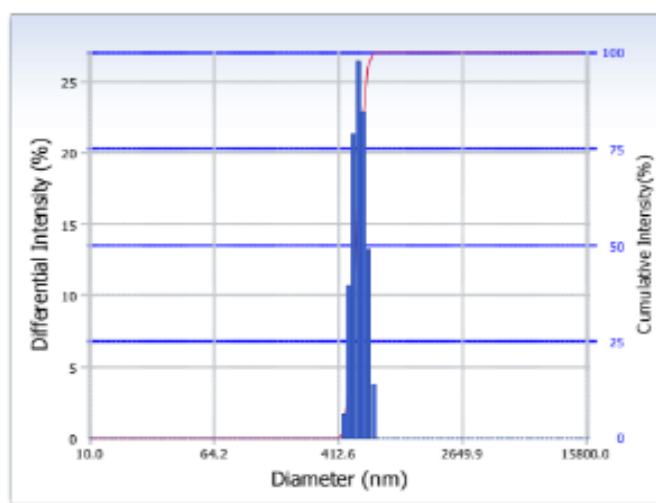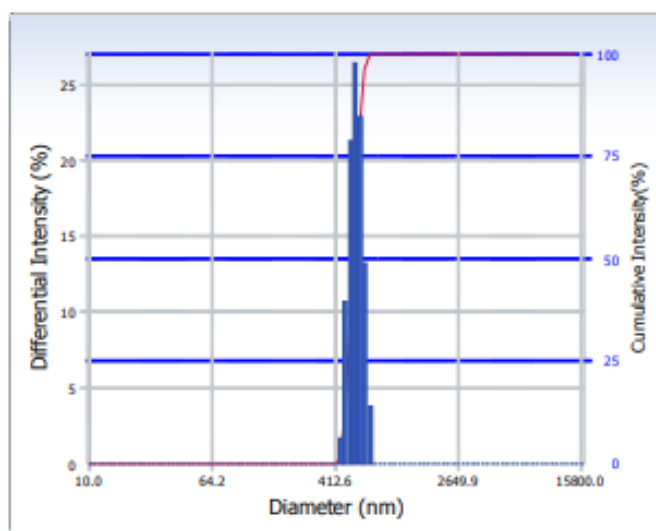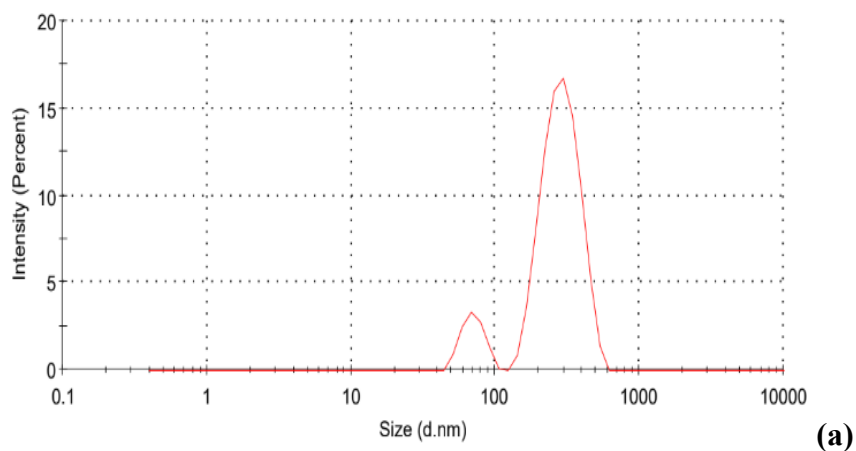
Figure 131: Particle size analysis of DT, NVP-FPV-DT, and M-NVP-FPV-DT

251

The average particle size was found to be 288.4 nm confirming that the new nanostructure was in the nanosize range. The PDI was found to be 0.385. The PDI indicates that the particle size was narrow and indicates that there was no such aggregation in the size of particles. The particle size of the drug NVP-FPV-DT was found to be 583.6 nm. The increment in size confirms the loading of the drug on DT. PDI was found to be 0.303 indicating that aggregation was further reduced, this may be due to steric hindrances. On mannosylation, there was an increment in particle size, which was found to be 765.3 nm and PDI was found to be 0.303. Figure 131 represents particle size analysis of DT, NVP-FPV-DT, and M-NVP-FPV-DT.

5.7.7.3.9 Zeta Potential

(a)

(b)

(c)
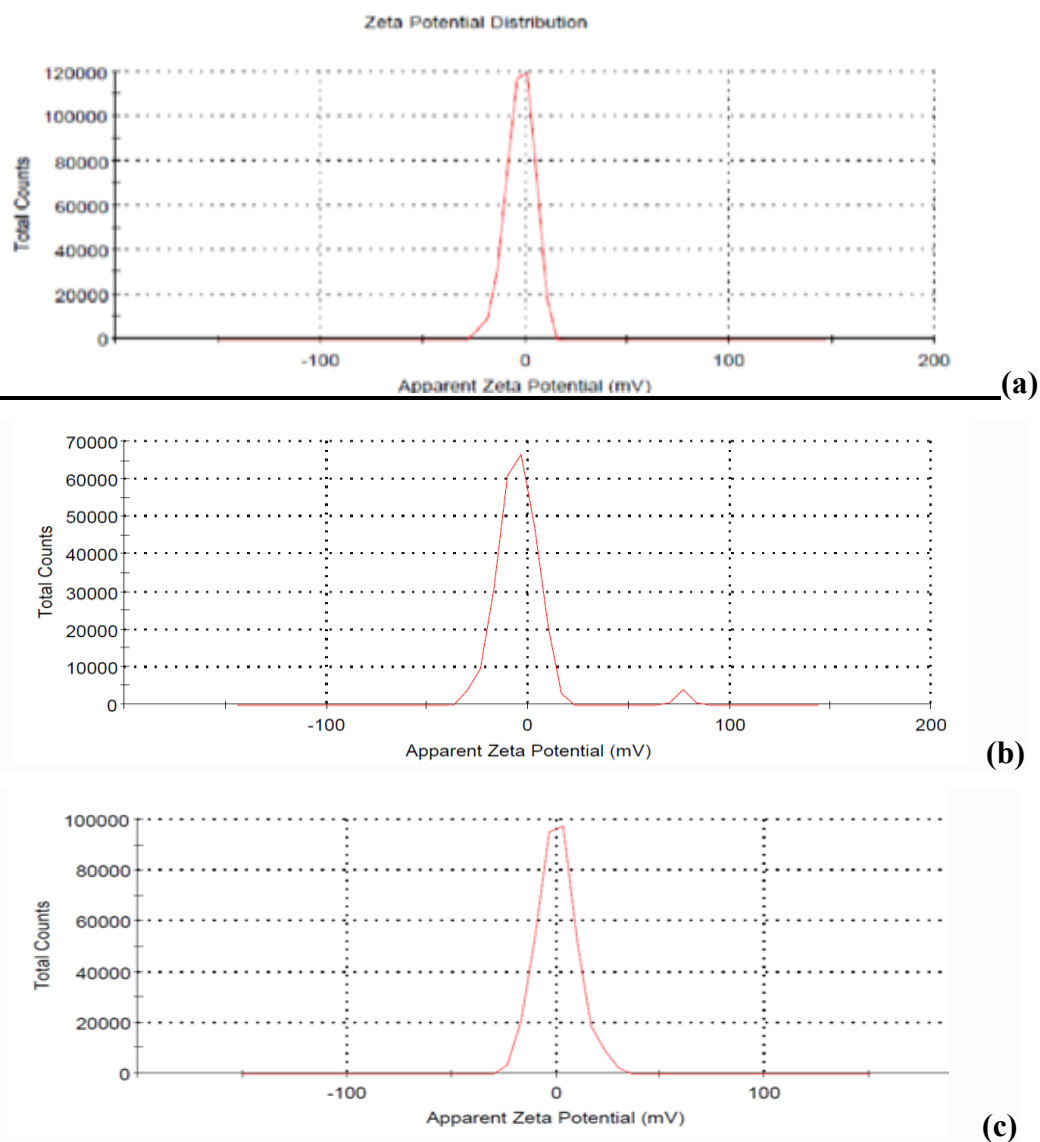
Figure 132: Zeta Potential of (a) DT, (b) NVP-FPV-DT, and (c) M-NVP-FPV-DT

Zeta potential is used to measure the charge on the surface of the nanotubes. Figure 132 represents the zeta potential of DT, NVP-FPV-DT, and M-NVP-FPV-DT. The value of Zeta potential was found to be -2.48. The negative charge may be contributed by the ionized carboxylic group on the surface. The zeta potential was found to be reduced as compared to COOH functionalized CNT and dendrimers. This indicates that the free surface functional group was reduced in the new structure. The zeta potential for NVP-FPV-DT further reduces to -0.362 which may be due to increases in –ve charges on the surface. The mannosylated structure shows positive zeta potential. It was found to be 0.510. The positive zeta potential was owing to the coating of mannose molecules on the surface. Table 49 represented the particle size, PDI, and zeta potential.

Table 49: Particle size, PDI, and zeta potential

Formulations	Z-average (nm)	PDI	Zeta potential (mV)
DT	277.9	0.358	-2.48
NVP-FPV-DT	1022	0.268	-3.62
M- NVP-FPV-DT	1058	0.192	0.510

5.7.7.3.10 Dispersibility test

The DT, NVP-FPV-DT, and M-NVP-FPV-DT were subjected to the dispersibility test to study the rate of dispersion of the prepared dispersions. The dispersion of DT NVP-FPV-DT and M- NVP-FPV-DT was prepared by dispersing 10 mg of the sample in 5 mL of distilled water. The system was sonicated for 5 min on the bath sonicator. After sonicating, the samples were kept for 24 h without disturbing the system. The dispersed system was examined at 0 h, 8 h, and 24 h. The system was found to be stable and did not settle down in deionized water. Dispersibility test of DT, NVP-FPV-DT, and M-NVP-FPV-DT at 0 h, 8 h, and 24 h in Figure 118.
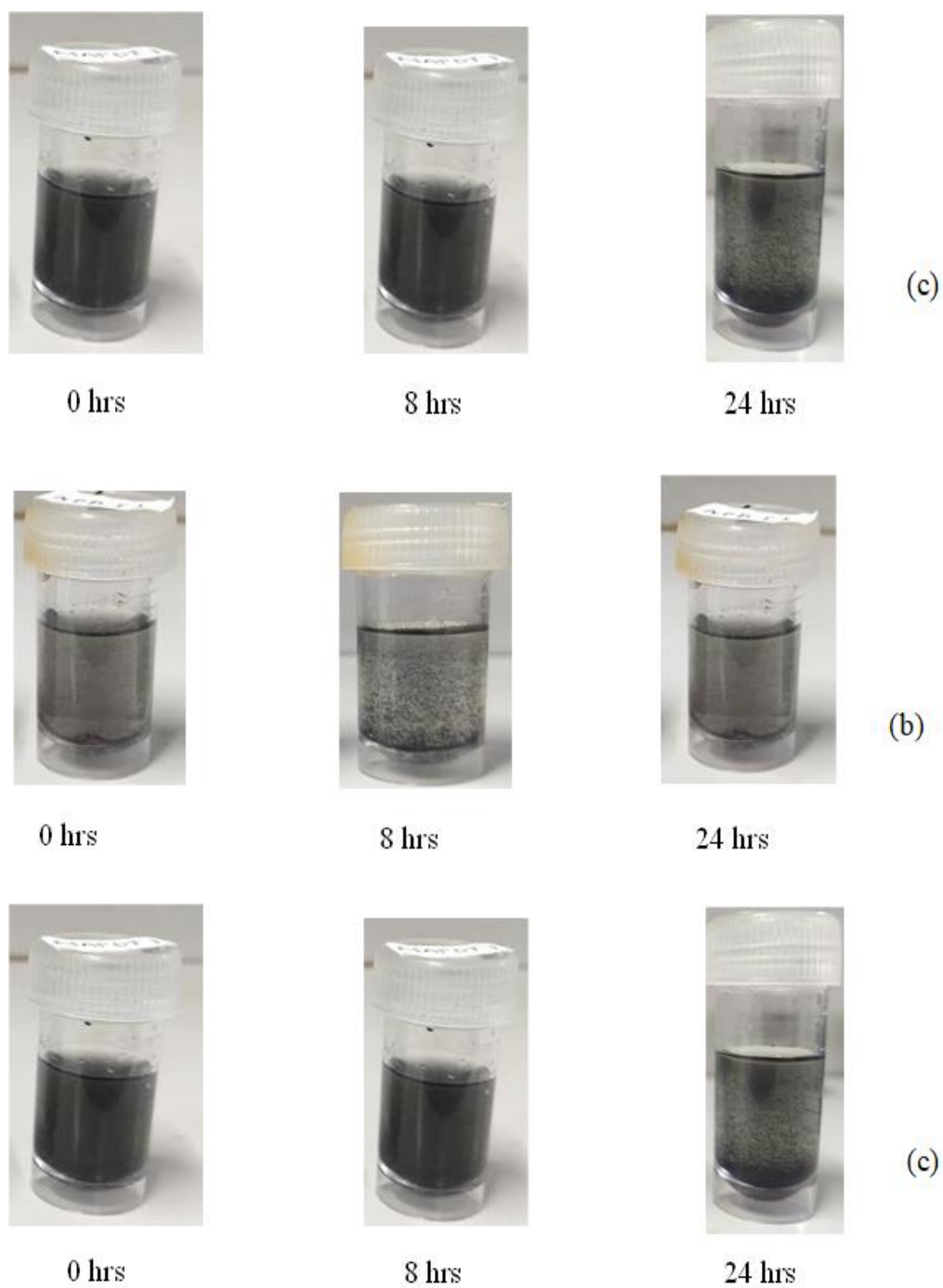
Figure 133:Dispersibility test of (a) DT (b) NVP-FPV-DT and (c) M-NVP-FPV-DT at 0 h, 8 h and 24 h

5.7.7.3.11 Entrapment efficiency

The drug entrapment efficiency of NVP in NVP-FPV-DT was found to be 69.65±0.76% and FPV in NVP-FPV-DT was found to be 47.59±0.62%. determined using an indirect method using a dialysis membrane (MWCO 7000 Da, Himedia, India). The drug can also entrap and form bonds inside the dendritic structure. The drug also binds to the side wall of MWCNT by π-π stacking. As with the new conjugate system, dendrimers on the surface have multiple binding sites available which results in higher drug loading (Tripathi et al., 2020).

5.7.3.12 *In vitro* drug release

5.7.3.12.1 *In vitro* drug release of NVP from NVP-FPV-DT at pH 7.4 and pH 5

Table 50: Drug release profile of NVP from NVP-FPV-DT

Time	% Cumulative drug release of NVP	
(h)	Acetate buffer pH 5	PBS pH 7.4
1	14.90±0.88	11.76±2.73
2	23.60±1.73	20.73±0.99
3	26.76±2.66	22.88±1.74
4	30.43±2.94	26.58±2.66
5	33.11±1.56	29.23±0.67
6	35.91±1.66	31.74±1.83
7	44.73±1.93	37.12±1.77
8	57.94±0.99	48.66±2.66
24	61.97±2.19	56.92±1.88
48	66.46±3.01	61.88±2.73
72	74.28±1.65	68.88±1.66
96	80.04±1.66	73.74±1.52

*The data was represented as Mean±SD (n=3)
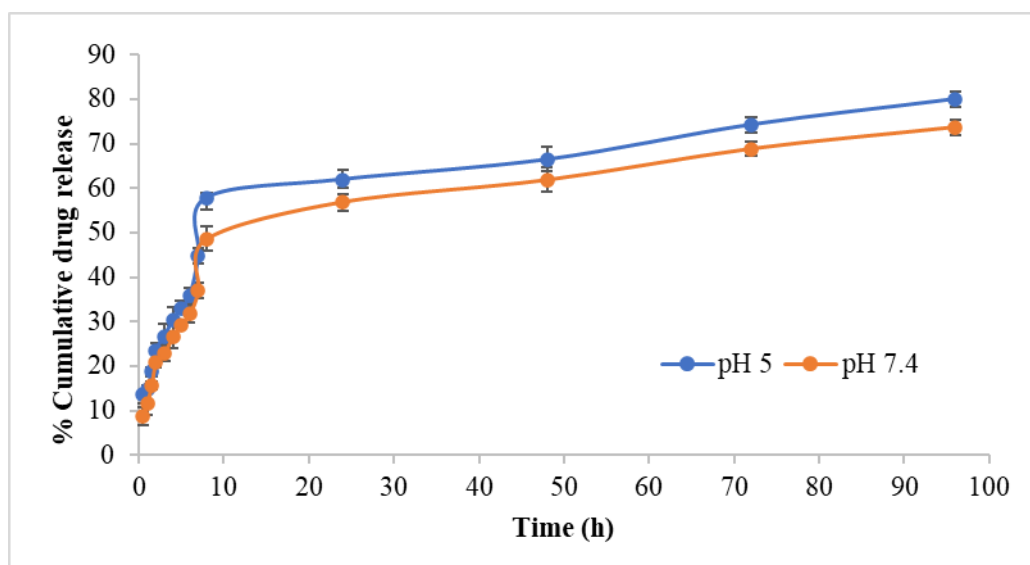
Figure 134: Drug release profile of NVP from NVP-FPV-DT for 96 h
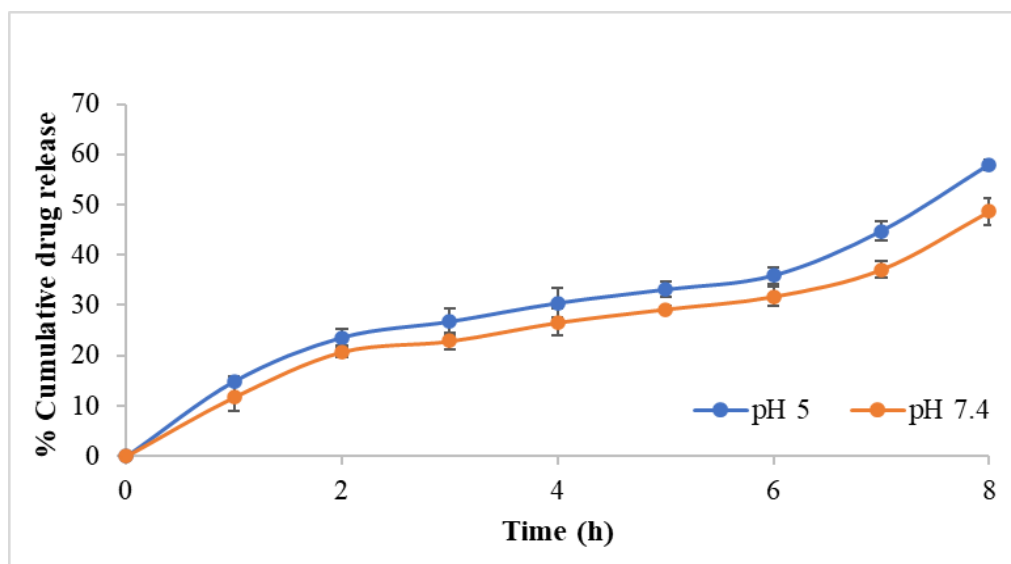
Figure 135: Drug release profile of NVP from NVP-FPV-DT for 8 h

Table 50 and Figure134 represent the drug release profile of NVP from NVP-FPV-DT at pH 7.4 and pH 5. The drug release study was performed to study the release pattern of the drug NVP from the NVP-FPV-DT. The drug release of NVP-FPV-DT was determined in pH 5 and pH 7.4 at 37 ˚C was carried out for 96 h. The medium consists of 40 % of methanol and 60% of the respective buffer. The NVP released from NVP-FPV-DT showed 80.04 ± 1.65% of drug release at pH 5 and 73.74±1.66% of drug release at pH 7.4 at the end of 96 h. The release took place in a sustained manner for 96 h. Higher release was observed at pH 5 as compared to pH 7.4. This may be due to the weekly basic nature of the drug NVP which ionizes readily at lower pH and leads to the

destruction of π-π interaction resulting in disruption of the carrier system. Due to the disruption of the carrier system repulsion forces increases between the drug and the carrier system, releasing the drug in the release system (Huang et al., 2011). The lower pH leads to the formation of free H^+ from the medium which can positively compete with hydrogen bond-forming groups. This causes the weakening of the drug-carrier interaction which results in increased release of the drug from the carrier system (Manyarara et al., 2018). The drug tends to release in a sustained manner due to the entrapment of the drug in the hydrophobic cavities of dendrimers. Also, the 5G structure of dendrimers tends to possess steric hindrance, due to the surface conjugation of primary amines. At lower pH, due to the surface amine group, the structure of dendrimers also develops a positive charge. NVP also tends to develop a positive charge which develops electrostatic repulsive force, which also promotes the release of the drug from dendrimer structures.

5.7.7.3.12.2 *In vitro* drug release profile of FPV from NVP-FPV-DT

Table 51: Drug release profile of FPV from NVP-FPV-DT

Time (h)	% Cumulative drug release of FPV	
	Acetate buffer pH 5	**PBS pH 7.4**
0	0±0	0±0
1	17.39±1.89	10.62±0.67
2	26.05±3.01	21.94±0.49
3	31.05±2.66	27.93±1.66
4	36.44±1.45	32.88±1.85
5	39.75±0.99	36.44±2.84
6	41.96±1.58	38.55±1.94
7	44.52±0.88	41.43±1.28
8	52.15±1.88	46.88±0.88
24	56.70±1.93	51.38±1.70
48	59.03±2.04	54.39±2.20
72	75.78±1.65	67.19±1.92
96	89.22±2.04	82.66±2.04

*The data was represented as Mean±SD (n=3)
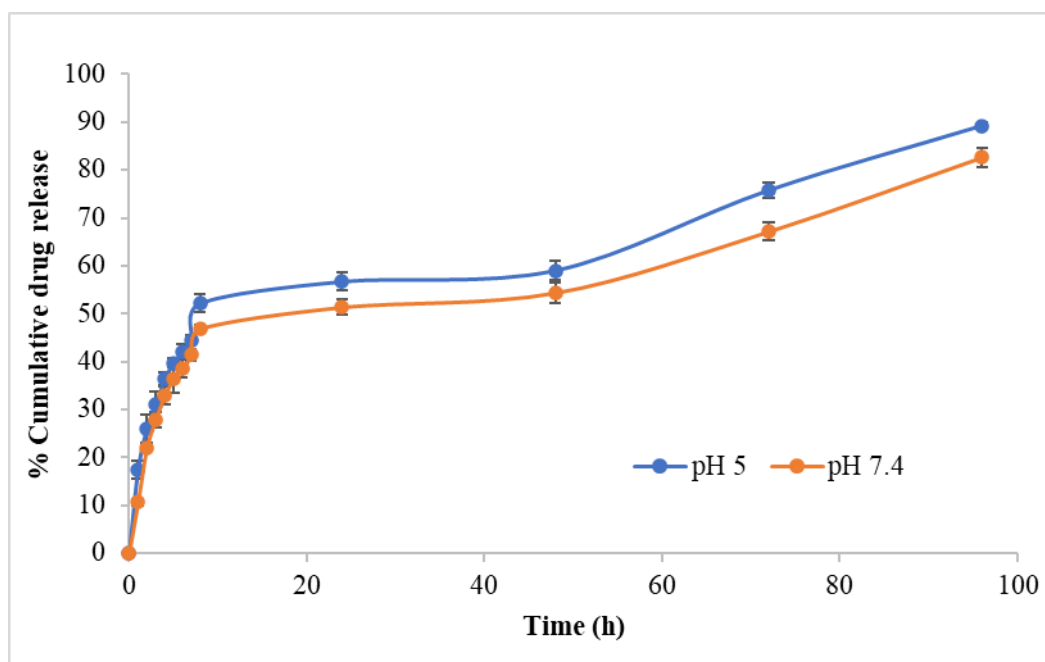
Figure 136: Drug release profile of FPV from NVP-FPV-DT for 96 h (n=3)
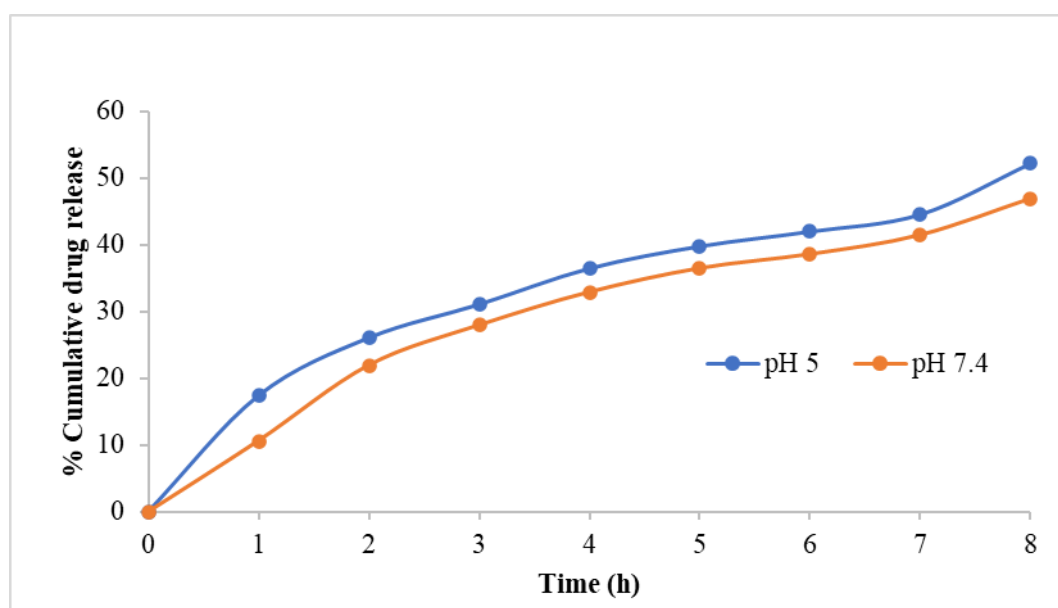
Figure 137: Drug release profile of FPV from NVP-FPV-DT for 8 h (n=3)

Table 51 and Figure 136 represent the drug release profile of FPV from NVP-FPV-DT at pH 7.4 and pH 5. Drug FPV revealed higher drug release at lower pH 5 (89.22 ± 0.64) as compared to pH 7.4 (82.66 ± 2.04). The drug tends to show higher solubility at lower pH around 3.3 than basic pH which increases the drug solubility in microphage pH. The drug tends to release in a sustained manner due to the entrapment of the drug in the hydrophobic cavities of dendrimers. Also, the 5G structure of

dendrimers tends to possess steric hindrance, due to the surface conjugation of primary amines. At lower pH, due to the surface amine group, the structure of dendrimers also develops a positive charge. FPV also tends to develop a positive charge which develops electrostatic repulsive force, which also promotes the release of the drug from dendrimer structures.

5.7.7.3.12.3 *In Vitro* drug release profile of NVP and FPV from M-NVP-FPV-DT at pH 7.4 and pH 5

Table 52: Drug release profile of NVP from M-NVP-FPV-DT

Time (h)	% Cumulative drug release of FPV	
	Acetate buffer pH 5	**PBS pH 7.4**
0	0±0	0±0
1	11.40±1.92	5.72±1.39
2	20.70±2.59	9.28±1.99
3	26.05±1.95	15.82±2.22
4	31.05±0.45	22.39±3.01
5	36.44±2.84	28.29±1.67
6	41.12±1.87	35.75±2.78
7	46.60±1.66	41.96±0.77
8	51.43±1.84	44.52±1.93
24	59.79±1.95	52.15±1.65
48	63.73±2.22	51.44±1.84
72	66.82±2.84	58.77±1.99
96	73.84±1.45	68.65±2.93

*The data was represented as Mean±SD (n=3)
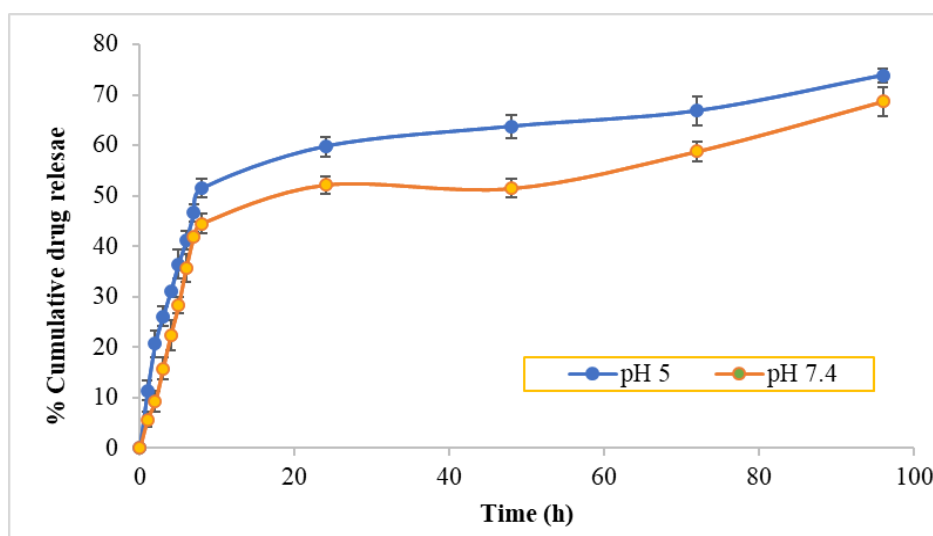
Figure 138: Drug release profile of NVP from M-NVP-FPV-DT for 96 h (n=3)

259
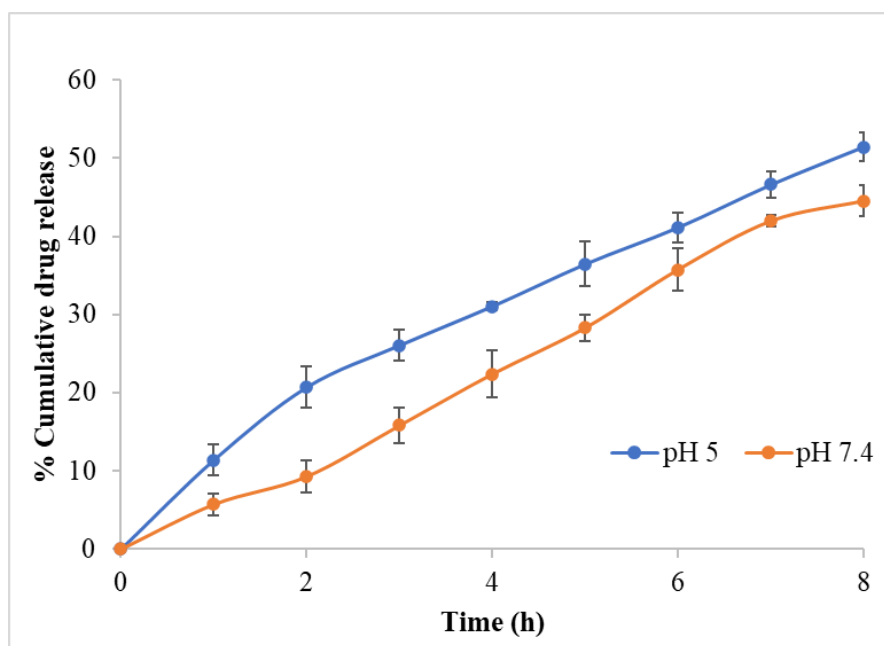
Figure 139: Drug release profile of NVP from M-NVP-FPV-DT for 8 h (n=3)

5.7.7.3.12.4 *In Vitro* **drug release profile of FPV and FPV from M-NVP-FPV-DT**

Table 53: Drug release profile of FPV from M-NVP-FPV-DT

Time (h)	% Cumulative drug release of FPV	
	Acetate buffer pH 5	**PBS pH 7.4**
0	0±0	0±0
1	11.40±1.92	4.59±0.85
2	20.70±1.02	11.31±1.39
3	26.05±1.96	14.01±1.56
4	30.05±2.34	17.81±1.84
5	34.44±3.23	22.97±2.13
6	39.75±1.92	34.81±2.96
7	40.96±2.77	39.99±1.99
8	42.52±2.44	42.85±2.64
24	52.15±1.89	48.36±1.64
48	60.44±0.99	56.70±1.94
72	69.77±0.58	63.73±2.34
96	79.84±1.56	74.38±1.44

*The data was represented as Mean±SD (n=3)
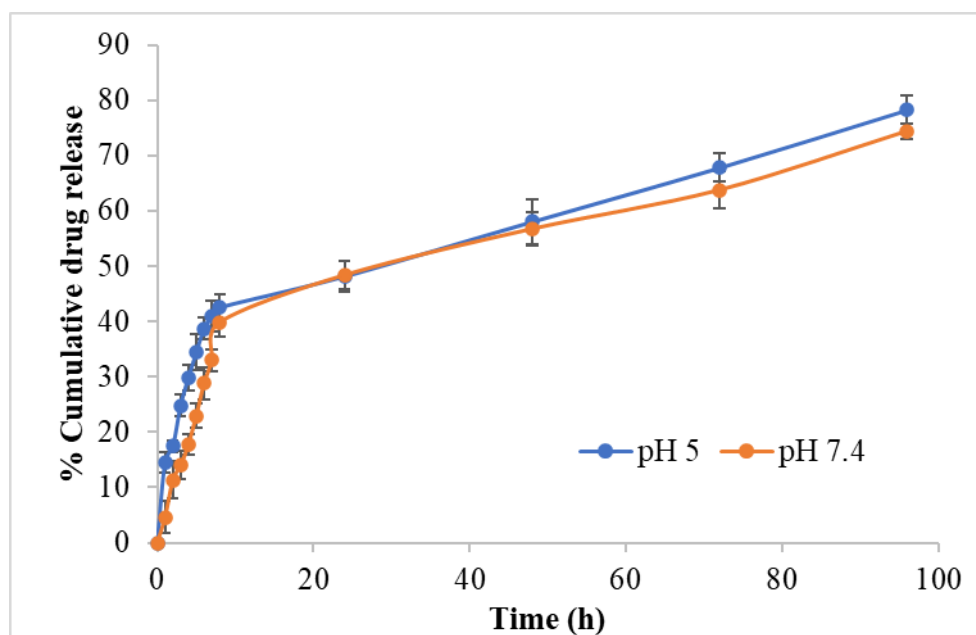
Figure 140: Drug release profile of FPV from M-NVP-FPV-DT for 96 h (n=3)
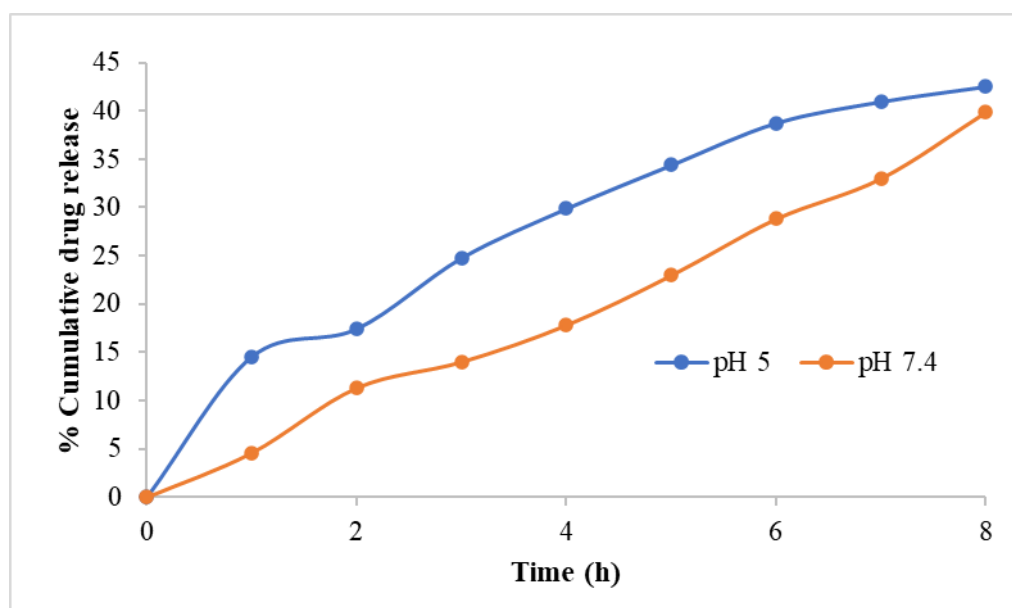
Figure 141: Drug release profile of FPV from M-NVP-FPV-DT for 8h (n=3)

Table 52 and 140 represent the drug release profile of NVP and FPV from M-NVP-FPV-DT at pH 5 and pH 7.4. Drug NVP showed 73.845±1.453 in pH 5 and 68.665±2.934 in pH 7.4. Figure 39 represents the drug release profile of NVP from M-NVP-FPV-DT at pH 5 and pH 7.4. Drug FPV showed 79.845±1.567 in pH 5 and 74.383±1.449 in pH 7.4. The drug release was reduced on mannosylation due to the presence of a protective surface coating of mannose which interfered with drug release of the drug.

From the release studies, it is suggested that the drugs NVP and FPV have better solubility at lower pH. Thus, when the system delivers the drug in the interior of the macrophages having pH 5, both the drugs will show higher release and solubility making the drug readily available for the action at the target site.

5.7.7.3.13 Drug Release Kinetics

5.7.7.3.13.1 Kinetic study of NVP from synthesized NVP-FPV-DT

Table 54: Drug release kinetics of NVP showing R^2 value and n from synthesized NVP-FPV-DT

S.No	Release	pH 5		pH 7.4	
		R^2	n	R^2	n
1	First-order	0.8412	-	0.8776	-
2	Zero-order	0.6760		0.7462	
3	Korsmeyer-Peppas	0.5580	0.5446	0.5943	0.5488
4	Higuchi	0.9005		0.9117	
5	Hixon	0.7901		0.838	

The drug release profile was subjected to different release kinetic models such as the Hixon Crowell model, the Korsmeyer-Peppas model, the Higuchi model, and first, and zero-order release kinetics. The release profiles at pH 5 and pH 7.4 were subjected to the release kinetics model. Table 54 represents the drug release kinetics of NVP showing the R^2 value and n from synthesized NVP-FPV-DT. Among the different models, the most-fitted model was found to be the Higuchi model. The best model was selected based on R^2 value, the R^2 for release profile pH 5 was found to be 0.9005 and for pH 7.4 was found to be 0.9117. The Higuchi model helps to understand the release of drugs from an insoluble matrix, wherein the factor affecting the drug release from dendrimers was owing to the higher solubility of the drug in the release medium. The release pattern showed a faster release at initial time points followed by a decrease in release with time. In this system concentration of the drug is much higher than it releases and acts as a driving force. As time proceeds concentration gradient changes reducing the diffusion subsequently reducing the drug release (Golshan et al., 2017).

The n component from the Korysmeyer-Peppas equation helps to study the release mechanism of the drug from the delivery system. The value for exponential n

was found to be 0.5446 for pH 5 and 0.5488 for pH 7.4. The value suggests that the non-fickian diffusion model governed the release. (Hooshyar et al., 2019).

The drug release was subjected to other release models, lowest R^2 value was found to be for the first order. The value for the first order was found to be 0.8412 for pH 5 and 0.8776 for pH 7.4, a lower value of R^2 makes it unsuitable. The zero-order model was also not fitted due to the low value of the correlation coefficient. It was 0.6760 for pH 5 and 0.7462 for pH 7.4. The Korsmeyer-Peppas model also showed a lesser R^2 value of around 0.5580 for pH 5 and 0.5943 for pH 7.4.The Hixon-Crowell model was also found unsuitable as the value of R^2 was found to be 0.7901 for pH 5 and 0.8380 for pH 7.4.

Thus, the best-suited model was the Higuchi model release mechanism. Figure 142 represents the drug release kinetics of NVP from NVP-FPV-DT at pH 5 and pH 7.4 such as First order release kinetics, Zero order release kinetics, Korsmeyer Peppas release kinetics, Higuchi release kinetics, and Hixon-Crowell release kinetics.
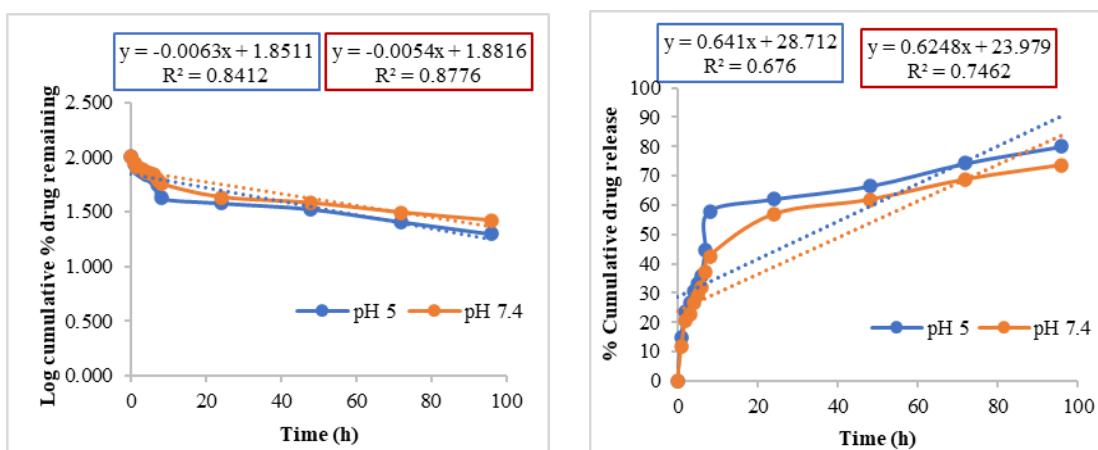
(a) First order release kinetics   (b) Zero order kinetics release
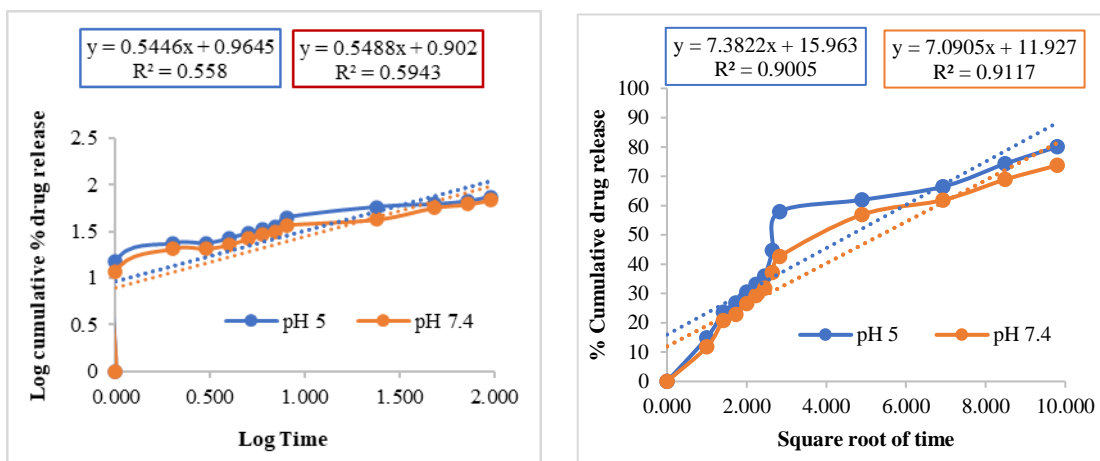
(c) **Korsmeyer Peppas release kinetics**

(d) **Higuchi release kinetics**
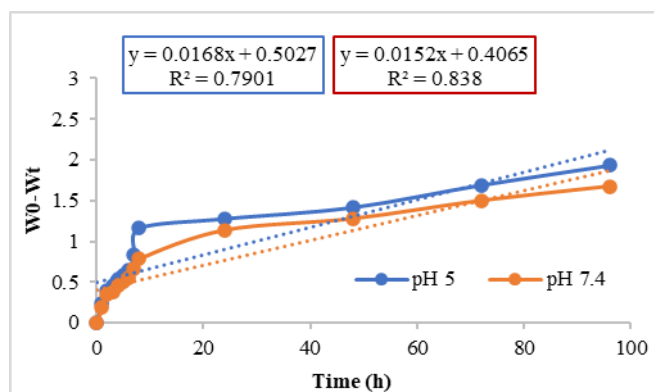
(e) **Hixon-Crowell release kinetics**

Figure 142: Drug release kinetics of NVP from NVP-FPV-DT

5.7.7.3.13.2 Kinetic study of FPV from synthesized NVP-FPV-DT

Table 55: Drug release kinetics of FPV showing R^2 value and n from synthesized NVP-FPV-DT

S.No	Release	pH 5		pH 7.4	
		R^2	n	R^2	n
1	First-order	0..9291	-	0.8683	-
2	Zero-order	0.8071		0.7070	
3	Korsmeyer-Peppas	0.5209	0.5130	0.5365	0.5256
4	Higuchi	0.9249		0.901	
5	Hixon	0.9134		0.8246	

The release profiles at pH 5 and pH 7.4 were subjected to the release kinetics model. Table 55 represents the drug release kinetics of FPV showing R^2 value and n from synthesized NVP-FPV-DT. Among the different models, the best-suited model

was found to be the Higuchi model. The best model was selected based on R^2 value, the R^2 for release profile pH 5 was found to be 0.9249 and for pH 7.4 was found to be 0.901. The Higuchi model helps to understand the release of drugs from an insoluble matrix, wherein the factor affecting the drug release from dendrimers was owing to higher solubility of drug in the release medium. The release pattern showed an initial fast release followed by a decrease in release with time. In this system concentration of the drug was much higher than it releases and acts as a driving force. As time proceeds concentration gradient changes reducing the diffusion subsequently reducing the drug release (Golshan et al., 2017).

The Korysmeyer-Peppas equation's n component aids in the investigation of the drug's release mechanism from the delivery method. For pH 5, the value of exponential n was determined to be 0.5130, and for pH 7.4, 0.5256. The number showed that the non-fickian diffusion model controlled the release. (Hooshyar et al., 2019).

The drug release was subjected to other release models, lowest R^2 value was found to be for the first order. The value for the first order was found to be 0.9291 for pH 5 and 0.8683 for pH 7.4, a lower value of R^2 makes it unsuitable. The zero-order model was also not fitted due to the low value of the correlation coefficient. It was 0.8071 for pH 5 and 0.7070 for pH 7.4. The Korsmeyer-Peppas model also showed a lesser R^2 value of around 0.5209 for pH 5 and 0.5365 for pH 7.4.The Hixon-Crowell model was also found unsuitable as the value of R^2 was found to be 0.9134 for pH 5 and 0.8246 for pH 7.4.

Thus, the most fitted model was the Higuchi model release mechanism. Figure 143 represents the drug release kinetics of FPV from NVP-FPV-DT at pH 5 and pH 7.4
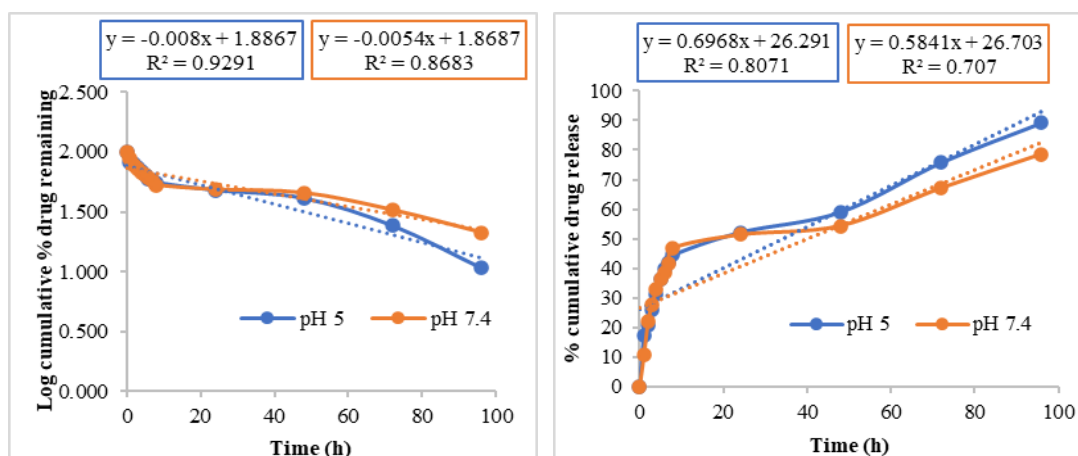
(a) First order release kinetics   **(b) Zero order release kinetics**
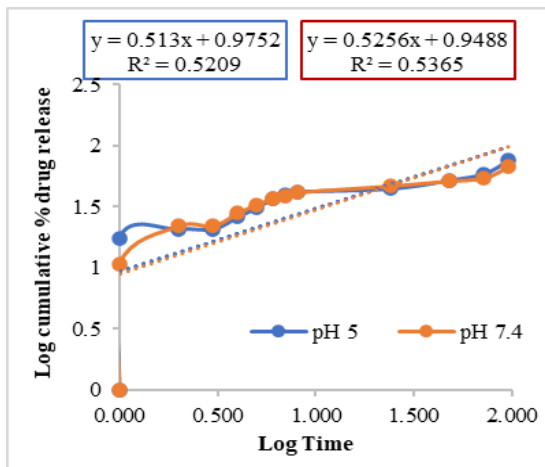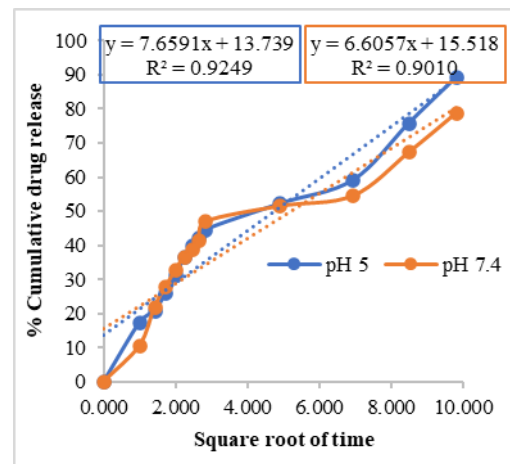
(b) Korsmeyer Peppas release kinetic   **(d) Higuchi release kinetics**
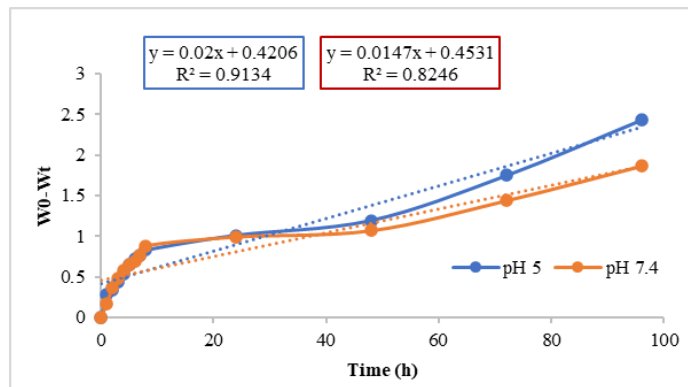
(e) Hixon-Crowell release kinetics

Figure 143: Drug release kinetics of FPV from NVP-FPV-DT

5.7.7.3.13.3 Kinetic study of NVP from synthesized M-NVP-FPV-DT

Table 56: Drug release kinetics of NVP showing R^2 value and n from synthesized M-NVP-FPV-DT

S.No	Release	pH 5		pH 7.4	
		R^2	n	R^2	n
1	First-order	0.7718	-	0.8886	
2	Zero-order	0.6149		0.784	
3	Korsmeyer-Peppas	0.5694	0.6474	0.8037	0.685
4	Higuchi	0.9077		0.901	
5	Hixon	0.7212		0.857	

The release profiles at pH 5 and pH 7.4 were subjected to the release kinetics model. Table 56 represents the drug release kinetics of NVP showing the R^2 value and n from synthesized M-NVP-FPV-DT. Among the different models, the best-suited model was found to be the Higuchi model. The best model was selected based on R^2 value, the R^2 for release profile pH 5 was found to be 0.9077 and for pH 7.4 was found to be 0.901. The Higuchi model helps to understand the release of drugs from an insoluble matrix, wherein the factor affecting the drug release from dendrimers was due to higher drug solubility in the release medium. The release pattern showed a faster release at initial time points followed by a decrease in release with time. In this system concentration of the drug was much higher than it releases and acts as a driving force. As time proceeds concentration gradient changes reducing the diffusion and subsequently reducing the drug release (Golshan et al., 2017).

The n component from the Korysmeyer-Peppas equation helps to study the release mechanism of the drug from the delivery system. If the value is less than o.5 then fickian diffusion was supposed to follow, if the value is between 0.5 to 1 non-fickian mechanism was followed. The value for exponential n was found to be 0.6474 for pH 5 and 0.685 for pH 7.4. The value revealed that the release was governed by the non-fickian diffusion model (Hooshyar et al., 2019).

The drug release was subjected to other release models, lowest R^2 value was found to be for the first order. The value for the first order was found to be 0.7718 for pH 5 and 0.8886 for pH 7.4, a lower value of R^2 makes it unsuitable. The zero-order model was also unsuitable as the value of the correlation coefficient was 0.6760 for pH 5 and 0.7462 for pH 7.4. The Korsmeyer-Peppas model also showed a lesser R^2 value

of around 0.5694 for pH 5 and 0.8037 for pH 7.4. The Hixon-Crowell model was also found unsuitable as the value of R^2 was found to be 0.7736 for pH 5 and 0.857 for pH 7.4.

Thus, the most-fitted model was the Higuchi model release mechanism. Figure 144 represents the drug release kinetics of NVP from NVP-FPV-DT at pH 5 and pH 7.4 such as First order release kinetics, Zero order release kinetics, Korsmeyer Peppas release kinetics, Higuchi release kinetics, and Hixon-Crowell release kinetics
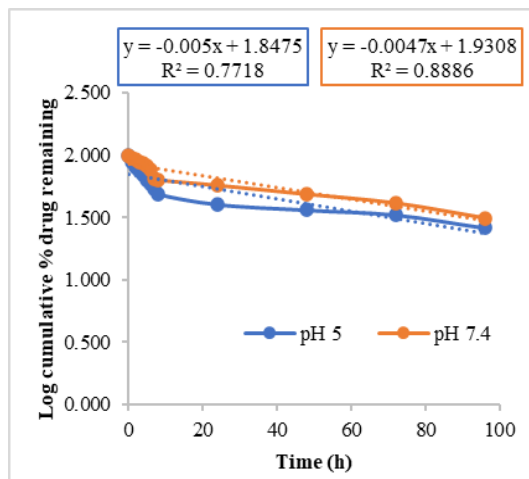
(a) First order release kinetics
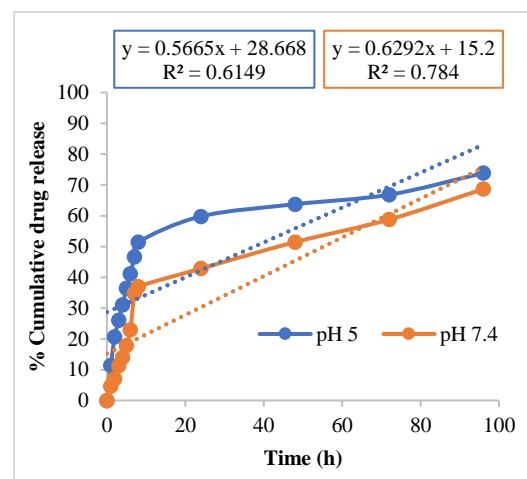
(b) Zero order release kinetics
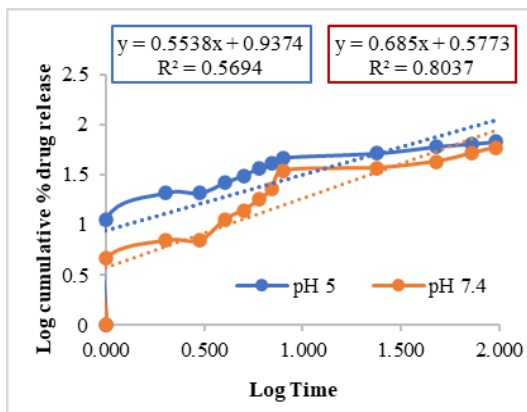
(c) Korsmeyer Peppas release kinetics
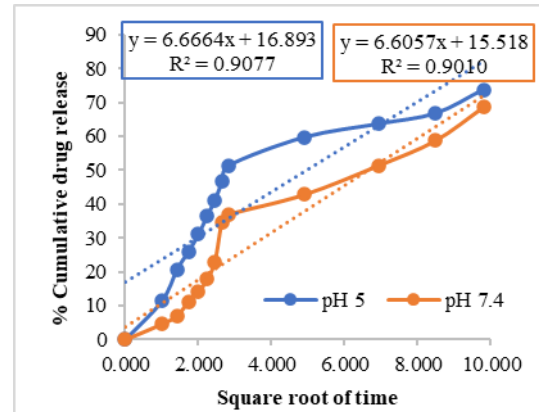
d) Higuchi release kinetics
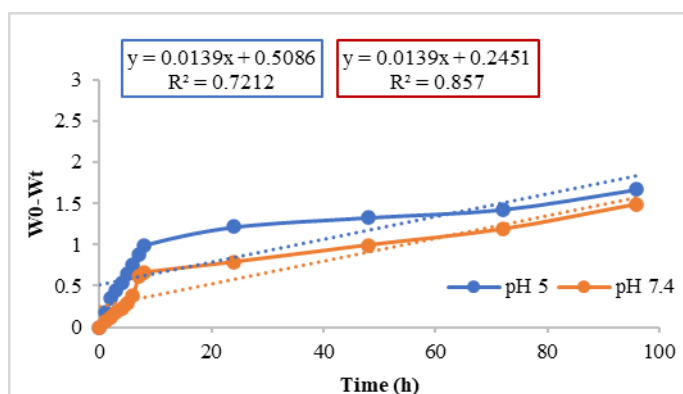
(e) Hixon-Crowell release kinetics

Figure 144: Drug release kinetics of NVP from M-NVP-FPV-DT

5.7. 7.3.13.4 Kinetic study of FPV from synthesized M-NVP-FPV-DT

Table 57: Drug release kinetics of FPV showing R^2 value and n from synthesized M-NVP-FPV-DT

S.No	Release	pH 5		pH 7.4	
		R^2	n	R^2	n
1	First-order	0.6184	-	0.9095	-
2	Zero-order	0.7567		0.7908	
3	Korsmeyer-Peppas	0.5747	0.5499	0.7605	0.66
4	Higuchi	0.9077		0.9010	
5	Hixon	0.5883		0.8752	

The release profiles at pH 5 and pH 7.4 were subjected to the release kinetics model. Table 57 represents the drug release kinetics of NVP showing the R^2 value and n from synthesized M-NVP-FPV-DT. Among the different models, the most-fitted model was found to be the Higuchi model. The best model was selected based on R^2 value, the R^2 for release profile pH 5 was found to be 0.9077 and for pH 7.4 was found to be 0.9010. The Higuchi model helps to understand the release of drugs from an insoluble matrix, wherein the factor affecting the drug release from dendrimers was owing to higher solubility of drug in the release medium. The release pattern showed a faster release at the initial time point followed by a decrease in release with time. In this system concentration of the drug was much higher than it releases and acts as a driving

force. As time proceeds concentration gradient changes reducing the diffusion subsequently reducing the drug release (Golshan et al., 2017).

The Korysmeyer-Peppas equation's n component aids in the investigation of the drug's release mechanism from the delivery method. For pH 5, the value of exponential n was determined to be 0.5499, and for pH 7.4, it was 0.66. The number showed that the non-fickian diffusion model controlled the release. (Hooshyar et al., 2019).

The drug release was subjected to other release models, lowest R^2 value was found to be for the first order. The value for the first order was found to be 0.6184 for pH 5 and 0.9095 for pH 7.4, a lower value of R^2 makes it unsuitable. The zero-order model was also not fitted as the value of the correlation coefficient was 0.7567 for pH 5 and 0.7908 for pH 7.4. The Korsmeyer-Peppas model also showed a lesser R^2 value of around 0.5747 for pH 5 and 0.7605 for pH 7.4. The Hixon-Crowell model was also found unsuitable as the value of R^2 was found to be 0.5883 for pH 5 and 0.8752 for pH 7.4.

Thus, the most-fitted model was the Higuchi model release mechanism. Figure 145 represents drug release kinetics of FPV from M-NVP-FPV-DT at pH 5 and pH 7.4.
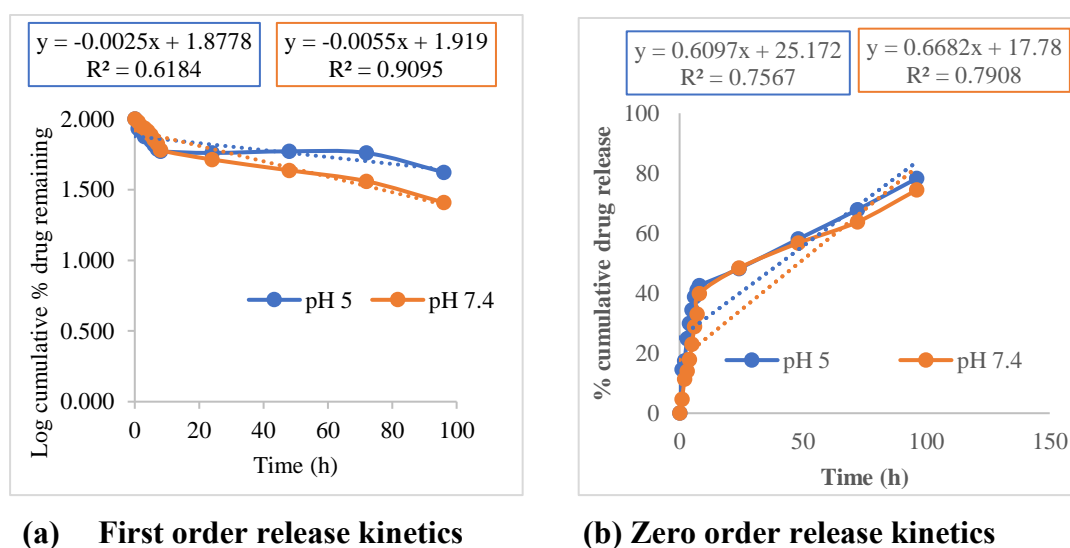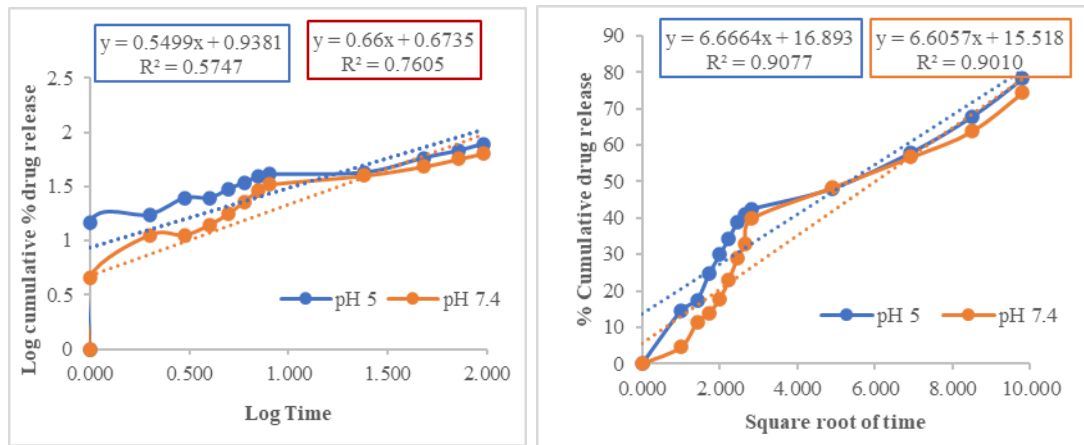
(a)   **First order release kinetics**   **(b) Zero order release kinetics**

(c) Korsmeyer-Peppas release kinetics   **(d) Higuchi release kinetics**
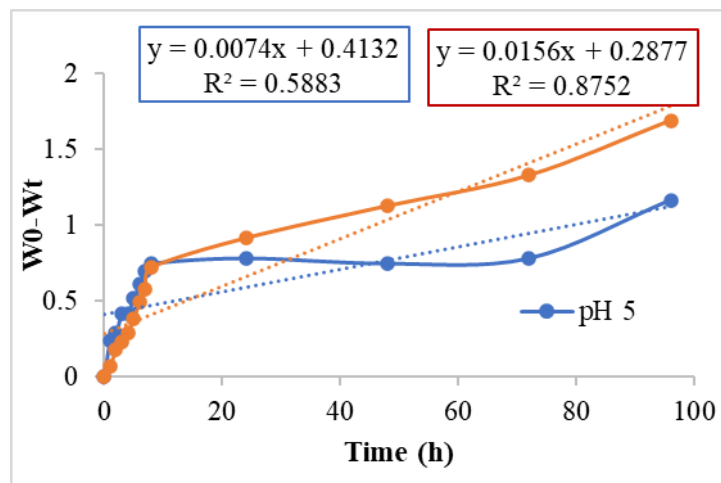
(e) Hixon-Crowell release kinetics

Figure 145: Drug release kinetics of FPV from M-NVP-FPV-DT

5.8 Stability studies

5.8.1 Physiochemical characterization

The stability studies were performed to evaluate the physical, chemical, and pharmacokinetic nature of the drug in the delivery system throughout the shelf life.

5.8 Stability studies

5.8.1 Physiochemical characterization

The stability studies were performed to evaluate the physical, chemical, and pharmacokinetic nature of the drug in the delivery system throughout the shelf life. The prepared NVP-DT, FPV-DT and NVP-FPV-DT, and M-NVP-FPV-DT were subjected to 4±2 °C, at room temperature (25±2 °C) and at accelerated temperature (40±2 °C) for 6 weeks and studied at the interval of 1 week and evaluated for the colour change, precipitation, turbidity, and consistency.

Table 58 tabulated the colour change, precipitation, turbidity, and consistency of NVP-DT, FVP-DT, NVP-FPV-DT, and M-NVP-FPV-DT. NVP-DT, FVP-DT, NVP-FPV-DT, M- NVP-FPV-DT does not show any significant change in dark and light at 4 ºC. Turbidity and precipitation were found to be higher in light-exposed samples as compared to the samples kept in the dark in RT and at accelerated temperature. Higher turbidity at accelerated temperature may be because of the polymerization of the free functional group. The formulation was found to be more stable in dark and in cool temperature (Soni et al., 2016).

Table 58: Stability studies of NVP-DT, FPV-DT, and NVP-FPV-DT

Storage condition	Light			Dark		
	4±2 °C	25±2 °C	40±2 °C	4±2 °C	25±2 °C	40±2 °C
NVP-DT						
Change in colour	-	+	+	-	-	+
Turbidity	+	+	++	+	+	++
Precipitation	+	4 weeks	3 weeks	-	-	5 weeks
Change in consistency	-	+	+	-	+	+
FPV-DT						
Change in colour	-	+	+	-	-	+
Turbidity	+	++	++	+	+	++
Precipitation	+	2 weeks	2 weeks	-	-	4 weeks
Change in consistency	-	+	+	-	+	+
NVP-FPV-DT						
Change in colour	-	+	+	-	-	+
Turbidity	+	++	++	+	+	++
Precipitation	+	3 weeks	2 weeks	-	-	5 weeks
Change in consistency	-	++	++	-	+	++
M-NVP-FPV-DT						
Change in colour	-	+	+	-	-	+
Turbidity	+	++	++	+	+	++
Precipitation	+	3 weeks	2 weeks	-	-	4 weeks
Change in consistency	-	++	+++	-	++	++

5.8.2 Drug leakage

A drug leakage test was determined for the leaking of the drug from the DT. NVP-DT, FPV-DT, NVP-FPV-DT, and M-NVP-FPV-DT were subjected to drug leakage test from the delivery system. NVP-DT, FPV-DT, NVP-FPV-DT, and M-NVP-FPV-DT were subjected to light and dark environment at 4±2 °C, 25±2 °C, and 40±2 °C. Table 59-64 and Figure 150-155 represent the % drug leakage from different formulations.

Table 59: % drug leakage of NVP from NVP-DT at different temperatures in dark and light conditions

Time	Dark cycle		
	4±2 °C	**25±2 °C**	**40±2 °C**
1 week	0.24±0.22	0.36±0.45	1.88±0.26
3 week	1.43±0.34	1.88±0.26	2.73±0.37
6 week	1.88±0.13	2.26±0.15	3.56±0.26
	Light cycle		
1 week	0.33±0.23	0.47±0.37	2.22±0.14
3 week	1.64±0.26	2.22±0.15	3.63±0.22
6 week	2.00±0.14	3.01±0.45	4.66±0.45
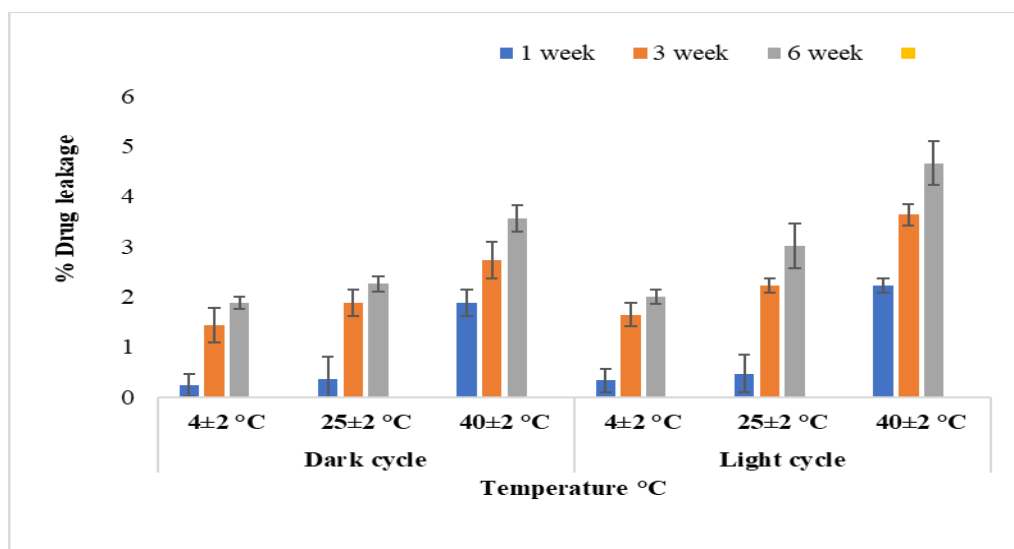
Figure 150: % Drug leakage of NVP from NVP-DT at different temperatures in dark and light conditions

Table 60: % Drug leakage of FPV from FPV-DT

Time	Dark cycle		
	4±2 °C	**25±2 °C**	**40±2 °C**
1 week	0.33±0.29	0.53±0.44	2.43±0.35
3 week	1.66±0.15	2.63±0.23	4.01±0.28
6 week	2.23±0.23	3.33±0.13	4.44±0.13
	Light cycle		
1 week	0.48±0.33	0.83±0.22	3.63±0.21
3 week	2.02±0.38	3.66±0.16	4.44±0.37
6 week	3.33±0.48	4.00±0.34	6.04±0.49
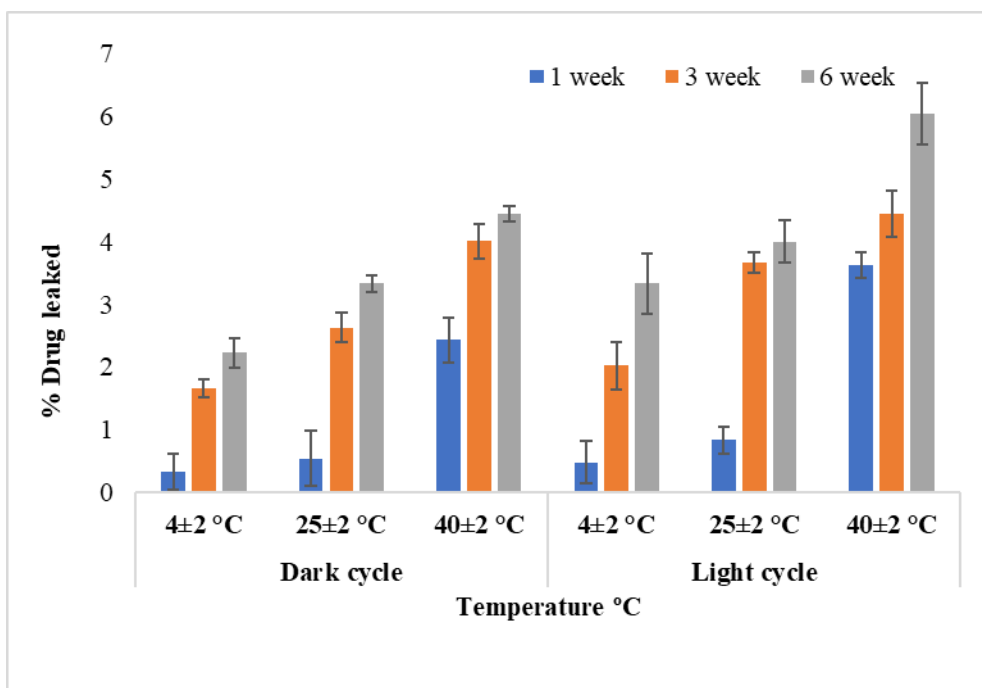
Figure 151: % Drug leakage of FPV from FPV-DT

Table 61: % Drug leakage of NVP from NVP-FPV-DT

Time	Dark cycle		
	4±2 °C	**25±2 °C**	**40±2 °C**
1 week	0.15±0.24	0.26±0.24	1.56±0.41
3 week	1.27±0.28	1.77±0.31	2.46±0.27
6 week	1.68±0.55	2.26±0.34	3.33±0.24
	Light cycle		
1 week	0.55±0.36	1.28±0.45	2.00±0.31
3 week	1.55±0.52	2.19±0.25	3.33±0.28
6 week	1.92±0.26	2.75±0.42	3.93±0.21
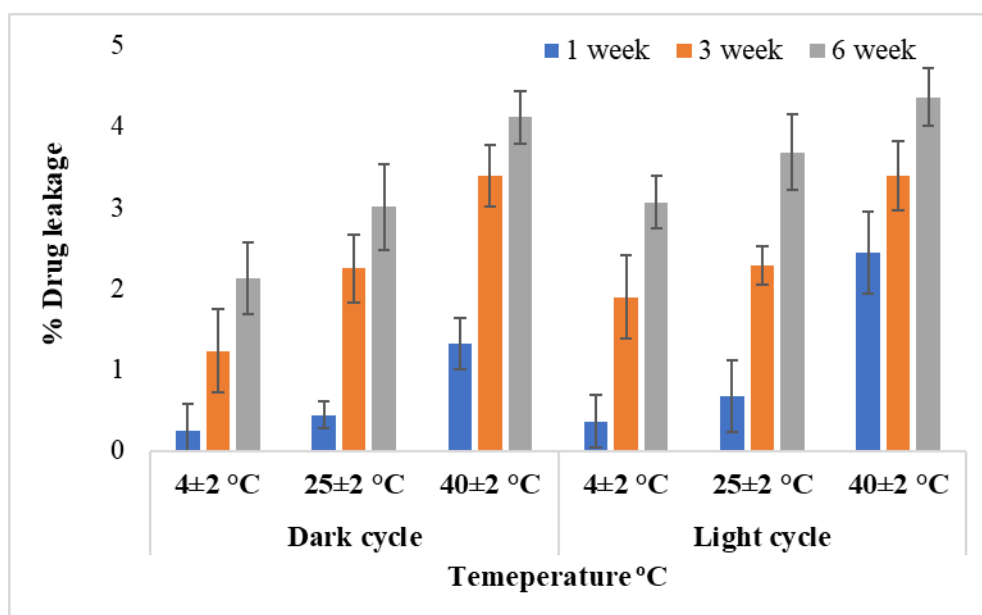
Figure 152: % Drug leakage of NVP from NVP-FPV-DT

Table 62: % Drug leakage of FPV from NVP-FPV-DT

Time	Dark cycle		
	4±2 °C	**25±2 °C**	**40±2 °C**
1 week	0.24±0.33	0.44±0.17	1.32±0.32
3 week	1.23±0.51	2.25±0.42	3.99±0.38
6 week	2.13±0.44	3.01±0.53	4.11±0.32
	Light cycle		
1 week	0.36±0.32	0.67±0.44	2.44±0.51
3 week	1.89±0.51	2.28±0.24	3.33±0.43
6 week	3.06±0.33	3.68±0.47	4.36±0.36
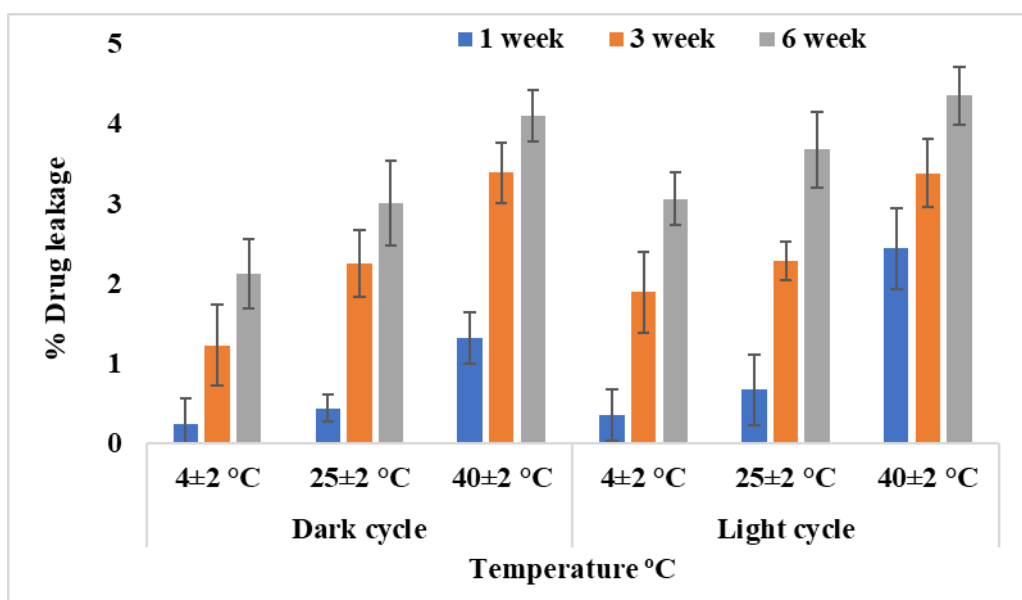
Figure 153: % Drug leakage of FPV from NVP-FPV-DT

Table 63: % Drug leakage of NVP from M-NVP-FPV-DT

Time	Dark cycle		
	4±2 °C	**25±2 °C**	**40±2 °C**
1 week	0.12±0.22	0.21±0.35	0.92±0.12
3 week	0.17±0.27	1.28±0.21	2.06±0.43
6 week	1.34±0.35	1.89±0.41	2.68±0.33
	Light cycle		
1 week	0.41±0.44	0.89±0.32	1.52±0.16
3 week	1.33±0.27	1.52±0.51	2.76±0.21
6 week	1.64±0.47	1.92±0.27	3.22±0.24
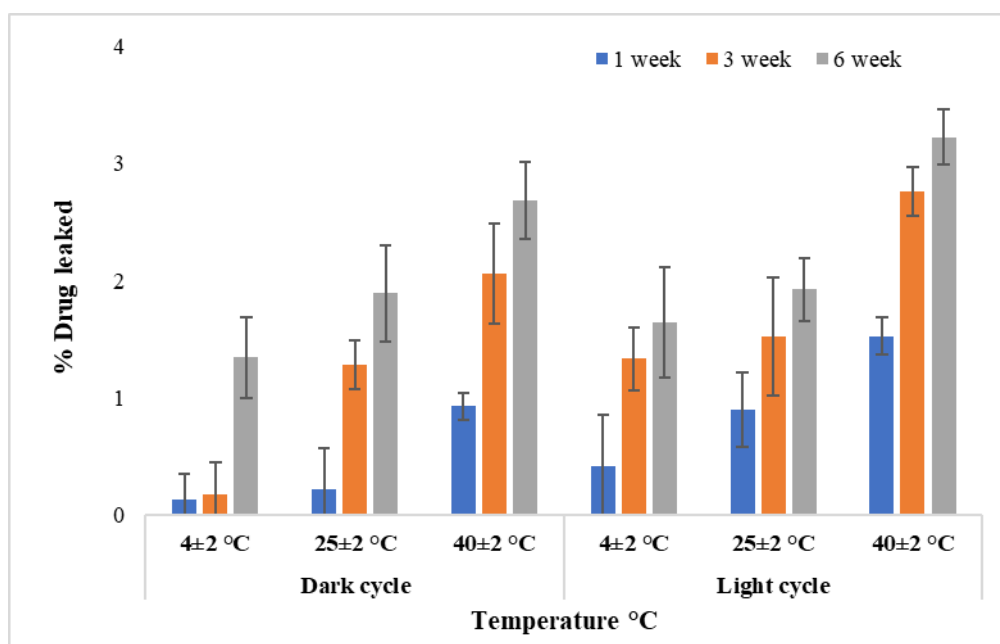
Figure 154: % Drug leakage of NVP from M-NVP-FPV-DT

Table 64: % Drug leakage of FPV from M-NVP-FPV-DT

Time	Dark cycle		
	4±2 °C	**25±2 °C**	**40±2 °C**
1 week	0.17±0.24	0.21±0.31	1.01±0.44
3 week	1.00±0.36	1.87±0.26	2.88±0.15
6 week	1.89±0.22	2.78±0.31	3.82±0.36
	Light cycle		
1 week	0.142±0.15	0.472±0.26	1.83±0.31
3 week	1.473±0.44	1.782±0.35	2.71±0.41
6 week	2.783±0.41	2.671±0.18	3.13±0.15
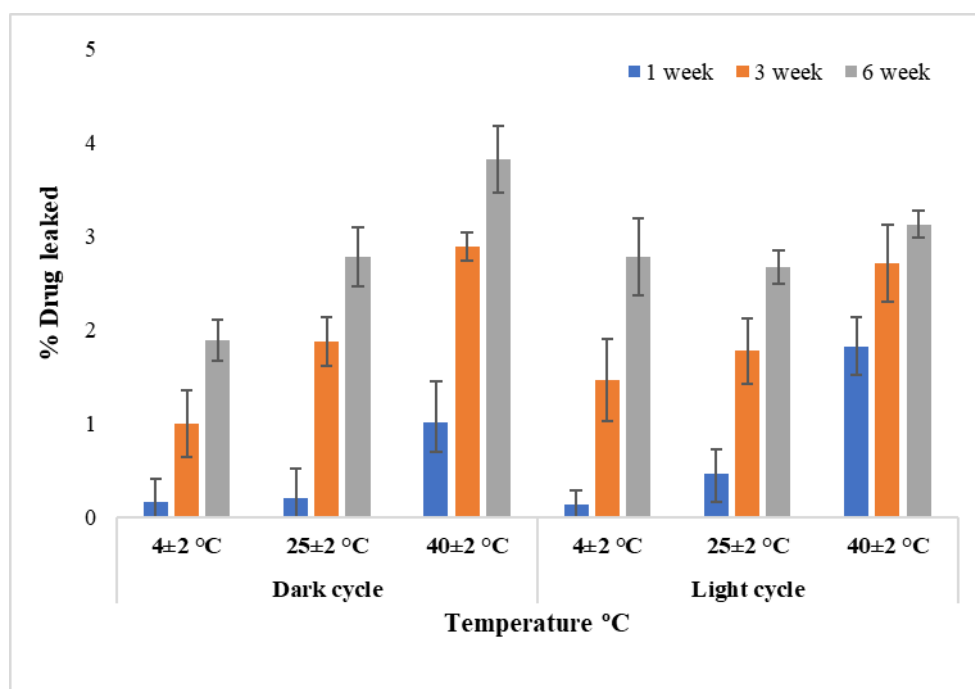
Figure 155: % Drug leakage of FPV from M-NVP-FPV-DT

All the formulations showed very low level of drug leakage at 4±2 °C as compared to RT and accelerated temperature. Dendriner structures tends to shrink at lower temperature which reduces the drug leakage. The leakage tends to increase with an increment of time. At RT (25±2 °C) the leakage was higher with FPV from FPV DT, this may be due to higher π- π stacking of drug on CNT or entrapped drug in dendrimers. NVP-FPV-DT showed reduced leaking as compared to NVP-DT and FPV-DT, this

may be due to the structural complexity of the system. M-NVP-FPV-DT further reduced leaking as compared to NVP-FPV-DT due to the steric effect of mannose which reduces the drug leakage. Accelerated temperature (40±2 °C) increases the leaking of the drug which may be due to structural deformation of dendrimers (Singh et al., 2016; Soni et al., 2016).

5.9 *In vitro* cell line studies

5.9.1 Cytotoxicity studies

MTT assay was performed to assess the cytotoxicity of the free drugs NVP, FPV, delivery system DT, M-DT, NVP-FPV-DT, and MNVP-FPV-DT with the equivalent dose of 5, 10, 25, 50, 100 µg/mL on macrophage cell lines and tabulated in Table 65. The MTT (3 -(4,5-dimethylthiazol-2-yl)-2,5-diphenyltetrazolium bromide) test is a calorimetric assay using non-radioactive materials to assess mitochondrial activity to study the cell viability following treatment with the developed delivery system.

From the study, it was clear that the viability of the cell decreases with an increase in the concentration. DT showed maximum toxicity which was due to the surface amine group of dendrimers attached to the surface of DT. Mannosylation improves the cytotoxicity as compared with plain DT due to the surface coating of the amine group with mannose. The plain drug FPV does not show cytotoxicity and the plain drug NVP showed a cell viability of 58.96±2.23 % at 100 µg/mL. The concentration-dependent cytotoxicity was observed with NVP-FPV-DT formulation. MWCNT has a nanoneedle-like structure that can cross the transmembrane of cell structures leading to its accumulation in cells. NVP-FPV-DT had surface amine groups which induced the toxicity. M-NVP-FPV-DT showed improved cell viability due to mannose coating on the surface of drug-loaded DT. Figure 156 represents the cell viability of plain drug NVP, FPV, delivery system DT, and M-DT and formulations.

Table 65: Cell viability studies

Conc. (µg/mL)	% Cell viability					
	DT	M-DT	FPV	NVP	NVP-FPV-DT	M-NVP-FPV-DT
Ctrl	100 ± 4.04	99.99 ± 0.70	103.89 ± 1.19	100.00 ± 1.96	99.99 ± 4.47	99.99 ± 1.69
5	71.16 ± 1.23	72.01 ± 1.16	102.85 ± 4.10	96.24 ± 4.93	72.24 ± 4.53	94.09 ± 2.93
10	68.65 ± 1.65	65.75 ± 1.56	100.00 ± 3.54	88.11 ±1.82	70.23 ± 2.92	81.06 ± 3.49
25	58.42 ± 2.44	58.11 ± 0.46	99.48 ± 5.30	72.83 ± 7.18	62.71 ± 4.61	73.96 ± 3.25
50	43.16 ± 1.26	53.07 ± 0.85	99.26 ±2.99	61.84 ± 4.73	51.73 ±1.27	71.97 ± 4.56
100	40.08 ± 3.03	53.63 ± 4.36	97.78 ±2.38	58.96 ± 2.23	43.11± 2.10	66.57 ± 2.52
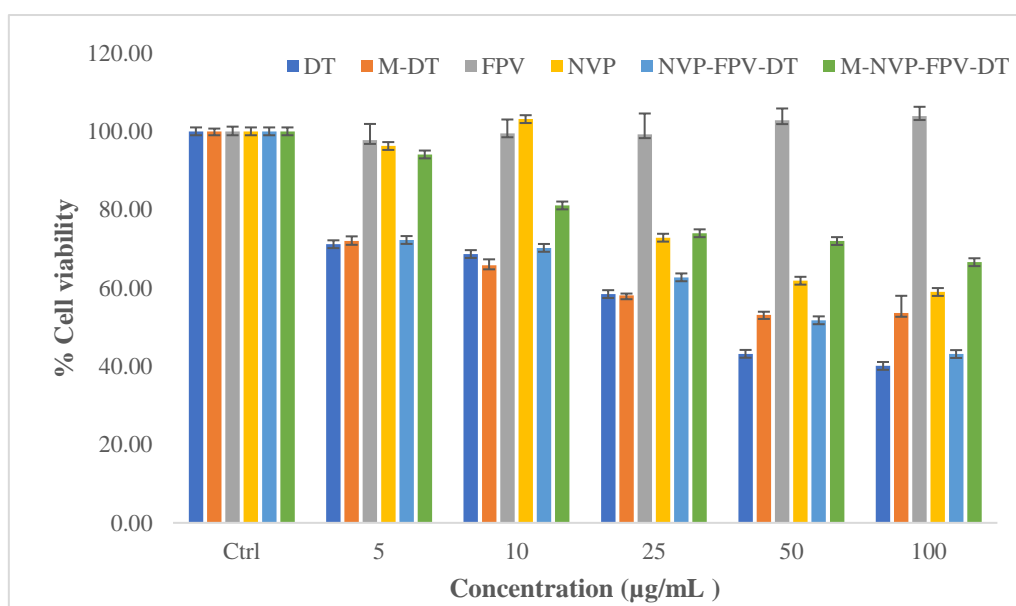
Figure 156: Cell viability studies

5.9.2 Cell internalization studies
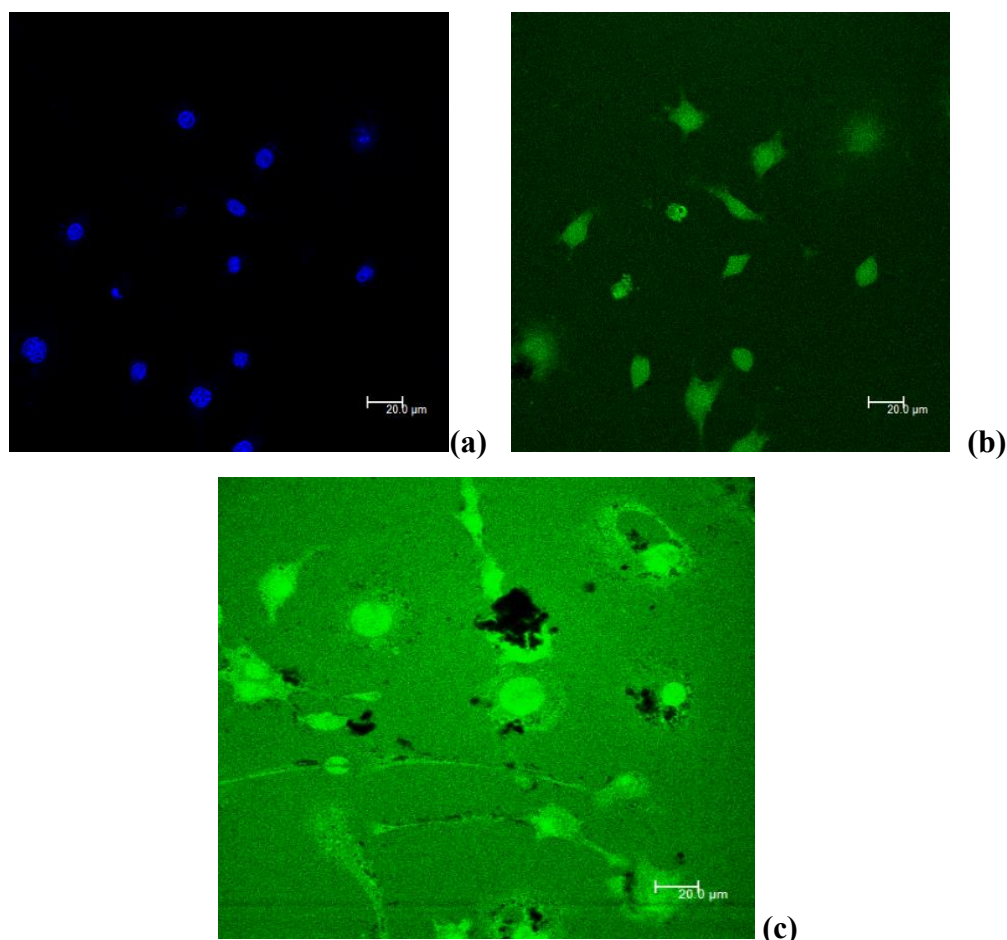
Figure 157: Confocal microscopic images of (a) Control (b) NVP-FPV-DT (c) M-NVP-FPV-DT

Cellular uptake studies were designed to explore the cell internalization of the designed delivery system using macrophage cell lines. Cellular uptake studies were carried out on NVP-FPV-DT and M-NVP-FPV-DT were observed using confocal microscopy. To identify the carrier, the systems were conjugated with FITC. M-NVP-FPV-DT showed greater intensity of fluorescence as compared to the non-mannosylated formulations (NVP-FPV-DT). The results suggest that the M-NVP-FPV-DT tends to show higher fluorescence intensity which was due to higher uptake of the mannosylated group due to receptor-mediated endocytosis and the nano needle-shaped structure of MWCNTs (Mehra et al. 2014). The nano-needle-specific mechanism also helps in the uptake of NVP-FPV-DT (Sharma et al 2016). Figure 157 represents the Confocal microscopic images of a) Control b) NVP-FPV-DT c) M-NVP-FPV-DT.

5.10 Animal studies

5.10.1 Bioanalytical Method Development

5.10.1.1 Selection of UV Wavelength

10 μg/mL solution was prepared and scanned at 400 to 200 nm using a UV spectrophotometer. The maxima for absorption of FPV, NVP, and AMP were found to be 265 nm for FPV and APV and 283 nm for NVP. The isosbestic point of three drugs in the mixture of the drugs was found to be 258 nm. The UV scan results are shown in Figure 158. Method development and validation were carried out at 258 nm.
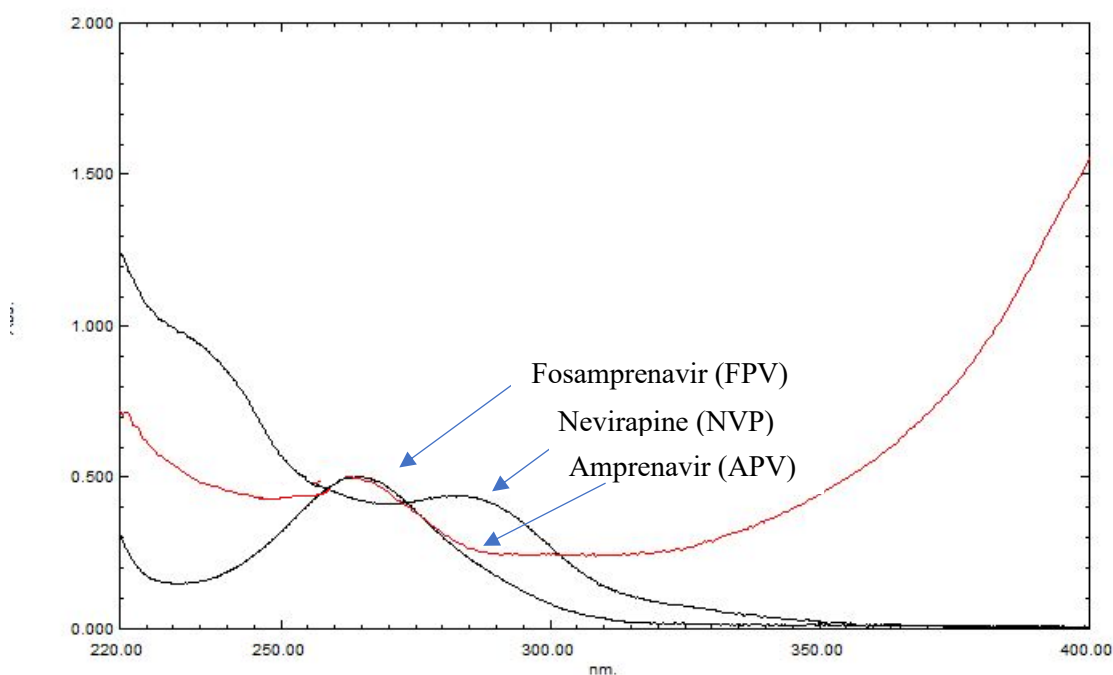
Figure 158: UV spectrum of FPV, APV, and NVP showing isosbestic point

5.10.1.2 Method development and optimization

Different trials were carried out using different solvent systems in varying ratios for the isolation of two drugs and the results were analyzed. The retention time of drugs tends to change with changes in mobile phage. Different trials were carried out using different concentrations of the water: methanol, and water: ACN in different concentrations. Figures 43-46 represent the different peaks in different solvent systems.
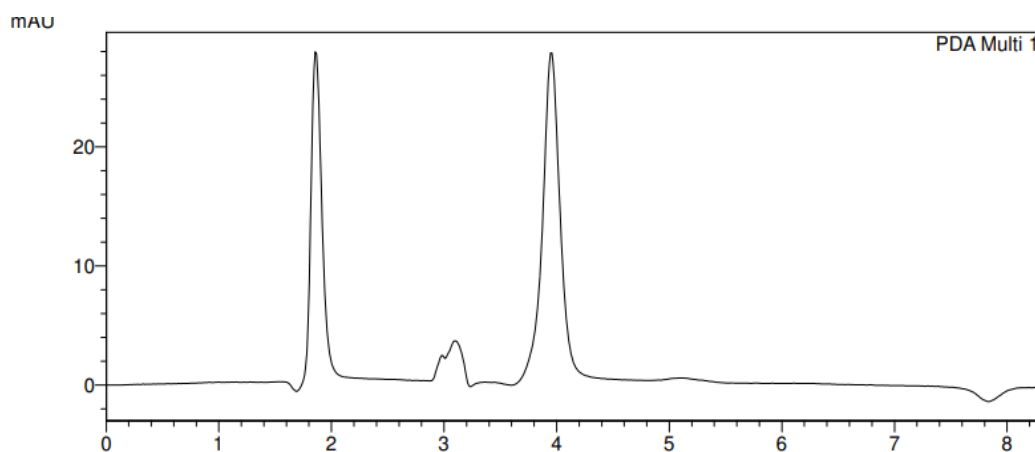
Figure 159: HPLC chromatogram using Water: Methanol (20:80) as solvent system
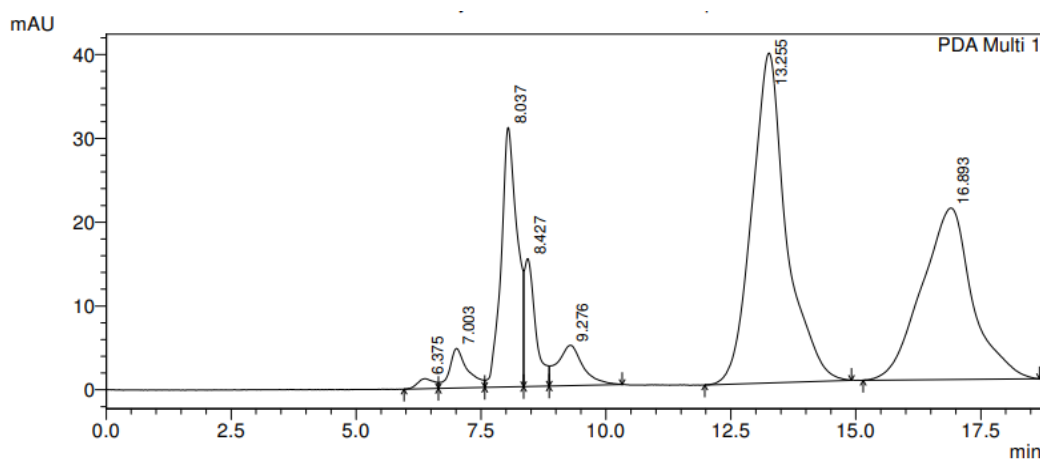
Figure 160: HPLC chromatogram using Water: Methanol (30:70) as solvent system
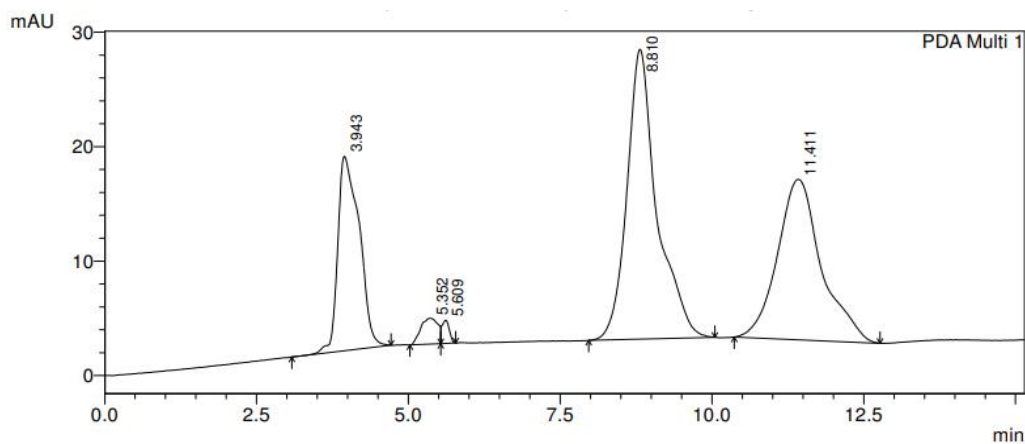
Figure 161: HPLC chromatogram using Water: Methanol (45:65) as solvent system

284
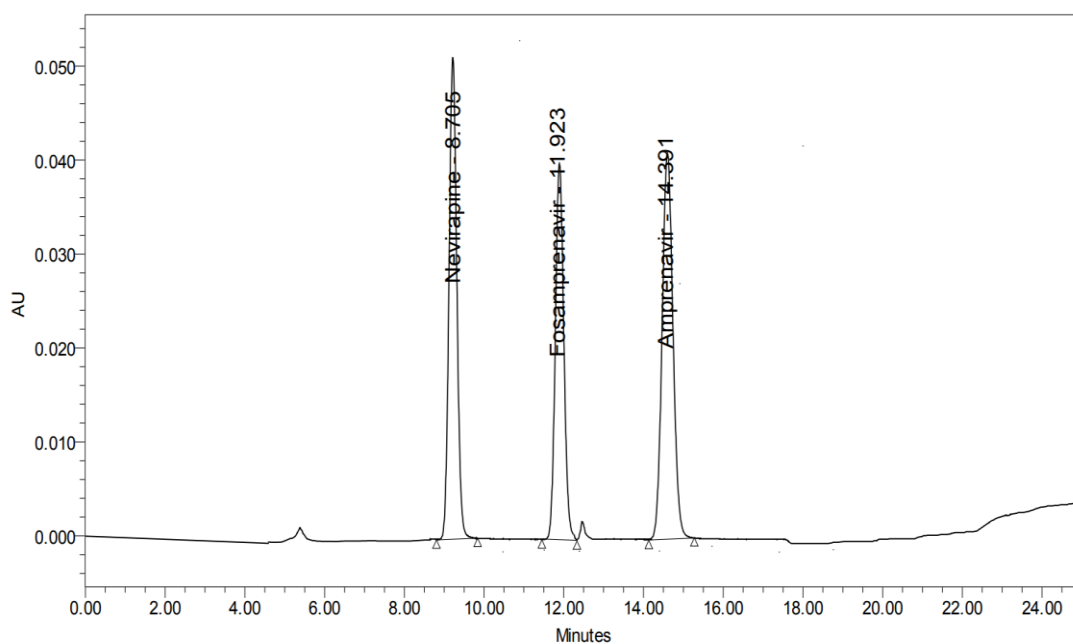
Figure 162: HPLC chromatogram using Methanol: Water: ACN as a solvent system
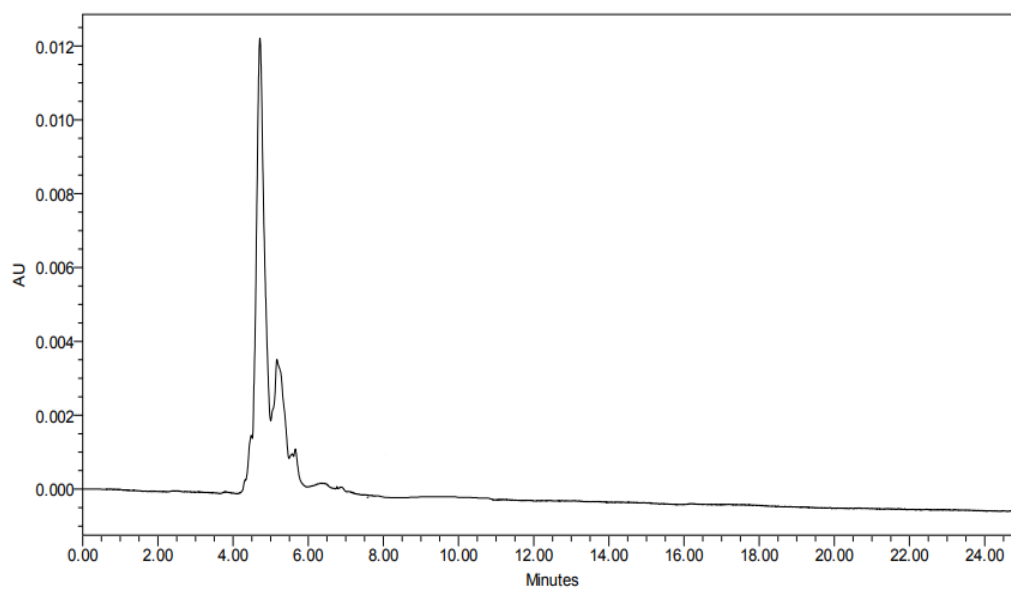
Figure 163: HPLC chromatogram of blank plasma

5.10.1.3 Method validation

5.10.1.3.1 System suitability

Table 65 shows the parameters describing the system's suitability parameters. Before a chromatographic system is put to use, it must first pass a test called the system suitability test, which evaluates the system to see whether it will perform as expected or not. When used consistently, the efficacy of any chromatographic system has the potential to undergo ongoing shifts, which can have an impact on the validity of the analytical findings. Better column efficiency is indicated when the value of the theoretical plate is greater than 2,000, the value of HETP is lower, and the tailing factor is higher. The findings that we received from this research suggested that the approach that was created has very excellent system adaptability (Ramadan et al., 2020).

Table 66: System suitability parameters for FPV and NVP

Sr.no	Parameters	Values			
		FPV	**APV**	**NVP**	**Limits**
1	Theoretical plates	8751	9366	3427	Depends on theoretical plates]
2	HETP	145.030	130.012	57.542	>2000
3	Tailing factor	1.0	1.05	1.01	> 2

5.10.1.3.2 Linearity and Range

The calibration curve for FPV, APV, and NVP was plotted. The linearity of the calibration curves was verified at a range of concentrations that extended from 0.2 to 3.2 µg/mL. The coefficient of correlation (R^2) was determined to be 0.9909 for FPV, 0.9879 for APV, and 0.9916 for NVP. The calibration curve is shown in Figures 47, 48, and 49 (El-Zahar et al., 2019).
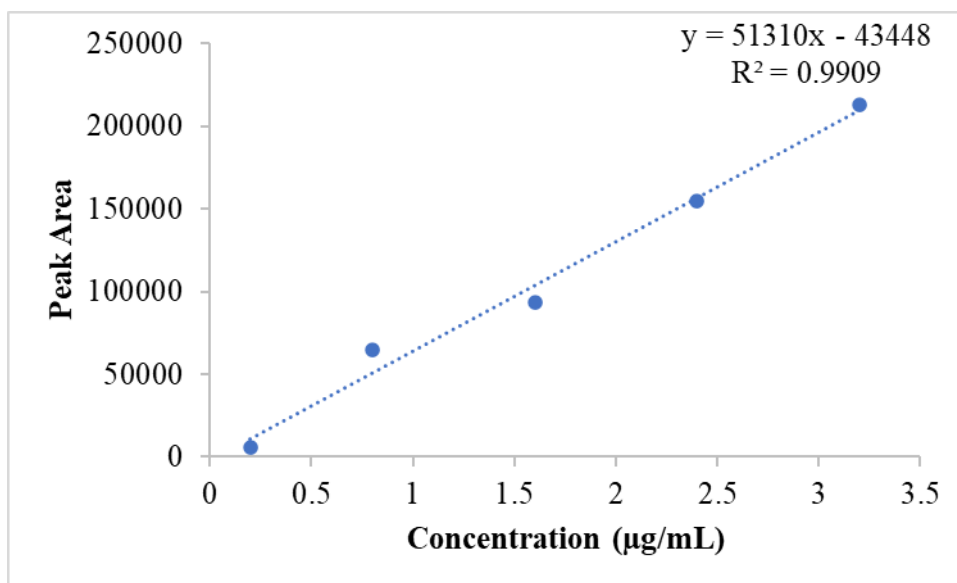
Figure 164: Calibration curve of FPV
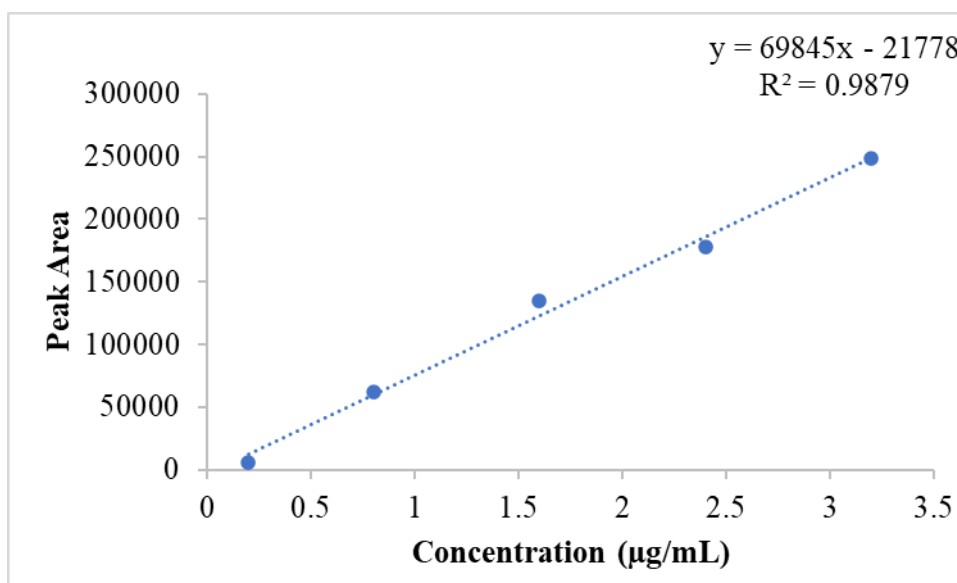
Figure 165: Calibration curve of APV
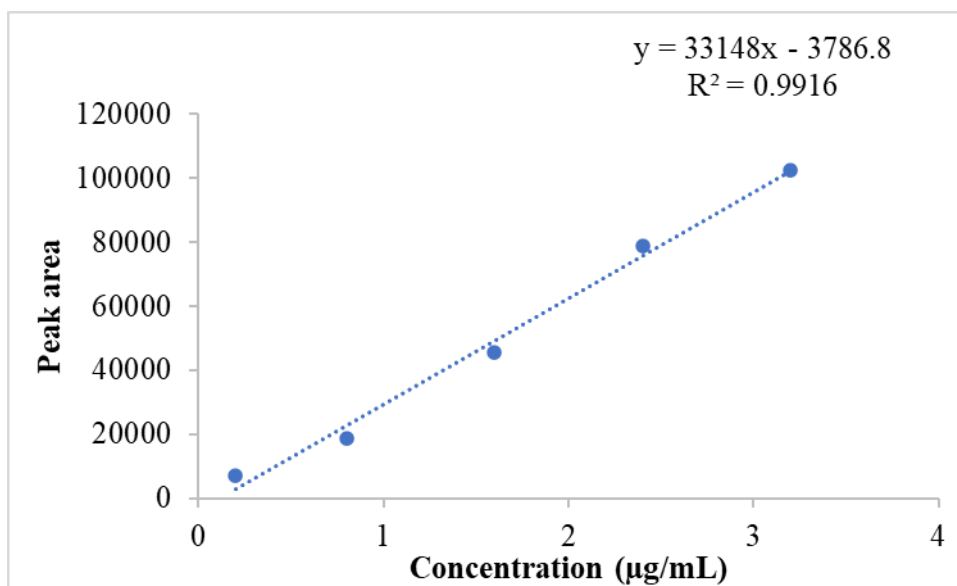
Figure 166: Calibration curve of NVP

5.10.1.3.3 Accuracy

Calculating the mean % recovery of the drugs from the low, medium, and high-quality controls was one way that the accuracy of the developed method was tested. According to the findings, the median percentage of recovery was within the allotted range, which was from 95% to 105% (Table 66). This was the case for all three levels. This demonstrates that the technique that was devised was reliable.

Table 67: Accuracy study for FPV, APV, and NVP

Drugs	Levels	The theoretical conc. of the standard solution (µg/mL)	Actual concentration has taken out from the mobile system (µg/mL) (mean ± SD) (n is 6)	% RSD	%Recovery (mean ± SD)	Mean recovery
FPV	LQC	1.06	1.0457 ±0.012	1.16	98.66	
	MQC	1.66	1.594 ± 0.0244	1.74	98.85	99.82
	HQC	1.92	1.860 ± 0.03	1.68	101.96	
APV	LQC	1.06	1.0596 ±0.009	0.86	99.96	
	MQC	1.66	1.6275 ± 0.025	1.57	101.72	99.82
	HQC	1.92	1.877 ± 0.027	1.47	97.77	
	LQC	1.06	1.079 ± 0.008	0.81	101.82	
	MQC	1.66	1.595 ± 0.009	0.60	99.71	100.33
NVP	HQC	1.92	1.909 ± 0.03	1.64	99.45	

5.10.1.3.4 Precision

We measured the % RSD for each of the 6 estimations of the LQC, MQC, and HQC solution at the intraday, interday, and interanalyst levels while maintaining the equivalent experimental settings. This allowed us to determine the precision of the approach that was created. It was found that the percentage relative variation was less than 2%, which demonstrates that the method that was devised was accurate.

Injecting LQC, MQC, and HQC allowed for the completion of both interday and intraday trials with successful results. Over three consecutive days, the peak locations that were independently discovered for FPV, APV, and NVP were repeatable and exact. The findings for both intraday and interday provide evidence that the devised approach has a high level of repeatability and accuracy. In this method, all of the data were expressed in % RSD, and they were consistently below the acceptable limit of % RSD < 2 (Binge et al., 2014). Table 67 presents the findings of the intraday and interday accuracy of FPV, APV, and NVP measurements.

Table 68: Precision study for FPV, APV and NVP

Parameters	Levels	A 1	A 2	A 3	A 4	A 5	A 6	Mean Area (cm^2)	SD	% RSD
					FPV					
Repeatability (Intraday)	LQC	97776	97001	99558	98733	98661	98134	98310.50	805.1134	0.81895
	MQC	129231	128821	126211	128761	129981	129761	128794.33	1238.866	0.961895
	HQC	148231	149761	146621	145581	144512	146721	146904.50	1708.262	1.162838
Intermediate Precision										
Interday 1	LQC	98823	97122	97841	97451	97386	99851	98079.00	960.9584	0.97978
	MQC	129982	129934	128892	129341	128852	124721	128620.33	1799.606	1.399161
	HQC	149761	148823	148764	148832	143213	148944	148056.17	2192.485	1.480847
Interday 2	LQC	97995	97312	97426	96845	95775	94591	96657.33	1146.898	1.186561
	MQC	128823	129982	126991	127811	128821	129342	128628.33	980.2758	0.762099
	HQC	148923	149912	146218	143912	148821	149231	147836.17	2098.543	1.419506
Interday 3	LQC	98994	98234	98561	98449	98341	98626	98534.17	243.3334	0.246953
	MQC	128235	126624	125832	127886	126921	129932	127571.67	1320.219	1.034884
	HQC	149231	148832	149921	147821	146692	147291	148298.00	1126.247	0.759448
Interanalyst	LQC	97812	97668	96565	99812	98562	98776	98199.17	1013.916	1.03251
	MQC	129923	126652	128421	129921	126721	129211	128474.83	1362.111	1.060216
	HQC	148823	149826	146721	148252	148971	143682	147712.50	2033.182	1.376446

APV									
Repeatability (Intraday)	LQC	96252	96392	96781	95782	95172	98453	96472.00	1019.865	1.057161
	MQC	134823	137782	134528	141182	139981	138218	137752.33	2446.924	1.776321
	HQC	156761	158234	159923	157823	158743	159853	158556.17	1114.216	0.702726
Intermediate Precision										
Interday 1	LQC	95672	96997	96712	96772	94531	96782	96244.33	877.0988	0.911325
	MQC	134832	139982	136272	138723	139465	139834	138184.67	1948.437	1.410024
	HQC	159834	157732	159943	157782	159932	156791	158669.00	1275.872	0.804109
Interday 2	LQC	96782	96773	96821	96881	96773	96882	96818.67	47.28871	0.048843
	MQC	136723	138892	137782	139962	137891	138992	138373.67	1039.354	0.751122
	HQC	158892	156672	154421	159621	156721	157721	157341.33	1688.528	1.073162
Interday 3	LQC	98342	98332	97821	95623	95612	99734	97577.33	1502.596	1.539903
	MQC	137821	138923	137781	137782	139982	136671	138160.00	1042.467	0.754536
	HQC	157782	159932	156721	157843	159832	157832	158323.67	1168.797	0.738233
Interanalyst	LQC	96784	96783	95672	95778	97882	96672	96595.17	736.2949	0.762248
	MQC	139841	136792	138832	136732	139843	138855	138482.50	1283.188	0.926607
	HQC	156723	159843	157898	156982	159981	154432	157643.17	1913.335	1.213713

291

NVP									
Repeatability (Intraday)	LQC	39013	39321	39336	39882	38776	39662	39331.67	370.2327	0.941309
	MQC	56996	56889	56901	55881	55732	55661	56343.33	589.8838	1.046945
	HQC	67544	67556	67432	66784	67921	68731	67661.33	585.7735	0.865743
Intermediate Precision										
Interday 1	LQC	39662	39551	39882	39901	39891	39881	39794.67	137.0166	0.344309
	MQC	56881	57812	56832	57832	56981	57342	57280.00	416.5089	0.727145
	HQC	67882	66892	66945	67843	68743	68672	67829.50	731.263	1.07809
Interday 2	LQC	39881	39565	39782	39673	39745	39882	39754.67	112.2923	0.282463
	MQC	57893	57993	59882	59662	59771	58332	58922.17	862.1662	1.463229
	HQC	67348	67843	66932	68942	69437	69564	68344.33	1022.857	1.496622
Interday 3	LQC	38943	39563	38554	39351	39883	38992	39214.33	437.1223	1.1147
	MQC	55783	56291	56778	55943	55933	55981	56118.17	332.0072	0.591622
	HQC	67241	68345	68163	67932	68996	69883	68426.67	833.8402	1.21859
Interanalyst	LQC	39452	38872	39342	38921	37845	38523	38825.83	535.9482	1.380391
	MQC	55672	55982	55673	55983	54893	53782	55330.83	782.4529	1.414135
	HQC	67892	68342	69876	68534	68443	67432	68419.83	752.1605	1.099331

*A represents Area

5.10.1.3.5LOD and LOQ

The limit of detection for FPV was 1.1 µg/mL and for APV was 0.02 µg /mL, and the limit of detection for NVP was also 0.02 µg/mL. The limit of quantitation for FPV, APV, and NVP was 0.1 µg /mL, 0.1 µg /mL, and 3 µg/mL, respectively.

5.10.1.3.6 Robustness

Table 69: Robustness study results for FPV, APV, and NVP

Variables	Value	Conc (µg/mL)	Avg. Area (cm²)	Std. Dev.	% RSD	% Recover
FPV						
Flow rate	0.3	1.6	113432	6.859	0.006	99.685
	0.5	1.6	138648	6.718	0.005	96.022
	0.7	1.6	157392	6.576	0.004	91.072
Wavelength	252	1.6	116708	171.120	0.147	96.287
	254	1.6	137502	172.534	0.125	94.374
	256	1.6	156618	173.948	0.111	104.040
APV						
Flow rate	0.3	1.6	125191	6.859	0.005	98.760
	0.5	1.6	136419	6.718	0.005	102.025
	0.7	1.6	144332	6.576	0.005	101.195
Wavelength	252	1.6	127395	171.120	0.134	102.379
	254	1.6	137688	172.534	0.125	98.937
	256	1.6	144489	173.948	0.120	98.685
NVP						
Flow rate	0.3	1.6	55689	6.859	0.012	98.760
	0.5	1.6	57393	6.718	0.012	101.025
	0.7	1.6	57399	6.576	0.011	102.195
Wavelength	252	1.6	55605	171.120	0.308	103.379
	254	1.6	56246	172.534	0.307	98.937
	256	1.6	57802	173.948	0.301	98.685

The fact that changing a few chromatographic conditions did not result in any noticeable shifts in the results indicated that the approach was resistant to the introduction of even relatively large amounts of arbitrary variation in the wavelength or flow rate. In every instance, the FPV, APV, and, NVP peaks were symmetric (tailing factor less than 2) and were distinguishable (resolution more than 2). According to Kumar et al. (2021), the fact that the % RSD of FPV, APV, and NVP retention periods were less than 1% implies that the established approach was reliable.

5.10.1.3.7 Stability studies

Table 70: Freeze thaw stability for FPV, APV, and NVP in plasma samples

	Conc. (µg /mL)	A 1 cm²	A 2 cm²	A 3 cm²	Mean cm²	SD	% RSD	Amount of drugs taken out in plasma sample (mg/mL)	% Recovery
FPV in plasma									
First Cycle	1.06	96623	96662	95612	96299	595.27	0.61	1.03	97.17
	1.6	126426	128981	127729	127712	1277.58	1.00	1.64	102.50
	1.92	148823	147892	145781	147499	1558.67	1.05	2.03	105.62
Second Cycle	1.06	97523	98712	94231	96822	2321.29	2.39	1.04	98.13
	1.66	126426	128232	127634	127431	920.00	0.72	1.64	98.60
	1.92	148823	148823	146623	148090	1270.17	0.85	2.04	106.22
Third Cycle	1.06	96734	96445	96734	96638	166.85	0.17	1.04	97.80
	1.66	126426	127723	128723	127624	1151.69	0.90	1.64	98.83
	1.92	148823	148756	142365	146648	3709.33	2.52	2.01	104.76
APV in plasma									
First Cycle	1.06	96552	95342	97123	96339	909.40	0.94	1.07	100.71
	1.66	134462	136623	137723	136269	1659.01	1.21	1.64	98.75
	1.92	156782	154462	156672	155972	1308.85	0.83	1.92	100.07
Second Cycle	1.06	95623	96534	97452	96536	914.50	0.94	1.07	100.98
	1.66	134823	137721	139956	137500	2573.62	1.87	1.66	99.81
	1.92	156761	156623	157723	157036	599.23	0.38	1.94	100.86
Third Cycle	1.06	96442	96812	96782	96679	205.50	0.21	1.07	101.17
	1.66	134823	135462	138867	136384	2173.94	1.59	1.64	98.85
	1.92	156761	157231	159314	157769	1358.77	0.86	1.95	101.41
NVP in plasma									
First Cycle	1.06	39123	39562	39425	39370	224.60	0.57	1.07	101.27
	1.66	56996	55342	56873	56403.67	921.48	1.63	1.59	95.62
	1.92	67544	65521	67142	66735.67	1070.96	1.60	1.90	98.91
Second Cycle	1.06	39886	39141	38923	39316.67	504.96	1.28	1.07	101.12
	1.66	56996	56692	56197	56628.33	403.28	0.71	1.59	96.03
	1.92	67544	65739	65784	66355.67	1029.37	1.55	1.89	98.31
Third Cycle	1.06	39734	39473	39645	39617.33	132.68	0.33	1.08	101.97
	1.66	56996	56594	56147	56579	424.69	0.75	1.59	95.94
	1.92	67944	67345	67685	67658	300.41	0.44	1.92	99.99

Table 71: Long-term stability for FPV, APV, and NVP in plasma samples

	Conc. (µg /mL)	A 1 cm²	A 2 cm²	A 3 cm²	Mean cm²	SD	% RSD	Amount of drug taken out in plasma sample (mg/mL)	% recovery
FPV in plasma									
Week 1	1.06	96083	97832	97943	97286	1043.31	1.07	1.05	98.99
	1.6	124721	126522	127734	126326	1516.06	1.20	1.62	100.95
	1.92	146061	149732	148835	148209	1913.81	1.29	2.04	106.34
Week 2	1.06	96902	96496	95213	96204	881.632	0.92	1.03	97.00
	1.66	128342	125281	124242	125955	2131.48	1.69	1.61	96.87
	1.92	145632	148231	145793	146552	1456.28	0.99	2.01	104.66
Week 3	1.06	95621	94723	97371	95905	1346.65	1.40	1.02	96.45
	1.66	128241	126372	128342	127652	1109.37	0.87	1.64	98.86
	1.92	139561	142721	144825	142369	2649.59	1.86	1.93	100.36
APV in plasma									
Week 1	1.06	96752	97732	95284	96589	1232.08	1.28	1.07	101.05
	1.66	137735	129452	136672	134620	4506.78	3.35	1.62	97.33
	1.92	151352	158231	152731	154105	3639.42	2.36	1.89	98.68
Week 2	1.06	94342	96945	97442	96243	1664.96	1.73	1.07	100.58
	1.66	135183	136932	139943	137353	2407.72	1.75	1.65	99.68
	1.92	158342	159436	156372	158050	1552.73	0.98	1.95	101.62
Week 3	1.06	94234	91845	93634	93238	1242.84	1.33	1.02	96.52
	1.66	136913	134453	132734	134700	2100.42	1.56	1.62	97.39
	1.92	157839	152856	153964	154886	2616.41	1.69	1.91	99.26
NVP in plasma									
Week 1	1.06	39673	39665	39584	39640.7	49.2375	0.12	1.08	102.04
	1.66	56934	56384	56773	56697	282.767	0.50	1.60	96.16
	1.92	67034	67935	66178	67049	878.596	1.31	1.91	99.40
Week 2	1.06	39282	38164	37923	38456.3	725.131	1.89	1.05	98.67
	1.66	56934	56184	55782	56300	584.695	1.04	1.58	95.43
	1.92	65941	66933	67881	66918.3	970.083	1.45	1.90	99.19
Week 3	1.06	38956	39923	40194	39691	650.791	1.64	1.08	102.18
	1.66	59671	58934	59745	59450	448.398	0.75	1.68	101.16
	1.92	68352	66384	66392	67042.7	1133.92	1.69	1.91	99.39

*A represents the Area

Table 72: Short-term stability for FPV, APV, and NVP in plasma samples

	Conc. (μg /mL)	A 1 cm²	A 2 cm²	A 3 cm²	Mean cm²	SD	% RSD	Amount of drug taken out in plasma sample (mg/mL)	% recovery
					FPV in plasma				
1 h	1.06	96453	96773	95934	96387	423.415	0.44	1.03	97.33
	1.6	124721	127782	128234	126912	1911.16	1.51	1.63	101.67
	1.92	142061	144134	142782	142992	1052.38	0.74	1.94	101.04
2 h	1.06	97342	96554	96573	96823	449.568	0.46	1.04	98.14
	1.66	126426	125623	128823	126957	1664.85	1.31	1.63	98.04
	1.92	146823	146523	142234	145193	2567.24	1.77	2.03	105.99
3 h	1.06	96442	96813	96273	96509	276.225	0.29	1.03	97.56
	1.66	126426	128436	129965	128276	1774.94	1.38	1.65	99.59
	1.92	143823	144243	139738	142601	2488.6	1.75	1.98	103.28
					APV in plasma				
1 h	1.06	96552	96353	97834	96913	803.792	0.83	1.08	101.48
	1.66	137735	134934	138234	136968	1778.79	1.30	1.65	99.35
	1.92	157352	157734	158451	157846	557.945	0.35	1.95	101.47
2 h	1.06	95623	95834	95442	95633	196.191	0.21	1.06	99.76
	1.66	134823	139231	136729	136928	2210.71	1.61	1.65	99.32
	1.92	156761	155623	154426	155603	1167.62	0.75	1.92	99.79
3 h	1.06	96442	97743	96342	96842	781.601	0.81	1.07	101.39
	1.66	134823	137362	137352	136512	1463.01	1.07	1.64	98.96
	1.92	153761	158375	154434	155523	2492.44	1.60	1.91	99.48
					NVP in plasma				
1 h	1.06	38945	39654	39554	39384.3	383.745	0.97	1.07	101.31
	1.66	56238	55745	56743	56242	499.012	0.89	1.58	95.33
	1.92	67341	67934	67153	67476	407.626	0.60	1.92	100.07
2 h	1.06	39334	39173	39823	39443.3	338.512	0.86	1.08	101.48
	1.66	56372	56981	56086	56479.7	457.111	0.81	1.59	95.76
	1.92	67352	65334	67632	66772.7	1253.76	1.88	1.90	98.97
3 h	1.06	39231	39124	39812	39389	370.215	0.94	1.07	101.32
	1.66	56943	56772	56172	56629	404.904	0.72	1.59	96.03
	1.92	66382	67912	67482	67258.7	789.071	1.17	1.91	99.73

*A represents Area

Plasma samples LQC, MQC, and HQC underwent freeze-thaw, short-term, and long-term stability experiments (Tables 69-71). All instances showed recovery > 95%

for FPV, APV, and NVP and % RSD less than two. Study results showed plasma drug stress and storage stability

Table 58 tabulated the colour change, precipitation, turbidity, and consistency of NVP-DT, FVP-DT, NVP-FPV-DT, and M-NVP-FPV-DT. NVP-DT, FVP-DT, NVP-FPV-DT, M- NVP-FPV-DT does not show any significant change in dark and light at 4 ℃. Turbidity and precipitation were found to be more in light-exposed samples as compared to the samples kept in the dark in RT and at accelerated temperature. Higher turbidity at accelerated temperature may be because of the polymerization of the free functional group. The formulation was found to be more stable in dark and in cool temperature (Soni et al., 2016).

5.10.2 Biodistribution studies

Biodistribution studies were performed to study the distribution of drugs to different organs including the liver, kidney, spleen, heart, and blood on Wister rats. Plain drug NVP showed higher levels in plasma in 1 h which subsides gradually in 24 h. Plain drug FPV showed little conversion to APV in 1h in plasma while maximum conversion in 8 h and the concentration reduces till 24 h. Formulation NVP-DT showed lower-level plasma concentration at 1 h which increases with time (8 h) and further reduces with time as compared to plain NVP (P < 0.05). FPV-DT showed a low level of drug FPV and lesser conversion to APV at 1 h, and at 8 h concentration of FPV reduced and the concentration of APV increased while the concentration of both FPV and APV decreased at 24 h. The formulation NVP-FPV-DT showed a maximum level of drug NVP at 8 h and maximum conversion of FPV to APV was observed at 8 h. M-NVP-FPV-DT showed a lower concentration of drug as compared to without mannose.

In the liver, plain drug NVP showed lesser accumulation as compared to plasma concentration increases with time. The plain drug FPV showed maximum conversion to APV at 8 h which may be due to the presence of cellulose phosphatase enzymes in the liver. NVP-DT showed higher concentrations of drug NVP in the liver as compared to plain drug NVP (P .0.05). FPV-DT showed higher conversion to APV in the liver at 8 h which reduces at 24 h. NVP-FPV-DT showed a higher level for NVP and APV at 8 h as maximum conversion took place in the liver as compared to plain drug NVP and APV (P < 0.05). M-NVP-FPV-DT showed a very high level of drug NVP (25.45 ±

0.48), low FPV concentration, and high APV concentration (20.44± 0.23). Conjugation with mannose increases the 3-fold localization of both drugs in the liver as compared to plain NVP (P < 0.05).

In the kidney, accumulation of both drugs was found to be higher at 8 h which gradually excreted through the kidney as. NVP-DT and FPV-DT showed higher levels of drug at 8 h. NVP-FPV-DT showed maximum drug level at 8 h. Kidney also showed abundant mannose receptors which showed higher uptake of the drugs. M-NVP-FPV-DT showed a higher level of drug NVP and efficient conversion of FPV to APV took place at 8 h, which gradually reduces due to renal clearance. The NVP level was found to be higher with NVP DT, NVP-FPV-DT and M-NVP-FPV-DT as compared to plain drug (P < 0.05).

In the heart, the plain drug concentration was found to be higher due to blood flow to the heart which reduces further with time. NVP-DT and FPV-DT showed higher drug concentrations at 8 h, similarly, NVP-FPV-DT showed higher drug concentrations at 8h. Heart cells have a lower number of mannose receptors. Hence, M-NVP-FPV-DT exhibits a lower concentration of drug accumulation in the heart as compared to the liver and kidney.

In the spleen, plain drugs exhibited a higher level of drug at 8 h, NVP-DT, and FPV-DT also showed higher drug levels at 8 h, and NVP-FPV-DT also showed a higher level accumulation at 8 h (P < 0.05). Spleen had a higher number of mannose receptors hence NVP-FPV-DT showed a higher accumulation of both drugs in the spleen as compared to the heart.

Table 73: Concentration of drugs NVP, FPV, and APV in plasma

Formulation code		Plasma (µg/mL)		
		1 h	8 h	24 h
NVP	NVP	8.23±0.12	4.21±0.221	1.26±0.22
FPV	FPV	4.54±0.13	1.54±0.142	0.01±0.24
	APV	0.25±0.16	6.43±0.281	1.36±0.19
NVP DT	NVP	1.54±0.13*	8.45±0.008	3.95±0.11
	FPV	2.24±0.19	3.35±0.241	1.45±0.16
FPV DT	APV	1.23±0.22	6.23±0.162	3.13±0.09
	NVP	2.24±0.25*	9.43±0.182	5.96±0.08
	FPV	1.02±0.18	1.23±0.109	0.12±0.14
NVP-FPV-DT	APV	0.45±0.09	7.12±0.115	4.02±0.18
	NVP	4.16±0.10	16.56±0.231	9.78±0.11
	FPV	1.98±0.11	2.02±0.262	1.04±0.15
M-NVP-FPV-DT	APV	3.08±0.11	11.02±0.182	7.01±0.16

*Values are represented as Mean±SD (n=3) #Stasticstically significant between treatment groups

Table 74: Concentration of drugs NVP, FPV, and APV in liver and kidney

Formulation code		Liver (µg/g of organ)			Kidney (µg/g of organ)		
		1 h	8 h	24 h	1 h	8 h	24 h
NVP	NVP	1.23 ± 0.34	4.23 ± 0.21	3.32 ± 0.33	1.12 ± 0.21	3.56 ± 0.11	2.14 ± 0.22
FPV	FPV	1.44 ± 0.29	0.264 ± 0.11	0.05 ± 0.29	1.22 ± 0.27	0.15 ± 0.21	0.03 ± 0.10
	APV	2.23 ± 0.22	6.32 ± 0.28	3.42± 0.11	2.03 ± 0.34	4.82 ± 0.221	1.22 ± 0.28
NVP DT	NVP*	8.56 ± 0.49	12.56 ± 0.32*	9.56 ± 0.39	6.52 ± 0.33*	10.65 ± 0.18*	1.04 ± 0.10
FPV DT	FPV	3.23 ± 0.49	1.63 ± 0.09	1.09 ± 0.21	1.13 ± 0.21	1.02 ± 0.10	0.07 ± 0.26
	APV	6.44 ±0.55	9.56 ±0.26	7.65 ± 0.25	3.92 ± 0.27	8.34 ± 0.21	3.97 ± 0.22
NVP-FPV-DT	NVP*	3.33 ± 0.39	8.45 ± 0.21	5.45 ± 0.33	2.45 ± 0.17	6.98 ± 0.22	1.98 ± 0.09
	FPV	2.66 ± 0.36	1.34 ± 0.36	1.08 ± 0.15	0.68 ± 0.10	0.96 ± 0.09	0.07 ± 0.21
	APV*	3.41 ± 0.44	7.23 ± 0.28	4.24 ± 0.16	2.69 ± 0.15	6.91 ± 0.12	0.99 ± 0.17
M-NVP-FPV-DT	NVP*	15.23 ± 0.48	34.45 ± 0.48*	20.23 ± 0.22*	8.12 ± 0.27*	20.33 ± 0.16*	1.74 ± 0.15
	FPV	1.88 ± 0.13	1.44± 0.02	1.88 ± 0.26	0.63 ± 0.36	1.84 ± 0.17	0.05 ± 0.21
	APV	10.23 ± 0.29*	22.44± 0.23*	17.23 ± 0.31*	5.28 ± 0.12	13.12 ± 0.21	0.84 ± 0.16

#Stasticstically significance between treatment groups

Table 75: Concentration of drugs NVP, FPV and APV in heart and spleen

Formulation code		Heart (µg/g of organ)			Spleen (µg/g of organ)		
		1 h	8 h	24 h	1 h	8 h	24 h
NVP	NVP	5.12 ± 0.14	3.36 ± 0.12	1.02 ± 0.22	0.88 ± 0.12	2.25 ± 0.22	1.45 ± 0.22
FPV	FPV	4.22 ± 0.15	0.12 ± 0.16	1.17 ± 0.25	0.92 ± 0.13	0.15 ± 0.14	0.04 ± 0.24
	APV	1.03 ± 0.27	5.12 ± 0.34	1.93 ± 0.12	0.98 ± 0.16	5.01 ± 0.28	2.95 ± 0.19
NVP DT	NVP	6.52 ± 0.29	9.56 ± 0.09*	5.62 ± 0.22	4.44 ± 0.13	9.25 ± 0.08*	5.65 ± 0.11
FPV DT	FPV	1.13 ± 0.24	1.09 ± 0.24	1.17 ± 0.14	1.97 ± 0.19	0.88 ± 0.24	0.72 ± 0.16
	APV	3.92 ± 0.33	8.48 ± 0.23	2.24 ± 0.09	1.59 ± 0.22	7.65 ± 0.16	4.45 ± 0.09
NVP-FPV-DT	NVP	2.45 ± 0.12	7.65 ± 0.15	2.16 ± 0.11	1.03 ± 0.25	6.56 ± 0.18	3.62 ± 0.08
	FPV	0.68 ± 0.13	0.74 ± 0.15	0.53 ± 0.16	0.48 ± 0.18	0.79 ± 0.10	0.07 ± 0.14
	APV	2.69 ± 0.09	5.52 ± 0.11	1.79 ± 0.25	2.03 ± 0.09	6.32 ± 0.11	3.01 ± 0.18
M-NVP-FPV-DT	NVP	2.12 ± 0.26	6.60 ± 0.09*	1.02 ± 0.21	5.88 ± 0.10	14.63 ± 0.23*	9.55 ± 0.11
	FPV	0.63 ±0.24	0.66 ± 0.24	0.44 ± 0.11	0.36 ± 0.11	2.69 ± 0.26	0.34 ± 0.15
	APV	3.28 ± 0.22	7.54 ± 0.28	2.85 ± 0.09	3.99 ± 0.11	13.55 ± 0.18	7.83 ± 0.16

#Stasticstically significance between treatment groups

BIODISTRIBUTION IN PLASMA
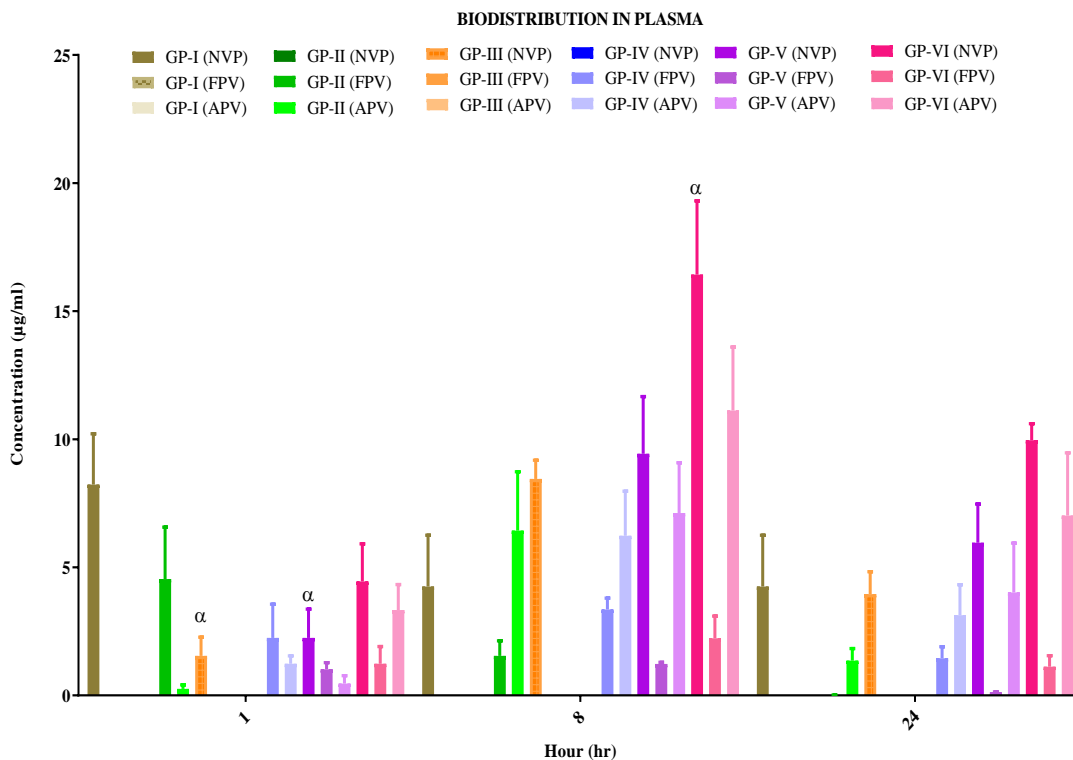
Figure 167: Biodistribution pattern of different formulations in plasma

The data was analyzed using one-way ANOVA followed by Tukey's test was performed ($P < 0.05$)

BIODISTRIBUTION IN LIVER
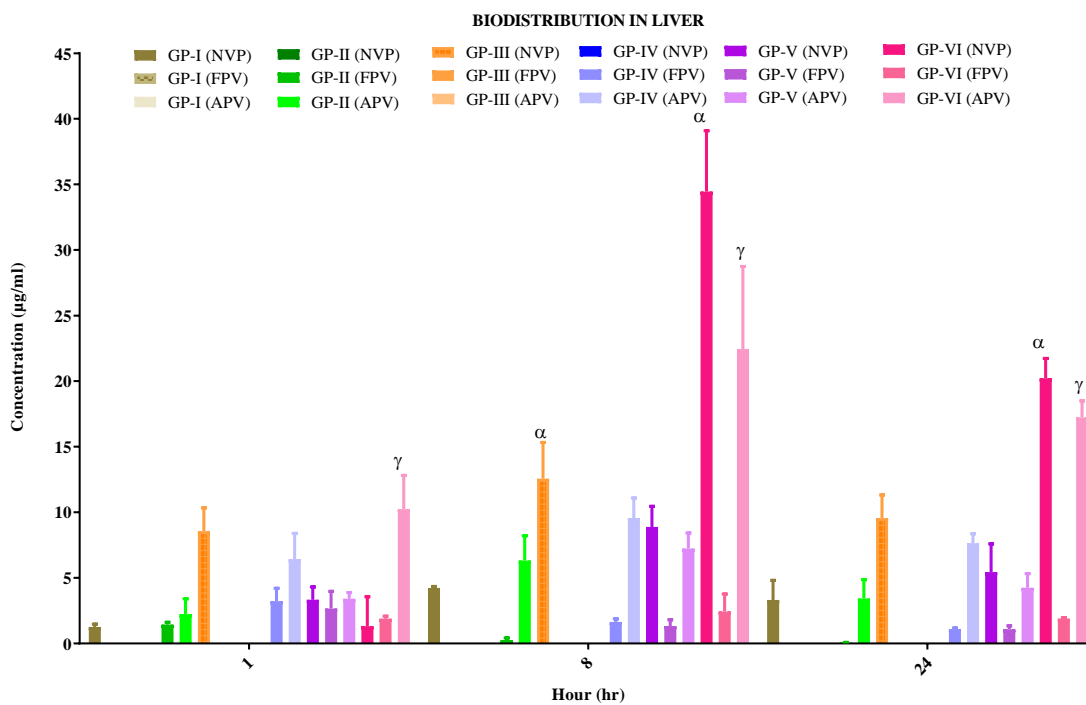
Figure 168: Biodistribution pattern of different formulations in the liver

The data was analyzed using one-way ANOVA followed by Tukey's test was performed ($P < 0.05$)

302
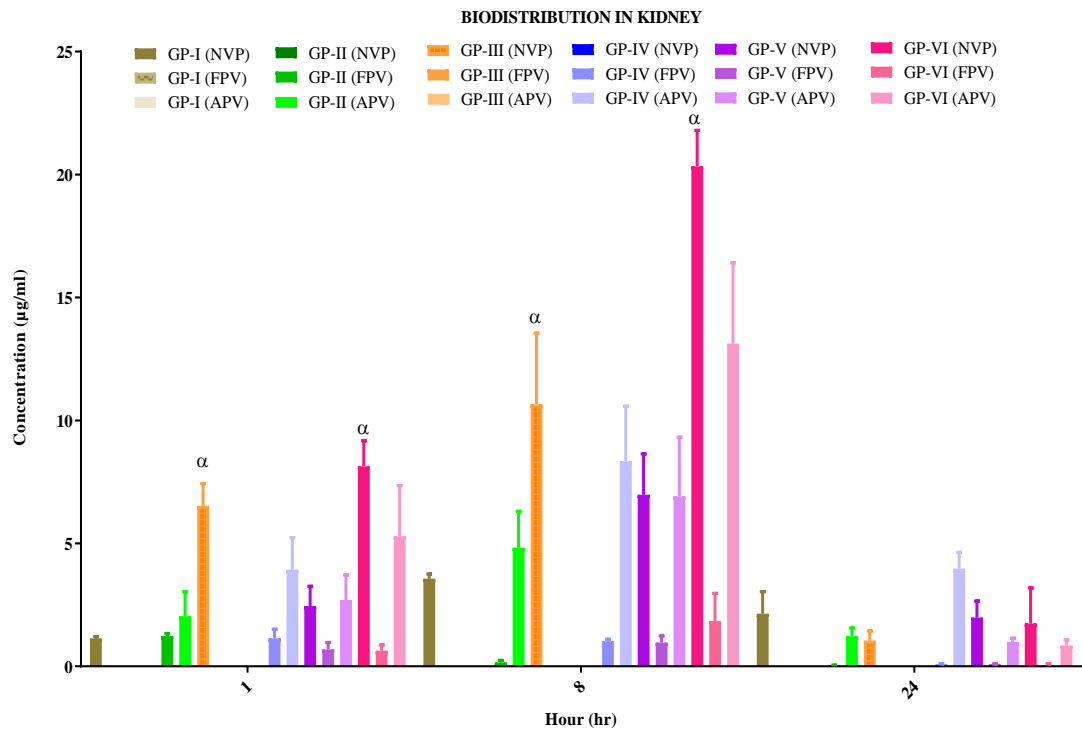
Figure 169: Biodistribution pattern of different formulations in the kidney
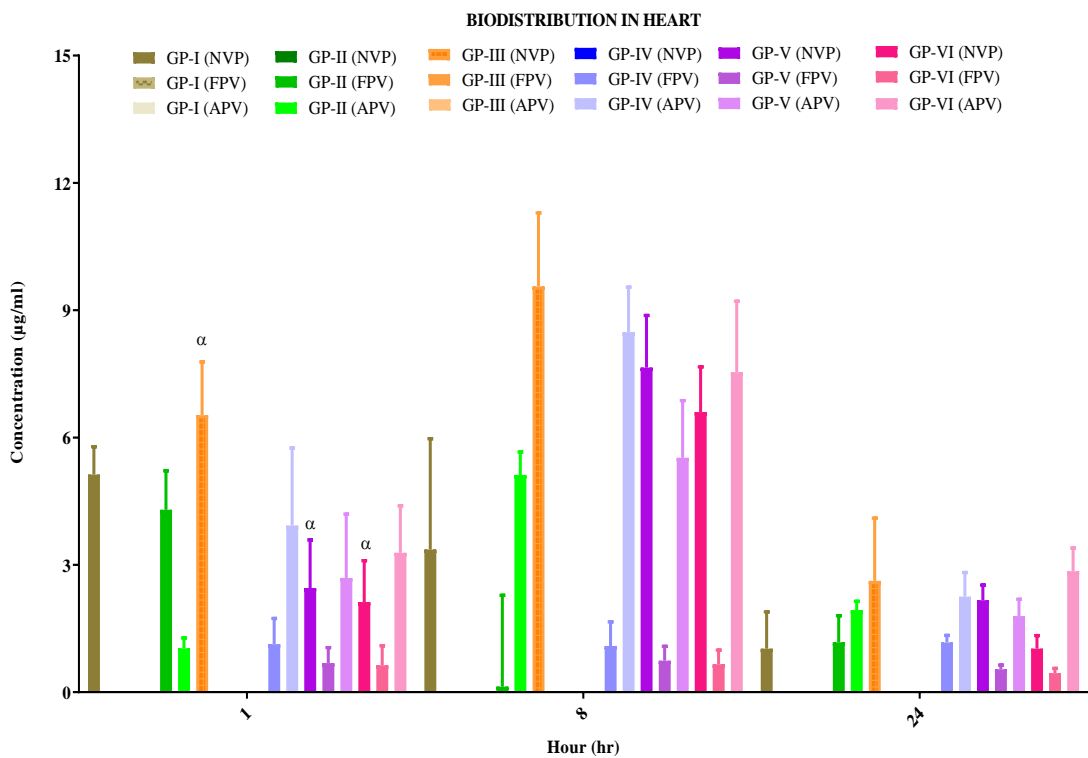
Figure 170: Biodistribution pattern of different formulations in the heart

*The data was analyzed using one-way ANOVA followed by Tukey's test was performed ($*P < 0.05$)

303
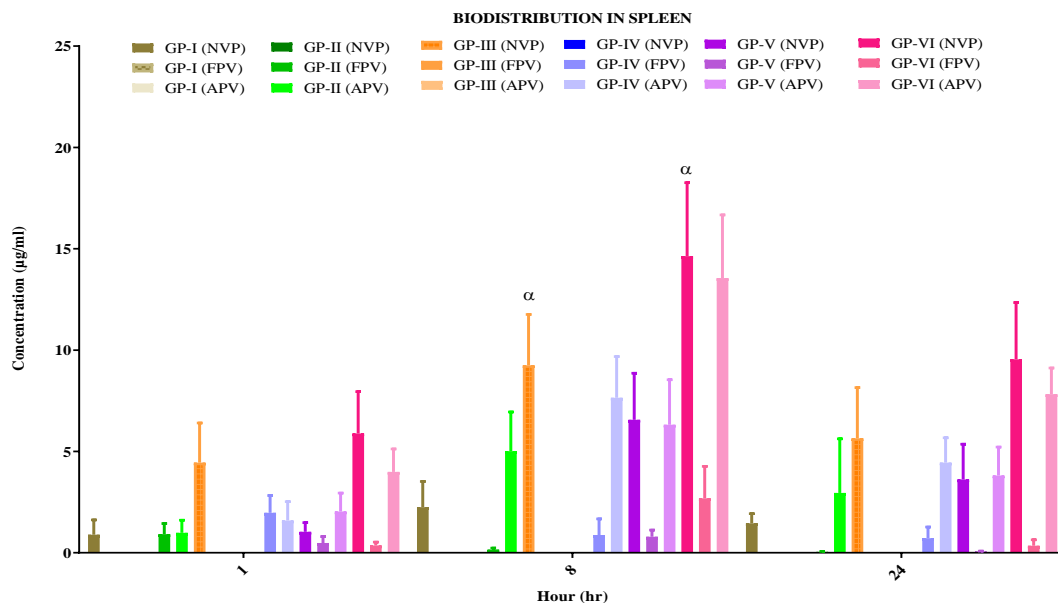
Figure 171: Biodistribution pattern of different formulations in the spleen

The data was analyzed using one-way ANOVA followed by Tukey's test was performed ($P < 0.05$)

5.10.3 Histopathological studies
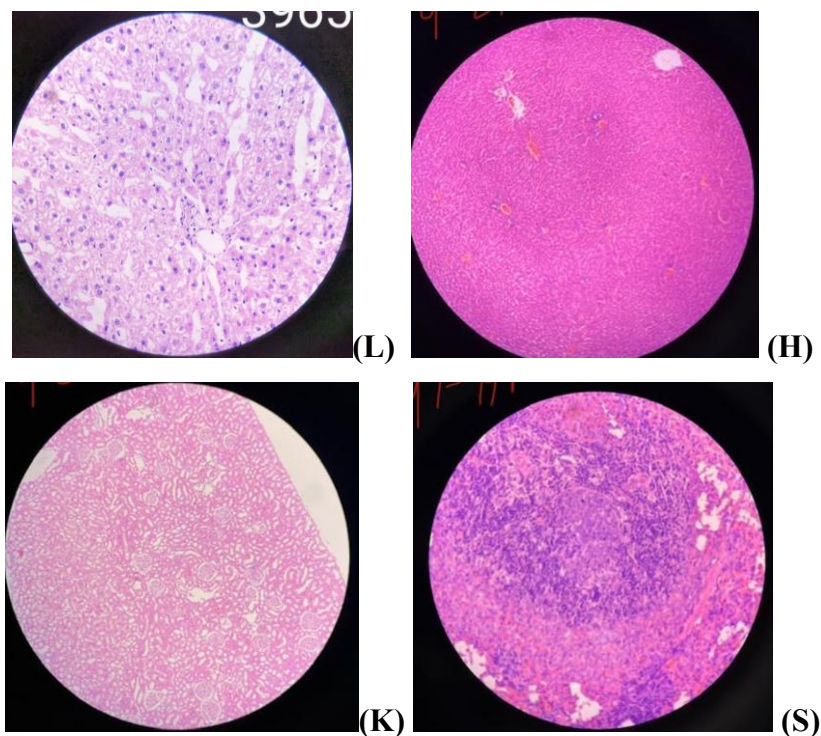
Figure 172: Histopathology of Liver (L), Heart (H), Kidney (K), and Spleen (S)

of vehicle control
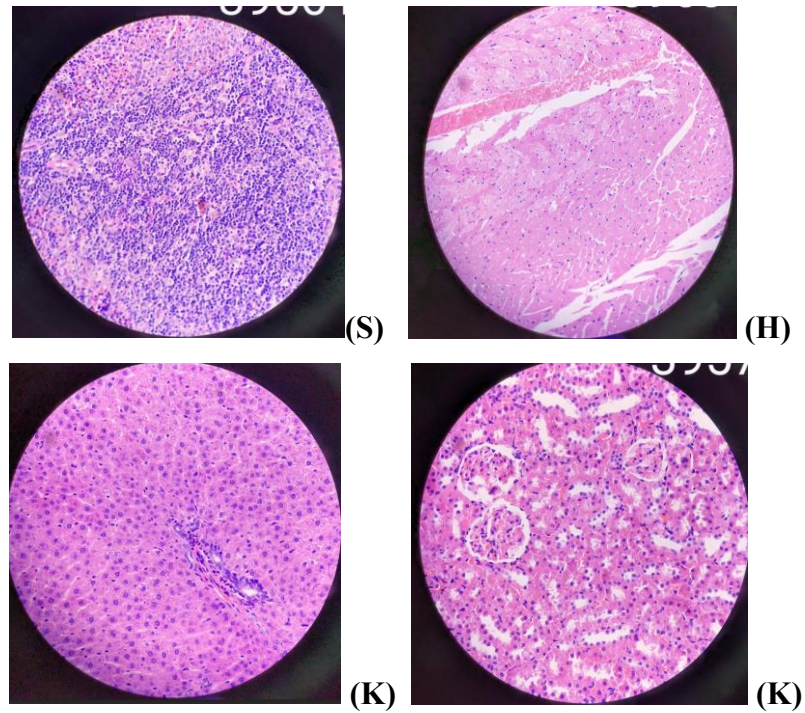
Figure 173: Histopathology of Liver (L), Heart (H), Kidney (K), Spleen (S) of plain drug NVP
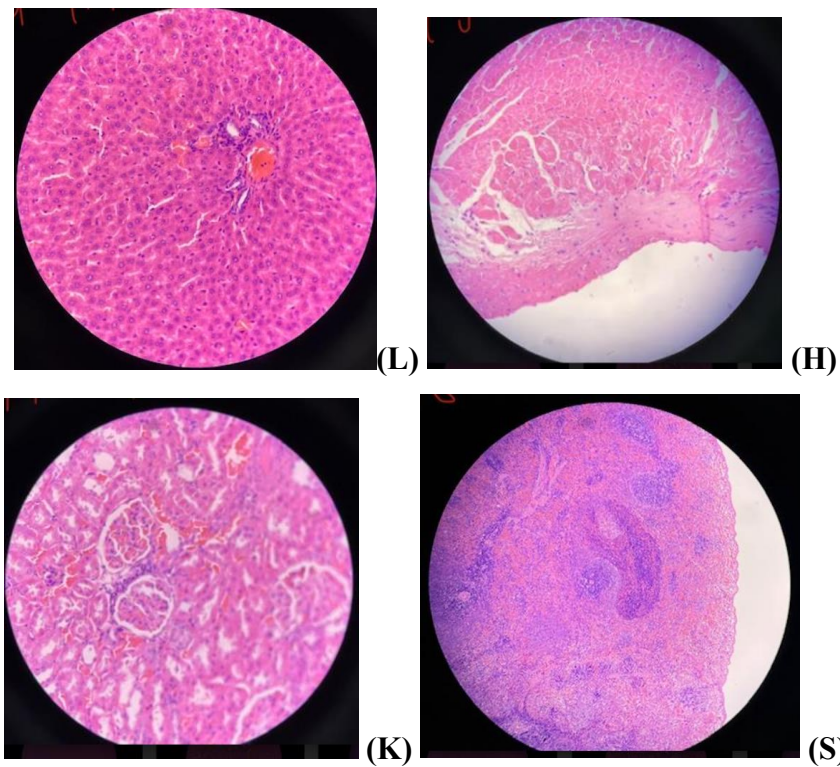
Figure 174: Histopathology of Liver (L), Heart (H), Kidney (K), and Spleen (S) of plain drug FPV

305
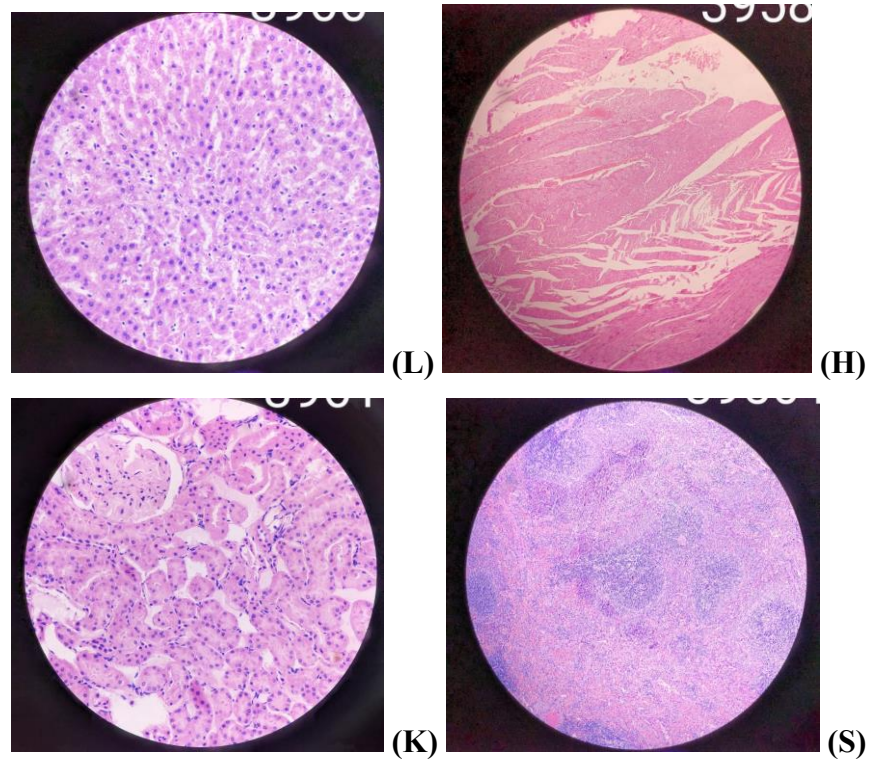
Figure 175: Histopathology of Liver (L), Heart (H), Kidney (K), and Spleen (S) of DT
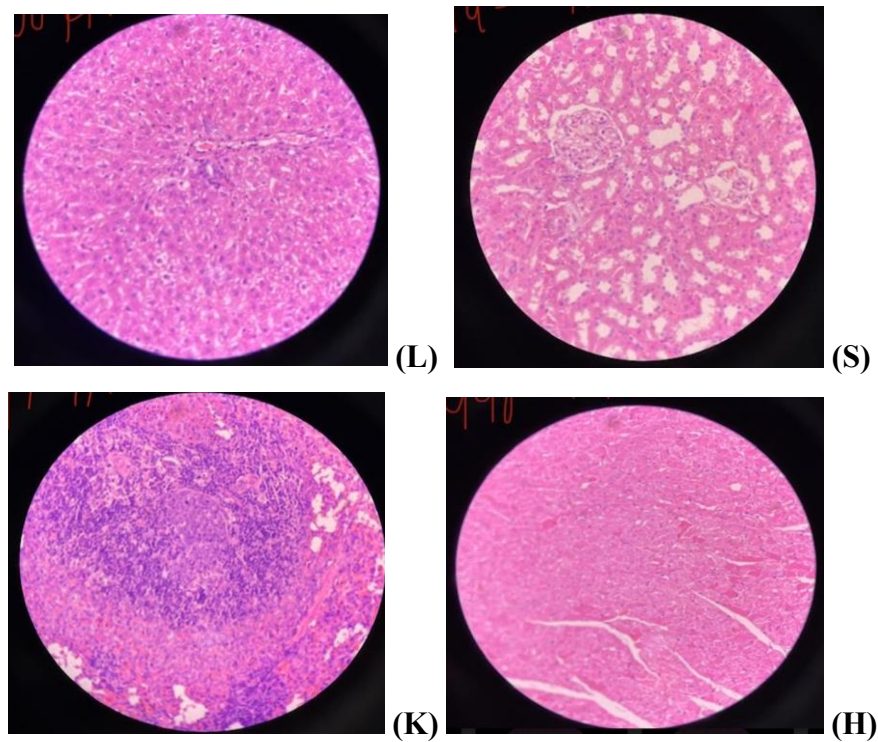
Figure 176: Histopathology of Liver (L), Heart (H), Kidney (K), Spleen (S) of M-DT

306
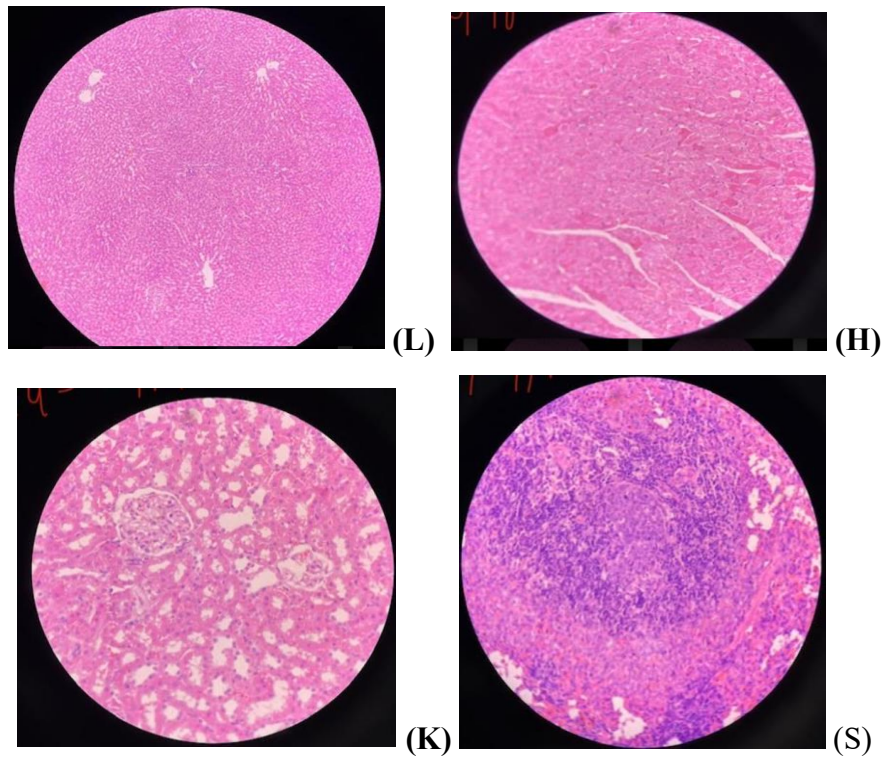
Figure 177: Histopathology of Liver (L), Heart (H), Kidney (K), and Spleen (S)

of NVP-DT
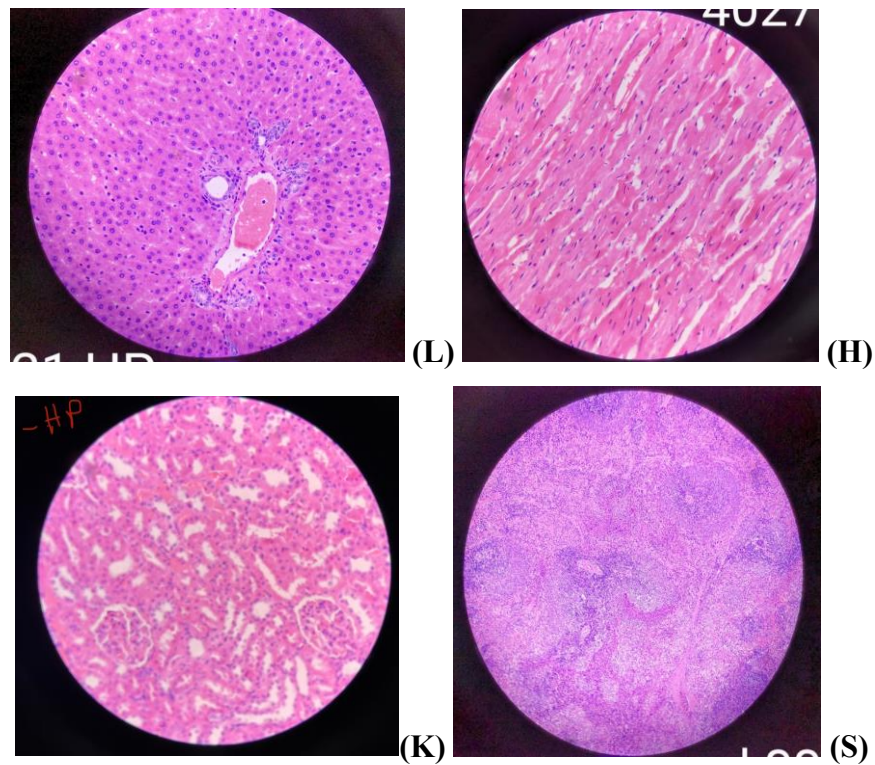
Figure 178: Histopathology of Liver (L), Heart (H), Kidney (K), and Spleen (S)

of FPV-DT
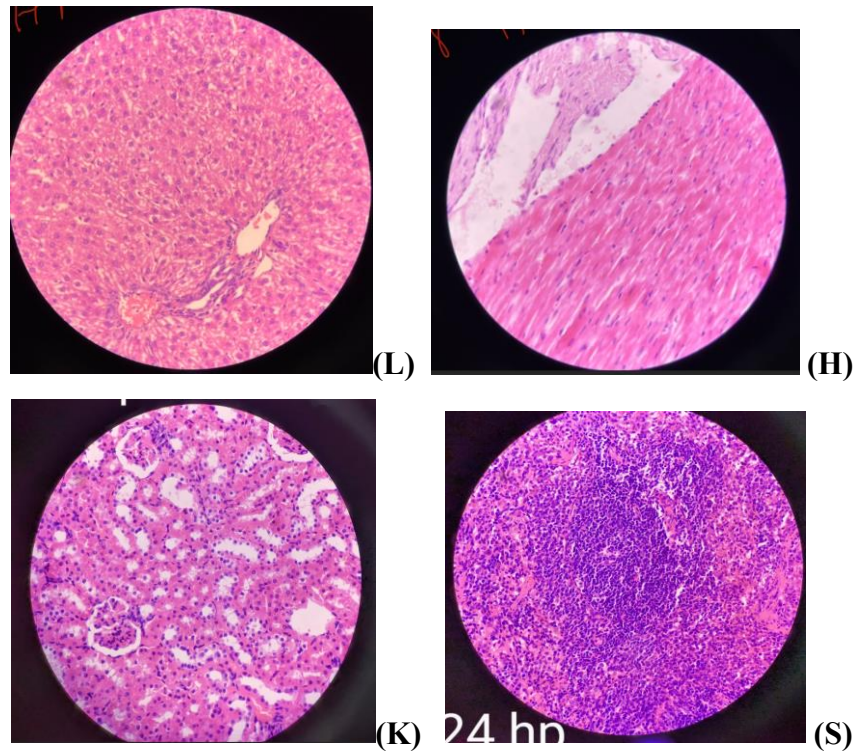
Figure 179: Histopathology of Liver (L), Kidney (K), Heart (H), Spleen (S) of NVP-FPV-DT
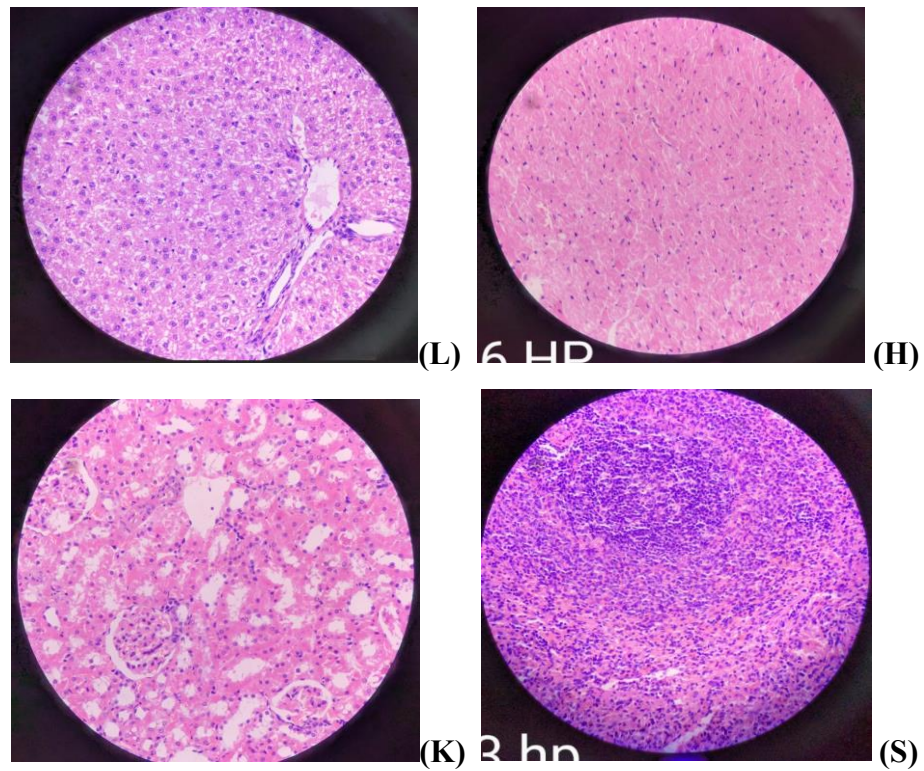
Figure 180: Histopathology of Liver (L), Heart (H), Kidney (K), and Spleen (S) of M-NVP-FPV-DT

Figure 50-58 represents the histopathological images of the different organs, liver, kidney, spleen, and heart. The result revealed that no histopathological changes were observed after injecting different formulations in Wister rats.

5.10.4 Haemolysis studies

RBC lysis studies were performed to study the interaction of the delivery system/ formulation with the red blood cell membrane *in vitro.* It gives a qualitative and quantitative indication of RBC damage due to the designed formulations. The study helps to determine the hemolytic toxicity of the different prepared formulations. Prepared formulations were subjected to a hemolytic test by adding formulation with the suspension of RBCs. The hemolytic activity was observed under an optical microscope and the sample was evaluated using a UV-spectrophotometer at 540 nm and the % hemolysis was calculated. Table 75 indicates the % Haemolysis by plain drugs NVP, FPV, and different formulations.

Dendritubes consist of dendrimers on the surface which consist of a surface amine group that causes haematotoxicity. Conjugation of the surface amino group leads to a reduction of haematotoxicity. Dendritubes caused the highest haematotoxicity (49.09±1.24), while conjugation with mannose (DT-M) drastically reduced the haematotoxicity and it was found to be 4.44±1.35 ($p < 0.05$). The plain drug NVP showed lesser haematotoxicity (15.960±2.17) while the drug FPV showed very high hemolysis (47.07±0.55). On conjugation, the haematotoxicity was drastically altered due to the conjugation of surface amine with drugs. FPV-DT showed reduced toxicity (29.69±1.34) ($p > 0.05$), while NVP-DT showed reduced toxicity (8.889±2.42) ($p < 0.05$) based on the intrinsic nature of the drugs. NVP-FPV-DT showed higher toxicity (20.202±0.82) ($p > 0.05$). The reason may be that during conjugation with the drug, there may be some surface amine groups that were not conjugated with the drug inducing toxicity. M-NVP-FPV-DT showed a drastic reduction in toxicity due to the surface coating of mannose on the surface of drug-conjugated DT (Mishra et al., 2014; Kesharwani et al., 2015)

Table 76: % Hemolysis by plain drugs NVP, FPV and different formulations

	% Hemolysis
DT	49.09±1.24
M-DT	4.44±1.35
FPV	47.07±0.55
NVP	15.96±2.17
FPV-DT	29.69±1.34
NVP-DT	8.88±2.42
NVP-FPV-DT	20.20±0.82
M-NVP-FPV-DT	6.86±1.41

*The data was analyzed using one-way ANOVA followed by Tukey's test was performed (*P < 0.05)
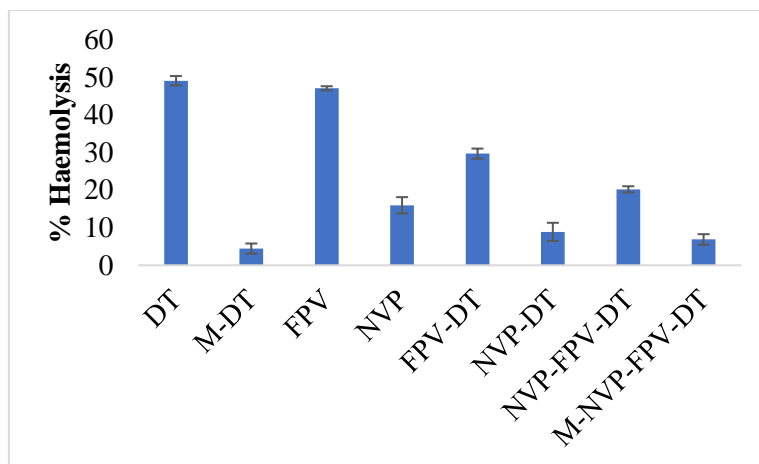
Figure 181: % Hemolysis by plain drugs NVP, FPV, and different formulations

*The data was analyzed using one-way ANOVA followed by Tukey's test was performed (*P < 0.05)
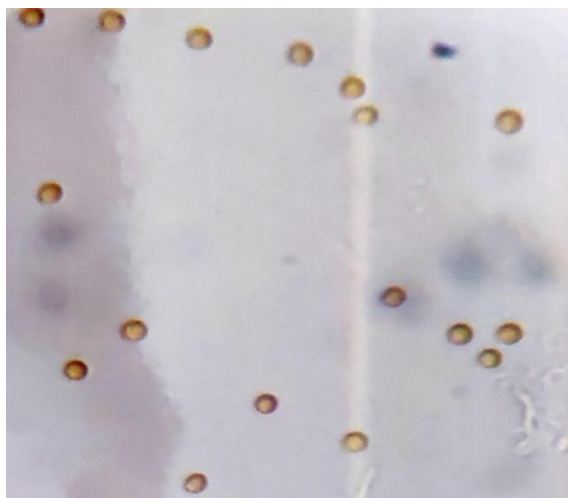
(a) Saline
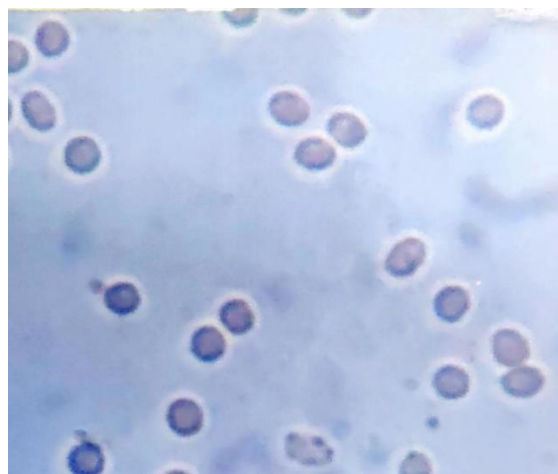
(b) Water
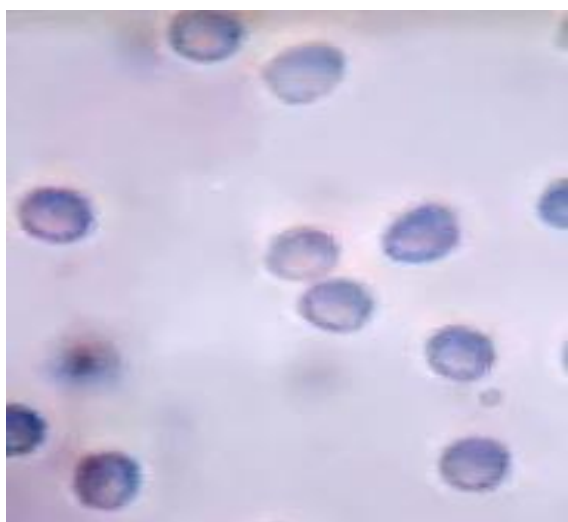
(c) DT
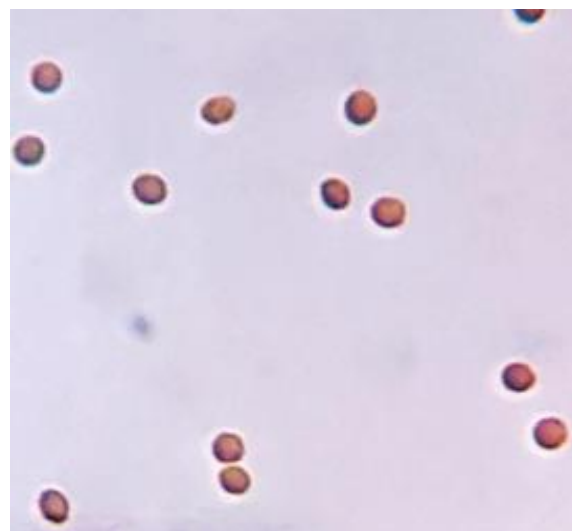
(d) MDT
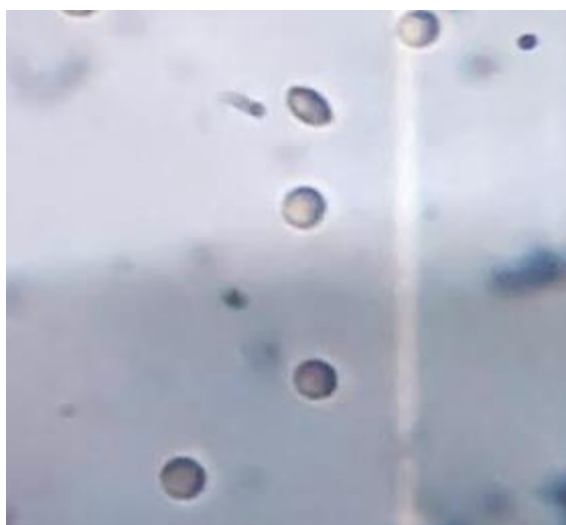
(e) FPV
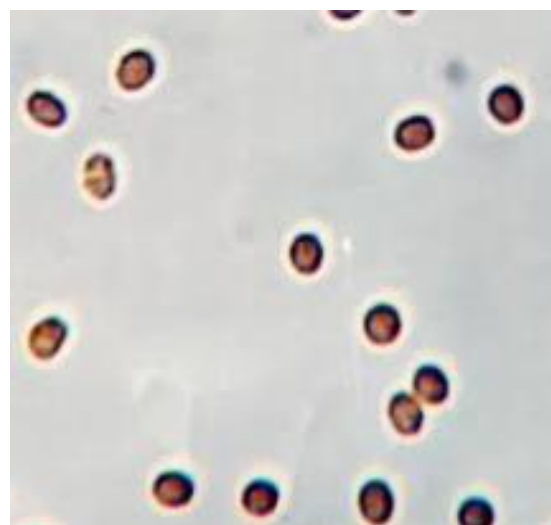
(f) NVP
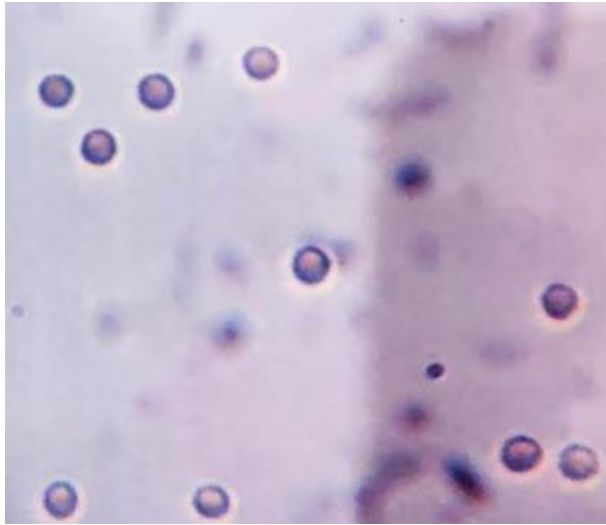
(g) NVP-DT
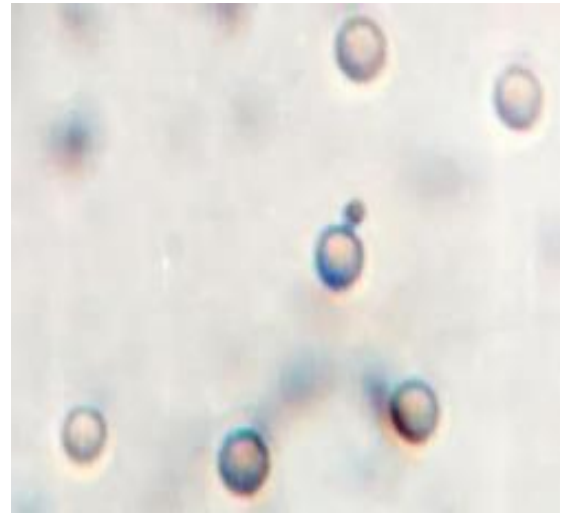
(h) FPV-DT
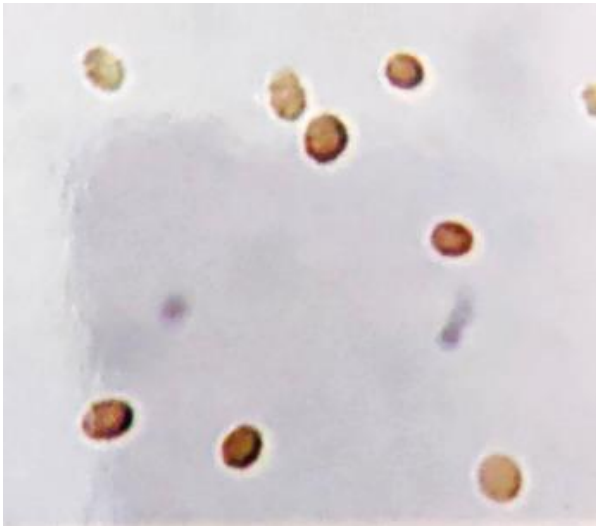
(i) NVP-FPV-DT
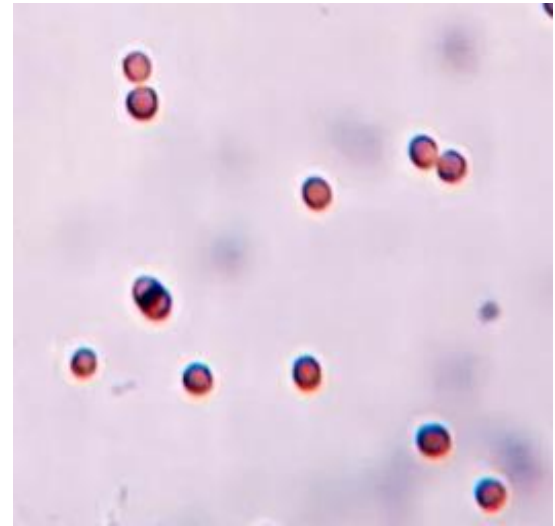
(j) M-NVP-FPV-DT

Figure 182: Photographs of RBC showing surface morphology (a) 100% Saline (b)100% Water (c) DT (d) M-DT (e) NVP (f) FPV (g) NVP-DT (h) FPV-DT (i) NVP-FPV-DT (j) M-NVP-FPV-DT

5.10.5 Hematological studies

Table 77: Hematological study of plain drugs NVP, FPV, and different formulations

Sample code	WBC count	RBC count	Hb	Platelet count	HCT	MCH
Vehicle Control	8.88±0.23	7.03±0.44	14.02±0.32	992±0.32	42.67±0.46	20.83±0.41
DT	11.34±0.44	4.45±0.62	9.34±0.44	561±0.46	30.49±0.45	16.44±0.62
M-DT	9.04±0.51	7.21±0.15	13.34±0.15	884±0.22	41.67±0.61	17.23±0.12
NVP	9.54±0.17	7.27±0.52	12.94±0.28	972±0.61	42.44±0.22	18.33±0.34
FPV	12.32±0.32	5.51±0.16	12.44±0.61	563±0.44	35.22±0.16	16.22±0.52
NVP-DT	8.94±0.44	7.883±0.42	13.12±0.37	856±0.32	42.23±0.31	19.17±0.66
FPV-DT	9.55±0.61	7.59±0.26	12.1±0.51	651±0.17	40.12±0.44	15.90±0.26
NVP-FPV-DT	9.28±0.51	7.51±0.34	11.23±0.38	776±0.42	41.44±0.27	17.22±0.52
M-NVP-FPV-DT	8.851±0.52	7.553±0.18	13.28±0.41	961±0.36	42.45±0.36	19.67±0.23

The data was analyzed using one-way ANOVA followed by Tukey's test was performed ($P < 0.05$)

Different formulations were subjected to hematological studies and their respective RBCs, WBCs, hemoglobin content, platelet count, HCT, and MCH were evaluated and compared. The vehicle control group showed readings that were near the standard level of different blood components. Hematological studies were conducted for DT and M-DT which are the designed delivery system. RBC and WBC count of DT were statistically different. RBC count was decreased and WBC count was increased this was due to the surface amine group of dendrimers present on the surface of DT. M-DT showed data similar to the control group indicating that the toxicity had been reduced due to the surface coating of the amine group with mannose (Agashe et al., 2006).

NVP samples were evaluated for different parameters indicating that the drug does not have any significant effect in 24 h (Nubila et al., 2012). FPV samples showed

significant differences in the RBC and WBC count ($p>0.05$). The RBC count was reduced as drugs tend to show hemolytic anaemia in 24 h, while the WBC count was increased (Torre 2007).

NVP-DT and FPV-DT showed the RBC and WBC count near normal which indicated that conjugation of the drug with the surface amine group of dendrimers reduces the cell lysis. NVP-FPV-DT showed all the hematological parameters near the control group but the value of RBC was slightly lower and the WBC count was slightly higher. The results are statically significant with (p value>0.05) M-NVP-FPV-DT showed results almost aligning with the control group indicating that the mannosylation reduces the toxicity of the prepared formulation (Mehra et al., 2013).

5.10.6 Future Scope

1. Detailed studies of pharmacokinetic parameters such as Cmax, tmax, AUC, and others.

2. Studies of potential interaction between dendrimers, CNTs, and DTs in vivo and its effects on pharmacokinetics.

3. Investigation of the long-term effects of DTs on human health and the environment.

4. Effects of mannose receptor alterations during disease state and its impact on the uptake of the drug.

5. The long-term impact on the efficacy and safety of the prepared structure needs to be investigated.

6. Studies related to potential adverse effects, long-term adverse effects, and HIV resistance due to the designed delivery system should be carried out

Chapter 6

Summary and Conclusion

Summary

The human immunodeficiency virus (HIV) is responsible for the development of acquired immunodeficiency syndrome (AIDS), which is responsible for more than 40.1 million deaths across the world. AIDS is a deadly disease caused by a retrovirus known as HIV.HIV has its impact throughout the world affecting the health system, education system as well as economic condition of the countries. Presently 38.4 million (33.9 - 43.8 million) people will be suffering from HIV worldwide in 2021. Different health agencies are striving hard for the betterment of HIV patients which can help them to lead a better life with the disease.

Acquired immunodeficiency syndrome is a life-threatening disease caused by the human immunodeficiency virus of the retroviridae family. The disease has engulfed 40.1 million people across the world and nearly 38.4 million individuals suffering from HIV. Different anti-HIV drugs in combinations termed HAART therapy were used to treat the disease but the efforts are in vain due to stringent dosage regimen, drug resistance, intracellular viral reservoirs, and severe adverse effects of the therapy. To bypass the problems of anti-retroviral therapy, it is a need of time to design a novel delivery system for the effective delivery of the drug to the target reservoir sites. It will improve the efficacy and efficiency of the drug and also help to manage adverse effects and drug resistance.

Dendrimers are the hyperbranched structure complex molecules consisting central core and branching units with multiple free functional groups. The structure shows good water solubility and biocompatibility make it suitable for the targeted delivery of the drug. They are formed by the successive addition of branching units to a core. It is feasible to exert specific control over the shape and size of dendrimers, and changed surface functional groups as a result of the methods that are employed to synthesize dendrimers. Therefore, for the dendrimers to selectively engage with the HIV envelope protein as well as receptors on the host cells, they have been engineered with specific functional end groups. This is done to inhibit the combination of HIV and the cells of the host, as well as the final phases of HIV replication. In addition to this, dendrimers that include a significant number of terminal groups and inner spaces act as vectors for the drug delivery, genes, and peptides that suppress HIV. Hydrogen bonds, electrostatic interactions, and hydrophobic interactions can bind these materials to

dendrimer peripheral groups or cavities. Either way, they are capable of performing both of these functions. Dendrimers would make chemical medications more stable and would facilitate the absorption of such drugs by cells through the use of functional end groups.

Multiwalled carbon nanotubes (MWCNT) are long tubular structures of nanosized diameter made up of graphene. It has unique thermal, physical, and electrical properties. The pristine MWCNTs are insoluble in water, to enhance the water solubility of the MWCNTs different functional groups can be attached to the surface of the MWCNT. CNTs have an open end or a capped end. SWCNTs are the outcome of CNTs being formed from a single sheet of graphene, whereas MWCNTs are the product of numerous graphene sheets being combined with MWCNTs. Pristine CNTs are practically insoluble in water. To improve the solubility of the pristine CNTs, surface functionalization with an organic group improves the solubility and opens the doors to the possibility of CNTs being used in bioapplications. They can adsorb or conjugate with a different medicinal compound due to the vast surface area that they possess. CNTs can be functionalized to improve their dispersibility in water or to render the correct functional groups that can attach to the therapeutic substance or desired tissue to activate a beneficial effect. This allows CNTs to be used to produce a therapeutic effect. The linked medicinal molecule may have an easier time penetrating through the target cell with the assistance of CNTs, which may then be used to cure ailments (Mishra et al., 2020).

The present work was designed to develop a novel conjugate system of 5th generation poly(propylene imine) (PPI) and the carboxylate functionalized MWCNTs for the delivery of anti-HIV drugs Nevirapine and Fosamprenavir calcium. The novel conjugate (DT) was prepared by conjugative surface amine group of

5G PPI dendrimers with the surface COOH of MWCNT. DT was evaluated for different spectroscopic and morphological studies which confirmed the attachment of dendrimers on the surface of MWCNTs. The drugs individually were loaded on dendrimers, COOH-MWCNT, and DT and characterized for different spectroscopic evaluation, morphological studies, and *in vitro* drug release and drug release kinetics.

Major target of HIV are the immune cell such as macrophages, monocytes by binding with CD4^{+} receptors of T cells. The virus tends to accumulate intracellularly

317

and tends to form viral reservoirs which are difficult to target by conventional delivery system. Macrophages have overexpression of mannose receptors, hence the delivery system can be conjugated with mannose for effective delivery of the drug to intracellular viral reservoirs. Anti-HIV drugs are usually given in combination to increase the efficacy and effectiveness of the drugs and to prevent drug resistance.

A delivery system was designed to deliver anti-HIV drugs Nevirapine and Fosamprenavir calcium using DT as a delivery system (NVP-FPV-DT). The drugs were conjugated with covalent bonding on the surface of DT. The designed structure was decorated with mannose for target efficiency (M-NVP-FPV-DT). The developed NVP-FPV-DT and M-NVP-FPV-DT were subjected to different spectroscopic analyses such as FTIR, Raman, and NMR spectroscopy. The spectroscopic analysis revealed the conjugation of NVP and FPV with DT.

It also confirmed the attachment of mannose on the surface of drug-loaded DT. XRD and DSC studies also support the conjugation of drugs NVP and FPV on the surface of DT. In the XRD diffractogram, different peaks were observed at 13.130º, 17.956º, and 22.665º were the peaks that were shifted from 13.915º and 25.455º peaks of NVP indicating the conjugation of drugs and delivery system. The broad peak at 25.00º corresponds to the peak of DT. In DSC, NVP-FPV-DT showed a peak at 235.08 ºC and another peak at 98.22 ºC. It was observed that the transition temperature showed a negative shift confirming the strong interactions between DT and drug NVP and FPV. M-NVP-FPV-DT showed a broad peak at 64.26 ºC, this may be due to the conjugation of mannose which causes distortion or alteration in the basic structure of the delivery system.

In SEM and TEM images, the image indicated the presence of a tube-like structure of carbon nanotubes with the spherical structure-dendrimer present on the surface of the MWCNT. the structure remains intact with drug loading and no structural defects were observed on drug loading.

The particle size of the drug NVP-FPV-DT was found to be 583.6 nm. The increment in size confirms the loading of the drug on DT. PDI was found to be 0.303 indicating that aggregation was further reduced, this may be due to steric hindrances. On mannosylation, there was an increment in particle size, which was found to be 765.3 nm and PDI was found to be 0.303. The zeta potential for NVP-FPV-DT further reduces

to -0.362 which may be due to increases in negative charges on the surface. The mannosylated structure shows positive zeta potential. It was found to be 0.510. The positive zeta potential was owing to the coating of mannose molecules on the surface.

The dispersibility test was done by dispersing the formulations in 5 mL distilled water and examined at 0 h, 8 h, and 24 h. The system was found to be stable and did not settle down in deionized water. Dispersibility test of DT, NVP-FPV-DT, and M-NVP-FPV-DT at 0 h, 8 h, and 24 h.

Entrapment efficiency of NVP-FPV-DT was found to be 69.65% for NVP and 47.59% for FPV. *In vitro* release studies of NVP-FPV-DT indicated 80.045±1.664% in acetate buffer pH 5 and 73.745±1.524 in PBS pH 7.4 of NVP and 75.787±1.657% in acetate buffer pH 5 and 67.192±1.924% in PBS pH 7.4 of NVP in 96 h. The drug release profile was subjected to different kinetic models and the drug release profile of NVP-FPV-DT was found to follow the Higuchi release pattern.

The stability study was conducted at 4±2 °C, at room temperature (25±2 °C), and at accelerated temperature (40±2 °C) for 6 weeks and studied at the interval of 1 week and evaluated for the colour change, precipitation, turbidity, and consistency. The formulation was found to be more stable in dark and in cool temperature. All the formulations showed a very low level of drug leakage at 4±2 °C as compared to RT and accelerated temperature. Dendrimer structures tend to shrink at lower temperature which reduces drug leakage. The leakage tends to increase with an increment of time.

The cell viability studies indicated that DT shows high cytotoxicity which was found to be reduced with mannosylation. NVP-FPV-DT showed cell viability of 43.1194 ± 2.10% at a concentration of 100 µg/mL which was found to be improved on mannosylation. The cell internalization studies indicated that mannosylation increases the uptake of the designed delivery system. cell viability decreases with an increase in the concentration. DT showed maximum toxicity which was due to the surface amine group of dendrimers attached to the surface of DT. Mannosylation improves the cytotoxicity as compared with plain DT due to the surface coating of the amine group with mannose. The cell internalization study results indicated that the M-NVP-FPV-DT tends to show higher fluorescence intensity which was due to higher uptake of the mannosylated group due to receptor-mediated endocytosis and the nano needle-shaped structure of MWCNTs.

Biodistribution studies indicated a higher accumulation of drugs in the liver, followed by the kidney, spleen, and heart. The hemolysis studies showed that the mannosylation reduces the RBC lysis. NVP-FPV-DT showed higher toxicity (20.202±0.82) (p> 0.05). The reason may be that during conjugation with the drug, there may be some surface amine groups that were not conjugated with the drug inducing toxicity. M-NVP-FPV-DT showed a drastic reduction in toxicity due to the surface coating of mannose on the surface of drug-conjugated DT. No histological evidence was observed with the liver, kidney, heart, and spleen.

Thus, from the study, it can be concluded that a novel conjugated system was developed that can load anti-HIV drugs NVP and FPV efficiently and can be targeted to the intracellular sites of viral reservoirs.

Chapter 7

Bibilography

Aavani P, Allen LJ. The role of CD4 T cells in immune system activation and viral reproduction in a simple model for HIV infection. Applied Mathematical Modelling. 2019 Nov 1;75:210-22.

Abbasi E, Aval SF, Akbarzadeh A, Milani M, Nasrabadi HT, Joo SW, Hanifehpour Y, Nejati-Koshki K, Pashaei-Asl R. Dendrimers: synthesis, applications, and properties. Nanoscale research letters. 2014 Dec;9(1):1-0.

Adar F. Introduction to interpretation of Raman spectra using database searching and functional group detection and identification. Spectroscopy. 2016 Jul 1;31(7):16-23.

Afshari R, Mazinani S, Abdouss M. Nanohybrid nanoparticles based on chitosan/functionalized carbon nanotubes as anti-HIV nanocarrier. Nano. 2015 Jan 9;10(01):1550010.

Aggarwal, Nidhi, Bushra Nabi, Sumit Aggarwal, Sanjula Baboota, and Javed Ali. "Nano-based drug delivery system: a smart alternative towards eradication of viral sanctuaries in management of NeuroAIDS. Drug Delivery and Translational Research. 2021: 1-22.

Agrahari AK, Singh AS, Mukherjee R, Tiwari VK. An expeditious click approach towards the synthesis of galactose coated novel glyco-dendrimers and dentromers utilizing a double stage convergent method. RSC Advances. 2020;10(52):31553-62.

Alamry KA, Georgiev NI, El-Daly SA, Taib LA, Bojinov VB. A highly selective ratiometric fluorescent pH probe based on a PAMAM wavelength-shifting bichromophoric system. Spectrochimica Acta Part A: Molecular and Biomolecular Spectroscopy. 2015 Jan 25;135:792-800.

Alavi SJ, Gholami L, Askarian S, Darroudi M, Massoudi A, Rezaee M, Oskuee KR. Hyperbranched–dendrimer architectural copolymer gene delivery using hyperbranched PEI conjugated to poly(propyleneimine) dendrimers: synthesis, characterization, and evaluation of transfection efficiency. Journal of Nanoparticle Research. 2017, 19(2), 49, 1-12.

Albayati TM, Abd Alkadir AJ. Synthesis and characterization of mesoporous materials as a carrier and release of prednisolone in drug delivery system. Journal of Drug Delivery Science and Technology. 2019 Oct 1;53:101176.

Altice F, Evuarherhe O, Shina S, Carter G, Beaubrun AC. Adherence to HIV treatment regimens: systematic literature review and meta-analysis. Patient preference and adherence. 2019;13:475.

Alvi Y, Khalique N, Ahmad A, Sameen S. A study on side effect of antiretroviral therapy among people living with HIV/AIDS. Journal of Pharmacovigilance and Drug Safety. 2019 Jun 30;16(1):22-5.

Amézqueta S, Subirats X, Fuguet E, Rosés M, Ràfols C. Octanol-water partition constant. Liquid-phase extraction. 2020 Jan 1:183-208.

Anzar N, Hasan R, Tyagi M, Yadav N, Narang J. Carbon nanotube-A review on Synthesis, Properties and plethora of applications in the field of biomedical science. Sensors International. 2020 Jan 1;1:100003.

Araga R, Sharma CS. One step direct synthesis of multiwalled carbon nanotubes from coconut shell derived charcoal. Materials Letters. 2017 Feb 1;188:205-7.

Auclair J, Morel E, Wilkinson KJ, Gagné F. Synergistic toxicity of PAMAM dendrimers and minocycline to rainbow trout hepatocytes. EC Pharmacology Toxicology 2017; 3(5):138–145.

Awasthi A, Kumar A, Kumar R, Vishwas S, Khursheed R, Kaur J, Corrie L, Kumar B, Gulati M, Kumar D, Kaushik M. RP-HPLC method development and validation for simultaneous estimation of mesalamine and curcumin in bulk form as well as nanostructured lipid carriers. South African Journal of Botany. 2022 Dec 1;151:529-37.

Badea MA, Prodana M, Dinischiotu A, Crihana C, Ionita D, Balas M. Cisplatin loaded multiwalled carbon nanotubes induce resistance in triple negative breast cancer cells. Pharmaceutics. 2018 Nov 13;10(4):228.

Barbier F, Mer M, Szychowiak P, Miller RF, Mariotte É, Galicier L, Bouadma L, Tattevin P, Azoulay É. Management of HIV-infected patients in the intensive care unit. Intensive care medicine. 2020 Feb;46(2):329-42.

Becken B, Multani A, Padival S, Cunningham CK. Human immunodeficiency virus I: history, epidemiology, transmission, and pathogenesis. In Introduction to Clinical Infectious Diseases, Springer, Cham 2019, pp. 417-423.

Bekker LG, Alleyne G, Baral S, Cepeda J, Daskalakis D, Dowdy D, Dybul M, Eholie

S, Esom K, Garnett G, Grimsrud A. Advancing global health and strengthening the HIV response in the era of the Sustainable Development Goals: the International AIDS Society—Lancet Commission. The Lancet. 2018 Jul 28;392(10144):312-58.

Bhandaru JS, Malothu N, Akkinepally RR. Characterization and solubility studies of pharmaceutical cocrystals of eprosartan mesylate. Crystal Growth & Design. 2015 Mar 4;15(3):1173-9.

Bharti SK, Roy R. Quantitative 1H NMR spectroscopy. Trends in Analytical Chemistry. 2012 May 1;35:5-26.

Bhatti, A. B., Usman, M., & Kandi, V. (2016). Current Scenario of HIV/AIDS, Treatment Options, and Major Challenges with Compliance to Antiretroviral Therapy. Cureus, *8*(3), 1–12.

Bhavyasri K, Srihitha G, Rambabu D, Sumakanth M. Development and Validation of Nevirapine—An Anti-Retro Viral Drug by UV-Visible Spectrophotometric Method and Its Degradtion Study under Various Stress Conditions. Saudi Journal of Biomedical Research. 2019;4:254-8.

Bhinge, S.D.; Malipatil, S.M.; Sonawane, L.V. Bioanalytical method development and validation for simultaneous estimation of cefixime and dicloxacillin by RP-HPLC in human plasma. Acta Chimica Slovenica, 2014**,** *61*(3), 580-586. PMID:25286213

Biagiotti G, Ligi MC, Fedeli S, Pranzini E, Gamberi T, Cicchi S, Paoli P. Metformin salts with oxidized multiwalled carbon nanotubes: In vitro biological activity and inhibition of CNT internalization. Journal of Drug Delivery Science and Technology. 2018 Oct 1;47:254-8.

Brown LB, Spinelli MA, Gandhi M. The interplay between HIV and COVID-19: summary of the data and responses to date. Current Opinion in HIV and AIDS. 2021 Jan 1;16(1):63-73.

Buber E, Kesik M, Soylemez S, Toppare L. A bio-sensing platform utilizing a conjugated polymer, carbon nanotubes and PAMAM combination. Journal of Electroanalytical Chemistry. 2017 Aug 15;799:370-6.

Campbell BC, Mitchell PJ, Churilov L, Yassi N, Kleinig TJ, Dowling RJ, Yan B, Bush SJ, Dewey HM, Thijs V, Scroop R. Tenecteplase versus alteplase before thrombectomy for ischemic stroke. New England Journal of Medicine. 2018 Apr 26;378(17):1573-82.

Ceciliani F, Morales GÁ, De Matteis G, Grandoni F, Ferreira RF, Roccabianca P, Lecchi C. Methods in isolation and characterization of bovine monocytes and macrophages. Methods. 2021 Feb 1;186:22-41.

Chamundeeswari M, Jeslin J, Verma ML. Nanocarriers for drug delivery applications. Environmental Chemistry Letters. 2019 Jun;17(2):849-65.

Chanvorachote B, Qiu J, Muangsiri W, Nimmannit U, & Kirsch LE. The interaction mechanism between lipopeptide (daptomycin) and polyamidoamine (PAMAM) dendrimers. Journal of Peptide Science 2015, 21(4), 312-319.

Chauhan A, Chauhan P. Powder XRD technique and its applications in science and technology. Journal of Analytical and Bioanalytical Techniques 2014 Sep 1;5(5):1-5.

Chauhan AS. Dendrimers for drug delivery. Molecules. 2018 Apr;23(4):938.

Chaurasia G. A review on pharmaceutical preformulation studies in formulation and development of new drug molecules. International Journal of Pharmaceutical Science and research. 2016 Jun 1;7(6):2313-0.

Che Marzuki NH, Wahab RA, Abdul Hamid M. An overview of nanoemulsion: concepts of development and cosmeceutical applications. Biotechnology & biotechnological equipment. 2019 Jan 1;33(1):779-97.

Chen B. Molecular mechanism of HIV-1 entry. Trends in microbiology. 2019 Oct 1;27(10):878-91.

Chmiel T, Mieszkowska A, Kempińska-Kupczyk D, Kot-Wasik A, Namieśnik J, Mazerska Z. The impact of lipophilicity on environmental processes, drug delivery and bioavailability of food components. Microchemical Journal. 2019 May 1;146:393-406.

Chopdey, Prashant K., Rakesh K. Tekade, Neelesh K. Mehra, Nishi Mody, and Narendra K. Jain. 2015. "Glycyrrhizin Conjugated Dendrimer and Multi-Walled Carbon Nanotubes for Liver Specific Delivery of Doxorubicin. Journal of Nanoscience and Nanotechnology 15(2):1088–1100.

Choudhary S, Gupta L, Rani S, Dave K, Gupta U. Impact of dendrimers on solubility of hydrophobic drug molecules. Frontiers in pharmacology. 2017 May 16;8:261.

Chountoulesi, Maria, Nikolaos Naziris, Natassa Pippa, Stergios Pispas, and Costas Demetzos. "Differential scanning calorimetry (DSC): An invaluable tool for the thermal evaluation of advanced chimeric liposomal drug delivery nanosystems." In Thermodynamics and Biophysics of Biomedical Nanosystems, pp. 297-337.

Chudoba D, Jażdżewska M, Łudzik K, Wołoszczuk S, Juszyńska-Gałązka E, Kościński M. Description of Release Process of Doxorubicin from Modified Carbon Nanotubes. International Journal of Molecular Sciences. 2021 Nov 5;22(21):12003.

Chun TW, Moir S, Fauci AS. HIV reservoirs as obstacles and opportunities for an HIV cure. Nature immunology. 2015 Jun;16(6):584-9.

Cihlar T, Fordyce M. Current status and prospects of HIV treatment. Current Opinion in Virology. 2016 Jun, 18: 50-56.

Clancy AJ, Bayazit MK, Hodge SA, Skipper NT, Howard CA, Shaffer MS. Charged carbon nanomaterials: redox chemistries of fullerenes, carbon nanotubes, and graphenes. Chemical reviews. 2018 Aug 15;118(16):7363-408.

Colino CI, Lanao JM, Gutierrez-Millan C. Targeting of hepatic macrophages by therapeutic nanoparticles. Frontiers in immunology. 2020 Mar 4;11:218.

Conway JM, Ribeiro RM. Modeling the immune response to HIV infection. Current opinion in systems biology. 2018 Dec 1;12:61-9.

Cordeiro CF, Bettio I, Trevisan MG. Studies on the characterization and polymorphic stability of Fosamprenavir. Anais da Academia Brasileira de Ciências. 2020 May 11;92.

Córdoba EV, Arnaiz E, Relloso M, Sánchez-Torres C, García F, Pérez-Álvarez L, Gomez R, de la Mata FJ, Pion M, Muñoz-Fernández MÁ. Development of sulphated and naphthylsulphonated carbosilane dendrimers as topical microbicides to prevent HIV-1 sexual transmission. Aids. 2013 May 15;27(8):1219-29.

Cribbs SK, Crothers K, Morris A. Pathogenesis of HIV-related lung disease: immunity, infection, and inflammation. Physiological reviews. 2020 Apr 1;100(2):603-32.

Cyganowski P, Wolska J. Nanocomposite membranes with Au nanoparticles for dialysis-based catalytic reduction-separation of nitroaromatic compounds. Reactive and Functional Polymers. 2022 Jan 1;170:105119.

da Silva EM, de Bustamante Monteiro MS, da Silva PS, Tavares MI. H NMR in Solution of Nanocomposites from Polycaprolactone–Nevirapine. Journal of Nanotechnology and Nano Science Research. 2021, 1(2), 1-10.

Dalle Vedove E, Costabile G, Merkel OM. Mannose and Mannose-6-Phosphate Receptor–Targeted Drug Delivery Systems and Their Application in Cancer Therapy. Advanced healthcare materials. 2018 Jul;7(14):1701398.

Das MK, Sarma A, Chakraborty T. Nano-ART and neuroAIDS. Drug Delivery and

Translational Research. 2016 Oct;6:452-72.

Date AA, Shibata A, Mcmullen E, Bruzzo KL, Belshan M, Zhou Y, and Destache CJ. HHS Public Access. 2018, 11(3):416–27.

de Béthune MP. Non-nucleoside reverse transcriptase inhibitors (NNRTIs), their discovery, development, and use in the treatment of HIV-1 infection: a review of the last 20 years (1989–2009). Antiviral research. 2010 Jan 1;85(1):75-90.

Deeks SG, Overbaugh J, Phillips A, Buchbinder S. HIV infection. Nature reviews Disease primers. 2015 Oct 1;1(1):1-22.

Desmecht, Antonin, Timothy Steenhaut, Florence Pennetreau, Sophie Hermans, and Olivier Riant. 2018. "Synthesis and Catalytic Applications of Multi-Walled Carbon Nanotube–Polyamidoamine Dendrimer Hybrids." Chemistry - A European Journal 24(49):12992–1.

Dharshini KP, Fang H, Devi DR, Yang JX, Luo RH, Zheng YT, Brzeziński M, Hari BV. pH-sensitive chitosan nanoparticles loaded with dolutegravir as milk and food admixture for paediatric anti-HIV therapy. Carbohydrate Polymers. 2021 Mar 15;256:117440.

Dlamini N, Mukaya HE, Van Zyl RL, Chen CT, Zeevaart RJ, Mbianda XY. Synthesis, characterization, kinetic drug release and anticancer activity of bisphosphonates multi-walled carbon nanotube conjugates. Materials Science and Engineering: C. 2019 Nov 1;104:109967.

Doitsh G, Galloway NL, Geng X, Yang Z, Monroe KM, Zepeda O, Hunt PW, Hatano H, Sowinski S, Muñoz-Arias I, Greene WC. Correction: Corrigendum: Cell death by pyroptosis drives CD4 T-cell depletion in HIV-1 infection. Nature. 2017 Apr;544(7648):124.

Doitsh G, Greene WC. Dissecting How CD4 T Cells Are Lost During HIV Infection. Cell Host Microbe. 2016 Mar 9;19(3):280-91.

Dong X, Sun Z, Wang X, Zhu D, Liu L, Leng X. Simultaneous monitoring of the drug release and antitumor effect of a novel drug delivery system-MWCNTs/DOX/TC. Drug Delivery. 2017 Jan 1;24(1):143-51.

Drug bank, https://go.drugbank.com/salts/DBSALT001228 accessed on 11 May 2023.

Duse PV, Baheti KG. Bioanalytical method development and validation for the determination of Favipiravir in spiked human plasma by using RP-HPLC. Journal of Pharmaceutical Research International 2021;33:275-81.

Edoul G, Chia JE, Vidal N, Guichet E, Montavon C, Delaporte E, Ngole EM, Ayouba A, Peeters M. High HIV burden and recent transmission chains in rural forest areas in southern Cameroon, where ancestors of HIV-1 have been identified in ape populations. Infection, Genetics and Evolution. 2020 Oct 1;84:104358.

Eloy AM. Proteins candidates for complementary diagnosis of goats naturally infected by Lentivirus. Virology & Mycology, v. 7, p. 53, 2018.

El-Zaher, A.A.; Hashem, H.A.; Elkady, E.F.; Allam, M.A. A validated LC-MS/MS bioanalytical method for the simultaneous determination of dapagliflozin or saxagliptin with metformin in human plasma. Microchemal. Journal. 2019, *149*, 104017, 1-9.

Esbjörnsson, J., Jansson, M., Jespersen, S. *et al*. HIV-2 as a model to identify a functional HIV cure. AIDS Research and Therapy 16, 24 (2019).

Eswarudu MM, Rao AL, Vijay K. Bioanalytical method development and validation for simultaneous determination of chlorthalidone and cilnidipine drugs in human plasma by RP-HPLC. International journal of research in pharmacy and chemistry. 2019;9(1):33-44.

Fanales-Belasio E, Raimondo M, Suligoi B, Buttò S. HIV virology and pathogenetic mechanisms of infection: a brief overview. Annali dell'Istituto superiore di sanita. 2010;46:5-14.

Faria, N. R., Rambaut, A., Suchard, M. A., Baele, G., Bedford, T., Ward, M. J., Tatem, A. J., Sousa, J. D., Arinaminpathy, N., Pépin, J., Posada, D., Peeters, M., Pybus, O. G., & Lemey, P. (2014). The early spread and epidemic ignition of HIV-1 in human populations. *Science*, 346(6205), 56–61. https://doi.org/10.1126/science.1256739

Filatova LY, Klyachko NL, Kudryashova EV. Targeted delivery of anti-tuberculosis drugs to macrophages: targeting mannose receptors. Russian Chemical Reviews. 2018 Apr 1;87(4):374.

Ford SL, Wire MB, Lou Y, Baker KL, Stein DS. Effect of antacids and ranitidine on the single-dose pharmacokinetics of fosamprenavir. Antimicrobial agents and chemotherapy. 2005 Jan;49(1):467-9.

Francis AP, Devasena T. Toxicity of carbon nanotubes: A review. Toxicology and industrial health. 2018 Mar;34(3):200-10.

Freed EO. HIV-1 assembly, release and maturation. Nature Reviews Microbiology. 2015 Aug;13(8):484-96.

Gadag S, Narayan R, Nayak Y, Nayak UY. Bioanalytical RP-HPLC method validation for resveratrol and its application to pharmacokinetic and drug distribution studies. Journal of Applied Pharmaceutical Science. 2022 Feb 5;12(2):158-64.

Gajbhiye V, Ganesh N, Barve J, Jain NK. Synthesis, characterization and targeting potential of zidovudine loaded sialic acid conjugated-mannosylated poly (propyleneimine) dendrimers. European Journal of Pharmaceutical Sciences. 2013 Mar 12;48(4-5):668-79.

Garcia A, Herrero MA, Frein S, Deschenaux R, Munoz R, Bustero I, Toma F, Prato M. Synthesis of dendrimer–carbon nanotube conjugates. physica status solidi (a). 2008 Jun;205(6):1402-7.

Garkal A, Avachat A. Development and in-vitro in-vivo characterization of in-situ gelling sustained-release nevirapine suspension. Journal of Drug Delivery Science and Technology. 2022 Jan 1;67:102938.

Ghoshal S, Mishra MK. Release Kinetic Profiles of 6-Mercaptopurine Loaded Covalently Functionalized Multiwalled Carbon Nanotubes. American Journal of Advanced Drug Delivery 2014;2:110-9.

Gill P, Moghadam TT, Ranjbar B. Differential scanning calorimetry techniques: applications in biology and nanoscience. Journal of biomolecular technique. 2010 Dec;21(4):167.

Global HIV and AIDS fact sheet 2021. Global HIV & AIDS statistics — Fact sheet | UNAIDS

Godbole MD, Sabale PM, Mathur VB. Development of lamivudine liposomes by three-level factorial design approach for optimum entrapment and enhancing tissue targeting. Journal of Microencapsulation. 2020 Aug 17;37(6):431-44.

Goku PE, Orman E, Quartey AN, Adu JK, Adosraku RK. A simple RP-HPLC method to simultaneously assay the contents of lamivudine, tenofovir, and nevirapine in fixed dose combined oral antiviral medicines. Journal of Chemistry. 2020 Sep 8;2020:1-9.

Golshan M, Salami-Kalajahi M, Roghani-Mamaqani H, Mohammadi M. Synthesis of poly (propylene imine) dendrimers via homogeneous reduction process using lithium aluminium hydride: Bioconjugation with folic acid and doxorubicin release kinetics. Applied Organometallic Chemistry. 2017 Nov;31(11):e3789.

Grobert N. Carbon nanotubes–becoming clean. Materials today. 2007 Jan 1;10(1-2):28-35.

Guerra J, Herrero MA, Carrion B, Pérez-Martínez FC, Lucío M, Rubio N, Meneghetti M, Prato M, Ceña V, Vazquez E. Carbon nanohorns functionalized with polyamidoamine dendrimers as efficient biocarrier materials for gene therapy. Carbon. 2012 Jul 1;50(8):2832-44.

Guideline WHO 2015 9789241509565_eng.pdf;jsessionid=140BA4B25E1C4B10129350DF2D841839 (who.int)

Guinto RR, Cahatol JJ, Lazaro KY, Salazar AF. Pathways Linking Climate Change and HIV/AIDS: An Updated Conceptual Framework and Implications for the Philippines. The Journal of Climate Change and Health 2021: 1100106.

Gulbake AS, Jain AV, Shilpi SA, KUMAR P, GULBAKE A. Mannosylated multiwalled carbon nanotubes assisted artesunate delivery for cerebral malaria. International Journal of Applied Pharmaceutics. 2019;11:24-30.

Gulbake AS, Jain AV, Shilpi SA, KUMAR P, GULBAKE A. Mannosylated multiwalled carbon nanotubes assisted artesunate delivery for cerebral malaria. International Journal of Applied Pharmaceutics. 2019;11:24-30.

Guo B, Liao C, Liu X, Yi J. Preliminary study on conjugation of formononetin with multiwalled carbon nanotubes for inducing apoptosis via ROS production in HeLa cells. Drug Design, Development and Therapy. 2018 Sep 7:2815-26.

Gupta R, Mehra NK, Jain NK. Fucosylated multiwalled carbon nanotubes for Kupffer cells targeting for the treatment of cytokine-induced liver damage. Pharmaceutical research. 2014 Feb;31:322-34.

Gupta S, Kesarla R, Omri A. Approaches for CNS delivery of drugs–nose to brain targeting of antiretroviral agents as a potential attempt for complete elimination of major reservoir site of HIV to aid AIDS treatment. Expert Opinion on Drug Delivery. 2019 Mar 4;16(3):287-300.

Gupta S, Nair AB, Attimarad M. Development and validation of bioanalytical method for the determination of hydrazinocurcumin in rat plasma and organs by HPLC-UV. Journal of chromatography B. 2020 Nov 1;1156:122310.

Gurpreet K, Singh SK. Review of nanoemulsion formulation and characterization techniques. Indian Journal of Pharmaceutical Sciences. 2018 Aug 31;80(5):781-9.

Haghighi F, Morsali A, Bozorgmehr MR, Beyramabadi SA. Nanostructures of PAMAM Dendrimers in Drug Delivery system for 5-fluorouracil. Журнал Сибирского федерального университета. Химия. 2020;13(3).

Haji, A.; & Shoushtari, A. M. Grafting of poly (propylene imine) dendrimer on polypropylene nonwoven: Preparation optimization, characterization, and application. Fibers and Polymers. 2019, 20, 913-921.

Hamedi, Sepideh, and Mojtaba Koosha. Designing a pH-responsive drug delivery system for the release of black-carrot anthocyanins loaded in halloysite nanotubes for cancer treatment. Applied Clay Science 197 (2020): 105770.

Harish V, Almalki WH, Alshehri A, Alzahrani A, Alzarea SI, Kazmi I, Gulati M, Tewari D, Chellappan DK, Gupta G, Dua K. Bioanalytical Method Development, Validation and Stability Assessment of Xanthohumol in Rat Plasma. Molecules. 2022 Oct 21;27(20):7117.

Haroun AA, Amin HA, Abd El-Alim SH. Immobilization and in vitro evaluation of soyasapogenol B onto functionalized multi-walled carbon nanotubes. IRBM. 2018 Feb 1;39(1):35-42.

Hassani M, Tahghighi A, Rohani M, Hekmati M, Ahmadian M, Ahmadvand H. Robust antibacterial activity of functionalized carbon nanotube-levofloxacine conjugate based on in vitro and in vivo studies. Scientific Reports. 2022 Jun 16;12(1):1-9.

Hatami Y, Heravi MM, Morsali A, Bozorgmehr MR. Experimental and theoretical Studies of Anti-HIV Medication Azidothymidine (AZT) Interactions with Non-

functionalized and Functionalized Nanotubes. Moroccan Journal of Chemistry. 2019 Jul 1;7(3):7-3.

Herrero MA, Toma FM, Al-Jamal KT, Kostarelos K, Bianco A, Da Ros T, Bano F, Casalis L, Scoles G, Prato M. Synthesis and characterization of a carbon nanotube−dendron series for efficient siRNA delivery. Journal of the American Chemical Society. 2009 Jul 22;131(28):9843-8.

Higuchi Y, Wu C, Chang KL, Irie K, Kawakami S, Yamashita F, Hashida M. Polyamidoamine dendrimer-conjugated quantum dots for efficient labeling of primary cultured mesenchymal stem cells. Biomaterials. 2011 Oct 1;32(28):6676-82.

Hileman CO, Funderburg NT. Inflammation, immune activation, and antiretroviral therapy in HIV. Current Hiv/aids Reports. 2017 Jun;14(3):93-100.

Himmel DM, Arnold E. Non-nucleoside reverse transcriptase inhibitors join forces with integrase inhibitors to combat HIV. Pharmaceuticals. 2020 Jun 11;13(6):122.

HIV, WHO report 2021. HIV (who.int)

Hooshyar, S. P.; Mehrabian, R. Z.; Panahi, H. A.; Jouybari, M. H.; & Jalilian, H. Synthesis and characterization of magnetized-PEGylated dendrimer anchored to thermosensitive polymer for letrozole drug delivery Colloids and Surfaces B. 2019, 176, 404-411.

Hosseini L, Mahboobnia K, Irani M. Fabrication of PLA/MWCNT/Fe3O4 composite nanofibers for leukemia cancer cells. International Journal of Polymeric Materials 2016;65(4):176-82.

Hsieh, Yu-Chen, Yu-Chuan Chou, Chun-Ping Lin, Tung-Feng Hsieh, and Chi-Min Shu. "Thermal analysis of multi-walled carbon nanotubes by Kissinger's corrected kinetic equation." Aerosol and Air Quality Research 10, no. 3 (2010): 212-218.

Huang H, Yuan Q, Shah JS, Misra RD. A new family of folate-decorated and carbon nanotube-mediated drug delivery system: synthesis and drug delivery response. Advanced drug delivery reviews. 2011 Nov 1;63(14-15):1332-9.

Hughes PJ, Cretton-Scott E, Teague A, Wensel TM. Protease inhibitors for patients with HIV-1 infection: a comparative overview. Pharmacy and Therapeutics. 2011 Jun;36(6):332.

Iannazzo D, Pistone A, Galvagno S, Ferro S, De Luca L, Monforte AM, Da Ros T, Hadad C, Prato M, Pannecouque C. Synthesis and anti-HIV activity of carboxylated and drug-conjugated multi-walled carbon nanotubes. Carbon. 2015 Feb 1;82:548-61.

ICH. https://database.ich.org/sites/default/files/Q2%28R1%29 Guideline.pdf, assessed on 18 April 2023.

Idris AO, Mamba B, Feleni U. Poly (propylene imine) dendrimer: A potential nanomaterial for electrochemical application. Materials Chemistry and Physics. 2020 Apr 1;244:122641.

Inkson BJ. Scanning electron microscopy (SEM) and transmission electron microscopy (TEM) for materials characterization. InMaterials characterization using nondestructive evaluation (NDE) methods 2016 Jan 1 (pp. 17-43). Woodhead publishing.

Jahagirdar P, Lokhande AS, Dandekar P, Devarajan PV. Mannose receptor and targeting strategies. Targeted intracellular drug delivery by receptor-mediated endocytosis. 2019:433-56.

Jain K, Verma AK, Mishra PR, Jain NK. Surface-engineered dendrimeric nanoconjugates for macrophage-targeted delivery of amphotericin B: formulation development and in vitro and in vivo evaluation. Antimicrobial agents and chemotherapy. 2015 May;59(5):2479-87.

Jain NK, Tare MS, Mishra V, Tripathi PK. The development, characterization and in vivo anti-ovarian cancer activity of poly (propylene imine)(PPI)-antibody conjugates containing encapsulated paclitaxel. Nanomedicine: Nanotechnology, Biology and Medicine. 2015;11(1):207-18.

Jain V, Maingi V, Maiti PK, & Bharatam PV. Molecular dynamics simulations of PPI dendrimer–drug complexes. Soft Matter 2013, 9(28), 6482-6496.

Janaszewska A, Lazniewska J, Trzepiński P, Marcinkowska M, Klajnert-Maculewicz B. Cytotoxicity of dendrimers. Biomolecules. 2019 Aug 1;9(8):330.

Javan F, Vatanara A, Azadmanesh K, Nabi-Meibodi M, Shakouri M. Encapsulation of ritonavir in solid lipid nanoparticles: in-vitro anti-HIV-1 activity using lentiviral particles. Journal of Pharmacy and Pharmacology. 2017 Aug;69(8):1002-9.

Jobli MI, Yao R, Luo Z, Shahrestani M, Li N, Liu H. Numerical and experimental studies of a Capillary-Tube embedded PCM component for improving indoor thermal environment. Applied Thermal Engineering. 2019 Feb 5;148:466-77.

Jose J, Charyulu RN. Prolonged drug delivery system of an antifungal drug by association with polyamidoamine dendrimers. International Journal of Pharmaceutical Investigation. 2016 Apr;6(2):123.

Karimi M, Solati N, Ghasemi A, Estiar MA, Hashemkhani M, Kiani P, Mohamed E, Saeidi A, Taheri M, Avci P, Aref AR. Carbon nanotubes part II: a remarkable carrier for drug and gene delivery. Expert opinion on drug delivery. 2015 Jul 3;12(7):1089-105.

Kaur A, Jain K, Mehra NK, Jain NK. Development and characterization of surface engineered PPI dendrimers for targeted drug delivery. Artificial cells, nanomedicine, and biotechnology. 2017 Apr 3;45(3):414-25.

Kaur D, Jain K, Mehra NK, Kesharwani P, Jain NK. A review on comparative study of PPI and PAMAM dendrimers. Journal of Nanoparticle Research. 2016 Jun;18:1-4.

Kayat J, Mehra NK, Gajbhiye V, et al. Drug targeting to arthritic region via folic acid appended surface-engineered multi-walled carbon nanotubes. J. Drug Target. 2016 Apr 20;24(4):318-27.

Kaynak N, Önen A, Karahasanoğlu M. Photoactive multi-walled carbon nanotubes: synthesis and utilization of benzoin functional MWCNTs. Journal of Materials Science. 2018 Jul;53(13):9598-610.

Kesharwani P, Gothwal A, Iyer AK, Jain K, Chourasia MK, Gupta U. Dendrimer nanohybrid carrier systems: An expanding horizon for targeted drug and gene delivery. Drug discovery today. 2018 Feb 1;23(2):300-14.

Kesharwani P, Jain K, Jain NK. Dendrimer as nanocarrier for drug delivery. Progress in Polymer Science. 2014 Feb 1;39(2):268-307.

Kesharwani P, Mishra V, Jain NK. Validating the anticancer potential of carbon nanotube-based therapeutics through cell line testing. Drug discovery today. 2015 Sep 1;20(9):1049-60.

Kesharwani P, Tekade RK, Jain NK. Formulation development and in vitro–in vivo assessment of the fourth-generation PPI dendrimer as a cancer-targeting vector. Nanomedicine. 2014;9(15):2291-308.

Khan H, Yerramilli AS, D'Oliveira A, Alford TL, Boffito DC, Patience GS. Experimental methods in chemical engineering: X-ray diffraction spectroscopy—XRD. The Canadian journal of chemical engineering. 2020 Jun;98(6):1255-66.

Khursheed R, Singh SK, Kapoor B, Gulati M, Wadhwa S, Gupta S, Prasher P, Kumar D, Dua K, Kumar LS, Babu UV. Development and validation of RP-HPLC method for simultaneous determination of curcumin and quercetin in extracts, marketed formulations, and self-nanoemulsifying drug delivery system. Re: GEN Open. 2021 Jan 1;1(1):43-52.

Khursheed R, Wadhwa S, Kumar B, Gulati M, Gupta S, Chaitanya MV, Kumar D, Jha NK, Gupta G, Prasher P, Chellappan DK. Development and validation of RP-HPLC based bioanalytical method for simultaneous estimation of curcumin and quercetin in rat's plasma. South African Journal of Botany. 2022 Sep 1;149:870-7.

Kiran AR, Kumari GK, Krishnamurthy PT. Carbon nanotubes in drug delivery: Focus on anticancer therapies. Journal of Drug Delivery Science and Technology. 2020 Oct 1;59:101892.

Klatt EC. Pathology of HIV/AIDS. The Mercer University of Medicine Savannah. 2017 Apr 25:6-50.

Kumar PD, Kumar PV, Selvam TP, Rao KS. PEG conjugated PAMAM dendrimers with a anti-HIV drug stavudine for prolong release. Research in Biotechnology. 2013 Mar 21;4(2).

Kumar PV, Asthana A, Dutta T, Jain NK. Intracellular macrophage uptake of rifampicin loaded mannosylated dendrimers. Journal of drug targeting. 2006 Jan 1;14(8):546-56.

Kumar R, Kumar R, Khursheed R, Awasthi A, Ramanunny AK, Kaur J, Khurana N, Singh SK, Khurana S, Pandey NK, Kapoor B. Validated Reverse Phase-High-Performance Liquid Chromatography Method for Estimation of Fisetin in Self-Nanoemulsifying Drug Delivery System. ASSAY and Drug Development Technologies. 2020 Sep 1;18(6):274-81.

Lahkar, S.; Das, M. K. Surface-modified polycaprolactone nanoparticles for the brain-targeted delivery of nevirapine. Journal of Nanoparticle Research, 2020, 22, 1-19.

Lee JH, Yeo Y. Controlled drug release from pharmaceutical nanocarriers. Chemical

engineering science. 2015 Mar 24;125:75-84.

Leksic E, Sepac D, Pavlicic D, inventors; Pliva Hrvatska doo, assignee. Solid state forms of fosamprenavir calcium salt and processes for preparation thereof. United States patent application US 12/986,125. 2011 Jul 7.

Lodhi N, Mehra NK, Jain NK. Development and characterization of dexamethasone mesylate anchored on multi walled carbon nanotubes. Journal of Drug Targeting 2013;21(1):67-76.

Lu DY, Wu HY, Yarla NS, Xu B, Ding J, Lu TR. HAART in HIV/AIDS treatments: future trends. Infectious Disorders-Drug Targets (Formerly Current Drug Targets-Infectious Disorders). 2018 Mar 1;18(1):15-22.

Lusic M, Siliciano RF. Nuclear landscape of HIV-1 infection and integration. Nature Reviews Microbiology. 2017 Feb;15(2):69-82.

Lyu Z, Ding L, Huang AT, Kao CL, Peng L. Poly (amidoamine) dendrimers: Covalent and supramolecular synthesis. Materials Today Chemistry. 2019 Sep 1;13:34-48.

Lyu Z, Ding L, Tintaru A, Peng L. Self-assembling supramolecular dendrimers for biomedical applications: Lessons learned from poly (amidoamine) dendrimers. Accounts of Chemical Research. 2020 Dec 4;53(12):2936-49.

Maartens G, Celum C, Lewin SR. HIV infection: epidemiology, pathogenesis, treatment, and prevention. The Lancet. 2014 Jul 19;384(9939):258-71.

Maciel D, Guerrero-Beltrán C, Ceña-Diez R, Tomás H, Muñoz-Fernández MÁ, Rodrigues J. New anionic poly (alkylideneamine) dendrimers as microbicide agents against HIV-1 infection. Nanoscale. 2019;11(19):9679-90.

Maingi V, Kumar MVS, & Maiti PK. PAMAM dendrimer–drug interactions: effect of pH on the binding and release pattern. The Journal of Physical Chemistry B 2012, 116(14), 4370-4376.

Maitre T, Muret P, Blot M, Waldner A, Duong M, Si-Mohammed A, Chavanet P, Aho S, Piroth L. Benefits and Limits of Antiretroviral Drug Monitoring in Routine Practice. Current HIV Research. 2019 May 1;17(3):190-7.

Maji I, Mahajan S, Sriram A, Medtiya P, Vasave R, Khatri DK, Kumar R, Singh SB, Madan J, Singh PK. Solid self emulsifying drug delivery system: Superior mode for oral delivery of hydrophobic cargos. Journal of Controlled Release. 2021 Sep 10;337:646-60.

Majoros IJ, Williams CR, Tomalia DA, Baker Jr JR. New dendrimers: synthesis and characterization of POPAM− PAMAM hybrid dendrimers. Macromolecules. 2008 Nov 25;41(22):8372-9.

Mallakpour S, Soltanian S. Chemical surface coating of MWCNT s with riboflavin and its application for the production of poly (ester-imide)/MWCNT s composites containing 4, 4′-thiobis (2-tert-butyl-5-methylphenol) linkages: Thermal and morphological properties. Journal of Applied Polymer Science. 2016 Jan 20;133(4).

Mallakpour, Shadpour and Samaneh Soltanian. 2016. "RSC Advances Fabrication and Applications." 109916–35.

Maneesh, M.U.; Ahmed, S.S.; Pasha, T.Y.; Ramesh, B.; Majumder, M. A simple bioanalytical method for simultaneous estimation of amlodipine and celecoxib in rat plasma by high performance liquid chromatography. Journal of Chromatographic Science, 2021, 59(7), 627-633.

Mangla B, Beg S, Alam O, Ahsan W, Haque A, Patel KS, Almalki WH, Alrobaian M, Kohli K. Systematic development and validation of RP-HPLC method for simultaneous estimation of tamoxifen and sulphoraphane with specific application for nanolipidic formulations. Arabian Journal of Chemistry. 2020 Nov 1;13(11):7909-20.

Manyarara TE, Khoza S, Dube A, Maponga CC. Formulation and characterization of a paediatric nanoemulsion dosage form with modified oral drug delivery system for improved dissolution rate of nevirapine. MRS Advances. 2018;3(37):2203-19.

Massoumi B, Ramezani M, Jaymand M, Ahmadinejad M. Multi-walled carbon nanotubes-g-[poly (ethylene glycol)-b-poly (ε-caprolactone)]: synthesis, characterization, and properties. Journal of Polymer Research. 2015 Nov;22:1-0.

Mehra NK, Jain NK. Development, characterization and cancer targeting potential of surface engineered carbon nanotubes. Journal of Drug Targeting. 2013;21(8):745-58.

Merino KM, Allers C, Didier ES, Kuroda MJ. Role of monocyte/macrophages during HIV/SIV infection in adult and pediatric acquired immune deficiency syndrome. Frontiers in immunology. 2017 Dec 5;8:1693.

Mirali M, Jafariazar Z, Mirzaei M. Loading tacrine Alzheimer's drug at the carbon nanotube: DFT approach. Lab-in-Silico. 2021, 2(1), 3-8.

Mishra V, Gupta U, Jain NK. Influence of different generations of poly (propylene imine) dendrimers on human erythrocytes. Die Pharmazie-An International Journal of Pharmaceutical Sciences. 2010;65(12):891-5.

Mishra V, Kesharwani P, Jain NK. Biomedical applications and toxicological aspects of functionalized carbon nanotubes. Critical Reviews™ in Therapeutic Drug Carrier Systems. 2018;35(4).

Mishra V, Kesharwani P, Jain NK. siRNA nanotherapeutics: a Trojan horse approach against HIV. Drug Discovery Today. 2014 Dec 1;19(12):1913-20.

Mishra V, Kesharwani P. Dendrimer technologies for brain tumor. Drug discovery today. 2016 May 1;21(5):766-78.

Mishra V, Singh M, Nayak P, Sriram P, Suttee A. Carbon nanotubes as emerging nanocarriers in drug delivery: An overview. International Journal of Pharmaceutical Quality Assurance 2020;11(3):373-8.

Mishra V, Yadav N, Saraogi GK, Tambuwala MM, Giri N. Dendrimer based nanoarchitectures in diabetes management: An overview. Current pharmaceutical design. 2019 Jun 1;25(23):2569-83.

Modi CD, Patel SJ, Desai AB, Murthy RS. Functionalization and evaluation of PEGylated carbon nanotubes as novel drug delivery for methotrexate. Journal of Applied Pharmaceutical Science. 2011 Jul 30(Issue):103-8.

Mohamed MA, Jaafar J, Ismail AF, Othman MH, Rahman MA. Spectroscopic Methods for Nanomaterials Characterization. 2017, 73-93.

Mohammed A, Abdullah A. Scanning electron microscopy (SEM): A review. InProceedings of the 2018 International Conference on Hydraulics and Pneumatics—HERVEX, Băile Govora, Romania 2018 Nov 7 (Vol. 2018, pp. 7-9).

Mohammed AM, Al-Khateeb IK, Haider AJ, Rahim RA, Hashim U. Preparation of DNA biosensor application from fuel oil waste by functionalization and characterization of MWCNT. Sensing and bio-sensing research 2017 Nov 1;16:1-5.

Mohan CK, Sekhar KB, Reddy BK. Bioanalytical method development and validation for the simultaneous determination of vildagliptin and telmisartan in rabbit plasma using RP-HPLC. Journal of Pharmaceutical Research International. 2021 Feb 13;33(1):76-86.

Monteiro MS, Chávez FV, Sebastião PJ, Tavares MI. 1H NMR relaxometry and X-ray study of PCL/nevirapine hybrids. Polymer testing. 2013 May 1;32(3):553-66.

Moranguinho I, Valente ST. Block-and-lock: new horizons for a cure for HIV-1. Viruses. 2020 Dec 15;12(12):1443.

Movasaghi Z, Rehman S, Rehman IU. Raman spectroscopy of biological tissues. Applied Spectroscopy Reviews. 2007 Sep 1;42(5):493-541.

Muda MR, Ramli MM, Isa SM, Halin DS, Talip LF, Mazelan NS, Anhar NA, Danial NA. Structural and morphological investigation for water-processed graphene oxide/single-walled carbon nanotubes hybrids. InIOP Conference Series: Materials Science and Engineering 2017 Jun 1 (Vol. 209, No. 1, p. 012030). IOP Publishing.

Murugan E, Geetha Rani DP, Srinivasan K, Muthumary J. New surface hydroxylated and internally quaternised poly (propylene imine) dendrimers as efficient biocompatible drug carriers of norfloxacin. Expert Opinion on Drug Delivery. 2013 Oct 1;10(10):1319-34.

Nahar UJ, Toth I, Skwarczynski M. Mannose in vaccine delivery. Journal of Controlled Release. 2022 Nov 1;351:284-300.

Naif HM. Pathogenesis of HIV infection. Infectious disease reports. 2013 Jun;5(S1):26-30.

Nalte YK, Arsul VA, Shep SG, Bothara SB. Solubility enhancement of nevirapine by cocrystallisation technique. Journal of Research in Pharmacy 2015 Aug;9(8):556-61.

Naqvi ST, Rasheed T, Hussain D, ul Haq MN, Majeed S, Ahmed N, Nawaz R. Modification strategies for improving the solubility/dispersion of carbon nanotubes. Journal of Molecular Liquids. 2020 Jan 1;297:111919.

Nayak Y, Avadhani K, Mutalik S, Y Nayak U. Lymphatic delivery of anti-HIV drug nanoparticles. Recent Patents on Nanotechnology. 2016 Aug 1;10(2):116-27.

Neelgund GM, Oki A, Luo Z. Antimicrobial activity of CdS and Ag2S quantum dots immobilized on poly (amidoamine) grafted carbon nanotubes. Colloids and Surfaces B: Biointerfaces. 2012 Dec 1;100:215-21.

Neto CM, Lima FC, Morais RP, de Andrade LR, de Lima R, Chaud MV, Pereira MM, de Albuquerque Júnior RL, Cardoso JC, Zielińska A, Souto EB. Rutin-functionalized

multi-walled carbon nanotubes: molecular docking, physicochemistry and cytotoxicity in fibroblasts. Toxics. 2021 Jul 22;9(8):173.

Nikzamir M, Hanifehpour Y, Akbarzadeh A, & Panahi Y. Applications of Dendrimers in Nanomedicine and Drug Delivery: A Review. Journal of Inorganic and Organometallic Polymers and Materials 2021, 1-16.

Noordadi M, Mehrnejad F, Sajedi RH, Jafari M, Ranjbar B. The potential impact of carboxylic-functionalized multi-walled carbon nanotubes on trypsin: A Comprehensive spectroscopic and molecular dynamics simulation study. PLoS One. 2018 Jun 1;13(6):e0198519.

Okafor NI, Nkanga CI, Walker RB, Noundou XS, Krause RW. Encapsulation and physicochemical evaluation of efavirenz in liposomes. Journal of Pharmaceutical Investigation. 2020 Mar;50:201-8.

Ordoñez JG, Andrade H. Synthesis and characterization of poly (propylene imine) dendrimers, as nanocarriers of Benznidazole: an in vitro controlled release assay. bioRxiv. 2022:2022-07.

Palmerston Mendes L, Pan J, Torchilin VP. Dendrimers as nanocarriers for nucleic acid and drug delivery in cancer therapy. Molecules. 2017 Sep;22(9):1401.

Pan BF, Cui DX, Xu P, Huang T, Li Q, He R, Gao F. Cellular uptake enhancement of polyamidoamine dendrimer modified single-walled carbon nanotubes. Journal of Biomedical & Pharmaceutical Engineering 2007;1(1):13-6.

Pandey P, Dahiya M. Carbon nanotubes: Types, methods of preparation and applications. Carbon. 2016 May;1(4):15-21.

Panzade P, Somani P, Rathi P. Nevirapine Pharmaceutical Cocrystal: Design, Development and Formulation. Drug Delivery Letters. 2019 Sep 1;9(3):240-7.

Parashar AK, Gupta AK, Jain NK. Synthesis and characterization of Agiopep-2 anchored PEGylated poly propyleneimine dendrimers for targeted drug delivery to glioblastoma multiforme. Journal of Drug Delivery and Therapeutics. 2018;8(6-A):74-9.

Pargoo EM, Aghasadeghi MR, Parivar K, Nikbin M, Rahimi P, Ardestani MS. Lamivudine-conjugated and efavirenz-loaded G2 dendrimers: Novel anti-retroviral nano drug delivery systems. IET nanobiotechnology. 2021 Sep;15(7):627-37.

Patel V, Rajani C, Paul D, Borisa P, Rajpoot K, Youngren-Ortiz SR, Tekade RK. Dendrimers as novel drug-delivery system and its applications. In Drug Delivery Systems 2020 Jan 1 (pp. 333-392). Academic Press.

Patel, H. K.; Gajbhiye, V.; Kesharwani, P.; & Jain, N. K. Ligand anchored poly (propyleneimine) dendrimers for brain targeting: Comparative in vitro and in vivo assessment. COCIS, 2016, *482*, 142-150.

Patil TS, Deshpande AS. Mannosylated nanocarriers mediated site-specific drug delivery for the treatment of cancer and other infectious diseases: A state of the art review. Journal of Controlled Release. 2020 Apr 10;320:239-52.

Patrikar S, Shankar S, Kotwal A, Basannar DR, Bhatti V, Verma R, Mukherji S. Predictors of first line antiretroviral therapy failure and burden of second line antiretroviral therapy. Medical Journal Armed Forces, India. 2017 Jan 1;73(1):5-11.

Pavia DL, Lampman GM, Kriz GS, Vyvyan JA. Introduction to spectroscopy. Cengage learning; 2014.

Pawar S, Wang YF, Wong-Sam A, Agniswamy J, Ghosh AK, Harrison RW, Weber IT. Structural studies of antiviral inhibitor with HIV-1 protease bearing drug resistant substitutions of V32I, I47V and V82I. Biochemical and biophysical research communications. 2019 Jun 30;514(3):974-8.

Pekamwar SS, Bhavar GB, Aher KB, Kakad SJ. Validated UV spectrophotometric and HPTLC method for determination of fosamprenavir calcium in pharmaceutical formulation. Austin Journal of Analytical and Pharmaceutical Chemistry 2015 Sep;2(4):1049-55.

Peng X, Ouyang J, Isnard S, Lin J, Fombuena B, Zhu B, Routy JP. Sharing CD4+ T cell loss: when COVID-19 and HIV collide on immune system. Frontiers in Immunology 2020 Dec 15;11:596631.

Perdomo-Celis F, Taborda NA, Rugeles MT. Follicular CD8+ T cells: origin, function and importance during HIV infection. Frontiers in immunology. 2017 Sep 29;8:1241.

Perisé-Barrios AJ, Jiménez JL, Domínguez-Soto A, de la Mata FJ, Corbí AL, Gomez R, Muñoz-Fernandez MÁ. Carbosilane dendrimers as gene delivery agents for the treatment of HIV infection. Journal of Controlled Release. 2014 Jun 28;184:51-7.

Piao Y, Tondare VN, Davis CS, Gorham JM, Petersen EJ, Gilman JW, Scott K, Vladár

AE, Walker AR. Comparative study of multiwall carbon nanotube nanocomposites by Raman, SEM, and XPS measurement techniques. Composites Science and Technology. 2021 May 26;208:108753.

Pistone A, Iannazzo D, Panseri S, Montesi M, Tampieri A, Galvagno S. Hydroxyapatite-magnetite-MWCNT nanocomposite as a biocompatible multifunctional drug delivery system for bone tissue engineering. Nanotechnology. 2014 Sep 29;25(42):425701.

Prabhu, R. H., Patravale, V. B., & Joshi, M. D. (2015). Polymeric nanoparticles for targeted treatment in oncology: current insights. International journal of nanomedicine, *10*, 1001–1018.

Prajapati SK, Jain A. Dendrimers for Advanced Drug Delivery. In Advanced Biopolymeric Systems for Drug Delivery 2020 (pp. 339-360).

Pruthi J, Mehra NK, Jain NK. Macrophages targeting of amphotericin B through mannosylated multiwalled carbon nanotubes. Journal of drug targeting. 2012 Aug 1;20(7):593-604.

Pubchem, https://pubchem.ncbi.nlm.nih.gov/compound/Nevirapine, 11 May 2023.

Pyreddy S, Kumar PD, Kumar PV. Polyethylene glycolated PAMAM dendrimers-Efavirenz conjugates. International Journal of Pharmaceutical Investigation. 2014 Jan;4(1):15.

Qi RL, Tian XJ, Guo R, et al. Controlled release of doxorubicin from electrospun MWCNTs/PLGA hybrid nanofibers. Chinese Journal of Polymer Science 2016;34(9):1047-1059.

R Benjamin, Sun. 2008. "基因的改变NIH Public Access." *Bone* 23(1):1–7.

Raja PB, Munusamy KR, Perumal V, Ibrahim MN. Characterization of nanomaterial used in nanobioremediation. InNano-Bioremediation: Fundamentals and Applications 2022 Jan 1 (pp. 57-83). Elsevier.

Rajora A, Nagpal K. Classification and Types of Dendrimers: Introduction and Chemistry. In Dendrimers in Nanomedicine 2021 Mar 22 (pp. 53-75). CRC Press.

Ramadon D, Courtenay A J, Permana, AD, Tekko, IA, McAlister E, McCrudden MT, McCarthy HO, Donnelly RFA sensitive HPLC-UV method for quantifying vancomycin in biological matrices: Application to pharmacokinetic and biodistribution studies in rat

plasma, skin and lymph nodes. Journal of Applied Behavior Analysis, 2020, 189, 113429, 1-28.

Ramana LN, Anand AR, Sethuraman S, Krishnan UM. Targeting strategies for delivery of anti-HIV drugs, Journal of Controlled Release. 2014, 192; Pages 271-283.

Ramana LN, Sethuraman S, Ranga U, Krishnan UM. Development of a liposomal nanodelivery system for nevirapine. Journal of biomedical science. 2010 Dec;17:1-9.

Ramanunny AK, Wadhwa S, Gulati M, Gupta S, Porwal O, Jha NK, Gupta PK, Kumar D, Prasher P, Dua K, Al Saqr A. Development and validation of RP-HPLC method for 1′-Acetoxychavicol acetate (ACA) and its application in optimizing the yield of ACA during its isolation from Alpinia galanga extract as well as its quantification in nanoemulsion. South African Journal of Botany. 2022 Sep 1;149:887-98.

Ramkumaar GR, Srinivasan S, Bhoopathy TJ, Gunasekaran S, Charles J, Ramesh J. Molecular structure, vibrational spectra, UV–vis, NBO, and NMR analyses on nevirapine using ab initio DFT methods. Journal of theoretical and applied physics. 2013 Dec;7:1-4.

Rao CR, Govindaraj A. Nanotubes and nanowires. Royal Society of Chemistry; 2011.

Rathod V, Tripathi R, Joshi P, Jha PK, Bahadur P, Tiwari S. Paclitaxel encapsulation into dual-functionalized multi-walled carbon nanotubes. AAPS PharmSciTech. 2019 Feb;20:1-3.

Razzazan A, Atyabi F, Kazemi B, Dinarvand R. In vivo drug delivery of gemcitabine with PEGylated single-walled carbon nanotubes. Materials Science and Engineering: C 2016 May;62:614-25.

Reddy KA, Kunchithapatham J, Dang R, Ramnarayanan C. Design and development of darunavir loaded self micro emulsifying drug delivery system using extreme vertices mixture design in a quality by design framework. Indian Journal of Pharmaceutical Education and Research. 2020 Apr 1;54(2):337-48.

Reddy YN, Sreeramulu J, Balaswami B. A new stability-indicating RP-HPLC-PDA method for simultaneous estimation of glecaprevir and Pibrentasvir in tablet dosage form. Research Journal of Pharmacy and Technology. 2019;12(2):625-31.

Rein A. RNA packaging in HIV. Trends in microbiology. 2019 Aug 1;27(8):715-23.

Rivero-Buceta E, Doyagueez EG, Colomer I, Quesada E, Mathys L, Noppen S, Liekens S, Camarasa MJ, Perez-Perez MJ, Balzarini J, San-Felix A. Tryptophan dendrimers that inhibit HIV replication, prevent virus entry and bind to the HIV envelope glycoproteins gp120 and gp41. European Journal of Medicinal Chemistry. 2015 Dec 1;106:34-43.

Rizvi SA, Saleh AM. Applications of nanoparticle systems in drug delivery technology. Saudi Pharmaceutical Journal. 2018 Jan 1;26(1):64-70.

Rosenblum, Daniel, et al. "Progress and challenges towards targeted delivery of cancer therapeutics." Nature communications 9.1 (2018): 1-12.

Rostron P, Gaber S, Gaber D. Raman spectroscopy, review. Laser. 2016; 21:24.

Roy U, Drozd V, Durygin A, Rodriguez J, Barber P, Atluri V, Liu X, Voss TG, Saxena S, Nair M. Characterization of Nanodiamond-based anti-HIV drug. Delivery to the Brain. Scientific reports 2018 Jan 25;8(1):1603. doi: 10.1038/s41598-017-16703-9.

Saluja V, Mankoo A, Saraogi GK, Tambuwala MM, Mishra V. Smart dendrimers: Synergizing the targeting of anticancer bioactives. Journal of Drug Delivery Science and Technology. 2019 Aug 1;52:15-26.

Samsodien H, Bapoo R, Doms TI, Harneker Z, Louw AS, Scheepers IC, Sonday AB, Geldenhuys B. FTIR, dissolution and anti-viral activity of nevirapine co-crystals. Pharmaceutica Analytica Acta, 8:9,1-10.

Santos A, Veiga F, Figueiras A. Dendrimers as pharmaceutical excipients: Synthesis, properties, toxicity and biomedical applications. Materials. 2020 Jan;13(1):65.

Sarkar M, Perumal OP, Panchagnula R. Solid-state characterization of nevirapine. Indian journal of pharmaceutical sciences. 2008;70(5):619.

Sathisaran I, Dalvi SV. Cocrystallization of an antiretroviral drug nevirapine: an eutectic, a cocrystal solvate, and a cocrystal hydrate. Crystal Growth & Design. 2021 Mar 12;21(4):2076-92.

Schank M, Zhao J, Moorman JP, Yao ZQ. The impact of HIV-and ART-induced mitochondrial dysfunction in cellular senescence and aging. Cells. 2021 Jan 16;10(1):174.

Scioli Montoto S, Muraca G, Ruiz ME. Solid lipid nanoparticles for drug delivery: pharmacological and biopharmaceutical aspects. Frontiers in molecular biosciences. 2020 Oct 30;7:587997.

Sedaghat S. Synthesis and modification of carboxylated multi wall nanotubes with atenolol. Soft Nanoscience Letters, 2014, 4, 75-81.

Sepulveda-Crespo D, Sanchez-Rodriguez J, Serramía MJ, Gomez R, De La Mata FJ, Jiménez JL, Muñoz-Fernández MÁ. Triple combination of carbosilane dendrimers, tenofovir and maraviroc as potential microbicide to prevent HIV-1 sexual transmission. Nanomedicine. 2015 Mar;10(6):899-914.

Shamard Charles. Global HIV Statistics: Complete Geographical Breakdown (verywellhealth.com). 2021. Accessed on 10 April 2023.

Shao N, Su Y, Hu J, Zhang J, Zhang H, Cheng Y. Comparison of generation 3 polyamidoamine dendrimer and generation 4 polypropylenimine dendrimer on drug loading, complex structure, release behavior, and cytotoxicity. International journal of nanomedicine. 2011 Dec 16:3361-72.

Sharma S, Mehra NK, Jain K et al. Effect of functionalization on drug delivery potential of carbon nanotubes. Artificial Cells, Nanomedicine, and Biotechnology 2016;44(8):1851-60.

Sharma S, Shyam Kumar CN, Korvink JG, Kübel C. Evolution of glassy carbon microstructure: In situ transmission electron microscopy of the pyrolysis process. Scientific reports. 2018 Nov 2;8(1):1-2.

Shegokar R, Singh KK. Surface modified nevirapine nanosuspensions for viral reservoir targeting: In vitro and in vivo evaluation. International journal of pharmaceutics. 2011 Dec 15;421(2):341-52.

Sherje AP, Jadhav M, Dravyakar BR, Kadam D. Dendrimers: A versatile nanocarrier for drug delivery and targeting. International journal of pharmaceutics. 2018 Sep 5;548(1):707-20.

Shi F, Zhuang X, Cui C, Zhang S. Synthesis, characterization and scale inhibition performance evaluation of novel dendrimers with the initiator core of pentaerythritol derivative. Desalination. 2022 Apr 15;528:115632.

Shi X, Wang SH, Shen M, Antwerp ME, Chen X, Li C, Petersen EJ, Huang Q, Weber Jr WJ, Baker Jr JR. Multifunctional dendrimer-modified multiwalled carbon nanotubes: synthesis, characterization, and in vitro cancer cell targeting and imaging. Biomacromolecules. 2009 Jul 13;10(7):1744-50.

Shirasu K, Yamamoto G, Nelias D, Hashida T. Mechanical and fracture properties of

carbon nanotubes. Carbon Nanotubes-Recent Progress. 2017 Dec 20.

Shokouhi S, Sohrabi MR, Mofavvaz S. Comparison between UV/Vis spectrophotometry based on intelligent systems and HPLC methods for simultaneous determination of anti-diabetic drugs in binary mixture. Optik. 2020 Mar 1;206:164304.

Silverstein RM, Bassler GC. Spectrometric identification of organic compounds. Journal of Chemical Education. 1962 Nov;39(11):546.

Singh DK, Sahu A, Wani AA, Bharatam PV, Kotimoole CN, Batkulwar KB, Deshpande AY, Giri S, Singh S. Stability behaviour of antiretroviral drugs and their combinations. 10: LC-HRMS, LC-MSn, LC-NMR and NMR characterization of fosamprenavir degradation products and in silico determination of their ADMET properties. European Journal of Pharmaceutics and Biopharmaceutics. 2019 Sep 1;142:165-78.

Singh I, Rehni AK, Kumar P, Kumar M, Aboul-Enein HY. Carbon nanotubes: synthesis, properties and pharmaceutical applications. Fullerenes, Nanotubes and Carbon Nanostructures. 2009 Jul 1;17(4):361-77.

Singh RP, Sharma G, Singh S, Patne SC, Pandey BL, Koch B, Muthu MS. Effects of transferrin conjugated multi-walled carbon nanotubes in lung cancer delivery. Materials Science and Engineering: C. 2016 Oct 1;67:313-25.

Singh S, Mehra NK, Jain NK. Development and characterization of the paclitaxel loaded riboflavin and thiamine conjugated carbon nanotubes for cancer treatment. Pharmaceutical Research. 2016 Jul;33:1769-81.

Singh V, Sahebkar A, Kesharwani P. Poly (propylene imine) dendrimer as an emerging polymeric nanocarrier for anticancer drug and gene delivery. European Polymer Journal. 2021 Sep 5;158:110683.

Singh, V.; Sahebkar, A.; & Kesharwani, P. Poly (propylene imine) dendrimer as an emerging polymeric nanocarrier for anticancer drug and gene delivery. Euopean Polymeric Journal 2021, *158*, 110683, 1-15.

Singhai NJ, Maheshwari R, Jain NK, Ramteke S. Chondroitin sulphate and α-tocopheryl succinate tethered multiwalled carbon nanotubes for dual-action therapy of triple-negative breast cancer. Journal of Drug Delivery Science and Technology. 2020 Dec 1;60:102080.

Sojka P, Wlaszczuk A, Olakowska E. Potential application of maraviroc in the therapy of neuropathic pain. Polski Merkuriusz Lekarski: Organ Polskiego Towarzystwa Lekarskiego. 2021 Oct 1;49(293):379-81.

Soni N, Jain K, Gupta U, Jain NK. Controlled delivery of Gemcitabine Hydrochloride using mannosylated poly (propyleneimine) dendrimers. Journal of Nanoparticle Research. 2015 Nov;17(11):458.

Srivastava N, Mishra Y, Mishra V, Ranjan A, Tambuwala MM. Carbon Nanotubes in Breast Cancer Treatment: An Insight into Properties, Functionalization, and Toxicity. Anti-Cancer Agents in Medicinal Chemistry (Formerly Current Medicinal Chemistry-Anti-Cancer Agents). 2023 Aug 1;23(14):1606-17.

Srivastava N, Mishra Y, Mishra V. Fosamprenavir calcium loaded dendrimers: formulation development, evaluation and hemolytic toxicity studies. International Journal of Applied Pharmaceutics. 2023, Vol 15, Issue 6, 342-352.

Srivastava N, Mishra V, Mishra Y, Ranjan A, Aljabali AA, El-Tanani M, Alfagih IM, Tambuwala MM. Development and evaluation of a protease inhibitor antiretroviral drug-loaded carbon nanotube delivery system for enhanced efficacy in HIV treatment. International Journal of Pharmaceutics. 2024 Jan 25;650:123678.

Su KY, Lee WL. Fourier transform infrared spectroscopy as a cancer screening and diagnostic tool: a review and prospects. Cancers. 2020 Jan 1;12(1):115.

Takassi MA, Zadehnazari A. Nanocomposites of triazole functionalized multi-walled carbon nanotube with chemically grafted polyimide: Preparation, characterization, and properties. Fullerenes, Nanotubes and Carbon Nanostructures. 2016 Feb 1;24(2):128-38.

Tan JM, Karthivashan G, Arulselvan P et al. Characterization and in vitro sustained release of silibinin from pH responsive carbon nanotube-based drug delivery system. Journal of Nanomaterials. 2014;439873:1-10.

Thakur CK, Neupane R, Karthikeyan C, Ashby Jr CR, Babu RJ, Boddu SH, Tiwari AK, Moorthy NS. Lysinated Multiwalled Carbon Nanotubes with Carbohydrate Ligands as an Effective Nanocarrier for Targeted Doxorubicin Delivery to Breast Cancer Cells. Molecules. 2022 Nov 2;27(21):7461.

Thiagarajan G, Greish K, Ghandehari H. Charge affects the oral toxicity of poly(amidoamine) dendrimers. European Journal of Pharmaceutics and Biopharmaceutics 2013 Jun; 84(2):330-4.

Toccafondi E, Lener D, Negroni M. HIV-1 capsid core: A bullet to the heart of the target cell. Frontiers in Microbiology. 2021 Apr 1;12:652486.

Tomalia DA, Christensen JB, Boas U. Dendrimers, dendrons, and dendritic polymers: discovery, applications, and the future. Cambridge University Press; 2012 (A) Oct 18.

Tomalia DA, Christensen JB, Boas U. Dendrimers, dendrons, and dendritic polymers: discovery, applications, and the future. Cambridge University Press; 2012 (B) Oct 18.

Torrelles JB, Schlesinger LS. Diversity in Mycobacterium tuberculosis mannosylated cell wall determinants impacts adaptation to the host. Tuberculosis (Edinb). 2010 Mar;90(2):84-93.

Tripathi PK, Gupta S, Rai S, Shrivatava A, Tripathi S, Singh S, Khopade AJ, Kesharwani P. Curcumin loaded poly (amidoamine) dendrimer-plamitic acid core-shell nanoparticles as anti-stress therapeutics. Drug development and industrial pharmacy. 2020 Mar 3;46(3):412-26.

Tunki L, Kulhari H, Sistla R, Pooja D. Dendrimer-based targeted drug delivery. InPharmaceutical Applications of Dendrimers 2020 Jan 1 (pp. 107-129). Elsevier.

Turchi M, Cai Q, Lian G. An evaluation of in-silico methods for predicting solute partition in multiphase complex fluids–A case study of octanol/water partition coefficient. Chemical Engineering Science. 2019 Apr 6;197:150-8.

Tzou PL, Rhee SY, Descamps D, Clutter DS, Hare B, Mor O, Grude M, Parkin N, Jordan MR, Bertagnolio S, Schapiro JM. Integrase strand transfer inhibitor (INSTI)-resistance mutations for the surveillance of transmitted HIV-1 drug resistance. Journal of Antimicrobial Chemotherapy. 2020 Jan;75(1):170-82.

Upadhyay S, Sharma N, Gupta KB, Dhiman M. Role of immune system in tumor progression and carcinogenesis. Journal of cellular biochemistry. 2018 Jul;119(7):5028-42.

Vacas-Cordoba E, Maly M, De la Mata FJ, Gomez R, Pion M, Muñoz-Fernández MÁ. Antiviral mechanism of polyanionic carbosilane dendrimers against HIV-1. International journal of nanomedicine. 2016;11:1281.

Vallari, Ana, Bodelle, P., Ngansop, C., Makamche, F., Ndembi, N., Mbanya, D., Kaptué, L., Gürtler, L. G., McArthur, C. P., Devare, S. G., & Brennan, C. A. (2010). Four new HIV-1 group N isolates from Cameroon: Prevalence continues to be low. AIDS Research and Human Retroviruses, 26(1), 109–115.

Varshosaz J, Taymouri S, Jafari E, Jahanian-Najafabadi A, Taheri A. Formulation and characterization of cellulose acetate butyrate nanoparticles loaded with nevirapine for HIV treatment. Journal of Drug Delivery Science and Technology. 2018 Dec 1;48:9-20.

Vatanpour V, Zoqi N. Surface modification of commercial seawater reverse osmosis membranes by grafting of hydrophilic monomer blended with carboxylated multiwalled carbon nanotubes. Applied Surface Science 2017;396:1478-1489.

Vidya Vijayan KK, Karthigeyan KP, Tripathi SP, Hanna LE. Pathophysiology of CD4+ T-cell depletion in HIV-1 and HIV-2 infections. Frontiers in immunology. 2017 May 23;8:580.

Vieira AC, Chaves LL, Pinheiro M, Ferreira D, Sarmento B, Reis S. Design and statistical modeling of mannose-decorated dapsone-containing nanoparticles as a strategy of targeting intestinal M-cells. International Journal of Nanomedicine. 2016;11:2601.

Visseaux B, Bertine M, Le Hingrat Q, Ferré V, Charpentier C, Collin F, Damond F, Matheron S, Hué S, Descamps D. HIV-2 diversity displays two clades within group A with distinct geographical distribution and evolution. Virus evolution. 2021 Jan;7(1):veab024.

Wang L, Su W, Liu Z, Zhou M, Chen S, Chen Y, Lu D, Liu Y, Fan Y, Zheng Y, Han Z. CD44 antibody-targeted liposomal nanoparticles for molecular imaging and therapy of hepatocellular carcinoma. Biomaterials. 2012 Jul 1;33(20):5107-14.

Wang M, Luo L, Bu H, Xia H. One case of coronavirus disease 2019 (COVID-19) in a patient co-infected by HIV with a low CD4+ T-cell count. International Journal of Infectious Diseases. 2020 Jul 1;96:148-50.

Wang X, Li B, Jing H, et al. MWCNT-mediated combinatorial photothermal ablation and chemo-immunotherapy strategy for the treatment of melanoma. Journal of Materials Chemistry B 2020;8(19):4245-4258.

Ward AR, Mota TM, Jones RB. Immunological approaches to HIV cure. In Seminars

in immunology 2021 Jan 1 (Vol. 51, p. 101412). Academic Press.

Wen S, Liu H, Cai H, Shen M, Shi X. Targeted and pH-responsive delivery of doxorubicin to cancer cells using multifunctional dendrimer-modified multi-walled carbon nanotubes. Advanced healthcare materials. 2013 Sep;2(9):1267-76.

WHO, https://www.who.int/about/accountability/results/who-results-report-2020-2021, Accessed on 28 April 2023.

Woodham AW, Skeate JG, Sanna AM, Taylor JR, Da Silva DM, Cannon PM, Kast WM. Human immunodeficiency virus immune cell receptors, coreceptors, and cofactors: implications for prevention and treatment. AIDS patient care and STDs. 2016 Jul 1;30(7):291-306.

World Health Organization. Global progress report on HIV, viral hepatitis and sexually transmitted infections, 2021: accountability for the global health sector strategies 2016–2021: actions for impact: web annex 2: data methods.

Wu Q, Lv H, Zhao L. Applications of carbon nanomaterials in chiral separation. TrAC Trends in Analytical Chemistry. 2020 Aug 1;129:115941.

Xiao T, Cai Y, Chen B. HIV-1 entry and membrane fusion inhibitors. Viruses. 2021 Apr 23;13(5):735.

Xu H, Li L, Fan G, Chu X. DFT study of nanotubes as the drug delivery vehicles of Efavirenz. Computational and Theoretical Chemistry. 2018 May 1;1131:57-68.

Yang S, Liu J, Ping Y, Wang Z, Zhang J, Zhang L, Cui L, Xiao Y, Qu L. Multi-functionalized single-walled carbon nanotubes as delivery carriers: promote the targeting uptake and antitumor efficacy of doxorubicin. Journal of Inclusion Phenomena and Macrocyclic Chemistry. 2022 Oct;102(9):801-17.

Yates A, Stark J, Klein N, Antia R, Callard R. Understanding the slow depletion of memory CD4+ T cells in HIV infection. PLoS Med (2007) 4(5):e177.

Yellepeddi VK, Ghandehari H. Pharmacokinetics of oral therapeutics delivered by dendrimer-based carriers. Expert opinion on drug delivery. 2019 Oct 3;16(10):1051-61.

Yetisgin AA, Cetinel S, Zuvin M, Kosar A, Kutlu O. Therapeutic nanoparticles and their targeted delivery applications. Molecules. 2020 May 8;25(9):2193.

Youssry, Mohamed, Maisa Al-Ruwaidhi, Mahdiyeh Zakeri, and Mohadese Zakeri.

"Physical functionalization of multi-walled carbon nanotubes for enhanced dispersibility in aqueous medium." Emergent Materials (2020): 1-8.

Zawawi NA, Majid ZA, Aini N, Rashid A. Effect of acid oxidation methods on multi-walled carbon nanotubes (MWCNT) for drug delivery application. International Journal of Advanced Scientific Research and Management 2016;1(11).

Zhang M, Guo R, Keri M, Banyai I, Zheng Y, Cao M, Cao X, Shi X. Impact of dendrimer surface functional groups on the release of doxorubicin from dendrimer carriers. The Journal of Physical Chemistry B. 2014 Feb 13;118(6):1696-706.

Zhang S, Zhang F, Pan Y, Jin L, Liu B, Mao Y, Huang J. Multiwall-carbon-nanotube/cellulose composite fibers with enhanced mechanical and electrical properties by cellulose grafting. RSC advances. 2018;8(11):5678-84.

Zhang X, Hui Z, Wan D, et al. Alginate microsphere filled with carbon nanotube as drug carrier. International Journal of Biological Macromolecules 2010;47(3):389-395.

Zhang, E.; Chu, F.; Zhao, T.; Chai, Y.; Liang, H.; Song, S.; Ji, A. Determination of fucoidan in rat plasma by HPLC and its application in pharmacokinetics. Pakistan Journal of Pharmaceutical Sciences, 2020, 33(1), 1-10.

Zhou Y, Vinothini K, Dou F, Jing Y, Chuturgoon AA, Arumugam T, Rajan M. Hyper-branched multifunctional carbon nanotubes carrier for targeted liver cancer therapy. Arabian Journal of Chemistry. 2022 Mar 1;15(3):103649.

Zhu W, Huang H, Dong Y, et al. Multi-walled carbon nanotube-based systems for improving the controlled release of insoluble drug dipyridamole. Experimental and Therapeutic Medicine 2019;17(6):4610-4616.

Zhu W, Huang H, Dong Y, Han C, Sui X, Jian B. Multi-walled carbon nanotube-based systems for improving the controlled release of insoluble drug dipyridamole. Experimental and Therapeutic Medicine. 2019 Jun 1;17(6):4610-6.

Zielińska A, Carreiró F, Oliveira AM, Neves A, Pires B, Venkatesh DN, Durazzo A, Lucarini M, Eder P, Silva AM, Santini A. Polymeric nanoparticles: production, characterization, toxicology and ecotoxicology. Molecules. 2020 Aug 15;25(16):3731.

Zuru DU. Theoretical model for the design and preparation of a CNT–ursonic acid drug matrix as HIV-gp120 entry inhibitor. Scientific African. 2019 Nov 1;6:e00177.

Annexure

LOVELY PROFESSIONAL UNIVERSITY

Centre for

Research Degree Programmes

LPU/CRDP/PHD/EC/20190715/001314
Dated: 10 Sep 2021

Neha Srivastava
Registration Number: 41700192
Programme Name: Doctor of Philosophy (Pharmaceutics)

Subject: Letter of Candidacy for Ph.D.

Dear Candidate,

We are very pleased to inform you that the Department Doctoral Board has approved your candidacy for the Ph.D. Programme on 21 Sep 2018 by accepting your research proposal entitled: "FORMULATION DEVELOPMENT, CHARACTERIZATION AND EVALUATION OF ANTI-HIV POTENTIAL OF DENDRIMER-CARBON NANOTUBES CONJUGATES (DENDRITUBES)" under the supervision of Dr. Vijay Mishra.

As a Ph.D. candidate you are required to abide by the conditions, rules and regulations laid down for Ph.D. Programme of the University, and amendments, if any, made from time to time.

We wish you the very best!!

In case you have any query related to your programme, please contact Centre of Research Degree Programmes.

Head

Centre for Research Degree Programmes

Note:-This is a computer generated certificate and no signature is required. Please use the reference number generated on this certificate for future conversations.
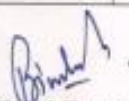
LOVELY
PROFESSIONAL
UNIVERSITY

Transforming Education Transforming India

Lovely
Institute of
Technology
(Pharmacy)

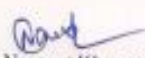Ref. No. : LPU/dop/69/220817/1560/002

Date: 17/8/2022

CERTIFICATE

This is to certify that the animals requested/ordered against the approved protocol(s) have not been earlier procured from any other source and are not exceeding the number of animals approved by IAEC. Further, the animals shall be transported and later maintained in a facility with basic infrastructure as per CPCSEA guidelines, Ministry of Environment and Forests, Government of India. These protocols for animals' study were approved on **13.04.2022** and none of the animals were taken earlier.

Proposal no	Title of the project	Name of Guide	No. of animals	Signature of guide
LPU/IAEC/2022/ 03	Biodistribution and heamolytic potential of dendrimer-carbon nanotubes conjugates (dendritubes). (Thesis Title: Formulation development, characterization and evaluation of anti-HIV potential of dendrimer-carbon nanotubes conjugates (dendritubes))	Dr. Vijay Mishra	81, SD/Wister rats, Either sex	

(Dr. Bimlesh Kumar)
Professor, School of Pharmaceutical Sciences,
Animal House In-Charge
Lovely Professional University, Phagwara

(Dr. Navneet Khurana)
Professor, COD, School of Pharmaceutical Sciences,
Lovely Professional University, Phagwara

(Dr. Monica Gulati)
Executive Dean,
Lovely Professional University, Phagwara

Jalandhar-Delhi G.T. Road (NH-1), Phagwara, Punjab (India)-144411
Ph : +91-1824-444039 Fax : +91-1824-240830   website : www.lpu.in

List of publications, patents and presentations

Publications related to research topic

1. Srivastava N, Mishra Y, Mishra V, Ranjan A, Tambuwala MM. Carbon Nanotubes in Breast Cancer Treatment: An Insight into Properties, Functionalization, and Toxicity. Anticancer Agents Med Chem. 2023 May 10. doi: 10.2174/1871520623666230510094850

2. Neha Srivastava, Yachna Mishra, Vijay Mishra. Fosamprenavir calcium loaded dendrimers: formulation development, evaluation and hemolytic toxicity studies. International Journal of Applied Pharmaceutics. 2023, Vol 15, Issue 6, 342-352. https://doi.org/10.22159/ijap.2023v15i6.49040

3. Srivastava N, Mishra V, Mishra Y, Ranjan A, Aljabali AA, El-Tanani M, Alfagih IM, Tambuwala MM. Development and evaluation of a protease inhibitor antiretroviral drug-loaded carbon nanotube delivery system for enhanced efficacy in HIV treatment. International Journal of Pharmaceutics. 2024 Jan 25;650:123678.

4. Srivastava N, Mishra Y, Mishra V. Dendrimers: A novel and efficient carrier for anti-HIV drugs. InAIP Conference Proceedings 2024 Feb 20 (Vol. 2986, No. 1). AIP Publishing.

5. N. Srivastava, Y. Mishra, S.K. Singh, V. Mishra*, Simultaneous Method Development and Validation of Fosamprenavir Calcium and Nevirapine by RP-HPLC in Dendrimer-Carbon Nanotubes Conjugates, Indian Journal of Pharmaceutical Scineces, Indian J Pharm Sci 2024;86(4):1366-1375.

Book chapter

1. Srivastava, Neha & Mishra, Yachana & Mishra, Vijay. (2023). Importance of Nanocarriers in Colon Cancer. 10.2174/9789815080506123010011.

Patents Applied

1. Neha Srivasatva, Yachana Mishra, Vijay Mishra. Anti-HIV drug nevirapine loaded dendritubes (Dendrimers-Carbon nanotubes conjugate): Development and evaluations. Request ID: 7147.

Copyright

1. Neha Srivasatva, Yachana Mishra, Vijay Mishra, Abhigyan Ranjan, Aditi Chattarji. Formulation development and characterization of dendrimers and carbon nanotubes (Dendritubes). Granted. Registration no: L-137356/2023. Dec 2023.

Presentations

Poster presentations

1. Neha Srivastava, and Vijay Mishra presented a paper on Development and characterization of nevirapine loaded dendrimers and multiwalled carbon

nanotubes for the treatment of HIV in IPA annual convention (IPAC 2021 virtual) held on July 16-17th, 2021 organized by Indian Pharmaceutical association, India.

Oral presentations

1. Neha Srivastava, Yachna Mishra and Vijay Mishra presented a paper on Dendrimers: A novel and efficient carrier for anti-HIV drugs in 3rd International Conference on "Functional Materials, Manufacturing and Performances" (ICFMMP-2022)" held on July29-30th, 2022 organized by Division of Research and Development, LovelyProfessional University, Punjab.

2. Neha Srivastava, Yachana Mishra, Vijay Mishra, Sachin Kumar Singh, presented a paper on Simultaneous method development and validation of Fosamprenavir and Nevirapine in HPLC, in "International conference of Pharmacy (ICP-2022) held on 9-10th November 2022 organized by school of pharmaceutical sciences, with Indian Pharmaceutical Association (IPA) at Lovely Professional university, Punjab.

Conferences Attended

1. International conference on Commercialization of Medicinal Plant products : Lab techniques to trade, "Phytocon 2018", organized by School of Pharmaceutical Sciences, Lovely Professional University, Phagwara, on 18 April 2018.

2. 21st Punjab Science Congress on "Scientific advances for inclusive development and environmental protection" organized by Punjab agricultural university, Ludhiana, on 7-9 February 2018.

3. 55th Annual conference of the Indian hospital pharmacist association and the hospital pharmacy foundation on "Hospital, clinical and community pharmacy: An Indian Scenerio" organized by Bengal School of Technology on 16 January 2021.

4. International Conference on "Pharmaceutical and Healthcare Challenges in Global Transformation" organized by Vishnu Institute of Pharmaceutical Education & Research on 11 April 2022.

5. 59th National Pharmacy week on "Pharmacist: Frontline Health professional" by Univercity school of Pharmaceutical Sciences, Rayat Bahra University, Mohali on 16-21 November 2020.

6. International conference on biological research and applied science (IBRAS 2021) organized by Jinnah University for women, Pakisthan on 20-21 January 2021.

Workshop

1. Workshop on "How to write and publish scientific article and manuscript" organized by Lovely professional University and Spinger Nature, on 15 April 2018.